Master of Science Thesis

CFD Investigation of the Ground Proximity Effect performance of a Commercial Aircraft

Kevin Mooi

October 4, 2019

Faculty of Aerospace Engineering

Delft University of Technology

CFD Investigation of the Ground Proximity Effect Performance of a Commercial Aircraft

Quantifying the Influence of Aircraft Geometry Configurations on Ground Effect Performance using a Modular-Meshing Approach

By

Kevin Mooi

in partial fulfilment of the requirements for the degree of

Master of Science
in Aerospace Engineering

at the Delft University of Technology,
to be defended publicly on Friday November 1, 2019 at 14:00 AM.

Supervisor:	Prof. dr. ir. G. Eitelberg	
Thesis committee:	Dr. ir. R. Dwight,	TU Delft
	Dr. ir. M. Hoogreef,	TU Delft

Acknowledgements

This MSc thesis marks the end of my studies at TU Delft. I would sincerely like to thank my thesis supervisor Prof. Dr. ir. Georg Eitelberg for his guidance and time during our many meetings. At the company where I performed my research, I want to thank Dr. ig. Rolf Emunds for all his time and patience in guiding me through the wondrous, exciting and challenging world of CFD research. I would like to thank Ir. Tobias Lange for his guidance, council and mentoring during my previous internship at the same company. Finally I want to express my thanks to Ir. Juergen Kotschote, for all his help and patience in obtaining the necessary information regarding the windtunnel tests.

Abstract

This thesis has two objectives: First, to investigate the behavior of typical twin engine commercial transport aircraft in ground effect under a wide range of conditions and geometry variations at the request of an aerospace company. And secondly, to add to the body of existing scientific knowledge on ground effect.

In order to identify the opportunities for adding scientific knowledge, first a literature study was conducted. The conclusion of this study proved that there is insufficient research literature available on wing-bodies in the ground effect to answer the investigation launched by the aerospace company.

A methodology was chosen to fulfill both objectives, namely generating ground effect performance data by means of CFD (Computational Fluid Dynamics) computations. The results are validated using existing wind tunnel measurements.

It was determined which data points had to be calculated to cover the parameter space and it was established that the required effort could be completed within the time frame of this thesis. The landing high-lift configuration was the principal configuration to be investigated. Using this baseline, the impact of the following changes on ground effect performance were determined: a) changes to the high lift settings b) change to the engine thrust setting c) changes to landing gear deployment d) changes to the nacelle size e) changes to the wingtip geometry.

After completing the calculation of all data points, it was also possible to develop a method that will enable engineers to calculate the effect of incremental changes in geometry and configuration, required for the initial stages of aircraft design.

The main conclusions in order of importance are:

I. For low to moderate angle of attack α, the ground effect is beneficial. Lift is increased by up to 3.5% of the total lift, drag is reduced by up to 33% of the total drag.
II. However, as $\alpha > 8.0°$, the ground effect becomes less beneficial and the ground effect can even be detrimental, leading to a loss of lift of up to 5.5% while still having a drag benefit of up to 33%.
III. The agreement between windtunnel data and CFD calculations is within 0.4% accuracy for the lift, and within 1.5% of the total drag value, except at the extreme case at moderate to high α and very close distance to the ground. Some of the differences can be explained in terms of practical problems in simulating the ground boundary conditions in the wind tunnel.
IV. The impact from a change to high lift setting and a change to thrust setting are most significant, with changes of up by up to 2% of total lift and up to 3.2% of total drag.
V. There is a smaller but still quantifiable impact from the gear effect and the nacelle effect.
VI. A change to wing tip geometry has a minor impact on ground effect behavior, as lift is changed by up to 0.26% of total lift, only between $10.0° \leq \alpha \leq 12.0°$.

Contents

List of Figures

List of Tables

Nomenclature

Greek Symbols

Γ	Circulation [m^2/s]
α	Angle of attack [deg]
α_{eff}	Effective Angle of attack [deg]
β	Sideslip Angle [deg]
γ	Ratio of specific heats [-]
$\delta_{aileron}$	Aileron Droop Angle [deg]
δ_{flap}	Flap Deflection Angle [deg]
δ_{slat}	Slat Deflection Angle [deg]
μ	Dynamic Viscosity [Pa s]
ρ	Density [kg/m^3]
τ_w	Wall Shear Stress [Pa]

Roman Symbols

AR	Aspect Ratio [-]
C_D	Drag Coefficient [-]
$C_{D\,friction}$	Skin Friction Drag Coefficient [-]
C_{D_i}	Induced Drag Coefficient [-]
$C_{D_{v.p}}$	Viscous Pressure Drag Coefficient [-]
C_L	Lift Coefficient [-]
C_N	Normal Force Coefficient [-]
C_M	Moment Coefficient [-]
C_Y	Side Force Coefficient [-]
D	Drag Force [N]
E	Internal Energy [j]
H	Enthalpy [j]
K_D	Spanwise Drag coefficient distribution [-]
K_L	Spanwise Lift coefficient distribution [-]
L	Lift Force [N]
L/D	Lift over Drag ratio [-]
P	Pressure [Pa]
P_{tot}	Total Pressure [Pa]
Re	Reynolds Number [-]
Ma	Mach Number [-]
V	Flow Velocity [m/s]
V_{tot}	Local Total Velocity ($V_{tot} = V_x + V_y + V\_z$) [m/s]
V_∞	Free Stream Velocity [m/s]
b	Wing span [m]
$b_{conventional\ wingtip}$	Wing span with conventional wingtip installed [m]
$b_{winglet}$	Wing span with winglet installed [m]
c	Chord length [m]
$\Delta c_{P_{GE}}$	Difference in pressure coefficient due to ground effect ($c_{P\,GE} - c_{P_{\frac{h}{b}=1.0}}$)
c_p	Pressure coefficient [-]
dV	induced Velocity [m/s]

h	Height above ground [m]
h/b	Height above ground non-dimensionalized by wing span [-]
u	Velocity in the airfoil direction [m/s]
t	Time [s]
u_τ	Wall shear stress velocity [m/s]
v	Kinematic Viscosity[m^2/s]
y_+	Non-dimensionalized wall distance

Abbreviations

AoA	Angle of Attack
CFD	Computational Fluid Dynamics
DES	Detached-Eddy Simulation
DNS	Direct Numerical Simulation
DNW	Deutsch Niederländische Windkanäle
DLR	Deutsches-Zentrum für Luft- und Raumfahrt
IGE	In Ground Effect
HTP	Horizontal Tail Plane
LES	Large-Eddy Simulation
MTO	Maximum Take-Off Thrust Setting
NACA	National Advisory Committee for Aeronautics
NASA	National Aeronautics and Space Administration
NLR	Netherlands Aerospace Centre
OGE	Out of Ground Effect
RANS	Reynolds-Averaged Navier-Stokes
SA	Spalart-Allmaras
SST	Shear Stress Transport
TFN	Through-Flow Nacelle
TKE	Turbulence Kinetic Energy
TPS	Turbine Power Simulator
VTP	Vertical Tail Plane
WIG	Wing-in-Ground-Effect

Introduction

This MSc thesis report presents a comprehensive investigation of the ground effect performance of a twin-jet, commercial transport aircraft. The research project was instigated by the request of a major aerospace company to gain knowledge on impact on ground effect performance due to changes made to the aircraft geometry and flight parameters, i.e. changes to the wingtip geometry, the engine nacelle and the engine thrust setting.

During the preliminary design phase of an aircraft, historical performance data is extensively used. For instance, if a larger engine is installed in an aircraft, an initial estimate for the change of performance due to this geometry change is made by verifying how a similar change impacted the performance of a previous aircraft design. Therefore reference (historical) data is needed during the preliminary design phase. This reference data was unavailable for ground effect performance, hence the request from the company to acquire more knowledge on ground effect performance.

The ground effect phenomenon occurs when the aircraft is close to the ground. This is typically defined as the height above ground being no higher than the aircraft wingspan. The downwash generated by the aircraft is now 'mirrored' by the presence of the ground, altering both the lift and drag characteristics. Historically this was seen as a predominantly positive effect, as it was thought that in ground effect the lift increases and the drag decreases. However, under specific conditions, such as flying close to the ground at high incidence and high flap settings, ground effect can actually be a negative effect, leading to a reduction in lift instead. This phenomenon is still not fully understood in scientific literature and is challenging to simulate.
During actual flight tests this is very difficult to measure, since it is dangerous to fly low above the ground for prolonged periods. It is also very challenging to maintain stable flight conditions during the test, due to the atmospheric turbulence and the safety requirements.
Measuring the ground effect in windtunnel is also challenging, as it requires the introduction of a moving ground plane, which introduces vibrations and additional complexity. Reynold's number effects can also pose additional challenges when investigating the ground effect in windtunnels, which may not be properly captured using windtunnel. For instance flow separation can be influenced both by Reynolds number and ground effect and thus can potentially be challenging to distinguish.
Finally there are the computational fluid dynamics (CFD) codes. These are used extensively in modern day ground effect research, but are not always fully validated for ground effect.

A requirement imposed by Delft University of Technology on any MSc thesis is that it has to add to the existing body of scientific knowledge. Therefore the first step is to investigate whether the initial research question is already answerable using existing literature sources. Subsequently this leads to a number of distinct phases of the thesis research project, which are documented below.

Phases of the Research Project

The research has been set up in a number of distinct phases:

1) **Definition of the initial research question**
    a) The initial generic research question stated by the aerospace company was to acquire more knowledge on the behavior of aircraft (wing-bodies) in ground effect for different geometric configurations.
    b) The requirement from Delft University was to add to the existing body of scientific knowledge on the ground effect literature

2) **Literature review:**
   A literature review was conducted to assess whether the initial research question could be answered using existing scientific literature. This review showed that this was not the case, as there are considerable gaps in the existing literature on ground effect. The literature review is presented in chapter 1.
3) **Finalizing the research question**
   a) Using the knowledge gained in chapter 1, the research question is subsequently finalized in chapter 2.
   b) Based on the findings of the literature study, the research question was re-phrased more precisely to fit both the objectives imposed by the company as well as from the university
   c) From then on this research question was the main driver of the research project
4) **Selecting the optimal methodology**
   a) Using the now defined research question, the optimal methodology to answer the research question was determined in chapter 3
   b) The research problem was practically defined in subchapter 3.1, in order to obtain a set of requirements which are imposed on the research method
   c) The next step was to decide what method should be selected for the research, which was done in subchapter 3.2. CFD was selected as the method of choice.
5) **Research Preparation**
   a) Preparations for the research, which had to be undertaken as a consequence of the chosen research method, are presented in subchapter 3.3:
   b) Decisions were made with respect to the set-up of the CFD solver, definition of the correct ground boundary conditions, turbulence model and modular meshing.
   c) The geometry of the aircraft, the air and the boundary conditions (ground) have to be discretized into a mesh for the CFD research. Meshing quality has a large impact on the accuracy of the CFD results, therefore considerable effort was spent in properly designing and validating the various meshes.
   d) Due to the large number of required meshes (more than 400), considerable effort was also made to optimize the required time for generating these meshes. For this purpose the use of modular mesh models for geometry components was also investigated and validated.
   e) This subchapter 3.3 must be seen as background reading for additional information on how the CFD data was generated.
6) **Validation of the initial CFD results using wind tunnel data.**
   A number of reference conditions were calculated using CFD and then compared to existing wind tunnel data. As there was good agreement between both results, the reliability of the meshing and CFD technique was thus established for a wide range of conditions.
7) **Systematic research**
   a) Using the now validated methods, a schedule was set up to perform a systematic calculation of a large number of different configurations. The calculated results were analyzed extensively, not just in terms of lift and drag but also with the purpose to understand what the aerodynamic changes are due to ground effect and to analyze how this is influenced by different parts of the geometry. This analysis is presented in chapter 4.
      i) The first subchapter presents a short summary of all the observed effects related to ground effect
      ii) The second subchapter presents an extensive analysis of impact of ground effect on aircraft aerodynamic performance for one geometry case. A baseline is thus established.
      iii) Every subsequent subchapter then addresses changes of one aspect of that geometry and examines how this changes ground effect performance compared to the baseline.

   b) During the systematic research, a number of unexpected results were identified and analyzed, such as early onset of stall in ground effect and a stronger than expected influence of the fuselage on the change in lift due to ground effect. This is also presented in chapter four.

8) **Development of methods to calculate incremental changes.**
   Based on the results of the systematic calculations, a set of polynomial fits were derived that enable engineers to calculate the requested lift and drag increments for various geometry and configuration changes. These polynomials are presented in the appendices.

9) **Continuous validation with wind tunnel results**
   While the systematic CFD research progressed, further comparisons were made with available wind tunnel results. This validation is presented in chapter 5.

10) **Remaining topics**
   Due to the extensive nature of the research question, a number of interesting phenomena not directly related to the research question were observed, but these were not always fully analyzed due to lack of time. These interesting topics for future research are briefly discussed in chapter 6.

1. Literature Survey

In this literature survey the current state of the research into the ground proximity effect will be documented. The goal of this survey is to identify gaps in the current state of scientific research, in order to formulate a well posed research question, which can add to scientific knowledge.

One of the driving topics in ground effect research are Wing-in-Ground (WIG) vehicles. These aircrafts spend their entire flight envelope cruising in the ground effect in order to benefit from the increased aerodynamic efficiency, which in turn results in a higher fuel efficiency. The most famous example of a WIG vehicle is the Russian built 'Caspian Sea Monster' or as the Russians know it, Korabl Maket (1). This 92m long, 544 ton craft flew over the Caspian Sea from 1966 to 1980 and is depicted in Figure 1.1.

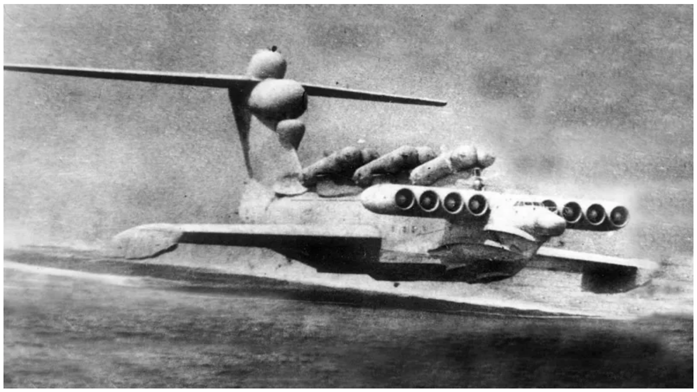

Figure 1.1 Caspian Sea Monster (2)

Another driving topic in ground effect research is racing car applications. Typically wings are installed at the front of the car within the ground effect to increase downforce and thus increase the grip of the tires (3), however this is often accompanied by an increase in drag (4). Since aerodynamic drag is a significant part of the total car drag, there is a clear incentive to minimize the drag of the front-wing while maintaining sufficient downforce.

As will become apparent in this report, the increase in aerodynamic efficiency desired by both the WIG and racing car research is most noticeable at low to moderate angle of attack (AoA), at $0° < \alpha < 10°$. This means that the majority of the literature on ground effect is focussed on this moderate AoA range. Therefore the available research at negative AoA and in the stall region is relatively limited.

Lift is the most important aspect of both the WIG and racing car applications. It is of paramount importance to either generate enough lift to carry the required payload or generate sufficient downforce to maintain grip on the tires. Drag is of secondary importance. This is reflected in the state of the literature: Almost every paper discussed here investigates lift in ground effect, while a much lower number also include drag in the calculations and/or measurements. Pitching moment and stability are only discussed in an even more limited number of papers.

The structure of this chapter will be as follows: In the first subchapter the historical perspective on the ground effect research will be discussed. The theory on the ground effect will be examined and it will be evaluated how the research has evolved from the first beginnings to the present day. In the second subchapter the tools used for ground effect research will be discussed, such as windtunnel experiments and computational methods. The emphasis will be discussing the particular challenges introduced when trying to model the ground effect,

such as what is the best way to simulate the ground plane or which turbulence model is the best with the purpose of CFD simulation in ground effect. An empirical ground effect model used by engineers will also be introduced in this chapter to get a feeling for how the ground effect is treated in practice.
The third subchapter will focus on modern day ground effect research and will represent the bulk of this literature survey. First the two-dimensional ground effect over a single-element airfoil will be discussed. Complexity will be added by introducing a multi-element airfoil and subsequently the introduction of three-dimensional, span dominated ground effect. Finally the behavior of a full wing-body configuration will be examined. The emphasis during this discussion will be on the change in lift due to ground effect, since this is also the focus of the majority of research papers. Of secondary importance is the drag, followed by the pitching moment. Once the effect of ground effect on lift, drag and pitching moment has been established, the dynamic ground effect and compressibility effect due to ground effect will be discussed. Finally in the fourth subchapter the gaps in the literature will be identified and discussed first. Once this is done, the research question for the MSc thesis will be established.

1.1 Historical Perspective

Before the state of the current research on ground effect is assessed, it is of interest to investigate the historical development of the research on the ground effect. It is also beneficial at this point to summarize the theory behind the ground effect. This will add context and understanding when discussing present-day research.

As early as 1921 the first theoretical predictions were being done for the ground effect. Wieselberg (5) introduced the concept of a mirrored wing (or 'image') which has since formed the basis of all theoretical predictions of the ground effect. He states: "*In order to investigate the change in resistance near the ground, we utilize the principle of reflection. We replace the surface of the ground by the wing '1 reflected the ground (Fig. 2) and calculate (by a method analogous to that for calculating the drag of a multiplate from the drag of a monoplane) in what manner the air flow about wing 1 will be affected by its image"*. Fig. 2 referenced in the quote can be seen in Figure 1.2.

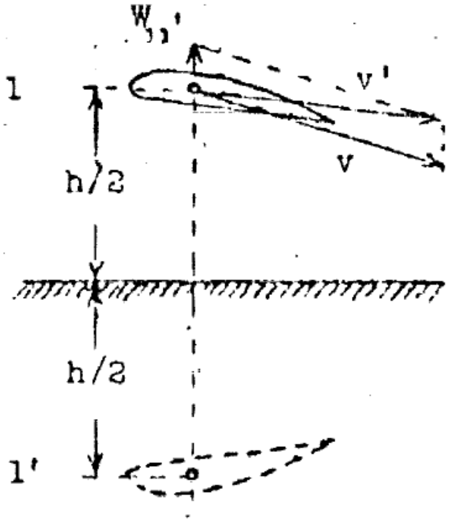

Fig. 2.

Figure 1.2 Mirrored image of the wing in ground effect (5)

Wieselberger used the then new Prandtl's lifting line theory to calculate the influence of the image wing. In this theory the lift of the wing is represented by a bound vortex filament, along with two trailing vortices from the wingtip, which as opposed to the bound vortex, are free vortices and move with the fluid (6). These vortices turn in opposite directions and both contribute to the downwash w and thus the induced drag. This is illustrated in Figure 1.3. Within a few years Prandtl discovered that the representation with a single horseshoe vortex was not accurate and instead represented the wake with an infinite number of horseshoe vortices, all coincident with the bound vortex or lifting line. This is illustrated in Figure 1.4.

If the wing is mirrored as shown in Figure 1.2, then it stands to reason that the lifting line and horseshoe vortices shown in Figure 1.4 are also mirrored. These mirrored vortices rotate in opposite direction to the original vortices and thus reduce the downwash. The influence of mirrored vortices on the downwash can be calculated using the law of Biot-Savart (7), given by equation 1.1.

$$\boldsymbol{dV} = \frac{\Gamma}{4\pi}\frac{\boldsymbol{dl} \times \boldsymbol{r}}{|\boldsymbol{r^3}|} \qquad (equation\ 1.1)$$

Here $\boldsymbol{dV}$ is the induced velocity at an arbitrary point P, Γ is the strength of the vortex filament and $\boldsymbol{r}$ is the vector from point P to the vortex filament $\boldsymbol{dl}$.

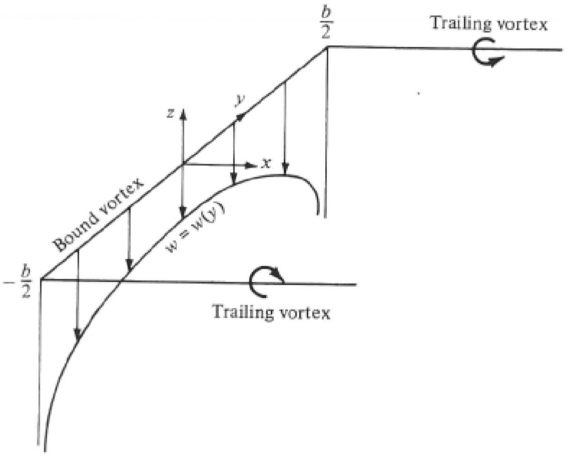

Figure 1.3 Downwash distribution for a single horseshoe vortex (6)

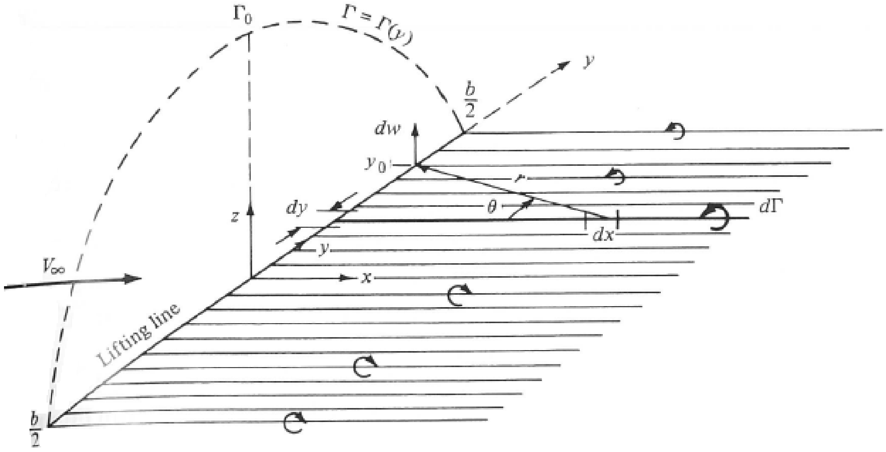

Figure 1.4 Superposition of an infinite number of horseshoe vortices along the lifting line (6)

So the ground effect reduces the downwash induced by the wing by means of the mirrored vortices, which act counter to the original vortices. This has two effects:

1. The induced drag is reduced

2. The effective angle of attack (AoA) α_{eff} increases. α_{eff} is given by $\alpha_{eff} = \alpha - \alpha_i$ (6). By reducing the downwash, the induced AoA α_i is reduced, thus α_{eff} increases. This means that for a given low to moderate AoA, the lift coefficient will be higher in the ground effect (IGE) as compared to out of ground effect (OGE). The slope of the lift curve increases as a result.

These two effects combined will cause the lift over drag ratio (L/D) to improve in the ground effect. This is shown in the original paper of Wieselsberger, reproduced here in Figure 1.5. Note that c_a is the lift coefficient C_L, while c_w is the drag coefficient C_D. Shown here are the Windtunnel results from IGE and OGE, as well as the calculations for IGE. The measurements were obtained from a monoplane model of 134cm span, with a fuselage and elevator with a surface area of 1675 cm^2 (5). There is a good agreement between the theory and the windtunnel experiment.

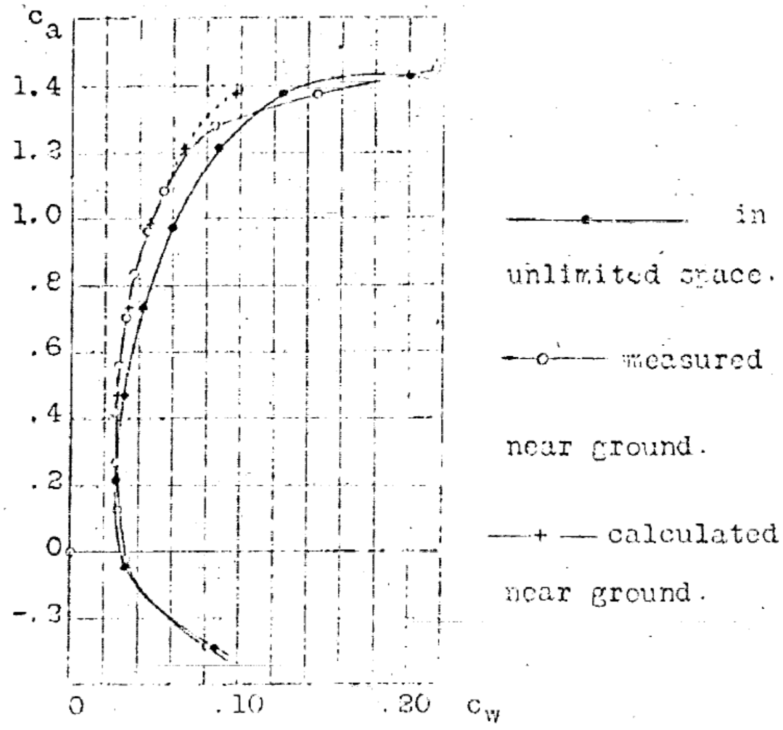

Figure 1.5 Polar in and out of ground effect (5)

Wieselsberger established the foundation for understanding the ground effect, but it soon become apparent that this was not the complete story. Up until now the ground effect has been treated as a 2D flow problem, with the change to the induced AoA as the only explanation given for the change in aerodynamic performance in the ground effect. A report from Pistolesi (8) from 1937 shows how much the field of research had advanced only fifteen years later. There are several studies reviewed (9) (10) which investigate the behaviour of a wing with infinite flat plates placed at the wing tip, in other words an airfoil. By now it was recognized that the ground effect is both a 2D and a 3D phenomenon. Another report is referenced where the author first examines the problem for an infinite wing and then attempts to extend this approach to a finite wing (11) and thus tries to improve on the theory of Wieselsberger. The venturi effect which occurs at very low and at negative angles of attack, causing an acceleration of the flow between the wing nose and the ground leading to strong suction on the lower side of the airfoil, was also already known by that time (12).

A 1955 report about the aerodynamic performance of a 42° swept wing in the ground effect highlights one area where research into ground effect is currently still lacking: "*Certain aspects* *of the effects of the ground interference on the aerodynamic characteristic of unswept wing have been thoroughly investigated both theoretically and experimentally (refs. 1 to 6), The experimental results of these investigations have shown that, in the high-lift range, theoretical calculations by existing method do not provide either a reliable estimate of the magnitude of the ground effect or an explanation of the phenomena involved at the stall*" (13). The research discussed up until now has primarily been focussed at low to moderate angles of attack, where the lift slope is still linear. In contrast, this report contains experimental measurements up until angles where stall occurs and the results will be briefly discussed below.

First an overview is given on the theoretical understanding of the ground effect at that time, which will be repeated briefly. The different ground interference effects are sketched in Figure 1.6. Three separate effects are detailed:

1. The mirrored trailing vortices as have been defined by Wieselsberger, corresponding to part a. in Figure 1.6.
2. The image of the bound vortex, identified in Figure 1.3, will induce a flow from back to front which has a vertical component at the back of the airfoil for low to moderate angles of attack, therefore increasing lift. However, for higher AoA or highly cambered airfoils this flow goes over the top surface of the airfoil, leading to a *reduction* in lift. These two separate cases are illustrated in part b. and c. of Figure 1.6.
3. The wing thickness is approximated by a source close to the airfoil nose and equivalent sink near the trailing edge. It is shown in part d. and e. of Figure 1.6 that the mirrored source-sink combination will increase the stream velocity over the airfoil, thus leading to an increase in lift. It can also be seen that this particular effect is independent of the AoA.

These separate effects combine towards the overall effect on the lift coefficient. At low to moderate angles of attack all three lead to an increase in lift and thus the lift curve slope is always increased with the AoA in this range. At high angles of attack the second effect becomes negative, and the net effect of all three effects summed together can be either positive or negative.

This is illustrated in Figure 1.7 and Figure 1.8. Figure 1.7 show the lift curves in ground effect for a wing with a neutral flap deflection angle where the ground effect increases both the lift curve slope as well as the maximum lift. The previously discussed venturi effect is also clearly visible, where at negative angles of attack the lift IGE is lower compared to OGE. Figure 1.8 shows the same set of measurements but now the flap angle is set to 60°. This clearly shows the negative influence of camber in the ground effect, because now the maximum lift is approximately 10% lower close to the ground, while the lift curve is still steeper due to the presence (proximity?) of the ground. Finally the report concluded that the sweep of the wing did not significantly influence the behaviour in the ground effect.

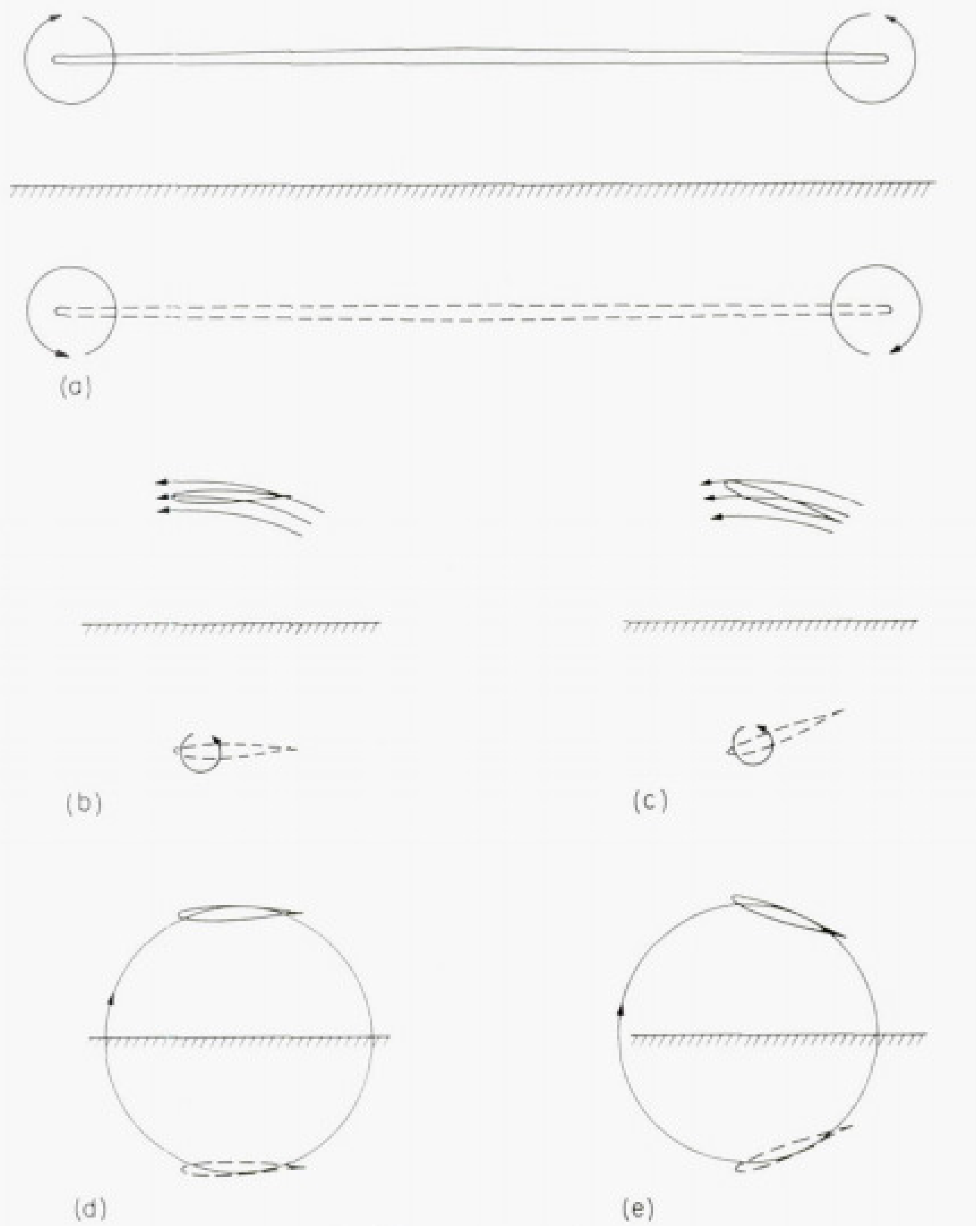

(a) Trailing vortices.

(b) Bound vortex (low angle of attack).

(c) Bound vortex (high angle of attack).

(d) Wing thickness doublet (low angle of attack).

(e) Wing thickness doublet (high angle of attack).

Figure 1.6 Sketch showing the interference effects of the reflected image of a wing in the presence of the ground (13)

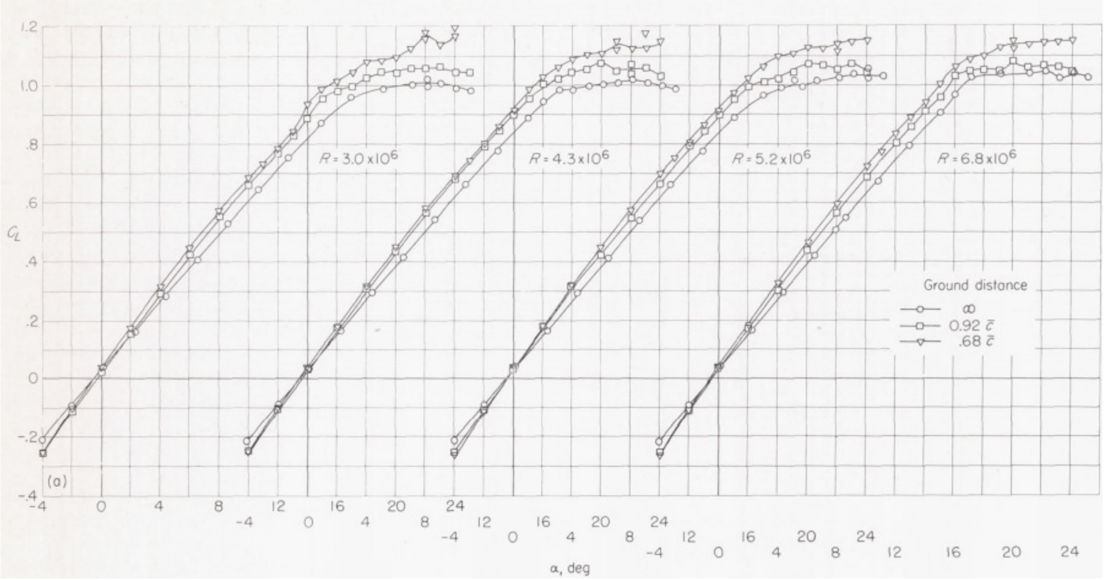

Figure 1.7 Lift Curves for varying Re Numbers and distance to ground for a 42° swept wing with no flaps (13)

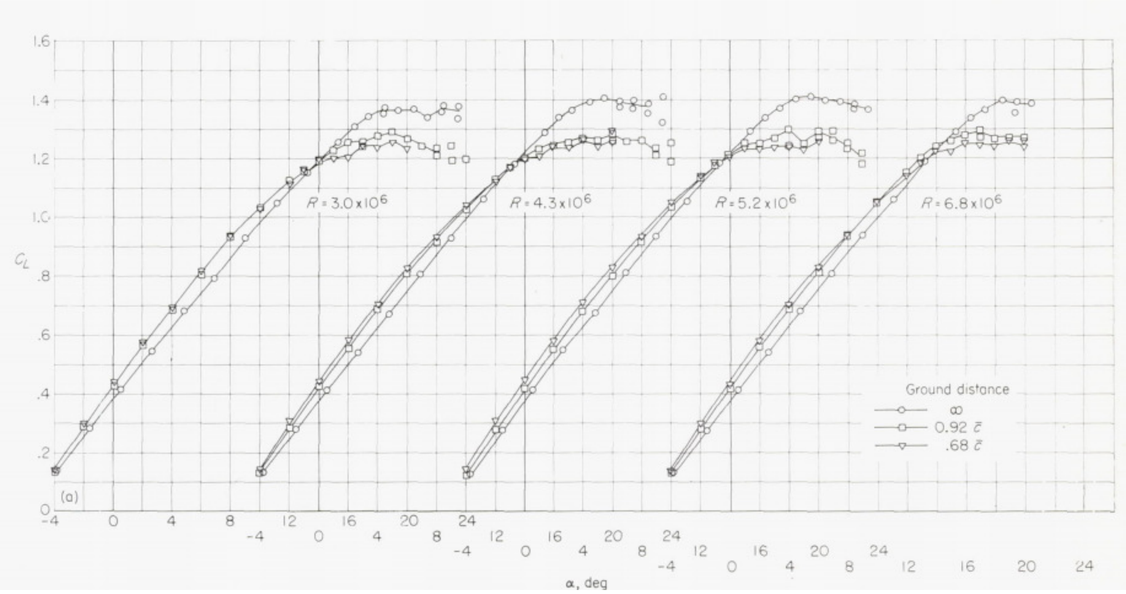

Figure 1.8 Lift Curves for varying Re Numbers and distance to ground for a 42° swept wing with 60° flap deflection (13)

This section ends with a reference to an exhaustive literature survey done in 1966 which attempted to provide a comprehensive collection / compilation of the scientific literature available at that time concerning ground effect (14). Also included in the report are references to the literature relevant to development and research into Wing-in-Ground effect craft, such as performance of propulsion systems in close proximity to the ground and naval engineering literature utilising aerodynamic effects. Figure 1.9 gives an overview of selected literature references categorised by research topic. It gives an impression of the state of scientific research into ground effect by 1966.

The remaining chapters of this literature survey will focus on discussing the modern day research. Two major advances compared to the literature presented up until now are the advent of numerical methods to calculate the flow around the wing in ground effect and more sophisticated windtunnel experiments. A moving belt will be added to many windtunnel experiments, which is a better representation of the real life situation where the aircraft flies over the ground (and thus the ground moves relative to the aircraft). Numerical computational fluid dynamics (CFD) methods, starting with the panel and vortex lattice method, and later evolving to solving the Euler and nowadays the Reynolds-averaged Navier-Stokes (RANS) equations, have allowed researchers to look at the ground effect in far greater detail than before.

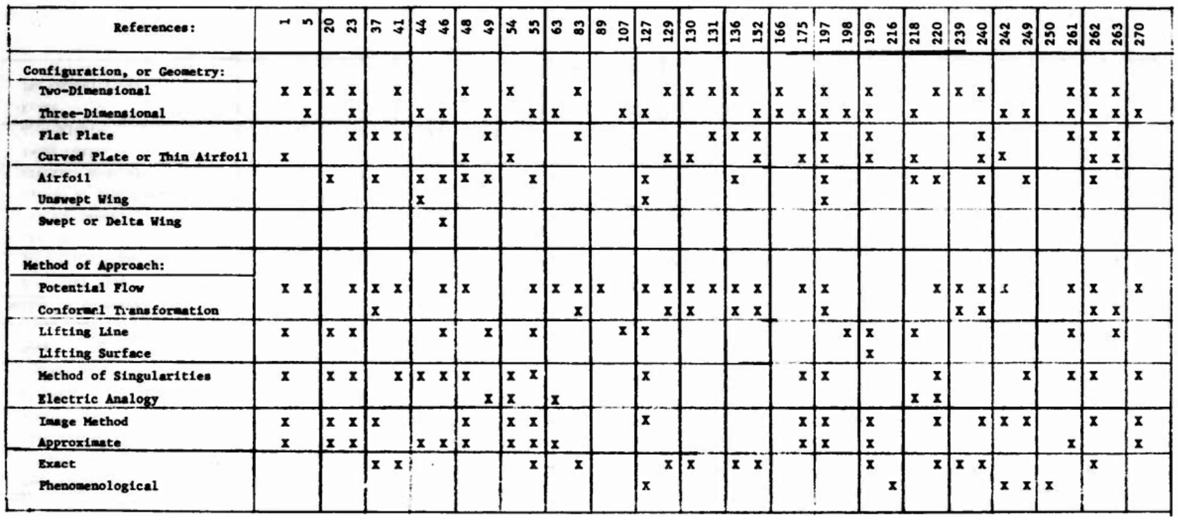

References:	1	5	20	23	37	41	44	46	48	49	54	55	63	83	89	107	127	129	130	131	136	152	166	175	197	198	199	216	218	220	239	240	242	249	250	261	262	263	270
Configuration, or Geometry:																																							
Two-Dimensional	X	X	X	X		X			X		X			X				X	X	X	X		X		X		X			X	X	X				X	X	X	
Three-Dimensional		X		X			X	X		X		X	X			X	X					X	X	X	X	X	X		X				X	X		X	X	X	X
Flat Plate				X	X	X				X				X						X	X	X			X		X					X				X	X	X	
Curved Plate or Thin Airfoil	X								X		X							X	X			X		X	X		X		X			X	X				X	X	
Airfoil			X		X		X	X	X	X		X					X				X				X				X	X		X		X			X		
Unswept Wing							X										X								X														
Swept or Delta Wing								X																															
Method of Approach:																																							
Potential Flow	X	X		X	X	X		X	X			X	X	X	X		X	X	X	X	X	X		X	X					X	X	X	X			X	X		X
Conformal Transformation					X									X				X	X		X	X			X						X	X					X	X	
Lifting Line	X		X	X				X		X		X				X	X									X	X		X							X		X	
Lifting Surface																											X												
Method of Singularities	X		X	X		X	X	X	X		X	X					X							X	X					X				X		X	X		X
Electric Analogy										X	X		X																X	X									
Image Method	X		X	X	X				X		X	X					X							X	X		X			X		X	X	X			X		X
Approximate	X		X	X			X	X	X		X	X	X											X	X		X									X			X
Exact					X	X						X		X				X	X		X	X					X			X	X	X					X		
Phenomenological																	X											X					X	X	X				

Figure 1.9 Categorisation of selected literature sources into various research topics (14)

1.2 Common Tools for Ground Effect Research

The focus of this literature survey is to gain an understanding of the state of scientific ground effect research. In order to evaluate the quality of the scientific literature, it is necessary to first establish an understanding of the tools used during ground effect research, which are primarily windtunnel experiments and CFD computations. It is of particular interest to establish the specific demands placed upon these tools by the ground effect.

First a brief overview will be given of CFD and the RANS equations in particular, since this will be the primary tool used during the thesis research. Wherever possible, a link will be made to determine the best practices for ground effect research. Secondly the additional complexities caused by the introduction of a ground plane, both in windtunnel research and CFD computations, will be examined. Finally an empirical calculation method will be introduced to determine the impact of the ground effect on the lift, drag and tail downwash of a transport aircraft.

1.2.1 CFD Simulations

During the thesis research, the primary simulation tool used to investigate the ground effect will be flow solutions obtained by solving the RANS equations. In this subchapter a brief overview of the Navier-Stokes equations and the RANS equations will be given first. Different turbulence models will be discussed and will be assessed to determine which model is best suited for use in ground effect computational research.

This subchapter is explicitly not meant to be an exhaustive resource for CFD and RANS solvers. There are many excellent sources available for this purpose, such as Anderson's Computational Fluid Dynamics book (15).

1.2.1.1 RANS Equations

A derivation of the Reynolds Averaged Navier-Stokes equations is presented in Appendix A – Derivation of the Navier-Stokes Equations. The derivation is based on information provided in the DLR TAU Technical Documentation (16).

1.2.1.2 Turbulence Models for Ground Effect Simulation

The Cartesian part of the Reynolds stress tensor, which was introduced in the RANS equations, is given by the Boussinesq hypothesis:

$$\bar{\rho}\tilde{R}_{ij} = -2\mu^{(t)}\tilde{S}_{ij}^{*} + \frac{2}{3}\bar{\rho}\tilde{k}\delta_{ij} \qquad (equation\ 1.2)$$

The eddy viscosity $\mu^{(t)}$ must be modelled by means of a turbulence model. Many modelling options exist and can be divided into the following classes:

1. Zero equation algebraic models such as the Baldwin-Lomax (17) and Cebeci-Smith (18) models. No additional governing equations are introduced, which reduces the computational complexity. The drawback is that these models are not very general and thus must be adapted to specific cases for optimal results. When optimized, these models can produce very accurate results compared to more complex turbulence models. However, these models break down when the flow becomes separated (19). Since high-lift flow is a topic of interest for the ground effect, which inherently contain separated flow, these models are of limited use for the ground effect application.

2. One-equation turbulence models add an additional equation to the governing equations based on the turbulence kinetic energy equation. An example is the Spalart-Allmaras (SA) (20) model which is a local turbulence model with a destruction term depending on the distance to the wall. Baldwin and Barth (21) have also come up with a one equation model. These models are more universal compared to zero equation models. However, these models still work best in the application they were designed for (e.g. airfoil and wing applications for the SA model) and become significantly less accurate when separation occurs (19).
3. Two-equation models introduce an additional equation which specifies a second turbulence scale. Three examples are the $k-\epsilon$ model (22) (23), the $k-\omega$ model (24) and the Menter-Shear Stress Transport (SST) (25) (26) model which is a combination of the previous two. The $k-\epsilon$ model breaks down for wall bounded flows (19), which is why the Menter-SST model uses the Wilcox $k-\omega$ near the walls. The drawback of the $k-\omega$ models is the high sensitivity to the free-stream value of the specific dissipation rate ω, which is why the $k-\epsilon$ model is used for the free stream. These models still lose accuracy as separation occurs, but to a lesser extent compared to the zero or one equation turbulence models.

Mahon and Zhang (27) performed a numerical turbulence model comparison study. An inverted airfoil, a derivative of the LS(1) – 0413 MOD profile, was investigated using the $k-\varepsilon$, the $k-\varepsilon\ RNG$, the realizable $k-\varepsilon$, the $k-\omega$, the Menter SST and finally the SA model. The results were then compared to experimental results. As the height above ground decreases, the difference between various models become more pronounced. This is shown in Figure 1.10 and Figure 1.11, where the pressure distribution at $\frac{h}{c}=0.224$ and $\frac{h}{c}=0.09$ can be seen respectively. In Figure 1.10 the difference between the models is relatively small, although there is some disagreement with experimental data, especially on the suction side. The Menter SST model seems most accurate in this situation. In Figure 1.11 much larger differences can be seen between the different models. Every model over-predicts the suction compared to the experiments, Menter SST to the least extent. Least accurate is the unmodified $k-\epsilon$ model, of which it has already been noted earlier that it breaks down with wall bounded flows. This is emphasised in Figure 1.13 which shows the lift coefficients for the Menter SST and the realizable $k-\epsilon$ model. At lower heights above ground there is a very large discrepancy of up to 25.1% between experimental data and the realizable $k-\epsilon$ model. In contrast Menter SST performs much better with a 5.2% difference at $\frac{h}{c}=0.09$.

The wake behind the airfoil was also analysed. In this case it was found that the realizable $k-\epsilon$ model was the most accurate model, while the Menter SST was least accurate. However the difference are less pronounced compared to the differences in pressure distribution discussed previously.

Finally the separation location was investigated for different turbulence models. The realizable $k-\epsilon$ model was more accurate than the Menter SST model. The latter predicts separation to occur earlier by approximately $0.08\ \frac{x_{sep}}{c}$, while the former has an error of approximately $0.05\ \frac{x_{sep}}{c}$. It should also be noted that the realizable $k-\epsilon$ model has accurate separation location predictions up to a lower height above ground compared to the Menter SST model.

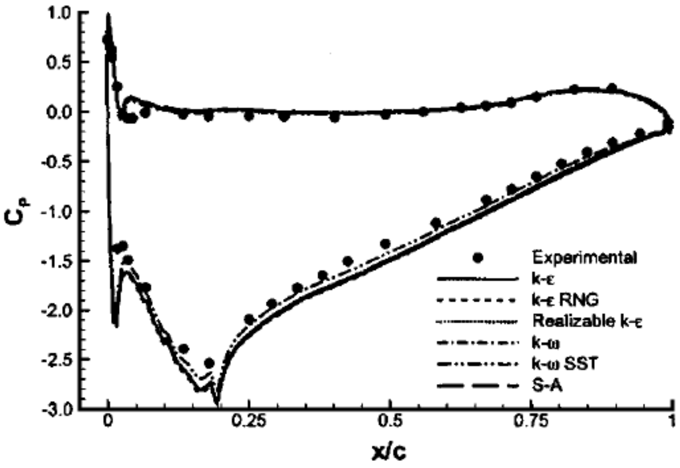

Figure 1.10 Pressure distribution in ground effect for different turbulence models at h/c = 0.224 (27)

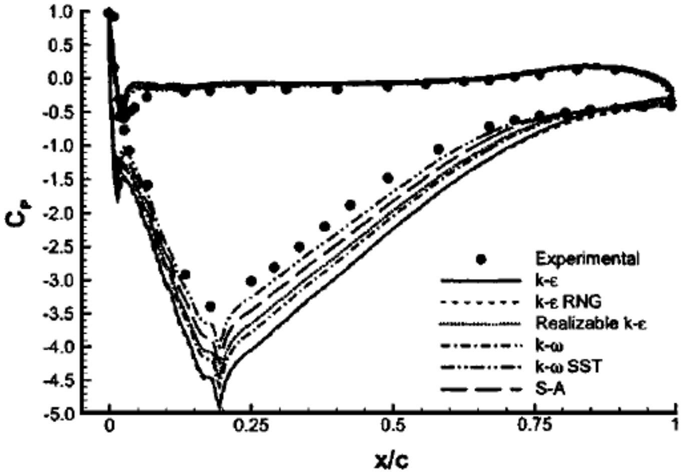

Figure 1.11 Pressure distribution in ground effect for different turbulence models at h/c = 0.09 (23)

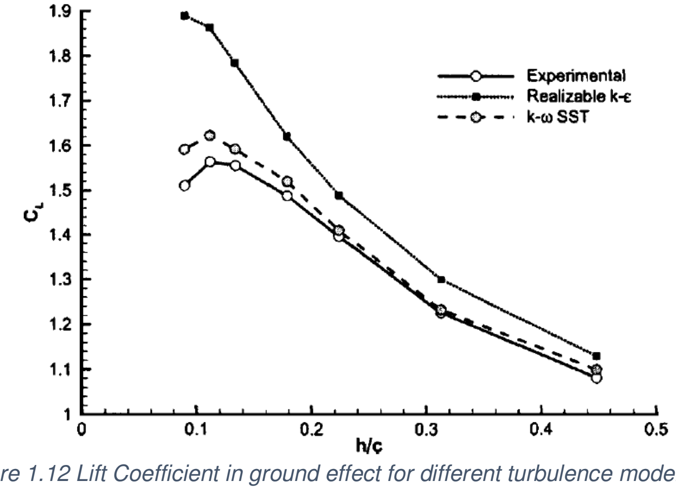

Figure 1.12 Lift Coefficient in ground effect for different turbulence models (27)

Doig et al. (28) performed a comparison for the SA, realizable $k-\epsilon$ model and Menter SST model in ground effect for a modified NASA GA(W)-2 LS [1]-0413 MOD inverted wing with an endplate. The differences between the models primarily manifested themselves at low heights above ground, when separation starts occurring, similar to the study from Mahon and Zhang. Unlike that study, here the differences between the models were found to be more subtle. The suction over the airfoil at low heights above ground is slightly under predicted by Menter SST and slightly over predicted by the realizable $k-\epsilon$ model and SA, thus no great qualitative differences could be found in lift and drag prediction. The wake is best predicted by the realizable $k-\epsilon$ model.

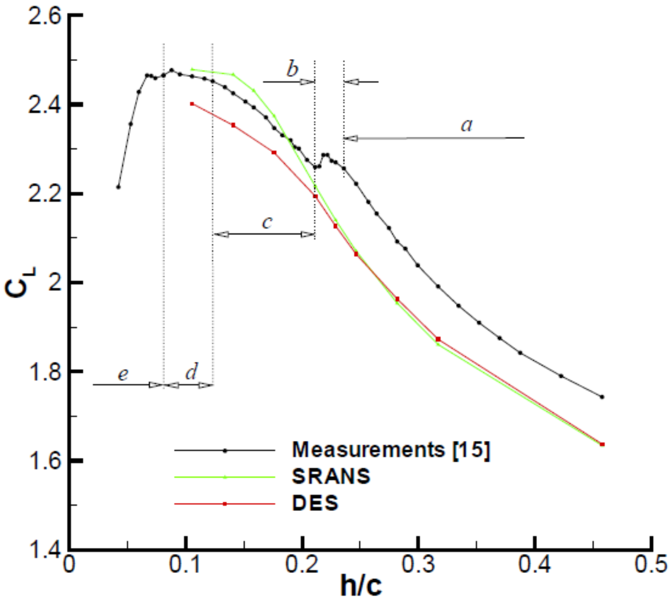

Figure 1.13 Comparison between different turbulence models for a double element wing in ground effect (29)

The turbulence equations discussed so far can be adapted for use with Detached Eddy Simulation (DES) (30), where the normal RANS equations are applied in the boundary layers and Large Eddy Simulation (LES) is used for the separated regions. LES resolves the larger turbulence scales numerically and models the smaller scales, but is still too computationally intensive to use for high Reynolds problems for several decades (31). DES can be used on smaller scale problems in a scientific setting, for example Heydner-Bruckner and Zhang (29). In this study a comparison is made between experiments, the DES and the SA turbulence models. Here it was found that the at larger heights above ground, above $h/c = 0.211$, both models predict a very similar lift coefficient with the same lift curve slope as in the experiments. As the height above ground is further reduced, as vortex breakdown occurs, the slope of the SA model suddenly becomes steeper, while both the DES and experimental results follow a flatter slope. This can be seen in Figure 1.13. The pressure distribution over the wing was also investigated at two locations, at the wing root and close to the wingtip (y/c = 0.93). At the wing root there was found to be little difference between the two turbulence models, both agreed with experiments on the pressure side and slightly under predicted the suction compared to the experiment. Close to the wing tip and at low heights above the ground the SA model significantly over predicted the suction, while the DES model showed good agreement with the experiment. Finally it was also found that the top and lower wing vortex were modelled more accurately by the DES turbulence model, which is of interest for vortex interaction with other parts of the vehicle or craft.

1.2.1.3 Conclusion

The choice of turbulence model can have a significant influence on the CFD results in the ground effect. At low heights above ground, the ground effect induces separation over the airfoil, which is when the performance of the different turbulence models diverges and the correct choice becomes important. The Menter-SST seems to give the best performance when investigating the pressure distribution and force coefficients over the airfoil, while the realizable $k-\epsilon$ model is the best choice if the wake of the wing is the most important aspect of the investigation. DES simulation will offer improved performance, but has the drawback of significantly increased computational cost.

1.2.2 Ground Simulation Techniques for CFD and Experimental Research

A key aspect of ground effect research is the accurate simulation of the ground plane. The simplest form of ground simulation is obtained by adding a simple flat plate under the model in the wind tunnel (32). However, this is an incorrect simulation of reality, since an aircraft flying over the ground is moving relative to the ground, while in this research situation the aircraft is fixed relative to the ground. A second source of errors is that a boundary layer will develop over the ground plane, which will interact with the boundary layer from the aircraft when the aircraft is positioned close to the ground, thus introducing an additional error in the results.

Several more accurate boundary conditions have been proposed and tested since the first windtunnel tests with a flat plate started. One of the earliest modifications was to introduce an inverted mirror image of the model (33), in an analogous fashion to the mirror image theory discussed in the previous chapter. However, this method of ground simulation quickly fell in disfavour. Nowadays the majority of the windtunnel research is performed with either a moving ground simulated by a belt (34) or still the simple method of a flat plate. Two additional methods are tangential boundary layer blowing (35) and by moving the model through the windtunnel (36), rather than moving the ground itself.

In this subchapter first the technology of the moving belt will be briefly explained. Next the influence of applying the correct ground simulation boundary condition will be discussed. This is important not just important for windtunnel testing, but holds equally true for CFD modelling of the ground effect.

1.2.2.1 Moving Belt

An example of a typical ground effect test section with moving belt is shown in Figure 1.76Figure 1.14. The aircraft is positioned directly above the moving belt. In front of the belt a boundary layer removal scoop is positioned, which is reinjected again behind the model. The scoop removes the boundary layer which has formed up to that point in the windtunnel, while the moving belt ensures that a new boundary layer does not start forming on the ground in proximity of the model.

There are a number of potential issues with a moving belt. First and foremost it adds a layer of complexity to the windtunnel tests, introducing additional costs and creating mechanical vibrations which may adversely influence the test results. The belt can experience local deformations due to the influence of the aerodynamic forces and can have a poor lifetime, as limited as having a maximum of twelve hours of testing capacity before needing to be replaced. Operating the belt can also be challenging due to manual controls and cooling tension on the belt (37). Therefore there needs to be a strong case to justify the additional complexity and costs of a moving belt.

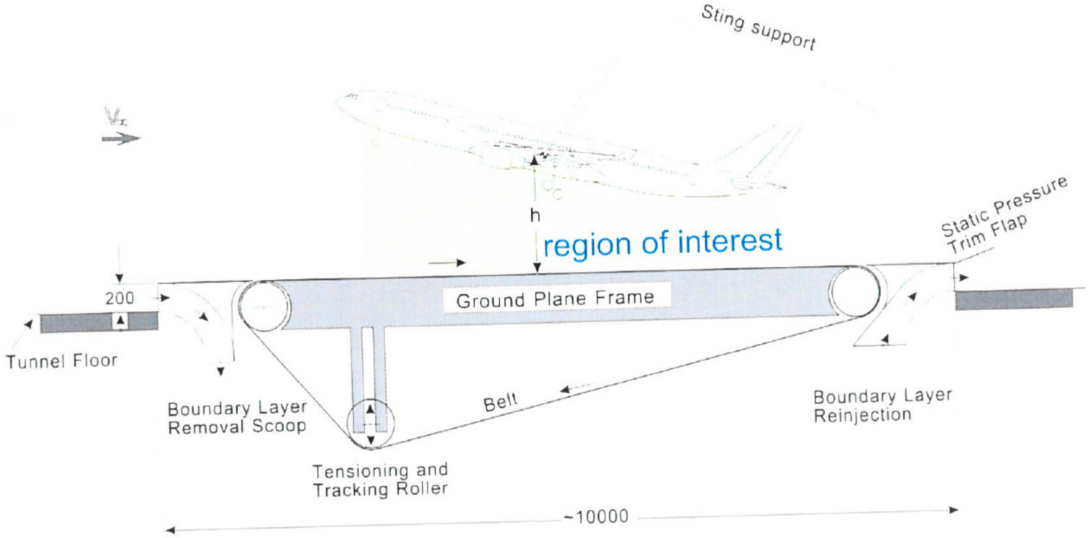

Figure 1.14 Test section of a windtunnel with a moving belt ground plane (38)

An example of the influence of the old moving belt of the Deutsch-Niederländische Windkanäle (DNW) can be seen in Figure 1.15, which shows the dependency of the force coefficients on the belt speed. The boundary conditions such as Ma, Re and AoA are unknown. At low heights above the ground such as $h/b = 0.1$ the impact on belt speed is significant. The change in lift coefficient due to ground effect ranges from $\Delta C_L = -0.0078$ with the belt switched on to $\Delta C_L = -0.022$ with the belt switched off. The drag increment increases by up to 16% when the belt is in operation.

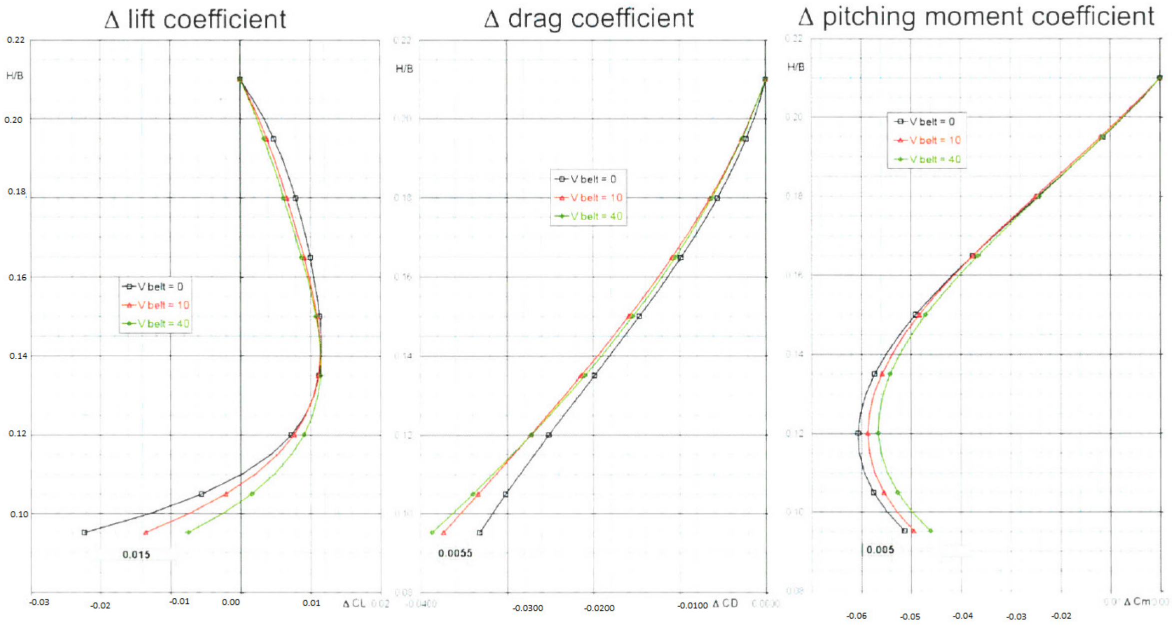

Figure 1.15 Change in force coefficients IGE due to moving belt (38)

1.2.2.2 Influence of different boundary conditions

Barber and Hall (39) have defined four possible boundary conditions for the ground simulation in CFD. Two have been mentioned before, ground stationary and the ground moving. A third option is to use the 'image' method. This is conceptually similar to placing a mirrored model in the windtunnel. This is accomplished in CFD by setting the boundary condition of the ground to Symmetry. The last boundary condition suggested by Barber was the ‘slip’ condition, where the ground was set to have zero shear stress. This would mean the ground moves at different speeds at different locations, so that the zero shear stress condition is enforced.

The impact of the different boundary conditions is shown in Figure 1.18. Most noticeable is the decrease in lift for the ground stationary boundary condition at $h/c < 0.25$, while all the other boundary conditions predict a lift increase and behave in a similar manner for the entire range of h/c. The maximum lift coefficient predicted for the image method is $C_{L_{max}} = 1.25$, while the slip and ground moving boundary conditions predict $C_{L_{max}} = 1.27$. A similar trend in lift behaviour was found by Firooz and Gadami (40) and Li et al (41) when comparing fixed and moving ground.

A similar situation can be found for the drag coefficient. Again as the height above the ground decreases, the ground stationary boundary condition under predicts the drag compared to the other three boundary conditions by as much as 28%. The maximum drag is the same for the slip, image and moving ground boundary condition, whereby the latter predicts a higher drag compared to the other two for most values of h/b. This can also be seen in the curves for the lift to drag ratio, where the ground moving has the worst lift to drag ratio for the large part of the range.

The flow was also been measured in a windtunnel by means of particle image velocimetry (PIV). This flow has been visualized in Figure 1.16 and Figure 1.17, showing the meanflow velocity and turbulence kinetic energy (TKE) for the ground moving and ground stationary boundary conditions respectively. The difference between the two boundary conditions in meanflow velocity and TKE at the bottom is obvious. In the case of a moving belt the flow field at the bottom of the windtunnel is far more uniform compared to the fixed ground.

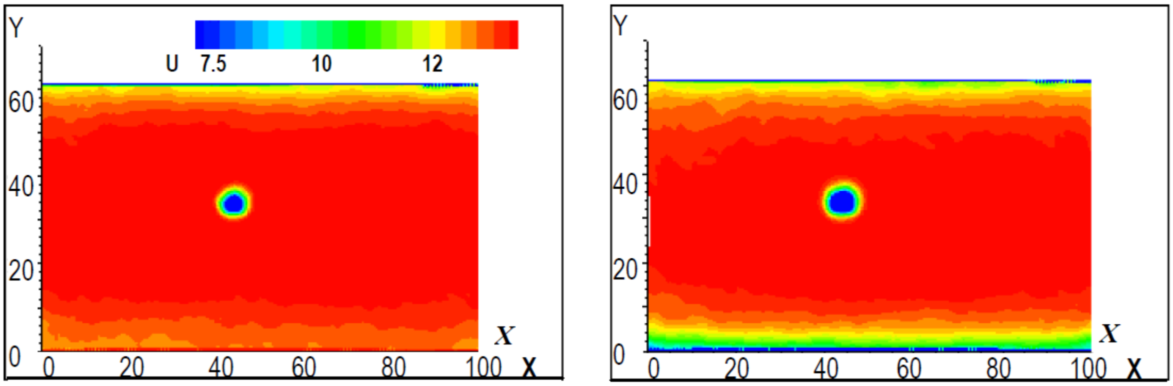

Figure 1.16 Experimental meanflow velocity with moving belt (left) and fixed ground (right) (39)

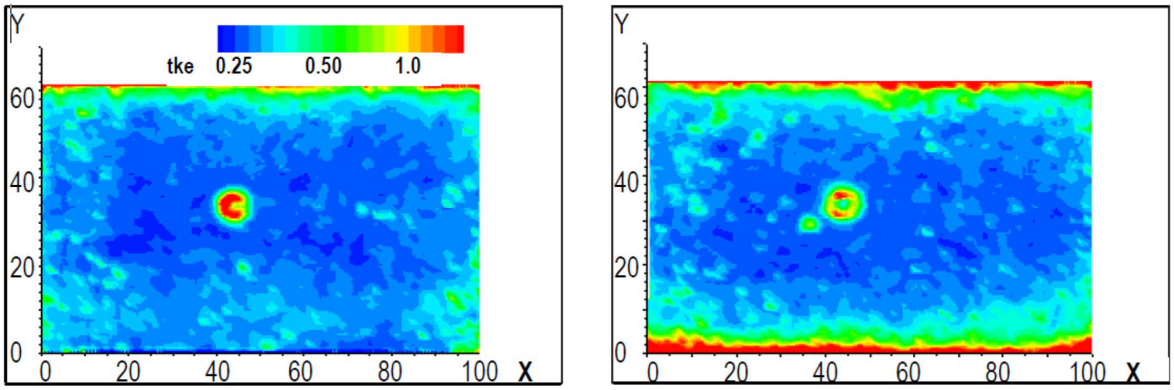

Figure 1.17 Experimental TKE with moving belt (left) and fixed ground (right) (39)

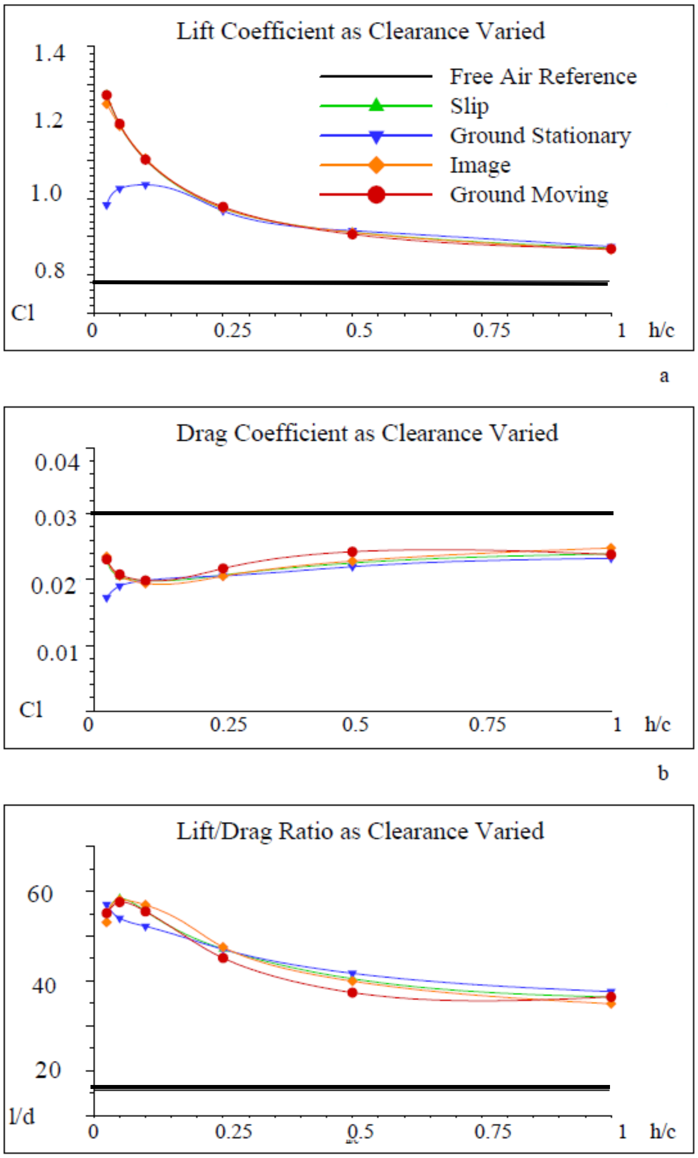

*Figure 1.18 Influence of the Ground Boundary Condition on the Lift and Drag of a NACA 4412 airfoil IGE Re=8.2*10^6 Ma=.315 α = 2.9° (39)*

1.2.2.3 Conclusion

It can be concluded that it is important to choose the correct ground boundary condition when investigating the ground effect. Significant differences of up to 28% have been observed using different boundary conditions. Multiple sources have found that the ground stationary boundary condition under-predicts the lift at small ground clearances compared to the physically correct boundary condition of a moving ground. It was found that the image and slip boundary conditions produce very similar results compared to ground moving, so these can also be applied. Since the use of boundary conditions can significantly influence the results, in the next chapter it will be noted explicitly for each study discussed which ground boundary condition was used.

1.2.3 ESDU Engineering Method for estimating Ground Effect

The ESDU 72023 (42) item provides a semi-empirical set of tools along which with the impact of the ground effect can be estimated for most aircraft. The changes in lift, drag and tail are treated separately and summarized in separate sections of this subchapter. First the general assumptions and applicability of these methods will be given, after which the methods will be explained.

1.2.3.1.1 Applicability and assumptions

- The ground is modelled as a mirrored image of the aircraft. Both the real and imagined wings are replaced by vortex systems of equal and opposing strength.
- Static treatment of the ground effect problem which is found to be a satisfactory assumption for real life applications
- Only the wing is taken into consideration when calculating the lift and drag changes. The new tailplane lift is calculated as a result of the changed pitching moment of the wing.
- Lift: the method is well validated with experimental and theoretical data for the range of $0 \leq C_L \leq 2$. The same validation was used for the range of $2 \leq C_L \leq 4$, but because the amount of data is somewhat limited and only contained data from unswept wings, caution should be used when applying the method to swept wings within this range.
- Drag: The same cautions apply here as the previous one for the lift. The $\frac{\Delta C_D}{C_D}$ obtained should be accurate within a margin of $0.15 \pm$.
- Caution should be taken applying this method to wings with a quarter point sweepback greater than 30°. Otherwise the accuracy of $\Delta\varepsilon$ should be within $2° \pm$.

1.2.3.1.2 Lift Calculation

The ESDU method for predicting the changes in lift consists of shifting the lift curve either by $\delta\alpha$ for constant C_L or by δC_L for constant α. This is indicated on figure 4.

$\delta\alpha$ can be calculated using equation 1.1. Parameter σ is a combination of h/b and is given by equation 1.2.

$$\delta\alpha = -\frac{\sigma C_L}{\pi A} \qquad (equation\ 1.3)$$

$$\sigma = e^{-2.48\left(2\frac{h}{b}\right)^{0.768}} \qquad (equation\ 1.4)$$

The incremental change in lift coefficient δC_L is given by equation 1.3. The parameters r, τ and N are given by equations 1.4-1.6 respectively. The reader is referred to the original ESDU document for a list of symbols.

$$\delta C_L = rC_L\left[\frac{N}{(1+\tau N C_L)^2} - 1\right] \qquad (equation\ 1.5)$$

$$r = \sqrt{1+\left(\frac{2h}{b}\right)^2} - \frac{2h}{b} \qquad (equation\ 1.6)$$

$$\tau = \frac{\frac{h}{\bar{c}}}{8\pi\left[\left(\frac{h}{\bar{c}}\right)^2 + \frac{1}{64}\right]} \qquad (equation\ 1.7)$$

$$N = 1 + (N' - 1)\left[1 + \frac{2}{C_L}\left(C_{m\frac{1}{4}} - C'_{m\frac{1}{4}}\right)\right] \qquad (equation\ 1.8)$$

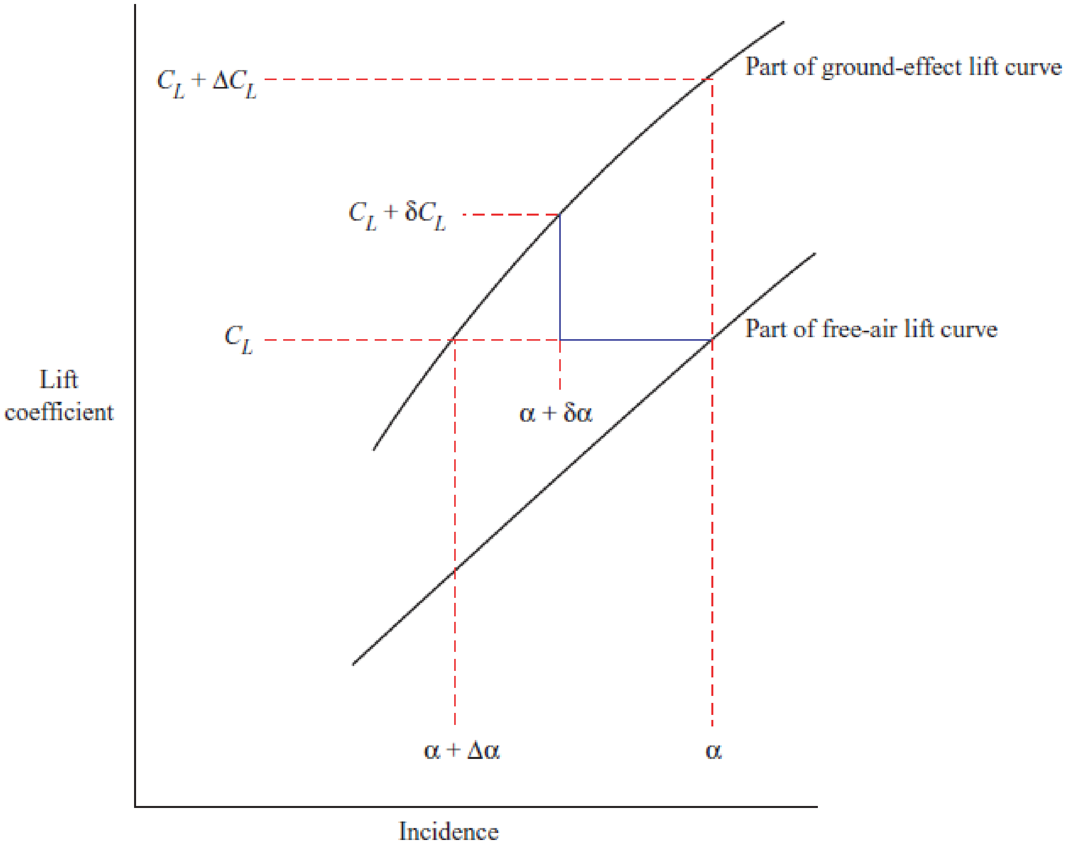

Figure 1.19 - Sketch of the shifting the CL-α curve to account for the ground effect (42)

If ΔC_L needs to be obtained, the stall region is avoided and the free air lift curve slope is linear over the range in consideration, then the above equations can be combined into equation 1.7.

$$\frac{\Delta C_L}{C_L} = \frac{1}{1 - \frac{a\sigma}{\pi A}} \left\{ \frac{a\sigma}{\pi A} + r \left[\frac{N}{\left(1 + \frac{\tau N C_L}{1 - \frac{a\sigma}{\pi A}}\right)^2} - 1 \right] \right\} \qquad (equation\ 1.9)$$

When the C_L is below 0.7, experiments suggest a correction needs to be applied for the wing thickness. This can be done by adding the factor ΔC_{Lt} to either ΔC_L or δC_L. ΔC_{Lt} can be calculated using equation 1.7. Equation 1.8 can be used to calculate ΔC_{Lt0}, where t represents the maximum thickness/chord ratio of the wing.

$$\Delta C_{Lt} = r(1 - 1.4C_L)\Delta C_{Lt0} \qquad (equation\ 1.10)$$

$$\Delta C_{Lt0} = -\frac{0.165t^{1.5}}{\left(\frac{h}{\bar{c}}\right)^{2.5}} \qquad (equation\ 1.11)$$

1.2.3.1.3 Drag Calculation

Using a similar approach as the sketch shown in figure 4, ΔC_D can be calculated using equation 1.9. The factor $1 + \delta$ can be found in ESDU 74035 or ESDU 01007 while the factor K can be found in ESDU Aero F.02.01.08.

$$\Delta C_D = \frac{\phi C_L}{\pi A} C_D - \left[\sigma - (2-\sigma)\frac{\phi C_L}{\pi A}\right] C_{Dv} \qquad (equation\ 1.12)$$

$$\phi = 0.00066\left[570\frac{b}{h} - 32\left(\frac{b}{h}\right)^2 + \left(\frac{b}{h}\right)^3\right] \qquad (equation\ 1.13)$$

$$C_{Dv} = \frac{1+\delta}{\pi A} C_L^2 + K^2(C_L - C_L')^2 \qquad (equation\ 1.44)$$

1.2.3.1.4 Calculation of the downwash on the tail

The angle of attack on the tail α_T is affected by the shift in angle of attack $\Delta\alpha$ of the entire aircraft as a result of the ground effect as well as the change in downwash due to the image wing $\Delta\varepsilon$.

$$\alpha_T + \Delta\alpha_T = \alpha + \Delta\alpha_t + \eta_T - (\varepsilon + \Delta\varepsilon) \qquad (equation\ 1.15)$$

The downwash $\Delta\varepsilon$ can be calculated as follows:

$$\Delta\varepsilon = \varepsilon_1[1 - \frac{b_{eff}^2 + 4(h_T - h)^2}{b_{eff}^2 + 4(h_T + h)^2} - \varepsilon \qquad (equation\ 1.16)$$

$$\varepsilon_1 = \varepsilon + \frac{d\varepsilon}{d\alpha}\Delta\alpha \qquad (equation\ 1.16)$$

$$h_T = z_T cos\alpha + h - x_T sin\alpha \qquad (equation\ 1.17)$$

Equations 1.16-1.19 explain how to get the factor $\frac{b_{eff}}{b}$.

$$\frac{b_{eff}}{b} = k_1 \quad (full\ span\ flaps\ or\ unflapped) \qquad (equation\ 1.18)$$

$$\frac{b_{eff}}{b} = \frac{k_1 k_2 C_L}{C_L - (1-k_2)C_L'} \qquad (equation\ 1.19)$$

$$k_1 = 0.085(7.56 + 3.5\lambda - \lambda^2) + 0.002(\lambda - 0.48)(A-6)(18.5-A) \qquad (equation\ 1.20)$$

$$k_2 = \sqrt{0.64 + 3.6\left(\frac{b_f}{b}\right) - \left(\frac{b_f}{b}\right)^2} - 0.8 \qquad (equation\ 1.21)$$

The tailplane lift is affected by its own image in an analogous way to the wing in section1.2.2. Thus:

$$\Delta C_{LT} = a_T\Delta\alpha_T = a\_T\{\Delta\alpha - \Delta\varepsilon + \frac{\beta[C_{LT} + a_T(\Delta\alpha - \Delta\varepsilon)]}{\pi A_T} \qquad (equation\ 1.22)$$

Finally the change in elevator angle $\Delta\eta$ in order to trim the aircraft can be calculated:

$$\Delta\eta = -\frac{\Delta C_{LT}}{a_e} \qquad (equation\ 1.23)$$

1.3 Literature Overview of Current Ground Effect Research

In this chapter the current state of the research into the ground effect will be documented. As has been mentioned previously, WIG vehicles and racing car applications are two of the driving forces in ground effect research. In both cases lift is the most important aspect for performance, followed by drag. This pattern can also be found when analysing the literature, as virtually every paper discusses the lift IGE while only approximately half of these also discuss the drag.

The structure of this chapter will reflect this distribution of the research. First the lift and pressure distribution of the simplest case, a single element airfoil affected by the chord dominated ground effect, will be reviewed. Next additional complexity will be added by introducing a flap to the airfoil and the changes it causes to the behaviour IGE will be evaluated. Finally it will be discussed how this behaviour changes when the ground effect for a finite wing is evaluated, in other words a three-dimensional flow.
The drag will be investigated subsequently. As mentioned before, the research on this topic is sparser, so by necessity the discussion of literature on drag will be briefer compared to lift.
Finally some miscellaneous topics on the ground effect will be discussed, such as the pitching moment, the dynamic ground effect and the influence of compressibility on the ground effect.

1.3.1 Lift & Pressure distribution

In this subchapter the lift-coefficient of an airfoil situated in the ground effect will be discussed as treated in the scientific literature. Data from multiple sources will be compared in order to identify the similarities and differences between them. First the discussion will be focussed on single-element airfoils, after which multi-element airfoils will be taken into consideration. Finally the discussion will be extended into the span dominated ground effect, where finite wings will be taken into consideration.

1.3.1.1 Single-Element Airfoil

In ground effect, there are three distinct angle of attack ranges wherein the lift coefficient is affected in a separate manner and by different underlying physical principles. These regions are:

1. At negative AoA there is a clear loss of lift IGE
2. In the linear part of the lift curve at low to moderate AoA the lift curve slope is becomes steeper and lift increases IGE compared to the same AoA OGE.
3. Separation occurs earlier in the presence of ground effect, so at high angles of attack near the stall region there is a loss of lift IGE.

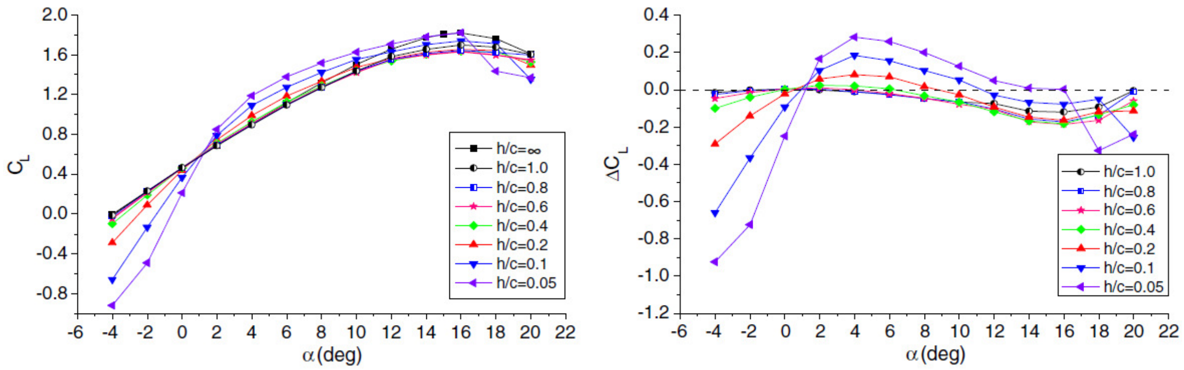

Figure 1.20 Lift Curve & Relative Lift Curve for a NACA 4412 Airfoil at $Re=6*10^6$ and Ma=0.26 (43)

This is shown in Figure 1.20 with the lift curve and relative lift curve of NACA 4412 airfoil (43). Qu et al. performed a numerical investigation using the RANS equations and the k-ω turbulence model. ANSYS FLUENT 14.5 was used to solve for the equations. This is a recent, very clear and extensive study and will be used as a primary source in this subchapter. Each AoA range mentioned above will be treated separately and other literature sources will be used to corroborate the evidence from Qu et al.

1.3.1.1.1 Negative to low AoA

The first distinct AoA range in the ground effect occurs at negative AoA until approximately $\alpha = 0°$, depending on the airfoil under investigation. At these AoA a convergent-divergent passage is formed between the ground and the lower side the airfoil: a venturi. This situation is illustrated in Figure 1.21. This causes the flow to accelerate, leading to a strongly increased suction of up to 180% on the lower side of the airfoil when in close $(h/c < 0.1)$ proximity to the ground. In contrast, the upper side of the airfoil is only very limitedly influenced by the ground effect at this range of AoA. The lift coefficient at $\alpha = -4°$ can be seen in Figure 1.22, where it is obvious that the majority of the lift loss observed in Figure 1.20 can be attributed to the pressure loss on the lower side of the airfoil due to the venturi effect. Finally the pressure distribution for this situation is shown in Figure 1.23. The very large increase in suction on the lower side of the airfoil can clearly be seen, the suction peak goes from ~ -1.9 in free to ~ -4.6 at h/c = 0.05.

Several literature sources show general agreement with the above, although none go on to discuss negative AoA in quite so much detail. One study by Angle et al. (44) focuses on the pitch stability of an airfoil in the ground effect and contains a comparison between the computed lift coefficient IGE and OGE for $-3° < \alpha < 15°$ for a flat plate. The computations were performed using the software tool FLUENT 6.2.16. The results can been in Figure 1.24, where the analytical solutions are provided by (45) and (6) respectively. It can be seen that at $\alpha < -0°$ the IGE solutions show up to 50% less lower lift compared to OGE solutions for the same AoA, which is in agreement with the discussion above.

A study by Smith et al. (46) compares a Computational Fluid Dynamics (CFD) code with experimental results for a NACA 4412 airfoil at low angles of attack. Figure 1.25 shows that at $\alpha = 0°$ there is a sharp lift decrease when the airfoil is placed close to the ground. There is also a good agreement between the experiment and CFD for this AoA.

Pátek et al (47) also found an increase in negative lift as a NACA0012 airfoil gets closer to the ground of AoA up to $\alpha = -6°$. At the height of $h/c = 0.15$ the lift coefficient went from $C_{L_{freestream}} \approx -0.7$ to $C_{L_{IGE}} = -1.4$.

Two additional studies will be mentioned here, where in both cases a finite wing was studied. Therefore 3D effects cannot be excluded in these cases. Nevertheless these show qualitative agreement at negative angles of attack with Qu et al, which is why these are mentioned here. No 3D studies were found that show a disagreement with Qu et al, which would be an improvement in performance IGE at negative AoA.

Figure 1.7 from (13) clearly shows the negative effect on the lift coefficient of the ground at negative AoA and has been discussed in the previous chapter. A NACA 64_1-112 airfoil was used in this study.

Zerihan and Zhang (48) performed windtunnel measurements on a single element wing in the ground effect with a highly cambered Tyrrell-26 airfoil and an aspect ratio of 5. End plates were used on the model, so the influence of 3D effects should be limited. Figure 1.26 shows the lift curve in ground effect for this experiment. Once again the lift is affected negatively by the ground effect at negative angles of attack. It can be observed that for Figure 1.7 and Figure 1.22 the ground effect becomes a negative at $\alpha \approx 0°$, while in Figure 1.26 this occurs at $\alpha \approx -6.5°$. Presumably this difference can be explained by the fact that the latter has a highly cambered airfoil, while the first two have a conventional airfoil with less camber.

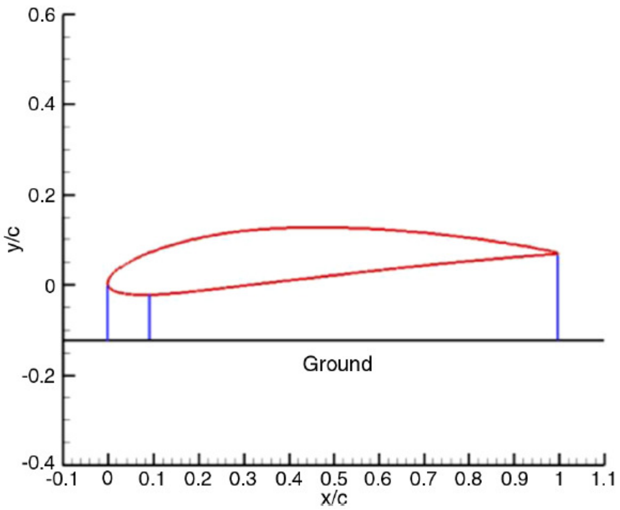

Figure 1.21 the Venturi effect illustrated at close proximity to the ground at α= -4° (43)

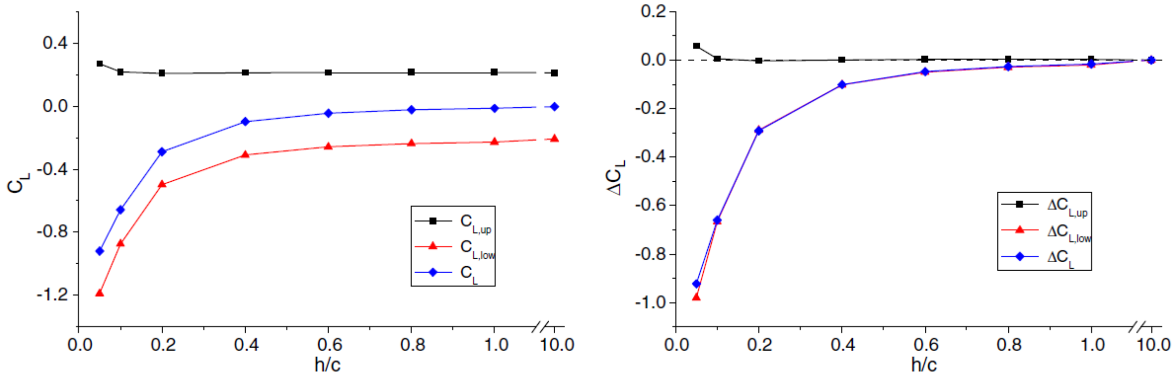

a) Lift coefficient **b) Lift coefficient increment**

*Figure 1.22 Lift Coefficient and incremental lift coefficient of a NACA 4412 Airfoil at Re=6*10⁶ and Ma=0.26 for α= -4° (43)*

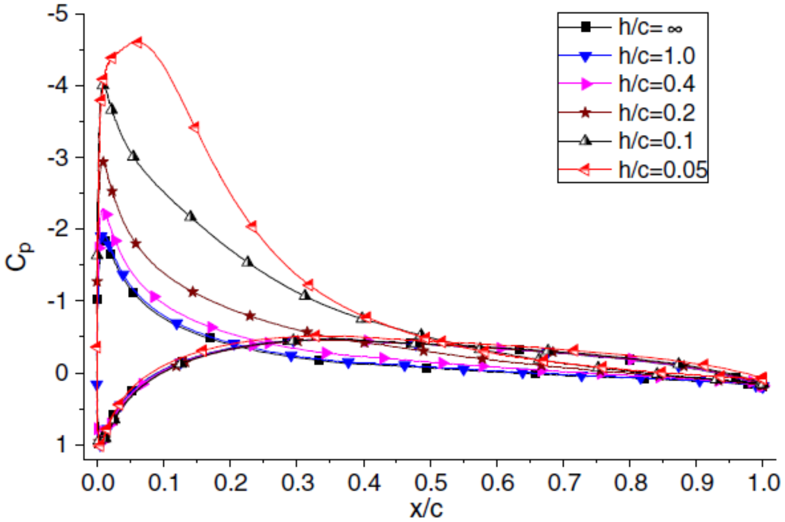

*Figure 1.23 Pressure distribution around a NACA 4412 Airfoil at Re=6*10⁶ and Ma=0.26 for α= -4° (43)*

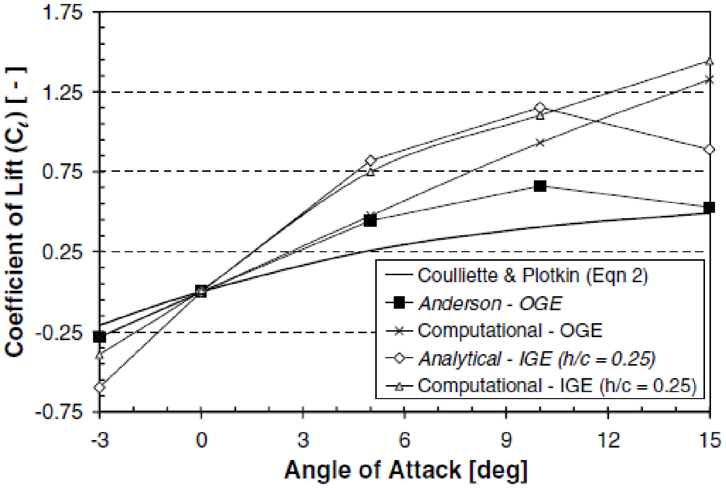

*Figure 1.24 Lift Coefficient for a flat plate OGE and IGE solved by various methods at Re =1.25*10^6 (44)*

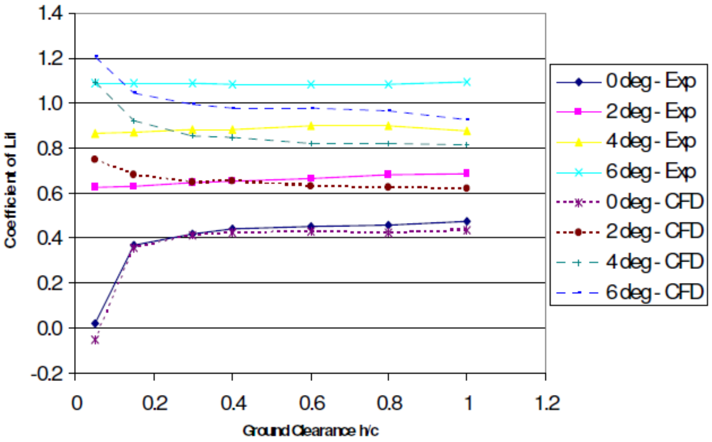

Figure 1.25 Experimental and CFD Lift Coefficient for a NACA 4412 airfoil $Re = 3 * 10^5$ $Ma \approx 0.1$ *(46)*

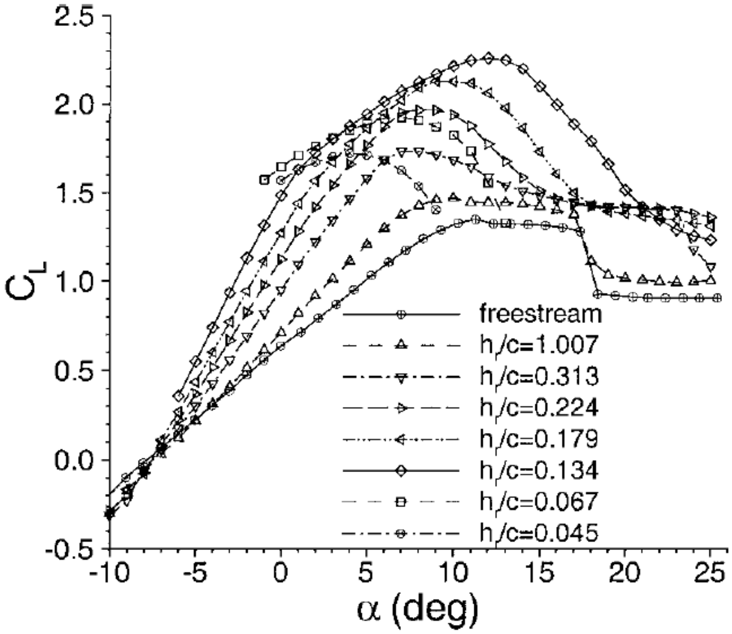

*Figure 1.26 Lift Coefficient in ground effect Re=2*10^6 Ma ~=0.1 (48)*

1.3.1.1.2 Low to Moderate Incidence

As mentioned previously, there is much research available which investigates the ground effect for low to moderate AoA, because this is the applicable flight regime for the WIG vehicles will be for the vast majority of the time. The overall trend is clear: Lift will increase in the ground effect at these AoA ranges. This phenomenon is well understood and can be corroborated by many different sources. Some examples are (44) (46) (49) (50) (32) (40) (51) (41).

First it will be examined in greater detail why the lift increases by first examining the pressure distribution around the airfoil and the streamlines, after which a physical explanation will be offered. Figure 1.27 from Qu et al. shows the pressure distribution for the NACA 4412 airfoil for $\alpha = 4°$ and $\alpha = 8°$. It can be seen that the pressure increases on both sides of the airfoil, with the exception of the suction peak at the nose of the upper side of the airfoil, which remains the same and even becomes stronger at $\alpha = 8°$ and $h/c = 0.05$. As a consequence the upper side of the airfoil experiences a stronger adverse pressure gradient IGE. The increase in pressure at the lower side of the airfoil is beneficial and is the main explanation for the increase in lift IGE.

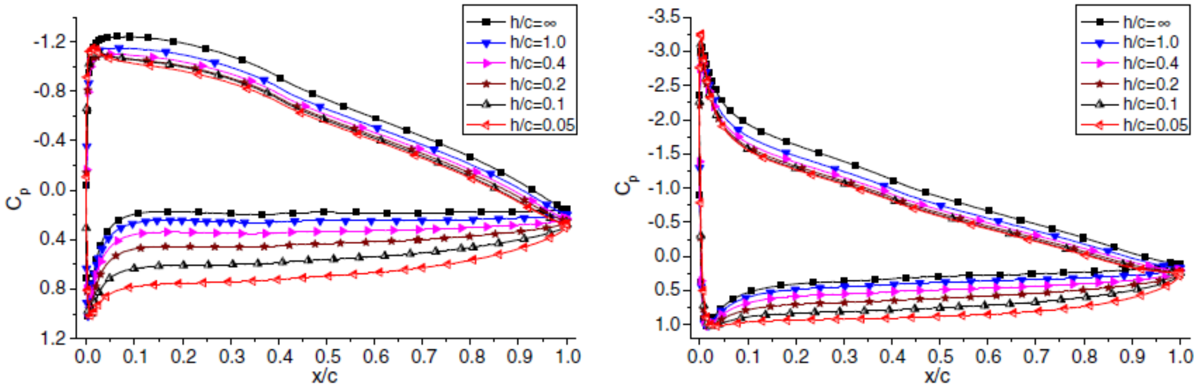

a) α = 4 deg **b) α = 8 deg**

*Figure 1.27 Pressure distribution around a NACA 4412 Airfoil at Re=6*10^6 and Ma=0.26 (43)*

This is illustrated further by Figure 1.28 where the lift coefficients for the lower and upper side of the airfoil are plotted separately. This confirms the findings from the pressure distribution, the lift produced by the upper side of the airfoil slowly decreases by the presence of the ground, while the lift coefficient of the lower side of the airfoil increases more rapidly. The sum of these two will result in a positive change to the overall lift coefficient at low to moderate AoA.

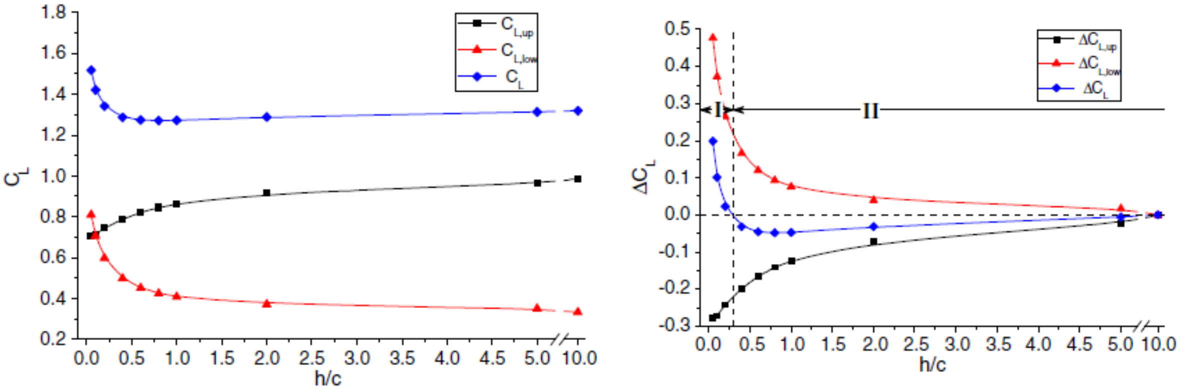

c) Lift coefficient for α = 8 deg **d) Lift coefficient increment for α = 8 deg**

*Figure 1.28 Lift change in ground effect for a NACA 4412 Airfoil at Re=6*10^6 and Ma=0.26 (43)*

Figure 1.29 shows the streamlines around the airfoil for $\alpha\ = 8°$, where G0, G1, G2 correspond to IGE with $h/c = 0.1$. F0, F1 and F2 are the same streamlines for the OGE situation. G1 and F1 are the streamlines which terminate at the stagnation point of the airfoil and reappear at the trailing edge. The two other streamlines are located either 0.1c above or under the stagnation streamline. In free air the airfoil starts deflecting the streamlines upwards at approximately $x/c = -25$ and deflects these downward once they have passed the airfoil. It can be seen that due to the presence of the ground the streamlines are deflected upwards at a far closer location to the airfoil, approximately $x/c =\ -1$. This is explained by the mirrored bound vortex, shown in Figure 1.6b. The counter clockwise mirrored circulation acts opposite to the deflection caused by the airfoil in free air, thus the streamlines become more parallel closer to the ground. This causes the effective AoA to decrease. This explains why the pressure is increased on the upper side of the airfoil in the ground effect.

The reduction of the effective angle of attack discussed above should also cause the pressure on the lower surface to decrease, yet this is not what is observed in Figure 1.27. The explanation for this is that all streamlines below G1 in Figure 1.26 are forced into the convergent passage between the lower side of the airfoil and the ground. This causes a 'blockage' effect, whereby the air speed is reduced and the pressure increases. This effect of the pressure increasing at the lower airfoil due to blockage effect is stronger at low to moderate AoA compared to the reduction of effective angle of attack which causes the pressure to decrease, which is why there is a net lift increase at these AoA ranges. The exact ratio between these two conflicting effects is dependent on both the height above ground and the AoA. It will be discussed in the next section how this ratio changes at high AoA.

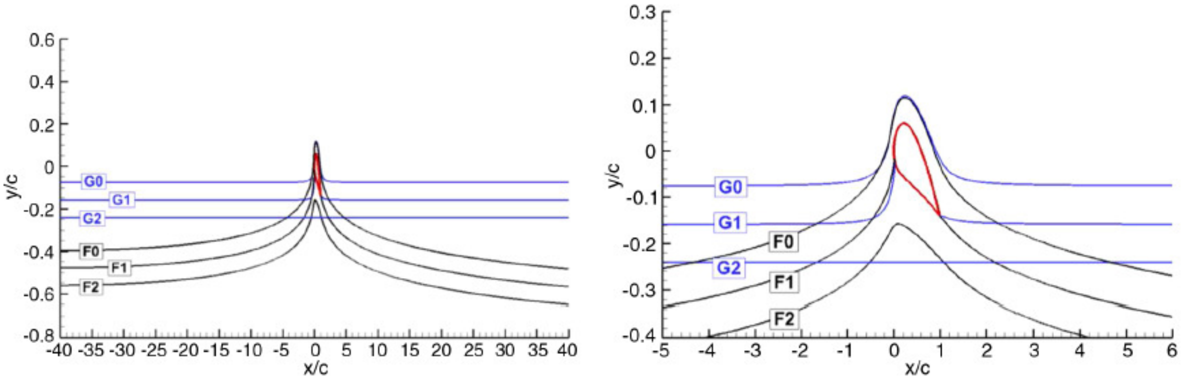

c) Global view of streamlines for α = 8 deg **d) Zoomed-in view of streamlines for α = 8 deg**

*Figure 1.29 Streamlines IGE (G) and OGE (F) for a NACA 4412 Airfoil at Re=6*10^{6} and Ma=0.26 (43)*

The remainder of this section will be spent briefly discussing corroborating evidence of the above from other sources. Figure 1.30 and Figure 1.31 show the experimental pressure distribution on a NACA 4412 airfoil at $\alpha\ = 4°$ and $\alpha\ = 8°$ for various heights above ground. These figures are directly comparable with Figure 1.27. While the exact magnitude of the pressure coefficient does not match, the overall trend is similar: For decreasing h/c the pressure increases at the upper airfoil surface and on the lower airfoil surface it increases *by a greater extent.*

A different study from Ahmed et al. (32) on a symmetrical NACA 0015 airfoil shows that for low to moderate angles of attack the pressure increase on the upper side is relatively insignificant, while the lower side of the airfoil experiences a significant pressure increase. This is shown in Figure 1.33.

Finally Figure 1.32 shows the pressure distribution as a result of a NACA 4412 airfoil with $\alpha\ = 6°$. These were obtained by solving the RANS equations with the SA turbulence model. It is evident that the increase in pressure on the lower side of the airfoil is more dominant compared to the decrease of suction on the upperside of the airfoil.

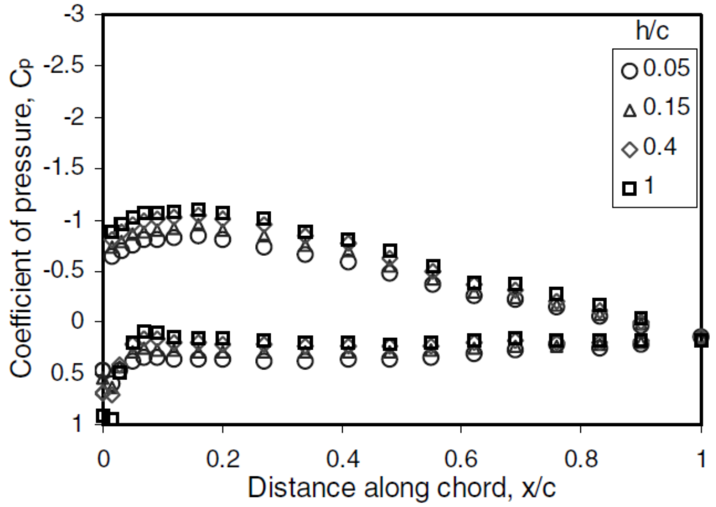

*Figure 1.30 Experimental Pressure distribution around a NACA 4412 Airfoil in ground effect with moving ground Re=3*10⁵ Ma=0.1 α = 4° (50)*

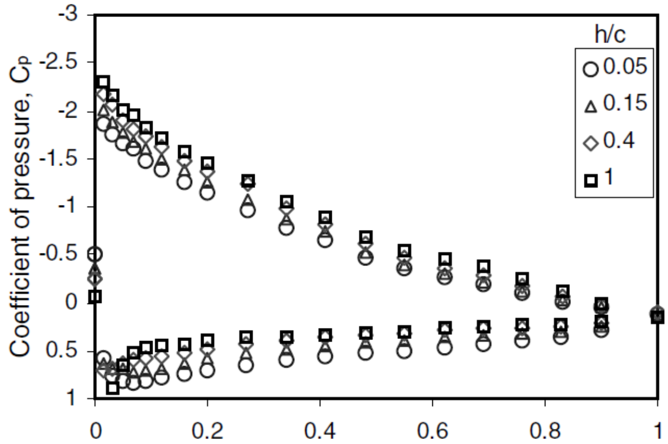

*Figure 1.31 Experimental pressure distribution around a NACA 4412 Airfoil in ground effect with moving ground Re=3*10⁵ Ma=0.1 α = 8° (50)*

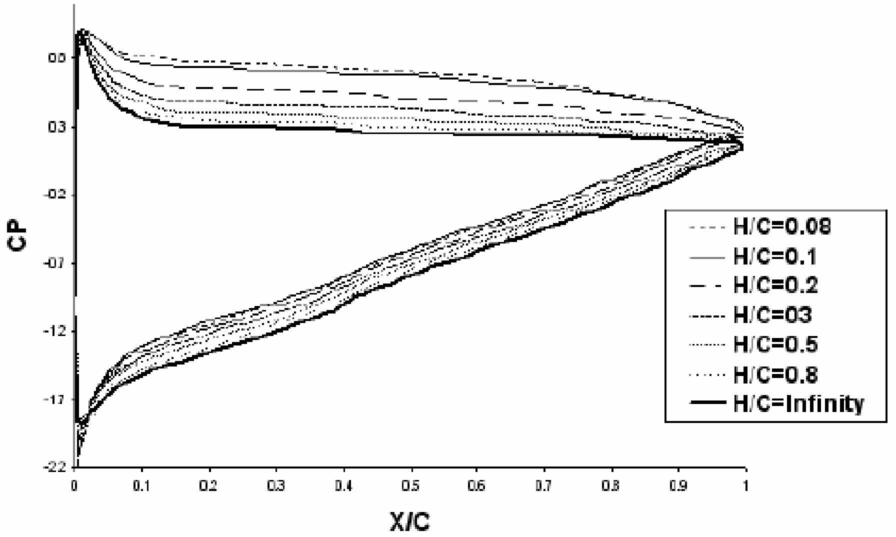

Figure 1.32 Pressure distribution around a NACA 4412 airfoil in ground effect with a moving belt Ma=0.1 α = 6° (40)

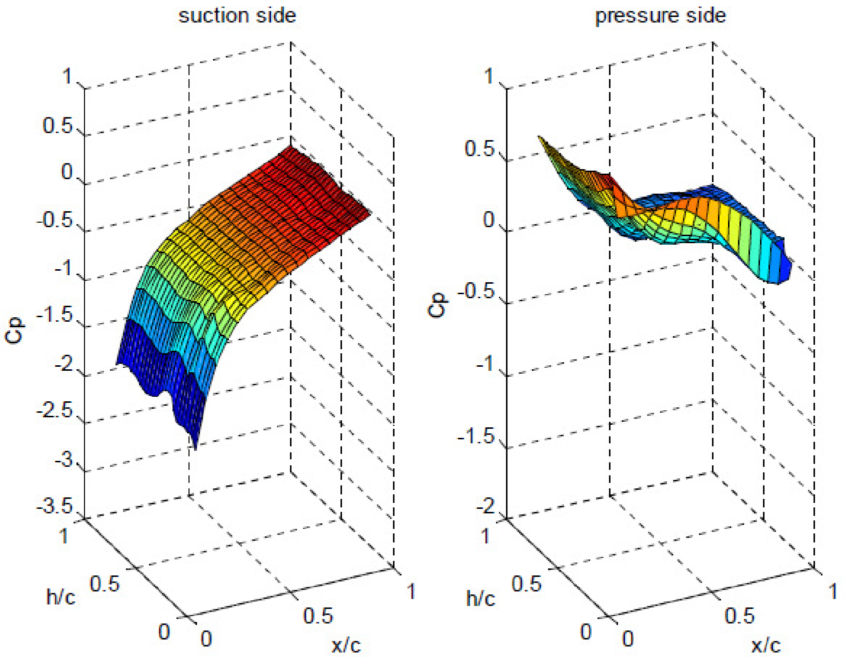

Figure 1.33 Experimental pressure distribution for a NACA 0015 airfoil in ground effect Re=unknown Ma = 0.1 α = 7.5° (32)

1.3.1.1.3 High Incidence & Stall

As has been mentioned previously, one of the main drivers of ground effect research are WIG craft. These craft spend their time almost exclusively in the low AoA regime. Therefore the literature on high AoA ground effect is relatively limited. The main source will be Qu et al (43).

Before the flow at high AoA in the ground effect is discussed, it is prudent to start with a word of caution at interpreting the results. CFD solvers for the RANS equations have been very successful during the past decades at simulating a wide range of flow conditions. But, as Jinaghua and Edwards (52) put it: "*However, the simulation of flow around a high-lift airfoil under static or dynamic stall remains a challenging task for the computational fluid dynamics (CFD) community. Such flows are characterized by high Reynolds number ( ) and the complexity of the turbulent boundary layer (including laminar to turbulent transition and separations)*."

Because of this, Qu et al have included a section in their report comparing the results of their calculations and experimental data from other sources in free air. This comparison is reproduced in Figure 1.34, the source of the experimental data is Abbott et al (53), the other CFD data is provided by Ockfen et al (54). The figure shows that at high angles of attack, as the airfoil approaches the stall region, the CFD computations overestimate the lift coefficient compared to the experimental results. Qu et al. attribute this to two causes. The first is that the turbulence model, SST k-ω, assumes fully turbulent flow which would delay separation of the flow on the upper airfoil. The second reason cited is that either the grid density should be increased or that a *higher-order* spatial discretization scheme (a second order scheme was used) should be used in order to more accurately predict the separation region. The above should be kept in mind while evaluating the results discussed below for high AoA ground effect flow.

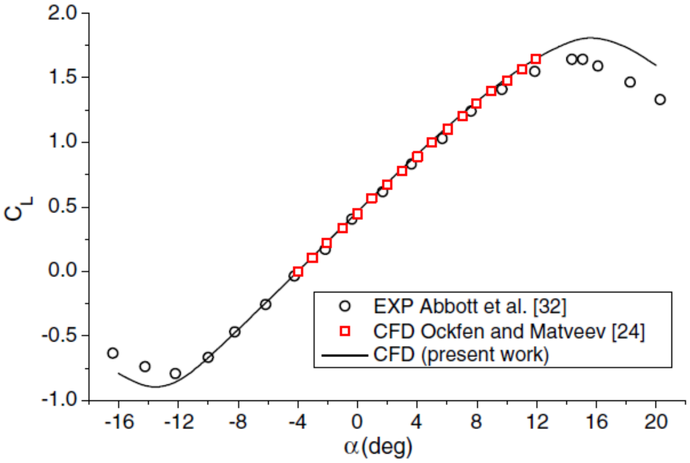

Figure 1.34 Lift Coefficient Comparison between CFD and Experimental Results for a NACA 4412 airfoil (43)

In the previous section it was seen that, when looking at the pressure distribution in ground effect for moderate AoA, as for example in Figure 1.27, that in the ground effect the suction peak at the nose of the airfoil becomes stronger and that the suction behind the suction peak drops faster compared to free-air, so the ground effect causes a stronger adverse pressure gradient to appear. This is especially evident in Figure 1.35, which shows the pressure distribution for the same airfoil at $\alpha = 16°$ and $\alpha = 18°$. The stronger adverse pressure gradient is evident. Near the trailing edge there is a plateau for the upperside of the airfoil, which indicates separated flow. The closer the airfoil is to the ground, the bigger is the region of separated flow. This is especially clear at $\alpha = 18°$ and $\frac{h}{c} = 0.05$, here the flow is completely separated over the entire airfoil, but if the distance to the ground is increases the flow is attached at the forward part of the airfoil. One final observation that can be made from Figure 1.35 is that the pressure rise on the lower side of the airfoil due to ground effect no longer increases with AoA. In other words, there seems to be a limit on how much the blockage effect can increase the pressure on the lower side of the airfoil.

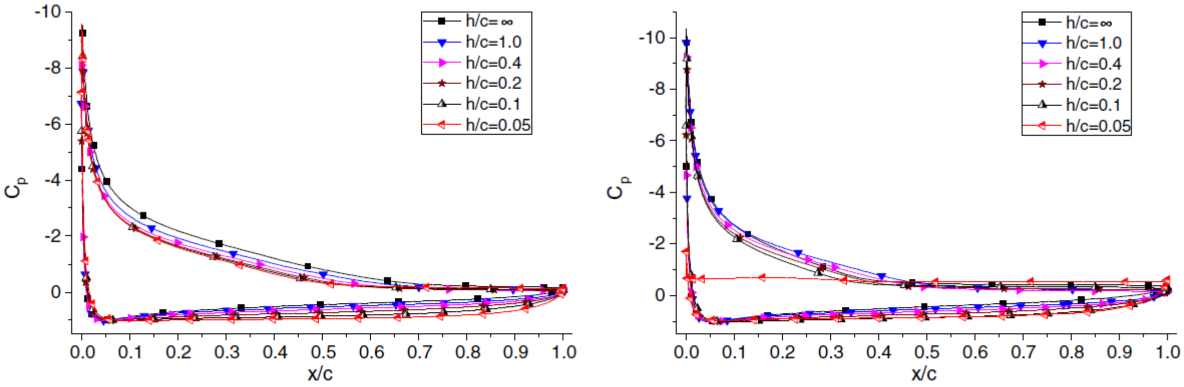

a) α = 16 deg **b) α = 18 deg**

*Figure 1.35 Pressure distribution around a NACA 4412 Airfoil at Re=6*10^6 and Ma=0.26 (43)*

This is confirmed by looking at the change in lift coefficient at these angles, shown in Figure 1.36. When going from $\alpha = 16°$ to $\alpha = 18°$, the lift increase due to the lower part of the airfoil remains the same and is comparable in magnitude to the lift increase observed at $\alpha = 8°$ in Figure 1.28. However as the AoA increases the decrease in lift on the upper side of the airfoil increases strongly, going from a relative change of $\Delta C_{L_{upper}} \approx -0.3$ at $\alpha = 8°$ to $\Delta C_{L_{upper}} \approx -0.7$ at $\alpha = 18°$ for $h/c = 0.05$ due to separation of the flow. This is confirmed in Figure 1.37

which shows the separation point on the upper side of the airfoil as a function of the height above ground. There is a clear trend that the separation point moves forward as the height above ground is reduced. Finally the streamlines can be observed in Figure 1.38 which again shows that in ground effect the flow becomes more separated at high AoA.

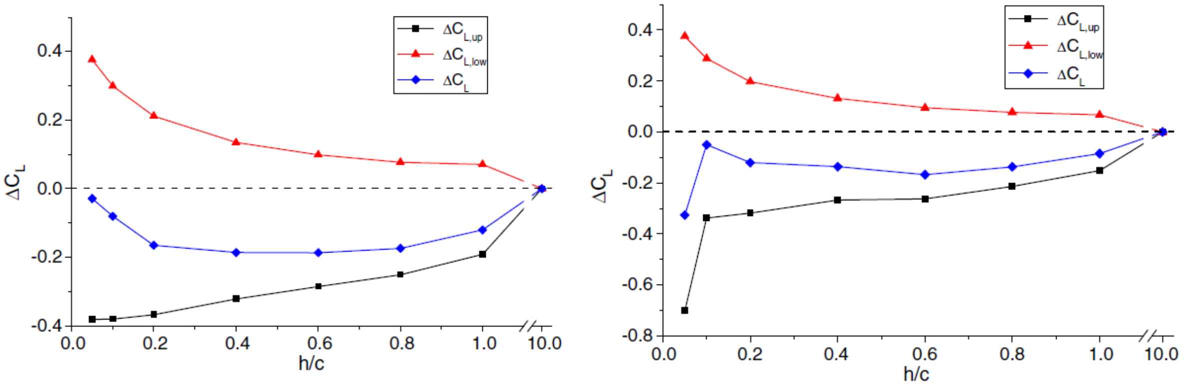

a) α = 16 deg **b) α = 18 deg**

*Figure 1.36 Lift change in ground effect for a NACA 4412 Airfoil at Re=6*10^{6} and Ma=0.26 (43)*

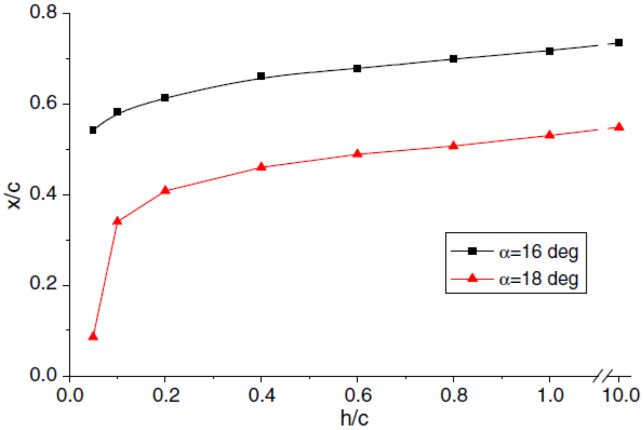

*Figure 1.37 Separation point as a function of height for a NACA 4412 Airfoil at Re=6*10^{6} and Ma=0.26 (43)*

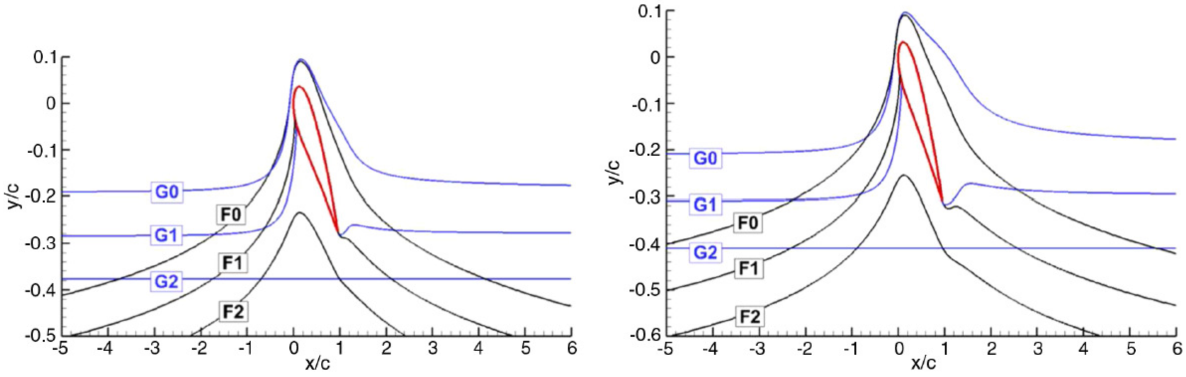

a) α = 16 deg **b) α = 18 deg**

*Figure 1.38 Streamlines IGE (G) and OGE (F) for a NACA 4412 Airfoil at Re=6*10^{6} and Ma=0.26 (43)*

One corroborative source for the above effects is Traub (55), who investigates a S8036 in a windtunnel at a low Reynolds number of Re = 1.2 *10^{5}. Figure 1.39 and Figure 1.40 show the influence of the ground effect on the lift coefficient. It can be observed how the maximum lift coefficient is reached at a height of $h/c = 0.4$. As the ground proximity is increased beyond that, the maximum lift is reduced. This is consistent with the observations from Qu et al.

Figure 1.26 showing the lift curve for a highly cambered wing, discussed in a previous section, shows that the maximum lift occurs at $h/c = 0.134$. Once again, when reducing the ground clearance further it results in a reduction of the maximum lift coefficient.

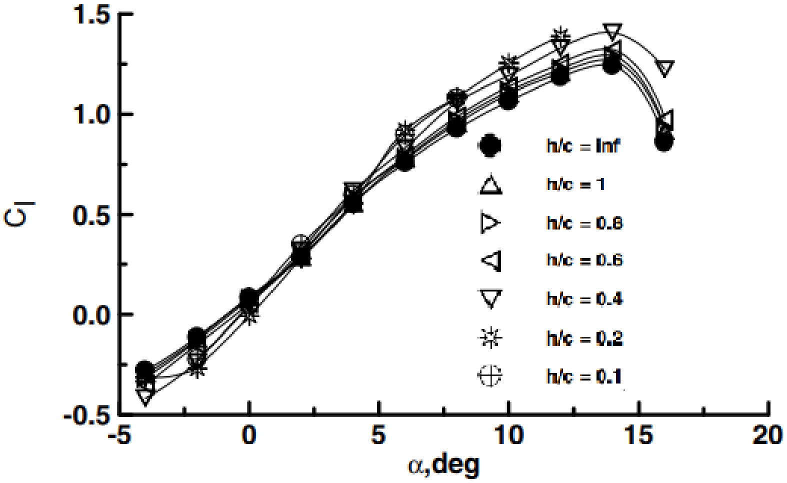

*Figure 1.39 Experimental results of a S8036 airfoil in ground effect Re=1.2*10^5 (55)*

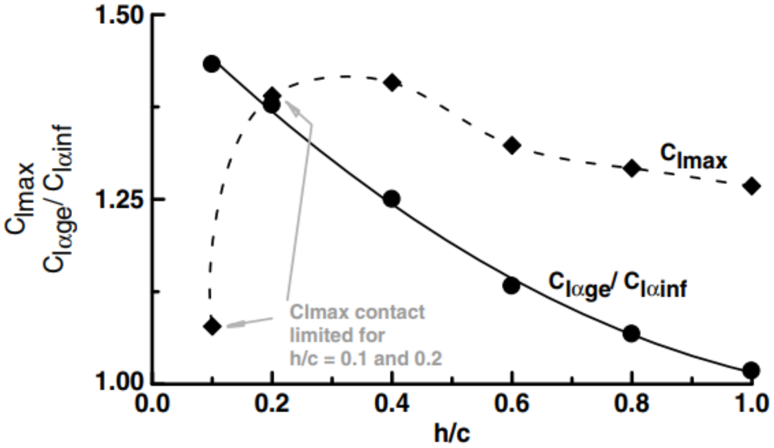

*Figure 1.40 Maximum Lift Coefficient of a S8036 airfoil in ground effect Re=1.2*10^5 (55)*

1.3.1.1.4 Conclusion

This subchapter concerning the influence of the ground effect on the lift and pressure distribution of a single element airfoil can be summarized by Figure 1.41, where the contours for the incremental lift change due to ground effect are shown. There are three distinct regions in this contour plot. The first, at low to moderate angles of attack, shows a net increase in lift, mainly due to the increase of pressure on the lower side of the airfoil. This is region I. As the angle of attack is increased, the pressure increase on the lower side of the airfoil remains similar in magnitude, while the reduction in suction at the upper side of the airfoil keep getting stronger with increasing AoA, resulting in a net loss of lift. This is region II in the figure. Region III occurs at negative AoA, where the lower side of the airfoil together with the ground forms a venturi shape, resulting in an increase on suction at the bottom side of the airfoil and the associated loss of lift.

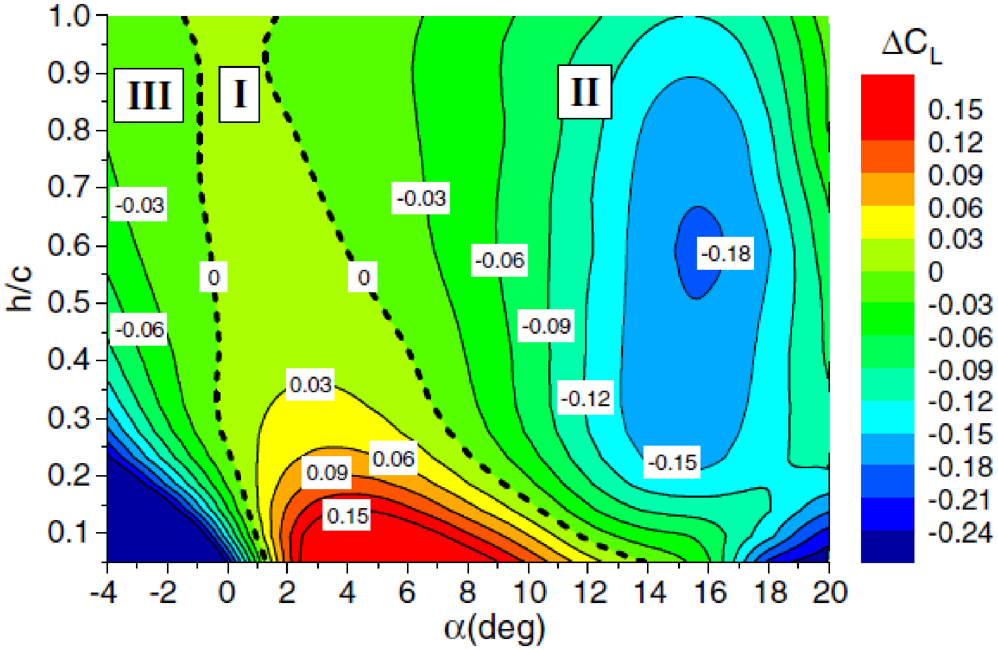

*Figure 1.41 Lift Increment contours for a NACA 4412 Airfoil at Re=6*10^6 and Ma=0.26 (43)*

The three regions outlined in Figure 1.41 hold true for a wide range of airfoils, multi-element airfoils and wings. The location and magnitude of each region will of course depend on the exact configuration under investigation.

1.3.1.2 Multi-Element Airfoil

Much of what has been said on the subject of single-element airfoils in ground effect also holds true for multi-element airfoils. This section will therefore focus primarily on the differences in ground effect behaviour which are introduced by multi-element airfoils.

According to Qu et al (56) the ground effect of a two-element airfoil can identified as having four separate characteristics, which can be summed to get the overall ground effect influence:

1. Each separate element in a multi-element airfoil is influenced by a change in AoA as if it were a single-element airfoil, as has been described in the previous section.
2. The reduction of effective AoA on the upper surface in the ground effect is strengthened by an increase in camber. This is illustrated in Figure 1.6. It was also found that the camber effect reduces the pressure increase on the lower surface, leading to a decrease in lift. This is called the camber effect.
3. The gap located between the main element and a (fowler) flap sees an increase in pressure and reduction of mass flow rate with reduced height above ground. This leads to a reduction of the suction peak on the flap just behind the gap and thus a lift reduction. This is called the gap effect.
4. An increase in flap deflection increases the magnitude of both the camber and the gap effect.

This is summed up in Figure 1.43 which shows the incremental lift change due to ground effect for a NACA 4412 airfoil with a 10°, 15° and 20° Fowler flap (FF) at moderate angle of attack. The further the flap is deflected, the more negative is the lift increment. This is consistent with Recant (57) where a NACA 23012 airfoil with a 40° flap angle was investigated. It was found that in the AoA range of $6° < \alpha < 12°$ the lift of the flapped airfoil continuously decreased as the ground was approached.

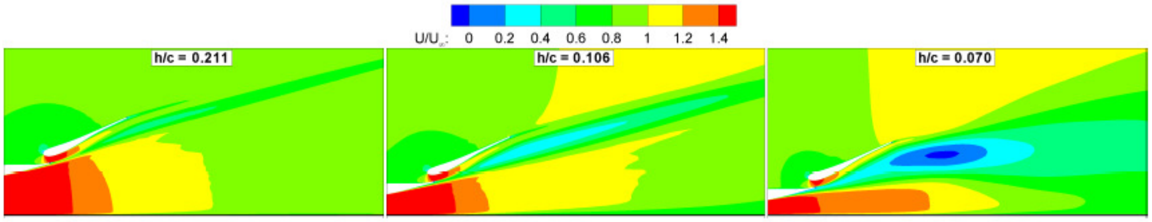

(a) Time-averaged streamwise velocity

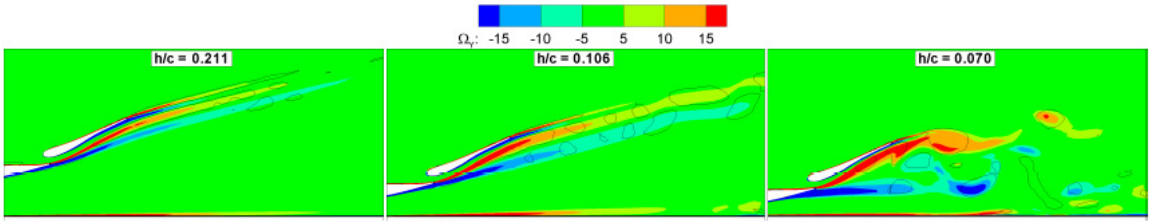

(b) Instantaneous Y vorticity

Figure 1.42 Contour plots from an inverted airfoil $Re=5.8*10^5$ $Ma=0.1$ $\alpha = 4°$ (29)

Ranzenbach (58) et al. found that a flapped airfoil would experience a negative change in lift at a higher height above ground compared to a similar unflapped airfoil. This is shown in Figure 1.44 where the unflapped NACA0015 airfoil is compared to the flapped NACA63$_2$-215 Mod B airfoil. This is further confirmed by Zherihan and Zhang (59) in Figure 1.45. Here it is shown that the low flap angle airfoil can get closer to the ground before experiencing a loss in downforce compared to the high flap angle airfoil due to the earlier onset of separation for this configuration. A discontinuity in the lift curve slope can also be observed which is not replicated by other sources. It was found that as h/c decreases, the boundary layer thickness increases. The wake thickness of the main airfoil element also increases, while the wake of the flap seems independent of height above ground. The wake of the main element increases in thickness with increasing flap deflection. IGE the wake of the main element does not touch the flap and does not immediately merge with the wake from the flap.

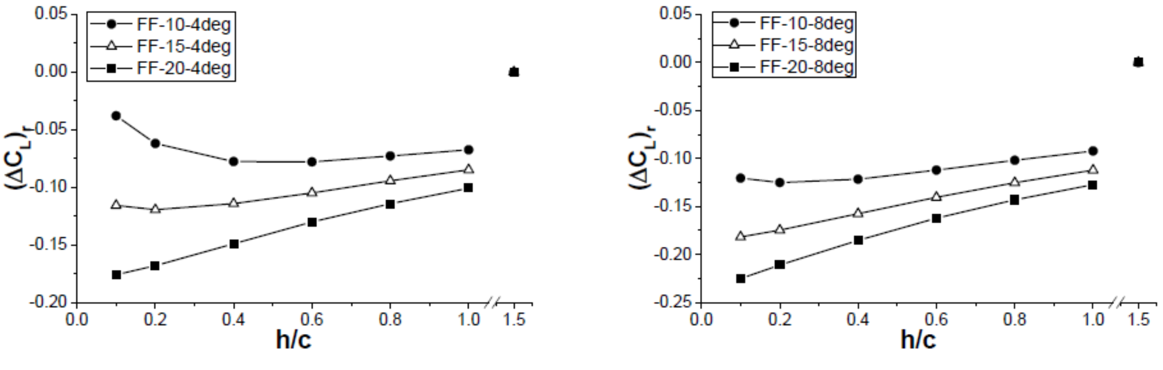

a) α = 4° **b) α = 8°**

Figure 1.43 Incremental lift change of a double-element airfoil in the ground effect $Re = 6*10^6$ $Ma = 0.26$ (56)

This increase in wake of the main element of the airfoil due to ground effect, while the wake of the flap behaves independently of ground effect was also found by Heyder-Bruckner and Zhang (29) using a Detached-Eddy Simulation. The wake is visualized in Figure 1.42, which show that at $\frac{h}{c} = 0.106$ the flow speed of the wake reduces to up to 20% of the free stream velocity. When the height is further reduced to $h/c = 0.070$ there is a significant area of flow reversal visible. In part (b) of Figure 1.42 it can be seen how the wake goes from steady at $h/c = 0.211$, to increased vortex shedding at $\frac{h}{c} = 0.106$, yet the wake from the flap and main airfoil are still clearly distinct. At $h/c = 0.070$ trailing edge separation occurs from the main element, with the wake of the upperside of the main element interacting with the flap, while the wake of the lower side of the airfoil starts interacting with the ground boundary layer.

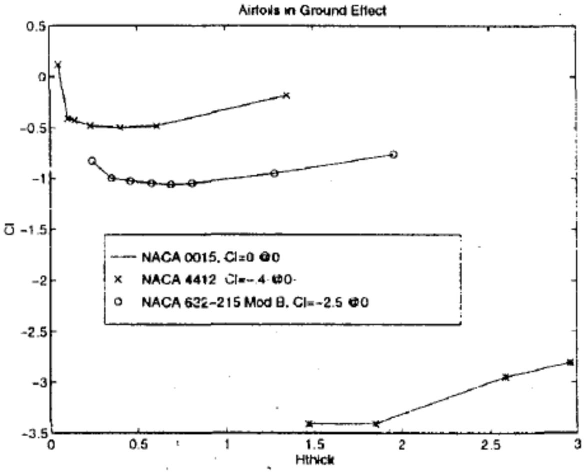

Figure 1.44 Lift Coefficient in ground effect for various airfoils (58)

The trend of increasing lift as the ground is approached, followed by a sudden sharp decrease in lift when the ground is further approached, as seen in Figure 1.45, was also observed by Qu et al (60) for a three-element airfoil for racing car applications. Pant (61) found that a higher downforce was produced by reducing the camber of the main element of a double-element inverted racing airfoil in ground effect.

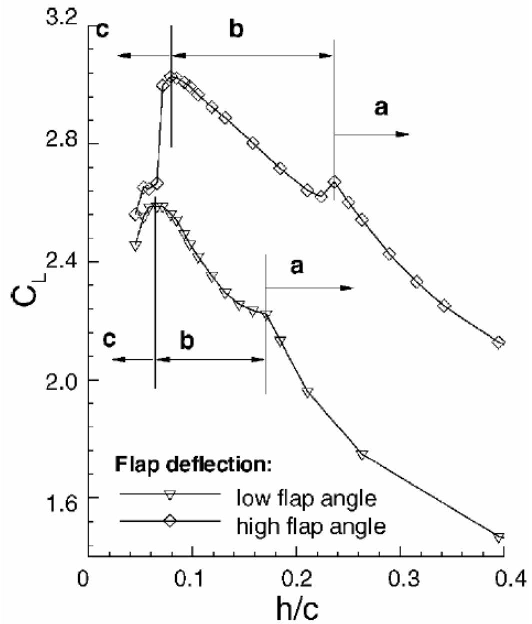

*Figure 1.45 Lift Coefficient for a modified General Aviation-Whitcomb airfoil in ground effect Re=7.35*10^5 Ma=0.1 (59)*

The gap effect is illustrated by Figure 1.46 which shows the decreasing mass-flow rate for both increasing flap deflection and decreasing height above ground. Figure 1.47 shows the pressure distribution for the NACA 4412 with a plain-flap (PF) and a FF for various heights above ground. The gap effect is observable, with the reduction of the flap suction peak for decreasing height above ground. As expected the pressure increase on the lower side of the airfoil is similar to that of a single-element airfoil. The increase of suction peak at the nose of the airfoil with decreasing height above ground is not observable, presumably because of the camber effect reducing the effective AoA.

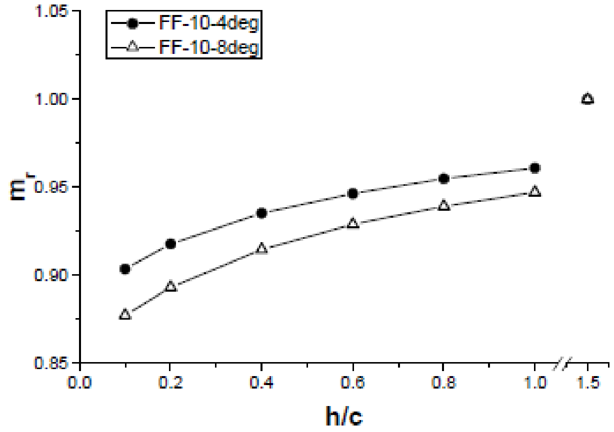

Figure 1.46 Massflow rate through the FF gap (56)

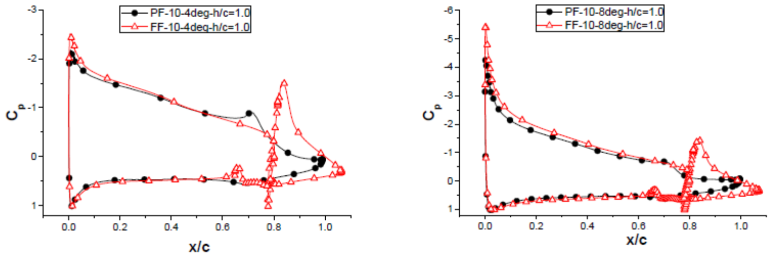

c) α = 4° and h/c = 1.0

d) α = 8° and h/c = 1.0

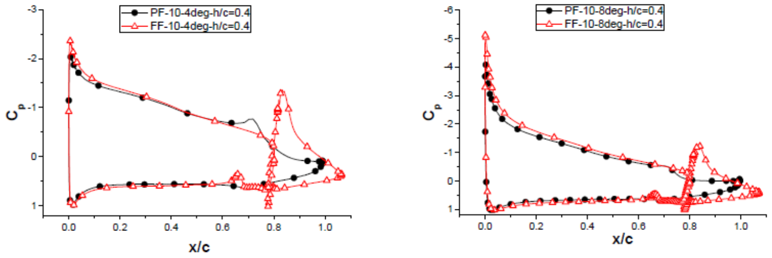

e) α = 4° and h/c = 0.4

f) α = 8° and h/c = 0.4

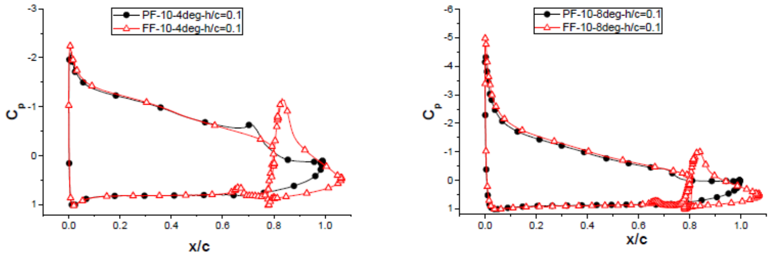

g) α = 4°and h/c = 0.1

h) α = 8° and h/c = 0.1

*Figure 1.47 Pressure Distribution around a flapped NACA 4412 airfoil in the ground effect Re = 6*10^6 Ma =0.26 (56)*

Figure 1.48 and Figure 1.49 show the experimental pressure distributions for the low and high flap angle case respectively, the lift curve of these is shown in Figure 1.45. For both cases a strong increase in suction can be observed as the ground is approached, with the overall distribution shape not changing significantly. It is evident that the suction peak located on the main element is influenced more significantly by the ground effect compared to the suction peak at the nose of the flap. For example in the low flap case the main element peak increases from $c_p \approx -2.6$ at $\frac{h}{c} = 1.97$ to a maximum of $c_p \approx -8.5$ at $h/c = 0.053$, while the suction peak at the flap goes from $c_p \approx -0.9$ to $c_p \approx -2.4$. This can be seen as evidence of the gap effect.

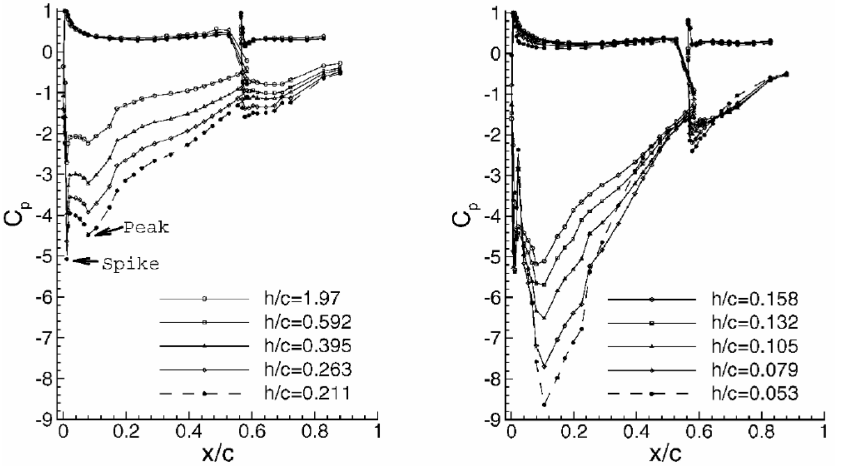

*Figure 1.48 Experimental pressure distribution for a modified General Aviation-Whitcomb airfoil with low flap angle in ground effect Re=7.35*10^5 Ma=0.1 $\alpha = 14.1°$ (59)*

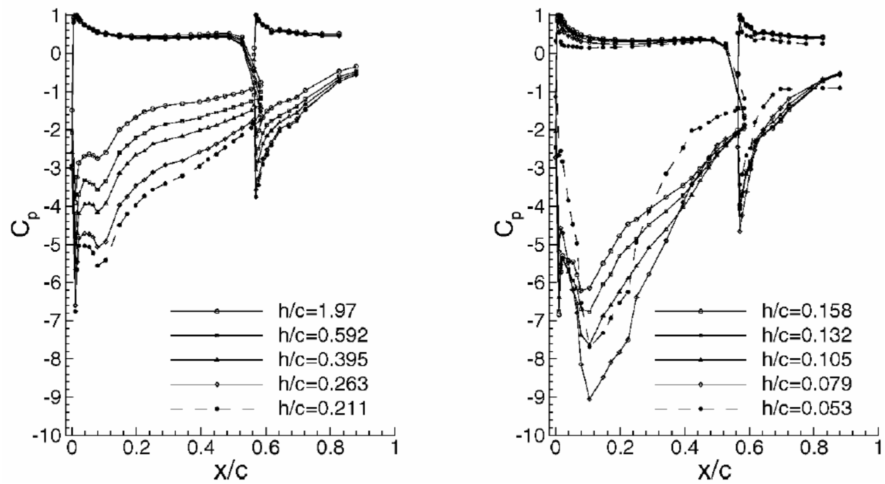

*Figure 1.49 Experimental pressure distribution for a modified General Aviation-Whitcomb airfoil with high flap angle in ground effect Re=7.35*10^5 Ma=0.1 $\alpha = 14.1°$ (59)*

Suguru Hase (62) investigated the ground effect on three 12% thickness airfoils, the NACA0012, NACA6212 and the NACA6712 respectively. The latter two airfoils both have 6% camber, but the NACA6212 is front loaded, while the NACA6712 is rear loaded, which is similar to adding more flap deflection. The measurements shown in Figure 1.50 indicated that the rear loaded NACA6712 performs worse IGE compared to the other two airfoils. The reason for this is explained in Figure 1.51. In the front loaded case, the mirrored vortex can influence the rear of the airfoil, since the original vortex is located near the front, thus the lift can be increased by the mirror vortex. With a rear loaded airfoil, the vortex is located near the rear, so the front of the airfoil is influenced by the mirrored vortex. This causes a lift decrease due to the direction in which the vortex acts. Hase and Eitelberg have determined that the limiting case for the lift of a front loaded airfoil is given by:

$$L = \rho u \, \Gamma_\infty \left(1 + \frac{1}{1 + 2\,\frac{h^2}{c^2}} \right) \qquad (equation\ 1.24)$$

Which in the case of $h \to 0$ yields double the free stream lift. The limiting case for the rear loaded airfoil is given by:

$$L = \rho u \, \Gamma_\infty \, \left(1 - \frac{c - x}{2h} \sin\beta \right) \qquad (equation\ 1.25)$$

Here $c - x$ is the distance of the circulating vortex to the trailing edge and β is the flow direction at the trailing edge. In this rear loaded case the lift decreases as the ground is approached. The lift of a real airfoil will be somewhere in between these two limiting cases. As flaps are selected, the airfoil becomes more rear loaded and thus in general performs worse in ground effect.

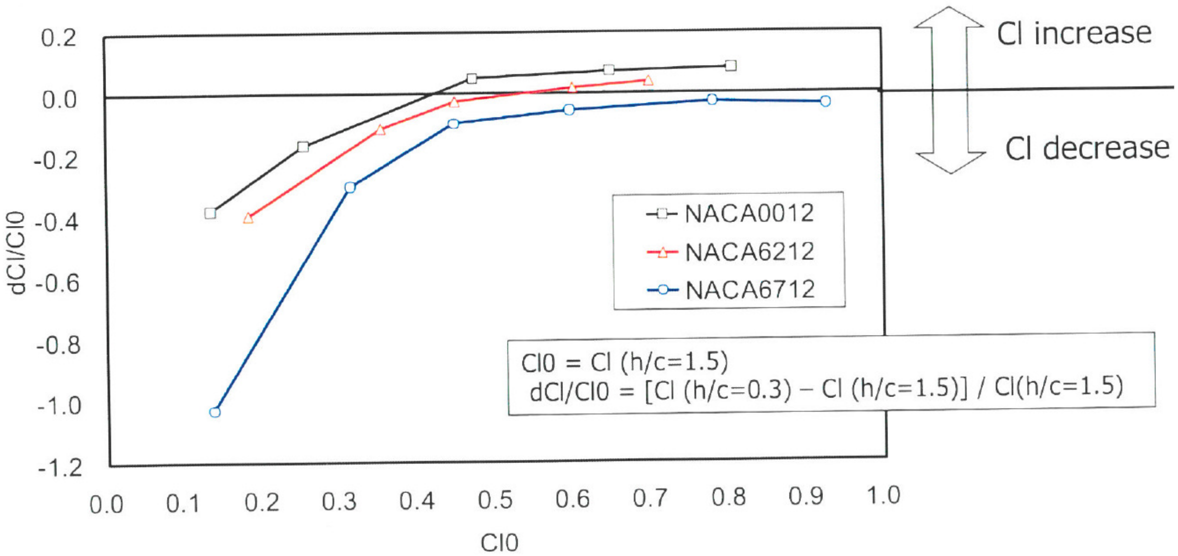

Figure 1.50 Lift change for front, neutral and rear loaded airfoil in ground effect (62)

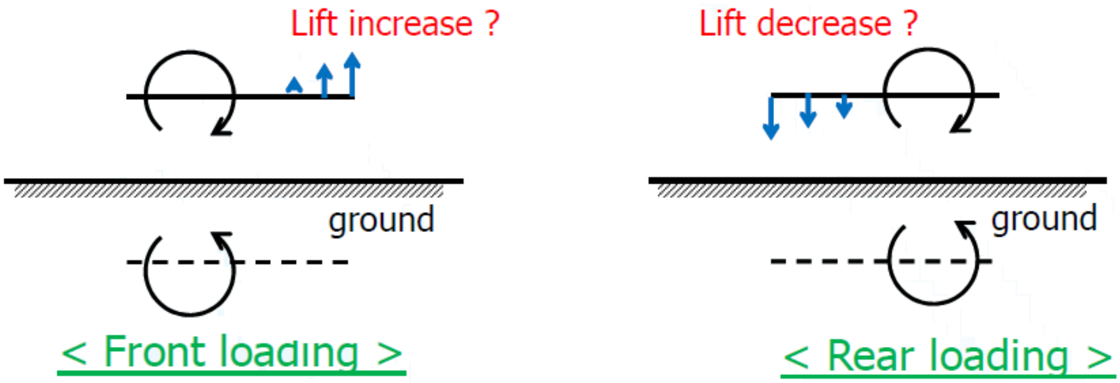

Figure 1.51 Front and rear loaded airfoils in ground effect (62)

1.3.1.3 Span Dominated Lift in Ground Effect

The principal change when evaluating the flow over a finite instead of an infinite wing is the introduction of the wing tip vortex and the accompanying change to induced drag (6). For that reason the wing tip vortex has been the main focus of investigation for the span dominated ground effect in literature (63). Han and Cho (64) found that the wing tip vortex downward movement behind the wing is hindered by the ground and that as a consequence the flow is forced outward in spanwise direction. An increase in wing loading, which OGE results in a more downward trajectory of the wing tip vortex results IGE in a trajectory further outward in spanwise direction. Qu et al. (65) expanded on this research by concluding that a regular wing in ground effect can be divided into two parts in spanwise direction: The inner part which can be viewed as quasi 2D and which behaves as an airfoil in ground effect, the second part is located at the wingtip where 3D effects dominate and the lift decreases IGE. Qu et al. confirmed the conclusion of Han and Cho that the wing tip vortex moves outward in spanwise direction due to ground effect, which is shown in Figure 1.52. They also found that the tip vortex rebounds from the ground due to a secondary vortex which is induced in the ground boundary layer. The change in location of the vortex in vertical direction is shown in Figure 1.53. The strength of the near-field wingtip vortex along the flow direction is partially dependent on the strength and interaction with the secondary vortex from the ground boundary layer.

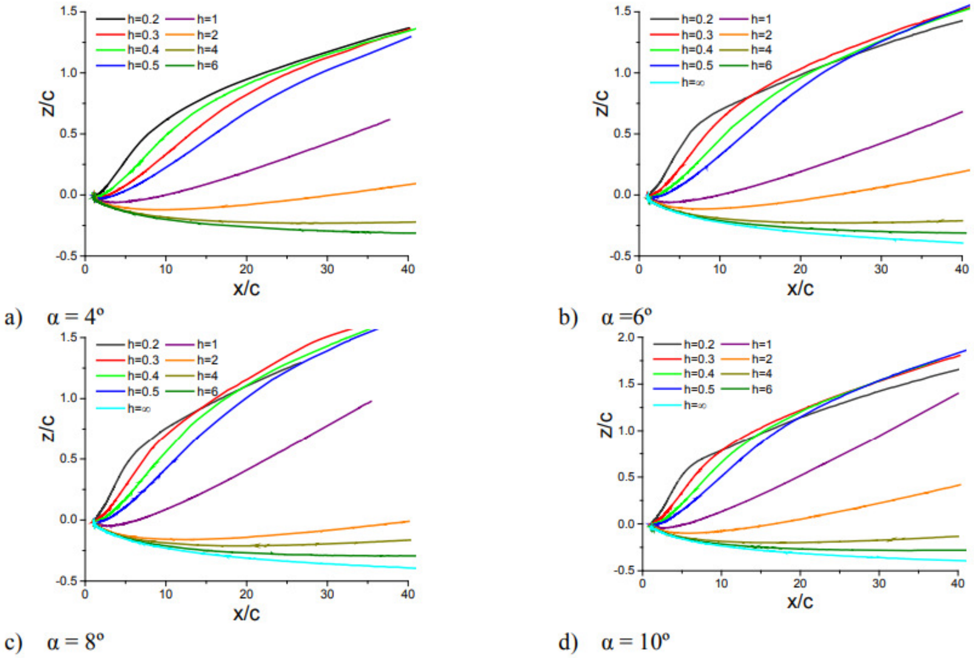

a) α = 4°

b) α =6°

c) α = 8°

d) α = 10°

Figure 1.52 Spanwise location of the wingtip vortex for a rectangular wing in ground effect (65)

A brief overview of the results of a numerical study on a multi-element, rectangular wing from Deng et al. (63) will now be presented. This is meant as an example of how a wing in ground effect can behave in terms of lift. The results are obtained using the RANS equations and the SA turbulence model using the ANSYS FLUENT solver. The change in lift due to ground effect is shown in Figure 1.54. The slat sees a small increase in lift due to the ground effect, while the main wing and flap lose lift in the ground effect. The lift loss of the flap is relatively more significant than the wing. The spanwise lift distribution due to ground effect is shown in Figure 1.55. It can clearly be seen that the lift loss due to ground effect is most significant near the wing tip, especially when very close to the ground at $h/c = 0.1$. The trend in lift distribution does not change IGE. Finally, the pressure distribution at two locations of the wing tip (the Z axis lies in spanwise direction) is shown in Figure 1.56. The spanwise trajectory for the wing tip vortex follows a similar trend as the trend depicted in Figure 1.52.

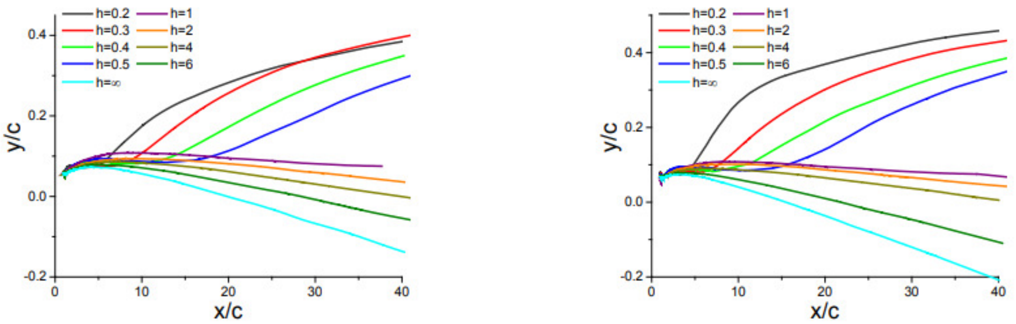

a) for α = 4°

b) α =6°

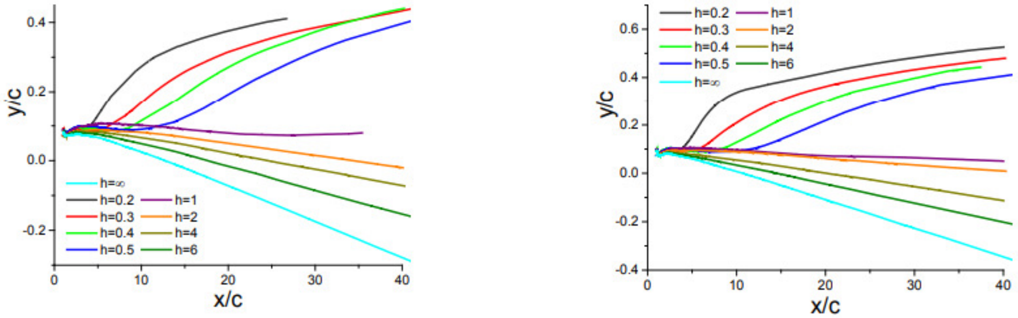

c) α = 8°

d) α = 10°

Figure 1.53 Vertical location of the wingtip vortex for a rectangular wing in ground effect (65)

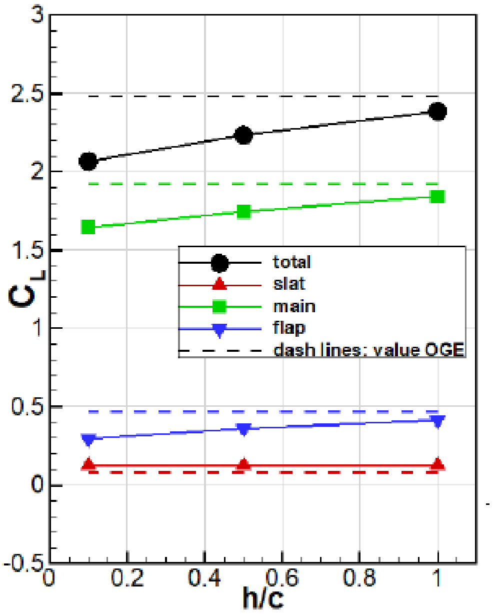

*Figure 1.54 Lift in ground effect for a rectangular multi-element wing Re = 9*10^6 Ma=0.2 $\alpha = 10°$ (63)*

The influence of the fuselage was investigated in a further study by Deng et al. (66) in 2017. In the author's own words, "A complex 3D wing body configuration in ground effect has never been analysed in the aerodynamics literature to date". A reference DLR-F6 wing body was studied numerically at a low AoA of $0° \leq \alpha \leq 1.5°$ for a low Reynolds number Re=7*10^5. The RANS equations were solved using ANASYS FLUENT and both the SA and SST k-ω model were used. After comparison with reference data OGE the choice was made to use SA for the ground effect study.

At low AoA the lift increased in ground effect, which is expected considering the prior literature. The spanwise trajectory of the wingtip vortex shifted more outward due to the influence of ground effect. The vorticity contours IGE and OGE are visualized in Figure 1.57 and Figure 1.58. Qualitatively it can be seen that the vorticity contours become flatter and broader IGE compared to OGE.

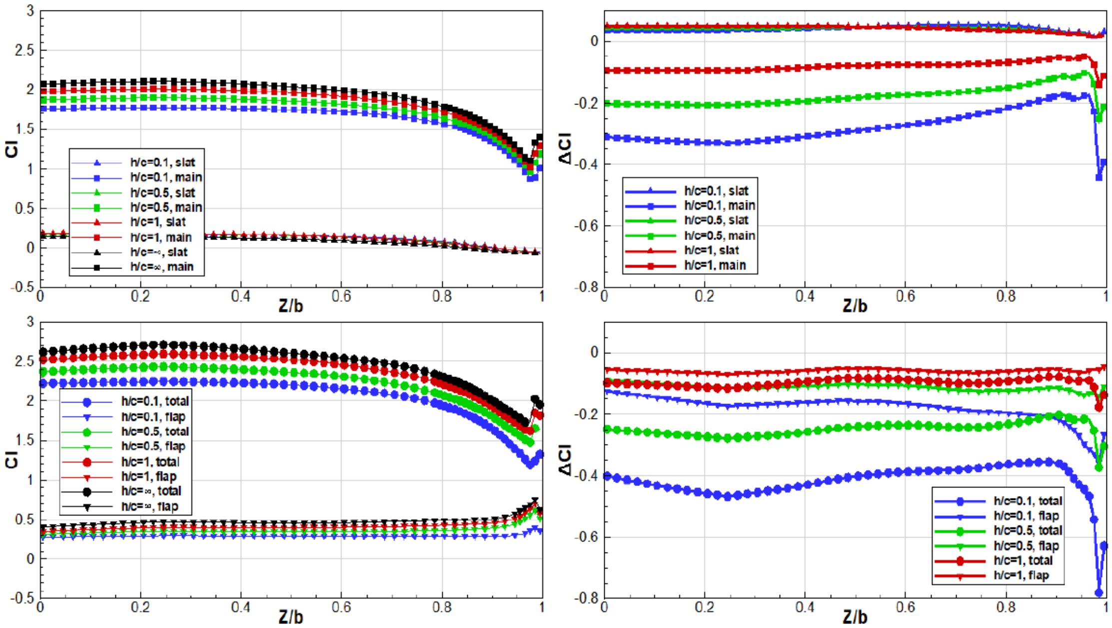

Figure 1.55 Spanwise lift distribution in ground effect for a rectangular multi-element wing Re = $9*10^6$ Ma=0.2 α = 10° (63)

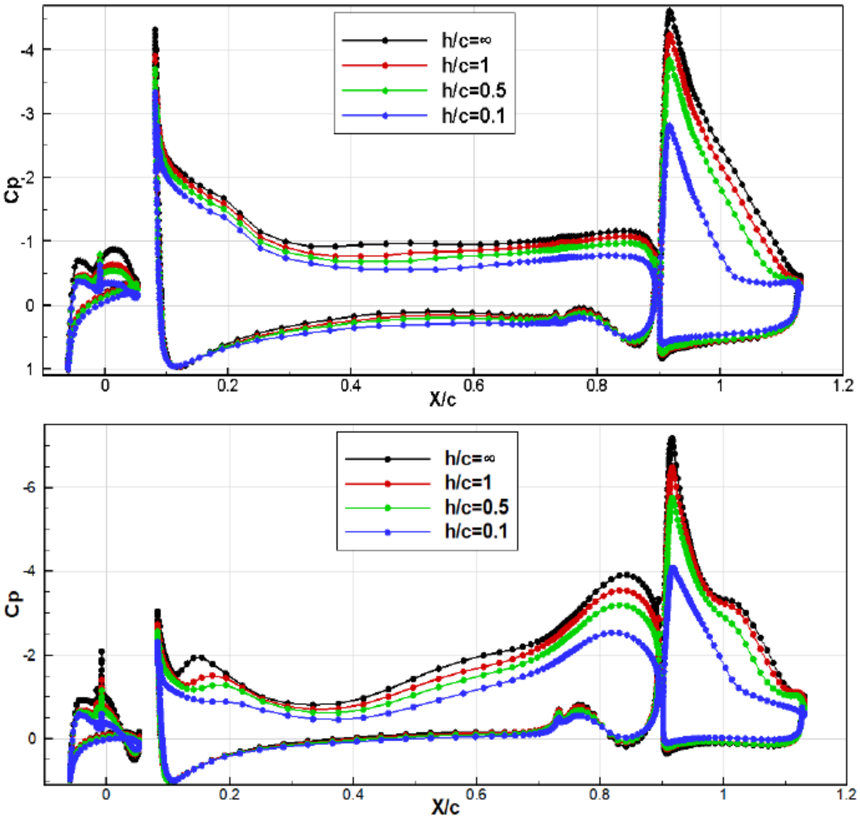

Figure 1.56 Pressure distribution lift distribution in ground effect for a rectangular multi-element wing at Z/b = 0.96 (top) and Z/b=0.99 (bottom) Re = $9*10^6$ Ma=0.2 α = 10° (63)

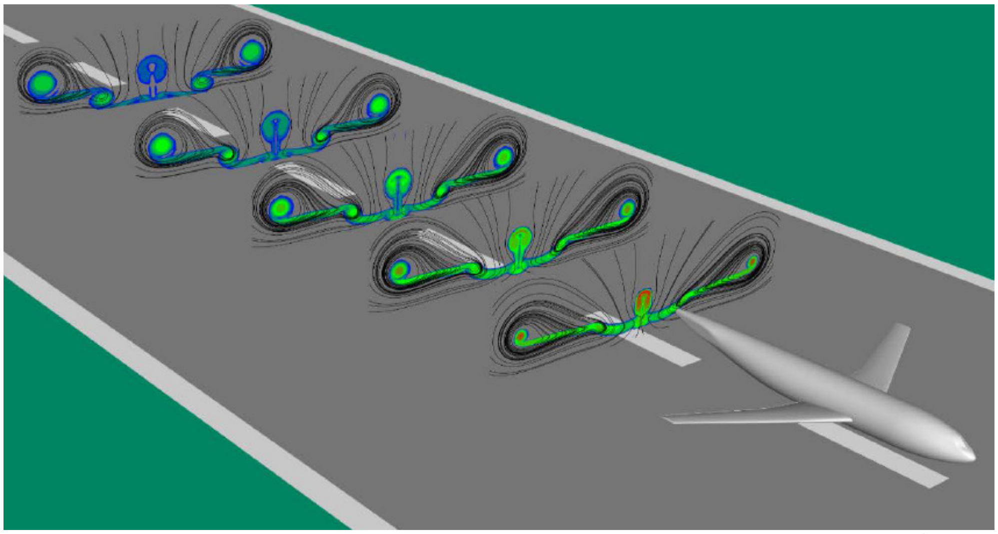

*Figure 1.57 Vorticity contours IGE behind a DLR-F6 Wing-body Re=7*10^5 Ma =0.175* $\boldsymbol{\alpha} = \mathbf{1.23°}\ \frac{\boldsymbol{h}}{\boldsymbol{c}} = \mathbf{0.5}$ *(66)*

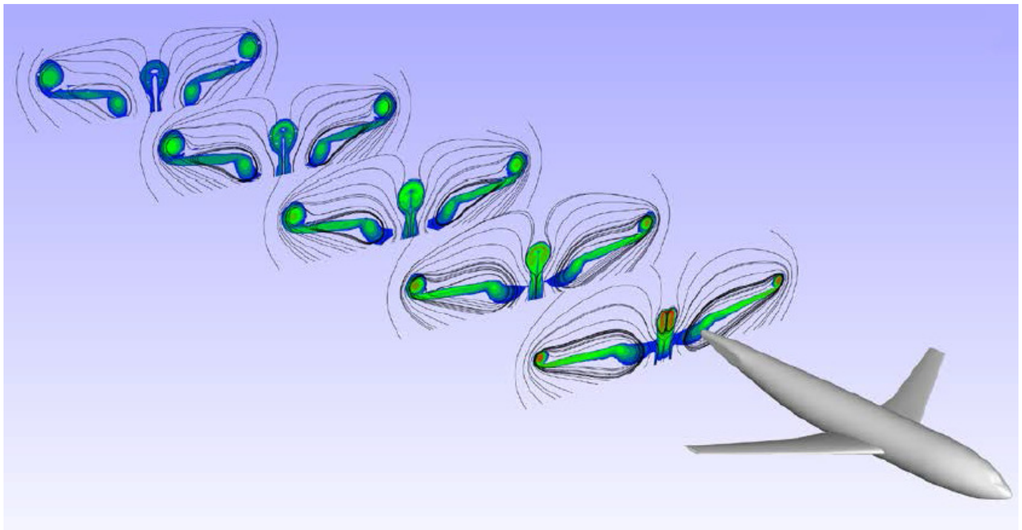

*Figure 1.58 Vorticity contours OGE behind a DLR-F6 Wing-body Re=7*10^5 Ma =0.175* $\alpha = 1.23°$ *(66)*

Van Muijden (67) investigated a crash of a Gulfstream G650 test aircraft making an un-commanded roll after stalling the right wing in close proximity to the ground (68). The stall AoA IGE was overestimated during the development phase of this aircraft. Thus, the pilots could exceed the safe AoA during take-off without any visual or auditory feedback from the on-board safety systems.

To investigate this phenomenon, Van Muijden performed a numerical simulation of a take-off run at conditions similar to those that occurred at the crash. The airfoil was an NLR 7301 and the wing resembled the planform of a small commercial aircraft. The Reynolds number reflected take-off conditions for a full-scale aircraft Re = 16.5*10^6, which is high compared to the other literature discussed in this chapter. This research also stands out for being one of the only numerical 3D RANS studies at high to very high AoA.

The lift curve for this configuration is shown in Figure 1.59. It can be seen that both the maximum lift coefficient decreases as well as the stall angle. OGE the maximum lift occurs at 19.5°, while at 4 meter above the ground the wing already stalls at 18°. The maximum lift coefficient is reduced by approximately 10%.

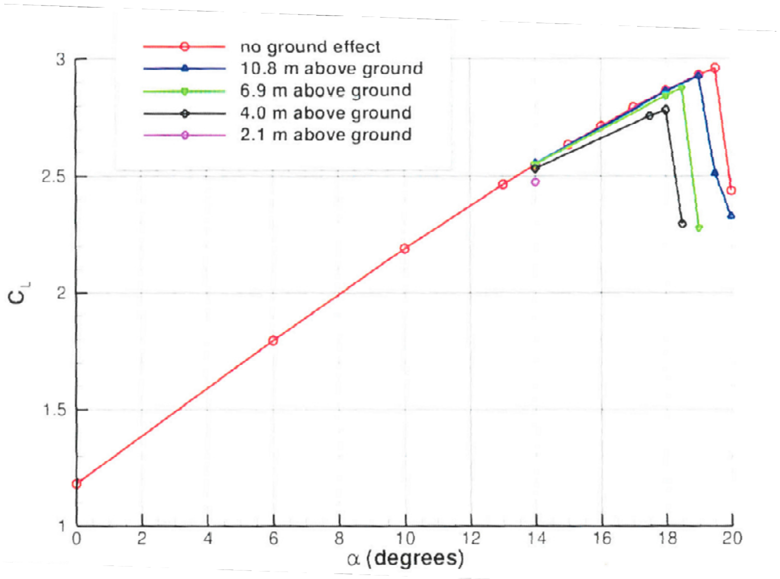

*Figure 1.59 Lift curve for an NLR 7301 Airfoil based wing Re = 16.5*10^6 Ma = 0.185 (67)*

Flaig (69) reported on the results of a test campaign of the ground effect around an Airbus A320 aircraft in a windtunnel with moving ground. Figure 1.60 shows the change in lift due to ground for three flap settings. The labels take-off II, take-off III and landing correspond to a flap setting of 10°, 20° and 40° respectively. It can be seen that an *increase* in flap deflection leads to a *reduction* of the lift increase of the ground effect. The point where maximum lift occurs at a lower AoA for an increase in flap deflection. The principal physical explanations for the observed lift changes are given as increased pressure at the lower side of the airfoil and a reduction in suction at the upper side of the airfoil.

The experiments on the A320 were done with Through-Flow-Nacelles (TFN) engines, equivalent to flight idle conditions and Turbine Powered Simulators (TPS) which could be used to simulate powered jets. This was used to evaluate the influence of engine propulsion on the ground effect. It was found that the lift is reduced when the TPS are used, as shown in Figure 1.61. This had two causes, the first that the flight-idle TFN nacelle creates a blockage effect, forcing air in between the fuselage and the nacelle causing a pressure increase. When TPS is used, the mass-flow at the nacelle becomes much higher due to turbine suction and thus the blockage effect is less significant. The second reason is that high velocity air exiting the turbine will decrease the pressure on the lower side of the airfoil and thus reduce lift. Finally it should be noted that the experiments were carried out at a free stream velocity of V = 70 m/s, while the maximum velocity of the moving belt was only 45 m/s (70). This will negatively affect the accuracy of the results.

Chawla et al. (71) performed a large windtunnel investigation on a low aspect ratio wing containing a 20% chord full span flap in the ground effect. The AoA ranged from 0° to 25° and the flap deflection angle was varied between 0° and 30°. The minimum height above ground was $\frac{h}{c} = 0.25$, which is relatively high compared to some other studies discussed here. End plates were installed at the wing which improved the lift in ground effect up to 17% at $\alpha = 5°$. A full lift-curve was shown using endplates. In this case the lift curve became steeper and the maximum lift coefficient increased due to ground effect at 0° flap deflection. It is unknown whether the increase in $C_{L_{max}}$ also occurs when the endplates at the wingtips are removed.

Weng et al. (72) analysed the flight-data recorder data of a twin-jet transport aircraft in ground effect using a fuzzy logic modelling technique. They found that the normal force coefficient increased from $C_{N_{OGE}} = 1.31$ to $C_{N_{IGE}} = 1.42$ at $\alpha = 3°$.

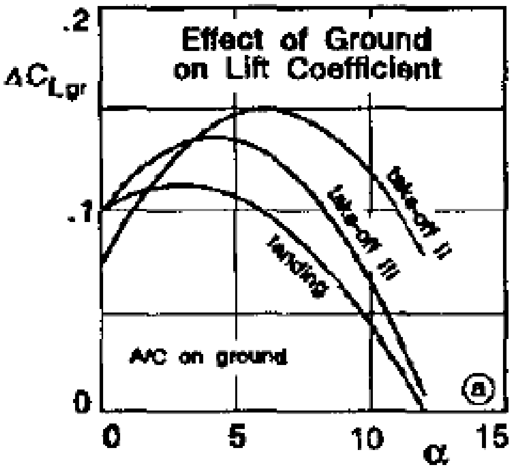

*Figure 1.60 Experimental change in lift coefficient for an Airbus A320 IGE Re=2.6*10⁶ Ma=0.2 (69)*

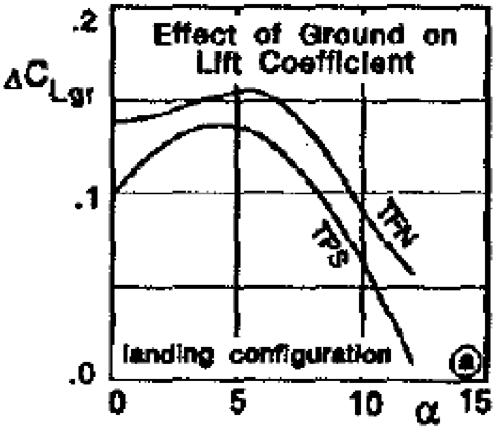

*Figure 1.61 Change in Lift due to different engine settings for an A320 IGE Re=2.6*10⁶ Ma=0.2 (69)*

The effects of sweep were investigated in two papers by NASA. Furlong and Bollech (13) studied the effects of sweep in ground effect for a 42° swept back wing with Reynolds numbers of up to 6.8*10^6 for a flapped and unflapped configuration. For the lift it was concluded that the increased slope of the lift-curve was comparable to the lift-curve slope of an unswept wing with flaps neutral. However, at high AoA it was found that the lift decrease for the flapped swept wing was far more severe compared to the flaps neutral swept wing. It was found that the maximum lift of the flap neutral wing was higher compared to an unswept flap neutral wing, while the maximum lift for the flapped wing was comparable to that of an unswept wing in ground effect. In other words, flap deflection seemed to negate the beneficial effects of sweep in ground effect. However this is an older study from 1955 and it would be beneficial to recreate these experiments with modern wind-tunnel practices such as a moving belt and modern numerical methods.

Curry et al. (73) investigated the ground effect on a forward swept X-29A research airplane by means of a test flight. Full scale investigation into ground effect poses many challenges, such as the fact that pilot control surface input, throttle adjustments and atmospheric turbulence are of a comparable order of magnitude as the ground effect and can thus easily render the data of a run useless. Yet these inputs are unavoidable in order to safeguard pilot safety. For the same reason very low heights above ground which are possible in the windtunnel and numerical simulation, have to be avoided in full scale test flight. A more thorough discussion on the challenges of full scale test flight in the ground effect is provided by Curry and Owens (74) and Baker et al (75).

The test flights of the X29-A showed a consistent lift increase of 17% at the moment of touchdown. This is less than predicted both by windtunnel results and inviscid panel methods. The authors attribute this discrepancy to the fact that both of these simulated the static ground effect, while the X29-A was continuously sinking and thus experienced dynamic ground effect. The dynamic ground effect will be further discussed in chapter 1.3.4. No comparison with unswept wings was made by the authors.

Katz and Levin (76) investigated the ground effect of a delta wing. The main conclusion reached was that a positive lift increase seen for other configurations was also found for a delta wing. This was corroborated two decades later by Curry and Owens (74) where comparisons were made between full-scale test flights, windtunnel measurements and numerical panel methods on the behaviour of a delta wing Tupolev TU-144 supersonic transport aircraft in ground effect. A clear increase in lift close to the ground was observed using all three methods. In contrast to the findings of the X29-A study discussed above, in this case of the steady flight tests (as opposed to dynamic flight tests) showed a slightly higher lift increase compared to wind tunnel testing and panel methods, with the caveat that these flight tests yielded poor quality data. In contrast the dynamic ground effect flight tests were of good quality and showed a good agreement with the steady-state windtunnel and numerical results.

Traub (55) compared a wing of aspect ratio (AR) of 3.46 with a wing with AR = 5.18. The high AR wing experienced the highest performance increase IGE, with the 78.7% lift over drag ratio (L/D) being an increase compared to a 70.9% increase for the lower AR wing.

The results from these different studies can be summed up as follows: For a 3D wing the change in lift over the wing can be separated into two distinct areas: inboard of the wingtip, the wing behaves as if it is quasi-2D and thus 2D effects dominate. This means that the lift over a wing in ground effect increases at low to moderate angles of attack and in many cases decreases at high AoA. Most studies show a reduction in the maximum lift coefficient. An increase in flap deflection causes the negative change in lift to occur at a lower AoA.
Only in the region of the wingtip do 3D effects start to dominate. The wingtip vortex moves both more upwards and outwards compared to OGE and interacts with the boundary layer of the ground. As the aspect ratio of the wing increases, the proportion of the wing which is affected by the wingtip vortex decreases and thus the aerodynamic performance in the ground effect improves with increasing AR. The behaviour of a wing in ground effect is not significantly influenced by wing sweep.

1.3.2 Drag Impact

In this subchapter the change in drag due to ground effect will be discussed. Similar to the case with lift, a clear distinction can be made between the 2D chord dominated ground effect and the 3D span dominated ground effect. Drag in ground effect is less extensively covered in literature compared to lift, so therefore this subchapter will be less detailed compared to the previous one. Many of the sources used in the previous chapter will be reused here.

1.3.2.1 Chord Dominated Drag in Ground effect

Many sources (46) (48) (49) (50) (41) (58) (59) (60) (77) (78) report an increase in airfoil drag due to ground effect, but the magnitude of drag increase varies significantly between different studies.

A typical example of drag in ground effect is given in Figure 1.62 with an approximately of 10% maximum increase in drag. A significant increase in drag is usually only observed in the region of $\frac{h}{c} < 0.3$. The drag increase is more significant for higher AoA. Barber and Hall (39) report a slight decrease in drag at $\frac{h}{c} > 0.3$ before a 15% increase in drag occurring as the ground clearance is further reduced. Ahmed et al. (50) found that the increase in drag could mainly be attributed to an increase in pressure drag on the lower airfoil, rather than skin friction drag. Zhang and Zherihan (59) report that the drag increase becomes more significant for higher flap deflections. A sharp drag increase is observed as the wake separates at very low height above ground. A 40% drag increase was found for the high flap deflection case and up to 80% for the low flap angle case, as shown in Figure 1.63. The lift curve of this configuration was discussed in subchapter 1.3.1.2 and shown in Figure 1.45.

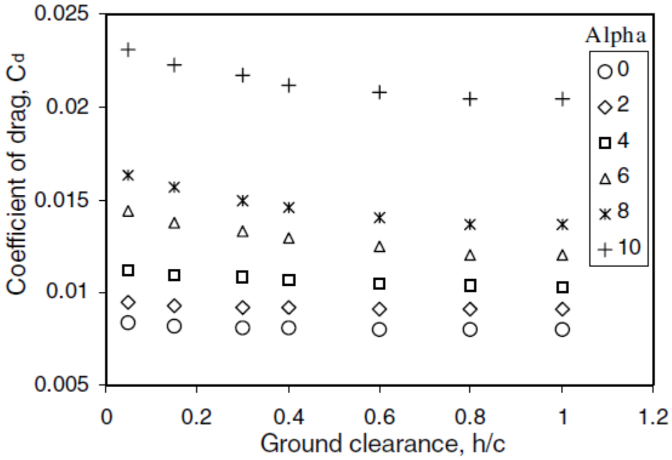

Figure 1.62 Drag due to ground effect for a NACA4412 airfoil $Re=3*10^5$ $Ma=0.1$ $\alpha = 4°$ (50)

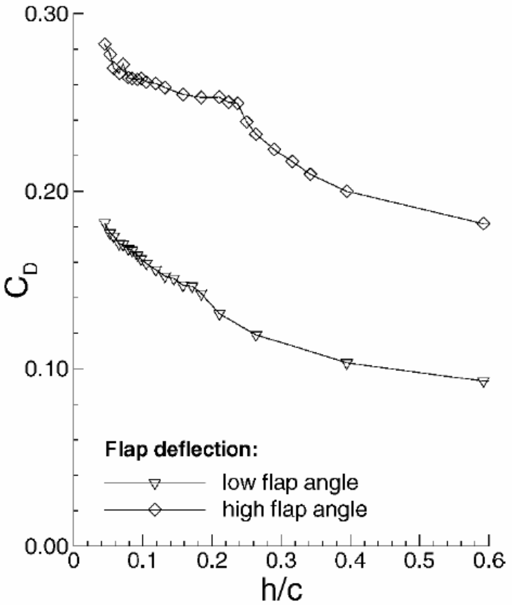

Figure 1.63 Drag for a modified General Aviation-Whitcomb airfoil in ground effect $Re=7.35*10^5$ $Ma=0.1$ (59)

In a separate study Zhang and Zherihan (79) found that drag also increases with flap deflection for a Gurney flap. Qu et al. (60) found that drag of a three-element inverted racing airfoil would increase by up to 300% as the height above ground was reduced. The L/D reduced from approximately 45 OGE to 15 very close to the ground, yet this airfoil still performed better than a comparable double-element airfoil IGE with 50% increase in lift and a 20% reduction in drag. Finally Van Muijden (67) reported a decrease in drag for reduced height above ground for a flapped airfoil at $\alpha = 14°$. However, no further details of this study are known so it is difficult to analyse why his results differ substantially from most of the literature. Pátek et al. (47) also report a drag reduction around a NACA 0012 airfoil for a wide range of AoA as obtained experimentally. However it should be noted that these experiments were done with a ground fixed boundary condition, which is the least accurate boundary condition. Figure 1.18 shows that the use of this boundary condition can indeed predict a drag decrease, while all the other, more correct boundary conditions predict an increase in drag as the ground is approached.

1.3.2.2 Span Dominated Drag in Ground Effect

While the drag increases in most cases for airfoils in the ground effect, this changes for the 3D case. One of the major benefits of flying in ground effect is the reduction of the induced downwash angle and thus a reduction in induced drag. This induced drag reduction is usually dominant compared to the airfoil drag increase, leading to an overall drag benefit of the wing.

An example of this is given by Deng et al (63) and can be seen in Figure 1.64. Here the drag is split in to the separate elements on the wing, the flap, slats and main wing. In this case the reduction in drag IGE is mostly apparent for the flap and to a lesser extent the slat. The drag distribution in spanwise direction is shown in Figure 1.65. The pressure distribution belonging to this situation at several locations is shown in Figure 1.56. Further details of the study are also provided there. The spanwise drag distribution can be split into two sections, similar as for the lift in Figure 1.55. There is a linear part from the wing root until approximately 90% of the span. Here a semi-monotone drag reduction can be seen. At the wing tip there is a sharp increase in drag reduction IGE, especially on the flap.
The drag of a DLR-6 wing-body model was investigated at low AoA in two separate studies by Deng et al. (66) (80). A small drag reduction of 2-4% was observed as the ground clearance decreased for $\alpha = 1.23°$. This small drag change can be expected at such a low AoA. Unfortunately higher AoA were not investigated in this study.

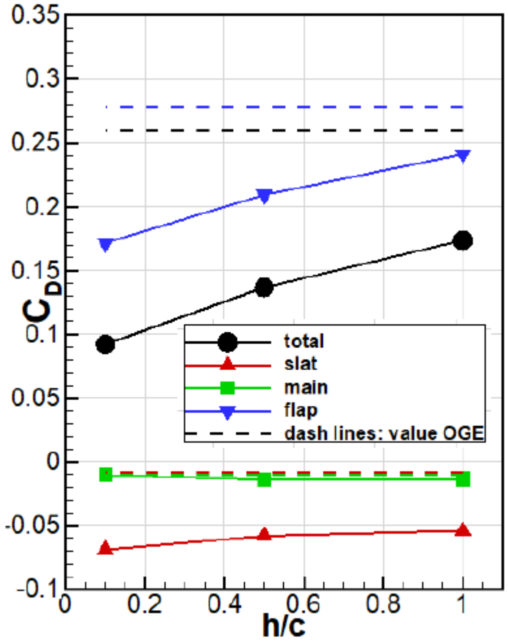

Figure 1.64 Drag in ground effect for a rectangular multi-element wing Re = 9*10^6 Ma=0.2 $\alpha = 10°$ (63)

Flaig (69) measured the drag of an Airbus A320 in a windtunnel. A significant drag reduction was found over the entire AoA range due to a reduction of the induced drag. Because the induced drag increases for increasing flap deflection, the magnitude of the drag reduction in ground effect is also increased with increasing flap deflection. This is shown in Figure 1.66.

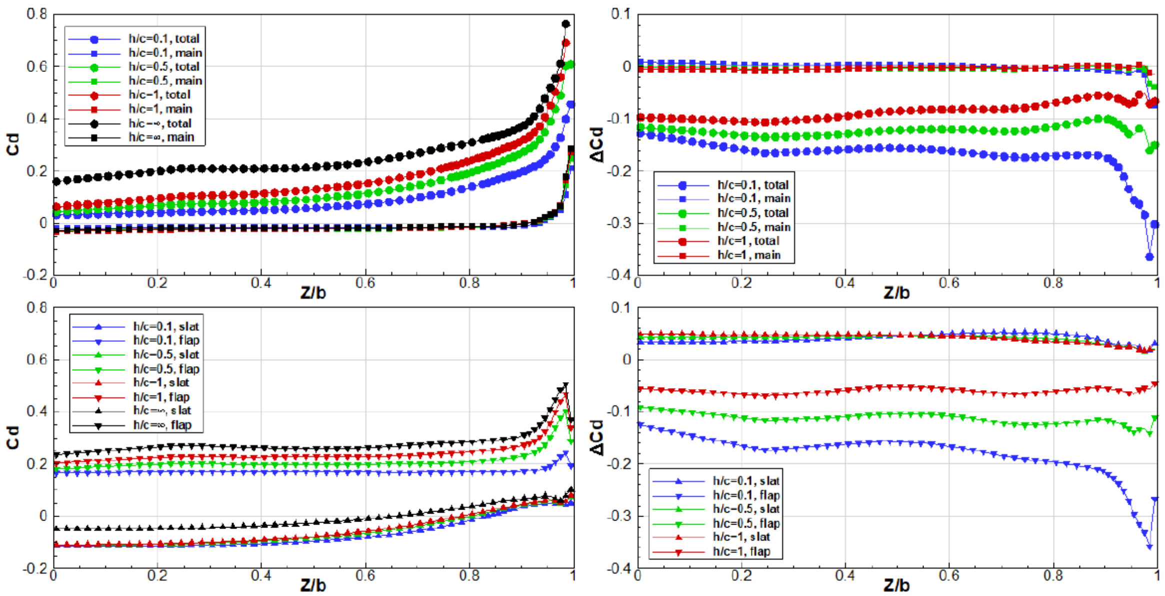

*Figure 1.65 Drag in ground effect in spanwise direction for a rectangular multi-element wing Re = 9*10^6 Ma=0.2 $\alpha = 10°$ (63)*

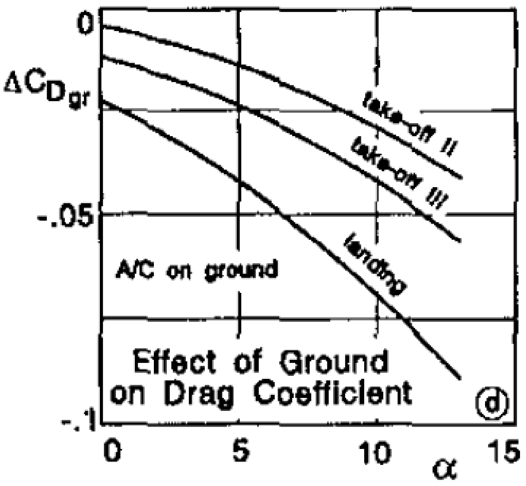

*Figure 1.66 Experimental change in drag due to ground effect for an Airbus A320 IGE Re=2.6*10^6 Ma=0.2 (69)*

The drag of a low-aspect ratio compound wing in ground effect was investigated by Jamei et al (81) at $\alpha = 2°$. The drag coefficient decreased from 0.042 at $h/c = 0.3$ to 0.0377 at $h/c = 0.05$, leading to an L/D increase from 5.6 to 7.6. The trend showed very good agreement with experiments. It was found that drag reduction of 24.7% could be obtained by using a compound wing over a normal rectangular wing IGE. Van Muijden (67) found a decrease in drag of up to 30% for the 3D case.

NASA published several studies (13) (74) on the ground effect for a (full) scale airplanes. The first study cited show that for a 42° sweptback wing the drag in unflapped condition can be improved by up to 20% and is beneficial over the entire AoA range. When a 60° flap deflection is introduced, at low to moderate AoA there is still a benefit of up to 15% reduced drag. At high AoA the drag is increased in ground effect, because of the earlier onset of flow separation in ground effect due to flap deflection, which significantly increases drag.
The second study cited concerns a full-scale testing of a TU 144 supersonic airplane. In this case most flight runs showed an increase in drag of up to 15% as the height above ground was reduced, which is the opposite of what would be expected based on the other studies

cited in this section. There can be three reasons for this. The first is that the landing configuration, high AoA and average of 8° elevon down increases drag in a similar way as to the previous study. A second is simply a problem with the data. The authors say the following: "*The consistency of the lift and pitching moment data is better than that of the drag data, which is expected, because the absolute magnitude of the drag increment caused by ground effect is much smaller than the force increment in the lift axis. Similar results were observed in previous ground-effect flight test studies*". The drag measurements are simply more susceptible to outside influences such as turbulence. The third reason for this discrepancy is that this is a delta-wing with canard configuration, and it is possible that this introduces some unforeseen effect that increases the drag in ground effect.

1.3.2.3 Conclusions

The drag produced by an airfoil tends to increase due to ground effect. This is caused mostly by an increase in pressure drag as a consequence of the modified pressure distribution on the lower side of the airfoil due to ground effect. Only a limited number of studies were found where an airfoil drag decrease was found in ground effect, one of which contained no details on how the calculations were obtained, the other study had used a less accurate boundary condition to simulate ground when compared to most other studies.
When 3D effects are taken into account the drag is generally reduced due to a reduction of the induced AoA and thus a reduction in induced drag. However some (full) scale studies from NASA with the Horizontal Tail Plane (HTP) included showed a drag increase due to ground effect.

1.3.3 Pitching Moment

It was found in section 1.3.1.3 that in some cases the lift decreases in the ground effect for a 3D case. Yet many engineering methods, aircraft databases and pilot's experience indicate a lift increase due to ground effect. One possible explanation for this discrepancy could be that all the studies mentioned implicitly discussed untrimmed wings. If there is a less nose down pitching moment due to ground effect, then for the trimmed condition the negative lift on the HTP can be decreased. Thus the hypothesis is that the aircraft as a whole will experience a lift increase, even if the isolated wing generates reduced lift IGE (67) .

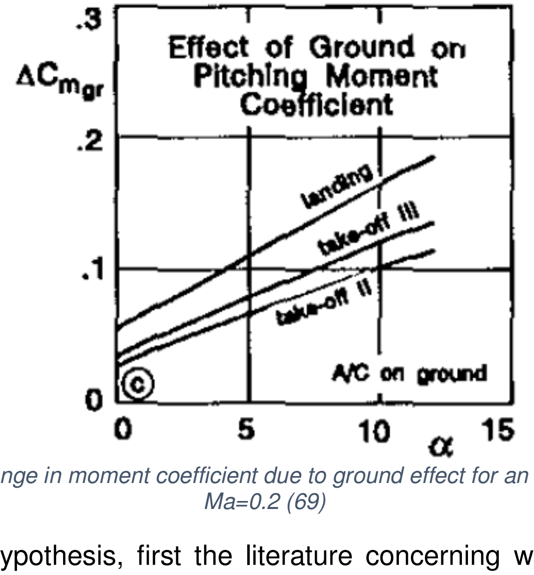

*Figure 1.67 Experimental change in moment coefficient due to ground effect for an Airbus A320 IGE Re=2.6*10^6 Ma=0.2 (69)*

To answer the above hypothesis, first the literature concerning wing-body aircraft will be discussed, since these bear the most resemblance to the real-life scenario. Flaig (69) performed a windtunnel investigation on an Airbus A320 twin-turbojet aircraft, which has been mentioned before in section 1.3.1.3. As shown in Figure 1.67 there is a linear increase in nose-up moment with an increase in AoA, which would require more positive lift from the HTP to compensate. The increase in nose-up moment becomes stronger with higher flap deflection. All this even holds true at high AoA where the increase in lift was already decreasing or even negative, as was seen in Figure 1.60. The change in moment coefficient was caused by the changing pressure distribution over the wing, causing it to become more forward loaded.

Deng et al. (66) investigated the moment coefficient around a DLR-F6 wing body IGE. Further details of this study have been given in section Span Dominated Lift in Ground Effect It can be seen that in this limited AoA range from $0° < \alpha < 1.23°$ there is a small increase in nose-up moment due to ground effect. It is primarily caused by an increase of pitching moment on the fuselage.

A follow up study from Deng et al. (80) used the same model to investigate the increased pitch up moment of the fuselage in ground effect in ground effect. The numerical setup was identical to the one study described above. It was found that a there was a dramatic pressure increase on the nose part of the fuselage due to the ground effect, resulting in a pitch up moment. The change in moment coefficient with ground effect is shown in Figure 1.69, where the strong change in nose up pitching moment is emphasised. It is unclear at this stage if this increased fuselage pitching moment holds true across a wide range of AoA and if it also occurs for similar shaped aircraft, for instance the Airbus A320 discussed previously.
Finally, it was concluded by Deng et al. that that the ground effect seemingly had a small effect on the formation of a laminar separation bubble near the wing-fuselage junction, but this requires further investigation.

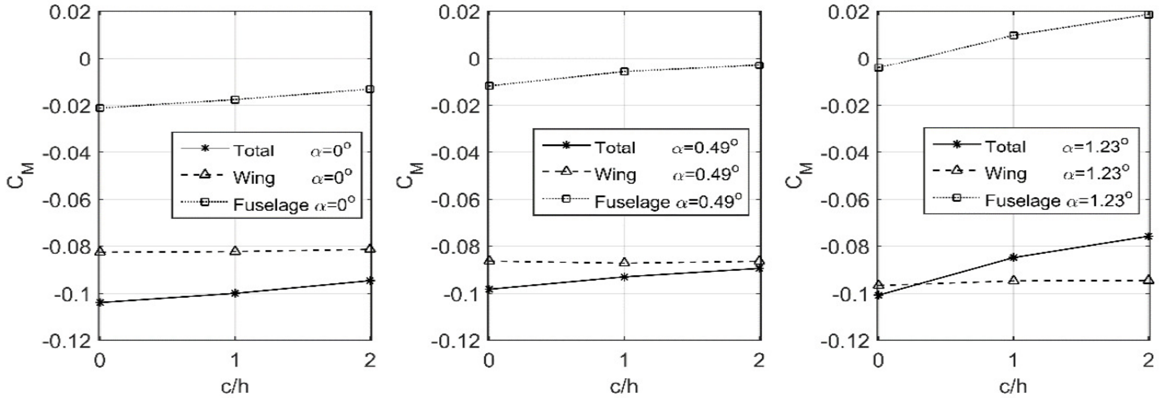

*Figure 1.68 Computational moment coefficient around a DLR-F6 Wing Body IGE Re=7*10^5 Ma =0.175 $\alpha = 1.23°$ (80)*

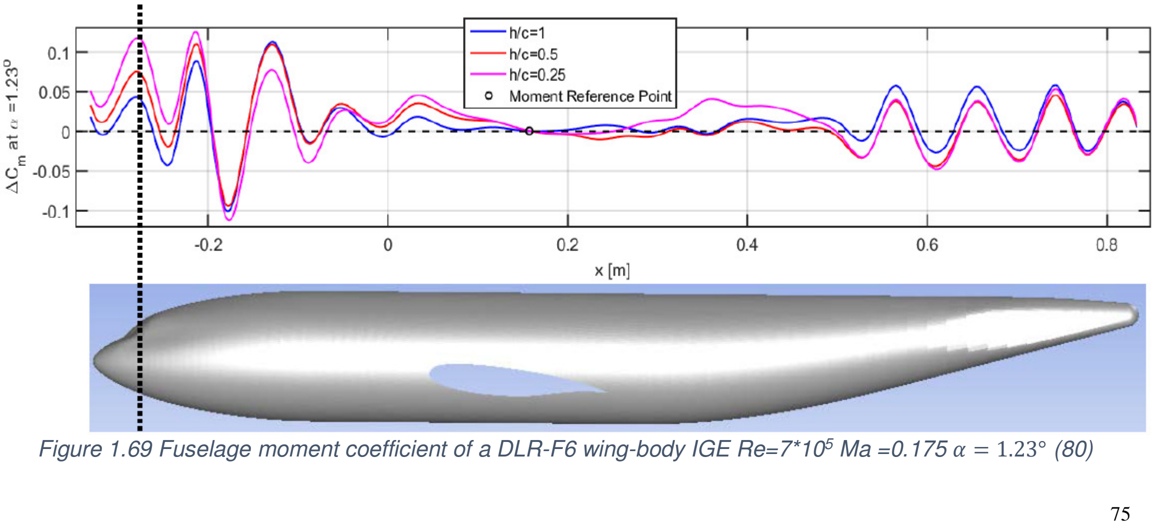

*Figure 1.69 Fuselage moment coefficient of a DLR-F6 wing-body IGE Re=7*10^5 Ma =0.175 $\alpha = 1.23°$ (80)*

Furlong and Bollech (13) found that for a 42° swept back wing there was a small variation in moment coefficient. When the flap settings were neutral the moment coefficient became slightly more negative IGE, while when there was a 60° flap deflection the moment coefficient became slightly more positive. This is consistent with the results of Flaig where the moment coefficient also became more positive with increase in flap deflection.
Van Muijden (67) found that moment coefficient on a wing resembling the wing of a Gulfstream G650 increased from $C_{M_{OGE}} = -0.692$ to $C_{M_{IGE}} = -0.612$ at $\alpha = 14°$.

Full scale flight tests with a Tupolev TU-144 Supersonic aircraft as reported by Curry et al. (74) also investigated the moment coefficient. Unlike the previous studies cited, here the moment coefficient became more negative IGE, going from $C_m \approx -0.02$ to $C_m \approx -0.012$. There was no further investigation into what the cause of the change in moment coefficient was. These measurements are consistent with Katz (76) who found that the pitching moment of a delta-wing decreased due to ground effect.

The chord dominated change in pitching moment due to ground effect has a different trend compared to the span dominated change. Molina and Zhang (51) show a decrease of up to $\Delta C_{m_{IGE_{max}}} = -0.09$. The pitching moment was independent of AoA. Only close to the ground, at $h/c = 0.16$ does C_m start increasing with AoA. This is caused by separation over large parts of the airfoil. Staufenbiel and Schlichting (82) found that the moment coefficient of a Clark-Y airfoil changed from $C_{m_{OGE}} = -0.18$ to $C_{m_{IGE}} = -0.31$ due to a backward shift of the neutral point caused by the increase in pressure on the lower side of the airfoil. Pátek (47) found that the moment coefficient for a NACA0012 airfoil increased IGE for low AoA and decreased at moderate to high AoA. Van Muijden found that the moment coefficient of a NLR 7301 airfoil with flap increased from -0.48 to -0.414. Weng et al. (72) found that the pitching moment of a twin-engine jet aircraft would decrease slightly in the ground effect from 0.055 to -0.051 at $\alpha = 3°$ and 30° flap deflection.

It can be concluded that the pitching moment for a full aircraft configuration does indeed tend to become more nose-up, decreasing the amount of negative lift from the HTP and increasing overall lift IGE. This effect can be caused both by a forward shift of the neutral point, as well as a change in pressure on the fuselage. An increase in flap deflection increases the nose-up shift of the moment coefficient. However it should be noted that not every study found this to be true, in a similar manner to that of the lift in a 3D case which was found to both decrease or increase depending on the exact wing and aircraft configuration.
In general the pitching moment becomes more nose-down when looking at the airfoil in isolation, ignoring span-wise effects due to the changing pressure distribution over the airfoil. However, many studies which discuss the lift and drag ignore the moment coefficient and thus the data is relatively limited and still inconclusive. For instance, the only airfoil study with a flap included in this literature survey actually showed an increase in moment coefficient rather than a decrease. Further research into this area would be interesting.

1.3.4 Dynamic Ground Effect

So far the ground effect has been treated as a purely static phenomenon – i.e. the wing has a certain height above ground and stays at that height indefinitely. While this is generally true for a WIG vehicle which will spend the majority of its flight time at the same altitude in the ground effect, it is not true for most other applications. A front wing of a racing car will go through both pitching and heaving motion during breaking (51), while conventional aircraft are always either climbing or descending close to the ground during a typical flight. Therefore these are not static but dynamic manoeuvres. In this subchapter it will be investigated how much this dynamic effect influences the behaviour in the ground effect and if the dynamic component of this effect is small enough to be negligible.

Weng et al. (72) analysed the data from the flight data recorder of a twin engine transport aircraft. Fuzzy logic modelling was used to establish a dynamic longitudinal aerodynamic model as a function of both the height above ground and the sink rate of the aircraft. Using this model, the change in behaviour in the ground effect induced by the dynamic aspect of the manoeuvre can be investigated. The change in normal force coefficient with changing sink speed, height above ground and side-slip angle β can be seen in Figure 1.70, the change in moment coefficient is shown in Figure 1.71. The descent speed for the dynamic ground effect was 12 ft/s. Using $h/b = 1$ as a reference point for the start of the ground effect, it can be seen that for no sideslip angle the lift increase due to ground effect is slightly larger in the dynamic case, $\Delta C_{L_{static}} \approx 0.09$, while $\Delta C_{L_{dynamic}} \approx 0.13$. It should be noted that maximum lift coefficient is slightly lower in magnitude IGE compared to OGE for the static case. This is atypical and casts some doubt as to the accuracy of these results. Since the source is from flight data recorders, perhaps there is still some noise scattered in the data.

The slope of the moment coefficient becomes steeper in the dynamic case. The dynamic ground effect causes the moment to be more nose down.

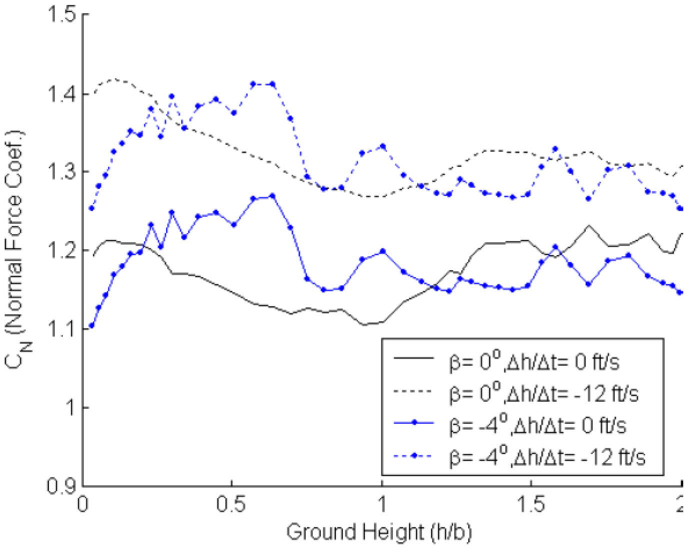

Figure 1.70 Normal force coefficient in static and dynamic ground effect $\alpha = 3°$ (72)

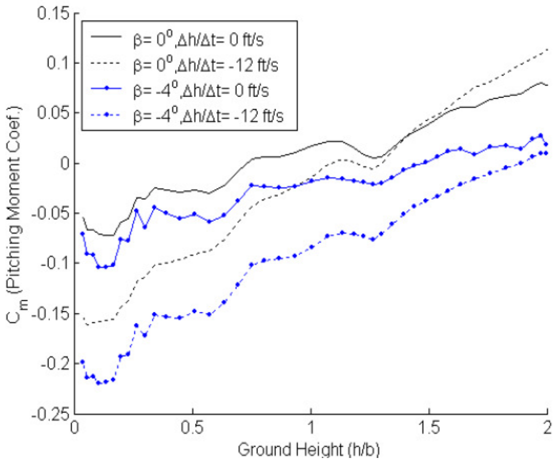

Figure 1.71 Moment coefficient in static and dynamic ground effect $\alpha = 3°$ (72)

Lee et al. (83) performed windtunnel tunnel experiments to compare the static and dynamic ground effect of a F-106B and XB-70 aircraft, both delta-wing aircraft. The vertical velocity was approximately 3 ft/s. In this case it was found that both the lift and drag increment was less in the dynamic case. At $\alpha = 14°$ the F-106 model experienced a lift increase of up to 24% in the static case, while the dynamic lift change was approximately 12%. For the case of drag this was 42.5% and 25% respectively. Chang and Muirhead (84) also found that highly swept wings always experience a lower lift and drag increments due to the ground effect compared to the static case. This was also found by Curry (85) when comparing dynamic flight results to static windtunnel measurements of a F16XL fighter aircraft.

Curry and Owens (74) compared full scale testing of a Tupolev Tu-144 supersonic aircraft with wind tunnel tests and computational results from panel methods of the same aircraft. The full scale dynamic measurements were obtained by keeping the aircraft at constant α. Two sets of measurements were performed, one where the aircraft stayed on level flight, measuring static ground effect, the second one with a constant descending glide path. The wind tunnel tests were also performed in both static and dynamic configurations with a fixed ground boundary condition. After analysing the data it was concluded that no significant differences could be observed between the dynamic and static cases. However, the data quality on the dynamic runs was relatively poor due to the experimental challenges faced and the authors also noted this conclusion conflicted with previous results in literature. As such, further research into this topic was recommended.

Ariyur (86) used a modified version of the lifting line theory to make a prediction of the change of lift and induced drag due to dynamic ground effect. As an example a calculation was made for the Gulfstream V aircraft. There it was found that in the dynamic ground effect the lift decreased and induced drag increased compared to the static ground effect. The change was linear with the descent angle.

Qu et al. (87) studied the behaviour of a NACA4412 airfoil in ground effect using the RANS equations at Re= $3*10^5$. Three regions were defined to describe the behaviour of the airfoil in the ground effect. The first region from $\infty > h/b > 1$ the airfoil behaves identical to the static ground effect. In the region from $1 > h/b > 0.5$ the dynamic ground effect cases produces slightly higher lift. Finally in the region from $0.5 > h/b > 0$ there is a dramatic increase in lift for the dynamic ground effect case. This is shown in Figure 1.72. The cause of the large lift increase is that the air below the airfoil is compressed by the descending airfoil and becomes trapped between the ground and the airfoil, causing a large pressure increase on the lower side of the airfoil.

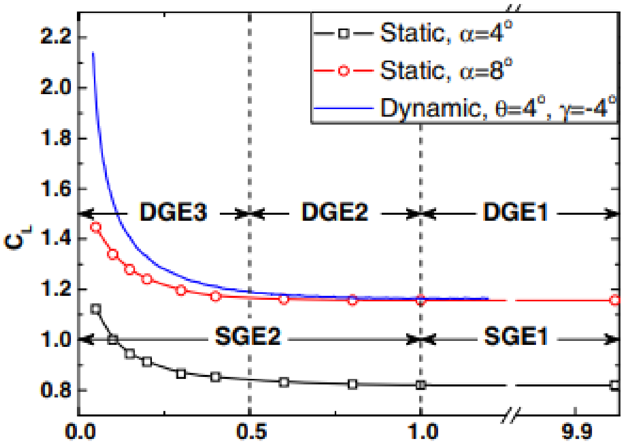

Figure 1.72 Lift Coefficient for static and dynamic ground effect for a NACA4412 airfoil Re=$3*10^5$ (87)

Mondal et al. (88) proposed a new CFD methodology to simulate the dynamic ground effect. In this proposal a structured grid block is positioned under the regular finite volume mesh. An unsteady computation is performed whereby the entire sinking grid moves downwards and the volumes which have already sunk through the (ground) domain are eliminated. This is illustrated in Figure 1.73. This method outlined above allows the entire landing phase including flare and touchdown to be simulated in one continuous unsteady calculation. In test runs for the 2D case it was found that a slight lift decrease of up to $\Delta C_L \approx -0.02$ was found compared to the static case. Results for the 3D case were not presented.

Molina et al. (51) investigated the aerodynamics of an inverted racing airfoil which is both heaving and pitching in the ground effect. They found that the downforce of the airfoil depended on the AoA (static case), and now additionally also on the rotational acceleration and rotational velocity. At low frequency the influence of the incidence is dominant. As the frequency increases, first rotational effects have a growing influence and at high frequencies the mass acceleration effect dominate the airfoil behaviour. At low frequencies the pitch mode was dominant, at high frequencies the heave mode became dominant. A hysteresis effect was also observed as separation of the suction surface occurred in the ground effect, induced by whichever mode is not dominant at the time. Finally, it was found that stall can occur below the static stall angle due to the earlier onset of separation and is a distinct phenomenon to dynamic stall. The influence of the oscillatory effects on the lift coefficients can be substantial, for instance $C_{L_{\alpha=8^\circ}} \approx 1.75\ \pm 0.1$.

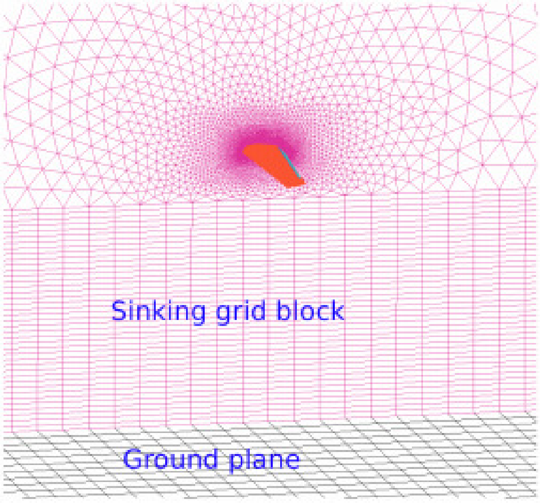

Figure 1.73 Sinking grid concept (88)

It can be concluded that the dynamic ground effect can have a significant effect on the lift and drag of an aircraft IGE. Modified lifting line theory says the lift will be reduced and the induced drag will be increased compared to static ground effect. Several studies on highly swept wings have found that the magnitude of both the lift and drag increments IGE can decrease by up to 42.5% in dynamic ground effect.

However, there are also studies where the dynamic ground effect shows a negligible difference compared to the static case. A study of flight data recorder analysis suggested an increase in lift for a twin-jet transport airplane due to dynamic ground effect. CFD analysis of a NACA4412 predicted a dramatic lift increase in the dynamic ground effect, which is either not measured or not present in the full-scale flight tests and windtunnel tests.

Historically this has been a difficult phenomenon to accurately measure. Ground effect windtunnel measurements are already quite complicated, adding a dynamic movement into the equation only adds further to the complexity. Full-scale flight tests are plagued by noisiness from many differences sources. CFD has been successfully used to study the static ground effect over the past two decades, but only in recent years has it started to being used for the dynamic ground effect. Perhaps this is the reason why there are conflicting studies on the impact of the dynamic ground effect. It is probable that over the coming years this phenomenon will be further clarified as CFD becomes more sophisticated and windtunnel instruments become ever more modern. In the meantime it can be concluded that the impact of the dynamic ground effect must be assessed on a case to case basis.

1.3.5 Compressibility Effects

Compressibility generally becomes impactful in aerodynamics at Mach numbers above 0.3 (6). However, it is possible that the channel between the ground and the airfoil can influence the flow in such a manner that compressibility effects become relevant at lower Mach Numbers. Three studies will be cited in this section where this was investigated.

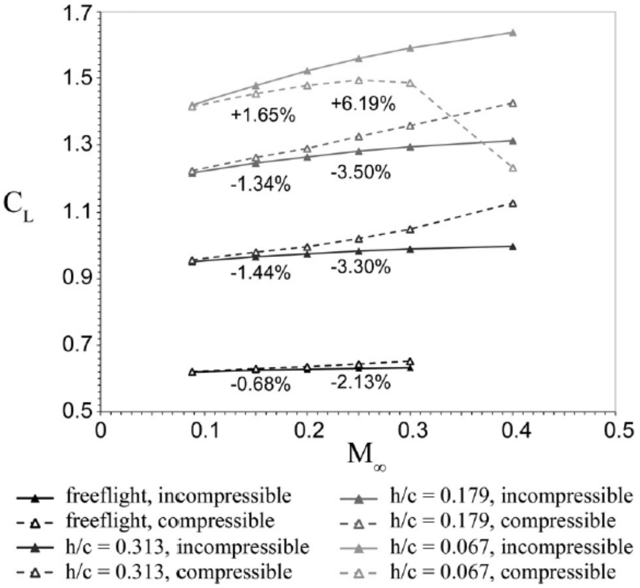

Figure 1.74 Influence of compressibility on lift in ground effect $\alpha = 3.45°$ (28)

The first study from Doig et al. (28) concerns an wing with endplate with an inverted T026 airfoil. The RANS equations are solved at for $0.0882 < Ma < 0.4$ and $0.459 * 10^6 < Re < 2 * 10^6$. The influence of compressibility for different heights above ground is shown in Figure 1.74. It can be seen that compressibility becomes more significant as the ground is approached. At $Ma = 0.25$ the incompressible solution in free air has under-predicts the lift by 2.13%, while at $h/c = 0.067$ the incompressible solution over-predicts the lift by 6.19%. As the Mach number is further increased this difference increases exponentially due to the formation of shocks at very low heights above the ground. A similar trend emerges for the drag coefficient and can be seen in Figure 1.75. For the heights of $\frac{h}{c} = 0.067$ and $\frac{h}{c} = 0.179$ the critical Mach number is already reached between Ma=0.3 and Ma=0.4. This is the cause of the strong decrease in lift and strong increase in drag at these locations. The critical Mach number in free flight for this wing configuration is far higher.

In the second study Hu et al. (89) computed the critical Mach number for a 30P30N three-element airfoil with a 30° flap and slat deflection by solving the RANS equations. The critical Mach number changes from approximately 0.33 in free air to 0.42 in ground effect, which can be seen in Figure 1.76. So in the case of a conventional airfoil the critical Mach number is increased due to ground effect. It was not investigated if this trend is dependent on slat, flap or incidence angle.

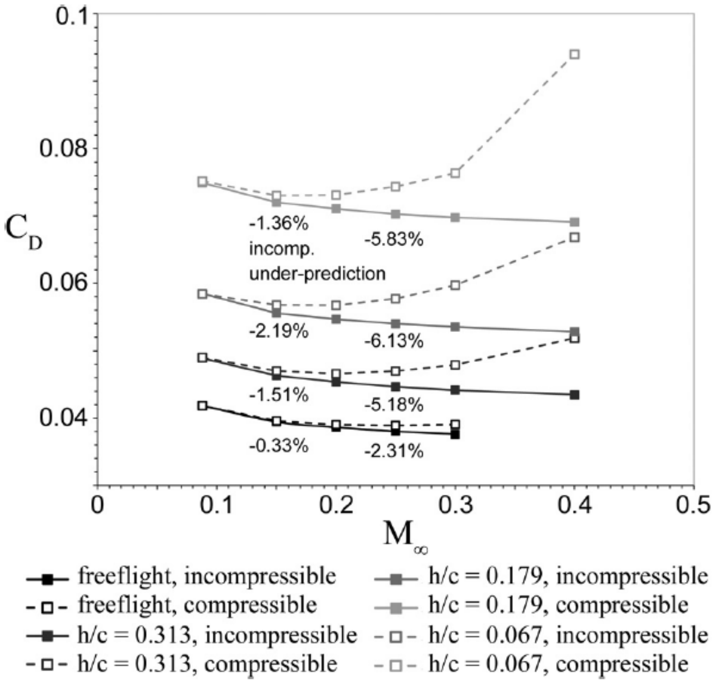

Figure 1.75 Influence of compressibility on drag in ground effect $\alpha = 3.45°$ *(28)*

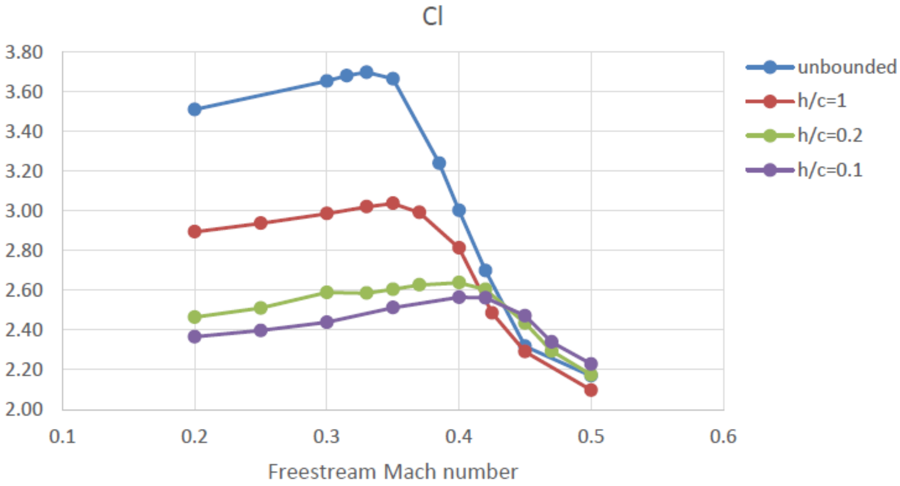

Figure 1.76 Influence of compressibility on lift in ground effect $\alpha = 10.0°$ *(89)*

Li et al. (41) performed an aerodynamic investigation of the RAE2822 in ground effect. Part of this investigation also covered the compressibility in ground effect, where it was found that the compressibility effect was not only dependent on Ma, but also on the height above ground and the AoA. Thus, their limited investigation was in agreement with the two studies cited above.

Based on the studies above it can be concluded that the critical Mach number will increase ground effect for the case of a conventional airfoil and decrease in the case of an inverted airfoil. The change of the critical Mach number can be very significant, up to 30% in either direction. It should be noted here that the amount of literature on this topic is limited and that the findings presented in this section have neither been confirmed nor denied by further studies. The effects of flap deflection and incidence variation on the critical Mach number in ground effect have not yet been systematically researched.

2. Research Question

In this section the research question for the MSc thesis will be formulated. The MSc thesis will be done in collaboration with Delft University of Technology and a major aerospace company. By definition, this thesis must add to the body of scientific knowledge, as well as provide the concerned company with the knowledge they require. Therefore, first the knowledge gaps in literature will be identified, based on the research presented in the previous chapters. Afterwards a research question will be formulated which fulfils both the scientific and industrial requirements.

2.1 Research Requirements imposed by the Aerospace Company

During the development of new aircraft by the aerospace company, incremental data from previous aircraft is often used to predict the parameters of the new aircraft. For example, if the size of the nacelle is changed, the initial estimate for the new lift and drag values are based on how a similar geometry change influenced the lift and drag values in other aircraft. So far this incremental data due to geometry changes has been lacking in the ground effect research. Therefore the aerospace company has expressed the necessity to conduct a systematic investigation of the performance of a twin-engine transport aircraft in the ground effect for different take-off and landing configurations.

2.2 Gaps in Scientific Literature on Ground Effect

It is worth noting that many studies in the literature have been dedicated either to WIG craft or race car performance. However, the aerospace company is mainly interested in the influence of Ground Effect on constructions that were not specifically designed for use in the ground effect.

It has been established that 2D ground effect is well understood. The performance of a single-element airfoil IGE has been covered in detail by many sources, including both computational and experimental data for a wide range of variables such as AoA, Mach and Reynolds number. There is little benefit for further research in this direction. An excellent example of literature on this subject is Qu et al. (43).

Multi-element airfoils have also been widely covered in literature, albeit less extensively compared to single-element airfoils, especially in computational studies. High AoA investigations are scarce, on the one hand due to the computational challenges, on the other hand because many multi-element airfoil ground effect studies concern inverted airfoils for racing applications. In this setting the high AoA close to stall is of less interest.

Simple wings in ground effect have been extensively studied as well. Due to the interest in dedicated WIG craft, many studies have focussed on low aspect ratio wings (90). However, NASA has performed windtunnel tests IGE during the past six decades for a wide variety of wing configurations, such as unswept (33), forward swept (73) and backward swept (13) wings including different flap settings. However, such a systematic investigation is lacking for computational research. Computational research has tended to focus on low to moderate $\alpha$with relatively simple geometries involving single-element airfoils. The change in wing-tip vortex behaviour for these simple geometries has been widely covered in literature. So there is an opportunity for a computational study into the behaviour of a more complex, multi-element wing across a wide range of AoA.

Contrary to static conditions, the dynamic ground effect is still not fully understood. There is a large variety of results and findings in literature, ranging from little influence of dynamic effects (74) to lift changes up to 20% (72). Therefore, there is also an opportunity for a systematic study to identify the factors influencing dynamic ground effect and to identify which aircraft configuration performs optimally in dynamic ground effect.

Another major gap in the scientific literature is the fact that there is a very limited amount of research done on wing-bodies in ground effect. As stated by Deng et al. (66) in 2017: "*It should be noted that this paper presents the computations for a wing-body in ground effect for the first time in the literature*". The aircraft model in question was a DLR-F6 wing-body with a simple, single-element wing and the computations were performed at low AoA of $0° < \alpha < 1.49°$. This implies that there is a complete lack of computational research for wing-bodies with complex, multi-element wings evaluated over a wide range of AoA. During this literature survey the only other research into the ground effect of a typical transport aircraft was the experimental research performed by Flaig (69) on an Airbus A320. Some full-scale flight testing has been done on transport aircraft, see references (74) and (72). However due to the limitations of full-scale testing it is difficult to perform an accurate and systematic investigation into the ground effect using this methodology. There is therefore an opportunity for further computational research into wing-bodies with complex, multi-element wings in ground effect.

To summarize the current gaps in research literature:

I. Research on bodies not specifically designed for ground effect.
II. Research in the region of high AoA involving multi-element airfoils.
III. Computational systematic research for a complex, multi-element wing across a wide range of AoA.
IV. Dynamic ground effect.
V. Computational research on a wing-body in ground effect.

This significant knowledge gap has now been included in the research question, where a number of the gaps mentioned above will be addressed as well.

2.3 Research Question

The research question can now be stated as follows:

1) *What are the incremental lift and drag changes in ground effect caused by changes to the geometry of a twin-jet transport aircraft as calculated in CFD for different values of flap and slat deflection angles, AoA and height above ground?*
    a) *The following changes to the aircraft geometry would have to be considered:*
        i) *Different engine size and different nacelle size*
        ii) *Change from a conventional wingtip to a winglet*
        iii) *Addition of the landing gear*
        iv) *Change of engine thrust setting*
    b) *What effect does a change in engine size have on the flowfield around the wing in ground effect?*
2) *Does the wake from the nose landing gear affect the flow over the wing in the presence of the ground effect?*
3) *How does the baseline CFD ground effect calculation agree with experimental data?*

Therefore, this research question will address both the research question from the aerospace company, and the following literature gaps, adding to the body of scientific knowledge on the ground effect:

- Research on bodies not designed specifically for ground effect (1)

- Research at high AoA involving multi-element airfoils (2)
- *Computational systematic* research for a complex, multi-element wing across a wide range of AoA (3)
- Computational research on a wing-body in ground effect (5)

3. Methodology

3.1 Problem Description

Based on the research question, the problem can now be defined as follows:

- Currently there is insufficient systematic research data related to ground effect, available to enable engineers to calculate performance changes due to various configuration changes (flap, slat) and performance changes due to (isolated) changes in the geometry of an existing aircraft.
- The effect of modifications to the engine size on the flow field around the wing is insufficiently understood.
- The effect of the nose landing gear on the flow over the wing in ground effect is insufficiently understood

The proposed method is as follows:

1) Generate a sufficient number of data points to cover the entire parameter space in such a manner that both main effects and interactions effects can be determined.
2) Analyze the flow phenomena around the aircraft for a wide range of α, h/b, flap/slat settings, with landing gear deployed/retracted, and both MTO and flightidle engine thrust.
3) Compare the CFD calculation results with wind tunnel measurements when available.
4) Develop a method that will enable engineers to predict the effect of incremental changes in configuration settings and geometry modifications.

The work carried out in the course of this thesis should contribute to a solution for the above mentioned problems. The aerospace company has indicated that the landing high-lift configuration is the most important condition to investigate. Previous windtunnel data had determined that for this configuration, interesting angles of attack are: $\alpha = [0°, 2°, 4°, 6°, 8°, 10°, 11°, 12°, 13°]$, so 9 in total. For each value of α, approximately 10 separate h/b measurements were taken. So for each combination of geometry and thrust setting, approximately 90 data points are required.
There are four main geometry variants to be considered resulting in 360 required data points. In addition to that the gear can be retracted and thrust setting can be changed and this would quadruple the number of data points. In order to limit the total number of data points, the latter two configurations have been calculated for extreme values of the other parameters only, and the effect can be interpolated for other settings. Therefore, whatever method is selected to generate the required data, it must in any case be able to produce more than 400 data points in a time and cost efficient manner.

3.2 Research methods available for Ground Effect Research

Three (simulation) methods are available when conducting ground effect research, namely flight-test using a full-scale aircraft, scaled windtunnel research or CFD simulations. In this subchapter the advantages and disadvantages of these methods with respect to ground effect research is discussed, based on the problem requirements posed in subchapter 3.1. At the end of this subchapter the most optimal method is selected for use during the thesis research.

3.2.1 Flight Test

Ground effect is a quite complex flow phenomena, especially when combined with high-lift flow of the aircraft, as is required for this research project. Therefore ideally there would be no simulation or modelling involved in ground effect research, but rather using direct

measurements from the real aircraft. This is the first and most important advantage of flight testing.
Additionally, both in CFD and in windtunnel research much effort needs to be expended in order to correctly simulate the ground boundary condition, while this occurs naturally during a full scale flight test.

Unfortunately, flight tests have several major drawbacks within the context of this research project:

1. Over 400 data points need to be generated during this research. It would be prohibitively expensive to do all these measurements during flight test, even when only taking the fuel and pilot salary costs into account, let alone the extra costs generated while changing the aircraft geometry.
2. There are significant operational measurement challenges involved. The pilot needs to maintain perfect level flight above the runway with a fixed height, which can be challenging given unavoidable atmospheric turbulence and wind velocity. It is very challenging to obtain data of sufficient accuracy.
3. In this proposed systematic research, the goal is to systematically vary α and h/b in order to explore the whole design space, while V_∞ remains fixed. This is possible in windtunnel and CFD, because for these cases $L \neq W$. However in flight test it is necessary that $L = W$, thus with fixed velocity the number of variable combinations that can be researched is limited.

3.2.2 Windtunnel Tests

For decades windtunnel experiments have been the main source of ground effect data and remain important today. Windtunnel data can be more accurate than CFD, especially when the flow becomes complex, at high α, low h/b and high flap deflection angle. A systematic exploration of the α and h/b parameter space is possible, unlike for flight test. Once the model and windtunnel are prepared, it is relatively cheap to perform a large number of runs at different test points, which is very important in the context of this research.

Disadvantages to a windtunnel ground effect experiment:

1. Additional complexity and cost are involved due to the modelling of the ground plane. For optimal results a boundary layer scoop and moving belt are required, which can be quite expensive.
2. Each geometry change adds complexity and cost to the model.
3. High initial cost to get the model prepared
4. Extra cost and complexity involved when more data is required than merely the lift, drag and moment data. For example, Particle-Image Velocimetry (PIV), pressure sensors on the wing or tufts on the winglet to detect wingtip stall all add to the complexity of the measurement setup and might influence the measurement results.
5. The Reynolds number will be lower compared to CFD and free flight, unless the choice is made to accept the extra cost and complexity associated with a cryogenically cooled windtunnel such as the European Transonic Windtunnel (91).

3.2.3 CFD Simulations

There are two main advantages to using the CFD for ground effect research. The first is that the setup time is shorter and the setup costs are lower to prepare the different required geometries. The second main advantage is that the information throughout the entire flowfield (pressure, velocity, streamlines, vorticity) are obtained unobtrusively and without additional costs for each separate CFD run, which significantly aids post-processing.

Some disadvantages to CFD simulation are listed below:

1. In case of CFD, use would be made of the steady RANS equations in combination with a turbulence model. Both the assumption of steady flow, as well as the accuracy of the turbulence model could be challenged at the parameter combination of high α, low h/b and high flap deflection angle. Thus CFD is potentially less accurate than windtunnel and flight test at certain parameter settings.
2. Windtunnel has high startup costs, but subsequently a low variable cost per data point. In contrast CFD has a low setup cost, but a higher variable cost per run. Given the large number of data points required for this research, windtunnel may still be the cheaper option.

3.2.4 Selection of Research Method

In Table 3.1 a comparison between the three different options is shown. These a briefly discussed below.

- *Cost* was discussed previously and is estimated in this table.
- *Data Quality* is defined as the combination of the accuracy of the data, as well as the physical correctness of the data. For example the flight test is a perfect representation of the physics, but due to atmospheric turbulence and pilot input some accuracy of the measurements is lost.
- *Availability of flow data* is a measure for how much data is available from this experiment. For instance, it is very challenging to measure the strength and location of the wing tip vortex during flight test, while this is relatively straightforward with CFD.
- *Ability to explore the parameter space* as discussed during the flight test section, not every combination of α and h/b can be measured during flight test if V_∞ remains fixed. No such limitations are present for windtunnel and flight test.
- *Feasibility* gives an estimate for how feasible it is to use each method for an MSc thesis. The feasibility of the CFD is estimated so highly, because the student was offered a position to conduct the research within the CFD department of the aforementioned aerospace company. This means that the computational resources and in-house expertise are available for the student to use, consequently it now becomes feasible to use this research method. This is the primary reason why CFD was chosen over windtunnel research as the principal research method.

Table 3.1 – Comparison of available research methods

Factor Method	Cost	Data Quality	Availability of flow data	Ability to explore the parameter space	Feasibility
Flight Test	---	++	+	-	---
Windtunnel	-	++	++	+++	-
CFD	+	+	+++	+++	++

3.3 CFD Setup

In this subchapter an overview will be given of the settings which were used while computing the CFD results. First the CFD setup will be discussed and the important choices which had to made will be highlighted. Afterwards an extensive discussion on the meshing process will be presented, since this was of significant influence on the quality of the results.

3.3.1 Governing Equations

The governing equations are presented as part of the literature survey in subsection 9.1.1 and 9.1.2. The CFD simulations will be run using the RANS equations. It is assumed that the solution is steady and time independent.

3.3.2 Turbulence Modeling

A discussion on the optimal turbulence model to be used during ground effect research is presented in subsection 1.2.1.2. It was concluded that the most accurate results were obtained using the realizable $k - \epsilon$ model and the Menter-SST model. From these two, the choice was made to use Menter-SST, since this model had worked well during previous CFD computations on the aircraft used for this ground effect investigation.

3.3.3 Ground Modelling

The optimal way to model the ground plane in CFD ground effect research was discussed in section 1.2.2. Here it was concluded that by setting the ground plane boundary condition to “moving“ produced optimal results, but this was also the most complex boundary condition to implement. Two other boundary conditions were almost as accurate, namely setting the ground plane as a mirrored plane or by setting the ground as an inviscid wall (“slip”). It was chosen to set the ground plane as an inviscid wall, both for ease of implementation and because good results were obtained in this manner during previous ground effect investigations conducted within the company.

3.3.4 CFD Solver

The CFD solver to be used for the generation of the required data is DLR-TAU 2017.1-p1. (16). In all computations the Reynold’s number was set to $Re_{CFD} = 19.6 * 10^6$. The Mach number was equal to 0.2.

3.3.5 Description of the Meshing Process and Investigation into the Mesh Quality

The quality of the mesh is of critical importance for the accuracy of the final computational result. For instance, if certain parts of the boundary layer are not captured accurately by the mesh, then this will negatively impact the accuracy of the result. Therefore it is crucial to ensure the use of a high quality mesh and to document the mesh characteristics and generator settings, since this could be important at a later stage when evaluating the computational results.

It must be noted here that generating meshes for ground effect studies is a computational- and labor intensive process. For a typical aircraft CFD study one mesh is generated, which can then be re-used for each new computation with different value of angle of attack. In contrast for ground effect CFD research, for each distinct combination of angle of attack and H/B, the position of the aircraft in relation to the ground changes, requiring a new mesh to be generated for each case, leading to high computational costs.

One way to reduce these computational demands is to use the so called ‘modular meshing’ approach. In this approach, instead of generating an entire new mesh for each change to geometry, α or h/b now only the local region where the change occurred will be recomputed and the remainder of the mesh will be reused. This approach has two distinct advantages, the first is that this can significantly reduce computation time. For instance, replacing the ground takes approximately ninety minutes of computation time, while generating an entire mesh from scratch can take up to thirty-six hours. The second advantage is that by only changing a local part of the mesh for a new case, large parts of the mesh remains identical compared to other cases. As discussed previously, mesh quality influences the final result, so by reducing the variation between different meshes, a more accurate comparison can be made between different geometrical cases. Unfortunately the modular meshing approach also has several disadvantages, the most important being that it can require compromises on overall mesh quality to function well and that it is significantly more labor intensive.

The goal of this section is first to explain how and with which software the mesh was computed and the principles behind mesh design. Secondly it will be explained which choices were made during the mesh design, which refinements were added to capture certain flow phenomena and the mesh will be visualized. The final part of the section will be dedicated to modular meshing. The different geometric modules will be discussed, as well as the compromises that must be made to the mesh quality in order to get the modular approach working. At the end of that subsection a comparison will be made between a modularly generated mesh and a normally generated mesh in order to determine both the magnitude and locations of the impact on the results caused by the modular approach.

3.3.5.1 Basic Mesh Principles and Mesh Generator Tool Description

This subsection will introduce the basic principles of mesh generation. First the requirements on the grid will stated. It will be discussed how the mesh is built up starting from the surface geometry. The meshing software used for producing these meshes will also be discussed.

Any grid used for solving the Navier-Stokes equations should preserve the conservation properties of these equations. This results in the following requirements (92):

- The grid should cover the entire domain.
- Individual elements should connect to each other seamlessly, so no overlapping and no space between elements should occur.

A second important requirement is that the grid should be smooth in order to minimize numerical errors (93). This means that (92):

- Individual elements should be as regular as possible.
- There should be no large difference between volumes of adjacent cells.
- There should be no large differences in stretching ratio between adjacent cells.

The mesh generating algorithm of Centaur (94) 12.5 fulfills all the requirements outlined above and is the tool used in-house at the aerospace company. Centaur can generate both structured and unstructured grids, as well as hybrid grids in which a structured grid is used in the boundary layer region and unstructured grids everywhere else. The meshes used during the thesis research consist of three distinct geometric elements, unstructured surface triangles, structured prism boundary layer elements and unstructured tetrahedrons:

1. The surface geometry is described by a mesh of unstructured triangles, which can be anisotropic along the wing for increased computational efficiency. An example of a surface mesh can be seen at the top left side of Figure 3.1. The prism and tetrahedral layers are built on top of the surface mesh, so errors in the surface mesh will propagate into the prism and tetrahedral layers. Poor initial geometry quality is often a source of problems in the surface mesh. The primary parameters available to the user to influence surface mesh generation are to control the minimum and maximum size of the triangle wall faces, the stretching factor at which the triangles grow away from any complex geometric features and finally to control the triangle clustering around complex geometry.
2. The prism mesh is formed perpendicular to the surface and is designed to fully capture the flow boundary layer. The prism layers are stretched in vertical direction as the distance from the surface is increased, illustrated at the top right side of Figure 3.1. This stretching allows for a high prism density close to the surface, where the strongest velocity gradients occur, while still maintaining computational efficiency by increasing the prism layer size away from the wall as the gradient of the boundary layer velocity is reduced. The primary parameters available to the user to influence prismatic mesh

generation are to define the number of prism layers to be formed, the thickness of the first layer and the stretching ratio by which each subsequent layer grows. Prism layers have the advantage that there is no numerical diffusion present, unlike tetrahedrons, and are thus far more suited to accurately capture the boundary layer flow. The disadvantages to this structured prism layer are higher computational costs and the fact that it is more difficult to form these structured layers around complex geometry compared to a tetrahedral mesh

The thickness of the first prism layer can be estimated using the non-dimensionalized wall distance y_+, which should be equal to a certain value, which is known in-house and is dependent on which turbulence model is used.

$$y_+ = \frac{u_\tau y}{v} \qquad (equation\ 3.1)$$

Here u_τ is the wall shear stress velocity, v is the kinematic viscosity and y is the distance normal to the wall.

$$u_\tau = \sqrt{\frac{\tau_w}{\rho}} \qquad (equation\ 3.2)$$

$$v = \frac{\mu}{\rho} \qquad (equation\ 3.3)$$

Here ρ is the air density and μ is the dynamic viscosity of the flow, which can be obtained from Sutherland's approximation law for viscosity (95).

There are two ways of obtaining the wall shear stress τ_w. The first method is by estimating the skin friction coefficient based on experimentally derived skin friction coefficient for turbulent flows over a smooth flat plate (96). When no flow information is available, an estimate for the skin friction coefficient C_{D_f} depending only on the running-length Reynolds number Re_x is given by:

$$\frac{1.0}{\sqrt{C_{D_f}}} = 1.7 + 4.15 \log_{10}\left(Re_x C_{D_f}\right) \qquad (equation\ 3.4)$$

Which can be related to the wall shear stress by:

$$C_{D_f} = \frac{\tau_w}{\frac{1}{2}\rho v^2} \qquad (equation\ 3.5)$$

Once flow information has been obtained, the wall shear stress can be accurately calculated using the definition:

$$\tau_w = \mu \left.\frac{\delta u}{\delta y}\right|_{y=0} \qquad (equation\ 3.6)$$

Here u is the velocity parallel to the wall.

3. Finally the rest of the volume is filled with unstructured tetrahedral elements. These elements have to match the prism layer. An example of a cutout through the tetrahedral layer can be seen in Figure 3.2. In general the further the tetrahedron is removed from a surface element, the larger that tetrahedral element will become. That is clearly visible in this example. The primary parameters available to the user to influence prismatic mesh generation are to change the stretching ratio by which the tetrahedral elements grow away

from the surface, to change the way by which the tetrahedral and prism layer boundary interface is formed and by changing the size of the first tetrahedral element which connects to the prisms.

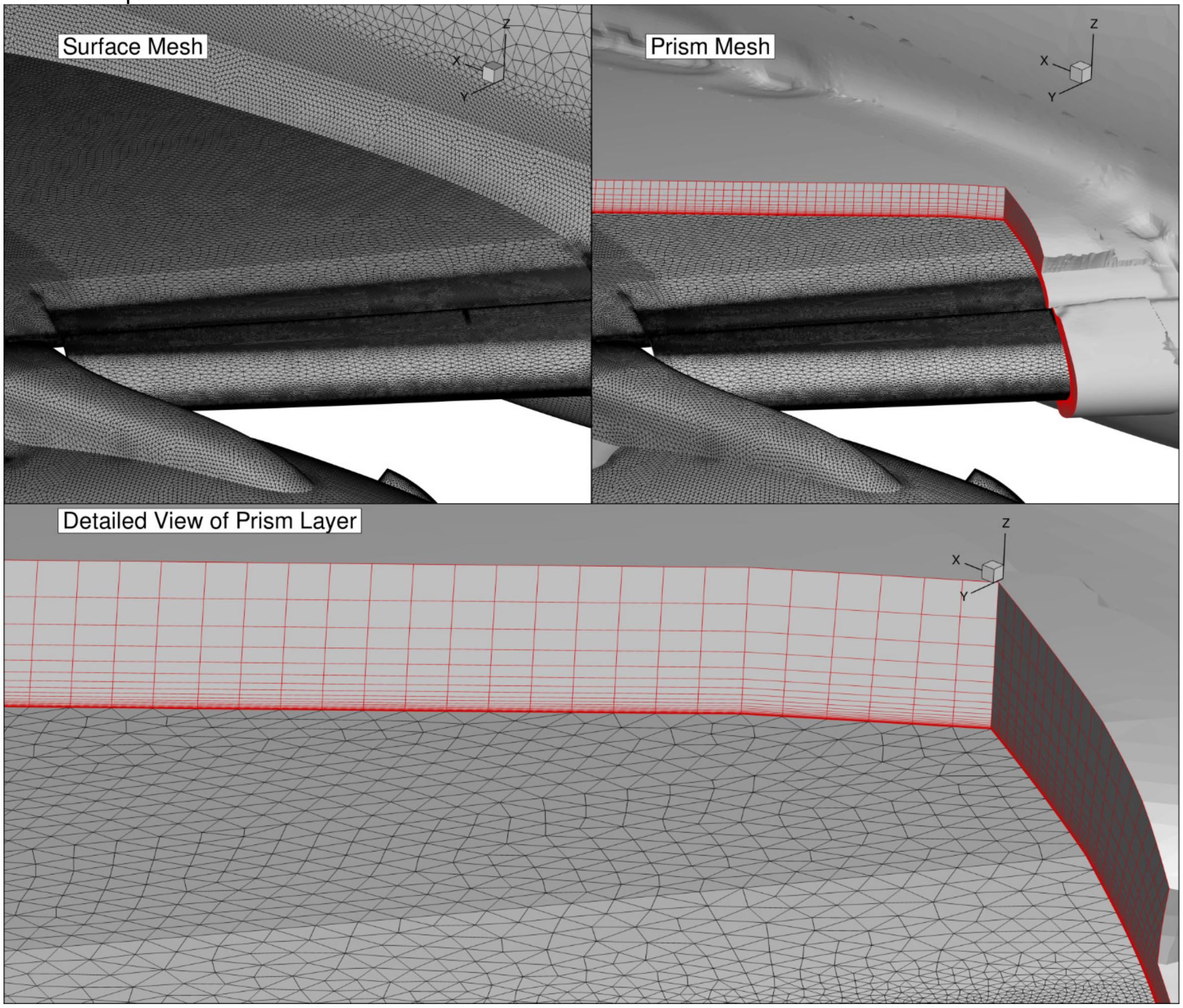

Figure 3.1 - Surface Mesh (left) and Prism Mesh (right). The prism layer mesh is highlighted in red, a detailed view can be seen in the bottom picture

Centaur allows the user to influence the mesh generation in two ways. The first method is by applying the global settings: the user specifies values of the parameters discussed above, which are then applied to the entire domain. But in a complex aerodynamic flow over a wing-body not every part of the domain should be treated equally. For example, the mesh density must be high in order to capture small scale flow phenomena such as the outboard slat vortex, but making the entire tetrahedral mesh very dense would be unnecessary and lead to significantly increased computational costs. Therefore, the approach is to set the global mesh density relatively low and then the user can choose to refine certain parts of the mesh to capture the flow in that area in more detail. These refinements are defined as **sources** within Centaur. The sources allow the user to specify the same parameters as available for the global settings, but are only applied to the local area as defined by the user.

An example of surface mesh refinement on the leading edge can be seen in Figure 3.1, the surface density is significantly increased. In contrast, a source has also been applied to the surface elements on the fuselage to make the surface elements at this location significantly larger to reduce computational costs. Another example of refinement can be seen in Figure 3.2, here the lower part of the tetrahedral cut-out is refined, which can be seen by the high and uniform mesh density in that region. In contrast the mesh in the upper half of Figure 3.2

has had no source applied to it and it can be seen that the mesh is less dense and that the density decreases as the distance from the wing increases.

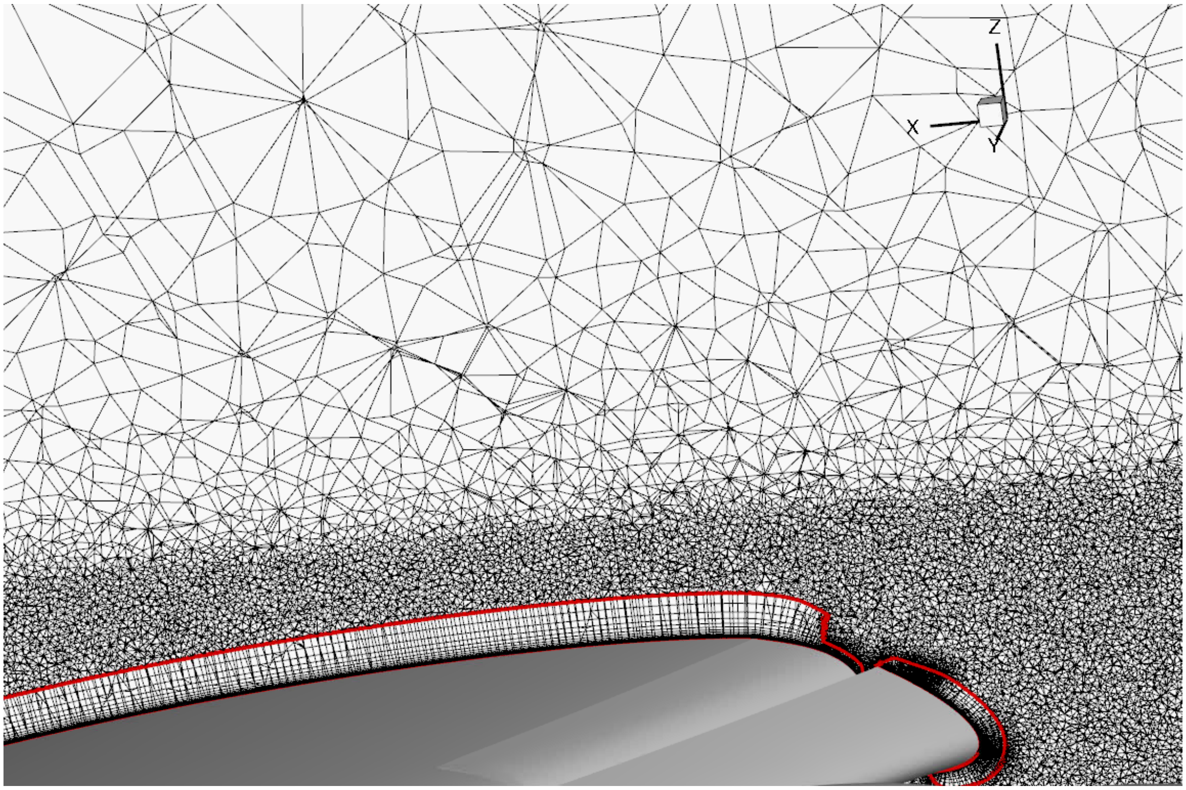

Figure 3.2 - Example of a cut-out of the tetrahedral layer. Highlighted in red is the prism layer.

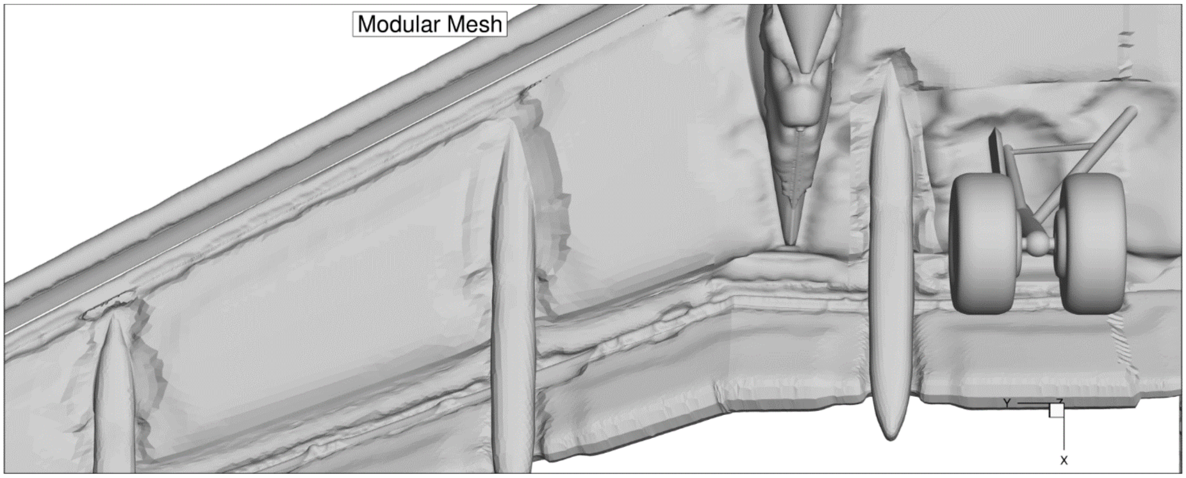

Figure 3.3 – Prism layer height reduction on the flap track fairings and the pylon-lower wing junction

Finally, it should be noted here that mesh creation is an iterative process, not only from the point of view of the user, but Centaur itself also uses an iterative mesh generation algorithm. Due to the complex geometries involved, conflicting requirements can be imposed on the mesh generating algorithm, for example prism layers from two different surfaces can grow into each other if located closer together, for instance at corner points. In this case the algorithm will either locally reduce the number of prism layers, defined as chopping, or reduce the height of the first prism layer, which reduces the height of the total prism stack. This is defined as pull-back. Both methods result in a reduction of prism layer height and both are used by the mesh generator during this thesis research. In the remainder of this subsection, whenever pull-back and/or chopping is visible, this will usually be referred to using the general term of prism layer height reduction unless it can clearly be seen that it is either chopping or pull-back. Figure 3.3 shows a reduction of prism layer height, which is visible in the corner region of the flap track fairing and the lowerside of the wing. There is a conflict between the prisms buildup from the sidewall of the flap track fairing and the prisms originating from the lowerside of the wing. A similar situation can be seen at the right side of the figure where at the pylon-wing junction and the wing-landing gear junction.

A similar set of conflicting requirements is also imposed on the mesh generation algorithm while generating the tetrahedral mesh. Because tetrahedrons are first built on top of the prism layer, changes made to the prism layer will directly influence the tetrahedral mesh. Due to the iterative nature of the algorithm these initially local changes can propagate throughout the mesh. Therefore local changes to the underlying geometry can cause significant changes in the mesh, for example by changing the nacelle.

Conclusion

The mesh is built from surface triangle elements, which are matched by prism elements which capture the boundary layer. The tetrahedral volume elements match the prisms and are used to discretize the remainder of the domain. It was discussed which parameters the user can use to influence mesh generation. Local changes to the geometry can cause changes which propagate through the mesh. Now that these basics have been established, the next subsection will introduce the final important aspect of mesh generation for this thesis, namely modular meshing.

3.3.5.2 Introduction to Modular Meshing

In the previous subsection the basic principles of meshing using Centaur have been introduced, this subsection will now expand on this by explaining the principles of modular meshing and by discussing the advantages and disadvantages associated with this approach.

One of the main objectives of this thesis research is to determine the behavior of a wing-body in ground effect and to determine how this behavior is influenced by changing the wing tip, engine and landing gear geometry. However, it was established in the previous subsection that a local change to geometry can cause changes which propagate through the mesh. That means that when comparing two cases with different geometries, not only will the computational results be different due to the change in geometry, but it will also be impacted by the changes in the mesh. Since the effect of the change in geometry can be relatively small (in the order of ±0.5 lift count), the changes due to the different mesh can have a significant impact on the final results and conclusions.

3.3.5.2.1 Advantages of Modular Meshing

The desire to minimize the influence of the mesh when comparing the final computational results is the primary reason why the modular meshing approach was chosen for this thesis research. Using this approach, the entire domain will be divided into a number of different modules, defined by the user. At the start of the meshing process a full mesh will be generated similar to the normal procedure. Once the full mesh has been generated, the user can now change the geometry by removing a certain module and replacing it with a module containing the desired changed geometry. In the normal approach, the mesh would now have to be re-calculated from the ground up and the new geometry would influence the mesh generation throughout the entire meshing domain. This is solved by using the modular approach, in this case only the mesh contained within the changed module is re-generated. Boundary conditions are imposed at the module border to force the new mesh within the module to match the already existing mesh on the outside. This offers the key advantage that changes made to the local geometry now no longer influence the entire mesh, but instead are contained within that module. Thus, when comparing the computational results from two modularly generated meshes, the results will be less impacted by the changes in the mesh than if the meshes would have been generated using the normal procedure, consequently it will be easier to identify the changes to the flow caused only by the changes to the geometry.

A second advantage of modular meshing is that the computation time is significantly reduced. For instance, it can take up to 36 hours to compute a full mesh, while it only takes approximately 45 minutes to calculate a new mesh for the wing-tip module or landing gear modules and changing the ground plane or the engine takes approximately ninety minutes. More than 400 meshes had to be calculated during the course of this thesis research, so the savings on computation time are significant.

3.3.5.2.2 Disadvantages of Modular Meshing

There are three disadvantages to using modular meshing and these are interrelated. The first and most significant disadvantage is that a modular mesh can cause local degradation in mesh quality. This is illustrated in Figure 3.4, which shows a comparison between a modularly generated prism mesh on the upper side and a normally generated prism mesh on the lower side, with the border between the modular wing-tip box and the remainder of the domain being indicated by the black line. The modular mesh clearly shows some local degradation in prism layer quality, with low prism height and prism height reduction evident on both the mainwing upper surface and on the slat. In contrast if the modular box is removed the prism layer looks cleaner and more uniform. Moving further away from the modular box border, both prism layers look very similar to one another and are of better quality compared to the wing-tip region. So it can be concluded that modular meshing can introduce a local reduction in mesh quality, which means that the flow is captured less accurately in that region compared to a non-modular mesh. However, this is an acceptable compromise, because the topic of interest for this thesis research are relative effects. For instance: how does the flow change in the ground effect compared to the flow out of the ground effect? If both sets of calculations contain a small but similar error, this will not invalidate the comparison.

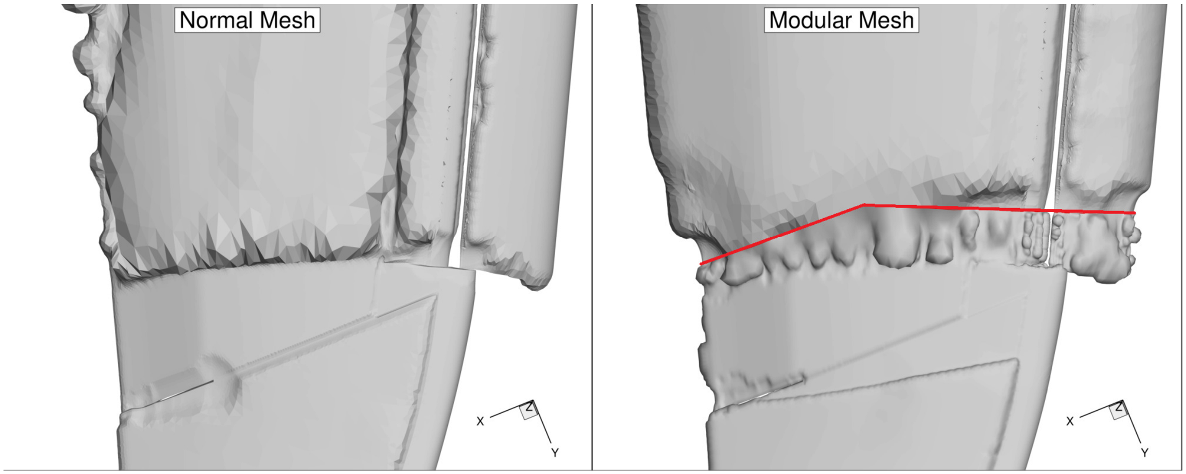

Figure 3.4 – Chopping located on the wingtip caused by modular meshing

The second disadvantage is related to the first: In order to minimize the degradation of the mesh caused by the modules, an iterative design process must be performed by the user in order to find an optimal shape of the modular box which minimizes the mesh degradation.

Since it can take up to 36 hours to generate a full mesh, using this iterative approach can be a time-consuming endeavor and should be taken into account while planning the research.

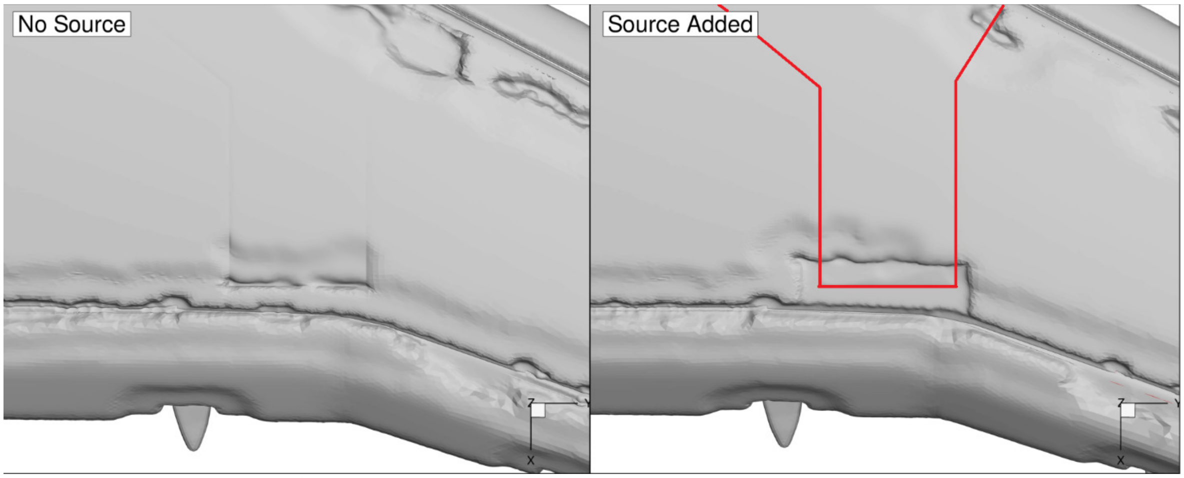

Figure 3.5 – The right part of the figure shows local mesh refinement to reduce prism pull-back and/or chopping on the mainwing upper side on the right compared to the original situation without a source on the left

The final disadvantage to modular meshing is that it can be necessary to degrade the overall mesh quality in order to get the modular approach to work reliably. When a new module is generated for an existing mesh, as a boundary condition to the mesh generator is imposed that at the module border the prism height must match the height of the existing prism mesh. The taller the original prism layer is, the more difficult it becomes for the algorithm to meet this constraint. At certain locations this becomes impossible, causing in the mesh generation algorithm to crash. This problem can be solved by reducing the original prism height, either by changing the global settings or by introducing a local source with which the prism height is reduced. An example of the latter can be seen in Figure 3.5, where the left side shows the original mesh before the source is introduced. At the rear border of the engine box module there it can be seen how the prisms layer height is reduced in a very local region. If this module is now replaced, it is impossible for the mesh generation algorithm to match these prisms exactly. Therefore, a source was introduced to locally reduce the prism height. This caused the prism layer to be uniform in height. This module can now be replaced without causing any problems for the mesh generator. It will be verified in subsection 3.3.5.5 if this source has any impact on the mesh quality.

3.3.5.2.3 Conclusion

Modular meshing allows the user to exchange and re-generate only a local section of the mesh without having to re-generate the entire mesh. The main advantage is that this results in a lower variance in the mesh, reducing the error caused by the mesh when comparing the computational results of cases with different geometries. Another advantage is a significantly reduced computation time compared to normal meshing, up to a 50 times lower. The main disadvantages are potentially long period of preparation, local mesh degradation and possibly user induced global mesh quality degradation. Now that the principle of modular meshing has been introduced, the next subsection will show the geometry of each module used for the thesis.

3.3.5.3 Overview of the Geometries Used During the Thesis Research

Elaborating on the principles of meshing and the concept of modular meshing discussed in the previous subsection, this subsection will now introduce the different geometries used during the ground effect research and will discuss the aspects which are relevant when evaluating the computational results presented in chapter 4. This subsection will also serve as a point of reference to which the reader will be referred back to should more information on the problem geometry be required. Due to confidentiality constraints, no absolute geometric dimensions can be presented in this subsection. First the geometry of the wing-body will be presented to which each module is attached. Each module used during this thesis research will then be discussed and detailed pictures will be presented. Finally, the geometry of the ground plane and the location and size of the far field will be presented.

3.3.5.3.1 Aircraft Geometry

Two different high-lift settings were investigated during this thesis research. The first is a typical take-off configuration, with significant slat deflection and limited flap deflection and aileron droop. The second configuration is the full landing setup, with maximum values for slat and flap deflection, as well as aileron droop. The exact values for each configuration can be seen in Table 3.2.

For each high-lift configuration, there are four sections of the geometry which can be changed during this thesis research:

1. Two different engines, one with a smaller and the other with a larger nacelle
2. Two different geometries at the wing tip: The first a conventional wingtip, the second a more modern winglet with 4% increased wingspan
3. Nose landing gear deployed or retracted
4. Main landing gear deployed or retracted

In this part first the main wing-body module will be discussed, since all the geometric variations mentioned above will be connected to the wing-body. Afterwards each individual geometric variation will be shown and briefly discussed.

Table 3.2 – Overview high-lift configurations

Parameter	*Take-Off Configuration*	*Landing Configuration*
δ_{slat}	22°	27°
δ_{flap}	10°	40°
$\delta_{aileron}$	5°	10°

Figure 3.6 shows the geometry of the main wing-body module. This module can be regarded as fixed, as it will remain unchanged throughout all the calculations performed for this thesis. All other modules are connected to this wing body module. As can be seen, a half model will be used to reduce the computational demands. This is a valid approach since the flow conditions will always be symmetrical, $\beta = 0°$.

The geometry consists of a typical single aisle commercial airliner fuselage. There is a cutout at the bottom front of the fuselage where the nose landing gear is located. This cutout can be seen in the bottom left of the side view part of Figure 3.6 and this is where the landing gear module will be connected. There is no horizontal tail plane installed on the fuselage, this implies that all the CFD runs will be performed in untrimmed flight condition.

The wing is a typical wing for a medium range twin-jet commercial airliner. There are three cutouts made into the wing. The first cut-out is located in the engine area where the engine modules can be attached and is depicted in Figure 3.7. The second cutout is located at the wing tip, where the wing-tip modules can be attached, depicted in Figure 3.8. The final cutout is located beneath the wing, between the fuselage and the engine nacelle. This is the attachment point for the main landing gear module, which shown on the lower part of Figure 3.9 and in the upper part of Figure 3.10.

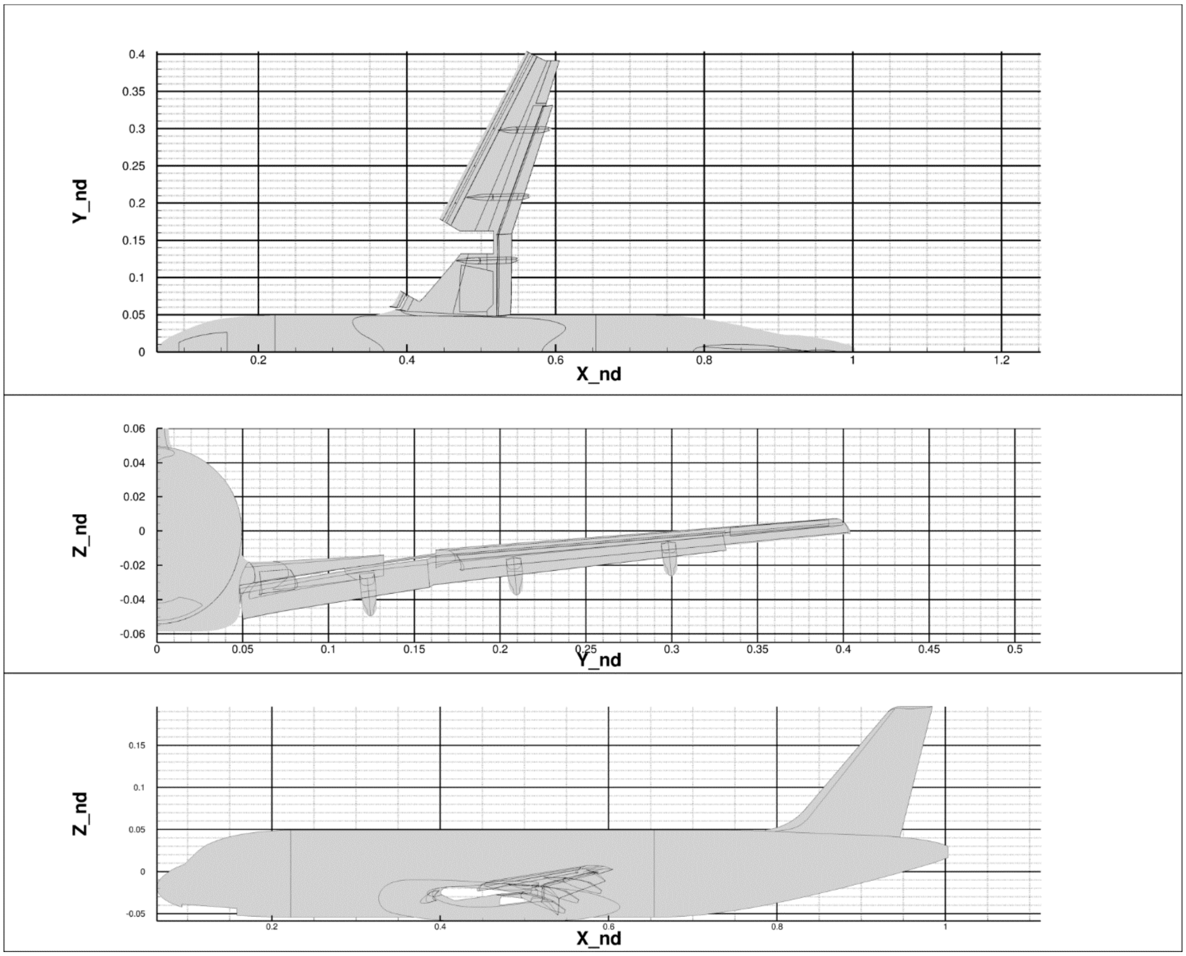

Figure 3.6 - Two-Dimensional View of the Wing-Body module

The wing contains inboard and outboard slats across the entirety of the leading edge. Flaps are located at inboard trailing, close to the fuselage, and continue outboard up until approximately 80% of the wingspan. Ailerons cover the remaining 20% of the trailing edge wingspan. There are three flap track fairings which guide flap deployment. Finally, it must be noted that the changes to slat, flap and aileron geometry were done without using a modular approach, so an entire new mesh was generated after the geometry was changed.

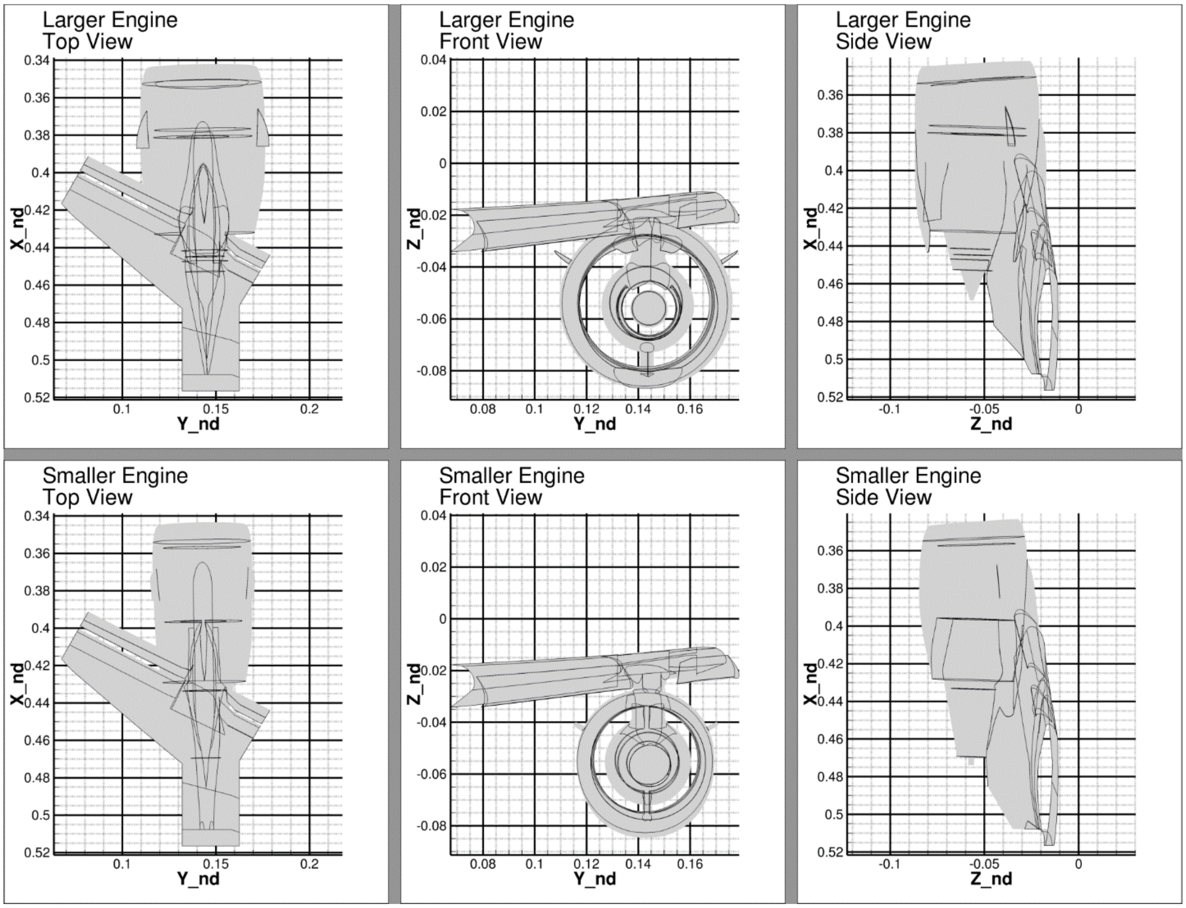

Figure 3.7 - Two-Dimensional View of the Engine modules (identical scales between top and bottom row)

The two different engine geometries can be seen in Figure 3.7. The scales on both the top and bottom row of pictures are identical. The most significant difference between the two geometries is that the diameter of the nacelle on the larger engine is increased by approximately 25%. The maximum thrust produced by the larger engine is also increased. It must be noted that both inboard and outboard strakes are installed on the same location on the nacelle for both engines.

Figure 3.8 shows both modules for wing tip geometry. The scale is the same for both the top and bottom set of pictures, so these can compared directly to determine the relative sizes. It can clearly be seen that the winglet module size is significantly larger compared to the wing-tip module. The wingspan is increased by approximately 5% when the winglet module is installed.

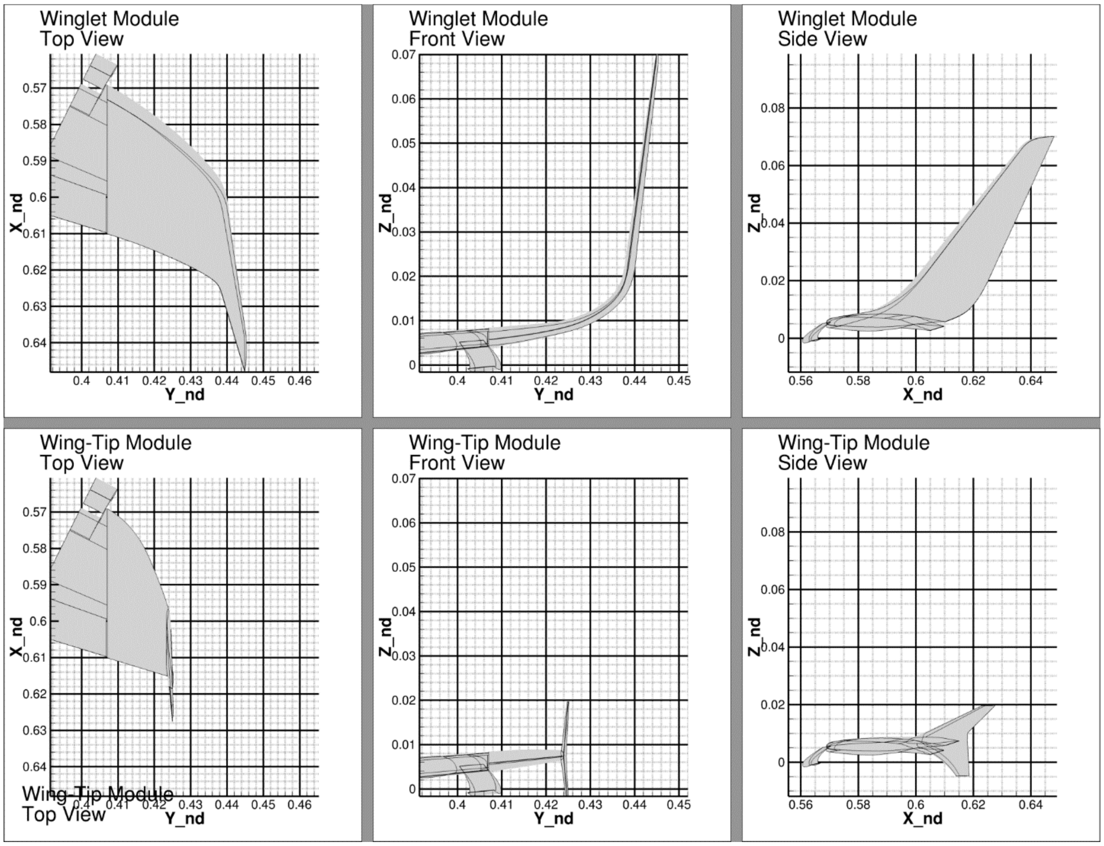

Figure 3.8 - Two-Dimensional View of the Wing-Tip modules (identical scales between top and bottom row)

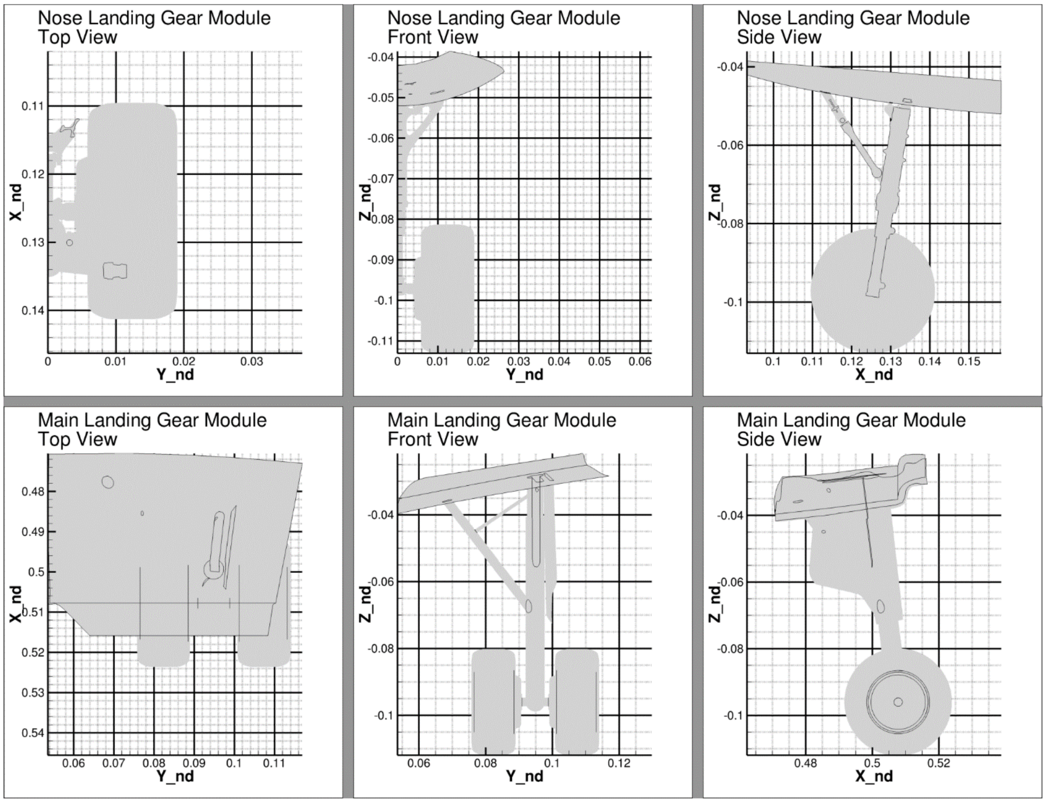

Figure 3.9 - Two-Dimensional View of the Landing Gear Modules

Figure 3.9 depicts the nose- and main landing gear in the deployed state. This is a simplified landing gear geometry, for instance no landing bay doors are modeled. The retracted state uses an identical fuselage panel, the landing gear geometry is simply removed from it.
Finally Figure 3.10 shows a three-dimensional view of the wing-body with all possible geometric variations. The top part of the figure shows the wing-body equipped with the larger nacelle, the winglet wingtip and the gear deployed. The flap and slat deployment angles correspond to the landing configuration. The bottom part of the figure shows the aircraft in take-off configuration, with gear retracted and the smaller wingtip and engine installed.

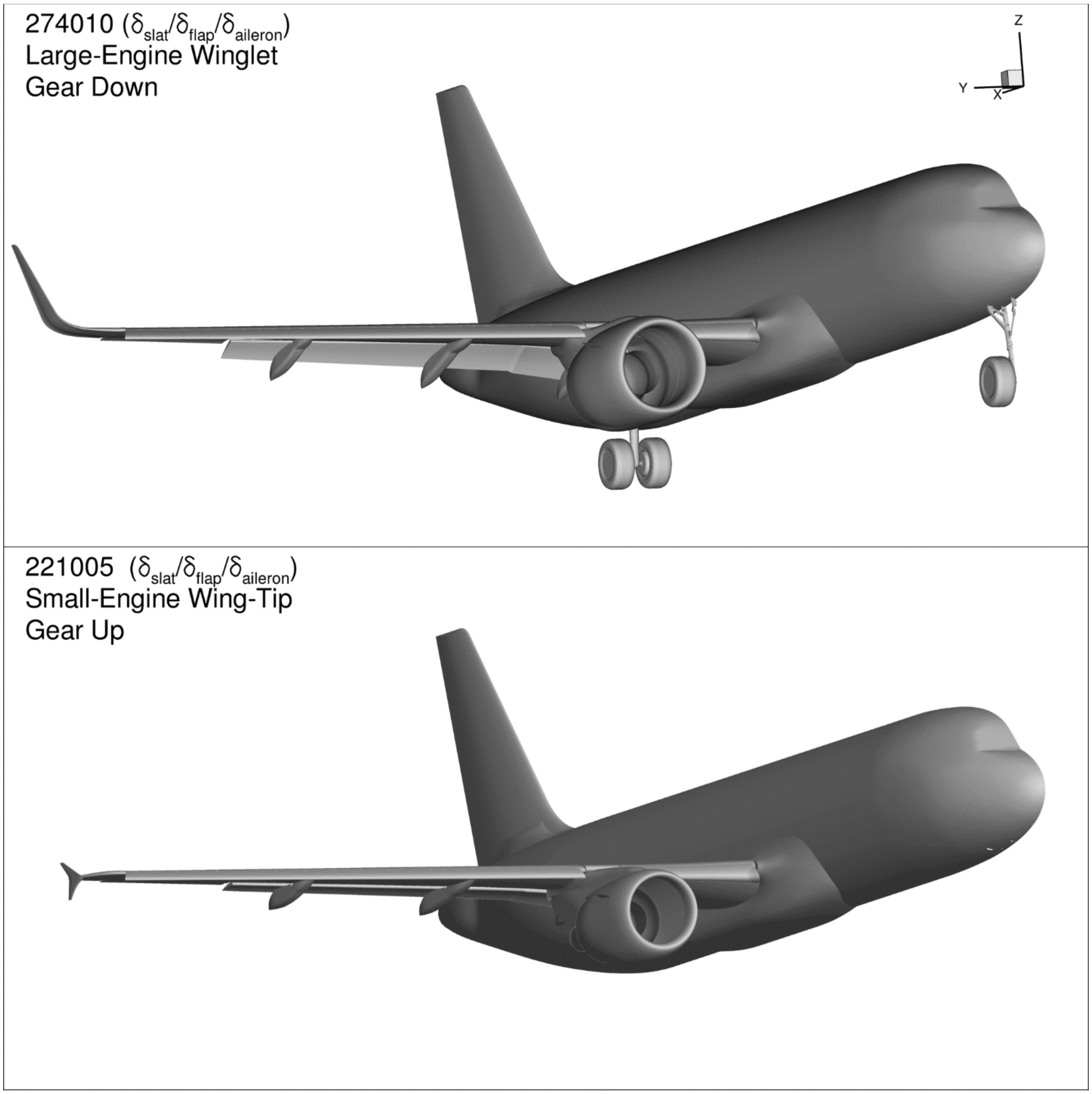

Figure 3.10 – Three Dimensional view of all the geometric variations used during the thesis research

3.3.5.3.2 Modular Boxes, Ground Plane and Far Field

In the previous part the geometry of the aircraft was discussed, now in this part first the modular boxes used for this module exchange will be shown. Secondly the modular box around the aircraft, which is used when changing the ground plane is discussed. Finally the far field module and ground plane module will be briefly discussed.

The top left part of Figure 3.11, displays in red the four different modular boxes discussed previously. Modular boxes may not intersect with other geometry, for instance the ground plane. Therefore an effort was made to 'shrink' the modular box around the landing gear, so that low values of h/b can still be obtained while using the modular meshing approach. The lowest achievable value obtained using this approach was $h/b = 0.114$. It should be noted in this context that the minimum achievable value of h/b when the wheels touch the ground at $h/b = 0.0947$.

In the top right part of Figure 3.11 the aircraft modular box is depicted in yellow. The entire mesh within the yellow modular box remains unchanged when the ground plane module is exchanged. The box has been designed to match the lower side of the aircraft geometry as closely as possible, in order to reduce the minimum distance to the ground before the aircraft module box would intersect with the ground plane.

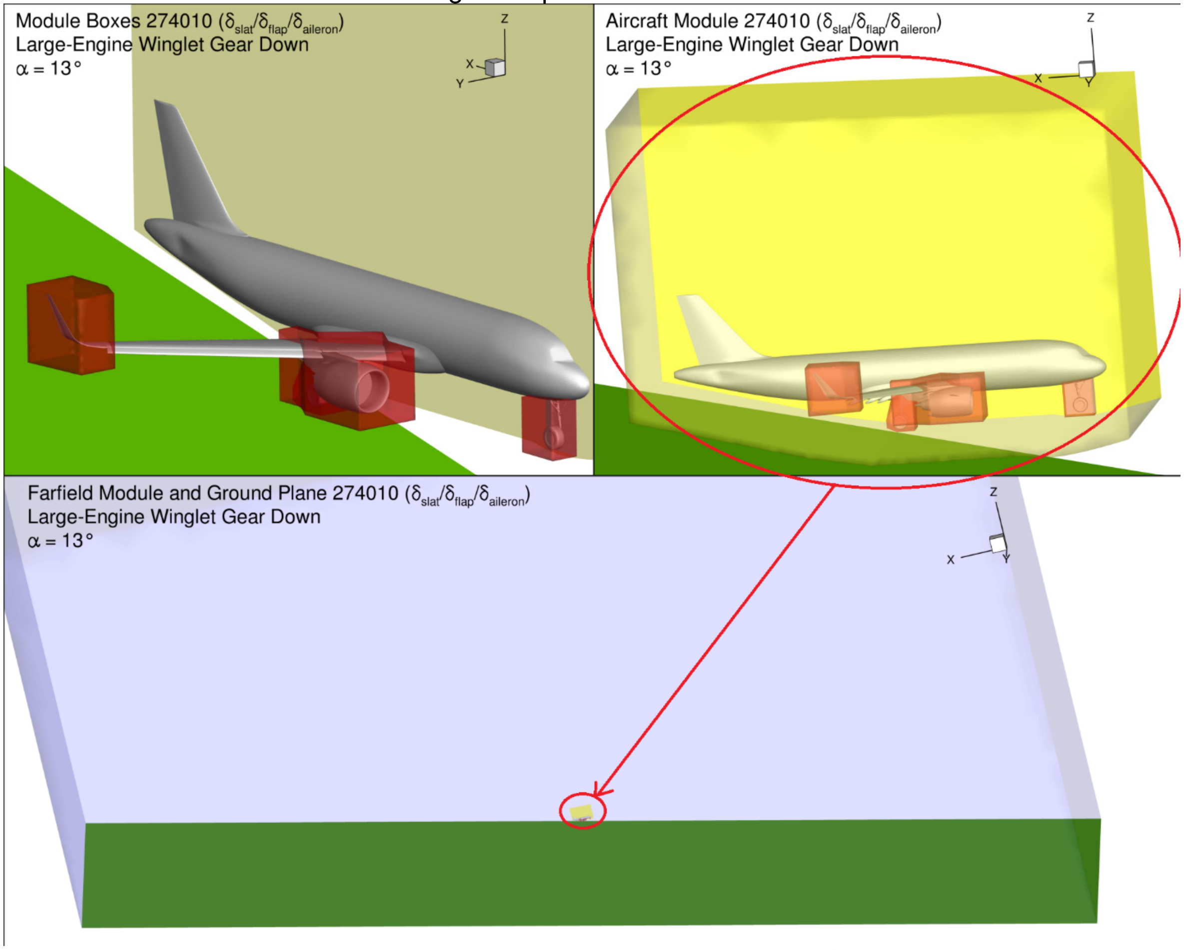

Figure 3.11 – Three-dimensional view showing the four modular boxes (red, top left picture), the aircraft modular box (yellow, top right picture) and the far field module (blue) including ground plane (green, bottom picture)

Finally, the lower picture of Figure 3.11 depicts the entire ground plane, as well as the lower part of the far field box, which is the limit of the computational domain. The far field border in x-direction is located approximately 25 fuselage lengths ahead and behind of the aircraft. The highest point of the far field box in z-direction is located approximately 12.5 fuselage lengths above the aircraft. When changing the height above ground and/or angle of attack, the ground plane is respectively translated or rotated relative to the aircraft, which maintains the same coordinate position for each different case. This approach simplifies the post-processing stage.

3.3.5.4 Description of the Mesh and local refinements

In this subsection a representative mesh used during the thesis research will be presented. Potentially problematic areas of the mesh will be identified and the local refinements to capture specific flow phenomena will be reviewed.

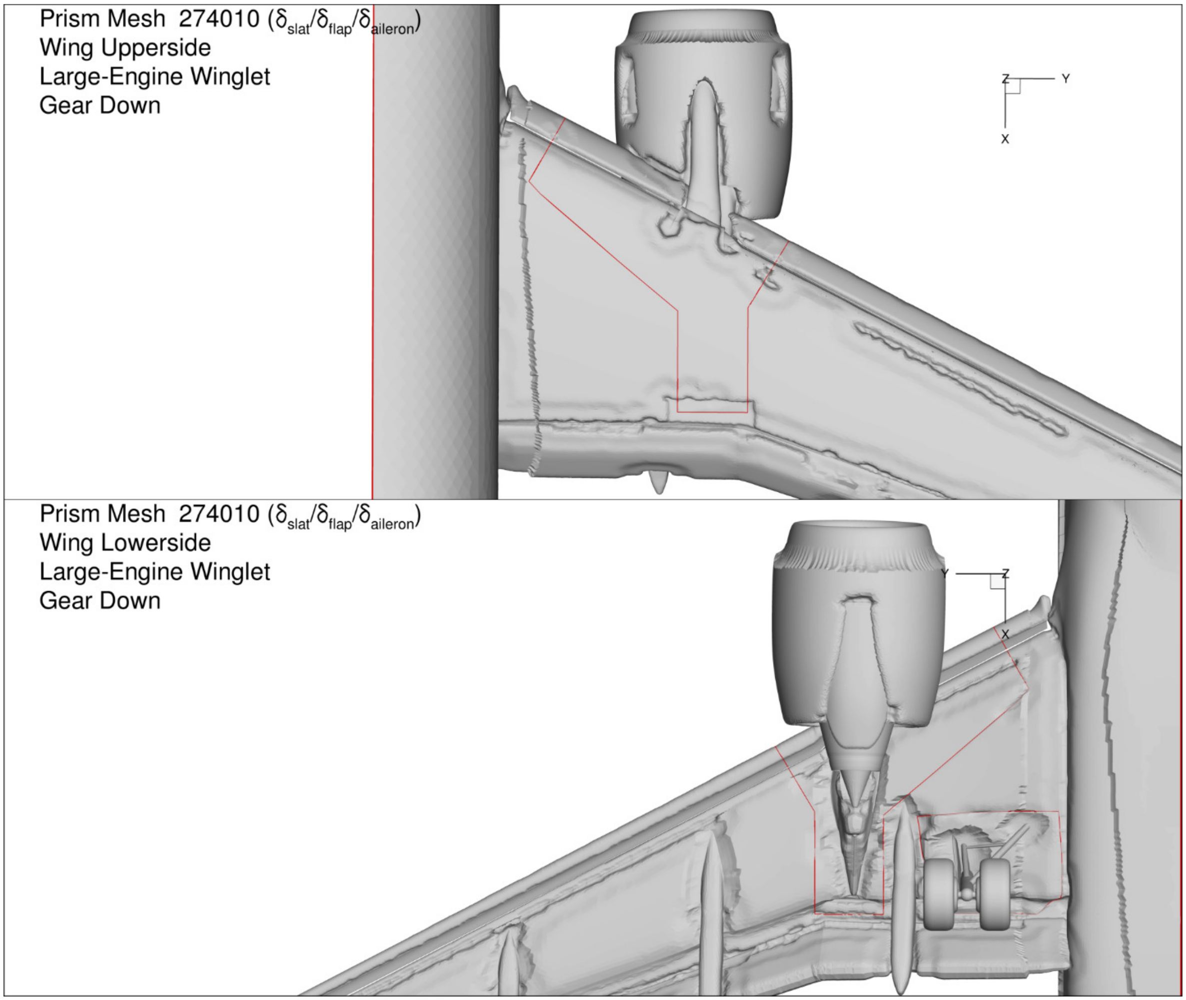

Figure 3.12 – Overview of the prismatic mesh on the inboard wing upper and lowerside

The prismatic mesh is shown in Figure 3.12 and Figure 3.13, which respectively show the in- and outboard part of the wing. The red lines show the borders between various modules. Certain exceptions aside, the mesh on the wing upper side looks uniform and shows good prism growth. On the wing upper side there is a region close to the wing leading edge where prism chopping has occurred. This is caused by slight discontinuity in the way the panels at the leading edge connect to the panels on the main wing, making it locally difficult for the mesh generator to build a full prism layer. This is a well-known problem. Sources have been introduced in that region, which have reduced the extent of the problem. Since this problem is located at the leading edge, the boundary layer there is still thin and is still fully captured in this region by the prism layer, despite the prism chopping. This will be verified and shown in subsection 3.3.5.5.

Another region of interest is the rear part of the engine box module, because here a source was introduced to reduce prism growth as discussed in section 3.3.5.2 (shown in detail in Figure 3.5). The same holds true for the prism chopping at the wing tip, this is shown in detail in Figure 3.4. Finally, it should be noted that there is some pull-back occurring on the wing lower surface in the region of the main landing gear. This is unavoidable and must therefore be accepted.

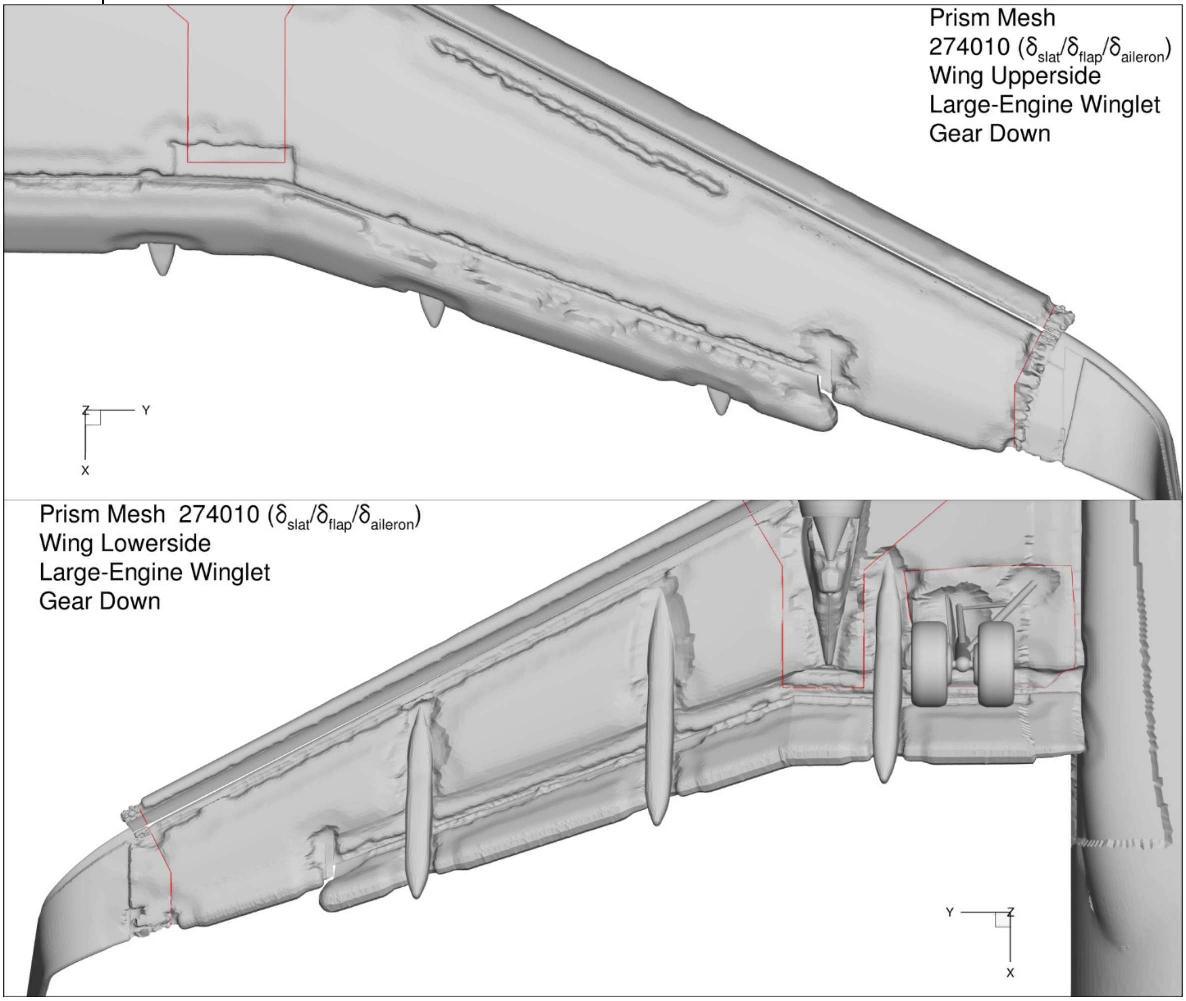

Figure 3.13 - Overview of the prismatic mesh on the outboard wing upper and lowerside

Figure 3.14 and Figure 3.15 show the surface mesh projected on top of the prismatic mesh for respectively the inboard and outboard part of the wing. By visualizing the surface mesh many of the mesh refinements become visible by looking at the change in mesh density.

The most significant refinements occur on the wing upper surface in the region behind the engine. The engine induces three separate vortices: two are induced by the inboard and outboard strake, while the third is induced by the pylon. A refinement is introduced for the latter which is visible as the highly dense area leading from the pylon toward the wing trailing edge. To the right of this pylon vortex refinement, there is a second refinement with slightly lower mesh surface density: This refinement is placed in that location to capture strake vortices. The normal wing mesh density can be observed to the right of this refinement. The third refinement is visible between the fuselage and the pylon vortex refinement. This refinement was introduced to capture any vortices induced by the nose landing gear. Finally, it should be noted that these refinements do not just refine the surface mesh, but also increase the density and/or shape of the tetrahedral volume mesh above it.

Another refinement is introduced at the wing upper side, to capture the horseshoe vortex which is present at the end of the outboard slat, close to the wing tip. This refinement is visible in Figure 3.15 by the dense area near the winglet.

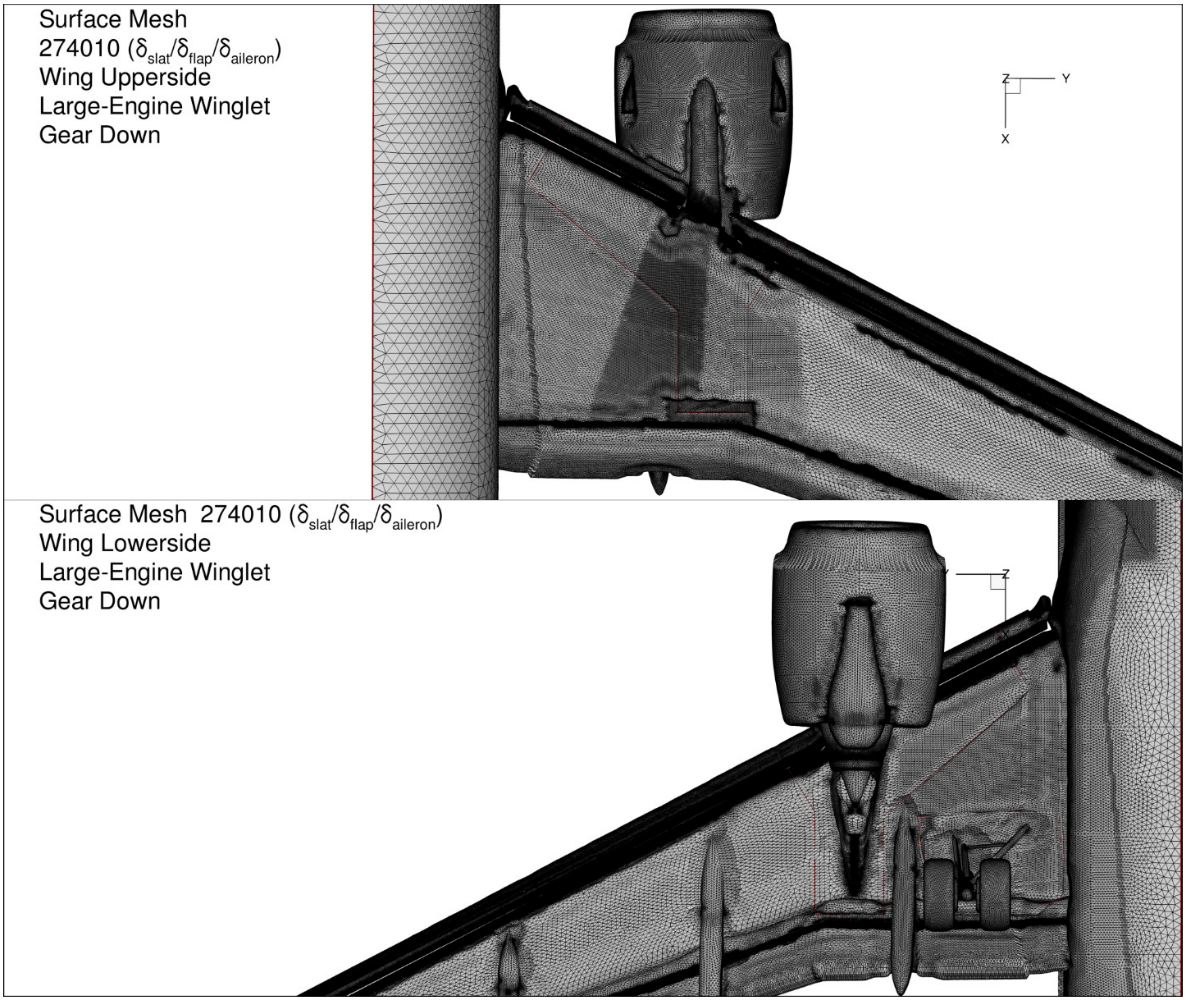

Figure 3.14- Overview of the surface mesh on the inboard wing upper and lowerside

No mesh refinement is added behind the winglet, so the wing tip vortex will not be captured with complete accuracy. From literature it is known that the wing tip vortex moves outward in span-wise direction and rebounds in vertical direction (65). Since this phenomenon is already well understood, it was decided not to expend time and effort into this topic during the thesis research.

A significant change to the mesh had to be incorporated as a consequence of modular meshing. It was mentioned in subsection 3.3.5.2 that it was necessary to reduce the prism height near the border of the modular box in order to be able to exchange modular boxes. Various settings of the global prism factor were tested, as well as a number of local prism refinements. From this investigation it was determined that the prism stretching factor had to be reduced from a value of 1.36 used in the reference mesh to 1.33 in the modular mesh. This means that the prism layer is reduced in height by approximately 29%. This is a significant decrease, but it was found that this was the only mesh set-up which enabled robust swapping of the modular boxes without constantly resulting in mesh generator crashes, which could then only be solved by tweaking the mesh settings for each case, in turn causing inconsistencies between meshes. Therefore it was decided to slightly compromise mesh quality in favor of higher mesh consistency, which increases the accuracy of the analysis when different cases are compared and relative effects are investigated.

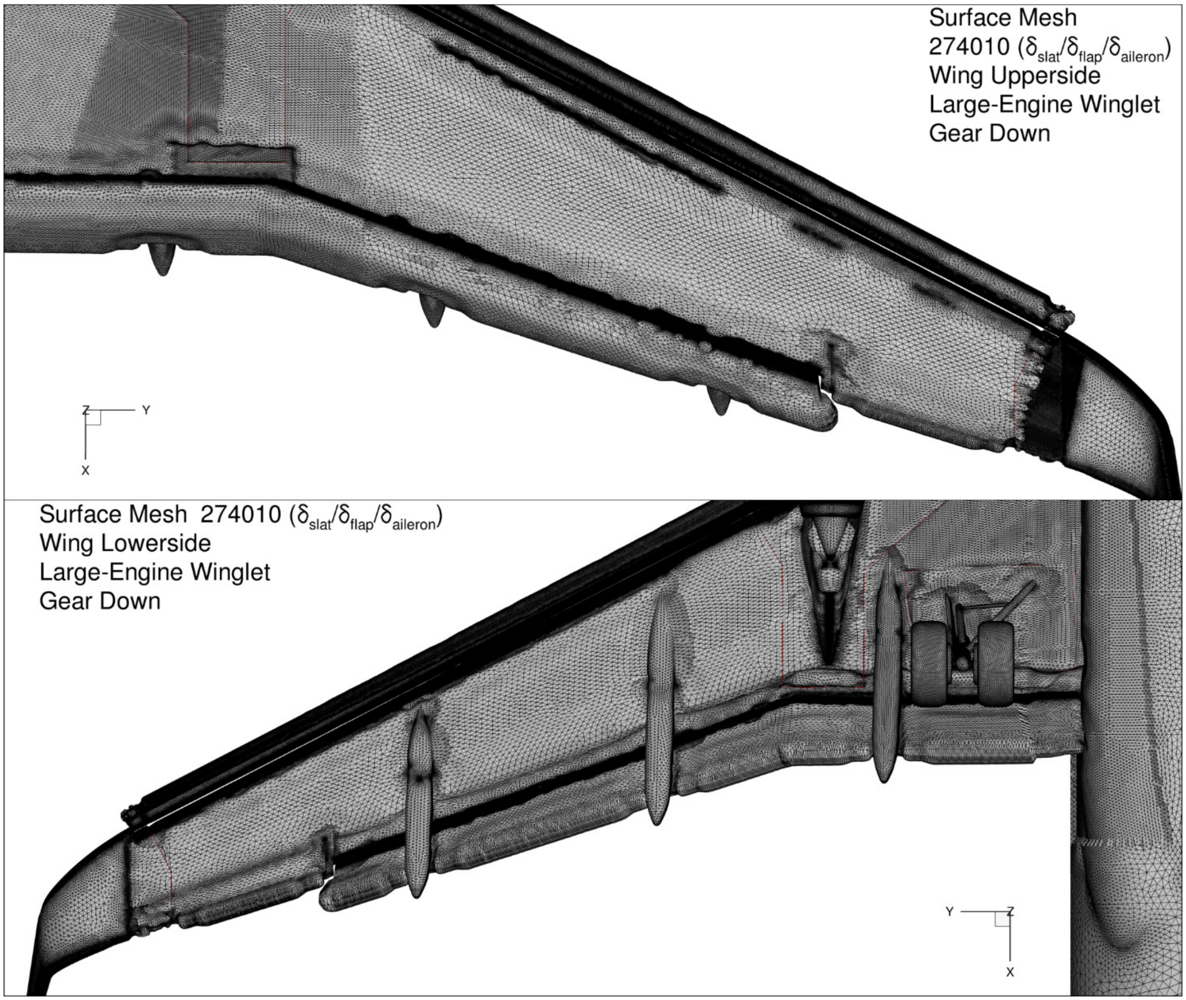

Figure 3.15 - Overview of the surface mesh on the outboard wing upper and lowerside

Various refinements have been depicted in this subchapter, the location and purpose of these has been discussed. It has also been discussed which adjustments had to be made to the mesh in order to allow for robust exchange of the various modules. Now the next part of this report will focus on first determining the impact of the modular meshing approach on mesh quality and secondly to determine the impact of reducing the prism stretching factor has on the mesh quality.

3.3.5.5 Evaluation of the Mesh Quality and Determination of the Impact from a Modular Meshing Approach

So far this subchapter has explained in detail the mesh philosophy used during the thesis work and the principles of the modular meshing approach. The resulting mesh has been visualized and refinements to the mesh have been highlighted. It has also been discussed which concessions had to be made to mesh quality in order to get the modular meshing approach to work consistently. Now in this subsection the consequences of these decisions are evaluated by comparing the mesh to a flight test validated mesh which has been used for previous work. This reference mesh without modular boxes will be compared to a modularly generated mesh with a similar prism stretching factor, in order to identify the differences caused only by the modular meshing. Next the modularly generated mesh will be compared to a mesh which was used for actual data production for this thesis. This production mesh has a reduced prism stretching factor, as was discussed in the previous part.

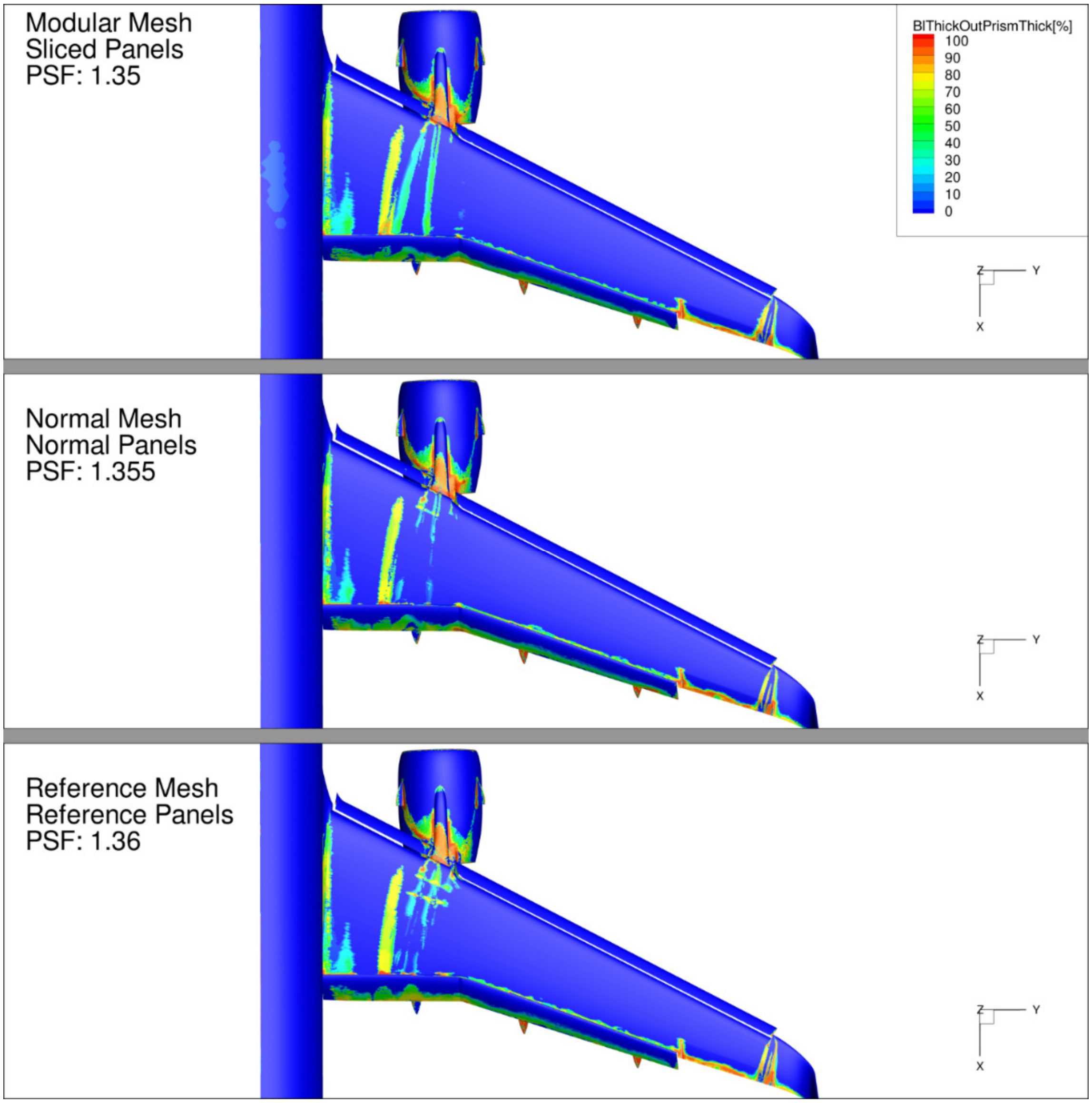

Figure 3.16 – Percentage of the boundary layer captured by the prism mesh on the wing upper surface for a modular (top), normal (middle) and reference (bottom) mesh as calculated by TAU_BL 8.0 $\alpha = 8.0°$

Figure 3.16 and Figure 3.17 show a comparison between three different meshes at how accurately the boundary layer is captured. This accuracy is measured as a percentage of the boundary layer that is located outside of the prism layer. Ideally the entire surface would be blue, which would indicate that the boundary layer is fully captured by the prism mesh.

The top mesh Figure 3.16 and Figure 3.17 is generated modularly with a prism stretching factor of 1.35. It does not include the sources described in the previous part, which locally reduce the prism stretching factor in order to be able to exchange modules. The second mesh, called normal mesh and positioned in the middle of the figures, is exactly the same mesh but with the modular boxes removed and the panels, which have to be sliced near the modular boxes, restored. The prism stretching factor is increased to 1.355, everything else remains unchanged. The third and final mesh included in this comparison is a reference mesh which has been used in-house and has successfully been validated using flight test data. This will be used as the reference mesh and ideally the final ground effect production mesh will generate identical results as this reference mesh.

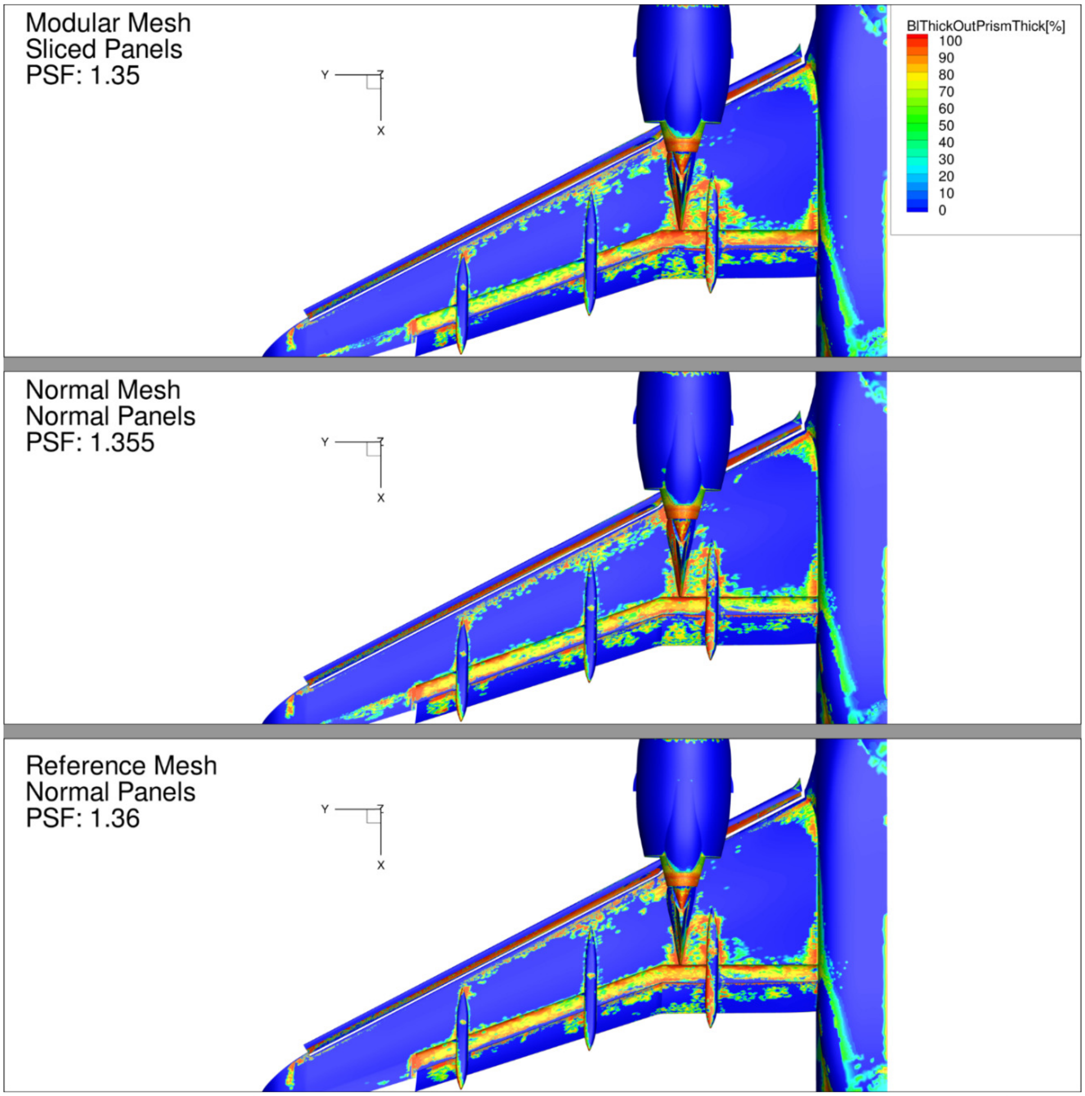

Figure 3.17 - Percentage of the boundary layer captured by the prism mesh on the wing lower surface for a modular (top), normal (middle) and reference (bottom) mesh as calculated by TAU_BL 8.0 $\alpha = 8.0°$

Figure 3.16 shows that there are three regions on the wing upper surface where the boundary layer is not fully captured. The first region is located at the inboard upper wing surface, where amongst others the inboard slat sidewall horseshoe vortex, the pylon vortex and the two strake vortices all are highly viscous regions which are due to their very nature not fully captured by the prism layer. This effect is slightly more pronounced on the top, modular mesh, which makes sense because the prism height is slightly reduced compared to the other two cases. However, it must also be noted that these vortices are unsteady phenomena and will shift slightly in time, so the differences between the three meshes in this location can also be explained by the unsteady nature of these phenomena.

The boundary layer at the upper side of the flap and aileron trailing edge is not fully captured by all three prism meshes. This area is located at the trailing edge of the wing, so the impact of this is relatively small and can be neglected. This is because the impact of the flap on flow over the wing is dominated by the front suction peak of the flap, which is fully captured by these meshes. In the outboard flap and aileron region there is also flow separation, which significantly increases the boundary layer thickness, explaining why it is not fully captured by the prism layer. The flow separation locations can be seen in Figure 3.18.

The final location where the flow is not fully captured by the boundary layer is at the nacelle-pylon junction. Due to the complex geometry at this location, there is significant prism layer height reduction in the region, as shown in Figure 3.12. This geometry also induces a complex flow and flow separation is present in this region, as shown in Figure 3.18.

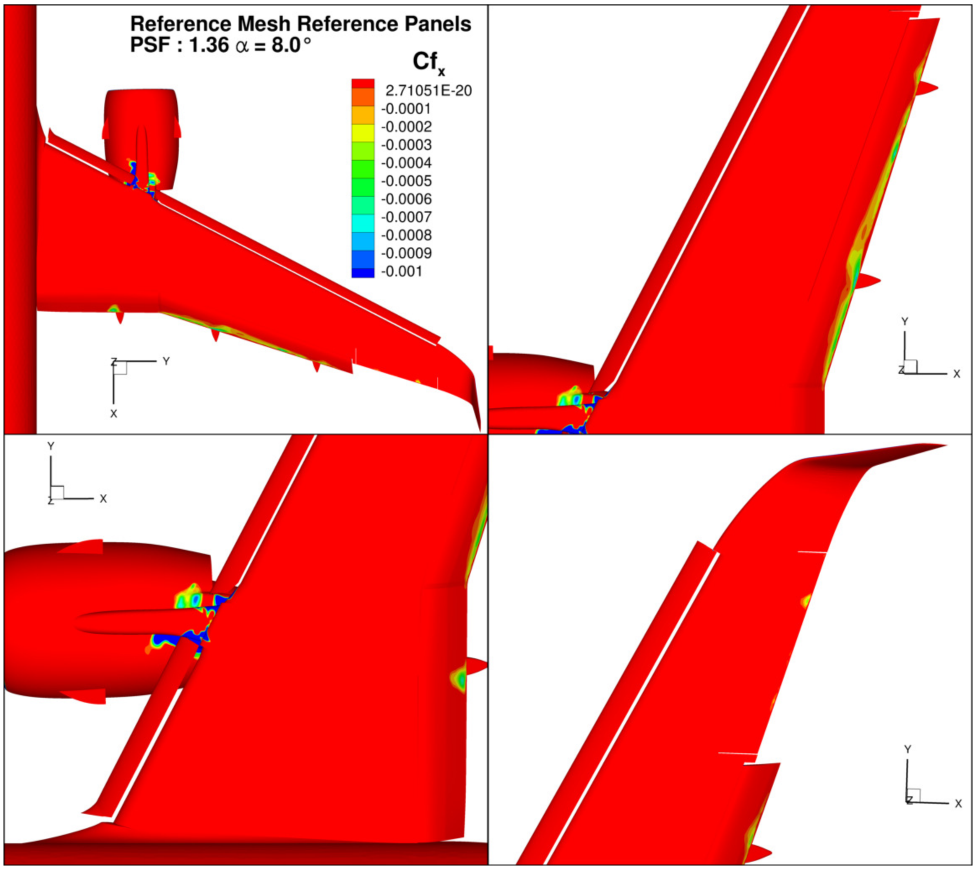

Figure 3.18 - Separation for the Reference Mesh, negative values of Cf$_x$ ***can*** *indicate separated flow*

The lower side of the wing, depicted in Figure 3.17 shows many similarities between the three cases. The boundary layers is not captured properly in the region below the wing where the flap is located when it is retracted. With the flap fully extended this region forms a ‘hollow’ area close to the lower wing trailing edge, where the flow is fully separated as shown in Figure 3.18, leading to increased boundary layer thickness which cannot be fully capture by the prism layer. The same holds true for the slat backskin where the flow is also separated over the entire span of the slat.

Differences between the three meshes can be observed at the lower side of the aileron near the trailing edge. In this region the boundary layer is not fully captured by the prism for the modular and normal mesh case, but this cannot be observed on the reference mesh.

From the above it can be concluded that the modular meshing approach and the presence of modular boxes does not significantly decrease mesh quality. No significant differences were found between the modularly generated mesh and the normal mesh. Compared to the reference mesh, the only region at which a difference can be observed is near the lowerside of the aileron trailing edge, where the reference mesh fully captures the boundary layer flow. Now that this has been established, a comparison between the modularly generated mesh and the final mesh used for data production will be made below.

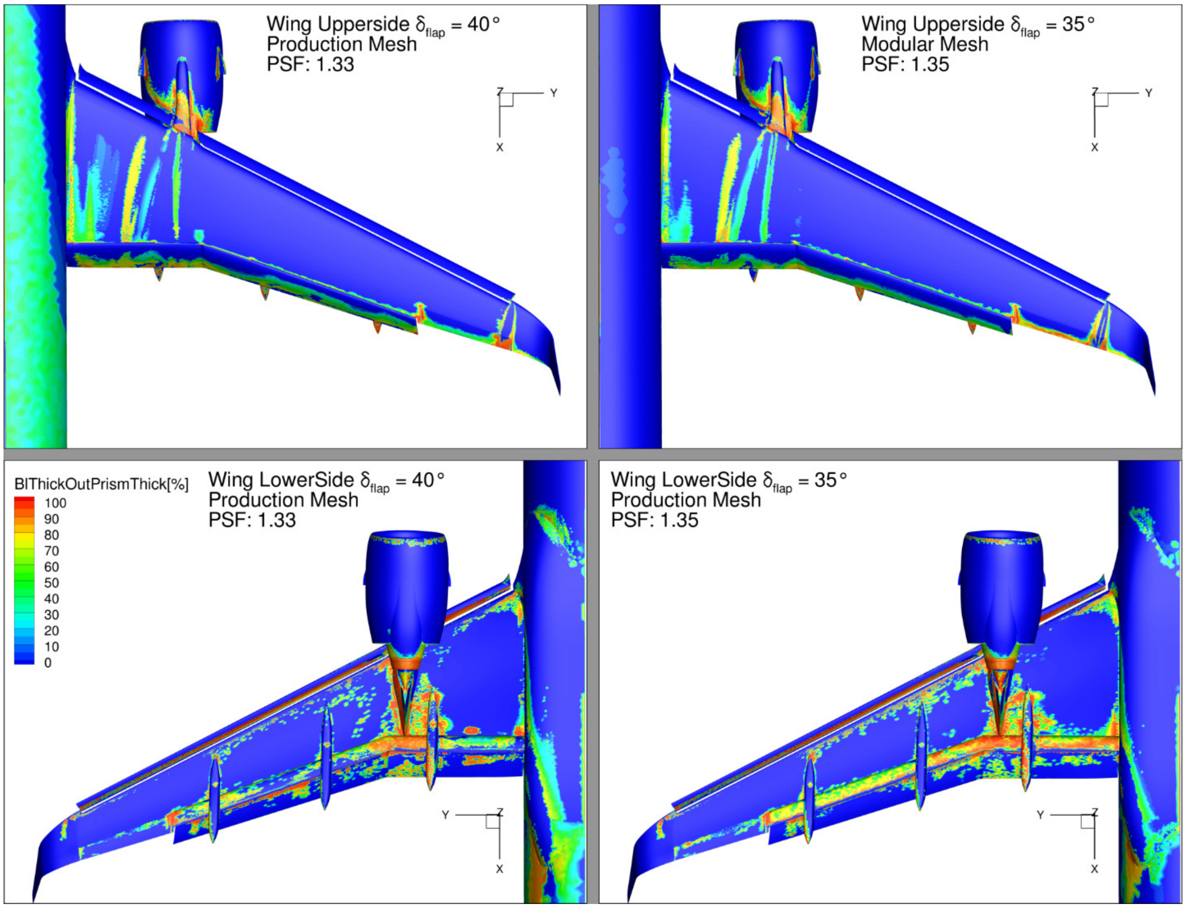

Figure 3.19 - Percentage of the boundary layer captured by the prism mesh on for a production (left) and modular (right) mesh as calculated by TAU_BL 8.0, α = 8.0°

The final mesh used for data production can be seen at the left side of Figure 3.19 for $\alpha = 8.0°$ and in Figure 3.21 for $\alpha = 12.0°$. The modular mesh is included at the right side of the figure. The prism stretching factor for these meshes are 1.33 and 1.35 respectively and the flap deflection on the production mesh is 40° instead of 35° for the modular mesh. The modularly generated mesh on the right is identical to the mesh shown in the top picture of Figure 3.16 and Figure 3.17.

Looking at just the wing, no major differences between the two meshes can be observed. The vortices on the upperside of the inboard wing are more visible in the production mesh, due to the lower prism height. In contrast the boundary layer near the upperside aileron trailing edge is captured more fully in the production case, most likely due to the change in flap deflection to 40°.

A significant difference between the two meshes can be observed when looking at the upper side of the fuselage. It can be seen on the top left part of Figure 3.19 that as the boundary layer becomes thicker over the fuselage, it can no longer be fully captured by the prism layer, because of the reduced prism stretching factor. Figure 3.20 offers an alternative view of the same data which shows in more detail where the differences between the meshes are located on the fuselage. It can be seen that this occurs primarily on the upper fuselage. Only near the belly on the lower part of the fuselage is there an observable difference, at this location the mesh with reduced prism height performs slightly worse.

Although there is a significant region on the upper fuselage in the production mesh where the boundary layer is not captured fully, this region is relatively unimportant for the purpose of this thesis research. The wing, winglet and nacelle regions are of primary importance, since it is expected that the most significant changes to the flow around the wing-body occur in these regions. Of secondary importance is the lower side of the fuselage, since a pressure increase is expected in this region due to the presence of ground. The upper side of the fuselage, the tail and the cockpit section are not expected to be significantly impacted by the ground effect, thus problems with the mesh in these regions are more acceptable.

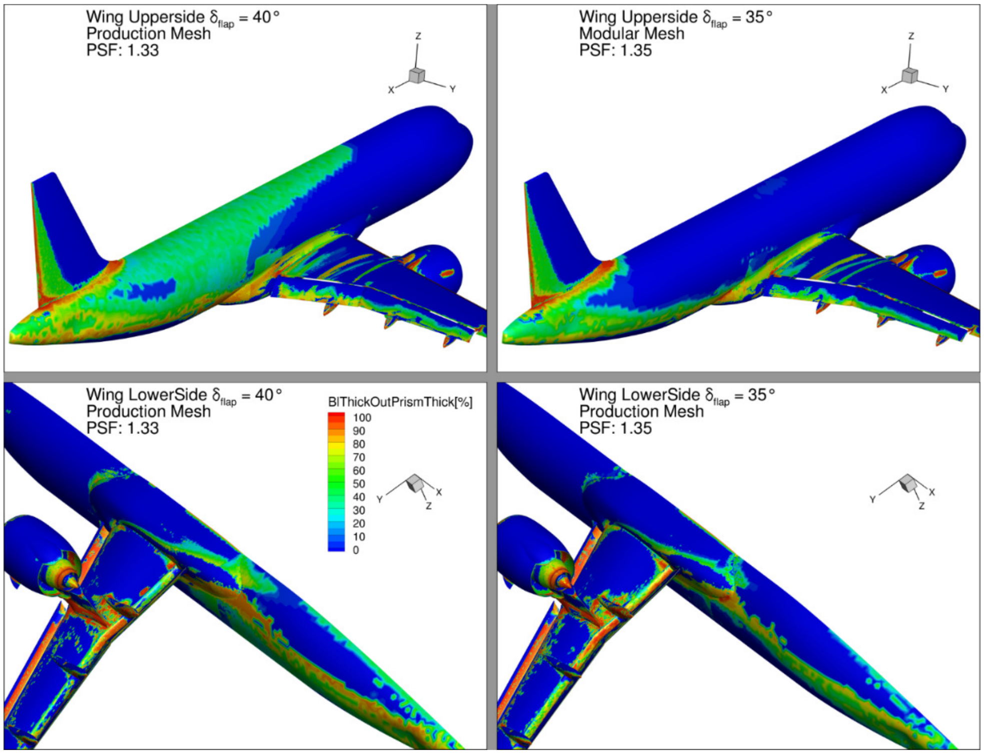

Figure 3.20 - Percentage of the boundary layer captured by the prism mesh on for a production (left) and modular (right) mesh as calculated by TAU_BL 8.0, α = 8.0° and seen on the fuselage

Two conclusions can be drawn from the observation of the insufficient quality of the prism mesh in this region:

1. The influence of the fuselage on the change in lift due to ground effect will be discussed in subsection 4.1.1.4. Any conclusions drawn with respect to the upperside of the rear part of the fuselage can be affected by the observations made here. However, since the lift is primarily an inviscid effect, the fact that the boundary layer is not fully captured should not have a significant impact on the lift calculations. However, more caution should be exercised while analyzing the drag over the fuselage.
2. This region of reduced mesh quality was discovered too late to apply the required modifications to the mesh, since that would invalidate comparisons made between calculations performed before and after the mesh got altered. It is expected that this problem could be fixed by applying a local source to the fuselage prism layer to increase the prisms stretching factor in that region only.

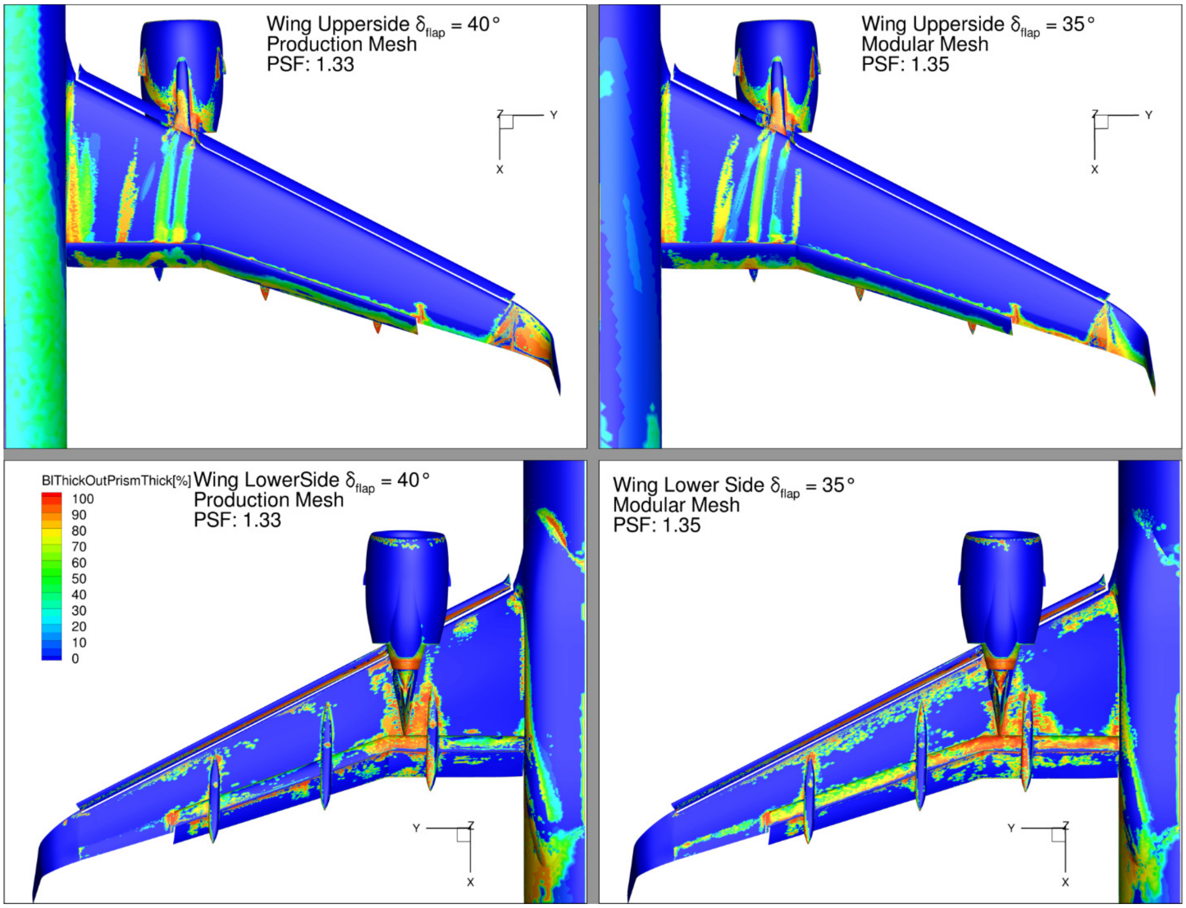

Figure 3.21 - Percentage of the boundary layer captured by the prism mesh on for a production (left) and modular (right) mesh as calculated by TAU_BL 8.0, α = 12.0°

3.3.5.6 Conclusions

The basics of the meshing process have been discussed in this section. The surface mesh consists of triangle elements. Prismatic elements form perpendicular to the surface elements and are used to discretize the boundary layer flow. Finally tetrahedral shaped elements are generated on top of the prism layer and are used to discretize the remaining part of the computational domain.

Modular meshing was used for the thesis research. The primary advantage lies in the fact that when the geometry is changed, only the mesh local of that geometry is modified and the remaining part of the mesh remains unchanged. This implies that when comparing computational results for different geometries, the influence of the mesh on that comparison is significantly reduced by using the modular meshing approach. The primary disadvantage of modular meshing is that it was necessary to reduce the height of the prism layer in order to make the process of switching modules reliable.

The quality of the mesh was also analyzed in this subsection, in order to determine the consequences of the choices made during the meshing process. It was concluded that there was no significant degradation in mesh quality due to the introduction of modular boxes. However there was a reduction in mesh quality associated with the choice of reducing the height of the prism layer to be able to reliably swap the modules. The consequence of this choice was that the boundary layer was not fully captured by the prism layer in the region of the upper fuselage, above and behind the wing.

4. Results and Discussion

This chapter represents the main body of work of the thesis, in which the results from the CFD campaign for a twin-jet transport aircraft in the ground effect are presented and analyzed in detail. The objective of this chapter is to answer the research questions presented in chapter 2.

A detailed description of the geometry used for the CFD campaign is given in subsection 3.3.5.3. The main emphasis of the CFD campaign was to generate data for the four different nacelle/wingtip combinations, summarized in Table 4.1. All four variants were in the landing high-lift configuration, with flaps and slats fully extended, and the landing gear deployed. The calculations were ran with two different engine thrust settings, namely maximum take-off (MTO) thrust, as well as the flightidle thrust setting. The majority of the data presented in this chapter is obtained with these four geometry variants.
It was of secondary importance to determine the ground effect behavior with take-off high-lift settings, as well as with the landing gear retracted. As a consequence, a smaller but still sufficient amount of data is available for these two geometry settings.

Table 4.1 – Summary of the four main geometric variants

Variant	Nacelle	Wingtip
#1	Large	Winglet
#2	Large	Conventional
#3	Small	Winglet
#4	Small	Conventional

Presented previously in Table 3.2, the high-lift settings for the landing configuration are $\left[\delta_{slat},\ \delta_{flap}, \delta_{aileron}\right] = [27.0°, 40.0°, 10.0°]$, which will be referred to as the landing high-lift configuration throughout this chapter. In later subchapters the take-off high-lift configuration will also be discussed, which has the following high-lift settings:
$\left[\delta_{slat}, \delta_{flap}, \delta_{aileron}\right] = [22.0°, 10.0°, 5.0°]$.

As discussed during the literature review in chapter 1, the influence of the ground proximity is non-dimensionalized as the ratio between the height above ground h and the wingspan b. It is assumed that the influence of the ground proximity is negligible at $h/b = 1.0$. That convention is followed throughout this report. Whenever relative effects are discussed and presented, it is always the change in lift or drag relative to the value at $h/b = 1.0$.
The chosen reference value for the wingspan is the span of the wing with winglet equipped, $b_{winglet}$ which is approximately 4% longer than with the conventional wingtip installed. It is a convention within the company that the smaller value of $b_{conventional\ wingtip}$ would be used as the reference, this small inconsistency with convention was discovered too late to correct it. It does not invalidate the results, but should be taken into account when comparing this data to other windtunnel or CFD data.

Table 4.2 shows the values that were used for angle of attack α and h/b throughout the CFD campaign. For each value of α, a new CFD computation had to be launched for each distinct value of h/b. This process had to be repeated for each geometry and thrust setting change. This resulted in an extensive CFD campaign comprising several hundred data points.

Table 4.2 – Values of the two variables used during the CFD campaign

α	$\frac{h}{b}$
0.0°	0.12
2.0°	0.128
4.0°	0.135
6.0°	0.155
8.0°	0.165
10.0°	0.18
11.0°	0.23
12.0°	0.31
13.0°	0.38
14.0°	0.41
15.0°	0.45
	0.625
	1.0

This chapter is structured as follows: In subchapter 4.1 an analysis is presented on the general behavior of this aircraft in ground effect, especially with respect to the change in lift and drag. This analysis is performed for the small nacelle, conventional wingtip geometry with flightidle thrust settings and gear deployed in the landing high-lift configuration. Counter-acting lift-enhancing and lift-reducing effects will be identified and their dependency on α and $\frac{h}{b}$ will be shown. This first subchapter will serve as a baseline for ground effect behavior, after which in the subsequent subchapters it will be discussed how a particular geometry change affects ground effect performance compared to that baseline geometry.

In subchapter 4.2 the influence of a change in thrust setting will be analyzed, using the same geometry used in subchapter 4.1. Next in subchapter 4.3 the high-lift setting will be changed to the take-off high-lift configuration with MTO thrust settings. This data can thus be directly compared to the data in subchapter 4.2. Subchapters 4.4 and 4.5 will look into the effect of changing nacelle size and wingtip respectively, for both the take-off and landing high-lift configuration. The final analysis is presented in subchapter 4.5, which will investigate how the influence of the ground effect changes when the landing gear is retracted. Early onset of stall due to ground effect is discussed in 4.7 and finally in subchapter4.8 there is a summary of all the observed effects.

4.1 General Ground Effect Behavior

In this section the change to lift and drag due to ground effect will be discussed and analyzed. This discussion will be limited to only one geometry variant, namely the case with a small nacelle, conventional wing-tip with gear deployed, in the landing high-lift configuration and flight-idle thrust setting. In short, a typical flight configuration used during the approach and landing phase of a flight.

The structure of this subchapter is as follows: First the behavior of the aircraft due to ground effect is analyzed in terms of change to global lift coefficient. Next the change in pressure distribution over the wing and fuselage is examined to determine how pressure change influences a change in lift. Subsequently this change in pressure can be compared to the change in spanwise drag changes due to ground effect. Cut-outs will be made along the wing to investigate the c_p distribution on the wing airfoil, as well as to determine the change to total velocity and total pressure close to the wing. A similar procedure will be followed to analyze the change in drag due to ground effect. Finally the changes to the flow due to ground effect will be visualized.

4.1.1 Lift Impact

4.1.1.1 Global Lift change due to Ground Effect

The relative change in lift due to ground effect in the range of $0° \leq \alpha \leq 13°$, as calculated by the in-house CFD post-processing tool FFD72 using the output ‘CL_S1MA’, can be seen in Figure 4.1. Positive values in these plots indicate that the lift is increased in ground effect.

As is evident from the results, there is some noise present in the data. Typically the CFD solutions converged to within $\pm 0.5\%$ of the total lift. Therefore, in order to further smooth the data, the assumption was made that there is a continuous relationship between α, h/b and the lift and drag of the aircraft. From this assumption a third order polynomial surface fit was constructed, which shows the trends in the data more clearly in. This is presented in Figure 4.2. Further details of the polynomial surface fit are given in Appendix K – Polynomial Surface Fit Plots. For ease of reading only three different h/b curves are shown, but these curves were generated based on the entire data set presented in Figure 4.1.

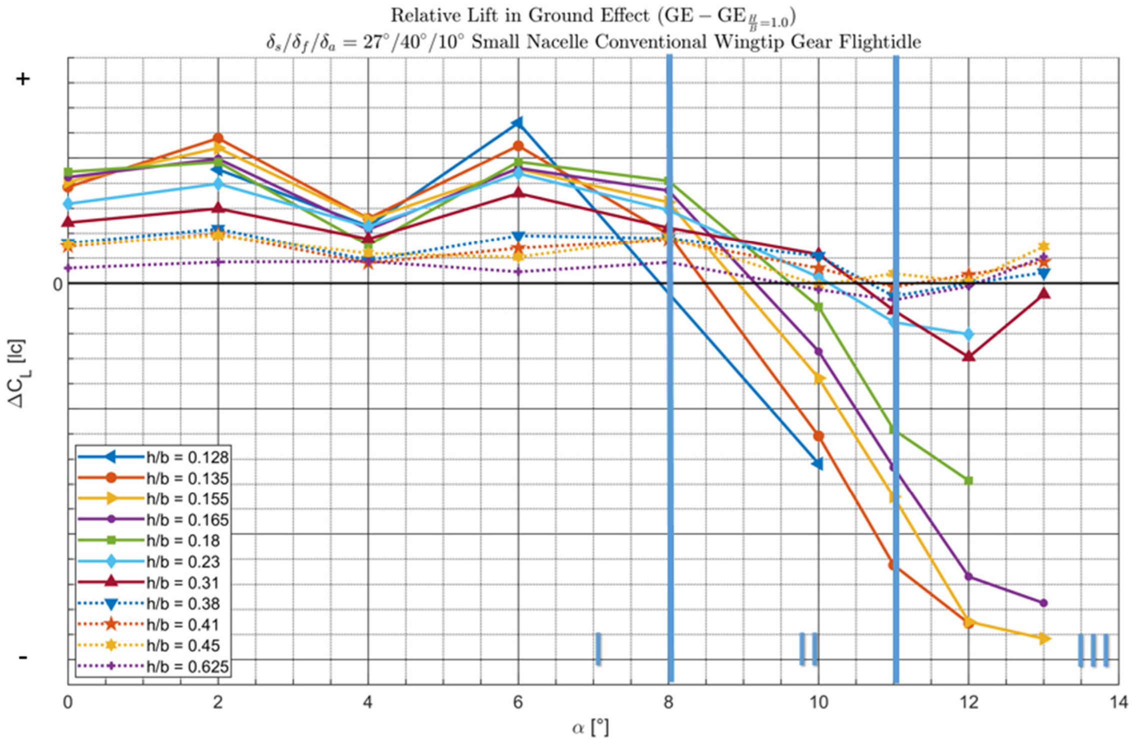

Figure 4.1 - Change in lift coefficient due to ground effect for a range of h/b for the small nacelle, conventional wingtip geometry with gear deployed in flightidle thrust conditions in landing configuration. Source: FFD72

Three distinct regions can be identified in these two figures, similar to what Qu et all (43) observed:

I. At low α, a lift increase of up to 3.5% can be observed.
II. There is an intermediate region at $8.0° < \alpha < 11.0°$, at which for moderate values of h/b there is still a small lift increase, but as the distance to the ground is decreased there is a relative loss of lift for the aircraft.
III. At high values of $\alpha > 11.0°$, there is a lift loss due to the ground effect for almost all values of h/b of up to 5.4%.

Both the lift increase at low α and lift decrease at moderate to high α become more pronounced as the distance to the ground is reduced. In other words, when the aircraft is closest to the ground, the largest absolute change to the lift is present, which is in agreement with the literature presented in chapter 1.

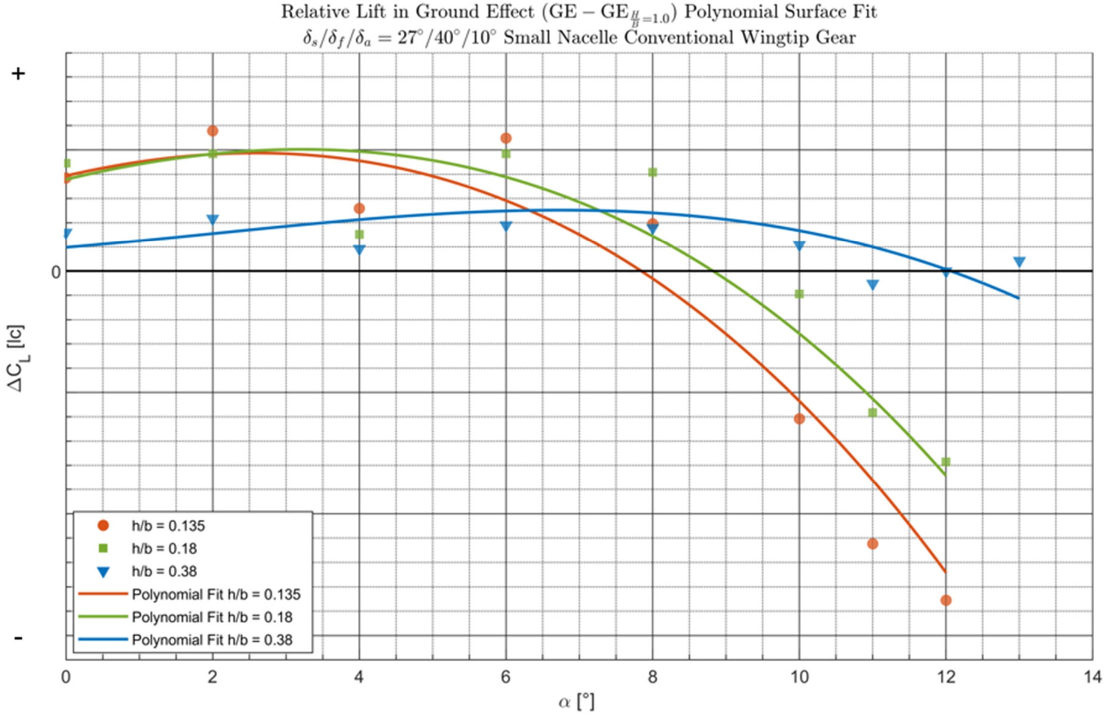

Figure 4.2 - Change in lift coefficient due to ground effect for a range of h/b for the small nacelle, conventional wingtip geometry with gear deployed in flightidle thrust conditions in landing configuration using a polynomial surface fit with same Y-Axis as figure 4.1. $R^2 = 0.8679$ *Source: FFD72*

In the remainder of this section, the mechanics behind the change in lift in ground effect for this particular geometric configuration will be discussed and explained by means of differential pressure plots, span wise lift distribution and 2D pressure and velocity distributions.

4.1.1.2 Relative Surface Pressure Distributions

4.1.1.2.1 General Observations

In order to get more insight into the causes of the change in lift of the aircraft in ground effect, the relative change to the pressure distribution over the wing is examined in this subsection. This differential pressure distribution is presented in Figure 4.3, Figure 4.4 and Figure 4.5 for respectively $\alpha = 4.0°$, $\alpha = 6.0°$ and $\alpha = 12.0°$. The contour of $\Delta C_{P_{GE}}$ is plotted in these figures:

$$\Delta c_{P_{GE}} = c_{P\,GE} - c_{P_{\frac{h}{b}=1.0}} \qquad (equation\ 4.1)$$

This means that for contour figures shown in this report, positive values of $\Delta C_{P_{GE}}$ imply that the pressure is increased in ground effect. The scale of the pressure change is the same for all three figures.

4.1.1.2.1.1 Wing Upper Side

By first investigating the upperside of the wing, it can be observed that in all cases there is an increase in suction across the entire length of the slat, labelled region A. This effect is strongest on the inboard slat and becomes weaker towards the wingtip. At $\alpha = 4.0°$ and $\alpha = 6.0°$ the leading edge of the mainwing also shows an increase in suction on the upperside due to ground effect, as well as an increase in pressure on the bottom part of the slat and the lower side of the mainwing leading edge. These are all lift-enhancing effects. At $\alpha = 12.0°$, only the upperside of the inboard slat still shows a significant suction increase, the other effects described above are no longer present.

In general in ground effect the upperside of the mainwing is subject to a pressure increase due to the bound mirror vortex reducing the stream velocity near the wing, resulting in a loss of lift on the wing upperside and effectively decreasing the camber (13) (56).

This increased pressure can be observed even more clearly on the flap upperside, where a significant reduction in the magnitude of the front suction peak is found, labelled region B. An example of this can be seen in Figure 4.10. This is in full agreement with the observations from Qu et al. (56), where it was found that due to ground effect, the mass flow rate in the flap gap decreased, thus reducing velocity through the gap and reducing the magnitude of the flap leading edge suction peak. Increasing the flap deflection angle or α further decreases this mass flow rate, resulting in a further reduced front suction peak on the flap, which reduces flap circulation and hence lift.

For all incidence angles, strange, unphysical looking spots with strong $\Delta C_{P_{GE}}$ gradient can be observed on the winglet, inboard flap and the wing upper surface behind the nacelle. These are shown in region C. These are caused by vortices, some of which are induced by the inboard and outboard slat end, the two strakes of the engine and wing-pylon junction. These vortices are inherently unsteady in nature, so when comparing their position in two different solutions, they will always be slightly shifted in position. This causes seemingly strong gradients to appear in the contour plots, which can safely be ignored.

Comparing the pressure differential at the upperside in front of the outboard flap and at the trailing edge of the wing, for the cases of $\alpha = 4.0°$ and $\alpha = 6.0°$ shows that there is a significantly higher pressure increase in this location for $\alpha = 4.0°$, which accounts for the relative reduction in global lift at $\alpha = 4.0°$ compared to $\alpha = 6.0°$.

Finally, it can be concluded that the pressure differential on the upperside of the wing shows a strong dependency on α. At low α the pressure increase is primarily concentrated on the flap region and the mainwing leading edge just in front of it. In contrast Figure 4.5 at $\alpha = 12.0°$ shows how there is a high increase in pressure over almost the entire surface area. At the inboard slat leading edge there is still an increase in the suction peak, but this is less significant compared to the case of $\alpha = 6.0°$.

4.1.1.2.1.2 Wing Lower Side

Similar to the upperside of the wing, the pressure on the lowerside also increases due to ground effect leading to a lift increase, labelled region D. In contrast to the wing upperside, now the pressure increase is relatively independent of α. This pressure increase is attributed in literature to the airflow being ‘blocked’ in the convergent channel between the wing lowerside and the ground (43), thus reducing the local flow velocity and increasing the static pressure. In subchapter 4.1.3 it is shown that in the ground effect, streamlines which would normally flow below the wing in free air flight conditions are diverted over the wing due to ground effect. This reduces the mass flow of the air below the wing and thus reduces the flow velocity.

That velocity reduction is shown for $\alpha = 6.0°$ and $h/b = 0.155$ in Figure 4.6, for a cut in the zx plane at a location close to the fuselage. Negative values of dV_{tot} indicate a decrease in flow velocity due to ground effect. Below the wing the total velocity is reduced by up to a maximum of approximately 7 m/s, which is 10% of the free stream velocity. The flow is accelerated locally over the slat and the front part of the mainwing and slows down strongly over the upperside of the flap by more than 10 m/s.

The total pressure differential due to ground effect is shown in Figure 4.7, whereby the conditions and cut location are exactly the same as previous image. There is no momentum loss causing the reduction in flow velocity beneath the wing. The wake from the flap shifts upwards in z-direction, away from the ground.

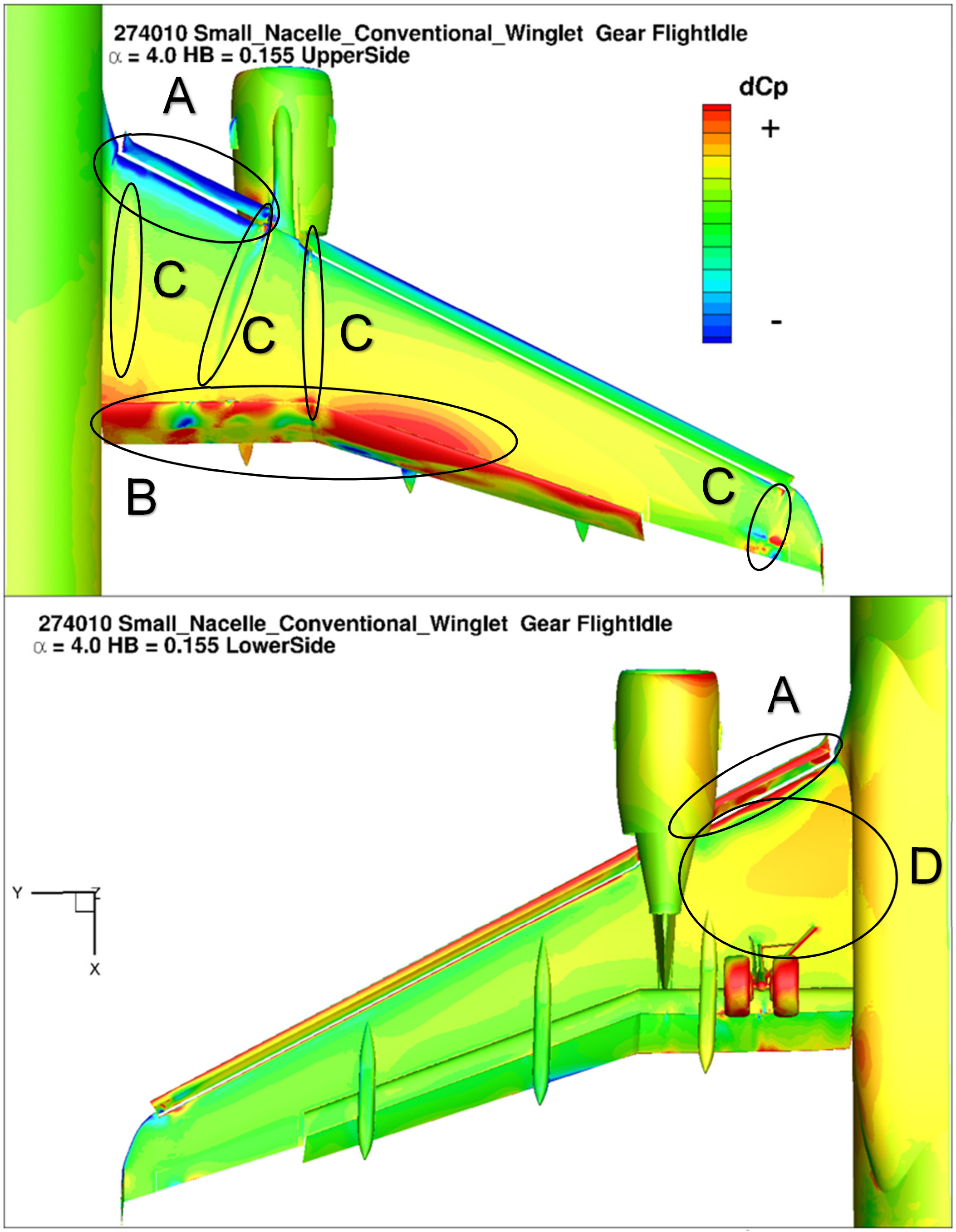

Figure 4.3 - Relative pressure change over the wing due to ground effect at $\alpha = 4.0° \ \frac{h}{b} = 0.155$,$(\Delta C_{P_{GE}} = C_{P\,GE} -$

While the pressure increase on the wing upperside is distributed over the entire wing span, the pressure increase on the lowerside is concentrated on the inboard wing between the engine nacelle and fuselage, as well as on the fuselage itself and on the inboard side of the nacelle. Almost no pressure increase can be observed on the lowerside of the flaps.

A possible explanation might be that for this particular flap deflection angle, the ground induced velocity, conceptually sketched in Figure 1.6, hits the flap lowerside perpendicularly, causing almost no change to the static pressure. This explanation is supported by analyzing the pressure distribution for the take-off configuration, for example in Figure 4.41 and Figure 4.42 (same dCp scale), which has a $10°$ flap deflection angle instead of $40°$. In this case with lower flap deflection, there is a stronger tangential component to the ground induced velocity on the flap lowerside, causing a stronger absolute pressure increase on the flap lowerside when compared to the landing configuration, even though the overall magnitude of the pressure increase on the remaining part of the lower wing is significantly lower for the take-off configuration.

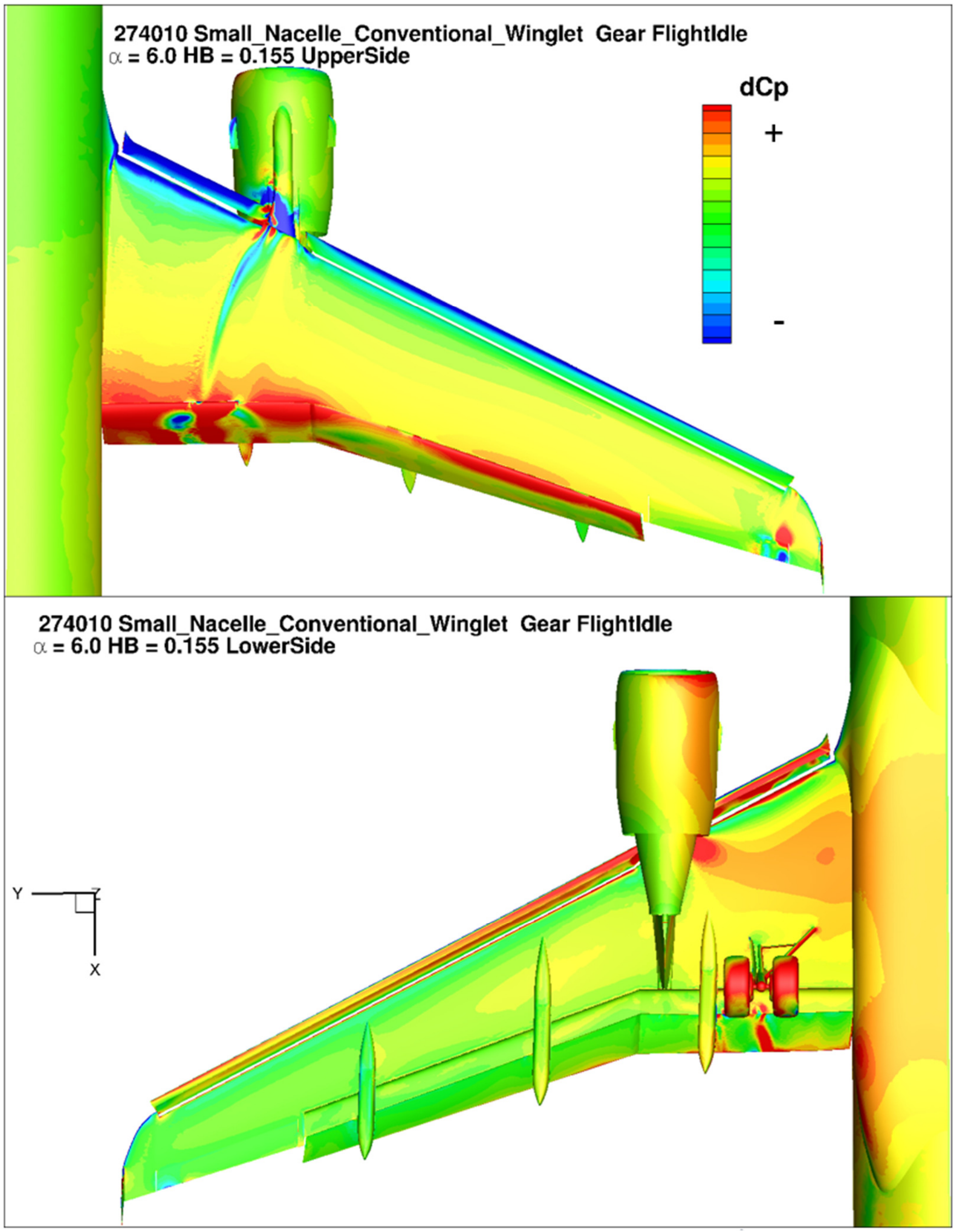

Figure 4.4 - Relative pressure change over the wing due to ground effect at $\alpha = 6.0°$ $\frac{h}{b} = 0.155$, $(\Delta C_{P_{GE}} = C_{P\,GE} - C_{P_{\frac{h}{b}=1.0}})$

The trends observed in Figure 4.1 and

Figure 4.2 can now be explained in terms of pressure changes on the wing. At low α, the pressure on the wing lowerside is already significantly increased due to ground effect, which enhances the lift. In contrast, the lift reducing pressure increase on the wing upperside is still relatively small, leading to a net increase in lift.

As α increases, the pressure on the wing upperside increases faster compared to the pressure rise on the lower surface. This reduces the lift benefit and eventually leads to a net reduction in lift.

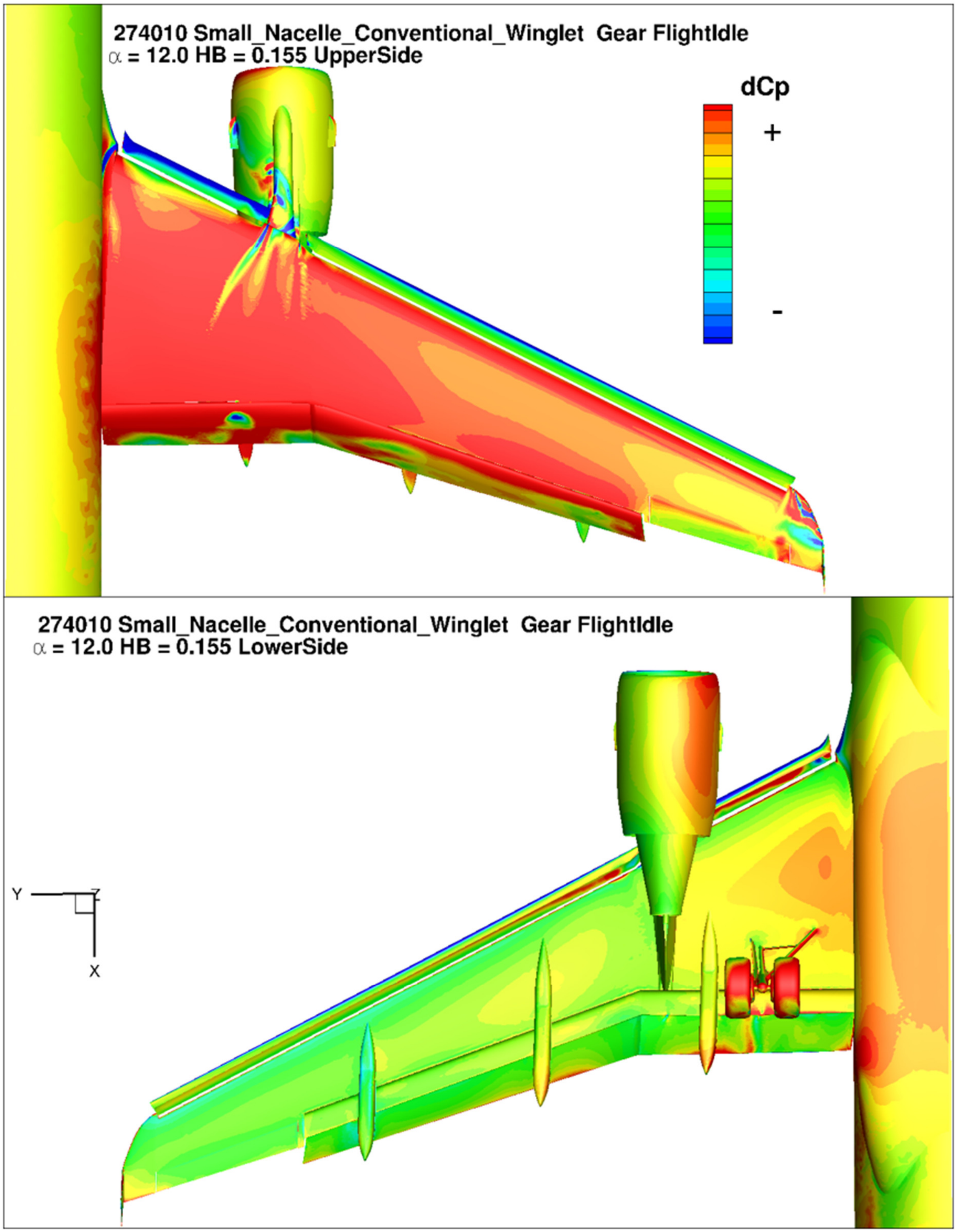

Figure 4.5 - Relative pressure change over the wing due to ground effect at $\alpha = 12.0°$ $\frac{h}{b} = 0.155$, $(\Delta C_{P_{GE}} = C_{P_{GE}} - C_{P_{\frac{h}{b}=1.0}})$

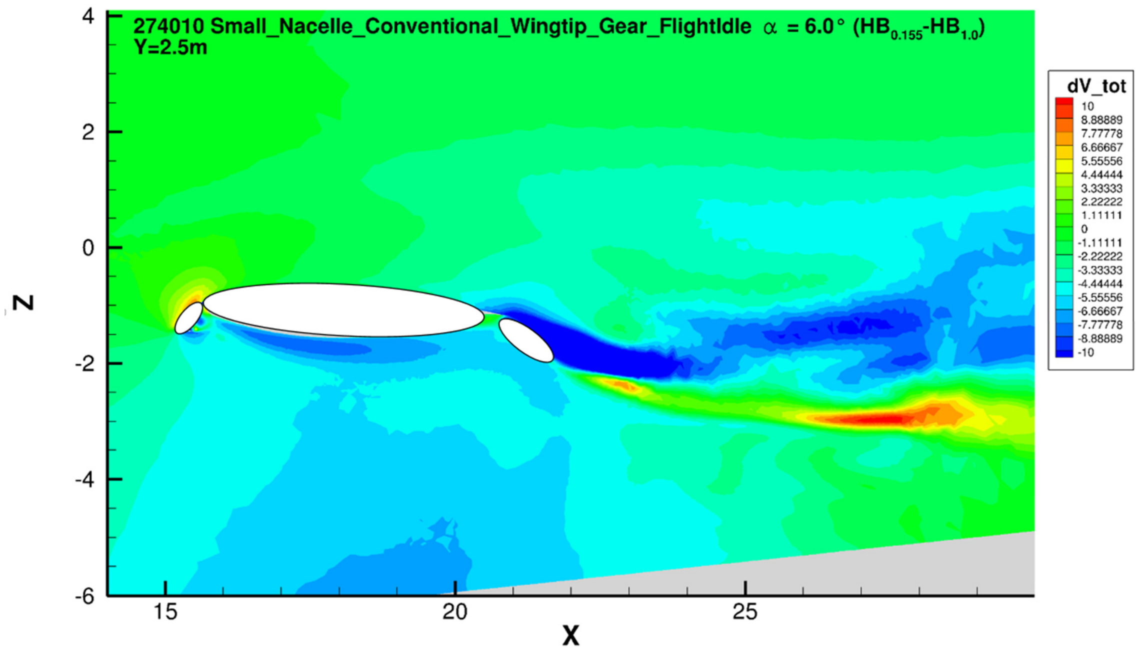

Figure 4.6 – Total velocity change (in m/s) due ground effect for the small nacelle, conventional winglet geometry in landing high-lift configuration with flightidle thrust settings $\alpha = 6.0°$

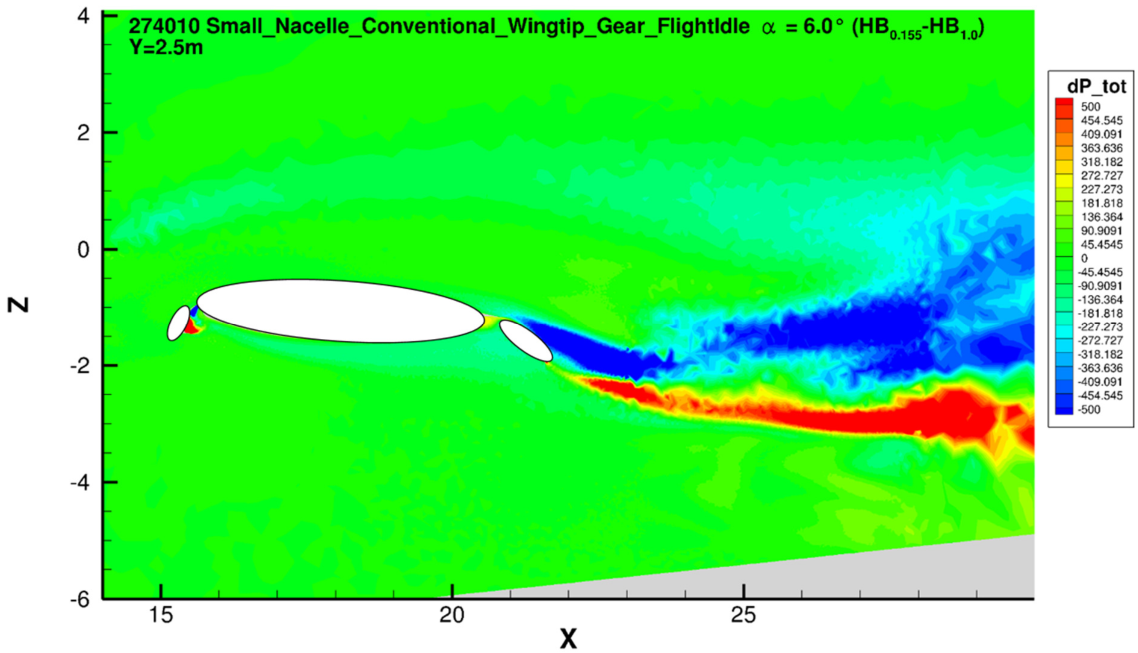

Figure 4.7 – Total pressure change (in Pa) due ground effect for the small nacelle, conventional winglet geometry in landing configuration with flightidle thrust settings $\alpha = 6.0°$

4.1.1.2.2 Deloading of the flap

At $\alpha = 4.0°$ in Figure 4.3, there is a reduction in lift increase compared to the closest data points $\alpha = 2.0°$ and $\alpha = 6.0°$ for low values of h/b. This is phenomenon can be observed to a lesser extent for most other configurations and thrust settings, which can be seen in Appendix E - Cut locations. One possible explanation for this observation is presented in Figure 4.8, where the flow separation on the outboard flap for $\alpha = 2.0°$, $\alpha = 4.0°$ and $\alpha = 6.0°$ is visualized by plotting the skin friction coefficient in x-direction, c_{f_x}. Negative values of c_{f_x} can indicate flow reversal and thus separation, as is the case on the flaps.

It can be seen that for $\alpha = 2.0°$ and $\alpha = 6.0°$ the separation on the outboard flap remains approximately the same in and out of ground effect, while for $\alpha = 4.0°$ there is a notable increase in the separated region in ground effect only, leading to a relative lift decrease. That can also be observed in Figure 4.11 which shows only for $\alpha = 4.0°$ a significant lift decrease of up to 5% in region of the outboard flap.

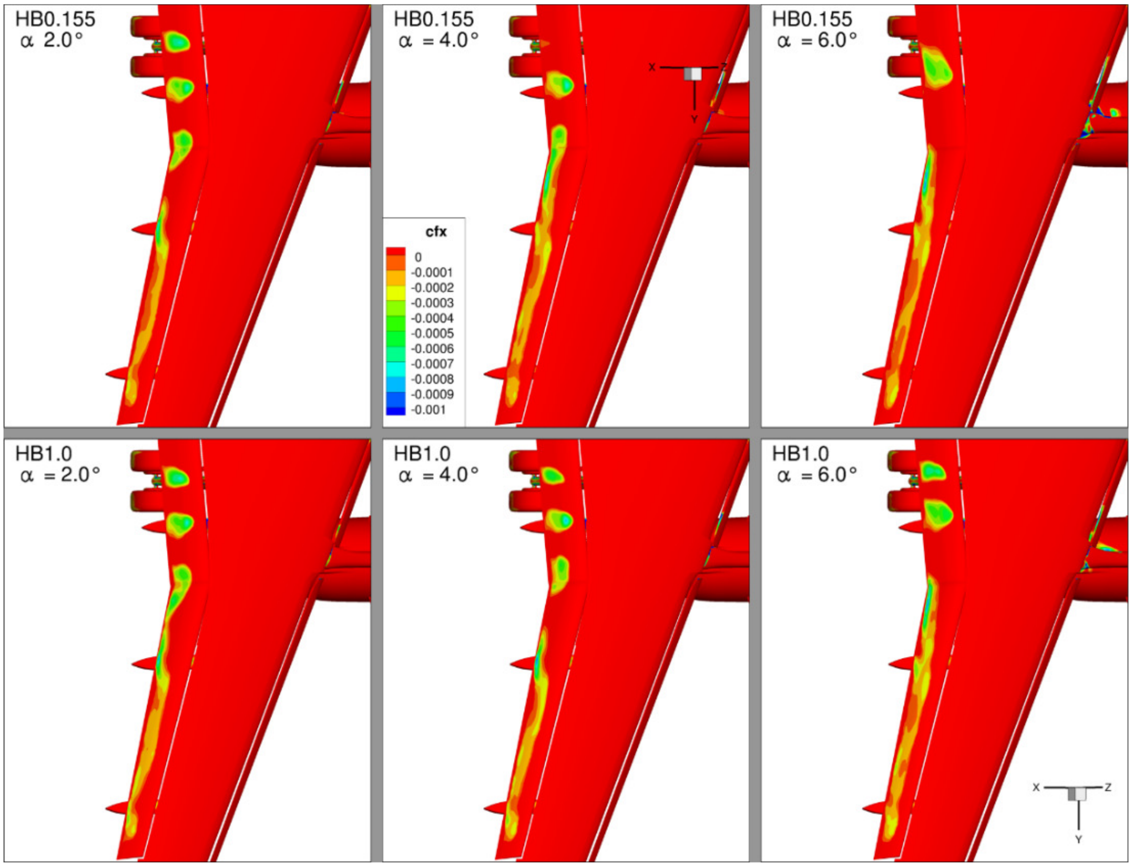

Figure 4.8 - Flow Separation location on the upperside of the outboard flap for low α. Small Nacelle, Conventional Winglet in landing configuration with flightidle thrust settings.

Figure 4.8 and Figure 4.9 show that the region of separation on the upperside of the inboard flap is reduced in ground effect across the range of $2.0° < \alpha < 12.0°$. This is caused by the reduction of the front suction peak on the flap leading edge, leading to deloading of the flap and a reduction of the adverse pressure gradient in ground effect, potentially resulting in a smaller separated flow region. This effect is illustrated in Figure 4.10, where C_p plots of the inboard flap are shown at $\alpha = 10.0°$.

The deloading of the flap is explained as follows: Out of ground effect, as the lift increases with α, the lift of the mainwing increases and thus the energy of the flow over the flap and into the flap gap decreases, causing it to become deloaded. At low α in ground effect, the mainwing lift is increased and thus the same mechanism will cause the flap to deload. But as α is increased in ground effect and the mainwing becomes deloaded due to ground effect, this will no longer be the cause for the flap to deload. However, as shown in Figure 4.5 for $\alpha = 12.0°$ and $h/b = 0.155$, the flap remains deloaded in ground effect even when the main wing itself is also significantly deloaded. That has also been observed in literature, where it was found that the mass flow rate though the flap gap of a 2-D multi-element airfoil is reduced in ground effect, even when the main wing element was also deloaded (56). The rate by which this is reduced increases with increasing α.

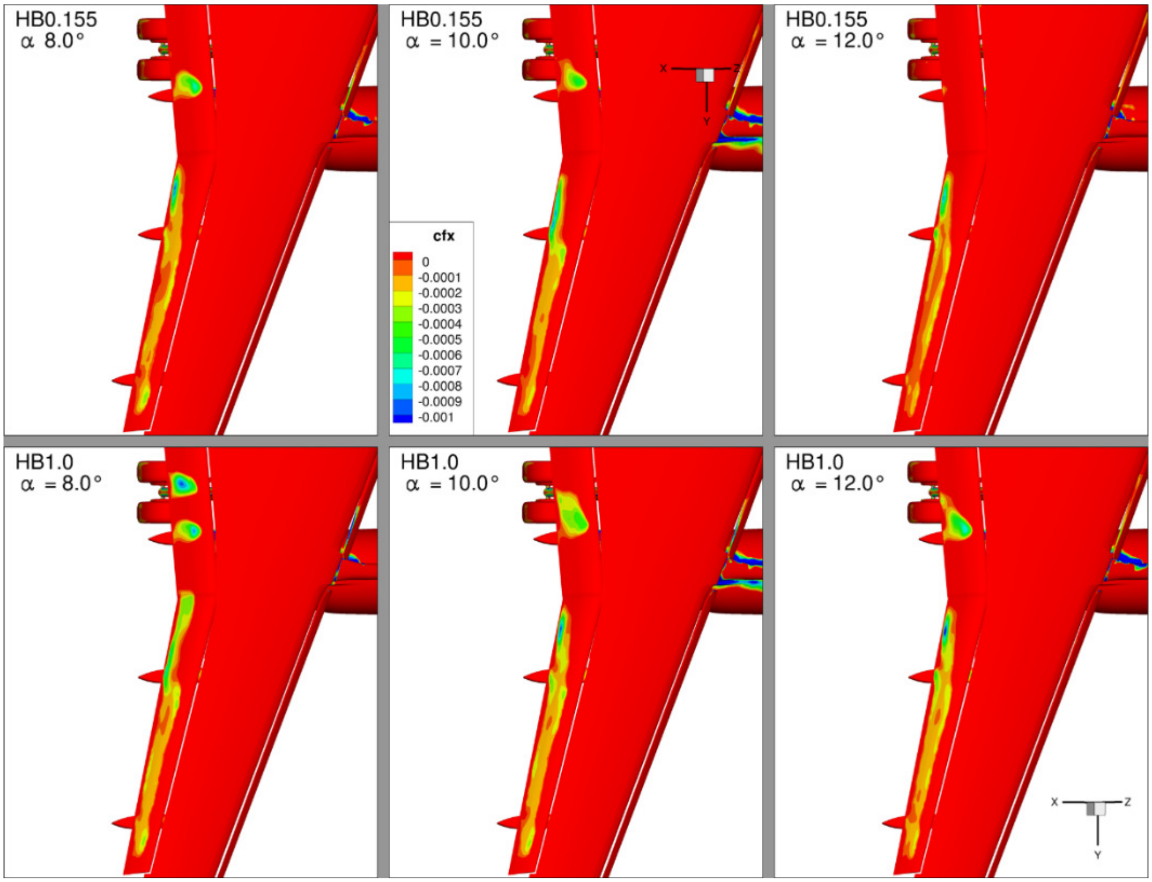

Figure 4.9 - Flow Separation location on the upperside of the outboard flap for moderate α. Small Nacelle, Conventional Winglet in landing configuration with flightidle thrust settings.

The wing becomes more frontally loaded in the ground effect. This is due to the flap becoming deloaded, together with the rear part of the main wing, while the slat and front of the mainwing become more loaded due to the suction increase on the upperside of the slat.

This also implies that the pressure gradient becomes more adverse in the ground effect. That can then lead to an early onset of stall and is discussed in more detail in subchapter 4.7.

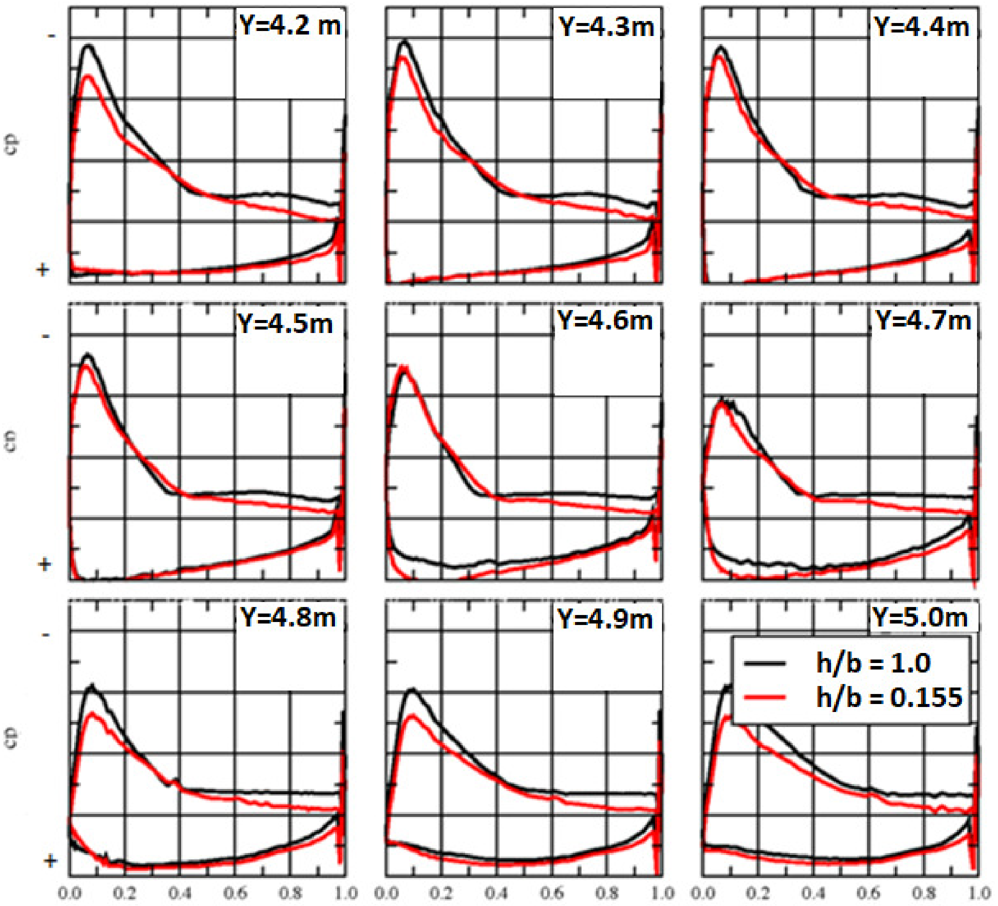

Figure 4.10 - Inboard Flap C_p Distribution small nacelle, conventional winglet geometry in landing configuration with flightidle thrust settings at $\alpha = 10.0°$

4.1.1.2.3 Summary of the Observed Effects Influencing Lift in Ground Effect

Based on the relative pressure distribution in ground effect the following effects can be summarized. These effects are categorized into lift enhancing and lift decreasing effects. For any combination of parameters α and h/b, all these effects are present and will counteract each other. It depends on the exact values of these parameters which effect is more dominant and thus whether the global lift coefficient is increased or decreased. The various effects are summarized below.

Lift Enhancing Effects:

- The suction on the slat upperside leading edge is increased over the entire length of the wing. This increase in suction is primarily caused by an increase in effective angle of attack, which the slat is very sensitive to. On the inboard slat the increase in suction is most significant.
- There is an increase in pressure on the lowerside of the inboard wing and on the lowerside of the fuselage, caused by the flow velocity reducing between the wing and the ground, the so-called blockage effect. This reduction in flow velocity under the wing is shown in Figure 4.6.
- A less significant pressure increase is present on the outboard part of the lower wing. It is most significant close to the nacelle and reduces towards the wingtip.
- The pressure on the lowerside of the nacelle is increased, especially at the side closest to the fuselage

Lift Reducing Effects:

- For all α the pressure on the flap upperside is increased due to a reduced mass flow rate through the flap gap, especially at the flap leading edge. This occurs over the entire span of the inboard and outboard flap.
- The pressure increases on the mainwing. The pressure increase is most significant at the trailing edge and reduces when moving towards the leading edge. This effect occurs over the entire wing span. At low α this pressure increase is relatively small compared to the other effects, in contrast at high α it becomes the dominant effect and also affects the upperside of the fuselage.

4.1.1.3 Spanwise Lift Distribution in Ground Effect

Now that the change in pressure distribution due to ground effect has been discussed in the previous subsection 4.1.1.2, the change in spanwise lift distribution can now be examined to get quantitative data. The change in lift due to ground effect could of course be obtained by integrating the surface pressure distributions which were discussed in the previous section, but use was made of the in-house tool FFD72 to obtain both the spanwise lift and drag distributions in order to use the standard data processing procedures followed at the company, as well as remove the risk of errors which would be introduced when writing a script to perform the surface integration.

Figure 4.11, Figure 4.12 and Figure 4.16 show the spanwise lift distribution over the wing-body with the incidence angle ranging from $0° < \alpha < 13°$. The top graph in each figure shows the absolute lift distribution, while the bottom graph shows the percentage change in lift distribution compared to the lift distribution at $h/b = 1.0$.
The wing-body geometry of the large nacelle-winglet variant can be seen in the background and has the correct scale in relation to the data shown in the figures. At the winglet the graph line stops before the geometry depiction ends, because the data from the conventional wingtip is shown, which has a shorter wingspan compared to the winglet geometric variant depicted here.

4.1.1.3.1 Low Incidence

For the lift distribution at low α, as shown in Figure 4.11, the largest lift increase on the wing can be seen between the fuselage and the nacelle. In this region local lift changes of approximately 5% can be observed. This is primarily caused by the pressure increase seen on the lower wing, which is shown in Figure 4.3, as well as the strong increase in suction on the inboard slats. Both the percentual lift change due to ground effect, as well as the absolute value of the lift are highest in this inboard region of the wing. Therefore, this area is of significant interest. At least two causes can be identified as to why this inboard region shows the strongest lift change in ground effect:

1. The absolute lift is strongest at the inboard wing region. Thus, the circulation of the bound mirror vortex is also strongest in this region, i.e. the influence of the ground effect will be strongest in this region
2. The inboard wing is closer to the ground compared to the outboard wing due to the dihedral present in the aircraft geometry, thus the influence of the ground effect is stronger according to the law of Biot-Savart.

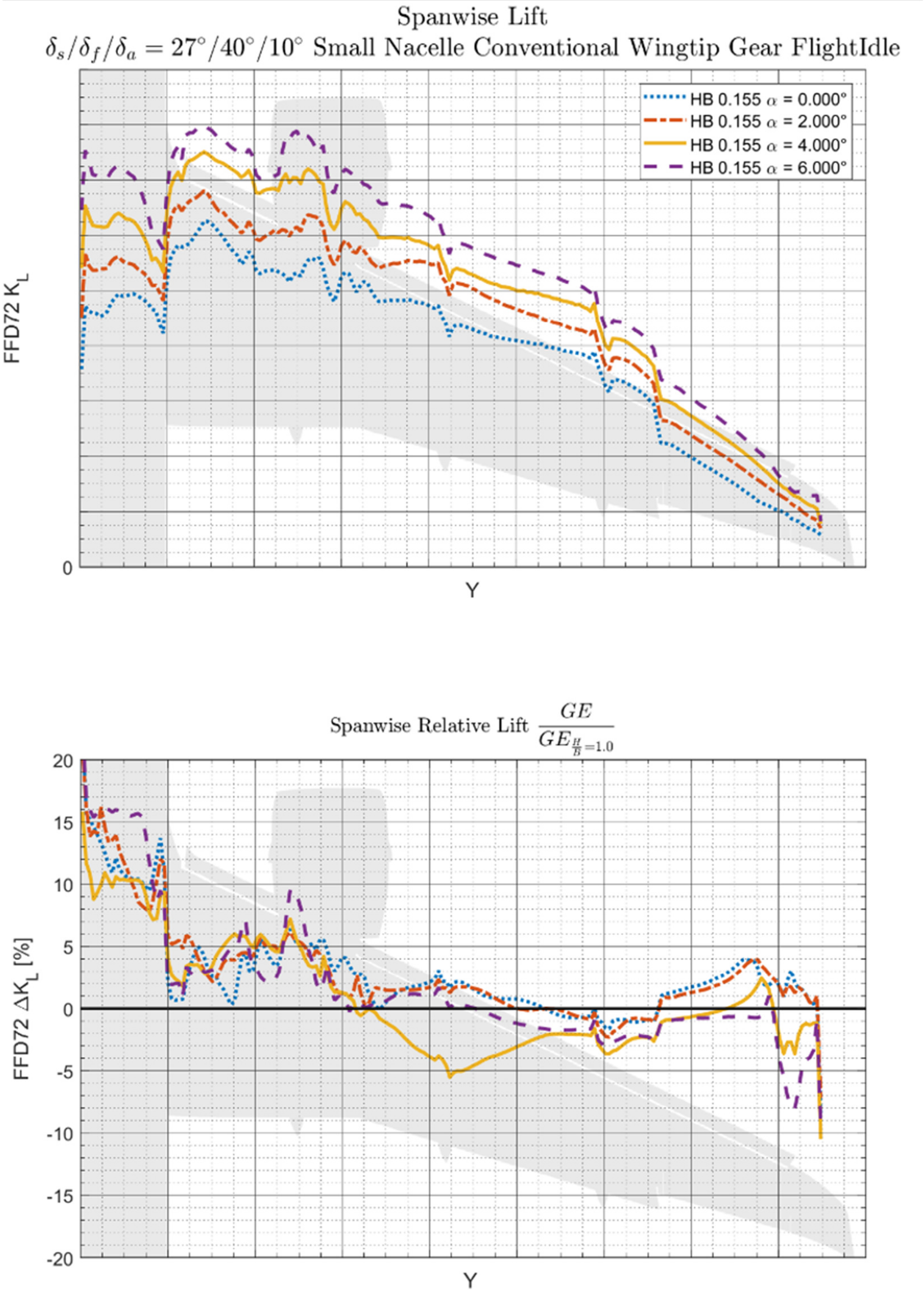

Figure 4.11 - Lift distribution along the wing-body for low α at $\frac{h}{b} = 0.155$

There is a limited change in lift due to ground effect in the middle section of the wing, located between the nacelle and aileron. Figure 4.3 and Figure 4.4 can be consulted to determine why this is the case: The pressure increase on the upper wing and flap in this region is counteracted by the suction increase on the slats, together with the slight pressure increase on the lower wing surface.

The reduction in lift on this part of the wing for $\alpha = 4.0°$, shown Figure 4.8 , was discussed in subsection 4.1.1.2.2. It was determined to be related to an increase in flow separation in the ground effect on the upperside of the outboard flap.

At the outboard section of the wing, the flap with 40° flap deflection ends and the aileron with only 10° aileron deflection begins. The difference in behavior in ground effect is seen by the upward moving kink in the relative lift distribution. The cause of this kink in the relative lift distribution can be seen in Figure 4.3, where the pressure is increased on the outboard flap but does not increase by the same order of magnitude on the aileron, due to it having a far smaller deflection angle, resulting in a more positive lift increment change in that region. As has been seen in literature (13), a higher flap deflection angle results reduces the lift increment in ground effect.

Finally it should be noted that there is a significant increase to the lift on the fuselage due to the ground effect, across the entire incidence range. The implications of this will be discussed separately in subsection 4.1.1.4.

4.1.1.3.2 Moderate Incidence

Figure 4.12 shows the spanwise lift distribution in ground effect for the range of $6° < \alpha < 11°$. As was seen in Figure 4.1, this is the critical range where the $\Delta C_{L_{GE}}$ changes from positive to negative.

As α increases, two regions can be identified where the lift increment changes. The first and most significant change occurs between the fuselage and the engine nacelle, labelled region A. For $\alpha = 6.0°$ and $\alpha = 8.0°$ there is still a small lift increase of on average 4% in this region. In contrast for $\alpha = 11.0°$ there is a lift decrease of approximately 7%. This decrease in relative lift with α is caused by the fact that in ground effect, with increasing α, the lift decreasing pressure rise on the upper wing is surface is increasing faster compared to counter-acting effect of the lift increasing pressure rise on the lower wing surface. The relative pressure increase on the bottom wing almost stops increasing at a certain point, while on the upper wing it keeps increasing with α.

The second region with strong lift increment change is located at the fuselage, region B. Here the lift increase reduces from 15% at $= 6.0°$ to $\alpha = 11.0°$. Identical to the inboard wing, the pressure increase on the lower fuselage increases slower compared to the pressure rise on the upper fuselage.

In the outboard of the wing where the outboard flap is located, region C, this same phenomenon of lift reducing pressure rise on the upper wing surface is occurring, albeit less strongly. The counteracting lift increase due to pressure rise on the lower wing surface is also less significant. Hence the relative lift change is only reduced by approximately up to 4% for this region in this incidence range.

Influence of Height Above Ground

The influence of different values of h/b on the spanwise lift distribution is shown in Figure 4.13. In general, it can be concluded that h/b determines the magnitude of the change due to ground effect, but has less influence on the shape of these curves. This holds especially true for the outboard part of the wing. Behind the nacelle there are some non-linear effects to be observed due to the engine influence, this is also the only region where there is a significant change in lift for the case of $h/b = 0.625$. Since this occurs only for the $\alpha = 8.0°$ case, this is most likely a numerical artifact present in the $h/b = 1.0$ reference solution.

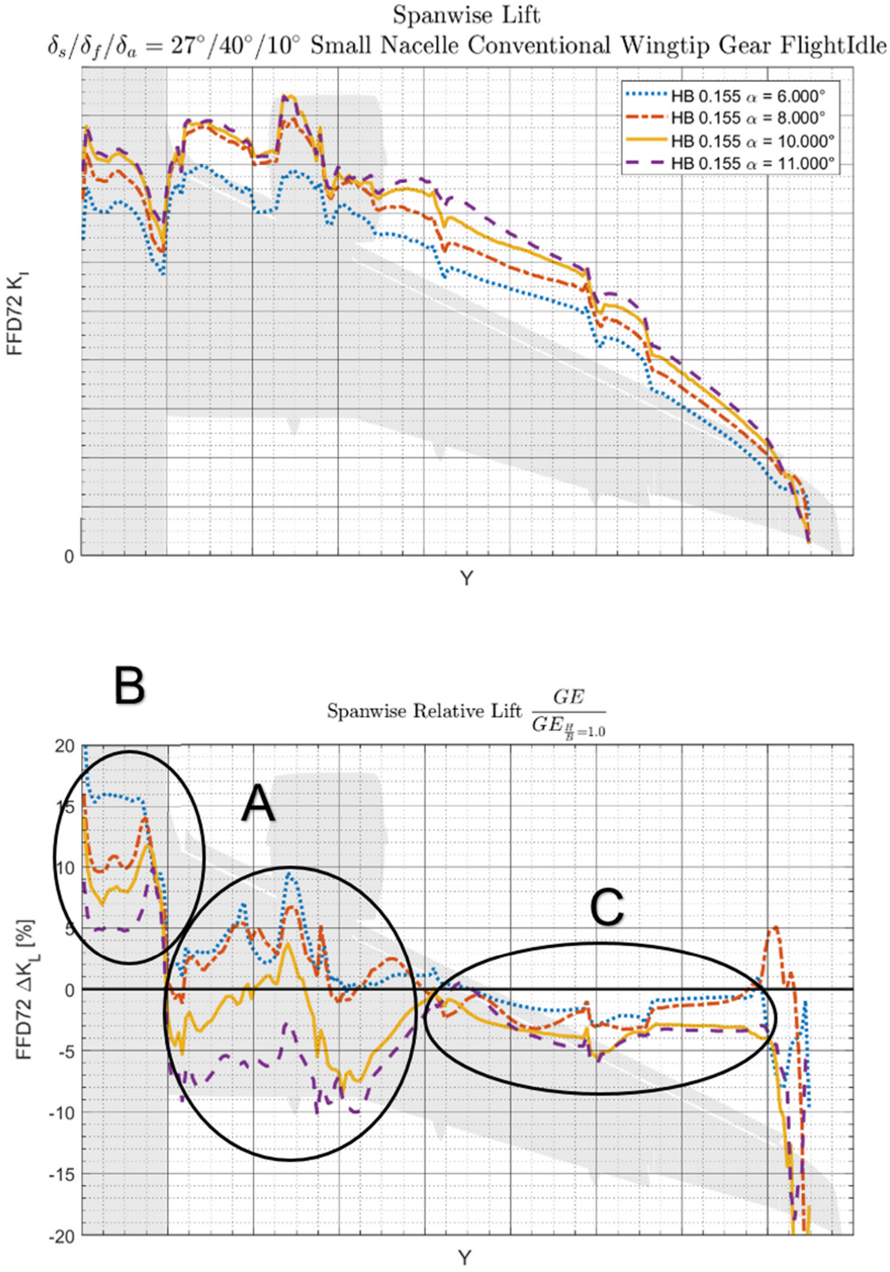

Figure 4.12 - Lift distribution along the wing-body for moderate α at $\frac{h}{b} = 0.155$

The kink close to the wingtip at $\alpha = 8.0°$, region D, where there is suddenly a strong increase in relative lift of up to 6% for all values of h/b , can be explained by inspecting the values of the friction coefficient in x direction c_{f_x}, seen in Figure 4.14. At $\alpha = 8.0°$ only, there is a region of separated flow on the outboard part of the upperside of the aileron for $h/b = 1.0$, which will lead to a reduction in lift in the reference computation. This region is not present in ground effect, leading to a relative lift increase in ground effect. No further explanation can be offered here for the occurrence of this separation region on the aileron for $\alpha = 8.0°$ at $h/b = 1.0$, other than to observe that this region is also present in computations with maximum take-off power applied, in computations with the landing gear removed and in computations where the large nacelle was exchanged. Thus, it could be a critical region where slight changes to the pressure distribution can be the difference between attached and separated flow. This region is affected by unsteady flow caused by the vortices from the end of the outboard slat and the wing D-nose. The unsteady nature of these vortices could be the reason why this separation region is present in some cases but not in others. Therefore, it is not necessarily a physical phenomenon caused by ground effect.

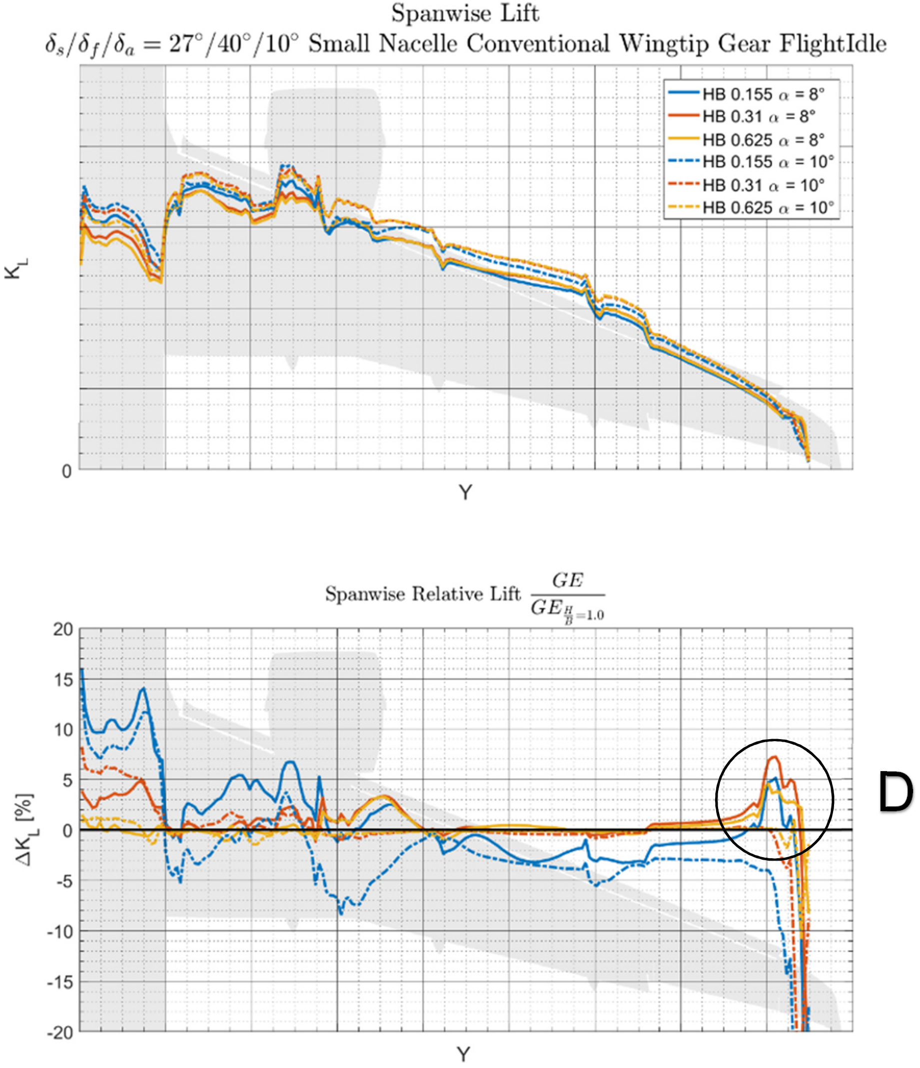
Spanwise Lift

$\delta_s/\delta_f/\delta_a = 27°/40°/10°$ Small Nacelle Conventional Wingtip Gear FlightIdle

Spanwise Relative Lift $\frac{GE}{GE_{\frac{H}{B}=1.0}}$

Figure 4.13 - Lift distribution along the wing-body for moderate α at $\frac{h}{b} = 0.155$, $\frac{h}{b} = 0.31$ and $\frac{h}{b} = 0625$

Figure 4.14 also shows that wingtip stall occurs earlier in ground effect for all angles shown here. This is due to the stronger adverse pressure gradient, created primarily by the increased suction peak on the leading edge of the wingtip. The same effect is also present when the winglet is equipped, as can be seen in Figure 4.15. Only one angle of α is shown in this figure, because since the winglet stall is more abruptly compared to the more gradual tip stall of the conventional wingtip, this effect is only visible at $\alpha = 11.0°$. At all other angles the flow over the winglet is either fully attached or fully detached.

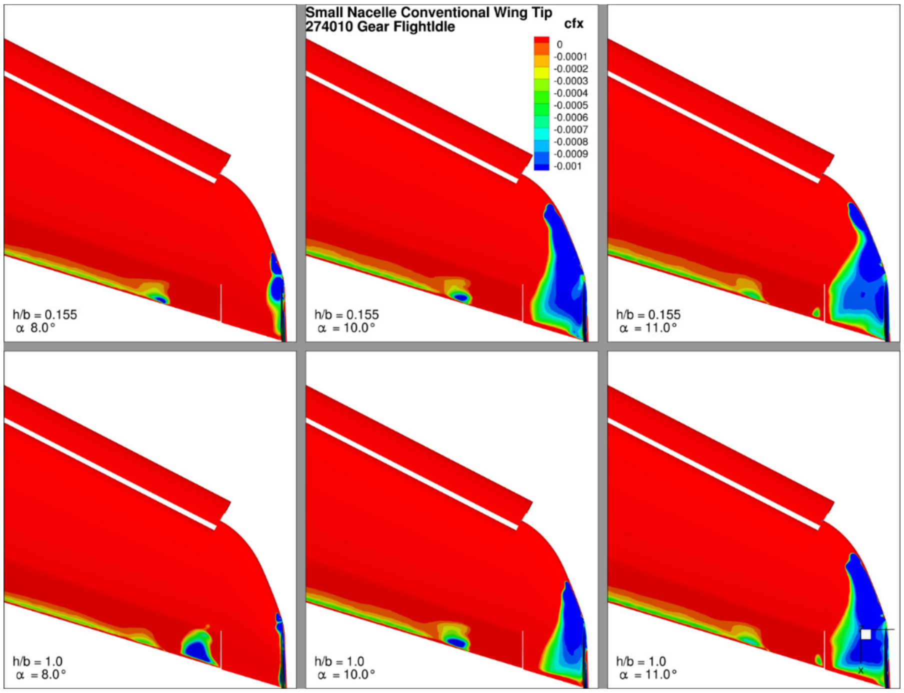

Figure 4.14 –Separation in the wingtip area at $\alpha = 8.0°$ (left), at $\alpha = 10.0°$ (middle), $\alpha = 11.0°$ (right) for $\frac{h}{b} = 0.155$ (top) and $\frac{h}{b} = 1.0$ (bottom)

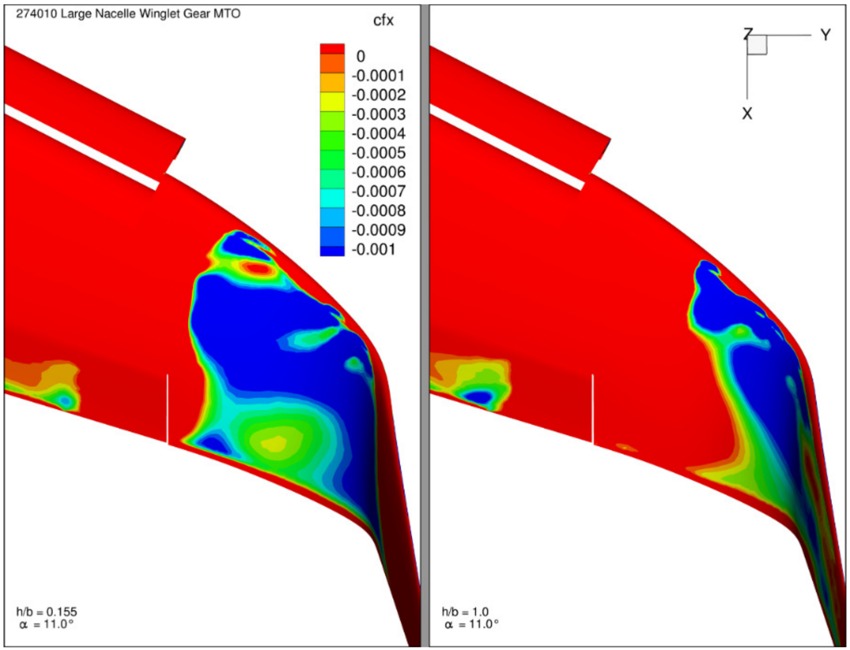

Figure 4.15 –Separation in the winglet area at $\alpha = 11.0°$ for $\frac{h}{b} = 0.155$ (left) and $\frac{h}{b} = 1.0$ (right)

4.1.1.3.3 High Incidence

As previously seen in Figure 4.1, at high α the lift increment continues to decrease due to ground effect. However it can be noted that the influence of the ground effect becomes less dependent on α, i.e. the non-linear part of the lift curve slope is reached. The relative lift change in ground effect over the wing becomes almost identical for $\alpha = 12.0°$ and $\alpha = 13.0°$, the one major observable difference is seen on the fuselage where the lift decreases strongly with increasing α.

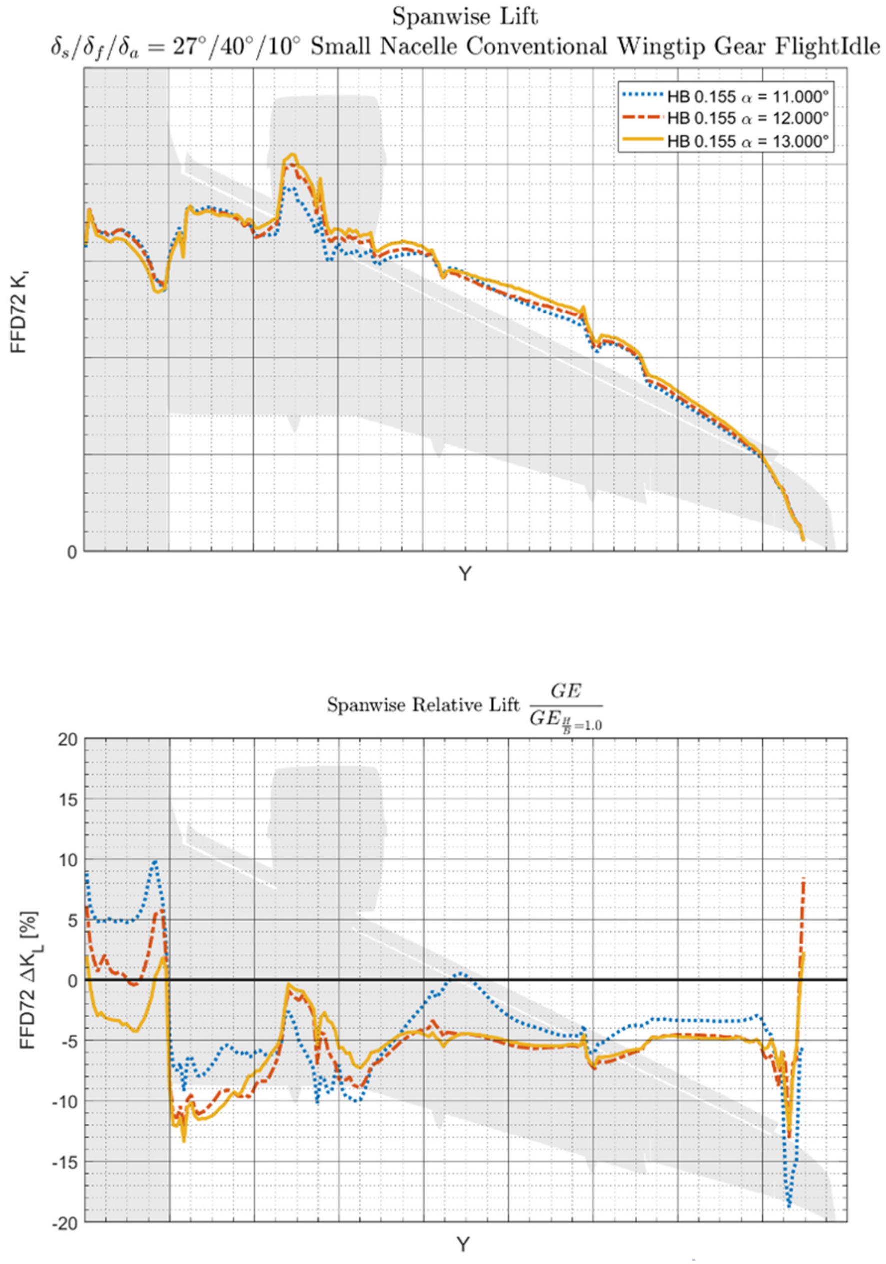

Figure 4.16 - Lift distribution along the wing-body for high α at $\frac{h}{b} = 0.155$

The absolute lift on the inboard wing section between fuselage and nacelle remains nearly independent of α, while the lift still increases as a function of α on the outboard part of the wing. At the wingtip there is a sharp decrease in lift due to ground effect at $\alpha = 11.0°$, due to a strong pressure rise on the leading edge of the wingtip, similar but stronger as to what can be observed on the wingtip in Figure 4.5. Since the wingtip is fully stalled at this α, as shown in Figure 4.14, there is a lot of unsteady flow in this region which is not fully captured by the steady RANS code used during these computations. Since the lift is already very small at the wingtip, fluctuations due to the unsteady nature of the flow can have a large impact on the relative change in this region.

4.1.1.4 Influence of the Fuselage on the Lift Change in Ground Effect

The simplest mental model that can be used to understand lift due to the fuselage is to imagine it merely as an extension of the inboard wing, used to connect the two wings together, since the fuselage will not induce circulation by itself. However it has been shown in Figure 4.3 until Figure 4.5 that there is a significant pressure increase present on the lowerside of the fuselage, similar but stronger than the pressure rise on the wing lowerside. In contrast on the fuselage upperside the pressure increase is less significant when compared to the pressure increase on the wing upperside immediately next to it. This may be explained by realizing that the influence of the mirrored vortex on a point on the aircraft is determined by the law of Biot-Savart (5), equation 1.1. The law states that the influence of the ground effect is reduced by the cube of the distance. For a wing, the difference in distance to the ground for the upper and lowerside is small, but for the fuselage this distance between the bottom and top part is more significant. Hence the upperside of the fuselage is influenced to a lesser degree by the ground effect compared to the upperside of the wing, which should result in a more positive lift increment due to ground effect.

This is exactly what can be seen in Figure 4.17 which shows separately the fuselage lift and wing lift as calculated by the tool CFD2LOADS, together with the total lift as calculated by FFD72. The fuselage ground effect lift increment is of the same order of magnitude as the wing lift increment, while in terms of the absolute lift the wing lift is approximately six times larger. Therefore, it can be concluded that the fuselage has a disproportionately large impact on the lift increment in ground effect for this particular combination of slat, flap and aileron deflection angles.

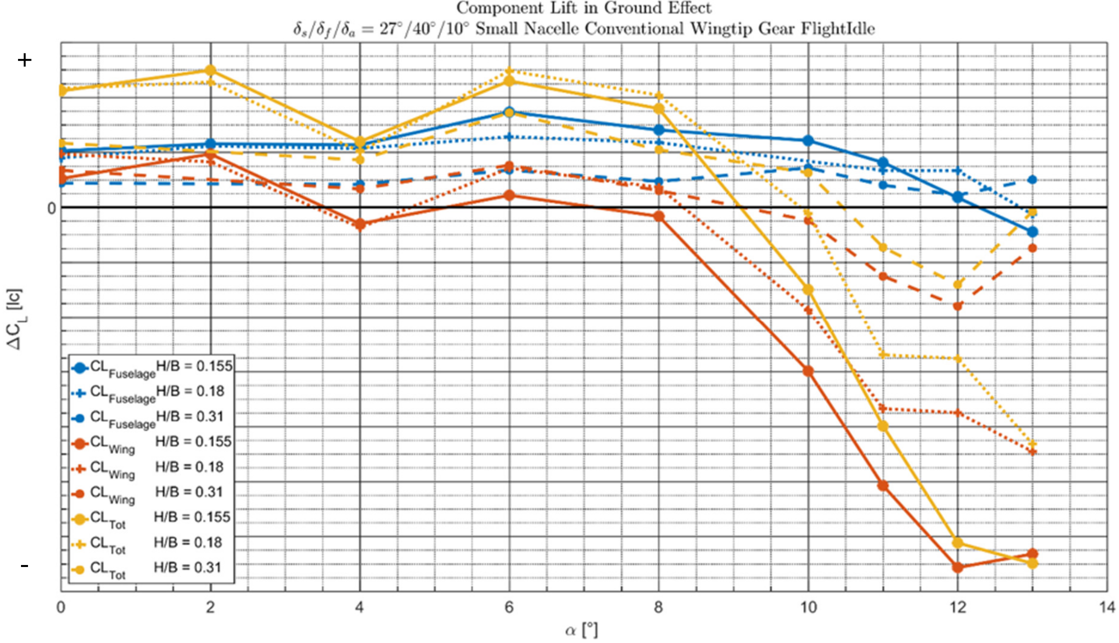

Figure 4.17 – Fuselage (blue), wing (red) and total lift (yellow) increments in ground effect for the small nacelle, conventional wingtip geometry with gear deployed in flightidle thrust conditions in landing configuration

The slope of the fuselage lift increment turns negative at $10.0° \leq \alpha \leq 13.0°$ for $h/b = 0.155$ and $h/b = 0.31$, while for the wing lift increment this is already the case at $\alpha = 8.0°$. The different behavior of the wing and fuselage in ground effect is explained by the fact that the fuselage upperside is located further away from the ground compared to the wing upperside, thus reducing this negative contribution to the lift increment compared to the wing. This is illustrated in Figure 4.4 for $\alpha = 6.0°$, which shows a strong pressure increase on the lowerside of the fuselage, while the pressure increase on the fuselage upperside is negligible in comparison. This is in contrast to the pressure change on the wing, where the pressure increase on the upper and lowerside is approximately in equilibrium, which is why the lift increment from the wing is approximately zero for this case.

Similar to the wing, the pressure increase on the fuselage lowerside does not increase as significantly at higher α compared to the pressure increase on the fuselage upperside. This is shown in Figure 4.5 for $\alpha = 12.0^\circ$, where the pressure on the fuselage upperside has been significantly increased compared to the case of $\alpha = 6.0^\circ$ in Figure 4.4. In contrast the pressure increase on the fuselage lowerside is only slightly increased between the two cases.

Finally, Figure 4.18 show that all of the above also holds true for the completely different geometric configuration, namely the large nacelle and winglet equipped and maximum thrust settings applied. In this case the fuselage lift increment is still the same order of magnitude as the fuselage, and stays positive up to higher values of α.

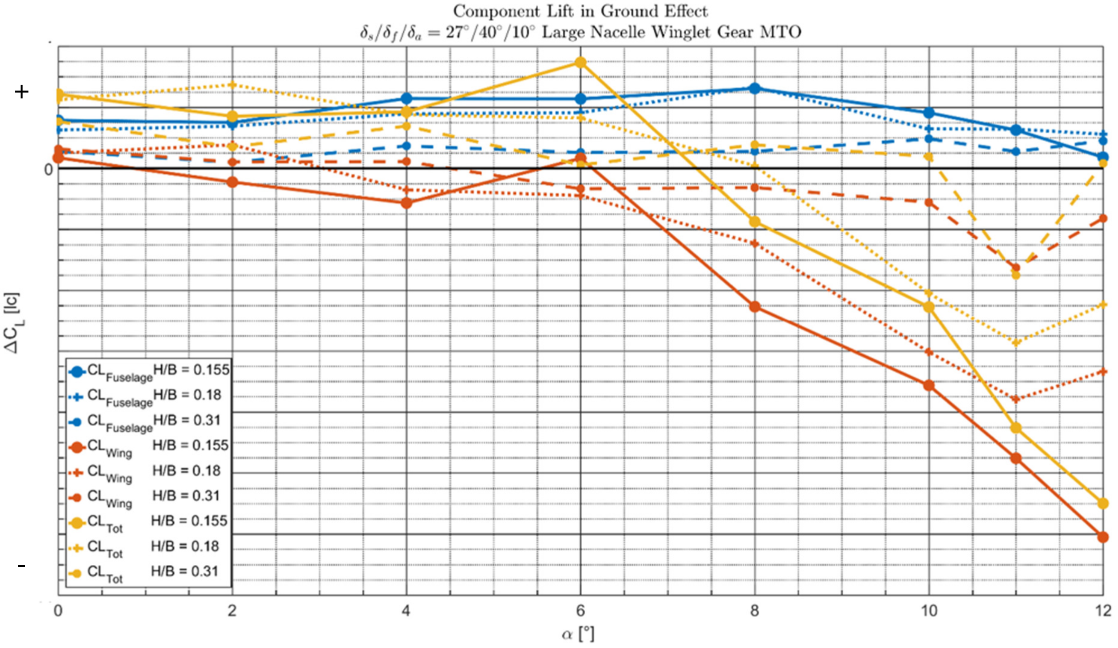

Figure 4.18- Fuselage, wing and total lift increments in ground effect for the Large Nacelle, Winglet geometry with gear deployed in maximum take-off thrust conditions

4.1.2 Drag Impact

4.1.2.1 Global Drag Change due to ground effect

The change in total farfield aircraft drag $C_{D_{tot}}$ due to ground effect is shown in Figure 4.19. The farfield drag consists of:

$$C_{D_{tot}} = C_{D_{Wave}} + C_{D_{v.p}} + C_{D_{induced}} + C_{D_{friction}} + C_{D_{jet}} + C_{D_{Inlet}} \qquad (equation\ 4.2)$$

Hereby $C_{D_{Wave}}$ is the wave drag coefficient, which is zero for this low speed simulation. $C_{D_{v.p}}$ is the viscous-pressure drag coefficient, also known as the form drag. $C_{D_{induced}}$ is the induced drag coefficient and $C_{D_{friction}}$ is the skin friction drag coefficient. $C_{D_{jet}}$ and $C_{D_{Inlet}}$ are two terms related to the engine drag and are assumed to be constant in the ground effect and will be neglected. Thus the drag change due to ground effect becomes:

$$\Delta C_{D_{tot_{GE}}} = \Delta C_{D_{friction_{GE}}} + \Delta C_{D_{v.p_{GE}}} + \Delta C_{D_{induced_{GE}}} \qquad (equation\ 4.3)$$

Figure 4.19 shows that the total drag change is negative across the entire range of α. In contrast to the change in lift due to ground effect, the drag always has a net benefit (reduction) in ground effect. With increasing α and reducing h/b the absolute drag benefit is increased. Across all the configurations evaluated the maximum drag reduction is up to approximately 22% at low α and up to 33% of the total aircraft drag at high α. All the drag data presented in this chapter is calculated using the in-house tool FFD72. The specific drag shown is $C_{D_{AICRAFT_{FF}}}$.

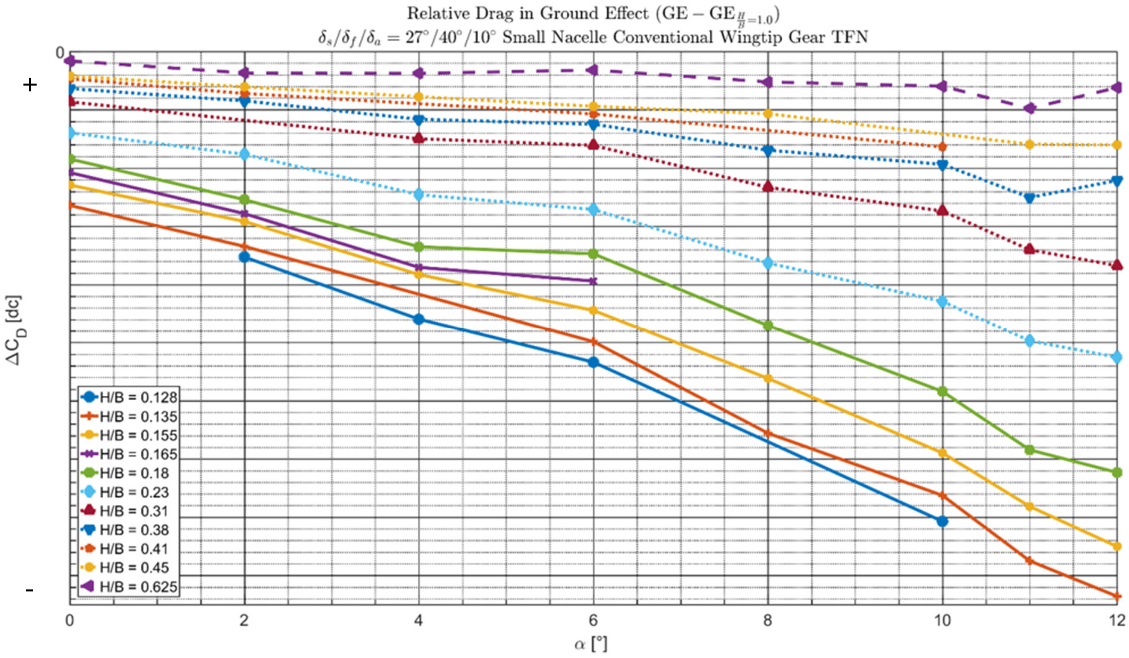

Figure 4.19 - Change in drag coefficient due to ground effect for a range of h/b for the small nacelle, conventional wingtip geometry with gear deployed in flightidle thrust conditions in landing configuration. Source: FFD72

It is known from literature (13) that the ground effect primarily reduces the induced drag, due to the mirrored tip vortex. Up to 62% of the total drag of this particular aircraft can be caused by the induced drag for the landing configuration. That explains the observations that can be made from the breakdown of the total drag in Figure 4.20, showing the relative influence of the induced drag and the viscous-pressure drag. Hereby the skin friction drag was not included, because it remained approximately constant in ground effect.

The change to induced drag is clearly the main driver for the drag reduction in ground effect. That can also be seen by the line of the total drag, which follows the same trend as that of the induced drag. A small reduction of approximately 9% to the viscous-pressure drag at $\frac{h}{b} = 0.155$ can be observed, which is independent of α up until $\alpha = 8.0°$, after which it linearly decreases to almost 0 at $\alpha = 13.0°$. For $h/b = 0.38$, a similar reduction is present, the benefit reduces from 4% at $\alpha = 8.0°$ to 2% at $\alpha = 13.0°$. It is not known what causes the viscous pressure drag benefit to diminish at higher α. It is not caused by a reduction of the pressure drag C_{D_P}, which is a component of the viscous-pressure drag. Because the pressure drag benefit actually increases in ground effect for higher values of α. For instance, for the configuration under discussion, the pressure drag ratio is $\frac{C_{D_P \frac{h}{b}=0.155}}{C_{D_P \frac{h}{b}=1.0}} = 0.778$ at $\alpha = 4.0°$ and $\frac{C_{D_P \frac{h}{b}=0.155}}{C_{D_P \frac{h}{b}=1.0}} = 0.7071$ at $\alpha = 12.0°$.

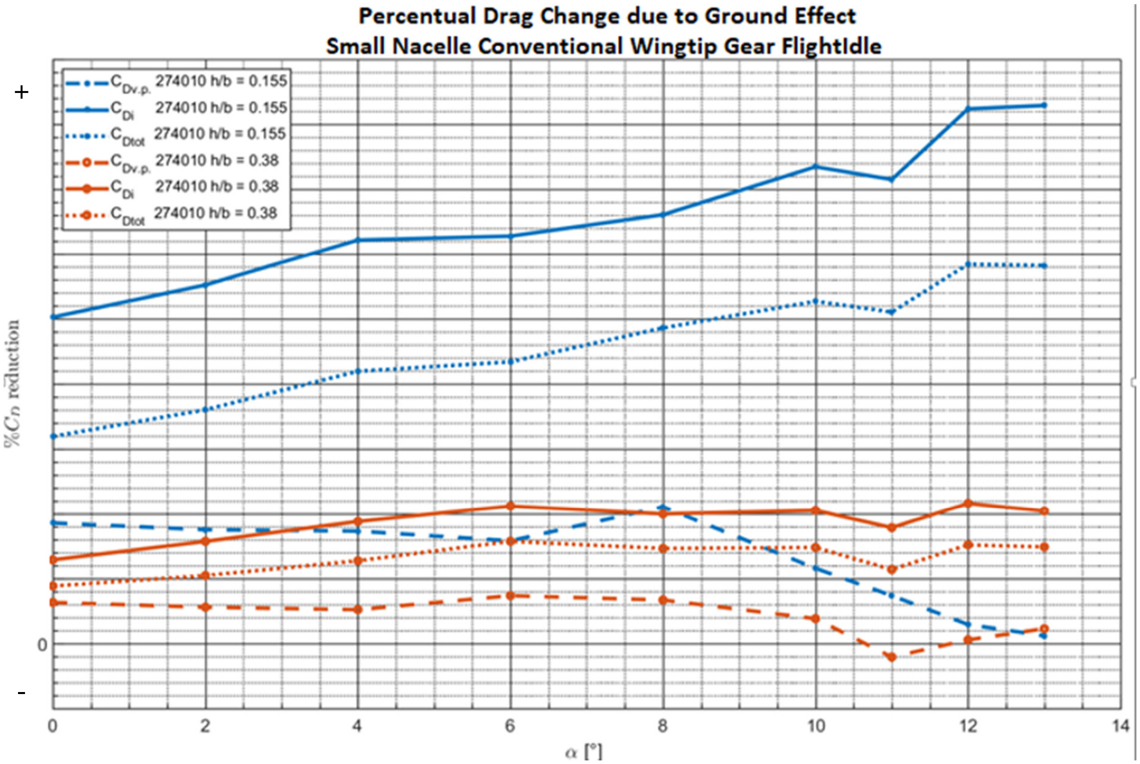

Figure 4.20 - Change to Viscous-Pressure Drag (dashed), Induced Drag (solid) and Total Aircraft Drag (dotted) in ground effect at HB=0.155 (blue) and HB=0.38 (orange) at Flightidle thrust setting. Source: FFD72

4.1.2.2 Spanwise Drag distribution

In this subchapter the spanwise total drag distributions will be discussed, similar to what was done for the lift in subsection 4.1.1.3. As shown in the previous subsection, the drag is reduced across all α, which was not the case for the lift which first increased and then decreased with increasing α. Therefore the graphs presented in this section will depict the full range of α available for the small nacelle, conventional wingtip case with gear deployed and flightidle engine thrust setting. Since the drag data is quite noisy, it was smoothed using a first degree Savitykz-Golay filter (97) as implemented by Matlab.

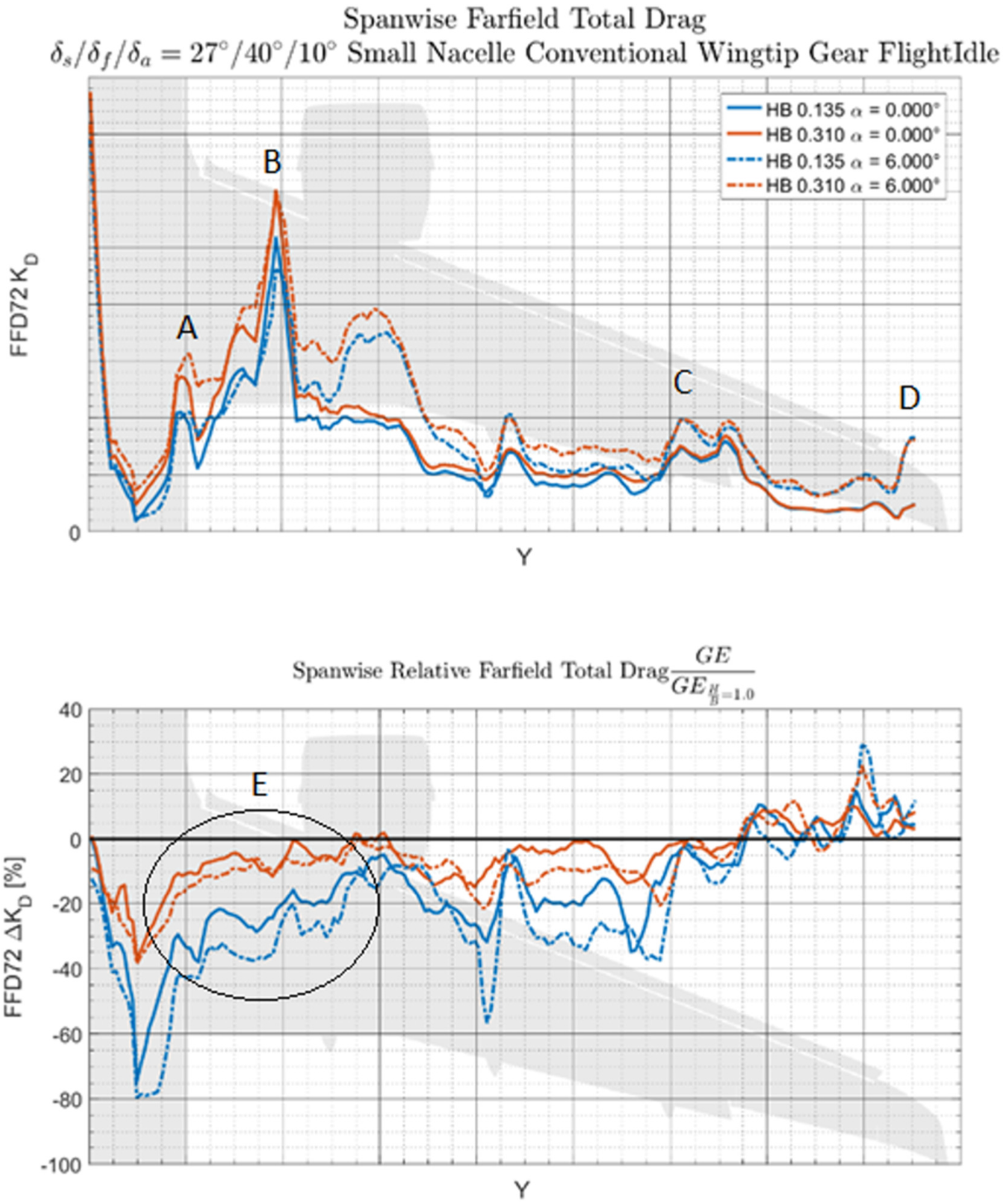

Figure 4.21 - Total Drag distribution along the wing-body for $0° \leq \alpha \leq 13.0°$ *at* $\frac{h}{b} = 0.155$ *and* $\frac{h}{b} = 0.31$

The total farfield drag distribution K_D as provided by FFD72 using the output file: “Plot_spanwise_jetblanked.dat”. The change due ground effect is shown in Figure 4.21 and Figure 4.22 for $0.0° \leq \alpha \leq 13.0°$, at $h/b = 0.155$ and $h/b = 0.31$, while Figure 4.23, Figure 4.24 and Figure 4.25 show the individual contributions of respectively the induced, the viscous-pressure and the skin friction drag. Significant differences in the absolute drag distribution are present at the wing-root junction (region A), behind the engine junction (region B), at the end of the outboard flap junction (region C) and finally at the wingtip junction (region D). In contrast the relative change to the total drag distribution remains qualitatively the same for all α, with only the magnitude of the relative drag increment increasing for higher α.

Drag is most significantly reduced in the area between the fuselage and the nacelle junction (region E). Here both the absolute value of the drag is comparatively large and the relative decrease in drag is significant. On the outboard flap area there is also a significant relative decrease in drag, but the absolute value of the drag is low in this area, thus this will have less impact on the overall drag change of the aircraft. Finally it can be seen that the drag increases strongly with α in the area of the wingtip. Figure 4.23 and Figure 4.24 show that this is a combination of the global increase in induced drag with α and a non-linear increase of the viscous-pressure drag related to the flow separation on the upperside of the winglet, which was discussed previously and is shown in Figure 4.14.

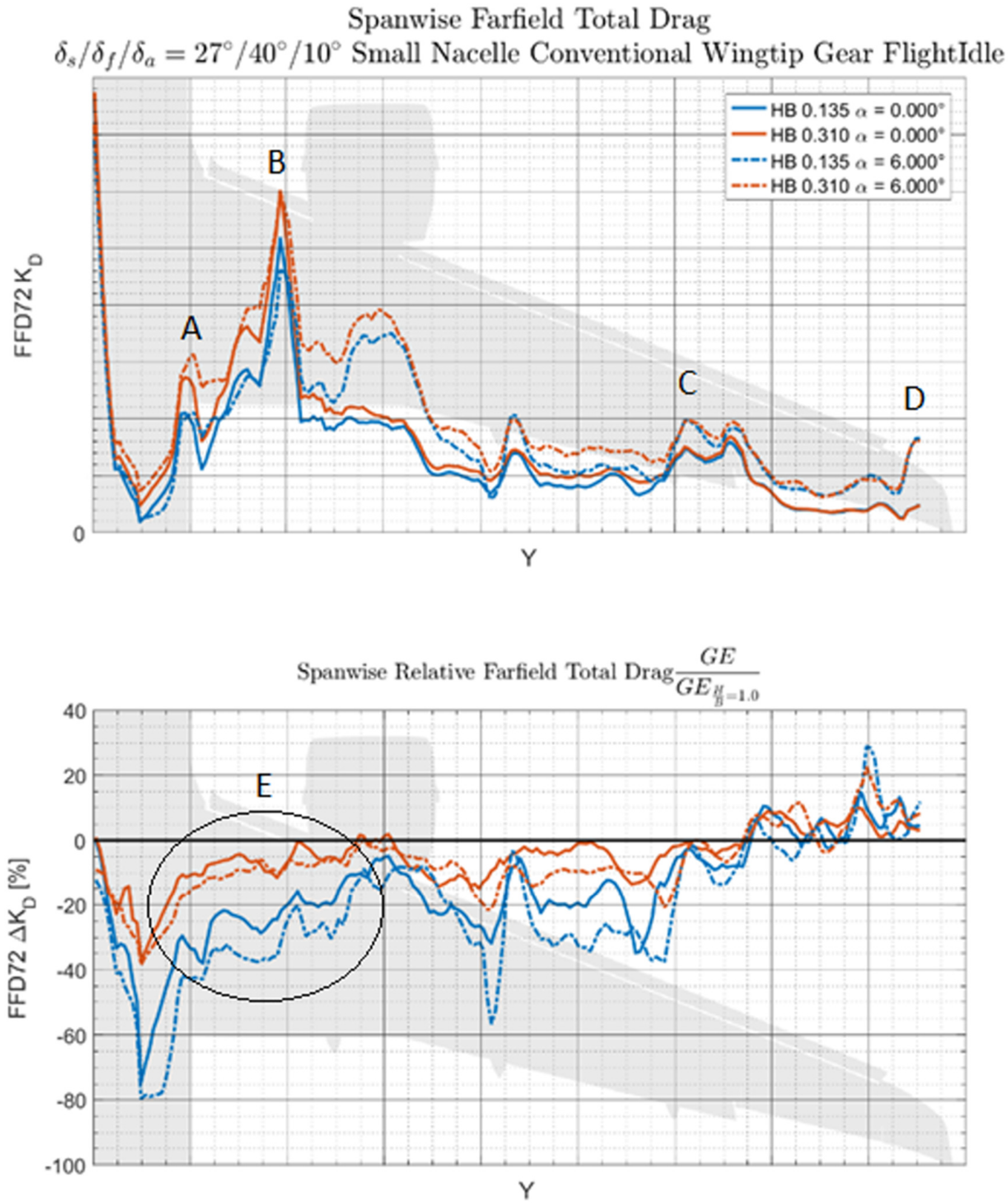

Figure 4.22 - Total drag distribution along the wing-body for high α at $\frac{h}{b} = 0.155$ and $\frac{h}{b} = 0.31$

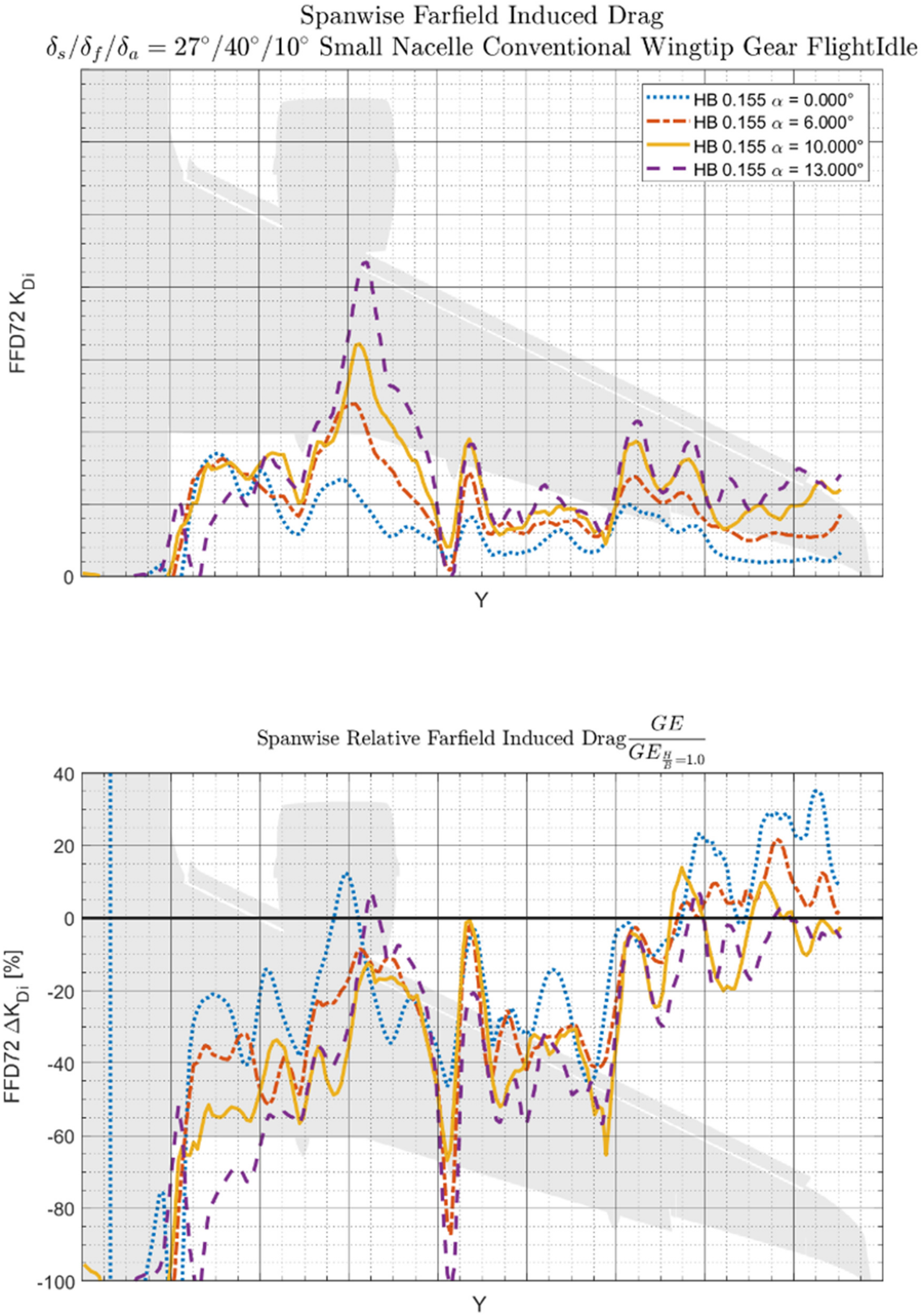

Figure 4.23- Induced drag distribution along the wing-body for $0° \leq \alpha \leq 13.0°$ at $\frac{h}{b} = 0.155$

Figure 4.23 shows that the induced drag is reduced along the entire wing span, except at the wing tip, where the induced drag is increases low to moderate α. The largest drag benefit is located at the inboard wing.

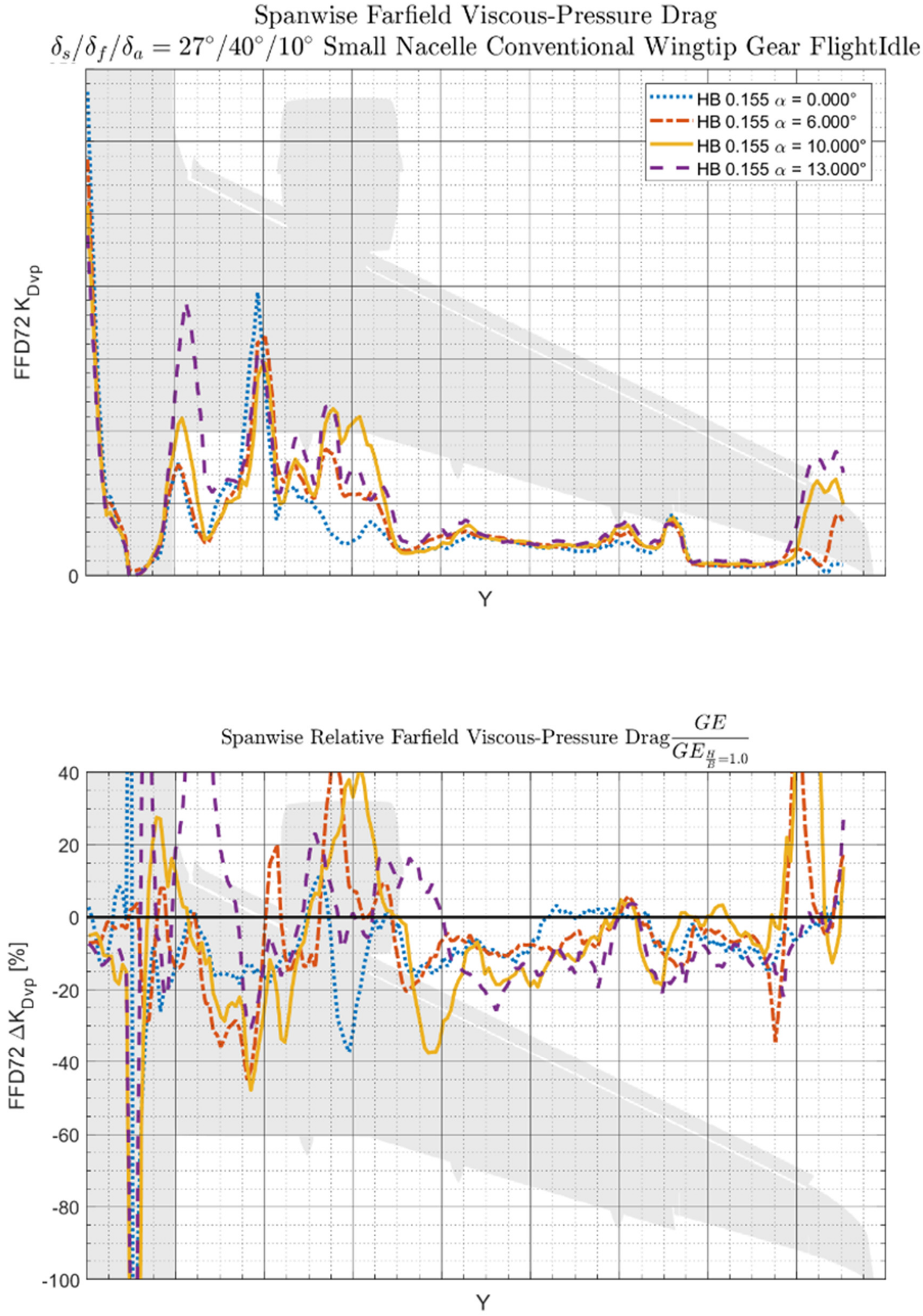

Figure 4.24 – Viscous-Pressure drag distribution along the wing-body for $0° \leq \alpha \leq 13.0°$ *at* $\frac{h}{b} = 0.155$

The relative change to the viscous-pressure drag is quite noisy, as can be seen in Figure 4.24. Concerning the outboard part of the wing, it stays almost constant with α, except for the location at the wingtip where separated flow occurs at higher values of α. There are two other locations along the wing where the viscous-pressure drag shows strong dependency on α. The first is located at the wing-root junction, which is where the vortex induced from the inboard slat is present. The second region of increased viscous-pressure drag is located behind the engine, where several vortices are present.

Finally it can be seen in Figure 4.25 that the skin friction is reduced by approximately 10% in ground effect. This is due to the reduced flow velocity over the wing. However the impact of this change is almost negligible, since the absolute value of the skin friction drag is up to an order of magnitude smaller compared to the viscous-pressure drag and induced drag for this high-lift configuration. Therefore the change to the skin friction drag is negligible compared to the change of the induced or viscous-pressure drag in ground effect and will not be further discussed in this report.

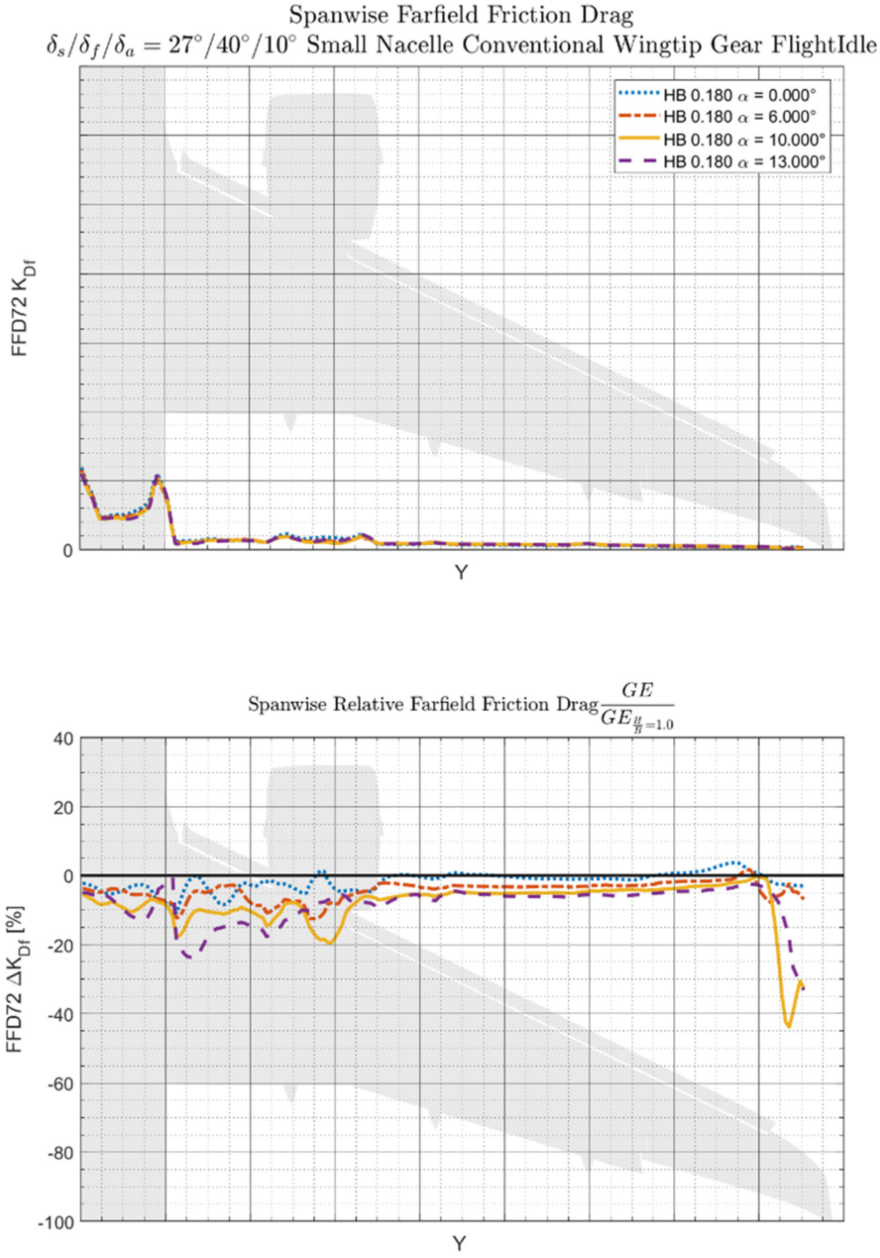

Figure 4.25 – Skin friction drag distribution along the wing-body for $0° \leq \alpha \leq 13.0°$ *at* $\frac{h}{b} = 0.155$

4.1.3 Three-Dimensional Flow Visualization

During the thesis work the flow changes due to ground effect were visualized in three-dimensions by means of plotting the total pressure iso-surfaces. Hereby the total pressure value of the iso-surfaces is chosen to be below the freestream total pressure, thus allowing for visualization of the wakes. By doing this for both in and out of ground effect, the shift in wake location due to ground effect can be observed. This is presented in in Appendix M – Total Pressure ISO-Surface Flow Visualization.

4.1.4 Conclusions

For the small nacelle, conventional wingtip geometry with gear deployed and landing high-lift configuration at flightidle thrust conditions, Lift is increased by up to 3.5% at $\alpha = 4.0°$ and is decreased by up to 5.5% at $\alpha = 13.0°$. The absolute value of the lift increment is highest when the aircraft is closest to the ground. As this distance is increased, the lift increment stays positive up until higher values of α.

Flow streamlines are deflected upwards, away from the ground, due to ground effect. This results in a lower mass-flow below the wing, decreasing flow velocity and increasing the pressure, which increase the lift. The upward deflection of the streamlines also increases the local angle of attack on the wing leading edge, leading to a lift enhancing increase in suction in this area.
At low α the pressure on the upper wing surface also increases, but not as strongly compared to the lower wing surface, which leads to a net increase in lift. At high α the lift-reducing pressure increase on the upper wing surface is dominant, causing the significant decrease in overall lift. The pressure increase on the upper wing surface increases more strongly with α and is distributed over a larger area of the wing. In contrast the pressure increase on the lower wing surface is limited to the area between the fuselage and the nacelle.

In chord wise direction the suction on the slat upperside and mainwing leading edge is increased across the entire range of α, while the upperside of the flap shows a significant pressure increase. The mainwing in between these two surfaces shows a small suction increase at very low α and a suction decrease for higher α.
It was found that due to the reduction of the suction peak on the flap, flap flow separation is reduced due to ground effect. The reverse is true at the winglet, due to the increased suction peak at the leading edge, there is a stronger pressure gradient in ground effect, leading to onset of earlier flow separation. This effect is more pronounced for the conventional wingtip compared to the winglet geometry.

The spanwise lift distribution showed that the most significant changes can be found on the wing between the fuselage and nacelle, as well as for the lift on the fuselage itself. The outboard wing section shows a small lift increase or decrease depending on α.

It was seen that the lift change over the fuselage is of the same order of magnitude as the lift change over the wing itself, while the absolute value of the lift is approximately six times lower for the fuselage compared to the wing at $h/b = 1.0$. The fuselage lift increment is more positive than the wing increment, because the upperside of the fuselage is located further away from the ground, thus reducing the negative contribution to the lift in ground effect, while the reverse is true for the lower side of the fuselage. Thus the lift enhancing influence of the ground effect is increased on the fuselage and the lift-reducing effects are reduced. The same is true to a lesser extent for the nacelle.

The drag is reduced by up to 33% due to the ground effect. That is primarily caused by a reduction of the induced drag. The magnitude of the drag reduction increases linearly with α

and increases as h/b decreases. The majority of the drag reduction can be attributed to a reduction of the induced drag of up to 42% at $\alpha = 13.0°$ and $h/b = 0.155$, caused by the mirrored wing tip vortex. As α and thus C_L increases, both the relative as well as the absolute value of the induced drag reduction due to ground effect increases. The viscous-pressure drag decreases by up to 9% in ground effect. There is a small reduction in the skin friction drag, but this is insignificant compared to the change to induced and viscous-pressure drag.

The spanwise drag distributions shows that the most significant drag reduction occurs on the inboard wing, between the fuselage and nacelle. The induced drag is reduced over the entire span of the wing, except at the wing tip where it increased slightly, especially for low α. Finally it was seen that the skin friction is reduced by approximately 10%, but that this reduction is negligible compared to the absolute value of the reduction of the viscous-pressure and induced drag.

4.2 Effect of Engine Thrust Setting in Ground Effect

In the previous subchapter it has been established how the aircraft behaves in ground effect for the small nacelle, conventional wing-tip, gear deployed, landing configuration and flight-idle thrust setting. In this subchapter only the thrust setting will be changed, namely to MTO thrust conditions and it will be investigated how this changes the behavior in ground effect is investigated.

The subchapter is structured as follows: First the change in lift is investigated. A comparison is made with the data presented in the previous subchapter to investigate the similarities and differences between the different thrust settings. An explanation is offered regarding the cause of the change in ground effect lift increment due to thrust setting. Finally the change in drag increment in ground effect for MTO thrust setting is analyzed.

4.2.1 Change in C_L

The lift change in ground effect for the small nacelle, conventional wingtip geometry with gear deployed and landing configuration high-lift settings with maximum take-off thrust engine settings can be seen in Figure 4.26. To obtain the change in lift in ground effect due to thrust setting, this Figure 4.26 can be directly compared to Figure 4.1 which shows the lift increment for the exact same configuration, with the only change being that here the flightidle thrust setting is applied. The difference between these two figures is plotted in Figure 4.27, which shows:

$$\Delta C_{L_{GE_{Thrust}}} = \left(C_{L_{GE}} - C_{L_{\frac{h}{b}=1.0}}\right)_{MTO} - \left(C_{L_{GE}} - C_{L_{\frac{h}{b}=1.0}}\right)_{Flightidle} \qquad (equation\ 4.4)$$

A third order polynomial surface fit is presented in Figure 4.28, based on the data shown in Figure 4.27. This shows the change lift increment due to thrust setting clearer. The polynomial surface fits for all four different geometry configurations are presented in Appendix K – Polynomial Surface Fit Plots.

Figure 4.27 shows that at low to moderate α, the range where the ground effect lift increment is positive, the MTO thrust setting *reduces* the magnitude of this *positive* lift increment by up to 2% of the total aircraft lift. In contrast at high α when the normal lift increment becomes negative, the high thrust setting *reduces* the magnitude of the *negative* lift increment by up to 0.5% of the total lift. Thus it can be concluded that a high thrust setting reduces the magnitude of the change in lift in ground effect.
For low α this conclusion holds true for all four different geometric configurations. In contrast, for the large nacelle geometry, presented in Appendix K – Polynomial Surface Fit Plots, the decrease in negative lift increment at high α is not present. Instead, there is still a lift *increase* for the flightidle settings of up to 1.1% of total aircraft lift.

This different trend at high α can be attributed to two explanations: The first is the fact that the uncertainty of the lift for the flightidle CFD solutions at high α, with the large nacelle, is quite high, in the same order of magnitude as the increments shown here. It could thus be that the noise masks the trend.
Another possible explanation for the different trends at high α is that different input settings had to be used for the CFD solver for the different engine geometries. The most notable change was related to switching off the Kato-Launder modification factor (98) (99) for the case of the large nacelle geometries with flightidle thrust settings only. If this modification was switched on in these conditions, the solution would not converge at high α. This issue was not present for the small nacelle geometry.

The Kato-Launder modification can be used for most two-equation models and reduces the amount of turbulent energy in stagnation regions of the flow, most notably for this aircraft geometry at the leading edge. Therefore, this solver setting can influence the calculated lift result and might be a reason why the trend at high α is different for the large and small nacelle. A limited check was performed to assess the impact of changing the Kato-Launder modification factor. It was found at moderate α that the impact was of the order of a 1 lift count. It is unknown if this changes at higher incidence angles. It did impact the convergence of the lift, which is why the uncertainty for the lift is higher for the large nacelle geometry.

The data shown here is similar to results found in literature from Flaig (69). There it was found in a windtunnel campaign that for a comparable aircraft, at low to moderate incidence, there was a positive difference of up to 4 lift counts present in the ground effect lift increment when TFN was used. The difference between power settings in the windtunnel reduces at high incidence, but still remains positive. Thus, this external data supports the trend that was observed in CFD only for the large nacelle geometry.

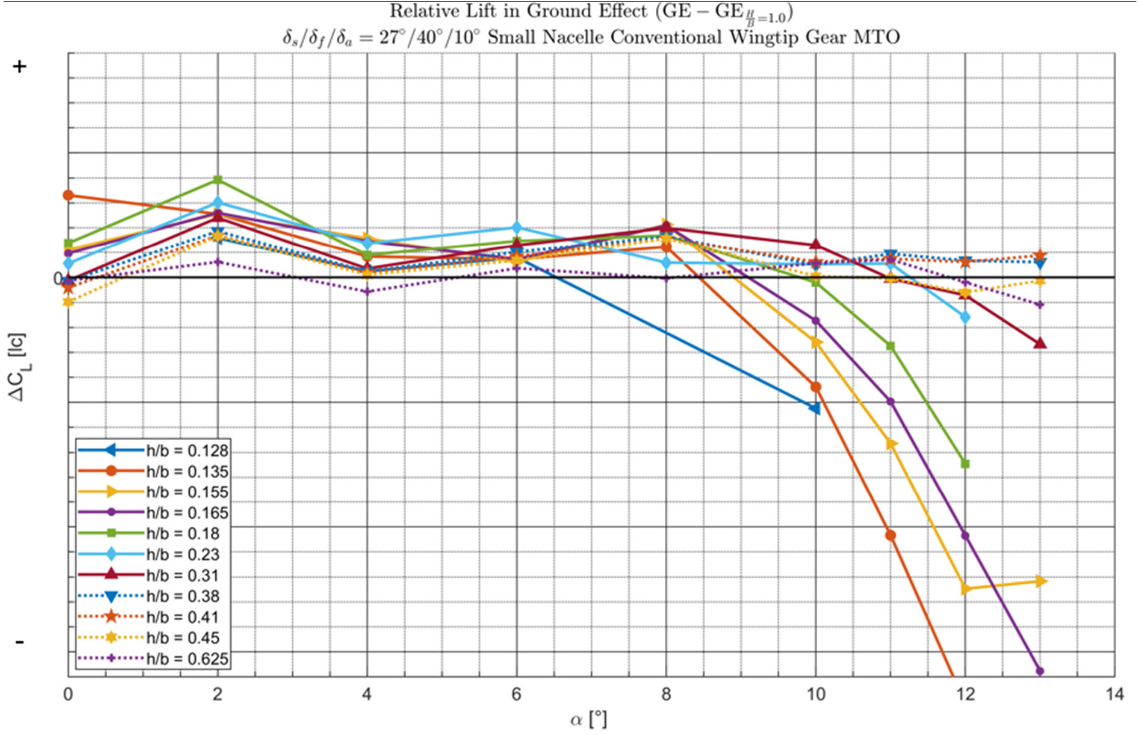

Figure 4.26 - Change in lift coefficient due to ground effect for a range of h/b for the small nacelle, conventional wingtip geometry with gear deployed in flightidle thrust conditions in landing lift configuration. Same Y-Axis scale as figure 4.1. Source: FFD72

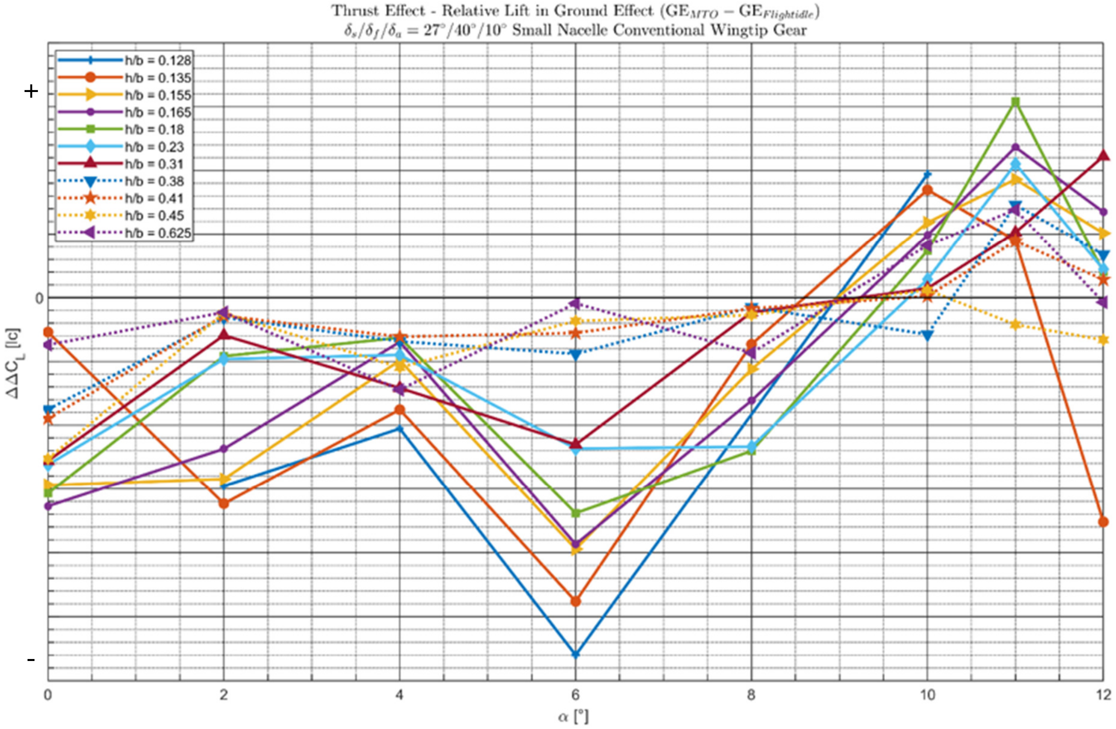

Figure 4.27 – Change to the incremental lift coefficient in ground effect due to engine thrust setting for a range of h/b for the small nacelle, conventional wingtip geometry with gear deployed in landing configuration. Source: FFD72

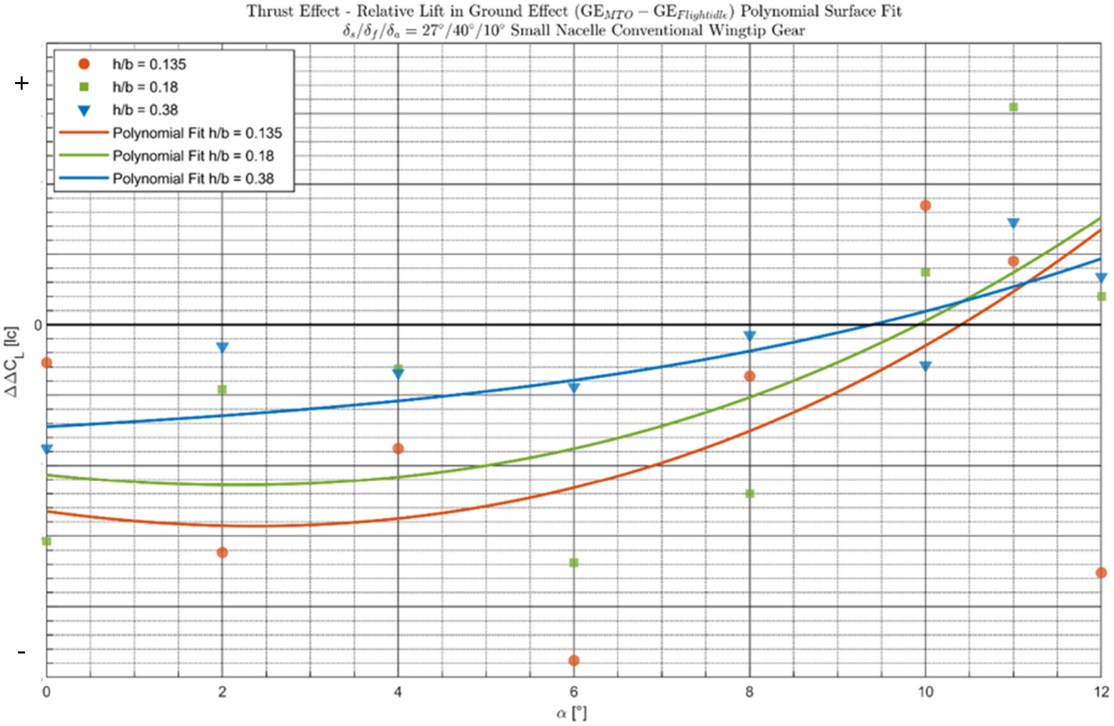

Figure 4.28 – Polynomial fit of change to the incremental lift coefficient in ground effect due to engine thrust setting for a range of h/b for the small nacelle, conventional wingtip geometry with gear deployed in landing configuration using a polynomial surface fit. $R^2 = 0.8517$ *Source: FFD72*

4.2.2 Causes of the change in C_L

In general, introducing a thrust effect to the flow around the wing will reduce the lift of the wing, because the velocity of the jet under the wing reduces the circulation around the wing. For this configuration, the absolute lift out of ground effect is reduced by approximately 1.5% to 2% when comparing the MTO lift setting with the flightidle setting at $h/b = 1.0$.

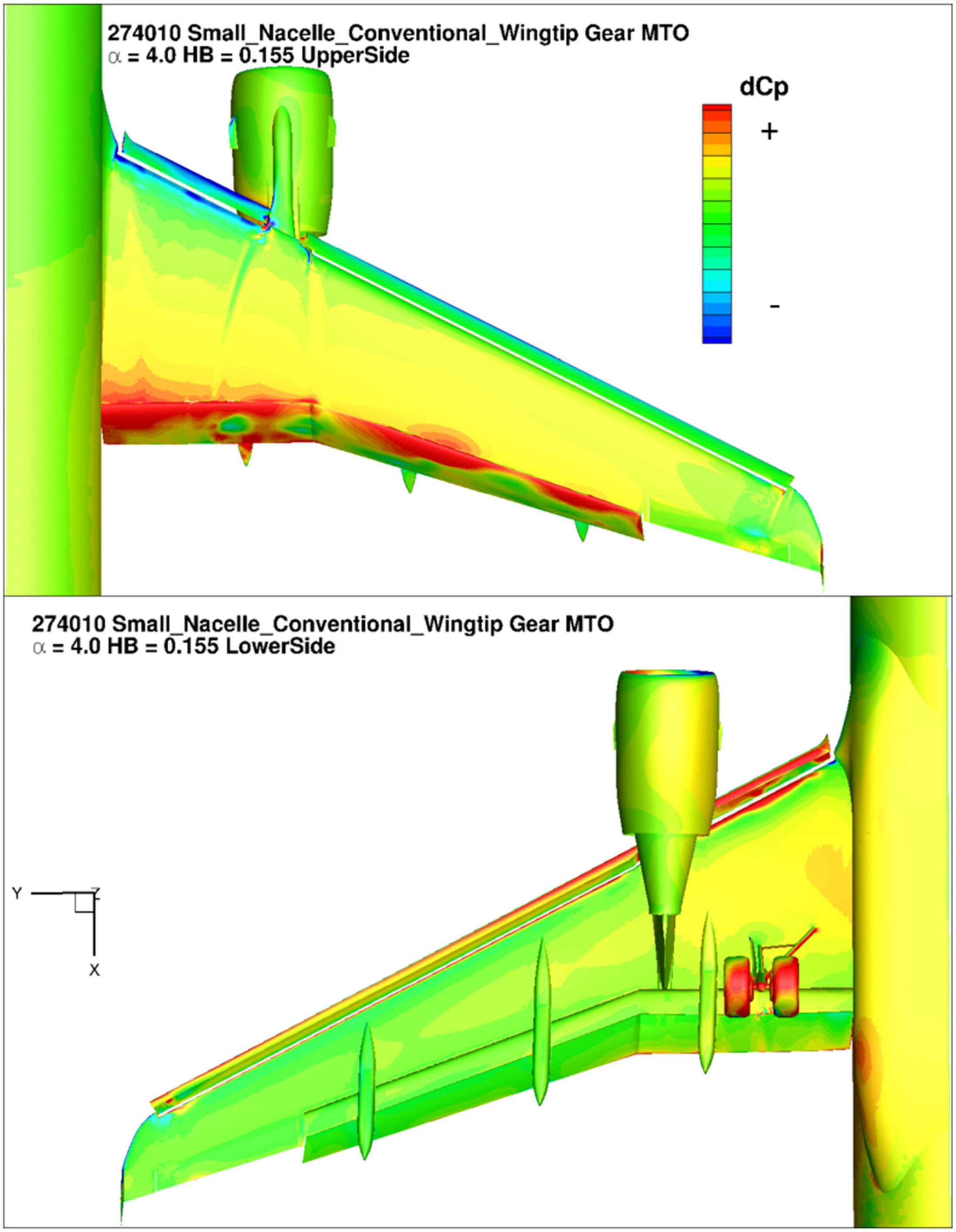

Figure 4.29 - Relative pressure change over the wing due to ground effect at $\alpha = 4.0° \ \frac{h}{b} = 0.155$, $(\Delta C_{P_{GE}} = C_{P\,GE} - C_{P_{\frac{h}{b}=1.0}})$

Figure 4.29 shows the relative pressure distribution at $\alpha = 4.0°$ and $h/b = 0.155$ for the small nacelle, conventional wingtip geometry with gear deployed and landing configuration settings with maximum take-off thrust engine settings applied. This figure can be directly be compared to Figure 4.3, the only differences between these two are caused by engine thrust setting. Two observations can be made when comparing these figures.

The first is that the suction increase on the leading edge of the slat and main wing is significantly stronger for the flightidle thrust setting. By increasing engine thrust in free air, the circulation over the wing becomes reduced, reducing α_{eff}. This in turn reduces C_p, especially at the slat which is known to be sensitive to small changes to α and leads to a reduction in suction, independent of ground effect.

Two possible explanations are presented here which might explain why there is a further reduction in suction in ground effect for the MTO thrust setting compared flightidle thrust. The first possible cause would be that the circulation reducing in influence of the engine jet is enhanced due to ground effect, leading to a higher reduction in α_{eff}.

Another possible explanation is that the engine inlet sucks in air at high thrust setting, which would otherwise flow over the leading edges of the wing, thus reducing the mass flow in that region. With reduced mass flow, there will be a reduced acceleration of the flow velocity around the leading edge, thus leading to a lower suction peak. This change in flow pattern due to engine thrust setting is illustrated in Figure 4.30, where ten different streamlines flowing over the inboard wing close to the engine are visualized for the four conditions of $h/b = 0.155$ and $h/b = 1.0$, with flightidle and MTO engine thrust setting applied to both cases. The streamlines in all four pictures all pass through the exact same series of points in front of the wing, just inboard of the engine. First of all the two left pictures in the figure, flightidle thrust conditions, out and in ground effect show that the streamlines are shifted upwards due to ground effect. At $h/b = 1.0$ five of the ten streamlines flow over the upperside of the wing, while at $h/b = 0.155$ the pressure is increased on the lowerside, deflecting some of these streamlines upwards. In this case eight of the ten streamlines flow over the upperside of the wing. This then explains why the suction peak at the slat and wing leading edge is increased due to ground effect, the flow is accelerated due to increased mass flow in ground effect.

The right side of the picture shows the same situation with MTO engine thrust settings applied. It shows that some of the streamlines which flowed over the wing with flightidle thrust setting applied, are now sucked into the engine. This locally reduces the airflow at the wing, leading to less air being deflected over the mainwing due to ground effect, causing a reduced suction peak on the slats and leading edge. The effective angle of attack is reduced in this region due to the engine thrust setting. For the MTO case the same amount of streamlines flow over the wing both in and out ground effect.

The change in pressure on the slat is shown in Appendix F – Thrust Effect Pressure Plots. Here it is shown that for the entire length of the inboard slat the suction peak is reduced for the MTO thrust setting. The only exception is at $\alpha = 2.0$ and $Y = 6.30\ m$, here the suction is increased with MTO thrust setting because it is located at the start of the outboard flap, right behind the engine, thus showing a very local increase in mass flow over the slat.

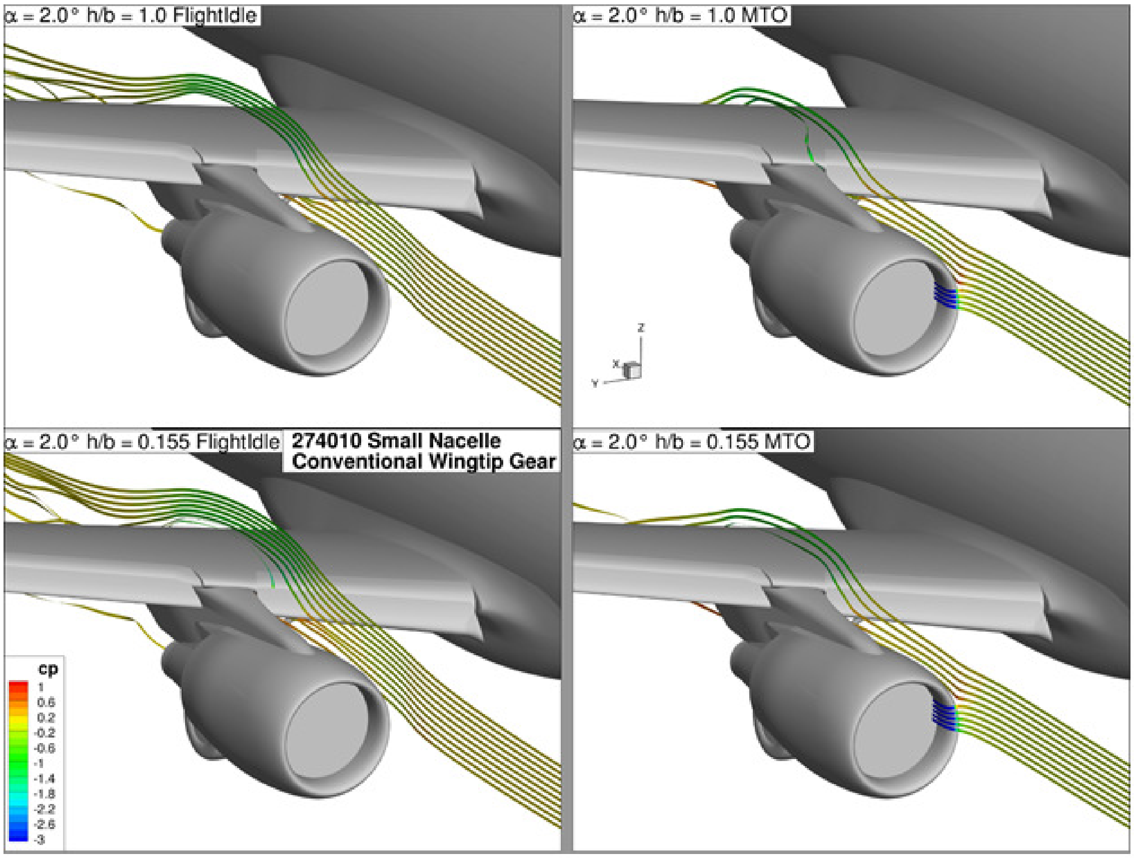

Figure 4.30- Change in streamlines over the inboard wing for different $\frac{h}{b}$ and engine thrust settings

The second observation when comparing Figure 4.29 to Figure 4.3 is that there is a reduction in the magnitude of the pressure increase on the lowerwing, when MTO thrust setting is applied. In ground effect the flow velocity is reduced below the wing, most significantly in the region between the fuselage and the nacelle. The jet from the engine will partially reaccelerate the flow below the wing, especially as the distance from the ground reduces and a venturi effect will further accelerate the flow.

The flow around the flap gap is also changed due to the MTO engine thrust settings. At high thrust setting the mass flow is increased behind the engine and below the wing. As α is increased, this engine induced flow is increasingly forced through the flap gap. This is also increased in ground effect, due to the ‘blockage’ effect of the ground. The increased flap gap mass flow induces an increased suction peak on the flap, thereby partially negating the reduction in flap suction peak caused by the ground effect. The C_p plots demonstrating this are present in Appendix F – Thrust Effect Pressure Plots .

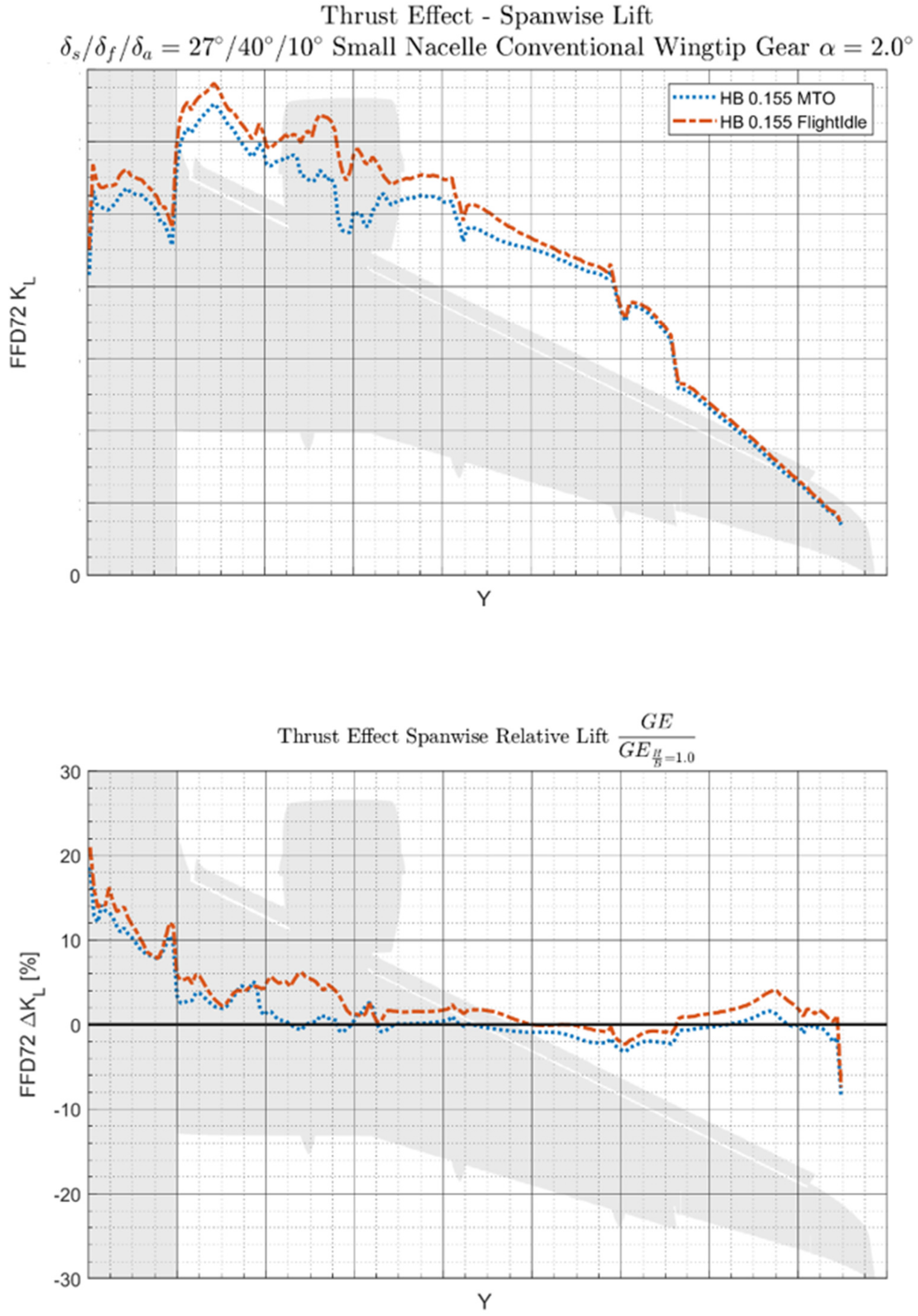

Figure 4.31 - Spanwise lift distribution showing the influence of thrust setting at $\alpha = 2.0^\circ$ *and* $\frac{h}{b} = 0.155$

Finally the influence of engine thrust setting on the spanwise lift distribution can be seen in Figure 4.31 and Figure 4.32 for respectively $\alpha = 2.0$ and $\alpha = 12.0$. At low α the lift is increased across the board for the case with flightidle thrust setting, mainly due to the increase in slat suction. As expected, the increase in lift is strongest around the area of the engine, both in the absolute as well as the relative lift distribution. At high α there is a lift increase for the MTO thrust setting, mostly due to the increased suction on the flap which becomes more significant at higher α, while the decrease in slat suction is relatively independent of α.

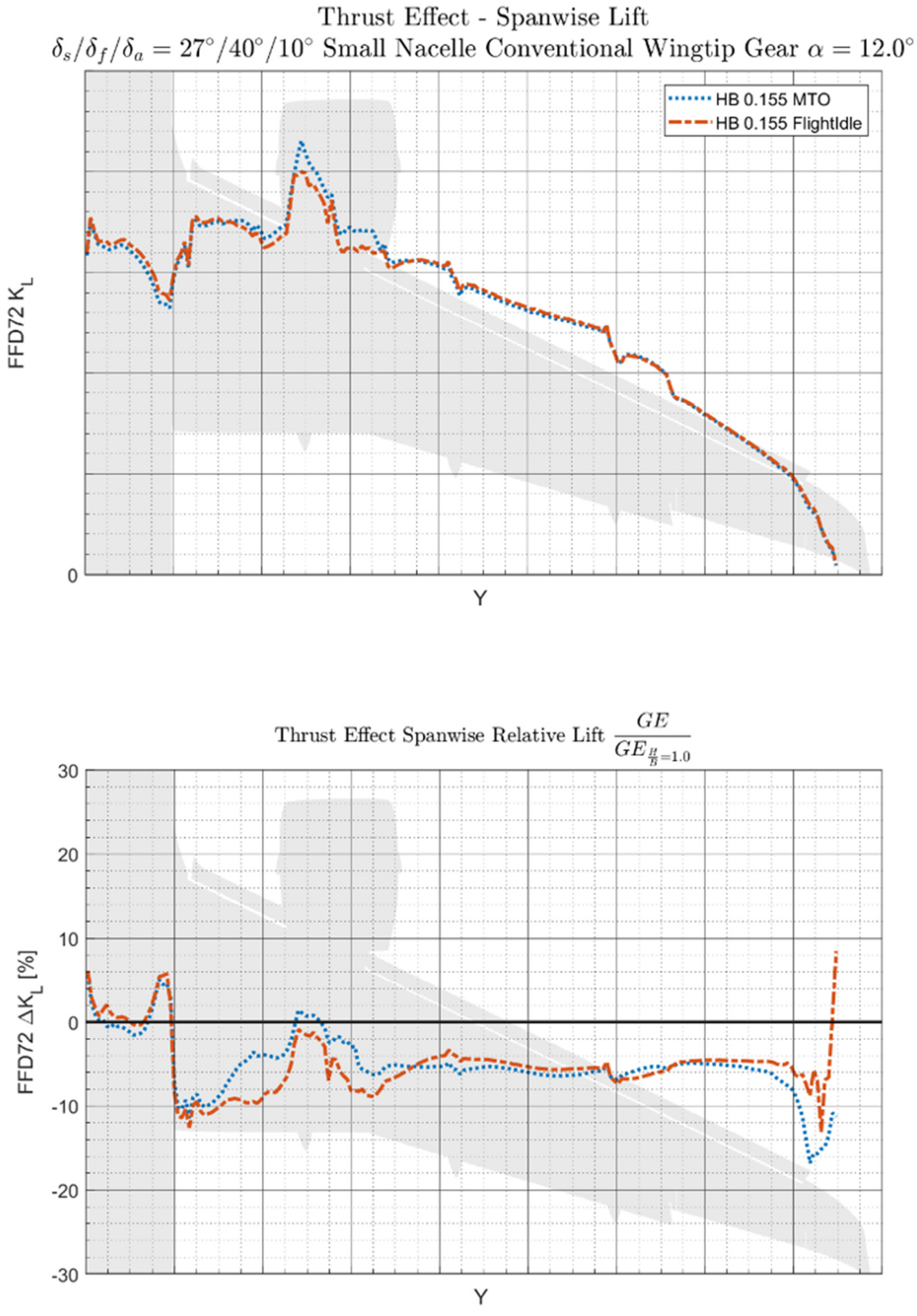

Figure 4.32 - Spanwise lift distribution showing the influence of thrust setting at $\alpha = 12.0°$ and $\frac{h}{b} = 0.155$

4.2.3 Change in Drag

When evaluating the change in lift in ground effect due to applying MTO engine settings, it became apparent that in essence the higher thrust setting reduced the influence of the ground effect. At low α, where the lift increment is positive, applying MTO engine settings reduced the magnitude of the lift increase. The reverse was true at high α, applying MTO engine settings in this case reduced the extent of the negative lift increment.

The same influence can be observed while evaluating the drag: Applying MTO engine settings reduces the drag reduction. This can be seen by comparing Figure 4.33 with Figure 4.19. The difference between these two figures is plotted in Figure 4.34, which shows:

$$\Delta\Delta C_{D_{GE}} = \Delta C_{D\,GE_{MTO}} - \Delta C_{D\,GE_{flightidle}} \qquad (equation\ 4.5)$$

Thus positive values in this figure indicate that there is a lower drag reduction for the MTO thrust setting compared to the flightidle thrust setting.

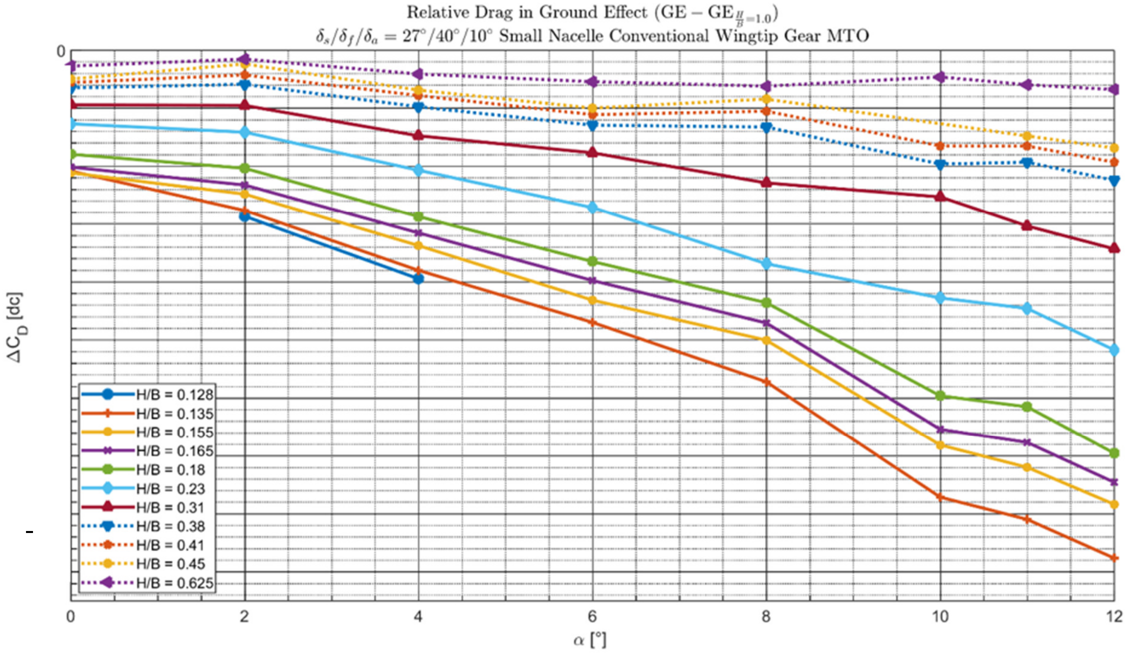

Figure 4.33 - Change in drag coefficient due to ground effect for a range of $\frac{h}{b}$ for the small nacelle, conventional wingtip geometry with gear deployed and MTO thrust settings in landing lift configuration. Source: FFD72

The magnitude of the drag reduction due to ground effect is reduced for the entire range of $0° \leq \alpha \leq 12°$ for MTO thrust setting by up to 4% of the total drag. With MTO thrust settings the drag is reduced by up to 38%, for the flightidle settings the drag is reduced by up to 42%.

This difference can be partially explained by the fact that the absolute lift coefficient is higher for the flightidle case. Since the induced drag is proportional to C_L^2, the absolute value of the induced drag will be higher for the flightidle thrust setting case. Assuming that the induced drag will be reduced by the same factor for both the flightidle and MTO thrust setting case, a higher *absolute* value of the induced drag will lead to a *higher reduction* in induced drag in the ground effect. However, at $\alpha = 12.0°$ difference in both absolute and incremental lift values for the two thrust settings are almost negligible, yet there is still a significant difference in drag increment. Thus the differences observed for the drag increment caused by different engine thrust setting are partially caused by the difference in lift, but this is not the only cause of this effect. No further conclusions investigations have been performed on this subject.

At $\frac{h}{b} \geq 0.45$ $\Delta\Delta C_{D_{GE}}$ becomes negative for $4.0 \leq \alpha \leq 8.0°$. This increase is most likely caused by the small oscillations in the CFD solution generated by the unsteady parts of the flow which cannot be fully modelled by the steady CFD solver.

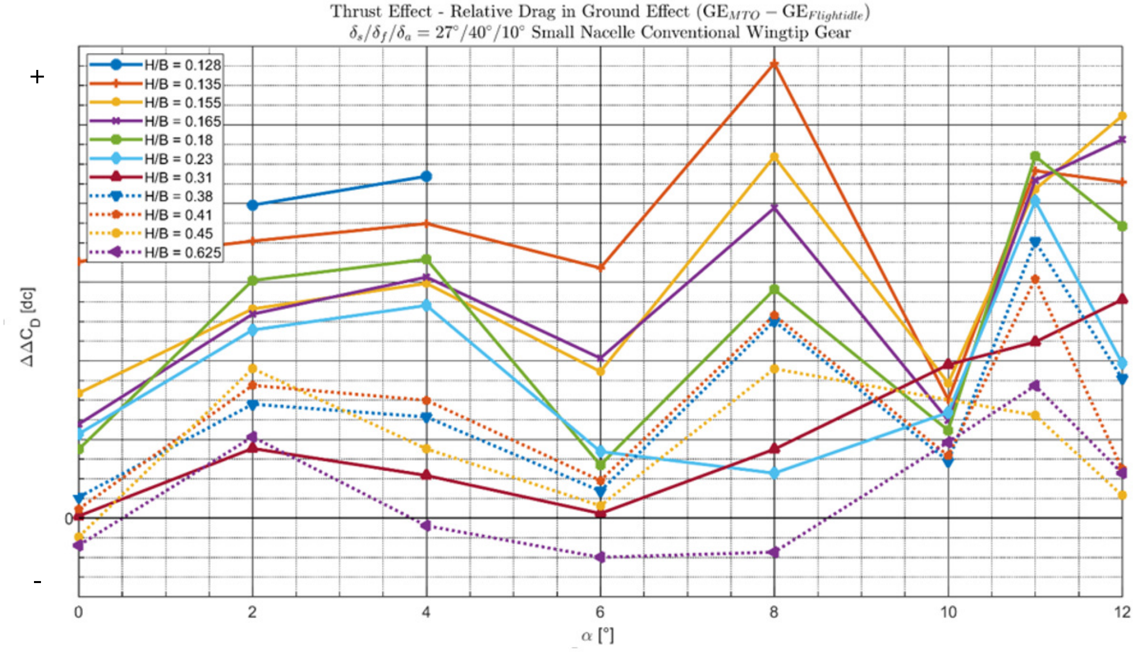

Figure 4.34 - Change to the incremental drag coefficient in ground effect due to engine thrust setting. Source: FFD72

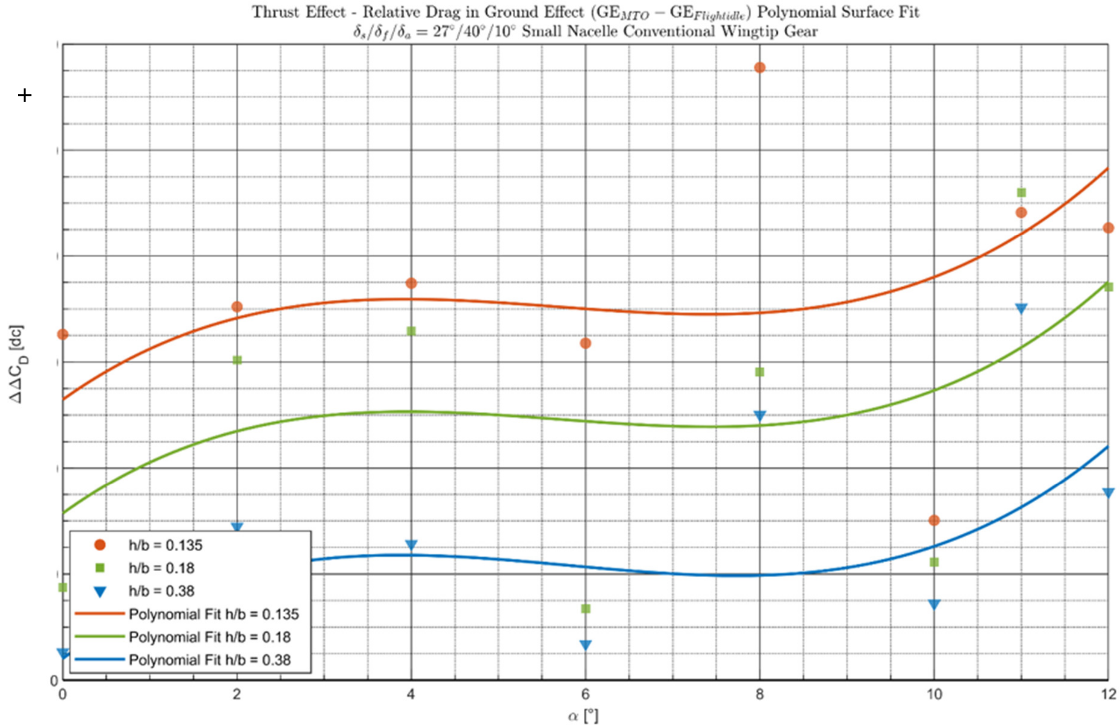

Figure 4.35 – Polynomial fit of change to the incremental drag coefficient in ground effect due to engine thrust setting for a range of h/b for the small nacelle, conventional wingtip geometry with gear deployed in landing configuration using a polynomial surface fit. Source: FFD72

The percentage change of the induced drag for both thrust settings is presented in Figure 4.36. The trend is that at lower to moderate α the induced drag for the flightidle case is further reduced, while at high α the induced drag is reduced by an approximately equal percentage.

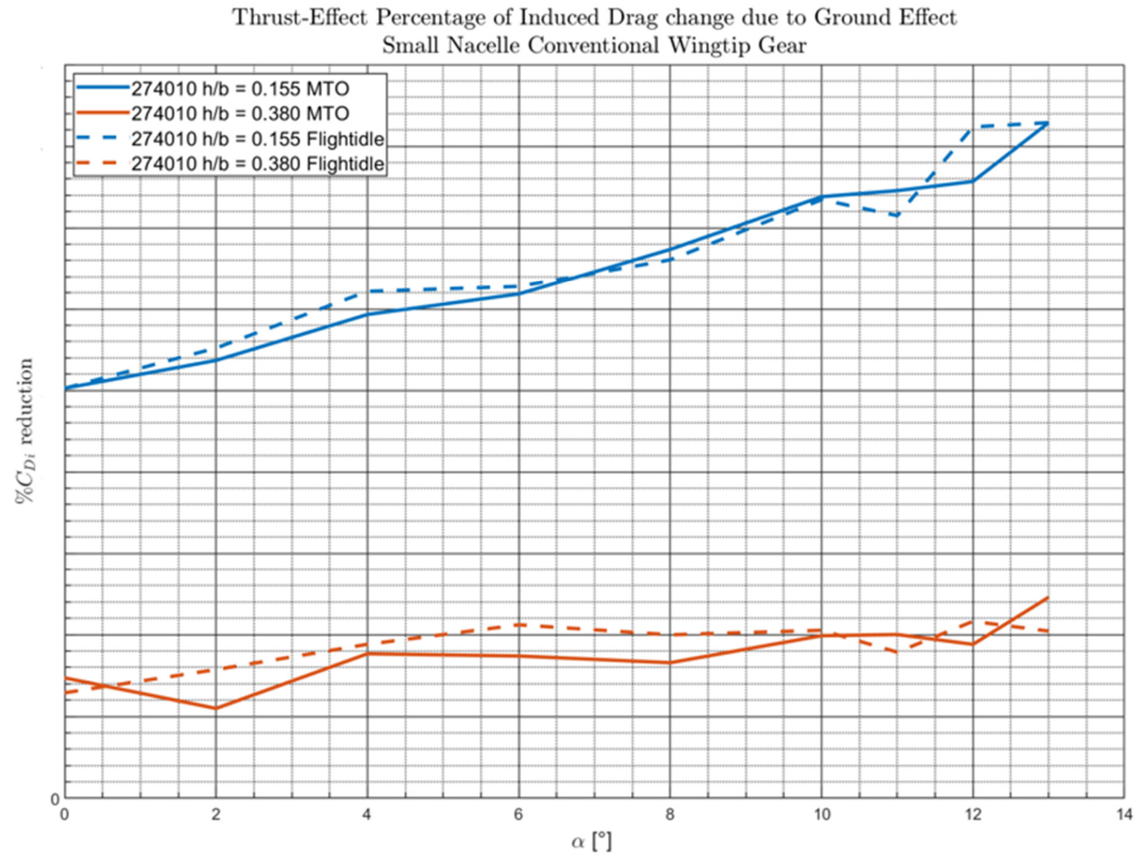

Figure 4.36 – Percentage for induced drag change for two thrust settings. Source: FFD72

The Spanwise drag distribution for the case of $\alpha = 2.0$ and $\alpha = 12.0$ can be seen in Figure 4.37 and Figure 4.38 respectively. At $\alpha = 2.0$ the drag is primarily changed behind the engine, where at flightidle thrust conditions the drag is further reduced in ground effect due to a combination of changing viscous-pressure drag and induced drag. At the wingtip the induced drag is increased for the flightidle case, because here the lift increment is higher, thus there is more induced drag at the wingtip.

For the case of $\alpha = 12.0$ similar observations can be made. The most significant drag reduction occurs for flightidle conditions in the region of the engine, which is the same region where the largest change in lift increment was observed. Similar to the case for $\alpha = 2.0°$, the wingtip induced drag is increased for the flightidle thrust condition.

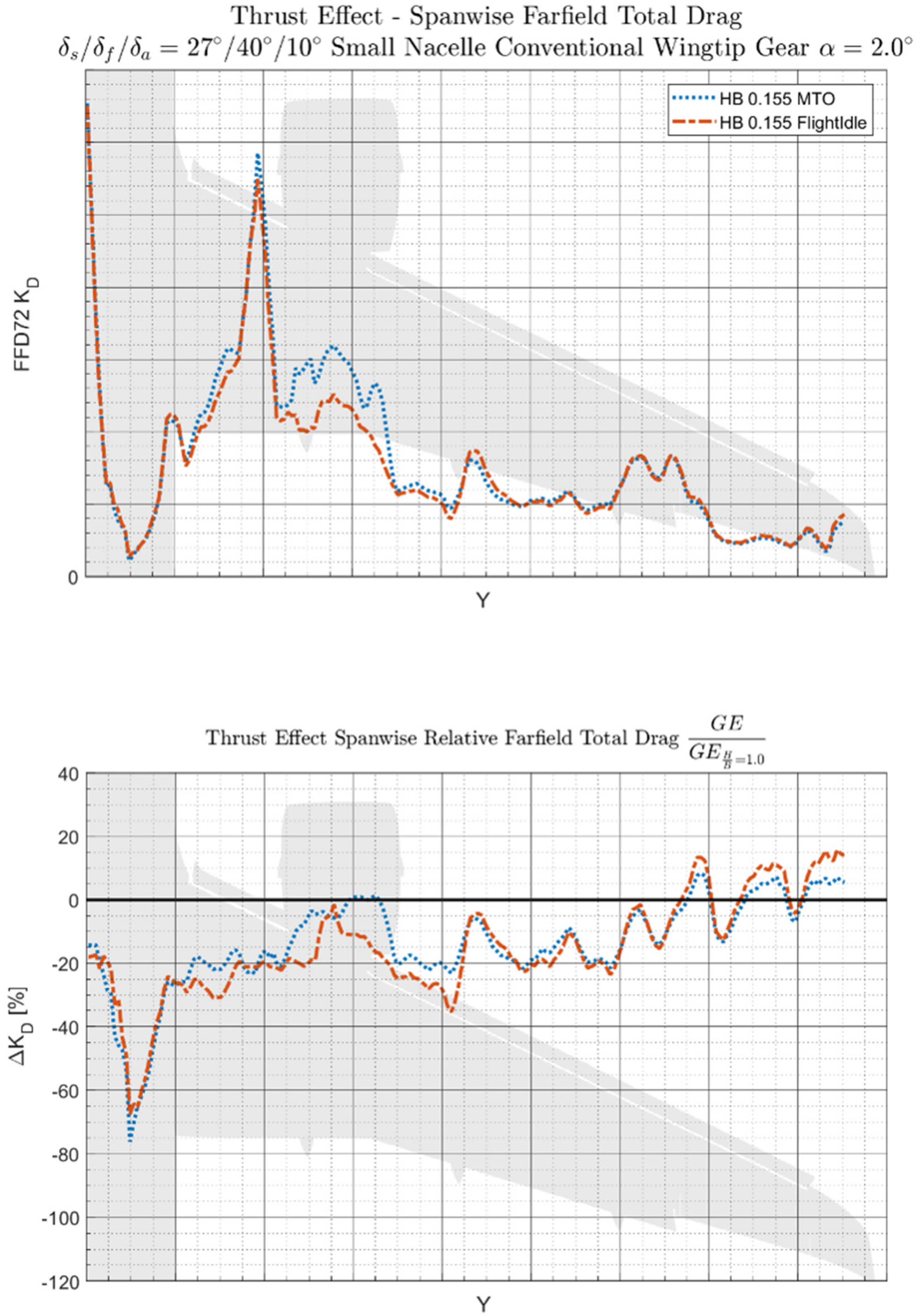

Figure 4.37 - Spanwise drag distribution showing the influence of thrust at $\alpha = 2.0°$ *and* $\frac{h}{b} = 0.155$ *Source: FFD72*

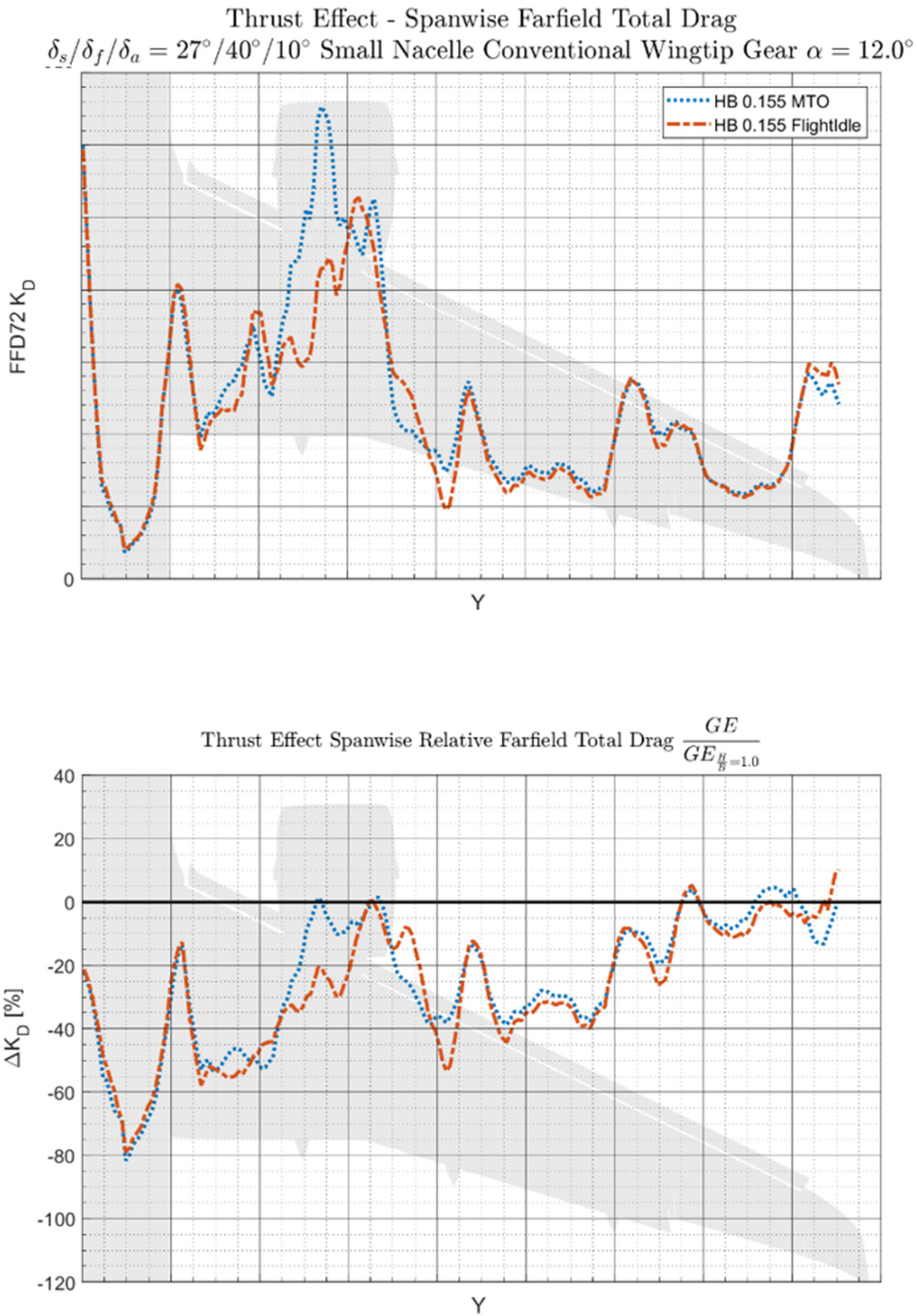

Figure 4.38 - Spanwise drag distribution showing the influence of thrust at $\alpha = 12.0°$ *and* $\frac{h}{b} = 0.155$ *Source: FFD72*

4.2.4 Conclusions

It was shown in this subsection that by applying maximum take-off instead of flightidle thrust settings, the influence of the ground effect on both the lift and drag is reduced. This has two causes:

1. At MTO thrust setting the engine sucks in air which would otherwise be deflected over the winger upper surface due to ground effect, which changes the local angle of attack on the leading edge in the region of the engine. This means that the magnitude of the suction increase which is normally present due to ground on the slat and mainwing leading edge, is reduced compared to when flightidle thrust settings are applied.
2. At higher α the jet from the engine increases the mass flow in the flap gap. This increases the suction on the flap leading edge, thereby counter-acting the suction decrease and lift loss caused by ground effect on this part of the wing.

These two effects combined cause a reduction of ground effect related lift by up to 2% of total lift increase at low α when MTO thrust settings are applied and a reduction of the ground effect related lift *decrease* at high α by up to 0.5% of total lift. Thus by applying MTO thrust settings the influence of the ground effect is reduced for all α.

The drag is reduced more significantly by up to 4% of total drag with flightidle thrust settings applied compared to MTO thrust. At low to moderate α this can be attributed to the higher lift for the flightidle case, resulting in a more significant induced drag benefit. At high α there is no longer a significant difference in absolute lift between the two thrust setting cases, but there is still a significant reduction in drag.

4.3 Effect of Flap Deflection in Ground Effect

In the previous subchapter, the influence of changing the engine thrust setting in ground effect was investigated for the case of the small nacelle, conventional wing-tip, gear deployed, landing configuration and MTO thrust setting. Now in this subchapter it is investigated how the behavior of this configuration changes when the high-lift settings are changed to the take-off setting, namely $22.0°$ slat angle, $10.0°$ flap angle and $5.0°$ aileron deflection is investigated.

After the extensive primary CFD campaign was completed, where the influence of the ground effect on the landing configuration was investigated, a smaller, secondary campaign was run for the take-off configuration. The scope of this campaign was more limited, calculations were performed only for $\alpha = 0.0°$, $\alpha = 6.0°$ and $\alpha = 12.0°$ for the MTO thrust setting, since this is a take-off high-lift setting it makes no sense to run these simulations at flightidle thrust setting. At a late stage of the thesis research, a few extra data points were added for $\alpha = 4.0°$ and $\alpha = 8.0°$ for a limited set of h/b values only. No CFD runs were performed with the gear retracted.

This subchapter is structured as follows: First the effect of the change in lift due to ground effect will be investigated for this take-off configuration, after which the change in drag will be discussed. Finally the conclusions will be presented.
The relative lift and drag curves for all four geometric variants are presented in Appendix C – Lift Increment Plots and Appendix D – Drag Increment Plots, in respectively section 9.3.3 and 9.4.3.

4.3.1 Change in Lift

The change in lift due to ground effect for the take-off configuration is shown in Figure 4.39 and can be directly compared with Figure 4.26, the only changed parameters between the two datasets are the slat, flap and aileron deflection angle.

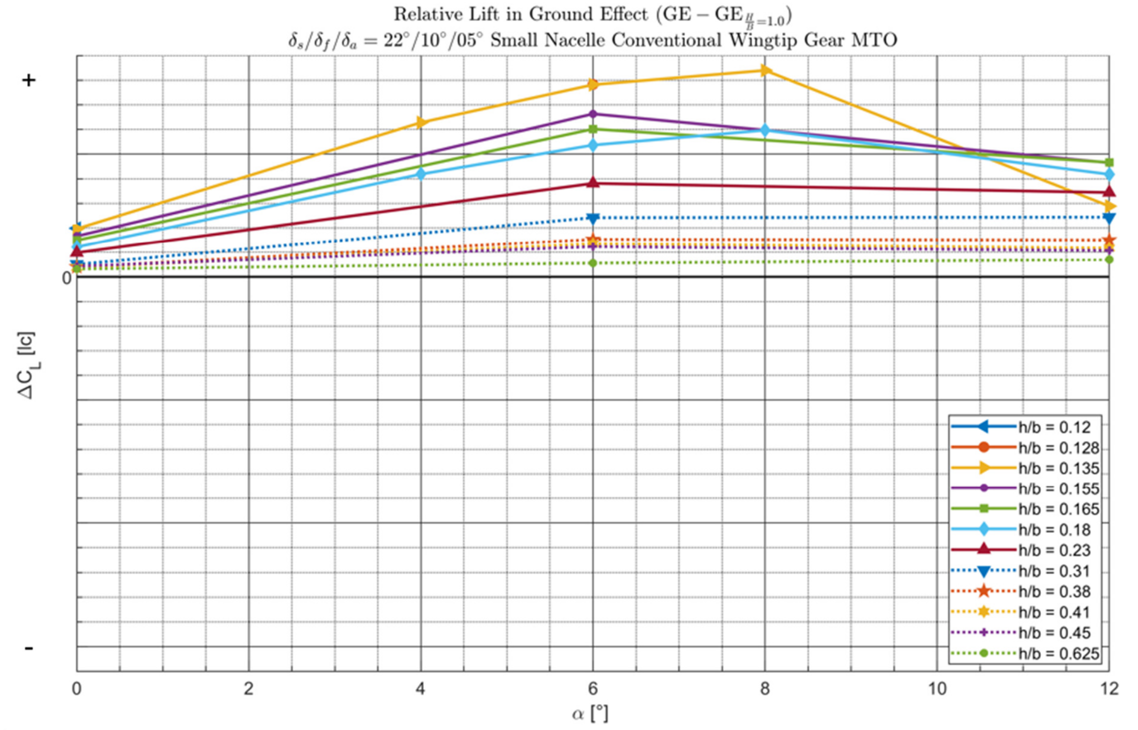

Figure 4.39 - Change in lift coefficient due to ground effect for a range of h/b for the small nacelle, conventional wingtip geometry with gear deployed in MTO thrust conditions in take-off configuration with same Y-Axis as figure 4.1. Source: FFD72.

Figure 4.39 shows that there is an increase in lift for the entire range of $0.0° \leq \alpha \leq 12.0°$ which is most significant at $\alpha = 8.0°$. This is in contrast to the case for the landing configuration, where it was shown previously that the lift increment already becomes negative in the region of $8.0° \leq \alpha \leq 10.0°$. Both the absolute and relative of the maximum lift increment is increased for the take-off configuration, up to 6.3% of total lift increase, compared to a maximum of 3.5% lift increase for the landing configuration.

A breakdown of the total lift increment into the individual contributions from the wing and the fuselage can be seen in Figure 4.40, which can be directly compared to Figure 4.18 to determine the influence of the high-lift configuration. The contribution from the fuselage remains relatively unchanged. The main difference can be observed at high α, where the landing configuration shows a reduction of the positive lift increment for the fuselage, while for the take-off configuration the fuselage lift increment is still increasing.

However, a significant difference can be observed for the change of lift increment on the wing. For the landing configuration, the contribution is zero to negative for the entire range α and becomes exponentially more negative for $\alpha > 10°$. In contrast, for the take-off configuration there is a positive lift increment for the entire range of α, which is larger than the increase in lift contribution from the fuselage. Only at $\alpha = 12.0°$ does the lift increment from the wing start being reduced. It is expected that as α would be further increased, the lift increment from the wing would turn negative, however no calculations were performed for this configuration for higher α.

The more positive ground effect lift increment for the take-off configuration, compared to the landing configuration, is expected based on literature (56) (69). Here it was found that flap deflection in ground effect reduces the effect angle of attack and reduces the mass flow rate through the flap gap, both causing a reduction in circulation. By reducing the flap deflection, the magnitude of these lift reducing effects is also reduced.

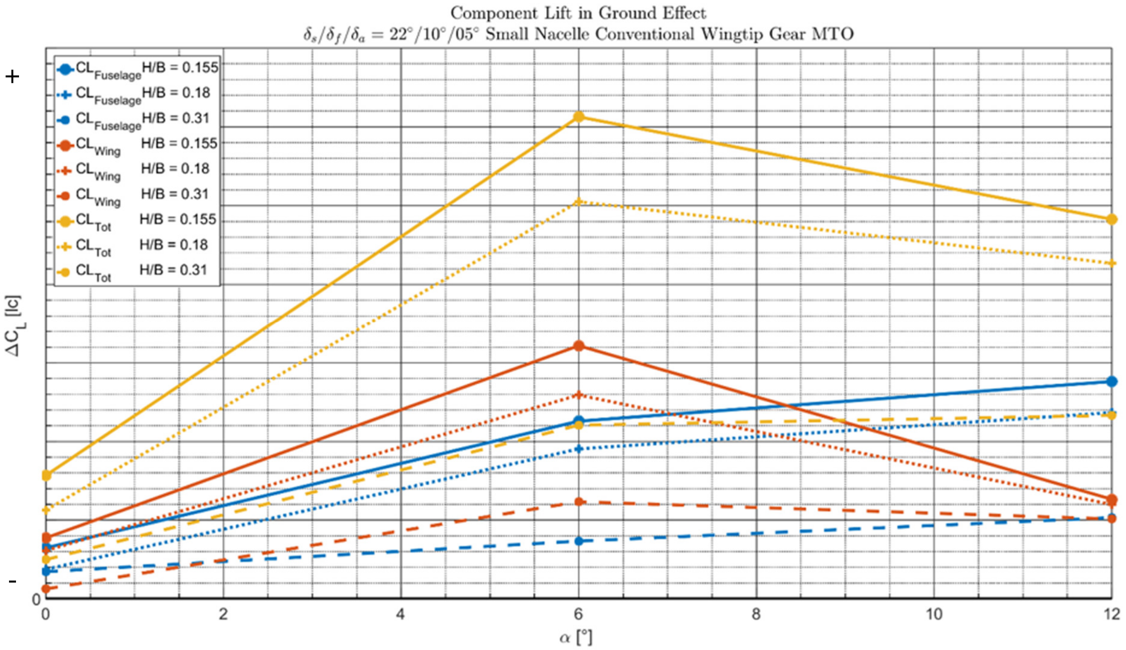

Figure 4.40 - Fuselage, wing and total lift increments in ground effect for the small nacelle, conventional wingtip geometry with gear deployed in MTO thrust conditions with the take-off configuration

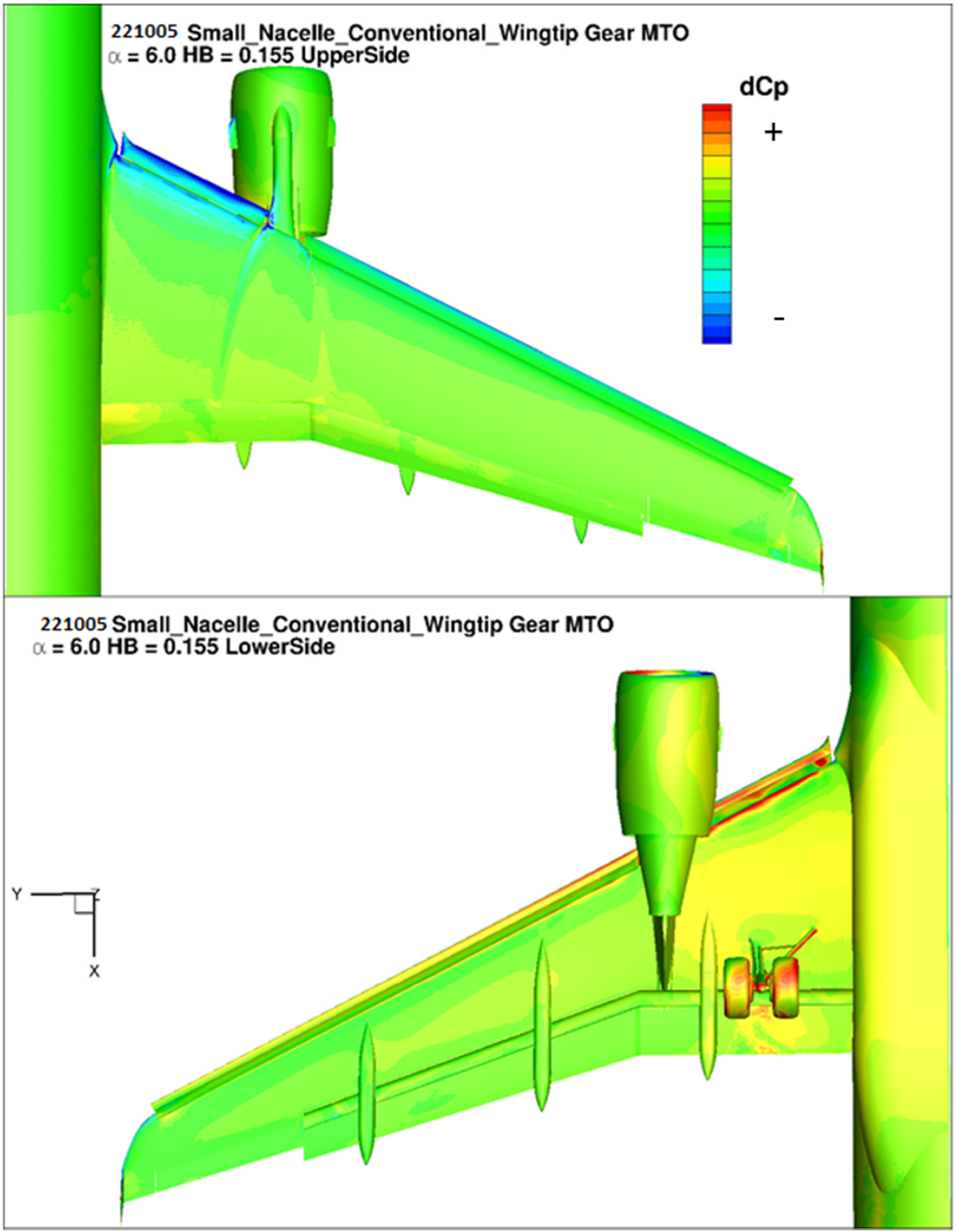

Figure 4.41 - Relative pressure change over the wing due to ground effect at $\alpha = 6.0°$ $\frac{h}{b} = 0.155$ *for the take-off configuration,* ($\Delta C_{P_{GE}} = C_{P_{GE}} - C_{P_{\frac{h}{b}=1.0}}$)

Figure 4.41 and Figure 4.42 show the relative pressure change due to ground effect for $\alpha = 6.0°$ and $\alpha = 12.0°$. Qualitatively the change in pressure is similar to that of the landing configuration. However, the pressure increase on the upperside of the mainwing and flaps is less pronounced compared to the landing configuration.

At $\alpha = 6.0°$ as shown in Figure 4.41 there is a significant pressure increase on the lower fuselage and inboard section of the lower wing, while the counteracting pressure on the upper surface of the wing has not yet increased as significantly, thus leading to the strong increase in lift, seen in Figure 4.39.

At $\alpha = 12.0°$, seen in Figure 4.42, there is now a strong increase in pressure observable on the upper wing surface. This pressure increase is similar to the pressure increase observed on the landing configurations, which becomes dominant for that configuration at $\alpha \geq 6.0°$. But for the take-off configuration the relative pressure on the lower wing is also still increasing, albeit not as significantly compared to the upperside. This results in a slightly lower positive lift increment due to ground effect. It is expected but not verified that if α increases further for this take-off configuration, the pressure increase on the upper surface becomes increasingly dominant eventually resulting in a negative lift increment.

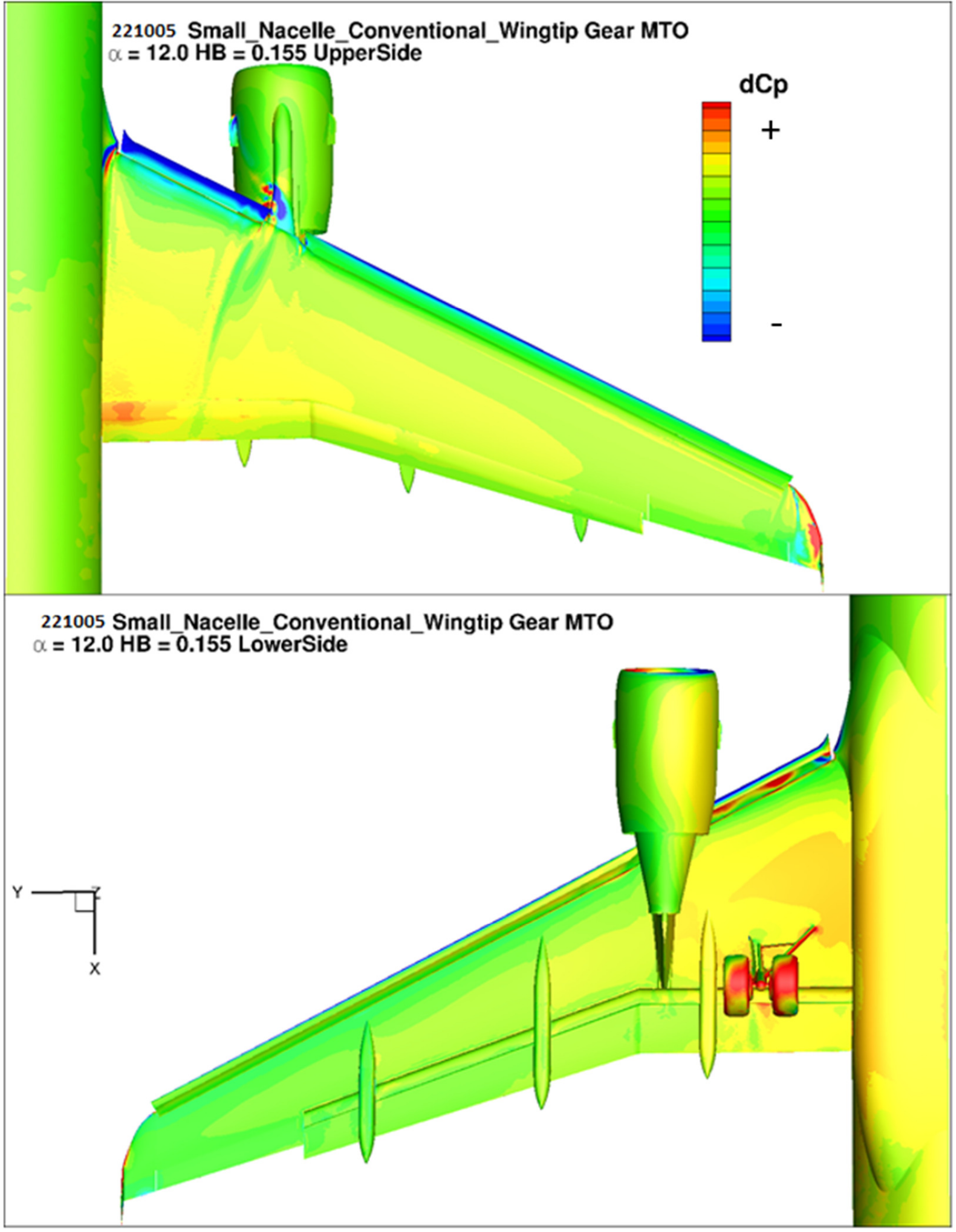

Figure 4.42 - Relative pressure change over the wing due to ground effect at $\alpha = 12.0°$ $\frac{h}{b} = 0.155$ for the take-off configuration, $(\Delta C_{P_{GE}} = C_{P_{GE}} - C_{P_{\frac{h}{b}=1.0}})$

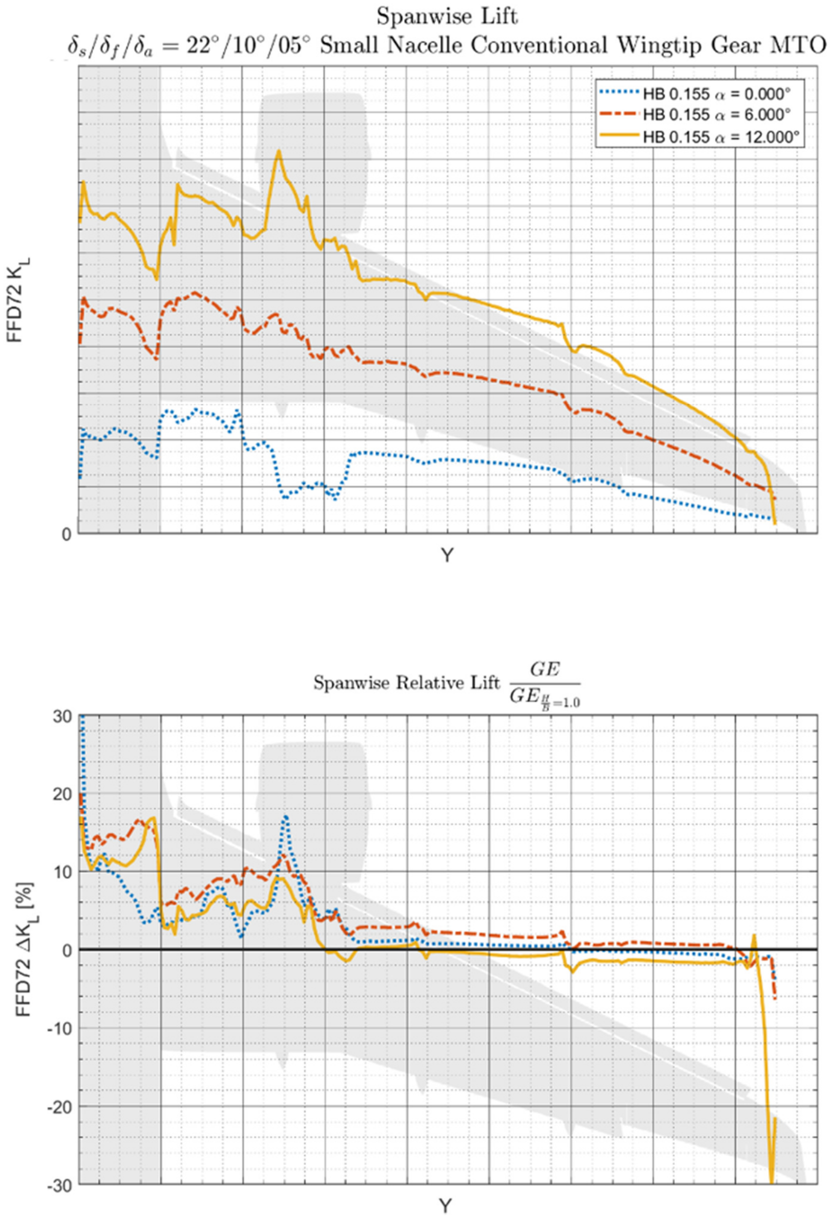

Figure 4.43 - Spanwise lift distribution for $0.0° \le \alpha \le 12.0°$ and $\frac{h}{b} = 0.155$ for the take-off configuration

The spanwise lift distributions for the three values of α calculated for this case are shown in Figure 4.43. An increase in lift is observable in the region of the fuselage and on the mainwing between the fuselage and nacelle. At $\alpha = 12.0°$ there is a strong lift decrease at the wingtip, this is caused by the earlier onset of wingtip stall, similar to that shown in Figure 4.14 for the landing configuration.

4.3.2 Change in Drag

The reduction in drag due to ground effect for the take-off configuration can be seen in Figure 4.44 and can be directly compared to Figure 4.33. The maximum drag decrease is strongly reduced from $\Delta C_{D_{max}} \approx -840\ [dc]$ in the landing configuration to $\Delta C_{D_{max}} \approx -310\ [dc]$ for the take-off configuration. This decrease in drag reduction is caused both by a decrease in the absolute value of the induced drag by a factor of two, which is caused by a reduction of approximately 40% in the lift coefficient compared to the landing configuration, as well as a decrease in value of the relative induced drag reduction. This is shown in Figure 4.45, at the same α the relative induced drag reduction is 5% to 10% lower compared to the landing configuration.

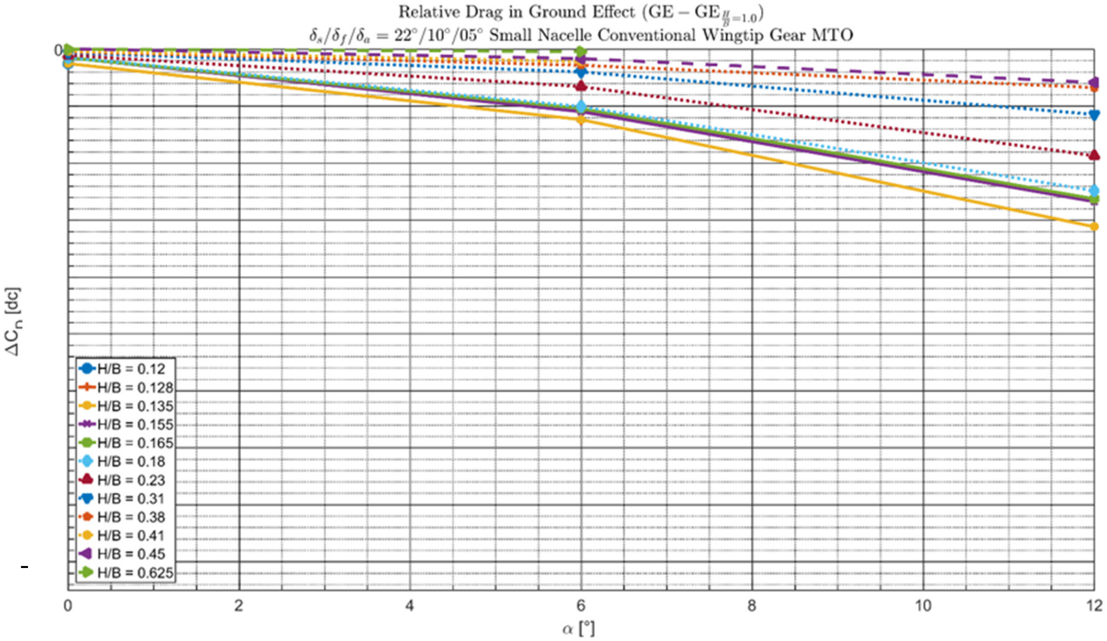

Figure 4.44 - Change in drag coefficient due to ground effect for a range of $\frac{h}{b}$ for the small nacelle, conventional wingtip geometry with gear deployed in MTO thrust settings with the take-off high- lift configuration. Y-axis scale identical to the landing configuration

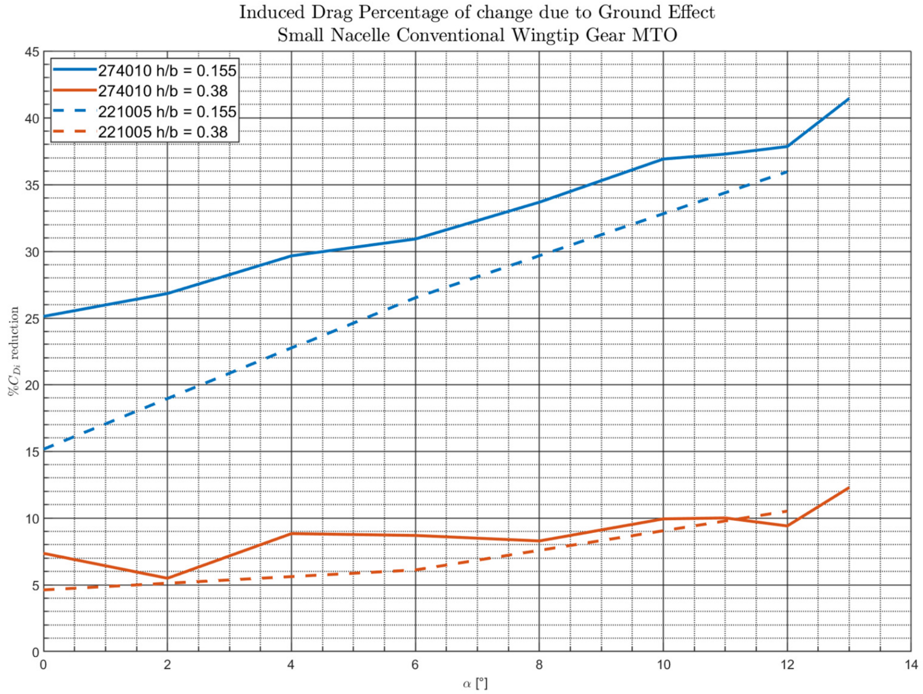

Figure 4.45 - Induced drag and the influence of lift coefficient on induced drag reduction for the small nacelle, conventional wingtip geometry with gear deployed in MTO thrust settings for two different high-lift configurations

Figure 4.46 shows the spanwise drag distribution at $h/b = 0.155$ for $0.0° \leq \alpha \leq 12.0$. At $\alpha = 0.0°$ the induced drag is an order of magnitude lower than at $\alpha = 12.0°$, which is why there is almost no drag change due to ground effect present at $\alpha = 0.0°$. In contrast, for the landing configuration there is already a significant amount of lift and thus induced drag present at low α, thus there is already a significant relative change in (induced) drag at $\alpha = 0.0°$ due to ground effect.

At $\alpha = 6.0°$ and $\alpha = 12.0°$ the relative change in drag for both the take-off and landing configuration are very similar, the most significant difference is the scale of the effects, not the trend. For the landing configuration in both the % value of the drag change, as well as the absolute drag values in are higher compared to the take-off configuration. Thus from the evidence presented here the high-lift settings scale the change in drag in ground effect only, but do not introduce significant new phenomena.

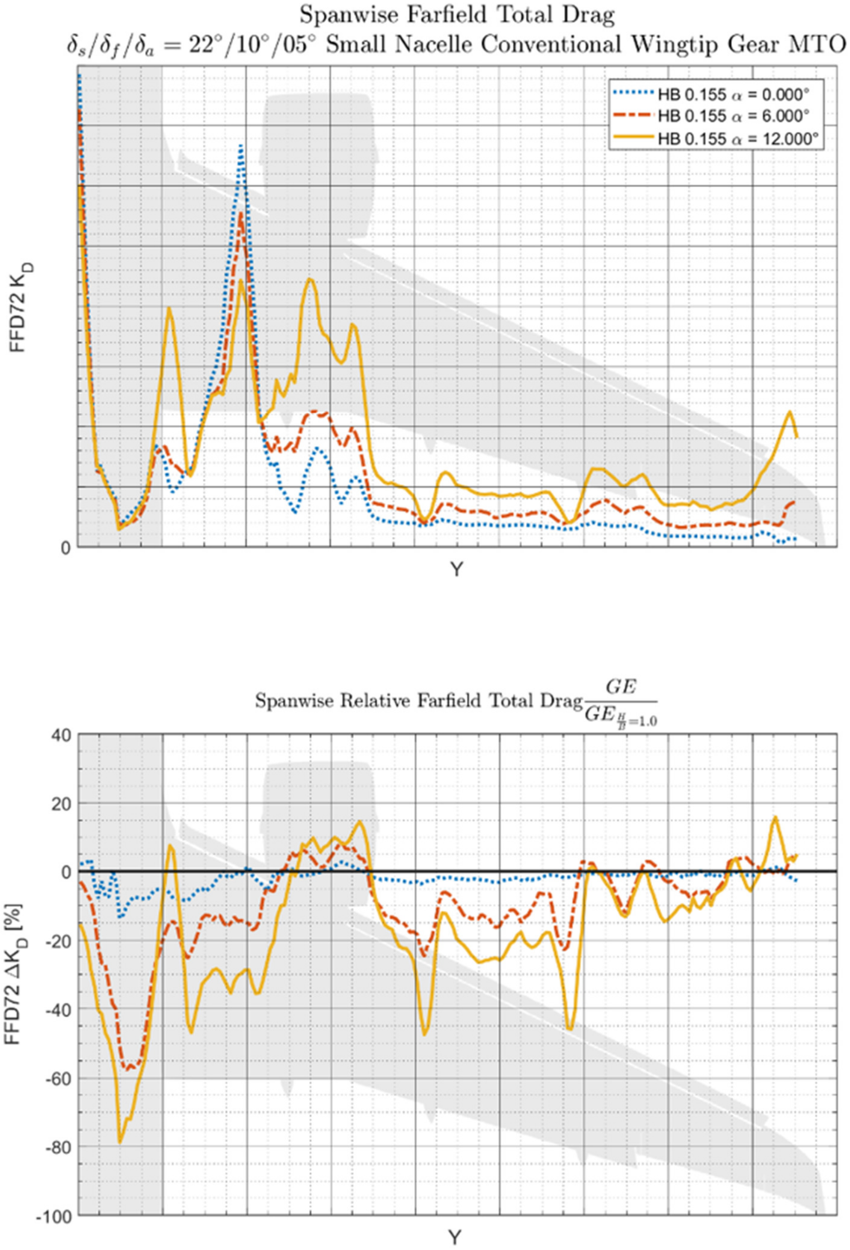

Figure 4.46 - Spanwise drag distribution for the small nacelle, conventional wingtip geometry with gear deployed and MTO thrust conditions at $0.0° \leq \alpha \leq 12.0°$ $\frac{h}{b} = 0.155$ *for the take-off configuration*

4.3.3 Conclusions

A CFD campaign was run utilizing take-off configuration of 22° slat, 10° flap and 5° aileron deflection. Compared to the landing configuration of 27° slat, 40° flap and 10° aileron deflection, the magnitude of the lift increment due to ground effect is increased from 3.5% to 6.3%. Furthermore, it stays positive across the entire range of $0.0° \leq \alpha \leq 12.0°$. At $\alpha = 12.0°$ and low h/b the magnitude of the lift increment starts decreasing and is expected to become negative as α is further increased. The difference in lift increment is primarily linked to a reduction in the flap deflection. This lower flap angle causes a less severe reduction in local angle of attack, a less severe reduction of the front flap suction and peak and a stronger pressure increase on the lower flap surface.

The benefit in drag reduction due to ground effect is significantly decreased for the take-off configuration by approximately a factor of two. It was found that both the magnitude and the relative value of the induced drag reduction decreases for the take-off configuration.

4.4 Effect of Engine Nacelle Size in Ground Effect

It was found during previous investigations that in ground effect, the sideways flow from the inboard wing towards the outboard wing increases, especially on the lower wing surface. This stronger sideways flow is caused by the previously discussed strong pressure rise on the lower inboard wing, between the fuselage and nacelle. During previous ground effect research on a large twin-jet transport aircraft it was found that the size of the engine nacelle influenced the magnitude of the increase sideways flow. This is also shown in Figure 4.47, at $\alpha = 8.0°$ there is an increase of up to 55% in side force C_y, which is defined as positive in the direction of the wingtip. This increase is stronger in both absolute and relative terms for the large nacelle. Given these observed differences in nacelle side force and sideflow on the wing, in this subchapter it is investigated if the change in nacelle size significantly influences the change to lift and drag in ground effect.

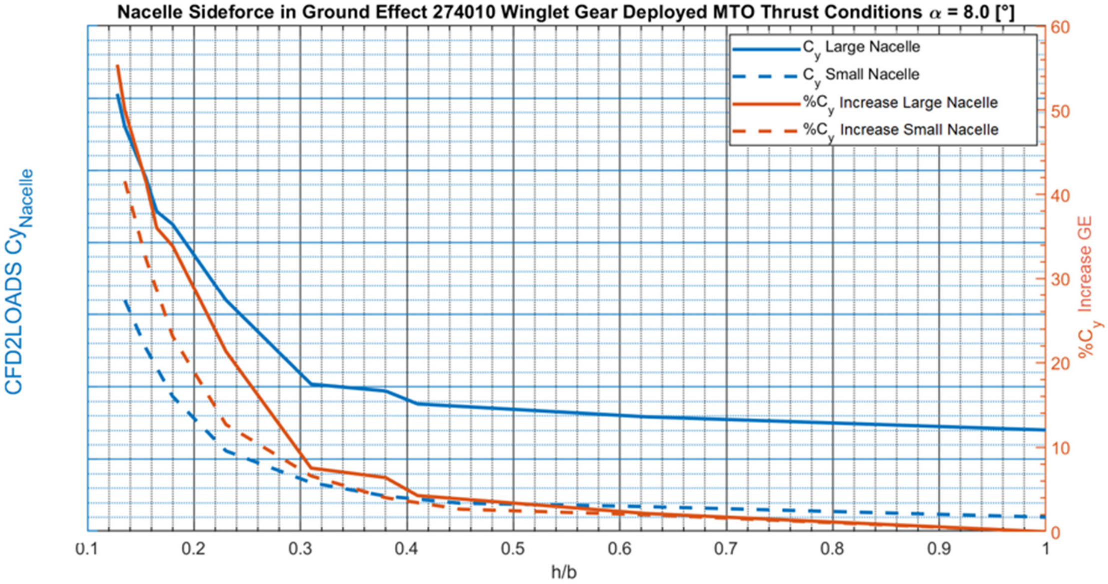

Figure 4.47 – Absolute (blue) and relative (orange) Nacelle side force change in ground effect for the winglet geometry with gear deployed and MTO thrust conditions in the landing configuration $\alpha = 8.0°$

First the influence of changing the nacelle on the ground effect lift increment is investigated, after which the change in drag increment will be discussed. After this the conclusions are presented.

4.4.1 Change in Lift

Appendix C – Lift Increment Plots contains lift and drag increment plots for the four different geometric configuration. Separate plots are provided for the landing configuration for MTO and flightidle thrust settings, as well as for the take-off configuration with just MTO thrust settings. Figure 9.6 to Figure 9.17 can be examined when researching the influence of the nacelle (and winglet) geometry change on the lift increment. A direct comparison from the data presented in the appendix between the four different geometric variations is presented in this section.

Figure 4.48 shows the lift change for the small and large nacelle with the winglet geometry installed for the take-off configuration, while Figure 4.49 shows the same but with the conventional wingtip geometry equipped. Figure 4.50 is a combination of the two previous figures, showing the lift increment for all four different geometry variants. Figure 4.51 and

Figure 4.52 are similar to Figure 4.50, but here the landing configuration is shown for the MTO and flightidle thrust setting respectively.

Firstly, it can be observed that the differences between the configurations are small, in the order off 1% of the total aircraft lift for the take-off configuration. This is in the same order of magnitude as the uncertainty in the CFD results for the landing-configuration, due to unsteady phenomena occurring which means the solution will never be fully converged when using the steady RANS equations. Therefore in this section the focus will be on analyzing the take-off configuration, after which an attempt will be made to extrapolate those results to the landing configuration.

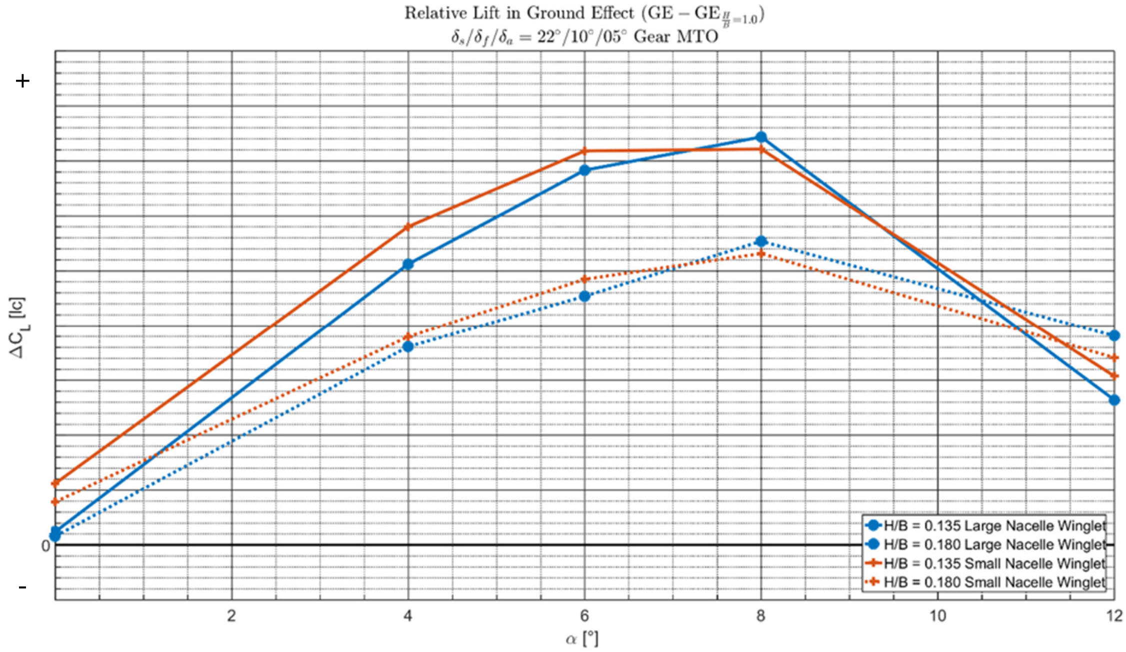

Figure 4.48 - Lift change due to ground effect showing the nacelle-effect for the conventional wingtip geometry with MTO thrust settings in the take-off configuration for $0^\circ \le \alpha \le 12^\circ$ *and* $\frac{h}{b} = 0.135\ and\ \ \frac{h}{b} = 0.18$

Figure 4.50 shows that the maximum lift increment, occurring at $\alpha = 8.0^\circ$, is higher for the cases with the small nacelle. But as α is increased further, the downward slopes of the lift increment is steeper compared to the cases with a large nacelle. This is similar behavior to that observed for the thrust-effect in subchapter 4.2. The smaller nacelle engine has a lower thrust coefficient by approximately 20%, thus it is possible that a significant part of the observed differences are caused not by the nacelle geometry, but by a thrust-effect. Ideally this would be checked by performing a CFD campaign for the take-off configuration with flightidle thrust settings, since for this setting the c_t vales for the large and small nacelles are identical. Unfortunately not enough time was available to complete this, so therefore this becomes a recommendation for future work.

For the flightidle thrust setting, landing configuration shown in Figure 4.52, it can be observed that the differences between the configurations seem less pronounced compared to the MTO thrust setting in Figure 4.51, but because of the previously mentioned CFD uncertainties no solid conclusion can be reached regarding this subject.

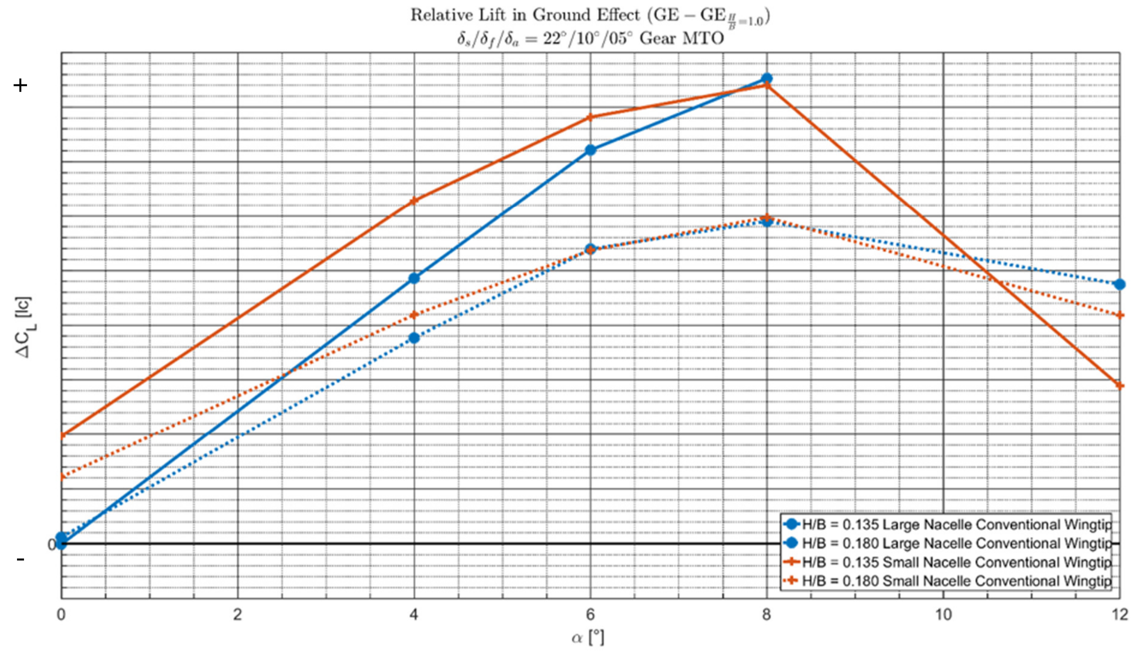

Figure 4.49 - Lift change due to ground effect showing the nacelle-effect for the conventional wingtip geometry with MTO thrust settings in the take-off configuration for $0° \leq \alpha \leq 12°$ *and* $\frac{h}{b} = 0.135\ and\ \frac{h}{b} = 0.18$. *Same Y-axis scale as figure 4.48.*

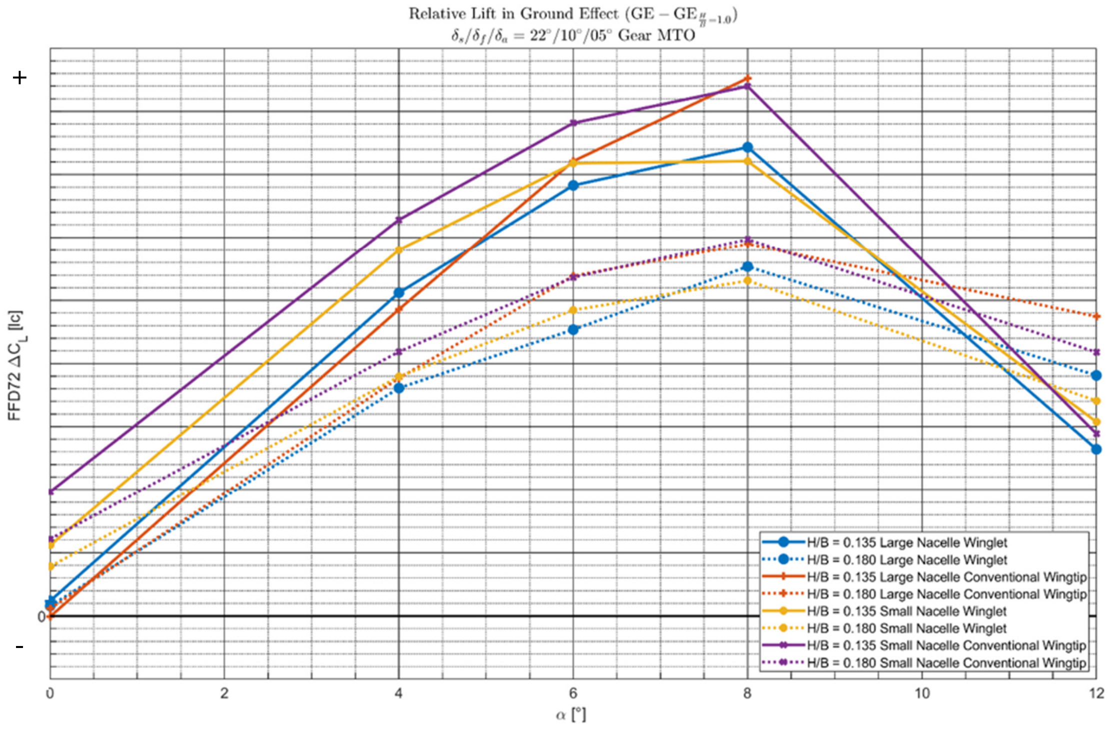

Figure 4.50 - Lift change due to ground effect for different configurations with MTO thrust settings in the take-off configuration for $0° \leq \alpha \leq 12°$ *and* $\frac{h}{b} = 0.135\ and\ \frac{h}{b} = 0.18$. *Same Y-axis scale as figure 4.48.*

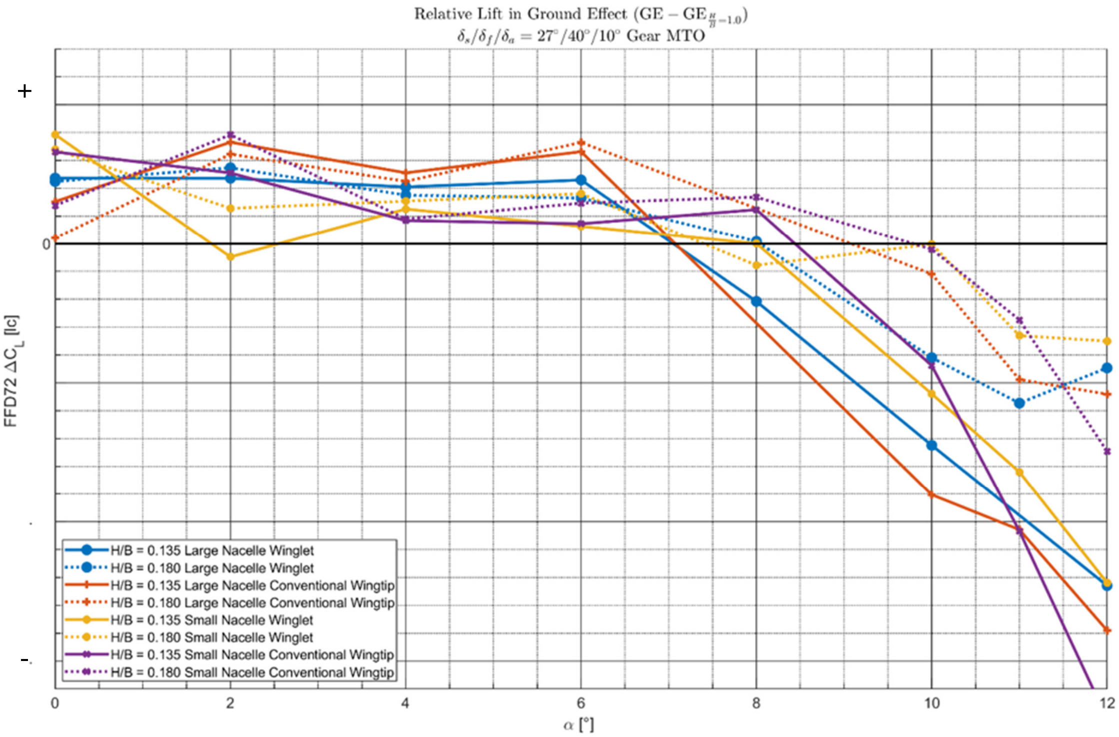

Figure 4.51 - Lift change due to ground effect for different configurations with MTO thrust settings in the landing configuration for $0° \leq \alpha \leq 12°$ *and* $\frac{h}{b} = 0.135\ and\ \frac{h}{b} = 0.18$

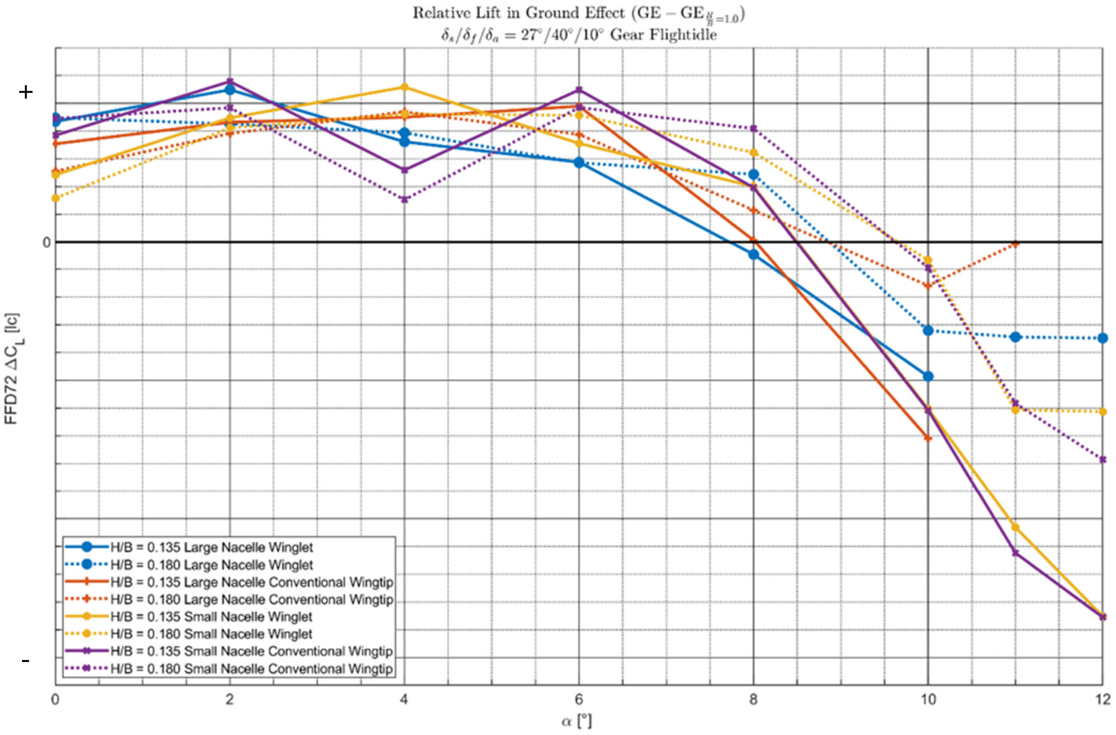

Figure 4.52 - Lift change due to ground effect for different configurations with flightidle thrust settings in the landing configuration for $0° \leq \alpha \leq 12°$ *and* $\frac{h}{b} = 0.135\ and\ \frac{h}{b} = 0.18$

The relative pressure change for the case with a large nacelle and small nacelle for $\alpha = 6.0°$ and $h/b = 0.135$ can be observed in Figure 4.53 and Figure 4.54 respectively. Differences can be observed in three distinct areas. The first is located on the top of the inboard slat, where the part closest to the large nacelle (furthest outboard) behaves differently compared to that part of the flap with the small nacelle installed. It seems as if the flow over this part of the slat is partially blocked by the nacelle, resulting in a significantly reduced influence of ground effect.

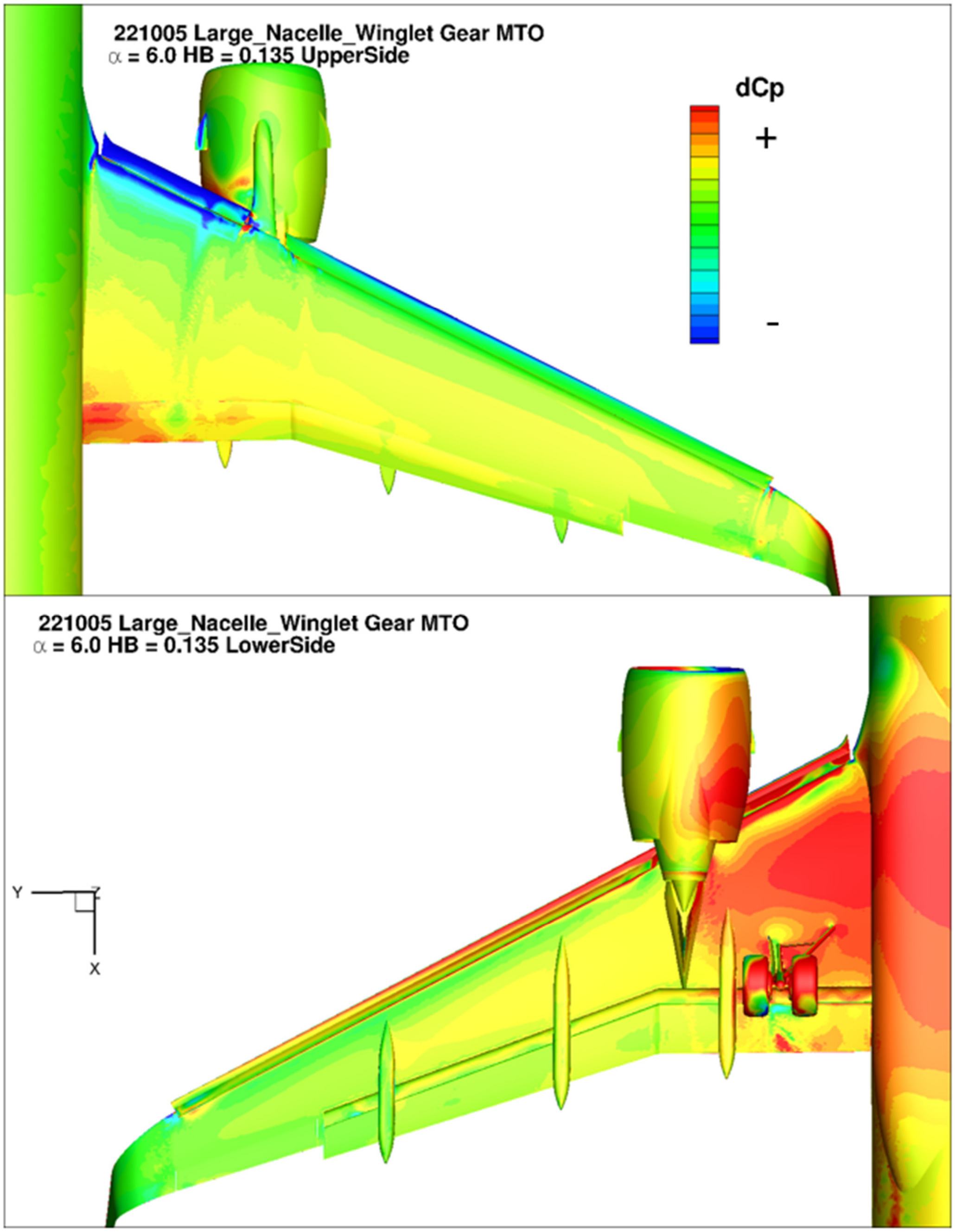

Figure 4.53 - Relative pressure change over the wing due to ground effect for the large nacelle, winglet geometry with gear deployed at $\alpha = 6.0°$ $\frac{h}{b} = 0.135$ *for the take-off configuration* $(\Delta C_{P_{GE}} = C_{P_{GE}} - C_{P_{\frac{h}{b}=1.0}})$

Differences in pressure can also be observed on the lowerside of the wing, where the pressure increase due to ground effect is slightly higher for the case of the large nacelle in the region between the fuselage and the nacelle. This effect is small but can also be observed for the landing configuration.

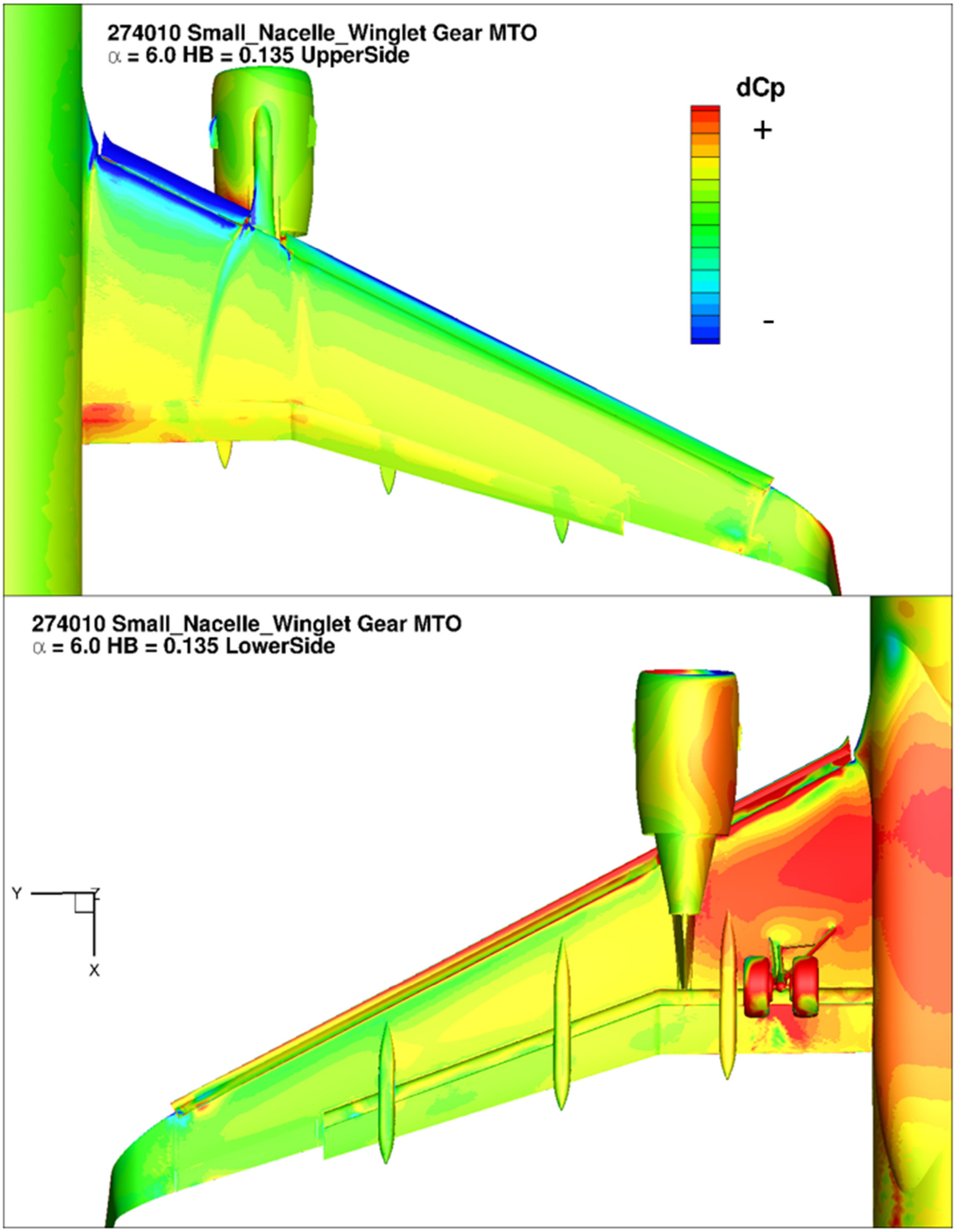

Figure 4.54 - Relative pressure change over the wing due to ground effect for the small nacelle, winglet geometry with gear deployed at $\alpha = 6.0°$ $\frac{h}{b} = 0.135$ *for the take-off configuration,* ($\Delta C_{P_{GE}} = C_{P_{GE}} - C_{P_{\frac{h}{b}=1.0}}$)

A more significant increase in pressure occurs on the large nacelle. Due to the larger circumference it is located closer to the ground, leading to an increased pressure rise on the bottom and side of the nacelle. This is shown in Figure 4.55 where the component lift of the entire wing, the inboard-slat and the nacelle is plotted for both the large and small nacelle for respectively $h/b = 0.18$. Of note is the fact that there seems to be a linear offset between the two geometries for the $C_{L_{Wing}}$ and $C_{L_{IB-Slat}}$, while for $C_{L_{Nacelle}}$ there is a different slope instead of a linear offset. At $\alpha = 6.0°$ the lift increment for the nacelle is approximately 0.08% of total lift higher for the larger nacelle. The lift increment on the inboard-slat is reduced by approximately 0.06% of total lift for the larger nacelle, caused by higher thrust coefficients associated with the large nacelle geometry which causes a stronger reduction in the circulation over the wing. The same effect also causes the wing lift increment to be reduced for the large nacelle geometry.

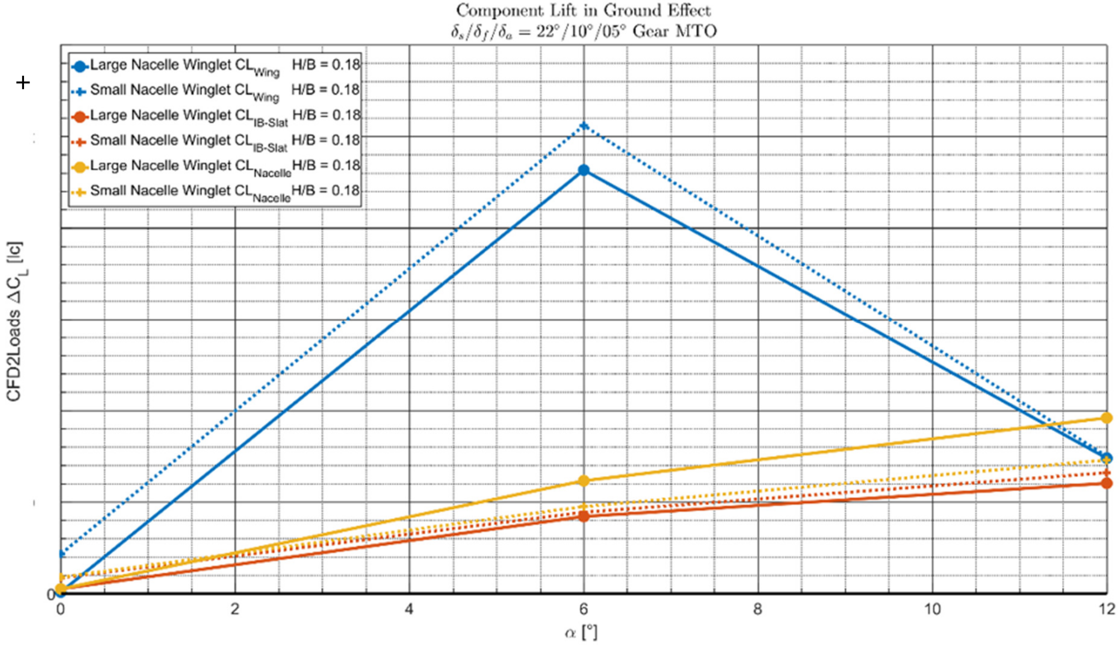

Figure 4.55 - Wing (Blue), IB-Slat (Red) and Nacelle (Yellow) lift in ground effect for the large nacelle and small nacelle geometry with gear deployed at $\alpha = 6.0°$ $\frac{h}{b} = 0.18$ for the take-off configuration

The spanwise lift distribution for all four geometric variants can be seen in Figure 4.56 for $\alpha = 6.0°$ and $h/b = 0.135$ and $h/b = 0.18$. As expected, the most significant differences in relative lift change are observable in the region of the nacelle. An increase in ground effect lift can be observed in this area (region C), just for the two small nacelle configurations. Very small differences in relative lift are observable at the inboard slat region (region B). Finally, at the fuselage (region A), the lift for the large nacelle and winglet configurations (blue lines) increases less than the other configurations with differences of up to 5%. No explanation can be offered regarding this observation. Figure 9.86 shows lift distribution for the same case at $\alpha = 12.0°$. No significant differences between the different configurations can be identified.

In Appendix I – Spanwise Lift Distributions comparing different Geometries in the Landing High-Lift Configuration the spanwise lift distribution for the landing configurations are presented. However, significantly more scatter in the data can be observed for the landing configurations, due to the presence of the previously mentioned unsteady flow phenomena. Due to this inherent noisiness and the fact small effects are being investigated, no firm conclusions can be drawn from these figures.

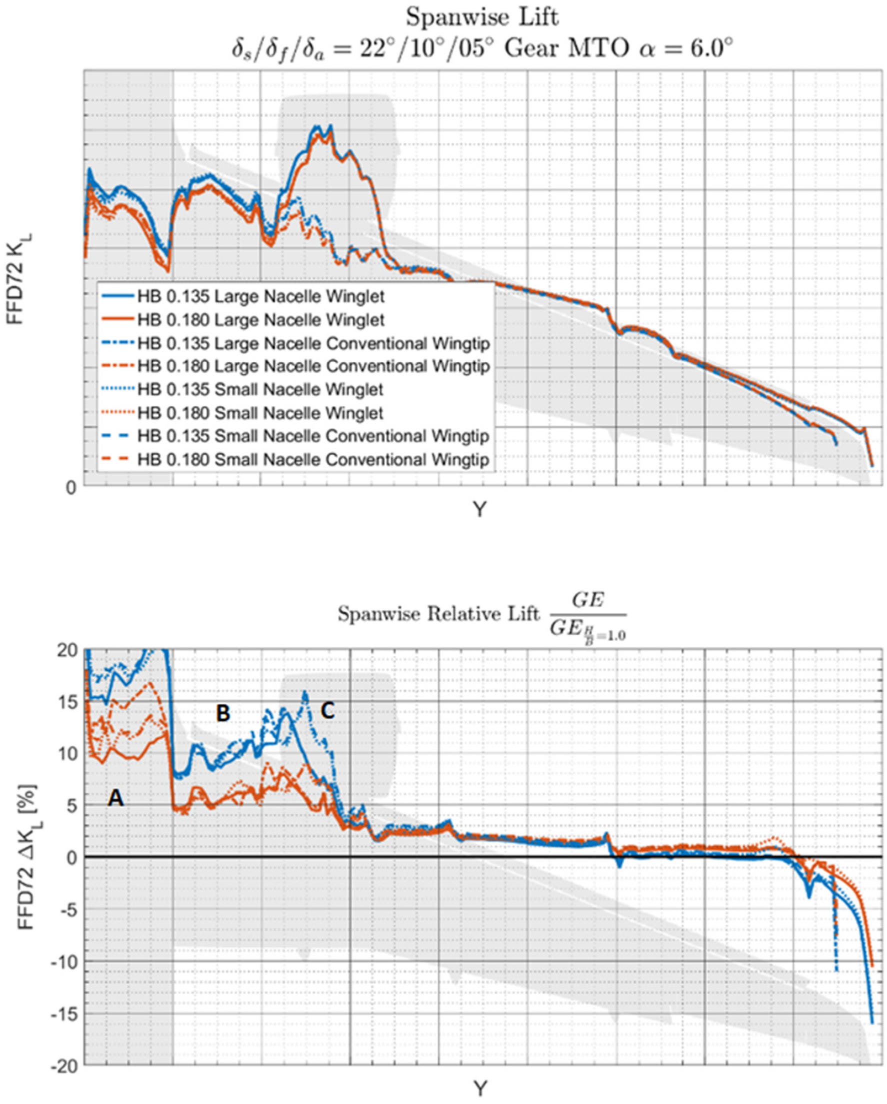

Figure 4.56 - Spanwise lift distribution for the large nacelle and small nacelle geometry with gear deployed and MTO thrust conditions at $\alpha = 6.0°$ $\frac{h}{b} = 0.135$ and $\frac{h}{b} = 0.18$ for the take-off configuration

4.4.2 Change in Drag

The change in drag due to all the different configurations can be seen in Figure 9.18 to Figure 9.29 in Appendix D – Drag Increment Plots. The information from these plots is synthesized in Figure 4.57, Figure 4.58 and Figure 4.59 where direct comparisons are made for the change in drag due to ground effect for the different geometric configurations for $h/b = 0.135$ and $h/b = 0.18$.

For the case of the take-off configuration, shown in Figure 4.57, it can be seen that in general the configurations with a small nacelle show a slightly larger drag decrease due to ground effect. This is consistent with the hypothesis formulated in section 4.4.1 that the primary cause of the difference observed between the large and small configuration for the MTO thrust condition are caused by the lower thrust coefficient of the small nacelle. It was shown in subchapter 4.2 that a lower thrust setting increases the drag reduction in ground effect.

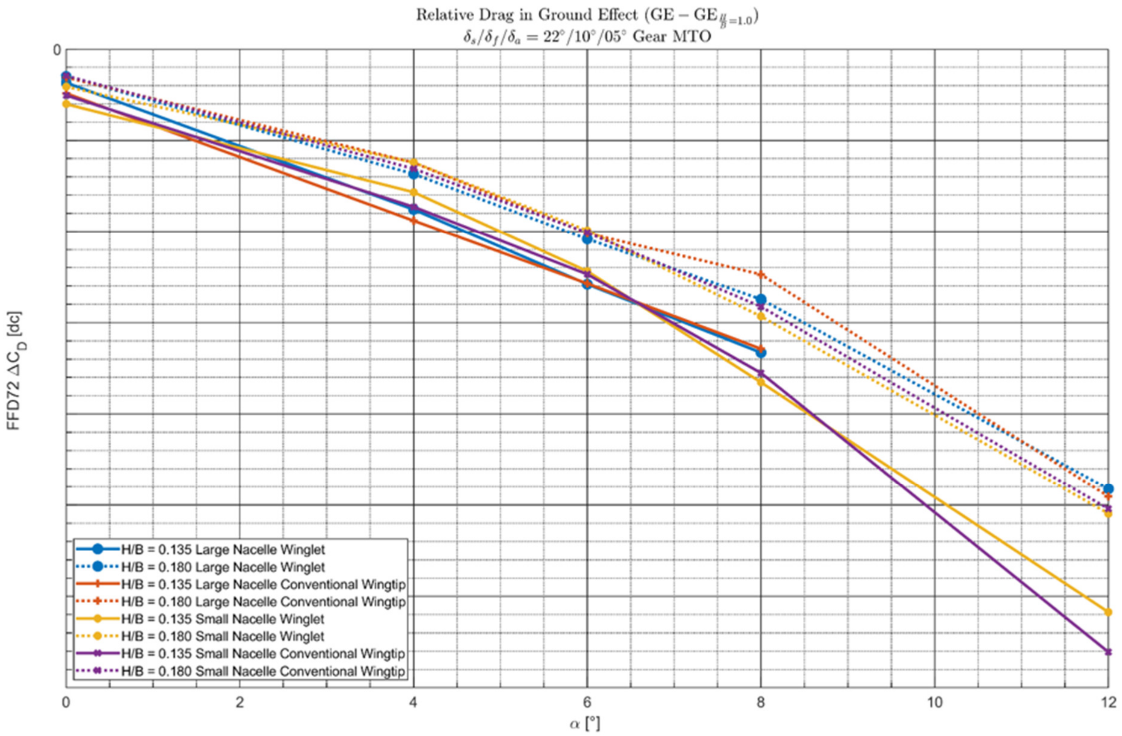

Figure 4.57 - Drag change due to ground effect for different configurations with MTO thrust settings in the take-off configuration for $0° \leq \alpha \leq 12°$ *and* $\frac{h}{b} = 0.135\ and\ \frac{h}{b} = 0.18$

This hypothesis is further supported when analyzing Figure 4.58 and Figure 4.59 which show the drag reduction in the landing configuration for MTO and flightidle thrust settings respectively. It is difficult to observe a clear trend in this data the data for the MTO case in Figure 9.88, but the general tendency is that the configurations with the small nacelle have a larger decrease in drag. This is more evident at high values of α. In contrast for the flightidle thrust settings there is no longer any trend visible, any nacelle influenced drag effects are small than the CFD uncertainty.

The diminished magnitude of the drag reduction for the large nacelle winglet geometry at $\alpha \geq 10.0°$ is caused by a large region of separated flow occurring on the upperwing surface for the flightidle thrust settings, causing a large increase in drag.

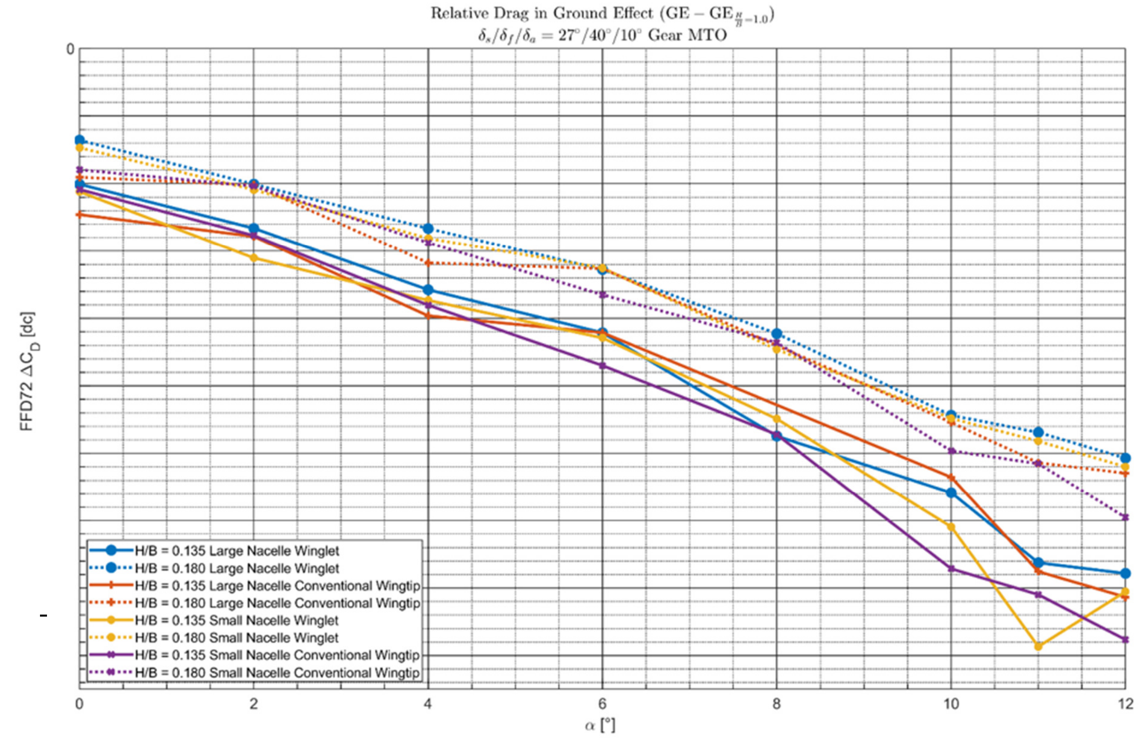

Figure 4.58 - Drag change due to ground effect for different configurations with MTO thrust settings in the landing configuration for $0° \leq \alpha \leq 12°$ *and* $\frac{h}{b} = 0.135\ and\ \frac{h}{b} = 0.18$

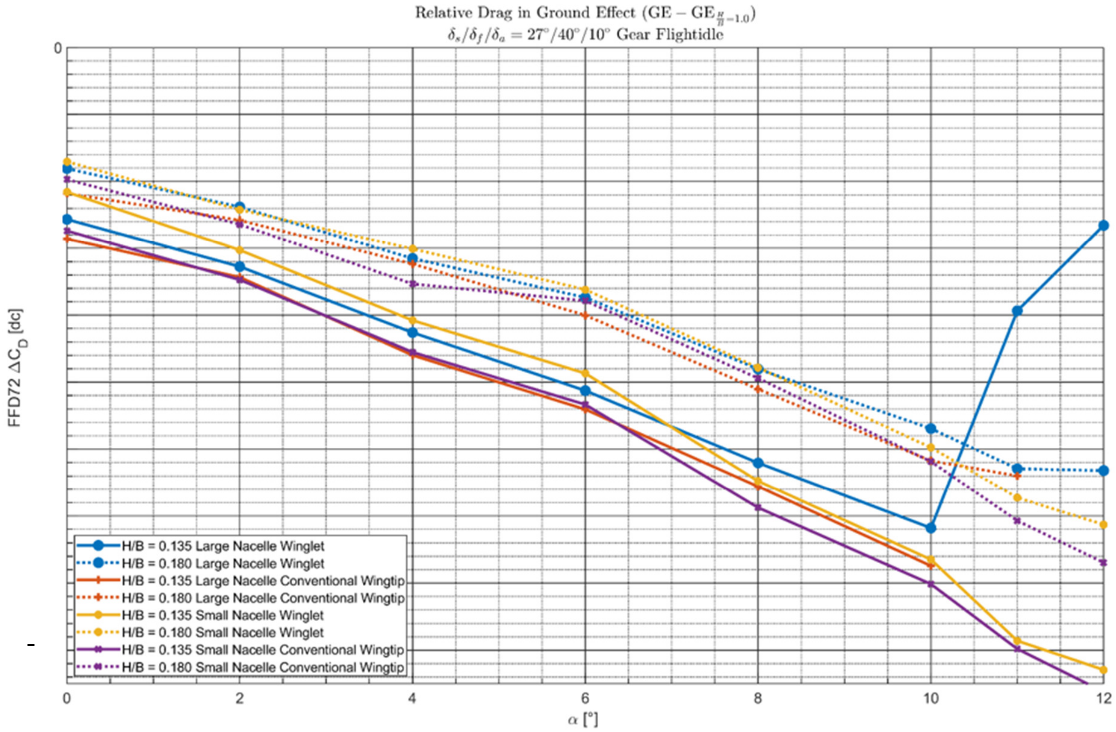

Figure 4.59 - Drag change due to ground effect for different configurations with MTO thrust settings in the landing configuration for $0° \leq \alpha \leq 12°$ *and* $\frac{h}{b} = 0.135\ and\ \frac{h}{b} = 0.18$*. Same Y-Axis scale as the previous figure.*

In order to identify changes caused to the spanwise drag distribution due to nacelle effect, the total spanwise total drag distributions are shown in Appendix J – Spanwise Drag Distributions comparing different Geometries. It must be concluded that the effect is small and relatively local. Outside of the immediate region of the engine no significant differences in drag change due to ground effect can be observed which are dependent on nacelle size.

4.4.3 Conclusions

Three separate nacelle effects on lift were identified:

1. The larger nacelle blocks the flow over the outboard part of the inboard-slat, which therefore has a lower lift increase in ground effect by up to 0.06% of total lift.
2. The lower side of the larger nacelle is located closer to the ground and thus the pressure increases more significantly here, leading to a lift increase of up to 0.08% of total lift.
3. A thrust effect is present due to the engine in the larger nacelle producing an approximately 20% higher thrust coefficient compared to the thrust from the engine in the smaller nacelle. This thrust-effect can be seen both in the lift and drag change and accounts for the majority of the observed effects. Most of the observed lift and drag differences disappear for the case of the landing configuration with flightidle thrust setting.

It should be emphasized here that the effects under consideration in this subchapter are small relative to the inherent uncertainty in the CFD results. To verify the hypothesis that the majority of the lift and drag differences between the small and large nacelle geometry are caused by the thrust effect, a recommendation for future research is to perform CFD simulations for the take-off configuration with flightidle thrust settings in which case the differences in lift and drag should be reduced. The evidence presented in this subchapter lead to the conclusion that the nacelle effect is of a smaller magnitude compared to the influence of flap setting or engine setting in ground effect.

4.5 Effect of Wing Tip Geometry in Ground Effect

The impact of wing tip geometry on ground effect performance is analyzed in detail in Appendix B – Analysis of the Influence of the Wingtip Geometry on Ground Effect Performance. This analysis is located in the appendix, because the impact of the tip effect is small compared to all the other effects discussed in this chapter. Therefore only the main conclusions are presented here.

Looking at the winglet in isolation, the performance in ground effect is only significantly changed in the range of $10.0° \leq \alpha \leq 12.0°$. This is due to the earlier onset of winglet stall in ground effect, which for this range only leads to a reduction in lift of up to 0.26% of total aircraft lift and drag is slightly increased.

It is also investigated whether the shape and size of the wingtip geometry impacts the ground effect performance of the overall wing. A limited effect on the outboard wing is present. No influence of wing tip geometry on ground effect performance is observed on the inboard wing section and fuselage.

4.6 Effect of Landing Gear in Ground Effect

It was noted previously that the lower wing area, especially between the nacelle and the fuselage, is one of the most affected areas in ground effect. Therefore it can be expected that whether the (main) landing gear is deployed or retracted will have an impact on the lift and drag change in ground effect. That will be investigated in this subchapter.

The subchapter is structured as follows: First the impact of landing gear deployment on the lift increment is investigated, after which the drag is examined. Next the influence of the nose-landing gear wake on the main wing leading edge is shown, after which the conclusions are presented.

4.6.1 Change in C_L

Figure 4.60 and Figure 4.61 show the double lift increment change in ground effect due to the gear effect for the large nacelle, winglet geometry with MTO thrust conditions and the small nacelle, conventional wingtip geometry with flightidle thrust conditions respectively. Shown on the y-axis of these figures is $\Delta\Delta C_{L_{Ge}} = \Delta C_{L_{GE_{Gear}}} - \Delta C_{L_{GE_{NoGear}}}$. Thus positive values on these two figures correspond to a more positive (or less negative for high α) lift increment when the landing gear is deployed.

Caution should be exercised when interpreting these results. At moderate α the uncertainty in the CFD results is in the order of 0.5% of total lift. Since now a double increment is being investigated, the uncertainty in the results is doubled to 1% of aircraft lift, which is the same order of magnitude as the influence of the gear on lift at low to moderate α. In Appendix K – Polynomial Surface Fit Plots, polynomial surface fits using the data presented in this chapter are shown in order to reduce the noise present in this data. Figure 9.100 and Figure 9.102 can be used for evaluating the data instead of the two figures presented below. Figure 4.62 presents the surface fit of Figure 4.60, with only three different h/b values included.

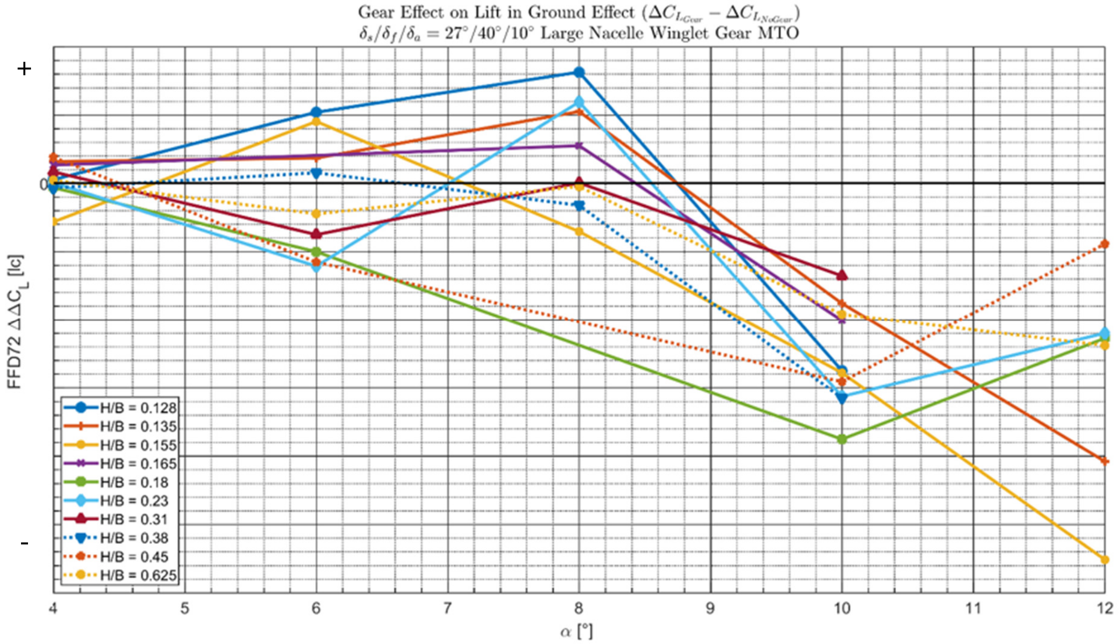

Figure 4.60 - Change to the incremental lift coefficient in ground effect due to landing gear deployment for the large nacelle, winglet geometry with gear deployed in landing configuration with MTO thrust setting

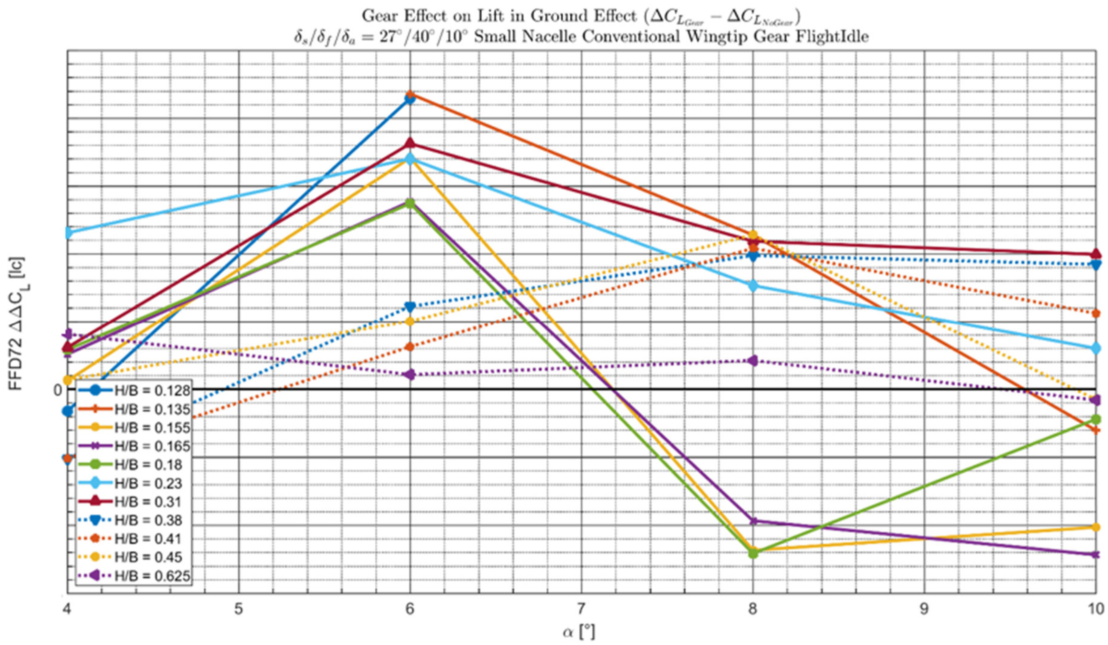

Figure 4.61 - Change to the incremental lift coefficient in ground effect due to landing gear deployment for the small nacelle, conventional wingtip geometry with gear deployed in landing configuration with MTO thrust setting

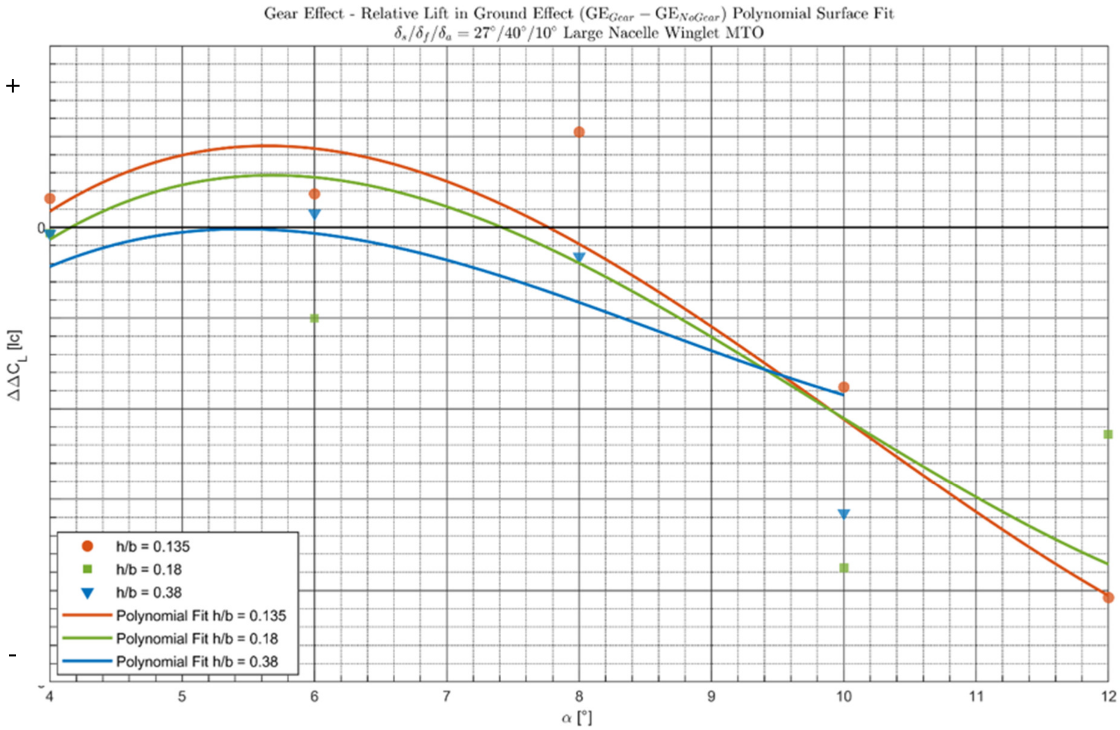

Figure 4.62 - Change in incremental lift coefficient due to landing gear deployment in ground effect for the large nacelle, winglet geometry in flightidle thrust conditions in landing configuration using a polynomial surface fit. $R^2 = 0.6724$

Low to Moderate Incidence

For low to moderate α the trend for both cases is that there is larger lift increment due to ground effect with gear deployed. For example, the pressure distribution for the small nacelle, conventional wingtip with no gear deployed is given in Figure 4.63, this figure can be directly compared to Figure 4.4 to see the differences caused by having the gear deployed. The pressure rise on the lower wing, close to the fuselage, is more significant, leading to a lift increase for the case with landing gear retracted. However, this lift increase is counteracted by a small pressure rise on the lower wing behind the engine, behind the landing gear on the flap and a suction increase on the inboard flap upperside for the case with gear deployed. These latter three effects are most likely either CFD artefacts and/or caused by unsteady flow phenomena, unlike the pressure increase on the lower wing when the landing gear is retracted which can be observed for many different combinations of α and h/b. The spanwise relative lift distribution shown in Figure 4.64 shows there is a higher relative increase in lift for the inboard wing, as well as the fuselage. No significant pressure difference on the fuselage can be observed when comparing Figure 4.63 to Figure 4.4, so perhaps this lift difference is caused by the nose landing gear. Due to lack of time the cause of the lift difference on the fuselage was not further investigated.

High Incidence

At high α the lift increment is more positive with gear retracted. This is driven by increased pressure differential on the lower side of the inboard wing and fuselage, when the gear is retracted. This is also shown in the lift distribution in Figure 4.65, where it is clear that the lift differential is located in the aforementioned regions.

This stronger pressure increase is caused by a more significant flow velocity decrease in ground effect, between the inboard wing and the ground, when the landing gear is retracted. This is shown in Figure 4.66 and Figure 4.67 with the landing gear deployed and retracted respectively. The cause of this stronger velocity decrease in ground effect when the main landing gear is retracted, is that when the landing gear is deployed out of ground effect, this already causes a significant reduction in flow velocity below the lower wing compared to gear retracted out of ground effect. Thus when ground effect is added to this situation with gear deployed, the velocity is already partially reduced and the further decrease in flow velocity due to ground effect is relatively smaller for this region. So this causes a smaller lift increment increase in ground effect for the gear deployed geometry when compared to the gear retracted case. This can be summed up as:

$$\Delta V_{gear} + \Delta V_{GroundEffect_{gear}} \approx \Delta V_{Groundeffect_{NoGear}}$$

Thus:

$$\Delta V_{GroundEffect_{gear}} < \Delta V_{Groundeffect_{NoGear}}$$

Whereby ΔV is the velocity differential below the wing where the main landing gear is located. Therefore at higher α, deploying the landing gear reduces the lift-increasing pressure rise on the lower wing. The difference is up to 1.7% of the total aircraft lift.

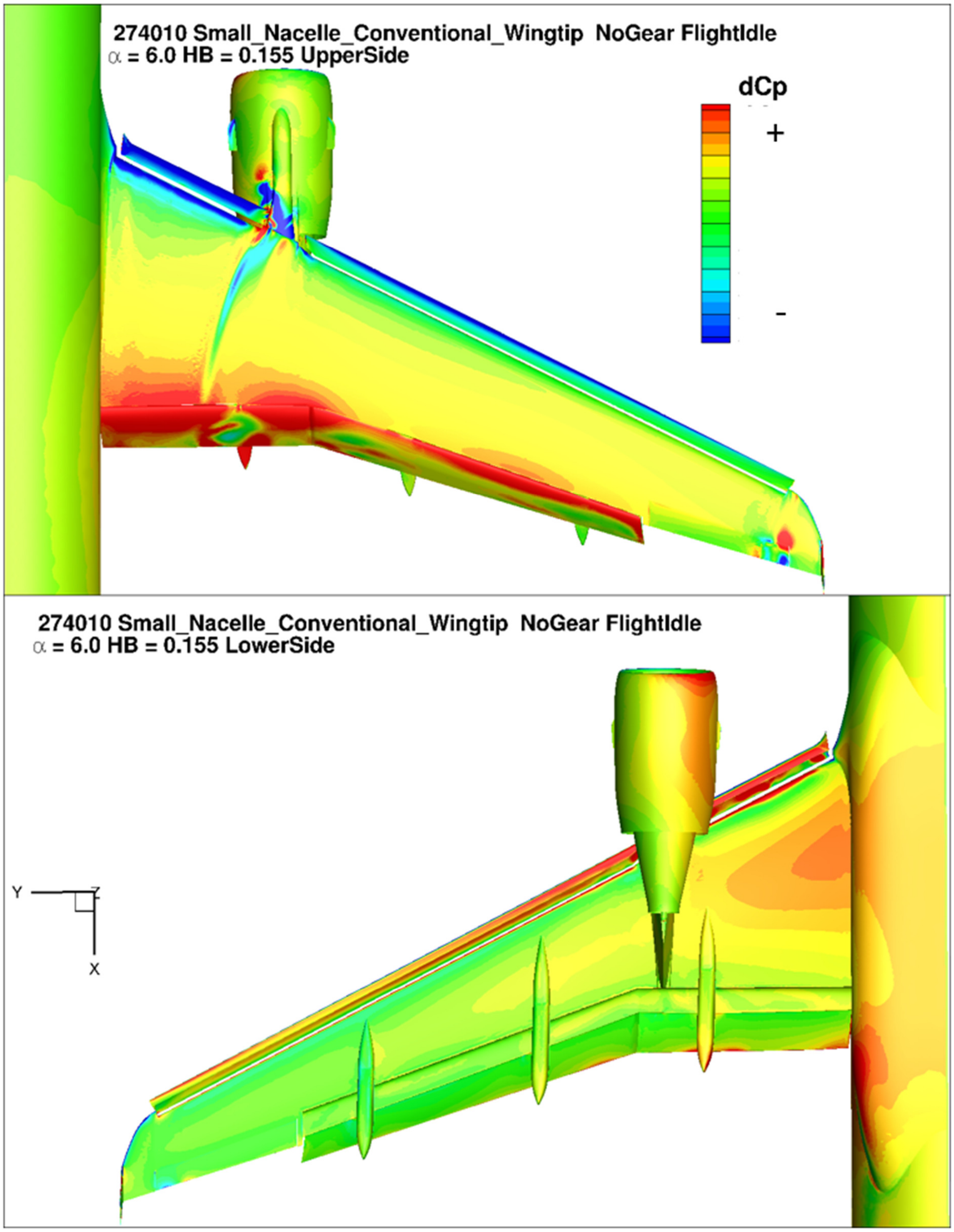

Figure 4.63 - Relative pressure change over the wing due to ground effect for the small nacelle, conventional wingtip geometry with gear deployed at $\alpha = 6.0°$ $\frac{h}{b} = 0.155$ *for the landing configuration at flightidle thrust conditions,* $(\Delta C_{P_{GE}} = C_{P\,GE} - C_{P_{\frac{h}{b}=1.0}})$

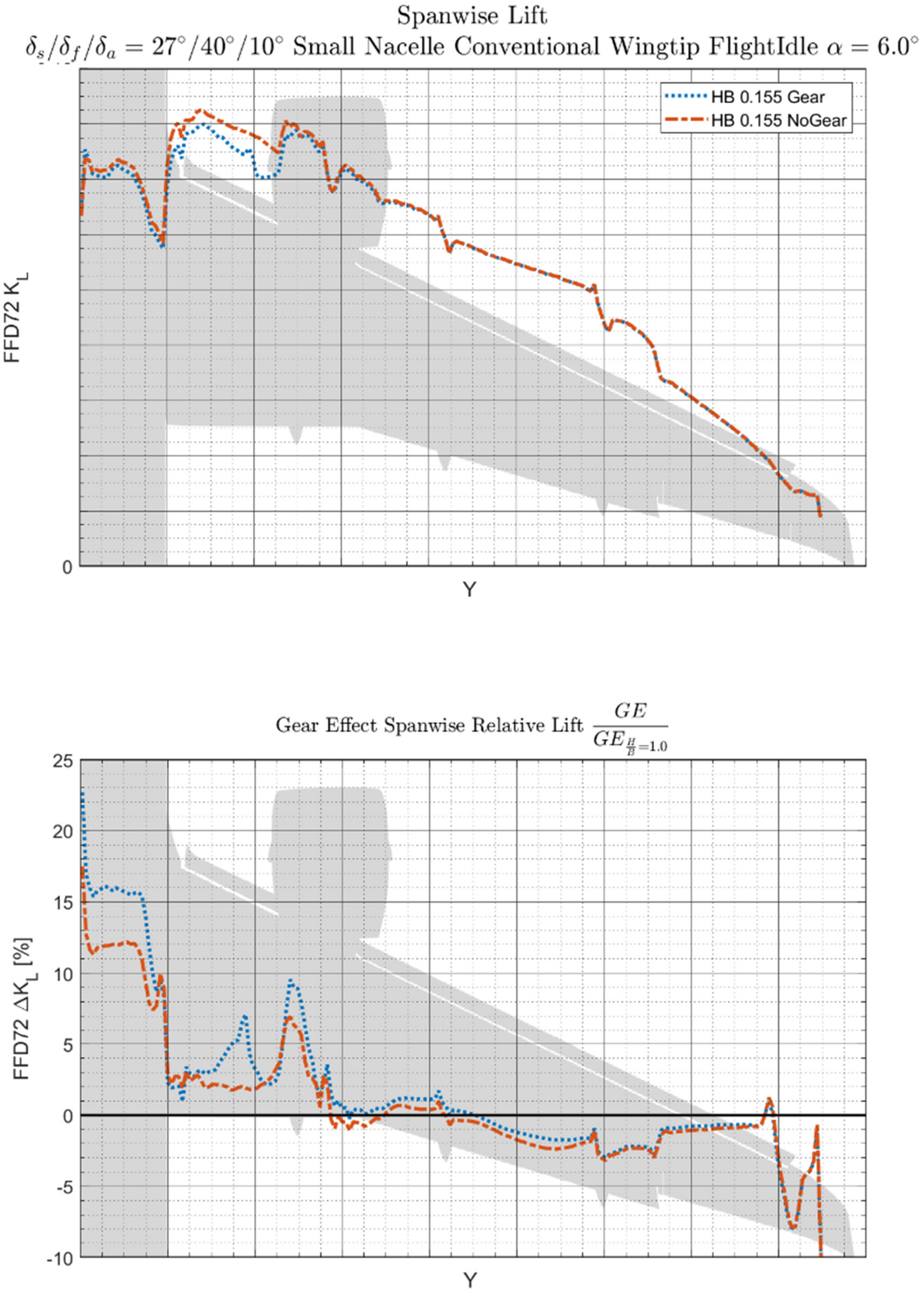
Spanwise Lift

$\delta_s/\delta_f/\delta_a = 27^\circ/40^\circ/10^\circ$ Small Nacelle Conventional Wingtip FlightIdle $\alpha = 6.0^\circ$

Gear Effect Spanwise Relative Lift $\frac{GE}{GE_{\frac{H}{B}=1.0}}$

Figure 4.64 - Spanwise lift distribution for the small nacelle, conventional wingtip geometry showing the gear effect at flightidle thrust conditions at $\alpha = 6.0^\circ$ $\frac{h}{b} = 0.155$ for the landing configuration

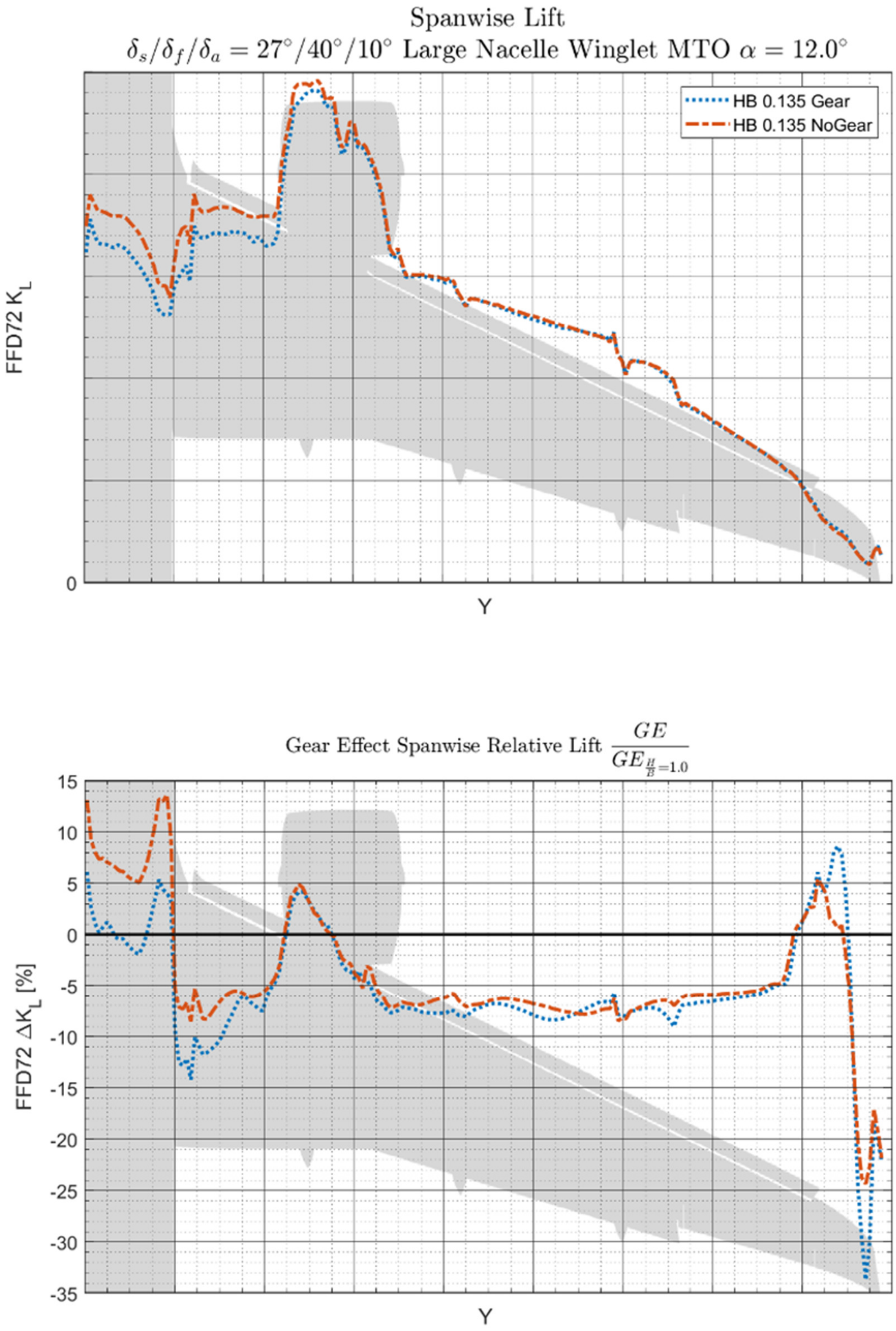

Figure 4.65 - Spanwise lift distribution for the large nacelle, winglet geometry showing the gear effect at MTO thrust conditions at $\alpha = 12.0°$ $\frac{h}{b} = 0.135$ for the landing configuration

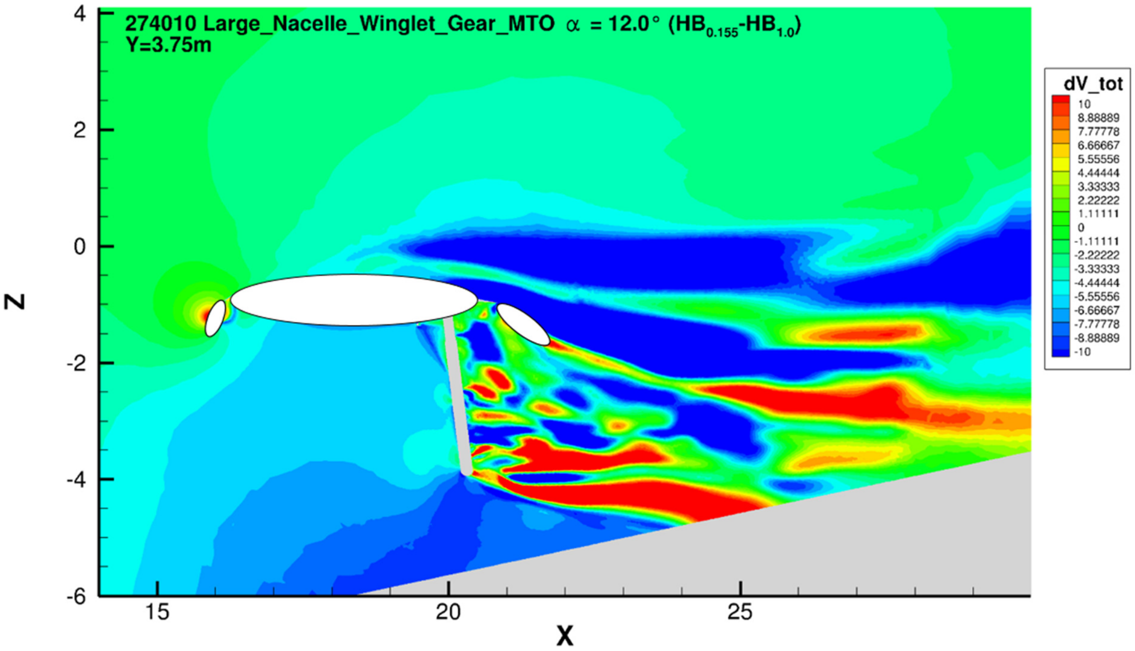

Figure 4.66 – Change in relative total velocity due to ground effect for the large nacelle, winglet geometry with gear deployed and MTO thrust conditions $\alpha = 12.0°$ $\frac{h}{b} = 0.155$ *for the landing configuration*

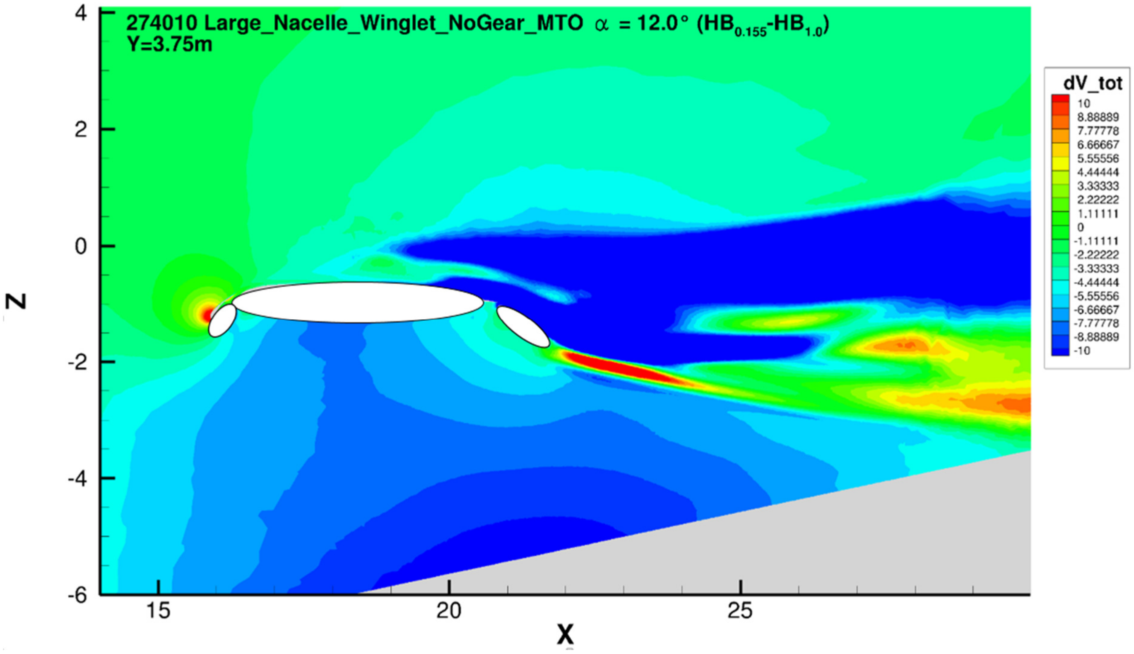

Figure 4.67 - Change in relative total velocity due to ground effect for the large nacelle, winglet geometry with gear retracted and MTO thrust conditions $\alpha = 12.0°$ $\frac{h}{b} = 0.155$ *for the landing configuration*

4.6.2 Change in Drag

Figure 4.68 and Figure 4.69 show the double drag increment change in ground effect due to gear effect for the large nacelle, winglet geometry with MTO thrust conditions and the small nacelle, conventional wingtip geometry with flightidle thrust conditions respectively. Positive values on these two figures indicate that the drag is reduced more strongly for the case with gear retracted. These plots are similar to the double increment lift plots in section 4.6.1 and the same note of caution must be used when interpreting these results. Due to the double increment any uncertainty in the CFD solution is amplified, thus there is some uncertainty in the data. For instance, the outlier at $h/b = 0.45$ and $\alpha = 10.0°$ is mostly caused by uncertainty in the CFD solution, rather than a physical effect. The polynomial fits of this data can be observed in Figure 9.101 and Figure 9.103 and are far easier to read compared to the raw data presented in this section.

There are two competing effects influencing the change in drag in ground effect due to gear effect. The first is that due to the previously discussed ground effect induced reduction in flow velocity below the wing, the drag on the main landing gear is reduced by up to 7% of the total ground effect drag reduction, or 2.2% of total aircraft drag, and is therefore not insignificant. This drag reduction as calculated by CFD2LOADS is shown in Figure 4.70 and is proportional to h/b. Figure 9.104 shows this drag reduction more clearly using the polynomial fit. The drag of the nose landing gear is also reduced in ground effect, but to a lesser extent.

With gear retracted, the lift coefficient out of ground effect is up to approximately 2% higher compared to gear deployed geometry. This increase in lift will lead to a higher induced drag component. As seen in section 4.3.2, with higher C_L both the relative and absolute value of the induced drag reduction due to ground effect increase. Thus for same α, the case with gear retracted will have a higher induced drag reduction compared to the gear deployed case. This effect counteracts the effect of reduced landing gear drag in ground effect.

This is why at low to moderate α the increased drag reduction due to the presence of the landing gear is dominant, as seen in Figure 4.68 and Figure 4.69. The drag is reduced more strongly with landing gear deployed by the same order of magnitude as the main landing gear drag reduction presented in Figure 4.70.

However, at higher α the lift increment becomes significantly less negative for the gear retracted case. This means that the differences in absolute value of C_L now increase further due to ground effect, rather than reduce as is the case at low α. This in turn means that now the induced drag (reduction) for the gear retracted geometry becomes more significant, which is why the double drag increment in Figure 4.68 becomes positive at $\alpha = 12.0°$. This is clearer in the polynomial fit presented in Figure 9.102.

The same tendency was observed for the case of the small nacelle, conventional wingtip geometry in Figure 4.69, but due to some doubts regarding the accuracy of the run at $\alpha = 12.0°$ this data was not included in the figure. This lack of data at $\alpha = 12.0°$ is also the cause of the polynomial fit in Figure 9.103 looking different to that of Figure 9.101. However due to the inherent uncertainty in this data, more research will be required to confirm the conclusions reached in this subchapter.

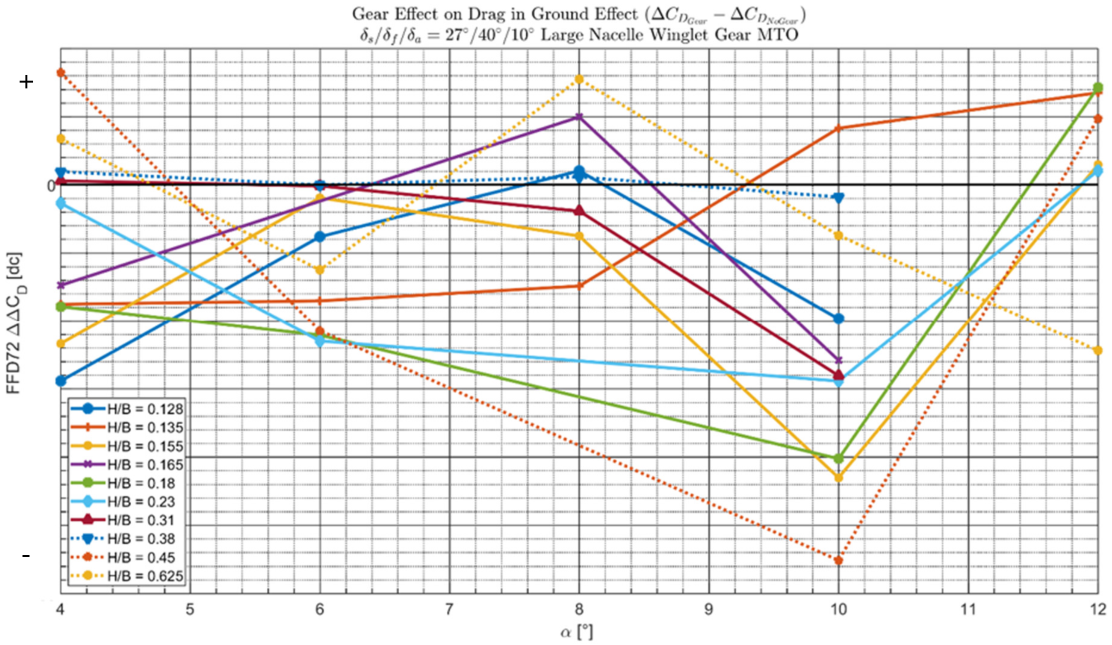

Figure 4.68 - Change to the incremental drag coefficient in ground effect due to landing gear deployment for the large nacelle, winglet geometry with gear deployed in landing configuration with MTO thrust setting

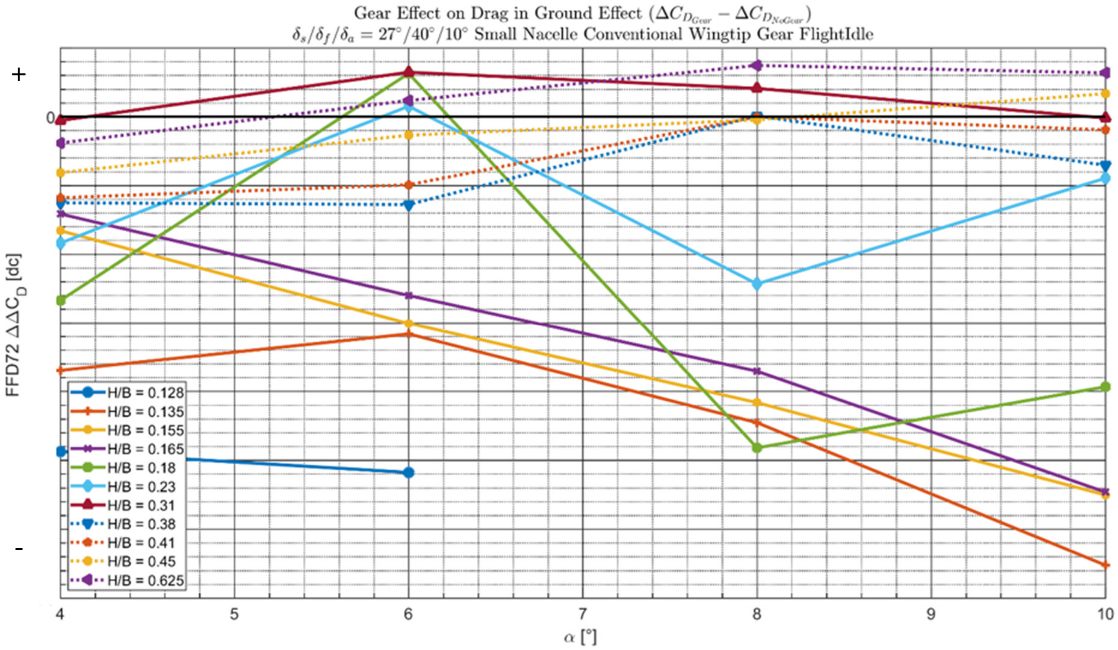

Figure 4.69 - Change to the incremental drag coefficient in ground effect due to landing gear deployment for the small nacelle, conventional wingtip geometry with gear deployed in landing configuration with MTO thrust setting

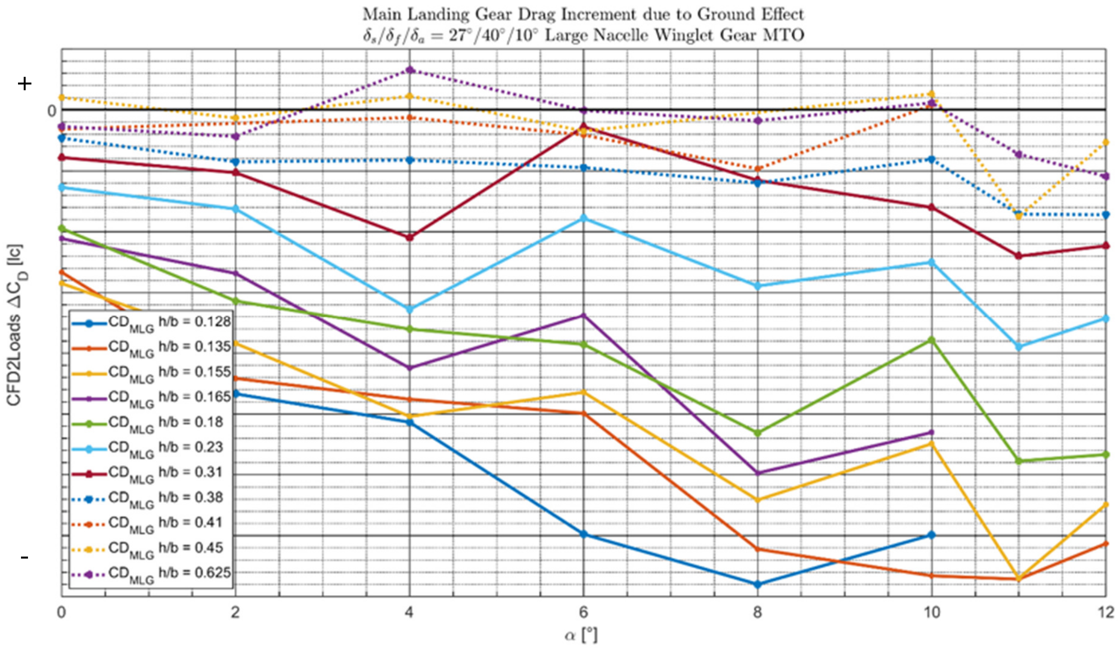

Figure 4.70 – Change to main landing gear drag coefficient in ground effect for the large nacelle, winglet geometry with gear deployed in landing configuration with MTO thrust setting

4.6.3 Flow Changes over the Main Wing due to Nose-Landing Gear

During this thesis project, the question arose whether the wake of the nose-landing gear for this aircraft geometry would affect the flow over the leading edge of the wing. An attempt was made to answer this question by means of a series of figures, which are located in Appendix L – Interaction between Nose Landing Gear Wake and Inboard Leading-Edge.

In this appendix it is concluded that the wake of the nose-landing gear does influence the flow over the main wing at certain combinations of α and h/b. No systematic investigation was performed to determine how this changes with α. It is also unknown if this effect is dependent on ground effect. It has been shown in this thesis that in ground effect the streamlines are shifted upwards away from the ground. Thus it is possible that the streamlines passing through the wake of the nose landing gear would flow beneath the main wing out of ground effect, but this would have be confirmed in future research.

4.6.4 Conclusions

The primary change caused by the deployed main landing gear in ground effect is that magnitude of the *relative* decrease in flow velocity below the inboard wing is reduced compared to when the gear is retracted. This results in a stronger pressure increase on the lower inboard wing, resulting in a lift benefit of up to 1.7% of total lift at high α. At low α the lift increase is not observable, it is uncertain if this is due to unknown flow phenomena or caused by the uncertainty in the CFD.

The drag benefit is more significant for the gear deployed case at low α by up to 2.2% of total drag. In contrast at high α, it is more significant for the gear retracted case by up to 0.46% of total drag. At low α the drag reduction on the main landing gear in ground effect is dominant, at high α the stronger induced drag reduction for the gear retracted case is dominant.
It was seen that the wake of the nose landing gear can affect the flow over the inboard leading edge of the main wing. It is unknown whether and/or how this changes with α and h/b.

4.7 Early Onset of Stall in Ground Effect

During the thesis investigation it was found that inboard wing stall occurred at very high α and low h/b, which occurs at significantly lower α compared to free air. The stall pattern is shown in Figure 4.71, whereby the massive region on the inboard wing shows the region of separated flow. This is the normal way that this wing stalls. It is known from literature that the maximum lift coefficient is reduced in ground effect (67), which has led to a fatal crash in the past (68). However, this early stall is not validated by windtunnel data, $\alpha = 15.0°$ was not reached in the available data.

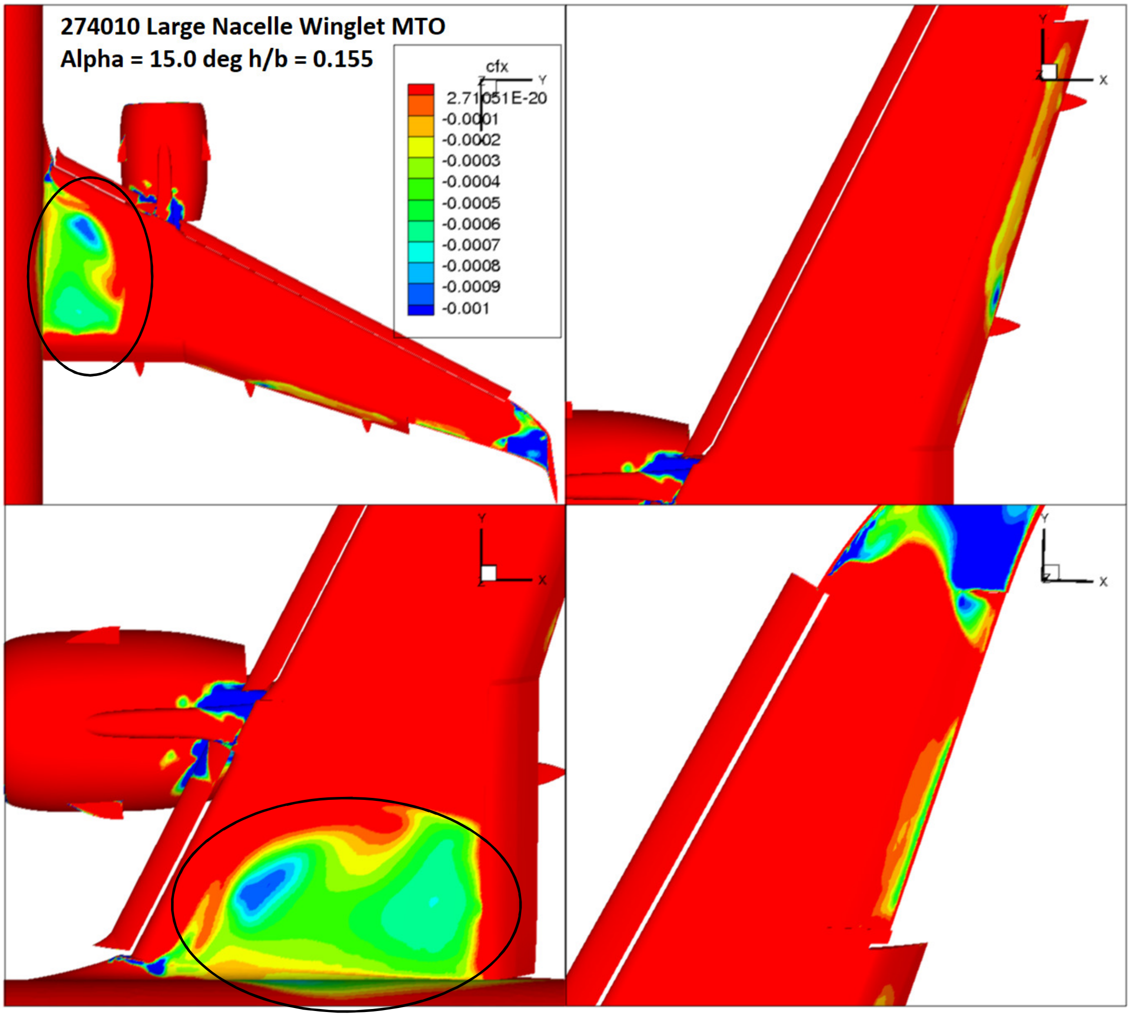

Figure 4.71- Inboard wing stall in ground effect $\alpha = 15.0\,° \ \frac{h}{b} = 0.155$

A possible reason for the early onset of stall was shown in section 4.1.3, where it was shown that the vortex induced by the onglet is moved upwards and away from the wing, due to ground effect. In free air, this vortex hits the upperside of the flaps, re-energizes the flow in that region and thus positively influences $C_{L_{MAX}}$. Usually a stall occurs when this vortex can no longer effectively re-energize the flap. In ground effect this vortex is adversely affected, thus it is likely that it detaches from the flap at a lower value of α.

Since early stall in ground effect was not part of the main research topic, no further investigation was performed to confirm or deny this hypothesis. However, it would be an interesting topic for future research.

4.8 Summary of the Observed Effects

A number of effects have been observed in this chapter. These are summarized below:

- Due to ground effect, streamlines get shifted upwards, slowing down the velocity under the wing and increase flow velocity over the wing leading edge. The influence of ground effect increases exponentially as the distance to the ground h/b is decreased.
  - This causes a lift enhancing effect of pressure increases on the lower wing surface, located most significantly between the fuselage and the engine nacelle, as well as on the fuselage itself. This pressure rise is already present at low α, causing lift to increase in ground effect.
  - The suction on the leading edge slat and main-wing leading edge increases in ground effect, most notably on the inboard section, leading to an increase in lift. This due to a local increase in angle of attack.
  - Pressure increases on the upper wing surface, causing the lift to decrease. At low α this pressure rise is limited to the upperside of the flaps. As α increases, this pressure increase becomes both larger in magnitude and spreads out over the entire area of the upperside of the wing, with the exception of the leading edge.
  - At low α, the pressure rise on the lower surface is dominant, leading to an overall positive change in C_L due to ground effect. In contrast at high α the pressure rise on the wing upperside is dominant, causing a decrease in C_L. Decreasing flap deflection increases the value of α at which ground effect lift increment becomes negative.
  - At the fuselage, there is a stronger lift enhancing benefit due to the ground effect compared to the wing. This is because the lowerside of the fuselage is located closer to the ground than the wing, leading to a stronger lift increase. At the same time it experiences much less of the lift destroying effect of the ground effect, since the fuselage upper surface is located further away from the ground than the mainwing.
  - The induced drag is reduced significantly due to the mirrored wing-tip vortex. A reduction of the induced drag of up to 42% is observed. The viscous-pressure drag, or form drag, reduces by up to 9% in ground effect.

- It is found that engine thrust reduces the influence of the ground effect. That has two causes:
  - At MTO thrust setting, the engine sucks in air which would otherwise be deflected over the wing upper surface due to ground effect, which changes the local angle of attack on the leading edge in the region of the engine. This means that the magnitude of the suction increase, which is normally present due to ground effect on the slat and mainwing leading edge, is reduced compared to when flightidle thrust settings are applied.
  - At higher α the jet from the engine increases the mass flow in the flap gap. This increases the suction on the flap leading edge, thereby counter-acting the suction decrease and lift loss caused by ground effect on this part of the wing.

- These two effects combined cause a reduction of ground effect related lift by up to 2% of total lift *increase* at low α when MTO thrust settings are applied and a reduction of the ground effect related lift *decrease* at high α by up to 1.5% of total lift. Thus by applying MTO thrust settings the influence of the ground effect is reduced for all α, the absolute value of the change in lift due to ground effect is reduced.
- The drag is reduced more significantly by up to 3.2% of total drag with flightidle thrust settings applied compared to MTO thrust.
- The differences caused by different size nacelles effect are threefold:

    - The larger nacelle has a higher thrust coefficient c_t, leading to an engine thrust effect
    - The lowerside of the large nacelle, is located closer to the ground, and thus sees a stronger increase in pressure in ground effect compared to the smaller nacelle, causing a lift benefit of up to 0.8% of total lift.
    - The larger nacelle blocks the flow over the slat leading edge in the immediate vicinity, which means the suction is no longer increased in that slat area. This leads to a lift reduction of up to 0.06% of total lift in ground effect.
- Changing the wingtip geometry causes small changes to lift and drag in the region local to the wingtip and to a lesser extent on the outboard wing section. This effect is an order of magnitude smaller than the gear or thrust effect.
    - In ground effect wing tip stall occurs earlier. Therefore ground effect has the most significant impact on wingtip performance, in the range of $10.0° \leq \alpha \leq 12.0°$, which is the region where the wingtip stalls.
- There is a more significant flow velocity decrease present under the wing when the main landing gear is retracted, resulting in a lift increase at high α.
    - The drag reduction of the main landing gear is significant, up to 7% of the total drag reduction benefit due to ground effect.
    - At high α the gear retracted case has a higher absolute lift value, independent of ground effect, of up to 2.13% increase. This causes a higher value of the induced drag and thus leads to a larger reduction of the induced drag in ground effect.
- It was found that stall can occur earlier than in free flight, at a combination of very high α and low h/b.

5. Validating the CFD Results Using Windtunnel Data

In the previous chapter an analysis was presented using the results from CFD simulations. In order to have confidence in this analysis, it is crucial to validate the accuracy of this CFD data. The validation is presented in this chapter using DNW windtunnel data as a reference.

The chapter is structured as follows. Subchapter 5.1 provides the relevant information on the windtunnel data. In subchapter 5.2 the comparison figures between windtunnel and CFD are presented and discrepancies between the two data sources will be identified. Then, in subchapter 5.3 possible causes for these discrepancies will be discussed. Finally the conclusions will be presented in subchapter 5.4.

5.1 Windtunnel Information

Data from two separate windtunnel test campaigns is used as a validation tool in this chapter. Both campaigns were conducted at DNW. The first campaign was completed in 1987 and concerned the take-off configurations. The goal was to catalogue ground effect performance data for this particular aircraft. This campaign was performed using TPS on the wings, simulating MTO thrust conditions. No moving belt was installed.

The second test campaign took place a year later and primarily concerned the landing configuration. The goal of this campaign was to investigate the influence of the newly installed moving belt on the ground effect performance data as well, which is also reflected by the test matrix. No effort was made to install TPS on the aircraft, but instead through-flow-nacelles (TFN) were used in order to save costs and reduce complexity.

These campaigns were held with a belt speed of $V_{belt} = 50\ m/s$. This is lower than the tunnel freestream velocity, $V_\infty \approx 68.64\ m/s$ depending on the exact temperature which shifts slightly throughout the tests. Table 5.1 shows the information on the high-lift settings for both windtunnel configurations.

In both test campaigns the Mach number was set to $Ma = 0.2$, which is the same value as for the CFD simulations. The Reynolds number for the windtunnel was approximately$Re_{WT} \approx 2.6 * 10^6$, which is significantly lower than the full-scale Reynolds number used in the CFD calculation: $Re_{CFD} = 19.6 * 10^6$.

The maximum achievable h/b in the windtunnel was $h/b = 0.625$. At this height the model was located in the tunnel center line. Out of ground effect data was produced by calculating wall corrections from four walls (4w) at $h/b = 0.625$. In ground effect, data was produced by only applying three wall corrections (3w), namely the wall corrections from the two walls and the ceiling. For each new settings of h/b, the wall corrections were re-calculated.

There are two different datasets available. Raw windtunnel data is present for the take-off configuration. Measurements were made at $\alpha = 0.0°$, $\alpha = 6.0°$ and $\alpha = 12.0°$. The wall corrections are applied to this data.

For the landing configuration, only post-processed data is available. The post-processing consisted of applying a polynomial fit over the entire data set. The polynomial is dependent on α and h/b. The data presented in the next subchapter for the landing configuration consists wholly of these calculated values, not measurements.

Table 5.1 – Overview high-lift configuration settings for the windtunnel data

Parameter	*W/T Take-Off Configuration*	*W/T Landing Configuration*
δ_{slat}	$22.0°$	$27.0°$
δ_{flap}	$10.0°$	$40.0°$
$\delta_{aileron}$	$0.0°$	$0.0°$
V_{belt}	$0\ [m/s]$	$50\ [m/s]$
$Propulsion$	TPS	TFN

5.2 Comparison between Windtunnel and CFD

Figure 5.1 and Figure 5.3 show the comparison between CFD and corrected windtunnel data for the take-off configuration. Concerning lift, the general agreement between the two data sources is quite good, within approximately 0.5% of the total lift. Both CFD and windtunnel show the same trend, especially for $\alpha = 6.0°$ and $\alpha = 12.0°$.

There is an offset of approximately 1% of the total lift between CFD and windtunnel for $\alpha = 12.0°$. This is most likely caused by a difference in reference values. This is evident at $h/b = 0.625$, region B, which shows for $\alpha = 12.0°$ that $\Delta C_{L_{WT}}$ is significantly negative. There is no physical explanation for why there would be a significant negative lift increment present at this high h/b. Therefore, in Figure 5.2 the line “WT $\alpha = 12.0°$” is adjusted by manually adding a fixed value to each data point on the curve, such that:

$$\Delta C_{L_{WT}}\Big|^{\frac{h}{b}=0.625} = \Delta C_{L_{CFD}}\Big|^{\frac{h}{b}=0.625} \qquad (equation\ 5.1)$$

Now it can clearly be seen that the lift increment change in CFD and windtunnel for this value of α is very similar, with the exception of $h/b = 0.135$ (region A in Figure 5.2), where for CFD only the lift increment becomes less positive. This is also present for $\alpha = 6.0°$, highlighted in region C.

The drag change shown in Figure 5.3 shows that there is an agreement between windtunnel in CFD within 1.5% of the total drag value. Both data sources follow a similar trend. There is an approximately linear shift between CFD and windtunnel, whereby the windtunnel predicts a slightly increased drag benefit. The cause of this offset is unknown, as it is not caused by a difference in absolute value of lift which could result in more induced drag to be present.

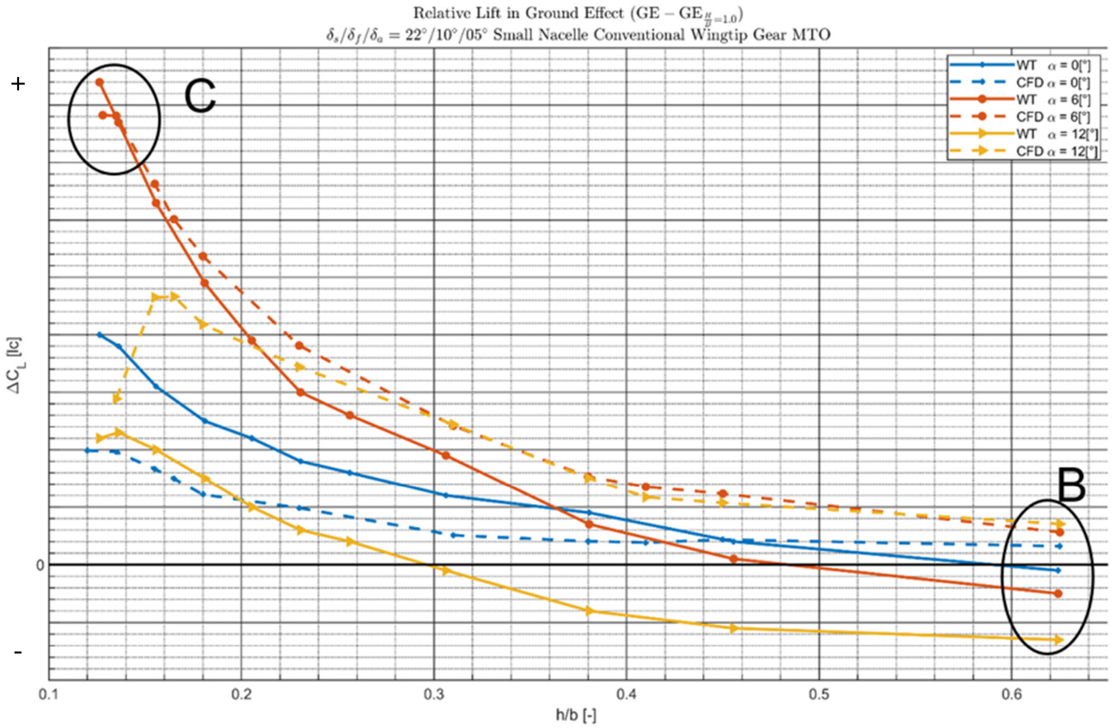

Figure 5.1 - Lift (FFD 72 CL_S1MA_NF) change due to ground effect from windtunnel and CFD for the small nacelle, conventional wingtip geometry with gear deployed and MTO thrust setting in the take-off configuration

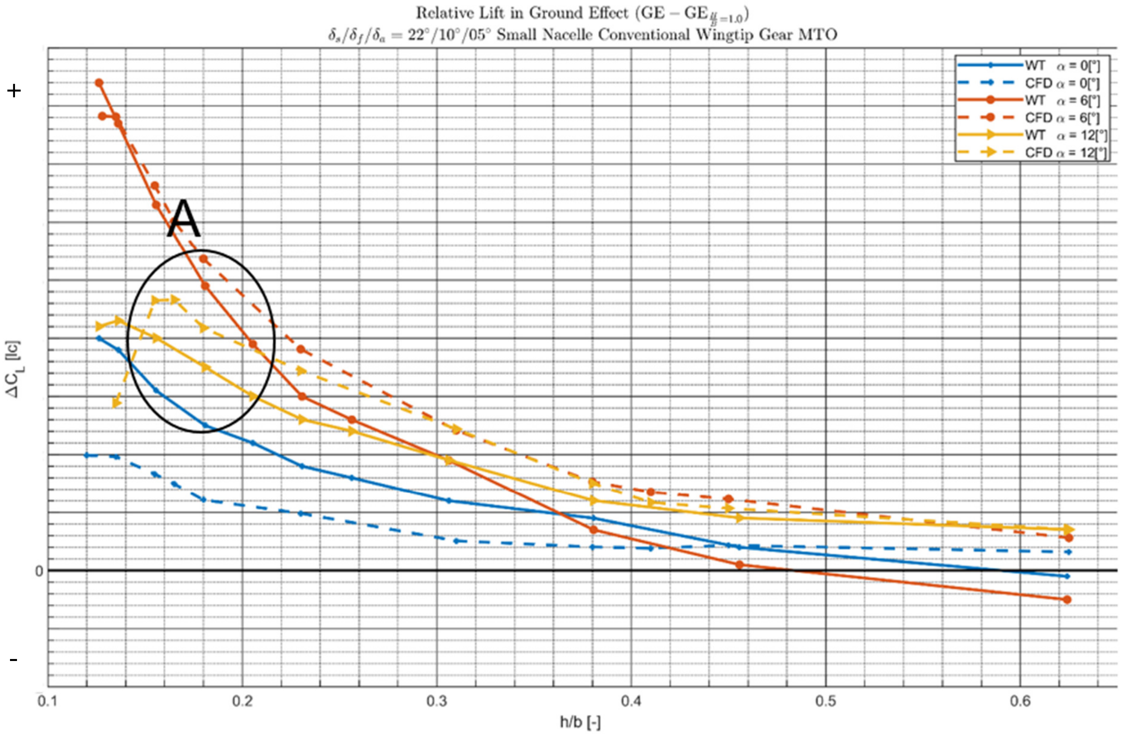

Figure 5.2 - Lift (FFD 72 CL_S1MA_NF) change due to ground effect from windtunnel and CFD for the small nacelle, conventional wingtip geometry with gear deployed and MTO thrust setting in the take-off configuration with manually adjusted values for the line WT $\alpha = 12.0°$

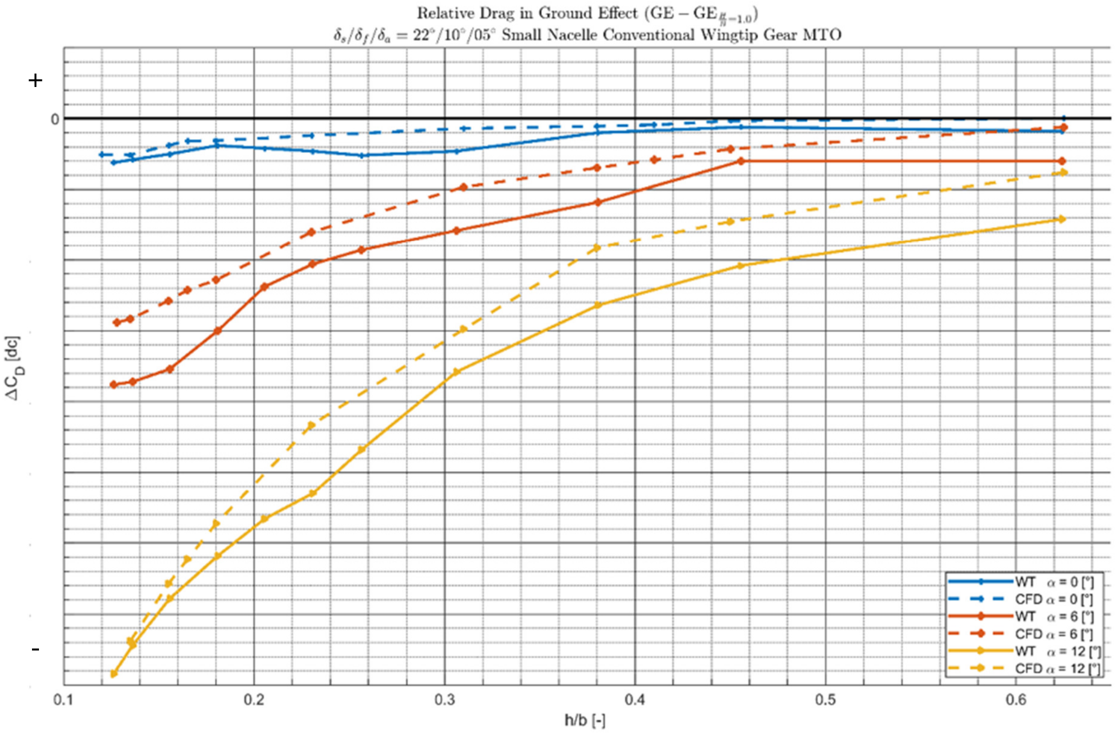

Figure 5.3 - Drag (FFD 72 CD_S1MA_FF) change due to ground effect from windtunnel and CFD for the small nacelle, conventional wingtip geometry with gear deployed and MTO thrust setting in the take-off configuration

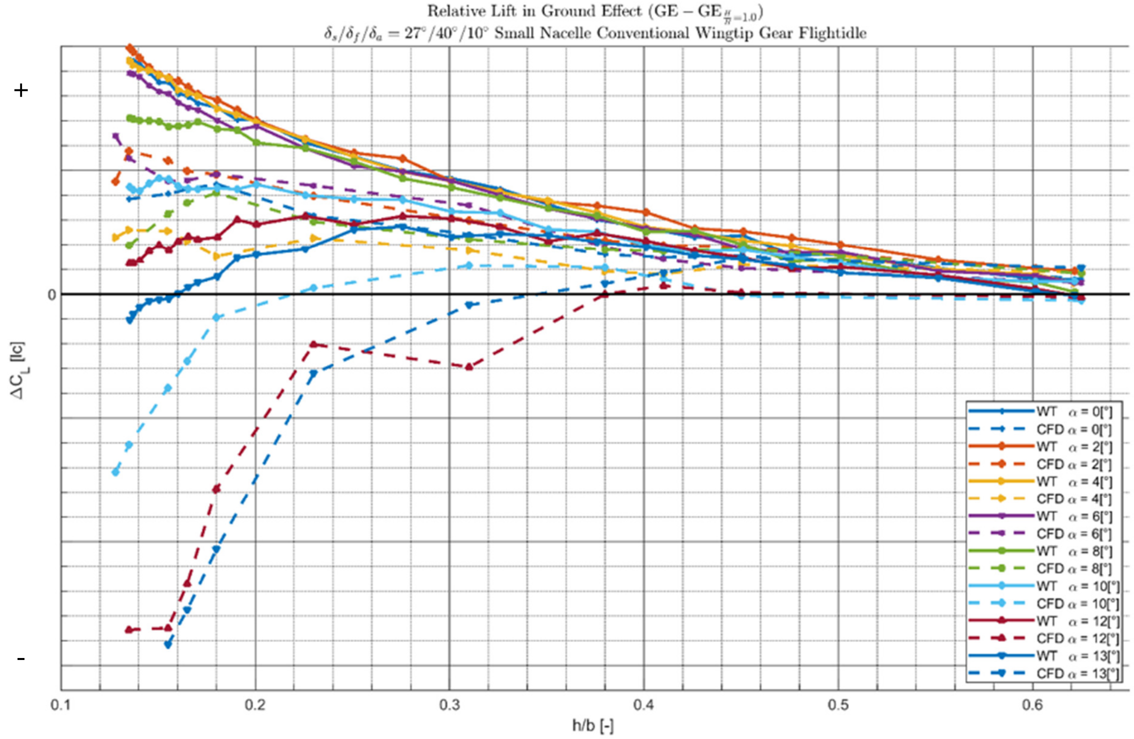

Figure 5.4 - Lift (FFD 72 CL_S1MA_NF) change due to ground effect from windtunnel and CFD for the small nacelle, conventional wingtip geometry with gear deployed and MTO thrust setting in the landing configuration

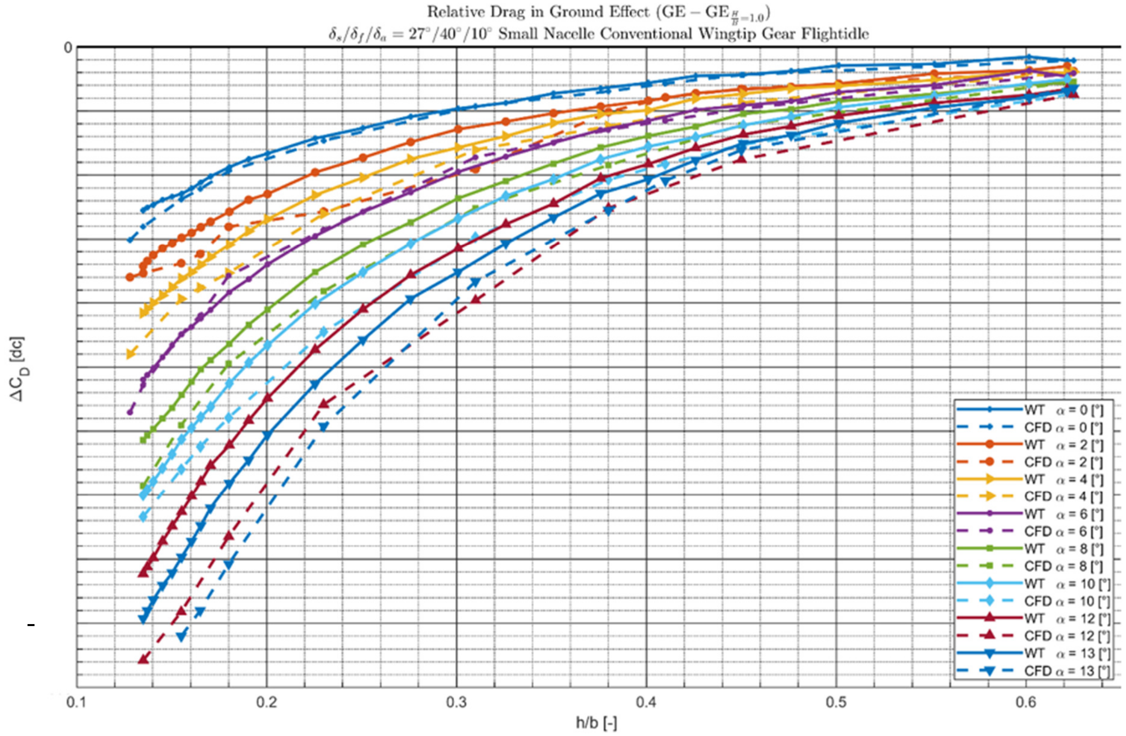

Figure 5.5 - Drag (FFD72 CD_S1MA_FF) change due to ground effect from windtunnel and CFD for the small nacelle, conventional wingtip geometry with gear deployed and MTO thrust setting in the landing configuration

Figure 5.4 shows the change in lift as simulated by CFD and windtunnel for the landing configuration. As previously discussed, the windtunnel data here is generated from a polynomial fit which is based on the corrected data.

The windtunnel data predicts a significantly more positive lift increment compared to CFD simulations. The highest lift increment present for windtunnel is $\Delta C_{L_{WT}}|^{\alpha=2.0^\circ} \approx 6.57\%$ of the total lift, while $\Delta C_{L_{CFD}}|^{\alpha=2.0^\circ} \approx 3.92\%$ of the total lift. This discrepancy gets larger for high α, where the CFD lift increment is negative up to 5.72% of the total lift. In the next subchapter possible causes for the observed discrepancies will be discussed.

Figure 5.5 shows the drag change comparison for the landing configuration. Interestingly enough, the drag reduction is now predicted to be higher by CFD, while for the take-off configuration this was reversed. The trend between windtunnel and CFD matches very closely, similar to what was observed in Figure 5.3. Only at $\alpha = 12.0^\circ$ and $\alpha = 13.0^\circ$ do the differences increase by up to 3.48% of the total drag. So similar to the lift data, only at high α do windtunnel and CFD data diverge significantly.

5.3 Discussion of identified differences

In the previous subchapter the most significant discrepancies between windtunnel and CFD were found to be present mainly for the lift increment on the landing gear configuration. In this subchapter some causes of these discrepancies will be discussed, such as different aileron droop angles, the difference in Reynold's number and the belt speed.

5.3.1 Effect of Different Aileron Droop Angles

The key difference in geometry between the CFD and windtunnel models are the aileron droop setting. Initially it was expected that the windtunnel data would follow the company convention

and have an aileron deflection of $\delta_{ail} = 10.0°$ in the landing configuration. Due to the age of this data, it took a long time to ascertain the true aileron setting used during the windtunnel campaign, which turned out to be $\delta_{ail} = 0.0°$. By this point it was no longer feasible to change this setting in the CFD models and redo many computations. To investigate the influence of this change in aileron droop, one h/b polar was produced with $\delta_{ail} = 0.0°$ at $\alpha = 10.0°$.
The aileron can be viewed as yet another flap. Thus it is expected that by reducing the aileron droop deflection, the lift increment will be influenced positively. This can be seen in Figure 5.6, where it is shown that by setting aileron droop to $0.0°$, the lift increment is increased by approximately 1% of total lift at equal h/b. This effect will be even stronger at higher values of α. Therefore it can be concluded that the aileron droop setting is partly responsible for the discrepancy observed at the landing configuration.

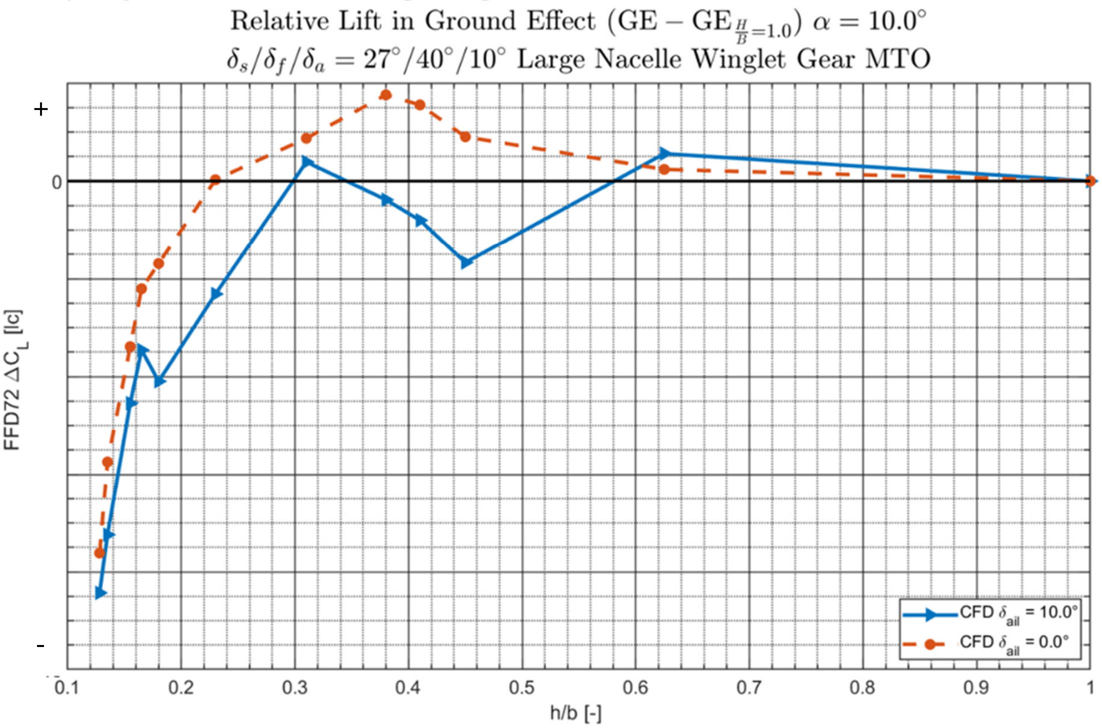

Figure 5.6- Effect of aileron droop setting on ground effect lift increment

5.3.2 Effect of the Reynold's Number difference

There is a significant difference in Reynold's number between the windtunnel and CFD, respectively $Re_{WT} \approx 2.6 * 10^6$ and $Re_{CFD} \approx 19.3 * 10^6$. This will cause differences in maximum lift, boundary layer thickness and transition location (98). It is not known if tripping devices were used on the aircraft model in the windtunnel to force transition.

No systematic studies were found which investigate the differences in ground effect performance caused by a Re variation of $2.0 * 10^6 < Re < 20 * 10^6$. Hsiun and Chen (99) showed that for $0.2 * 10^6 < Re < 2.0 * 10^6$ significant differences in ground effect lift and drag increment are present, but it is not clear how this translates to higher values of Re.

It was shown in chapter 4 that in ground effect there is an earlier onset of wingtip stall. In many cases at $\alpha = 12.0°$ there is not yet tip stall present in free air, but tip stall is already present in ground effect. Previous work from the author of this report has found that for this type of aircraft, the angle of attack at which tip stall occurs can vary by up to several degrees due to variation of the Reynolds number. The critical region at which this happens is $2.0 * 10^6 < Re <$

$7 * 10^6$. Therefore a possible explanation for the discrepancy between windtunnel and CFD visible at $\alpha = 12.0°$ (as shown in region A in Figure 5.2) would be that tip stall occurs only for low h/b in CFD, but is already present in windtunnel for all h/b, i.e. both in and out of ground effect, thus not changing the lift increment.

5.3.3 Belt Speed

No belt was present for windtunnel measurements for the take-off configuration. Figure 1.18 indicates the effect this omission can have on the ground effect measurements, whereby the windtunnel corresponds to the ground stationary curve and the CFD data has been obtained using the 'slip' boundary condition. It is shown that at low height above ground, the ground stationary boundary condition has a lower lift increment and a stronger reduction in drag. This could explain why the drag benefit for the CFD is lower compared to windtunnel, especially at $\alpha = 0.0°$ and $\alpha = 6.0°$.The influence of the belt speed is not at as evident for the lift increment from this source.

For the landing configuration, the belt speed is $50\, m/s$ while $V_\infty \approx 68.64\, m/s$. These speeds are sufficiently close to each other that any ground boundary condition based effects become negligible compared to other effects.

5.3.4 Limits of the CFD

The largest discrepancies between CFD and windtunnel data are found for the lift increment at high α and low h/b for the landing configuration. These parameters are at the limit of the of the CFD simulation capabilities. The implicit assumption when using the steady RANS equations is that there is steady flow, but this is no longer fully the case at these parameter values due to significant regions of separated flow over the flaps and wingtip. For better results at these conditions it could be beneficial to use the unsteady-RANS (uRANS) equations. However, this approach is significantly more computationally expensive.

A comparison between CFD and windtunnel data for a different aircraft in ground effect is shown in Appendix N – Windtunnel and CFD Ground Effect Lift Increment Comparison for a Different Commercial Jet Aircraft. Different high-lift configurations with a δ_{flap} of $8.0°$, $14.0°$ and $22.0°$ are shown in Figure 9.115, Figure 9.116 and Figure 9.117 respectively. A similar trend can be observed, which is that at a δ_{flap} of $8.0°$ and $14.0°$ there is a good agreement between CFD and windtunnel, while at $\delta_{flap} = 22.0°$ the CFD lift increment becomes significantly more negative at high α and low h/b.

5.4 Conclusion

It was found that there is a good agreement between the ground effect lift and drag increments from windtunnel experiments and the CFD results presented in this thesis, especially for the take-off configuration. The agreement is in the order of within approximately 0.5% of the total lift, and within 1.5% of the total drag value. At high flap deflection, high α and low h/b there is a significant discrepancy in the predicted lift increment, whereby the CFD simulation predicts a more negative lift increment. The trend of the predicted ground effect drag change is very similar for both CFD and windtunnel results, but at high α and low h/b the discrepancy rises by up to 3.48% of the total drag. CFD overestimates the drag benefit compared to windtunnel for the landing configuration, whereas it under-predicts the drag benefit for the take-off configuration.

Possible causes of the observed discrepancies are:

- Different aileron droop setting are used, which is $0.0°$ for windtunnel and $10.0°$ for CFD.
- Different Reynolds number, which is $Re_{WT} \approx 2.6 * 10^6$ and $Re_{CFD} \approx 19.3 * 10^6$ respectively
- There is no moving belt present for the take-off configuration windtunnel experiments, which will adversely influence the accuracy of those results
- At high flap deflection, high α and low $\frac{h}{b}$ the steady flow assumptions underlying the RANS equations may no longer be completely valid, leading to some inaccuracies.

6. Open Topics and Recommendations for Further Research

Throughout this thesis investigation, a number of questions have remained unanswered due to time constraints. In this chapter an overview of these topics will be presented and recommendations for future research will be provided.

6.1 Engine Nacelle Effect with Identical Thrust Coefficient

While investigating the nacelle effect, it was found that it was difficult to answer this question conclusively. One of the reasons was that the thrust coefficients for the two small and large nacelle were different, which made it difficult to isolate the influence caused by the nacelle geometry change. Data was available for the flightidle case in landing configuration, but the nacelle effect turned out to be of the same order of magnitude as the inherent uncertainty of the CFD data at this high flap deflection setting.

Therefore the recommendation for future research is as follows:
Perform the computations at lower flap deflection settings. Use either the flightidle power setting, or when it is required to perform the computations with MTO power setting, ensure beforehand that the C_t values are identical between the two nacelle geometry cases.

6.2 Constant Lift Coefficient when comparing Wing Tip Geometry

By exchanging the conventional wingtip with the modern winglet geometry, the wingspan of the aircraft is increased by approximately 4%. This will increase C_L at identical α and change the shape of the lift distribution over the wing, thus introducing additional variables which make the analysis on the winglet effect more challenging. The best alternate approach would be to instead have the CFD solver iterate to a chosen value of C_L, thereby eliminating one variable in the comparison.

This approach was known and considered before the research started, but to conform to company best practices and to enable easier comparisons with reference (windtunnel) data, it was decided to perform the calculations at fixed α anyway. For future research in which the influence of wingtip geometry is most important, it is recommended to switch this approach and focus on iterating to a certain value of C_L.

6.3 Influence of Ground Effect on the Nose-Landing Gear Wake Encountering the Wing Leading Edge

It was seen in section 4.6.3 that at a certain α and h/b, the wake from behind the nose-landing gear encounters the leading edge of the mainwing. This removes energy from the flow at this critical location, which in turn will lead to a decrease in lift. In this thesis no further investigation of this phenomenon was made. It is unknown if this effect is ground effect related and if there is a dependency on α. Thus, there is ample opportunity for a future, more in-depth investigation on this subject.

6.4 Investigate Stall in Ground Effect

It was shown in subchapter 4.7 that for some cases the CFD simulation predicted a very early onset of stall when the aircraft is close to the ground at $13.0° \leq \alpha \leq 15.0°$. This resulted in a stronger separation on the inboard wing upper surface, in a manner and location similar to the normal stall behavior in free flight, but at a significantly lower α. Earlier onset of stall and reduction of $C_{L_{MAX}}$ in ground effect is not unheard of in scientific literature (67), but not fully understood either. It would be of interest to discover whether the observations on early stall onset made in this thesis are physically correct, or if this is related to CFD settings and the aforementioned limits to the CFD accuracy. It should be mentioned here that these observations were made at the combination of parameter settings for which there was the lowest agreement between windtunnel and CFD. See subchapter 5.2 and Figure 5.4.

7. Conclusions

An extensive CFD campaign investigating ground effect was completed. Throughout the campaign changes were made to the geometry of the nacelle and wingtip, as well as deploying and retracting landing gear and changing the high-lift configuration. Finally this was done for both flightidle and MTO thrust configurations.

The following ground effect related changes to aerodynamic performance of the aircraft were observed:

- For the landing configuration, low α shows a positive lift increment, whereas at high α a negative lift increment is present.
    - Lift increase is caused due to more air being deflected over the wings, rather than under them. This results in the following lift-enhancing effects:
        - A pressure increase on lower main wing due to a decrease in flow velocity under the wing. The pressure increase is primarily located between the fuselage and nacelle.
        - A suction increase on the slat and wing leading edge due to an increase in the local angle of attack.
        - A pressure increase on the lower side of the engine nacelle and fuselage.
    - Lift-decreasing effects are:
        - For all α the pressure on the flap upperside is increased, especially at the flap leading edge due to a reduced mass-flow rate through the flap gap. This occurs over the entire span of the inboard and outboard flap. This effect is reduced with lower flap deflection angle.
        - A pressure increase on the mainwing upperside. That increase is most significant at the trailing edge and reduces when moving towards the leading edge. This effect occurs over the entire wing span. At low α this pressure increase is relatively small compared to the other effects. In contrast, at high α it becomes the dominant effect and also affects the upperside of the fuselage.
    - At low α the pressure increase on the lower wing is dominant, causing an overall lift increase. As α increases, the lift-reducing pressure increase on upper wing increases in magnitude faster compared to the lift-enhancing pressure on the lower wing surface. Depending on h/b, between $8.0° \leq \alpha \leq 11.0°$ the pressure rise on the upper wing surface becomes dominant, leading to an overall reduction in aircraft lift.
    - Lift is increased by up to 3.5% at $\alpha = 4.0°$ and is decreased by up to 5.5% at $\alpha = 13.0°$.
    - The influence of the ground effect increases exponentially as the distance to the ground is reduced.

- Drag is reduced by up to 33% due to the ground effect. That is primarily caused by a reduction of the induced drag. The magnitude of the drag reduction increases linearly with α, and increases as h/b decreases. The drag reduction can mostly be attributed to a reduction of the induced drag of up to 42% at $\alpha = 13.0°$ and $h/b = 0.155$, caused by the mirrored wing tip vortex. The viscous-pressure (form) drag is reduced by up to 9%.

- By applying MTO instead of flightidle thrust settings, the influence of the ground effect is reduced:
    1. At MTO thrust setting the engine sucks in air which would otherwise be deflected over the winger upper surface due to ground effect. This modifies the local angle of attack

on the leading edge in the region of the engine. That means that the magnitude of the suction increase on the slats, which is normally present due to ground effect on the slat and mainwing leading edge, is reduced compared to when flightidle thrust settings are applied.

2. At higher α the jet from the engine increases the mass flow in the flap gap. This increases the suction on the flap leading edge, thereby counter-acting the suction decrease and lift loss caused by ground effect on this part of the wing.

   These two effects combined cause a reduction of ground effect related lift by up to 2% of total lift *increase* at low α when MTO thrust settings are applied and a reduction of the ground effect related lift *decrease* at high α by up to 0.5% of total lift. Thus by applying MTO thrust settings the influence of the ground effect is reduced for all α, the absolute value of the change in lift due to ground effect is reduced.
   The drag is reduced more significantly by up to 4% of total drag with flightidle thrust settings applied compared to MTO thrust.

- Reducing the flap deflection from $\delta_{flap} = 40.0°$ to $\delta_{flap} = 10.0°$ results in a positive lift increment up until $\alpha \approx 12.0°$ instead of $\alpha \approx 9.0°$
  - Higher flap deflection values reduces the value of α at which the ground effect lift increment becomes negative.
  - The absolute value of the induced drag *reduction* is diminished by approximately 50%, the relative induced drag reduction is slightly decreased.

- The effect of changing the size of the engine nacelle is threefold:
  - 1) The larger nacelle blocks the flow over the outboard part of the inboard-slat, which therefore has a lower lift increase in ground effect by up to 0.06% of total lift.
  - 2) The lower side of the larger nacelle is located closer to the ground and thus the pressure increases more significantly here, leading to a lift increase of up to 0.08% of total lift.
  - 3) A thrust effect is present due to the engine in the larger nacelle producing an approximately 20% higher thrust coefficient compared to the thrust from the engine in the smaller nacelle. This thrust-effect can be seen both in the lift and drag change and accounts for the majority of the observed effects. Most of the observed lift and drag differences disappear for the case of the landing configuration with flightidle thrust setting.

  The impact of changing nacelle size is significantly smaller compared to the impact of changing the high-lift configuration and the engine thrust settings.

- The influence of changing the wingtip geometry is limited to the local, outboard area. The largest differences of up to 0.26% of total aircraft lift are observed at the range of $10.0° \leq \alpha \leq 12.0°$, which is when wingtip stall occurs. Impact of ground effect is very limited here because the chord of the wing is small compared to the inboard wing, and due to dihedral, the wingtip is located significantly further away from the ground.

- A deployed main landing gear counteracts the impact of ground effect below the wing. This is because both ground effect and the main landing gear reduce flow velocity below the wing. The combined effect is of a lower magnitude than the individual components, thus the magnitude of the lift-enhancing pressure rise on the lower wing is reduced with landing gear deployed.
  - Due to the lower velocity below the main wing, the main landing gear drag is reduced by up to 20% in ground effect. This is up to 7% of the total ground effect related aircraft drag reduction.

  - At $\alpha = 12.0°$ and $h/b = 0.155$, it was observed that the wake of the nose-landing gear hits the wing leading edge, reducing the local lift in this region. It is not known if this is a ground effect related phenomenon.

- Early onset of stall in ground effect was found occur at $\alpha \geq 13.0°$, but this effect is not validated by external data.

- The CFD data was validated using a DNW windtunnel campaign. It was found that for the take-off configuration there was a good to very good agreement between CFD and windtunnel, 0.5% of the total lift.
  - The agreement was not as good for the landing configuration lift increment. Especially at high α, CFD predicts a considerably more negative lift increment by up to 5.72% of the total lift in extreme cases. There is better agreement for the drag prediction, and the predicted trend is very similar. CFD predicts a slightly more significant drag benefit.
  - Possible causes for the discrepancies between windtunnel and CFD are:
    - Different aileron droop setting, $0.0°$ for windtunnel model and $10.0°$ for CFD, which can cause a discrepancy of up to 1% of total lift.
    - Difference in Reynolds number, $Re_{WT} \approx 2.6 * 10^6$ and $Re_{CFD} \approx 19.3 * 10^6$
    - Windtunnel belt speed which is below the freestream velocity
    - Limits of CFD: The largest discrepancies are found at high α, low h/b and high flap deflection. In this regime the steady assumptions underlying the CFD no longer fully apply, which will cause the CFD to lose accuracy for these conditions.

8. Bibliography

1. Caspian Sea Monster. *Wikipedia.* [Online] [Cited: August 24, 2018.] https://en.wikipedia.org/wiki/Caspian_Sea_Monster.
2. Tarantola, Andrew. This "Caspian Sea Monster" was a giant Soviet Spruce Goose. *Gizmodo.* [Online] [Cited: August 24, 2018.] https://gizmodo.com/this-caspian-sea-monster-was-a-giant-soviet-spruce-go-1456423681.
3. *A further evaluation of the ground plane suction method for ground simulation in automotive wind tunnels.* G.W., Carr and Eckert, W. 1994. SAE 940418.
4. *Measurement of formula one car drag force on the test track.* Crewe, C.M., Passmore, M.A. and Symonds, P. 1996. SAE 962517.
5. *Wing Resistance Near the Ground.* Wieselsberger, C. s.l. : Zeitschrift fur Flugtechnik und Motorlufschiffahrt, 31 May 1921, Vol. 10, pp. 145-147.
6. Anderson, J.D.,. *Fundementals of Aerodynamics - Fifth Edition in SI Units.* Singapore : McGraw-Hill, 2007. ISBN 978-1-259-01028-6.
7. Karamcheti, K. *Principles of Ideal Fluid Aerodynamics.* New York : John Wiley & Sons, Inc., 1966.
8. Pistolesi, E. *Ground Effect - Theory and Practice.* Washington : NACA, 1937. TM No.828.
9. *Abbildungstheoretische Grundlagen fur das Problem des Tragflugels in Erdbodenähe,.* Müller, W. s.l. : Z.M.M, 1931.
10. *The Lift on a Flat Plate Between Parallel Walls.* Rosenhead, L. s.l. : Royal Society, 1931. A 132.
11. *Il Problema dell'ala in Vicinanya del Suolo.* Pistolesi, E. 4, s.l. : L'Aerotechnica, 1933, Vol. 13, pp. 351-360.
12. *Untersuchungen über das Verhalten von Tragflügelprofilen sehr nahe am Boden.* Dätwyler, G. Zurich : Mitteilung aus dem Inst. für Aerodynamik, 1934.
13. Furlong, C & Bollech, T. *Effect of ground interference on the aerodynamic and flow characteristics of a 42° sweptbackwing at Reynolds numbers up to 6.8e6.* Washington : NACA, 1955. Report 1218.
14. Foshag, W. *Literature search and comprehensive bibliography of wings in ground effect and related phenomena.* s.l. : Department of the Navy, 1966. Report 2179 / Aero Report 1098.
15. Anderson, J.D. *Computational Fluid Dynamics.* Singapore : McGraw-Hill Book Co., 1995. ISBN 0-07-113210-4.
16. Deutsches Zentrum für Luft- und Raumfahrt e.V. *Technical Documentation of the DLR TAU-Code Relase 2017.1.0.* Braunschweig / Göttingen : Institute of Aerodynamics and Flow Technology, 2017.
17. *Thin Layer Approximation and Algebraic Model for Seperated Turbulent Flows.* Baldwin, B. and Lomax, H. Huntsville, Alabama : 16th Aerospace Sciences Meeting, 1978.
18. Cebeci, T. and Smith, A.M.O. *Analysis of Turbulent Boundary Layers.* s.l. : Academic Press, 1974. 978-0124313040.
19. *Turbulence Modeling: An Overview.* Wilcox, D. C. Reno, Nevada : 39th Aerospace Sciences Meeting & Exhibit, 2001. AIAA 2001-0724.
20. *A One-Equation Turbulence Model for Aerodynamic Flows.* Spalart, P.R. and Allmaras, S.R. Reno, Nevada : 30th Aerospace Sciences Meeting & Exhibit, 1992. AIAA-92-0439.
21. *A One-Equation Turbuelence Transport Model for High Reynolds Number Wall-Bounded Flows.* Baldwin, B.S. and Barth, T.J. Reno, Nevada : 29th Aerospace Sciences Meeting, 1991. AIAA 91-0610.
22. *Application of the Energy Dissipation Model of Turbulence to the Calculation of Flow Near a Spinning Disc.* Launder, B.E. and Sharma, B.I. 2, s.l. : Letters in Heat and Mass Transfer, 1974, Vol. 1.

23. Shih, T.H., et al. *A New k-e Eddy-Viscosity Model for High Reynolds Number Turbulent Flows - Model Development and Validation.* s.l. : NASA, 1994. NASA Technical Memorandum 10721.
24. *Reassessment of the Scale-Determining Equation for Advanced Turbulence Models.* Wilcox, D. C. s.l. : AIAA Journal, 1988, Vol. 26.
25. *Two-Equation Eddy-Viscosity Turbulence Models for Engineering Applications.* Menter, F.R. s.l. : AIAA Journal, 1994. AIAA 92-0439.
26. *Ten Years of Industrial Experience with the SST Turbulence Model.* Menter, F.R., Kuntz, M. and Langtry, R. Antalya, Turkey : 4th International Symposium on Turbulence, Heat and Mass Transfer, 2003.
27. *Computational Analysis of Pressure and Wake Characteristics of an Aerofoil in Ground Effect.* Mahon, S. and Zhang, X. 3, s.l. : Journal of Fluids Engineering, 2005, Vol. 127.
28. *The Influence of Compressibility on the Aerodynamics of an Inverted Wing in Ground Effect.* Doig, G., Barber, T.J. and Neely, A.J. s.l. : Transactions of the ASME, 2011, Vol. 133. 061102-12.
29. *Detached-Eddy Simulation of a Double-Element Wing in Ground Effect.* Heyder-Bruckner, Jacques and Zhang, Xin. January 2010. AIAA Aerospacing Meeting Including the New Horizons Forum and Aerospace Exposition. p. 59.
30. *Comments on the feasibility of LES for Wings, and on a hybrid RANS/LES approach.* Spalart, P.R:, et al. Greyden, Columbus OH : First AFOSR International Conference on DNS/LES, 1997.
31. *Extra-large Eddy Simulation of Massively Seperated Flows.* Kok, J.C., et al. Reno, Nevada : 42th AIAA Aerospace Sciences Meeting and Exhibit, 2004. AIAA 2004-264.
32. *Experimental investigation of the flowfield of a symmetrical airfoil in ground effect.* Ahmed, M. R., et al. Orlando, Florida : 21st Applied Aerodynamics Conference, 2003. AIAA 2003-4065.
33. Pink, M.P. and Lastinger, J.L. *Aerodynamic Characteristics of Low-aspect-ratio Wings in Close Proximity to the Ground.* Washington : National Aeronautics and Space Administration, 1961. NASA TN D-926.
34. *Features of DNW's New Moving Belt and Overview of Aero Test Systems.* Senft, V. Zwolle : Symposium on Experiments and Simulation of Aircraft in Ground Proximity, 2013.
35. *Ground Effect Simulation in the F1 High Reynolds Wind Tunnel.* d'Ozouville, G. and Escande, L. Zwolle : Symposium on Experiments and Simulation of Aircraft in Ground Proximity, 2013.
36. *Measurement of ground effect and boundary-layer transition by towing wind tunnel.* Yoshioka, S., et al. 2, s.l. : The Japan Society of Fluid Mechanics, 2009, Vol. 41.
37. *DNW-LLF Upgrade Ground Simulation.* Hegen, S. Zwolle : Experiments and Simulation of Aircraft in Ground Proximity, 2013.
38. *Way of Working with the DNW-LLF Moving Belt Ground Plane.* Stelte, P. Zwolle : Symposium on Experiments and Simulation of Aircraft in Ground Proximity, 2013.
39. *Aerodynamic ground effect: A case study of the integration of CFD and Experiments.* Barber, Tracie. June 2006, International Journal of Vehicle Design.
40. *Turbulence flow for NACA 4412 in Unbounded Flow and Ground Effect with Different Turbulence Models and Two Ground Conditions: Fixed and Moving Ground Conditions.* Firooz, A. and Gadami, M. 2006. International Conference on Boundary and Interior Layers.
41. *Aerodynamic investigation of RAE2822 airfoil in ground effect.* Li, S., et al. Qingdao, China : 7th International Conference of Fluid Mechanics, 2015.
42. Emslie, K., et al. *Low Speed longitudinal aerodynamic characteristics of aircraft in ground effect.* s.l. : ESDU 72023.
43. *Airfoil Aerodynamics in Ground Effect for Wide Range of Angles of Attack.* Qu, Q, et al. 4, s.l. : AIAA Journal, 2015, Vol. 53.
44. *Pitch Stability Analysis of an Airfoil in Ground Effect.* Angle II, G. M., et al. 3, Morgantown, West Virginia : Journal of Aircraft, 2009, Vol. 46.
45. *Aerofoil Ground Effect Revisited.* Coulliette, C and Plotkin, A. 992, s.l. : The Aeronautical Journal, 1996, Vol. 100.

46. *The Validation of an Airfoil in the Ground Effect Regime using 2D CFD Analysis.* Smith, J. L., Graham, H. Z. and Smith, J. E. Washington : AIAA Aerodynamic Measurement Technology and Ground Testing Conference, 2008. AIAA 2008-4262.
47. *Experimental and Computational study of Ground Effect on Airfoil Section.* Patek, Z., Vrchota, P. and Cervinka, J. Daejeon, Korea : ICAS 2016 - 30th Congress of the International Council of the Aeronautical Science, 2016.
48. *Aerodynamics of a single element Wing in Ground Effect.* Zerihan, J and Zhang, X. 6, s.l. : Journal of Aircraft, 2000, Vol. 37.
49. *Experiments on the Aerodynamics of a Cambered Airfoil in the Ground Effect.* Ahmed, M.R., T.Takasaki and Kohomoa, Y. January 2006. 44th AIAA Aerospace Sciences Meeting and Exhibit. p. 258.
50. *Aerodynamics of a NACA4412 Airfoil in Ground Effect.* Ahmed, M. R., Takasaki, T. and Kohama, Y. 1, s.l. : AIAA Journal, 2007, Vol. 45.
51. *Aerodynamics of a Pitching and Heaving Airfoil in Ground Effect.* Molina, J, Zhang, X and Alomar, A. 4, Southampton : AIAA Journal, 2016, Vol. 54.
52. *RANS and LES/RANS Simulation of Airfoils under Static and Dynamic Stall.* Jinaghua, K. and Edwards, J. R. Grapevine, Texas : 51st AIAA Aerospace Sciences Meeting, 2013. AIAA 2013-0955.
53. Abbott, I. H., Von Doenhoff, A. E. and Stivers, L. Jr. *Summary of Airfoil Data.* s.l. : NASA, 1945. NASA TM-824.
54. *Numerical Study of Wing Aerodynamics in Ground Proximity.* Ockfen, A. E. and Matveev, K. I. New York : ASME 2008 International Mechanical Engineering Congress and Exposition, 2008.
55. *Experimental and Analytic Investigation of Ground Effect.* Traub, L. W. 1, Prescott, Arizona : Journal of Aircraft, 2015, Vol. 52.
56. *Aerodynamics and Flow Physics of a Two-Element Airfoil in Ground Effect .* Qu, Q., et al. Kissimmee, Florida : 53rd AIAA Aerospace Sciences Meeting, 2015. 10.2514/6.2015-0550.
57. Recant, I.G. *Wind-Tunnel Investigation of Ground Effect.* Washington D.C. : NACA, 1939. TN 705.
58. Ranzenbach, R., Barlow, J. B. and Diaz, R. H. *Mutli-element Airfoil in Ground Effect - An Experimental and Computational Study.* Maryland : American Institutde of Aeronautics and Astronautics, 1997. AIAA-97-2238.
59. *Aerodynamics of a Double-Element Wing in Ground Effect.* Zhang, X. and Zerihan, J. 6, Southampton : AIAA Journal, 2003, Vol. 41.
60. *Numerical Investgation of the Aerodynamics of an Inverted Three-Element Airfoil in Ground Effect for Race Car Application.* Qu, Q., et al. Washington, D.C. : AIAA AVIATION Forum, 2016. 10.2514/6.2016-4180.
61. *Camber Reduction to Mitigate Burst Wakes in Inverted Mutli-element Airfoils Operating in Ground Effect.* Pant, P. New Dehli, : 2018 Applied Aerodynamics Conference, 2018. 10.2514/6.2018-4117.
62. *Ground Effect Investigation on Two-Dimensional Airfoils.* Hase, Suguru. Zwolle : DNW Symposium on Experiements and Simulation of Aircraft in Ground Proximity, 2013.
63. Deng, N., Qu, Q. and Agarwal, R.K. *Numerical Study of the Aerodynamics of Rectangular Multi-Element Wing in Ground Effect.* Atlanta, Georgia : AIAA AVIATION Forum, 2018. 10.2514/6.2018-4115.
64. *Unsteady Trailing Vortex Evolution behind a Wing in Ground Effect.* Han, C. and Cho, J. 2, Seoul : Journal of Aircraft, 2005, Vol. 42.
65. *Near-field Wingtip Vortex Characteristics of a Rectangular Wing in Ground Effect.* Qu, Q., et al. San Diego, California : AIAA SciTech Forum, 2016. 10.2514/6.2016-1781 .
66. *Numerical Study of the Aerodynamics of DLR-F6 Wing-Body in Unbounded Flow Field and in Ground Effect.* Deng, N., Qu, Q and . Agarwal, R.K. Grapevine, Texax : AIAA SciTech Forum, 2017. 10.2514/6.2017-1424.
67. *Numerical Simulation of the impact of ground proximity on maximum lift.* van Muijden, J. Zwolle : DNW Symposium on Experiments and Simulation of Aircraft in Ground Proximity, 2013.

68. National Transportation Safety Board. *Crash During Experimental Test Flight Gulfstream AeroSpace Corportation GVI (G650), N652GD.* Washington : s.n., 2011. NTSB/AAR-12/02 PB2012-910402.
69. *Results of Wind Tunnel Ground Effect Measurements on Airbus A320 Using Turbine Power Simulation and Moving Tunnel Floor Techniques.* Flaig, A. Seattle, WA : AIAA 16th Aerodynamics Ground Testing Conference, June 1990. AIAA 90-1427.
70. *DNW-LFF Upgrade Ground Simulation.* Hegen, S. Zwolle : DNW Symposium Experiments and Simulation of Aircraft in Ground Proximity, 2013.
71. *Wind-Tunnel Investigation of Wing-in-Ground Effects.* Chawla, M.D., Edwards, L.C. and Franke, M.E. 4, s.l. : Journal of Aircraft, 1990, Vol. 27.
72. *Analysis of Dynamic Ground Effect for a Jet Transport in Crosswind.* Weng, C., Lan, C. E. and Ho, C. Providence, Rhode Island : AIAA Atmospheric Flight Mechanics Conference and Exhibit, 2004. AIAA 2004-5066.
73. Curry, R.E., Moulton and Kresse, J. *An In-Flight Investigation of Ground Effect on a Forward-Swept Wing Airplane.* Edwards, California : NASA, 1989. NASA Technical Memorandum 101708.
74. Curry, R.E. and Owens, L.R. *Ground-effect characteristics of the TU-144 Supersonic Transport Airplane.* Edwards, California : NASA, October 2003. NASA/TM-2003-212035.
75. Baker, P.A. and Schweikhard, W.G., Young, W.R. *Flight Evaluation of Ground Effect on several Low-Aspect-Ratio Airplanes.* Edwards, California : NASA Flight Research Center, 1970. NASA TN D-6053.
76. Katz, J. and Levin, D. *Measurements of Ground Effect for Delta Wings.* s.l. : Journal of Aircraft, 1984. 10.2514/3.44988.
77. *Aerodynamic Characteristics of a Two-Dimensional Airfoil with Ground Effect.* Hsiun, C.M. and Chen, C. K. 2, Taiwan : Journal of Aircraft, 1996, Vol. 33.
78. *Measurements of Aerofoil Characteristics by Method of Towing.* Kikuchi, M., et al. 676, s.l. : Transactions of the Japan Society of Mechanical Engineers, 2002, Vol. 68.
79. *Aerodynamics of Gurney Flaps on a Wing in Ground Effect.* Zerihan, J. and Zhang, X. 5, s.l. : AIAA Journal, 2001, AIAA Journal, Vol. 39.
80. *Numerical Study of Fuselage Aerodynamics of DLR-F6 Wing-Body in Ground Effect.* Deng, N., Qu, Q. and Agarwal, R.K. Denver, Colorado : AIAA AVIATION Forum, 2017. 10.2514/6.2017-4234.
81. *Numerical Investigation on Aerodynamic Characteristics of a Compound Wing-in-Ground Effect.* Jaemi, S., et al. 5, s.l. : Journal of Aircraft, 2012, Vol. 49.
82. *Stability of Airplanes in Ground Effect.* Staufenbiel, R. W. and Schlichting, U.-J. 4, Aachen : Journal of Aircraft, 1988, Vol. 25.
83. *Experimental Investigation of Dynamic Ground Effect.* Lee, P., Lan, C.E. and Muirhead, V.U. 6, Lawrence, Kansas : Journal of Aircraft, 1989, Vol. 26.
84. *Effect of Sink Rate on Ground Effect of Low-Aspect-Ration Wings.* Chang, R. C. and Muirhead, V. U. s.l. : Journal of Aircraft, 1987, Vol. 24.
85. Curry, R. E. *Dynamic Ground Effect for a Cranked Arrow Wing Airplane.* Edwards, California : American Institute of Aeronautics and Astronautics, 1997. AIAA-97-3649.
86. *Prediction of Dynamic Gorund Effect Through Modified Lifting Line Theory.* Ariyur, K. B. Ontario, Canada : 23rd AIAA Applied Aerodynamics Conference, 2005. AIAA 2005-4610.
87. *Numerical Simulation of the Flowfield of an Airfoil in Dynamic Ground Effect.* Qu, Q., et al. 5, s.l. : Journal of Aircraft, 2014, Vol. 51.
88. *Dynamic Ground Effect Analysis Using a Novel Sinking Grid Methodology.* Mondal, P., et al. Washington : 34th AIAA Applied Aerodynamics Conference, 2016. 10.2514/6.2016-4167.
89. *Numerical Determination of Critical Mach Number of a Three-Element Airfoil in Unbounded Flow and in Ground Effect.* Hu, B., Qu, Q. and Agarwal, R.K. Atlanta, Georgia : 2018 Applied Aerodynamics Conference, 2018. 10.2514/6.2018-4114.
90. *Aerodynamic investigation of three-dimensional wings in ground effect for aero-levitation electric vehicle.* Moon, Y.J., Oh, H. and Seo, J. Seoul, Korea : Aerospace Science and Technology, 2005.

91. ETW GmbH. ETW - European Transonic Windtunnel. [Online] 2. [Cited: May 27, 2019.] ww.etw.de.

92. Blazek, J. *Computational Fluid Dynamics: Principles and Applications.* Oxford : Elsevier, 2001. ISBN 0 08 043009 0.

93. *Discretization of the Navier-Stokes Equations and Mesh Induced Errors.* Baker, T.J. Mississipi : Proceedings of the 5th International Conferefence on Numerical Grid Generation in CFD, 1996.

94. CentaurSoft. CENTAUR Software from CentaurSoft - Mesh (Grid) Generation for CFD and Computational Simulation. [Online] 2 18, 2018. https://www.centaursoft.com/.

95. White, F.M. *Viscous Fluid Flow - Third Edition.* Singapore : McGraw-Hill, 2006. ISBN 007-124493-X.

96. *Turbulence and Skin Friction.* von Kármán, T. 1, s.l. : Journal of the Aeronautical Sciences, 1934, Vol. 1.

97. *Smooth and Differentitation of Data by Simplified Least Squares Procedures.* Savitzky, A and Golay, M.J.E. 8, s.l. : Analytical Chemistry, 1964, Vol. 36. DOI: 10.1021/ac60214a047.

98. A. Elsenaar, Travis W. Binion, E. Stanewsky. *Reynolds Number Effects in Transonic Flow - Volume 303 of NATO AGARD-AG.* s.l. : AGAARD, 1988. 9789283504924.

99. *Aerodynamic Characteristics of a Two-Dimensional Airfoil with Ground effect.* Hsiun, C-M. Chen, C-K. 2, Tainan, Taiwan : Journal of Aircraft, 1996, Vol. 33.

100. *A New Method of Interpolation and Smooth Curve Fitting Based on Local Procedures.* Akima, H. 4, Boulder, Colorado : Journal of the Associaton of Computing Machinery, 1970, Vol. 17.

101. *Approximate Riemann Solvers, Parameter Vector, and Difference Schemes.* Roe, P.L. 43, s.l. : Journal of Computational Physics, 1981.

9. Appendices

9.1 Appendix A – Derivation of the Navier-Stokes Equations

9.1.1 Navier-Stokes Equations

The Navier-Stokes equations are a coupled system of non-linear partial differential equations for solving a viscous flow. They form the mathematical basis for the RANS solvers. So far no general analytical solution exists for these equations, hence the need for numerical solution methods. The Navier-Stokes equations are given below, for the full derivation see (6).

The continuity equation:

$$\frac{\delta\rho}{\delta t} + \nabla \cdot (\rho \boldsymbol{V}) = 0 \qquad (equation\ 9.1)$$

The momentum equation:

$$\frac{\delta(\rho u)}{\delta t} + \nabla \cdot (\rho u \boldsymbol{V}) = -\frac{\delta p}{\delta x} + \rho f_x + F_{x_{viscous}} \qquad (equation\ 9.2)$$

$$\frac{\delta(\rho v)}{\delta t} + \nabla \cdot (\rho v \boldsymbol{V}) = -\frac{\delta p}{\delta y} + \rho f_y + F_{y_{viscous}} \qquad (equation\ 9.3)$$

$$\frac{\delta(\rho w)}{\delta t} + \nabla \cdot (\rho w \boldsymbol{V}) = -\frac{\delta p}{\delta z} + \rho f_z + F_{z_{viscous}} \qquad (equation\ 9.4)$$

The energy Equation:

$$\frac{\delta}{\delta t}\left[\rho\left(e + \frac{V^2}{2}\right)\right] + \nabla \cdot \left[\rho\left(e + \frac{V^2}{2}\right)\boldsymbol{V}\right] = \rho\dot{q} - \nabla \cdot (p\boldsymbol{V}) + \rho(\boldsymbol{f} \cdot \boldsymbol{V}) + \dot{Q}_{viscous} + \dot{W}'_{viscous} \qquad (equation\ 9.5)$$

This is a system of five equations and six unknowns, ρ, p, u, v, w, e. The system is closed by adding the equation of state, which is in the case for a perfect gas:

$$p = \rho RT \qquad (equation\ 9.6)$$

Or for the more general case:

$$p = (\gamma - 1)\rho\left(E - \frac{u^2 + v^2 + w^2}{2}\right) \qquad (equation\ 9.7)$$

This adds the temperature T as the seventh unknown, which can be obtained when assuming a perfect caloric gas by:

$$e = c_v T \qquad (equation\ 9.8)$$

The Navier-Stokes equations can be rewritten in conservative form, as used by the TAU solver (16):

$$\frac{\delta}{\delta t}\iiint\limits_V \vec{W} dV = \iint\limits_{\delta V} \bar{\bar{F}} \cdot \vec{n} dS \qquad (equation\ 9.9)$$

Hereby $\vec{W}$ is the vector of the conserved quantities:

$$\vec{W} = \begin{pmatrix} \rho \\ \rho u \\ \rho v \\ \rho w \\ \rho E \end{pmatrix} \qquad (equation\ 9.10)$$

V is an arbitrary control volume with boundary δV and normal vector $\vec{n}$. $\bar{\bar{F}}$ is the flux density tensor and consists of the flux vectors of all three axis directions:

$$\bar{\bar{F}} = \left(\vec{F}_i^C + \vec{F}_v^C\right) \cdot \vec{e}_x + \left(\vec{G}_i^C + G_v^C\right) \cdot \vec{e}_y + \left(H_i^C + H_v^C\right) \cdot \vec{e}_z$$

The inviscid and viscous contributions are given separately by:

$$\vec{F}_i^C = \begin{pmatrix} \rho u \\ \rho u^2 + p \\ \rho uv \\ \rho uw \\ \rho Hu \end{pmatrix} \qquad (equation\ 9.11a)$$

$$\vec{F}_v^C = \begin{pmatrix} 0 \\ \tau_{xx} \\ \tau_{xy} \\ \tau_{xz} \\ u\tau_{xx} + v\tau_{xy} + w\tau_{xz} + \kappa_l \frac{\delta T}{\delta x} \end{pmatrix} \qquad (equation\ 9.11b)$$

$$\vec{G}_i^C = \begin{pmatrix} \rho v \\ \rho uv \\ \rho v^2 + p \\ \rho vw \\ \rho Hv \end{pmatrix} \qquad (equation\ 1.12a)$$

$$\vec{G}_v^C = \begin{pmatrix} 0 \\ \tau_{xy} \\ \tau_{yy} \\ \tau_{yz} \\ u\tau_{xy} + v\tau_{yy} + w\tau_{yz} + \kappa_l \frac{\delta T}{\delta y} \end{pmatrix} \qquad (equation\ 9.12b)$$

$$\vec{H}_i^C = \begin{pmatrix} \rho w \\ \rho uw \\ \rho vw \\ \rho w^2 + p \\ \rho Hw \end{pmatrix} \qquad (equation\ 9.13a)$$

$$\vec{H}_v^C = \begin{pmatrix} 0 \\ \tau_{xz} \\ \tau_{yz} \\ \tau_{zz} \\ u\tau_{xz} + v\tau_{yz} + w\tau_{zz} + \kappa_l \frac{\delta T}{\delta z} \end{pmatrix} \qquad (equation\ 9.13b)$$

9.1.2 Reynolds-Averaged Navier-Stokes Equations

The Navier-Stokes equations could in principle be fully solved numerically for the entire computational domain using Direct Numerical Simulation (DNS). Unfortunately the prohibitive computational costs make this unfeasible for anything but the simplest of cases, since these costs rise proportional to the cube of the Reynolds Number. Therefore, in order to reduce the computational complexity of solving the Navier-Stokes equations, some of the non-linear parts of the equations are averaged. The continuity, momentum and energy equation then become respectively (16):

$$\frac{\delta\bar{\rho}}{\delta t}+\frac{\delta}{\delta x_k}\left(\bar{\rho}\widetilde{U}_k\right)=0 \qquad (equation\ 9.14)$$

$$\frac{\delta\left(\bar{\rho}\widetilde{U}_i\right)}{\delta t}+\frac{\delta}{\delta x_k}\left(\bar{\rho}\widetilde{U}_i\widetilde{U}_k\right)+\frac{\delta}{\delta x_k}\left(\bar{\rho}\tilde{R}_{ik}\right)=-\frac{\delta\bar{p}}{\delta x_i}+\frac{\delta\bar{\tau}_{ik}}{\delta x_k} \qquad (equation\ 9.15)$$

$$\frac{\delta\left(\bar{\rho}\tilde{E}\right)}{\delta t}+\frac{\delta}{dx_k}\left(\bar{\rho}\widetilde{H}\widetilde{U}_k\right)+\frac{\delta}{\delta x_k}\left(\bar{\rho}\tilde{R}_{ik}\widetilde{U}_i\right)=\frac{\delta\left(\bar{\tau}_{ik}\widetilde{U}_i\right)}{\delta x_k}-\frac{\delta\bar{q}_k}{dx_k}-\frac{\delta q_k^t}{\delta x_k}+\bar{\rho}D^{\tilde{k}} \qquad (equation\ 9.16)$$

In the above equations, the overbar denotes the weighted average, while the tilde denotes a mass weighted average as given by for example:

$$\widetilde{H}=\frac{\overline{\rho H}}{\bar{\rho}} \qquad (equation\ 9.17)$$

The Reynolds-Averaged Navier-Stokes equations introduce additional terms which need to be modelled instead of solved. In particular there is the introduction of the Reynolds stress tensor:

$$\bar{\rho}\tilde{R}_{ij}=\overline{\rho u_\imath"u_\jmath"} \qquad (equation\ 9.18)$$

The half of the trace of the Reynolds stress tensor is called the kinetic turbulence energy:

$$\bar{\rho}\tilde{k}=\frac{1}{2}\bar{\rho}\tilde{R}_{kk} \qquad (equation\ 9.19)$$

the turbulent heat-flux vector and the diffusion of kinetic turbulence energy are respectively:

$$q_i^{(t)}=\overline{\rho h"u_\imath"} \qquad (equation\ 9.20)$$

$$\bar{\rho}D^{(\tilde{k})}=-\frac{\delta}{\delta x_k}\left(\overline{\rho u_\imath"u_\imath"u_k"}-\overline{\tau_{\imath k}u_\imath"}\right) \qquad (equation\ 9.21)$$

Whereby the “ indicates a fluctuation around mass weighted average.

The average of the viscous stress is given by:

$$\bar{\tau}_{ik}=2\bar{\mu}\tilde{S}_{ij}^{*} \qquad (equation\ 9.22)$$

With traceless strain rate tensor:

$$\tilde{S}_{ij}^{*}=\tilde{S}_{ij}-\frac{1}{3}\tilde{S}_{kk}\delta_{ij} \qquad (equation\ 9.23)$$

And the simple strain rate tensor

$$\tilde{S}_{ij}=\frac{1}{2}\left(\frac{\delta\widetilde{U}_i}{\delta x_j}+\frac{\delta\widetilde{U}_j}{\delta x_i}\right) \qquad (equation\ 9.24)$$

Sutherland’s law can be used to compute the average molecular viscosity:

$$\frac{\bar{\mu}}{\mu_{REF}} = \left(\frac{\bar{T}}{T_{REF}}\right)^{\frac{3}{2}} \frac{T_{REF} + S}{\bar{T} + S} \qquad (equation\ 9.25)$$

Finally the average molecular heat flux is given by:

$$\bar{q}_i = -\lambda \frac{\delta \tilde{T}}{\delta x_i} \qquad (equation\ 9.26)$$

The average molecular heat conductivity λ can be derived from the definition of the Prandtl number. The averaging of the ideal gass law does not introduce any changes compared to the original equation. The average specific total energy and enthalpy change in the following manner:

$$\tilde{E} = \tilde{e} + \frac{1}{2}\widetilde{U}_k \widetilde{U}_k + \tilde{k} \qquad (equation\ 9.27)$$

$$\widetilde{H} = \tilde{h} + \frac{1}{2}\widetilde{H}_k \widetilde{H}_k + \tilde{k} \qquad (equation\ 9.28)$$

Whereby:

$$\tilde{e} = C_v \tilde{T} \qquad (equation\ 9.29)$$

$$\tilde{h} = C_p \tilde{T} = \tilde{e} + \frac{\bar{p}}{\bar{\rho}} \qquad (equation\ 9.30)$$

9.2 Appendix B – Analysis of the Influence of the Wingtip Geometry on Ground Effect Performance

In subchapter 4.4 the change in global lift and drag coefficient for the different configurations was shown. The focus for that subchapter was to determine the differences in lift and drag increment in ground effect caused by the nacelle geometry, now in this subchapter the focus will be on using that same data to determine the influence of the wingtip geometry on ground effect lift and drag.

One important note is that the winglet geometry has a wingspan which is increased by approximately 5% compared to the conventional wingtip geometry. However all CFD runs have been performed using the same reference value of the span b, which was the value of $b_{Winglet}$ corresponding to the winglet geometry. Therefore the results for the conventional wingtip case were interpolated to the correct value of wingspan $b_{conventionalWingtip}$ using an Akima (100) spline interpolation as implemented in the EGAAG STET excel toolset. This interpolation has been performed for the global lift and drag increments discussed below, but not for the spanwise lift and drag distribution discussed in the subsection

9.2.1 Change in C_L and C_D

9.2.1.1 Global Lift and Drag Coefficient

Figure 4.50, Figure 4.51 and Figure 4.52 show the lift increment for respectively the take-off MTO, landing MTO and landing flightidle configurations. No clear trends in terms of lift increment dependency on winglet geometry can be determined from this data. For the take-off configuration in Figure 4.51 the conventional wingtip geometry shows a higher lift increment of up to 0.4% of total lift when the smaller nacelle is equipped, while when the larger nacelle is installed it is now the winglet geometry which shows a higher lift increment of up to 0.26% of total lift. As α increases to the point that wingtip stall occurs ($\alpha \approx 12.0°$), the difference between due to the wingtip lift are reduced. As the CFD uncertainty is increased in for the two landing configurations*, it becomes impossible to discern any clear trend with respect to wingtip geometry.* Thus it can be concluded that any effect of the wingtip geometry on the global lift increment change in ground effect is small and in the same order as the CFD uncertainty at high lift conditions.

The same conclusion can be taken from evaluating the global drag increment changes in Figure 4.57, Figure 4.58 and Figure 4.59. No clear drag dependency on wingtip geometry can be found.

9.2.1.2 C_L-C_D Polars

Because no clear trends can be determined from the global lift and drag increment, the remainder of this section will be focused on the local lift and drag from the winglet only. Figure 9.1 shows the C_L–C_D curves for both the winglet and conventional wingtip geometry in the full landing configuration. The C_D values here a calculated by CFD2Loads 5.3 and is obtained by integrating the values of c_f and c_p over the wingtip surface. The data is taken from the incidence values of $0.0° \leq \alpha \leq 12.0°$. The corresponding pressure distributions along the wingtip are shown in Appendix G – Wing Tip Pressure Coefficient Plots, Figure 9.40 to Figure 9.51.

Figure 9.1 shows that at low incidence there is no strong influence of the ground effect on the wingtip behavior. For both the winglet and conventional wingtip case there is a slight decrease in drag (increase in negative drag) and a small decrease in lift for the same α, the effective angle of attack is reduced. Figure 9.40 to Figure 9.42 show that the slight lift loss is caused by a slight decrease in suction on the upperwing surface behind the leading edge suction peak. The reduction in suction in this region is also the cause of the reduction in pressure drag due to the shape of the airfoil geometry.

It was seen in previous subchapters that the winglet stall occurs at lower α for the ground effect, which is shown in Figure 4.14 and Figure 4.15. This is also quantitatively shown in Figure 9.1, where the maximum lift coefficient is reduced by approximately 0.26% of total lift for the winglet and by 0.17% of total lift for the conventional wingtip. Once separation on the winglet occurs, the drag is increased significantly and the lift is decreased. As the winglet is fully stalled, the differences between the in and out of ground effect case become almost negligible. This is also illustrated in the c_p distribution for $\alpha = 12.0°$ shown in Figure 9.45 for the winglet geometry and Figure 9.51 for the conventional wingtip geometry, which can be compared with $\alpha = 11.0°$ in Figure 9.44 and Figure 9.50 respectively where the difference between in and out of ground effect are more significant.

Now that the limited local influence of the ground effect on the wingtip lift and drag is known, the next section will discuss if changing the local wingtip geometry will significantly influence the ground effect behavior of the rest of the wing.

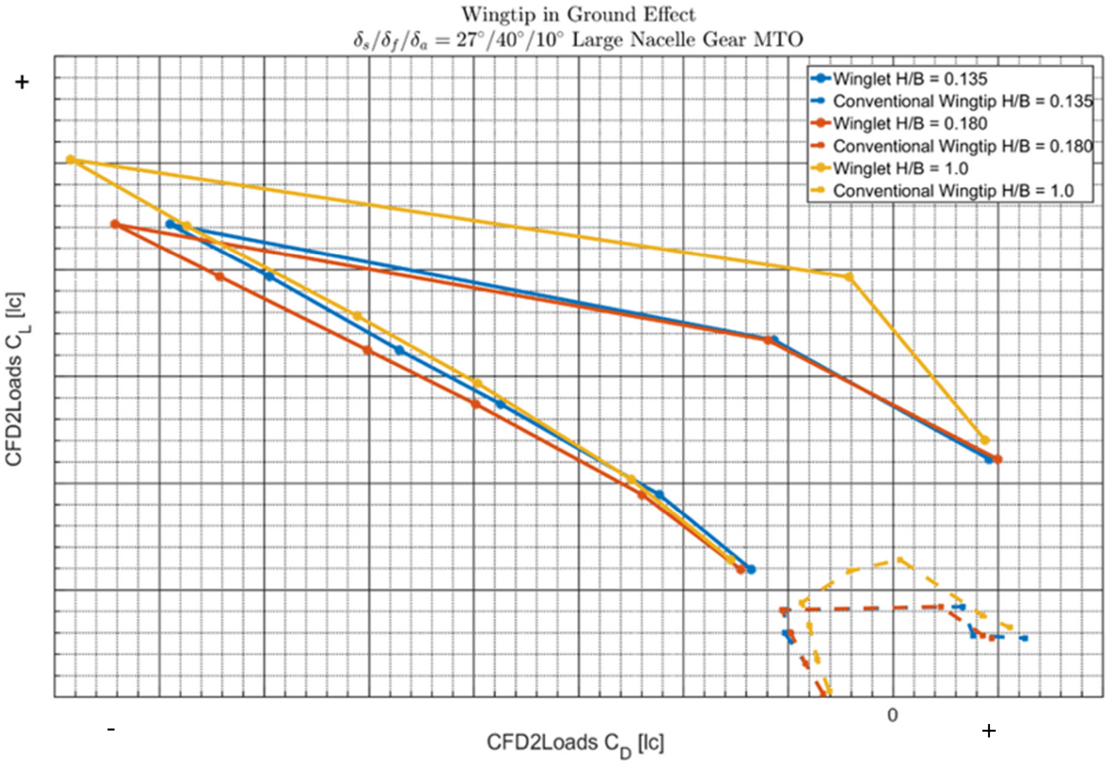

Figure 9.1 - $C_L - C_D$ curve for the Winglet and Conventional Wingtip in and out of ground effect for the large nacelle, full landing configuration with MTO thrust settings and gear deployed

Note that the negative drag shown here is purely a bookkeeping effect, related how the drag is calculated by the tool CFD2Loads. This is known within the department, it should not be considered to be an error.

9.2.2 Change in spanwise lift and drag distribution

9.2.2.1 Spanwise lift distribution change

Figure 4.56 shows the spanwise lift distribution for the take-off configuration at $\alpha = 6.0°$ and $h/b = 0.135$ and $h/b = 0.18$. As discussed previously some small differences could be observed in this figure concerning the nacelle effect. In comparison to the nacelle effect, the changes due to the wingtip geometry are even smaller. Very small changes in lift increment of up to 1% are present at the outboard wings section near the aileron.

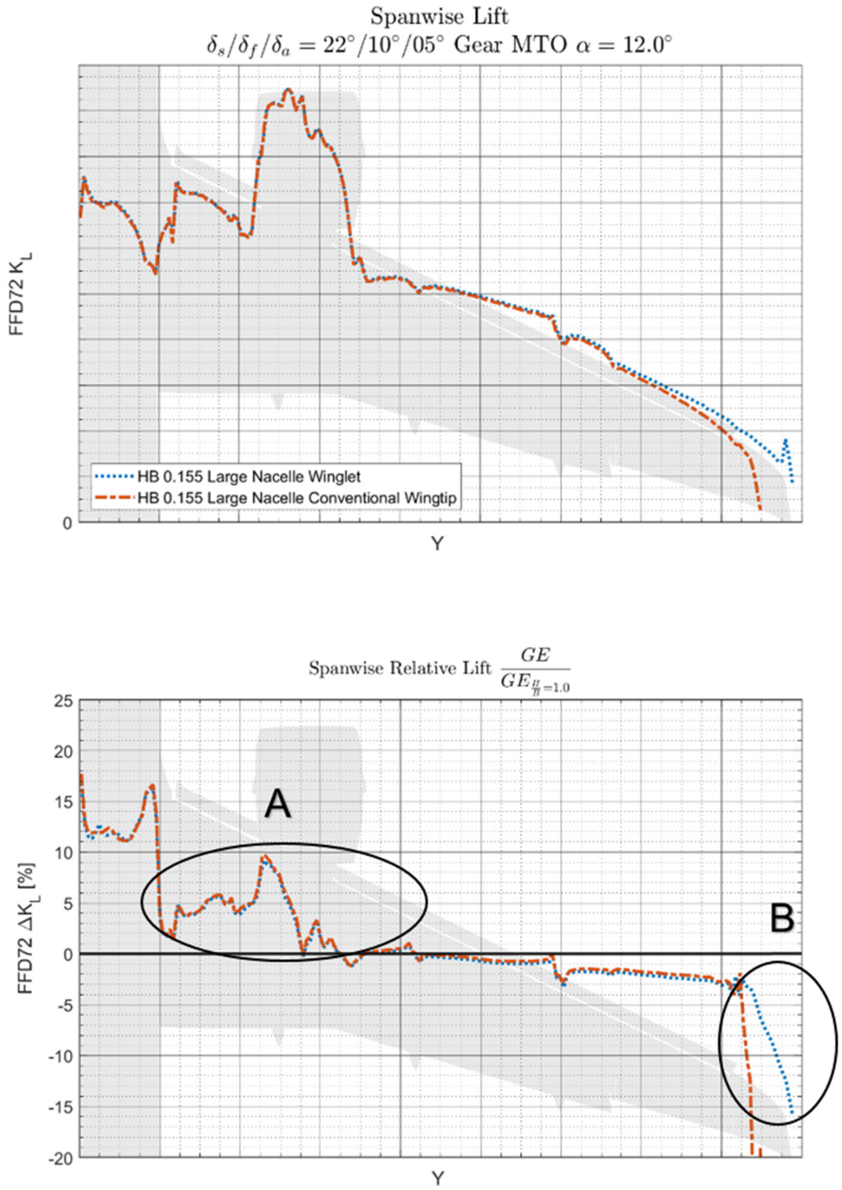

Figure 9.2 - Spanwise lift distribution for the large nacelle geometry with gear deployed and flightidle thrust conditions at $\alpha = 12.0°$ $\frac{h}{b} = 0.155$ for the take-off high lift configuration

The differences due to wingtip geometry become slightly more pronounced when evaluating that same outboard wing section for the landing configuration, which is shown at same α and h/b values in Figure 9.84 for the MTO thrust setting and in Figure 9.85 for the flightidle thrust setting. Here changes of up to 3% are visible for the local lift increment, whereby the trend is that conventional wingtip has a slightly less negative value of the lift increment.

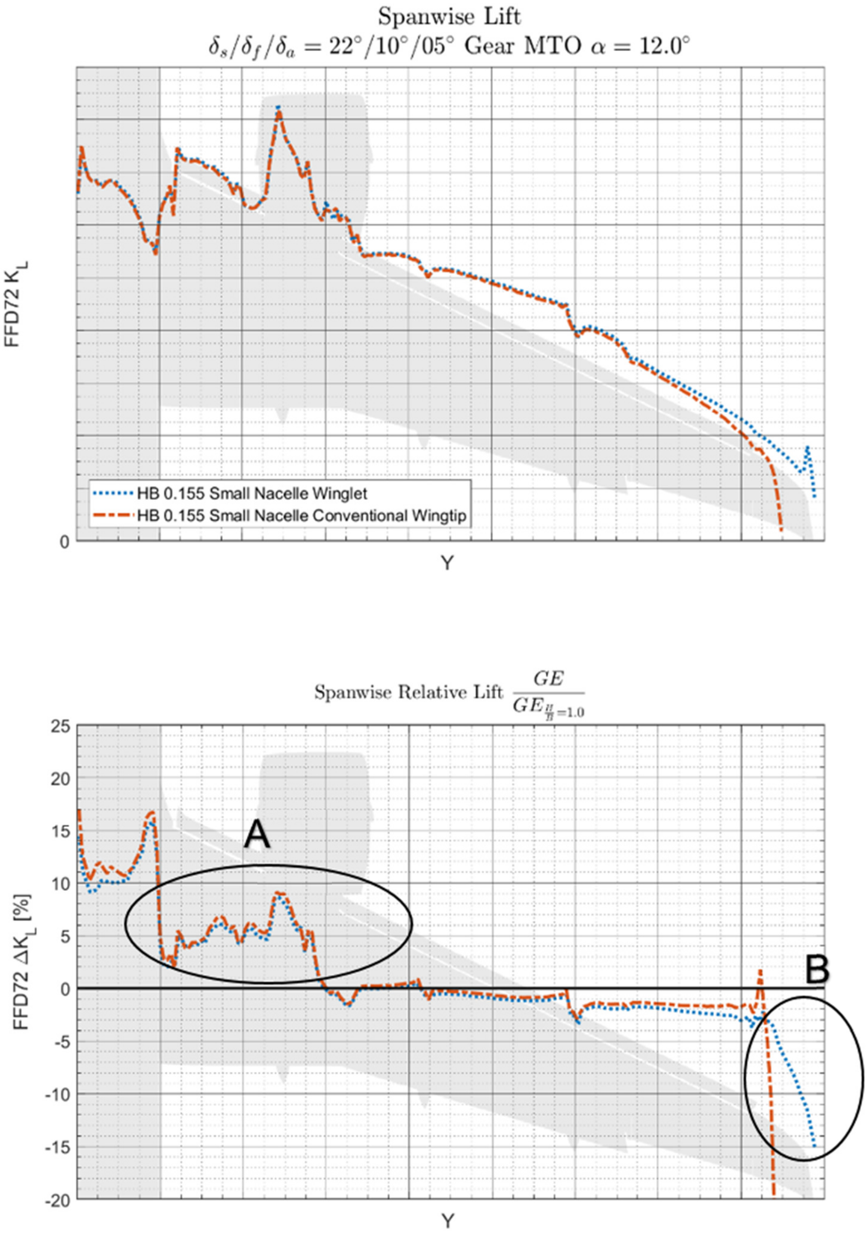

Figure 9.3 - Spanwise lift distribution for the small nacelle geometry with gear deployed and flightidle thrust conditions at $\alpha = 12.0°$ $\frac{h}{b} = 0.155$ for the take-off high lift configuration

Investigating at higher incidence angle, Figure 9.2 and Figure 9.3 show the spanwise lift distribution at $\alpha = 12.0°$ for respectively the large and small nacelle geometries. These figures show that at the wingtip (marked as region B), the conventional wingtip geometry has significantly worse performance in ground effect due to the wingtip stalling only in ground effect. That separation is also shown on the wingtip C_p distribution in Figure 9.37 for the winglet and Figure 9.39 for the conventional wingtip.

Almost no changes to the lift occur on the inboard area and at the fuselage (marked as region A), even with the same nacelle geometry, only local effects close to the wingtip can be

observed. There is a very small change in ground effect lift increment on the outboard wing area, in the order of less than 1%. These observations disprove the hypothesis that the ground effect behavior of the entire wing gets changed due to a change in spanwise lift distribution on the wing, caused by the wingspan extension when the winglet is installed. This conclusion remains valid at lower values of α.
It would be of interest to see the results for this configuration at flightidle thrust settings to see if the lift differences would also be present in that case. Unfortunately no time was available to produce this data. Another direction for future research would be to perform CFD runs whereby the solution is iterated to a certain fixed of C_L value, so that a 'fair' comparison can be made in ground effect at identical C_L between the different geometries.

9.2.2.1 Spanwise drag distribution change

Figure 9.88, Figure 9.89 and Figure 9.90 show the drag distribution for respectively the take-off high lift setting for MTO thrust setting and the landing configuration for the MTO and flightidle thrust setting. These drag distributions are inherently noisy and as such it is difficult to take firm conclusions based on these plots. The most significant differences are present at the wingtip itself, where there is a very sharp and strong peak of up to 100% drag increase present for only the winglet geometry for all three cases. It is not known what causes this strong drag increase, but it is present across a wide range of α. However, this is a strong relative change of a small absolute value, so the impact on the global drag value is very limited.

This local influence is also seen in Figure 9.4 and Figure 9.5, which show the total drag distribution for the exact same settings as shown in the previous section in Figure 9.2 and Figure 9.3 for the lift. Allowing for the fact that the drag data is inherently noisier compared to the lift data, Figure 9.4 and Figure 9.5 show that the most significant differences in ground effect drag performance caused by wingtip geometry are present at the wingtip and to a lesser extent on the outboard wing section, marked in region A. No clear influence of wingtip geometry on the drag distribution on the inboard section of the wing or fuselage can be observed.

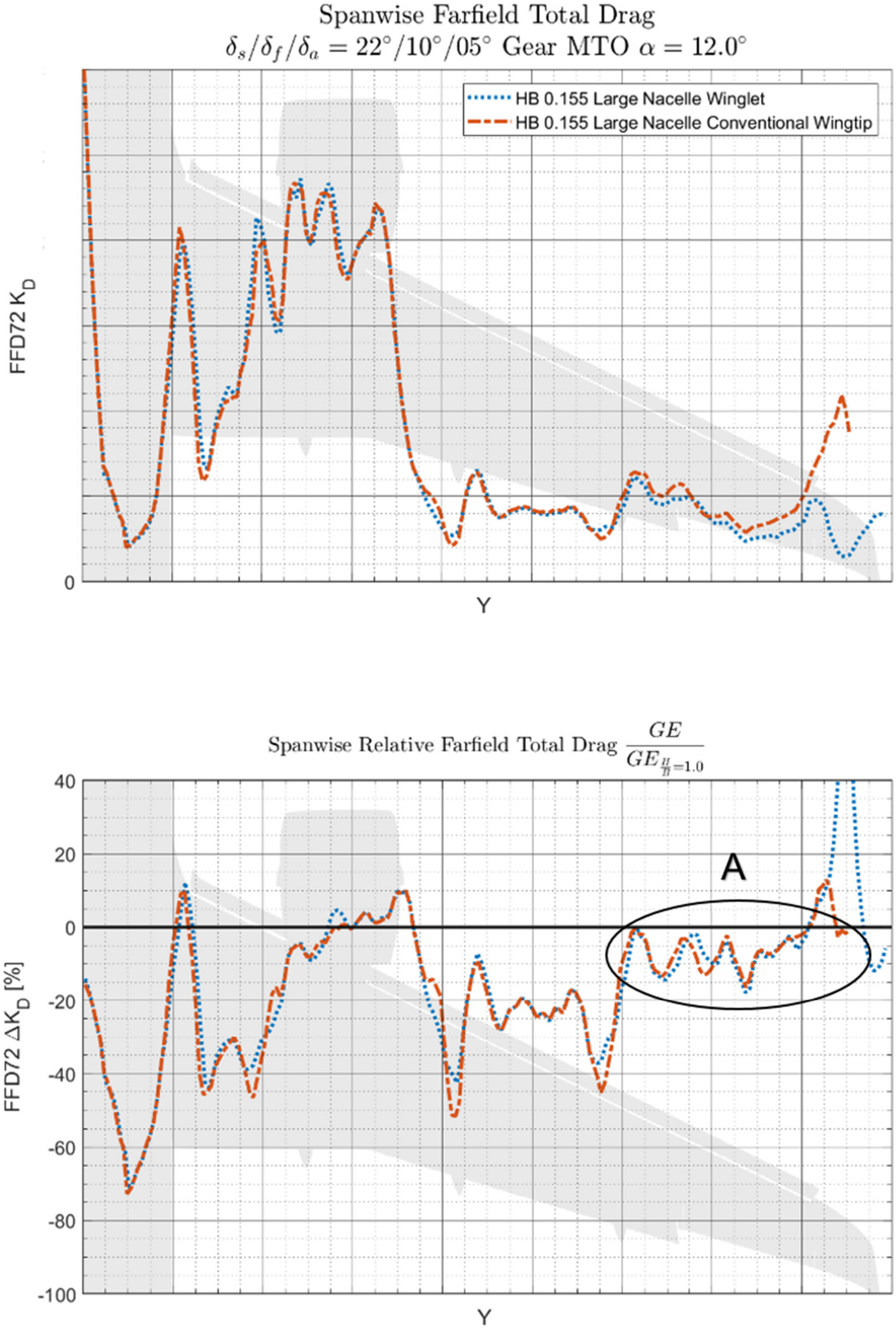

Figure 9.4 - Spanwise drag distribution for the large nacelle geometry with gear deployed and flightidle thrust conditions at $\alpha = 12.0°$ $\frac{h}{b} = 0.155$ *for the take-off high lift configuration*

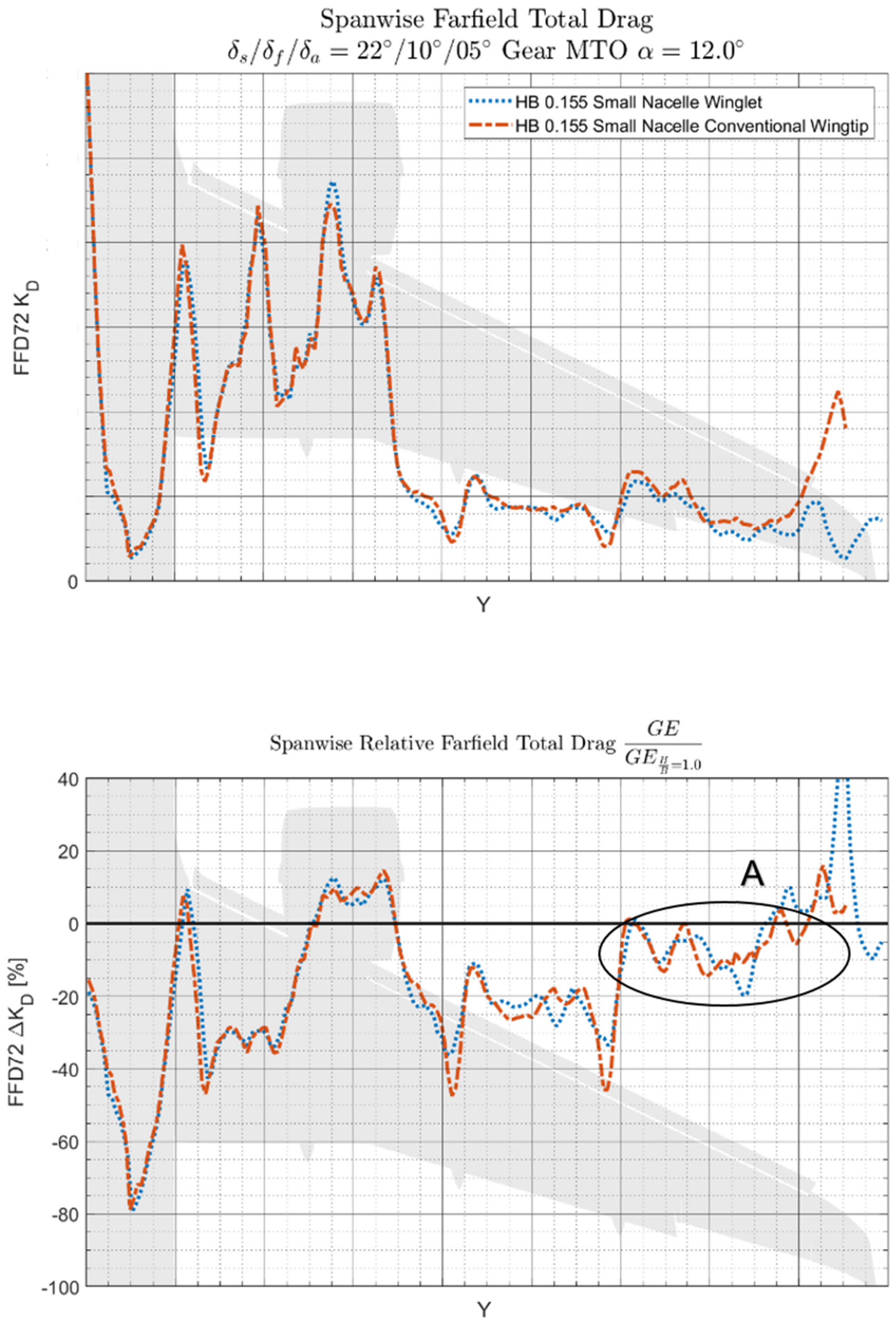

Figure 9.5 - Spanwise drag distribution for the small nacelle geometry with gear deployed and flightidle thrust conditions at $\alpha = 12.0°$ $\frac{h}{b} = 0.155$ for the take-off high lift configuration

9.2.3 Conclusions

It can be concluded that the influence of the ground effect on only the winglet lift is limited compared to the thrust, engine and landing gear effect. Only in the narrow range of $10.0° \leq$

$\alpha \leq 12.0°$ are clear differences present of up to 0.26% of total lift and slight change in drag due to ground effect. This is caused by the earlier onset of wingtip stall in ground effect. At lower and higher α the wingtip is either fully stalled or there is fully attached flow present, in that case the differences caused by ground effect are minimal and are limited to a small decrease in suction on the upper wingtip surface behind the leading edge suction peak.

No clear evidence was found that ground effect behavior over the entire wing gets changed by changing the wingtip geometry (and thus changing wingspan). The outboard wing section shows very limited changes of up to 1% in lift change due to ground effect. There was no clear influence found of wingtip geometry changing the ground effect behavior of the inboard wing section.

The same conclusion is reached when discussing the drag. Local to the wingtip a strong relative change in drag is present for the winglet geometry only and small differences on the outboard wing section are present, while the drag on the fuselage and inboard wing section remain unchanged.

9.3 Appendix C – Lift Increment Plots

In this appendix the lift increment data for the three high-lift configurations is presented, being the take-off configuration with MTO thrust settings, the landing configuration with MTO thrust settings and the landing configuration with flightidle thrust settings. For each configuration, the four data plots are provided, corresponding to the four geometry variants discussed in subsection 3.3.5.3. The scale of the Y-Axis is the same for all plots of the landing configuration, and for all plots of the take-off configuration.

9.3.1 Landing High-lift configuration – MTO Thrust Conditions

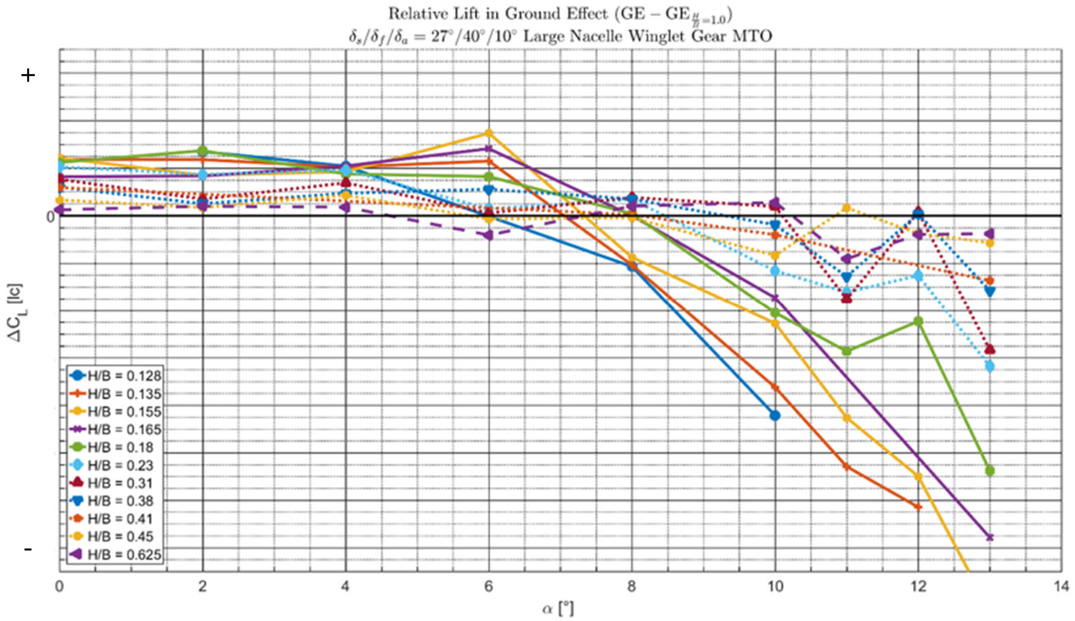

Figure 9.6 - Change in lift coefficient due to ground effect for a range of h/b for the large nacelle, winglet geometry with gear deployed in MTO thrust conditions in landing configuration

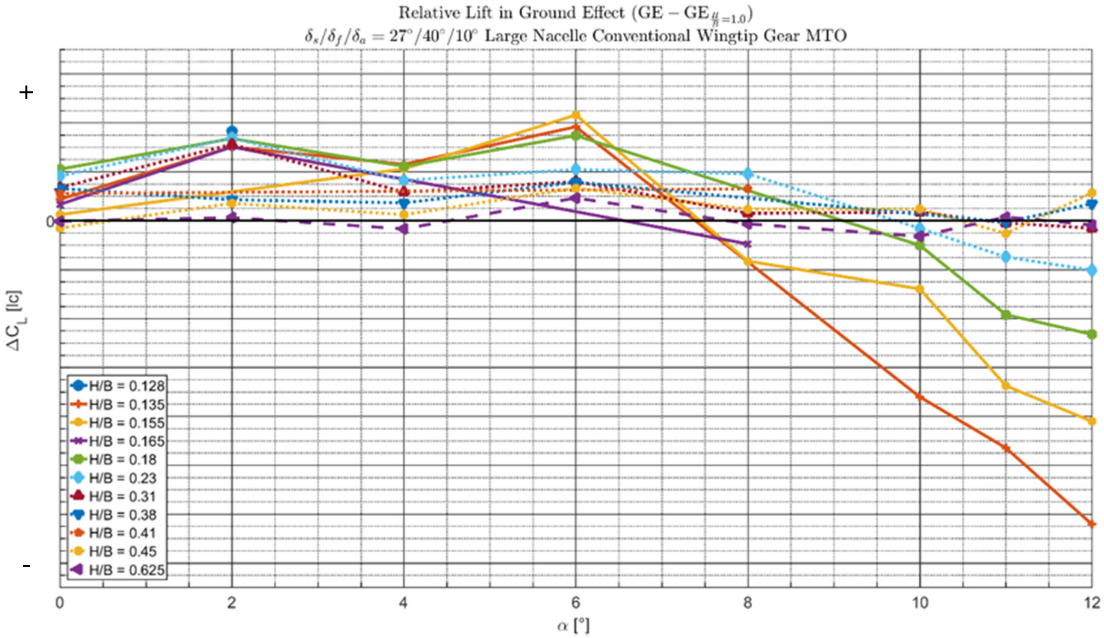

Figure 9.7 - Change in lift coefficient due to ground effect for a range of h/b for the large nacelle, conventional wingtip geometry with gear deployed in MTO thrust conditions in landing configuration

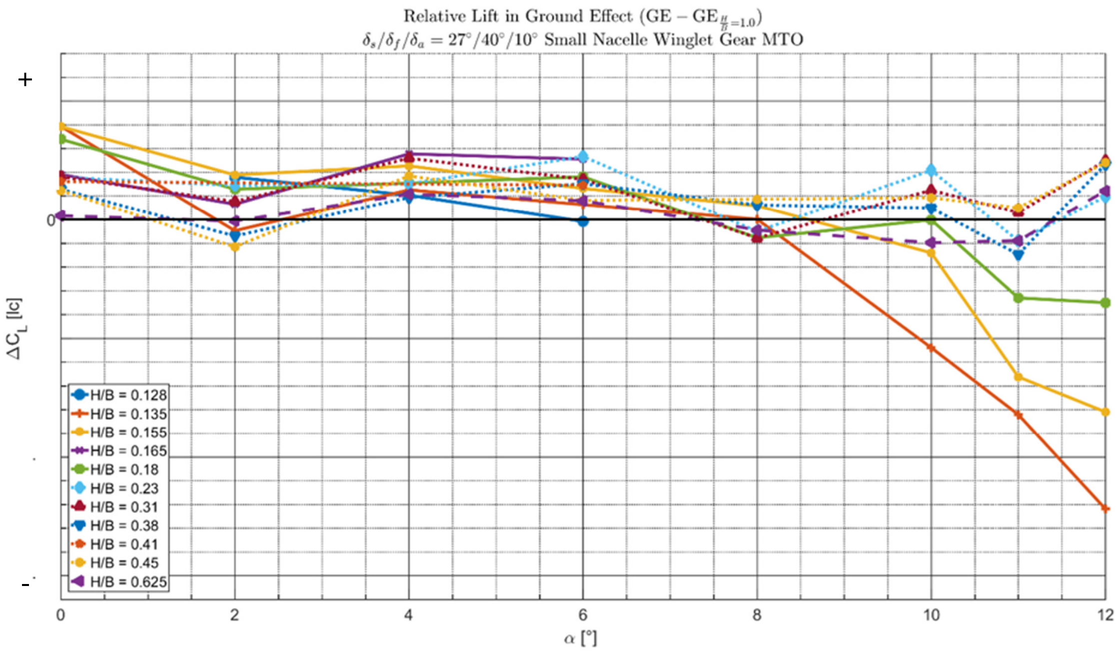

Figure 9.8 - Change in lift coefficient due to ground effect for a range of h/b for the small nacelle, winglet geometry with gear deployed in MTO thrust conditions in landing configuration

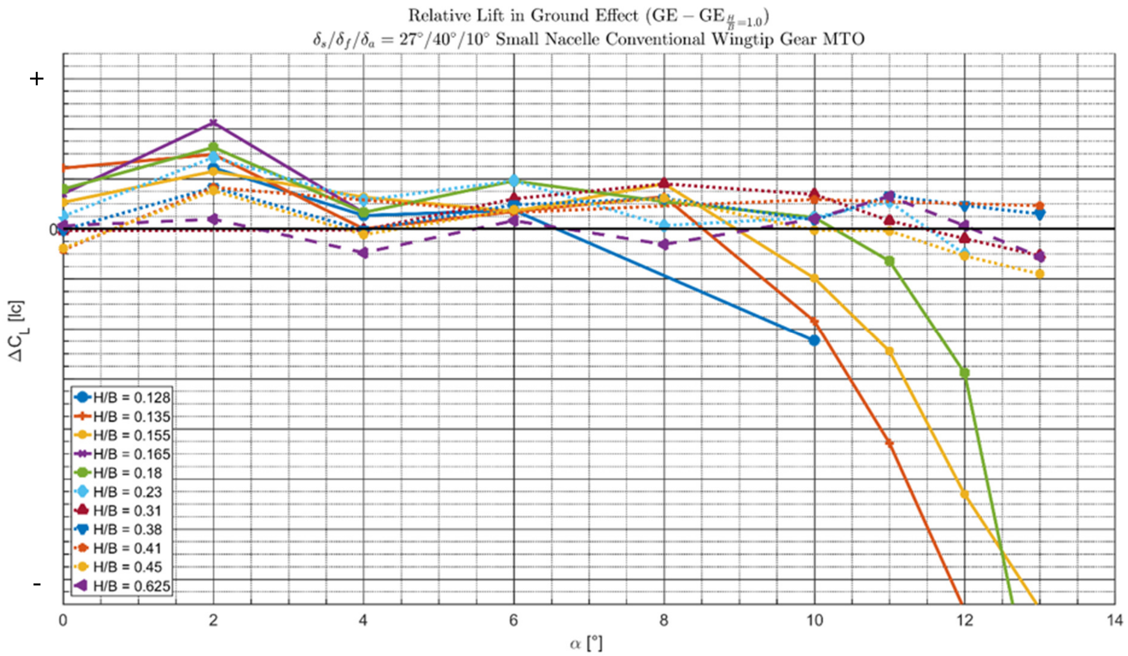

Figure 9.9 - Change in lift coefficient due to ground effect for a range of h/b for the small nacelle, conventional wingtip geometry with gear deployed in MTO thrust conditions in landing configuration

9.3.2 Landing High-lift configuration – Flightidle Thrust Conditions

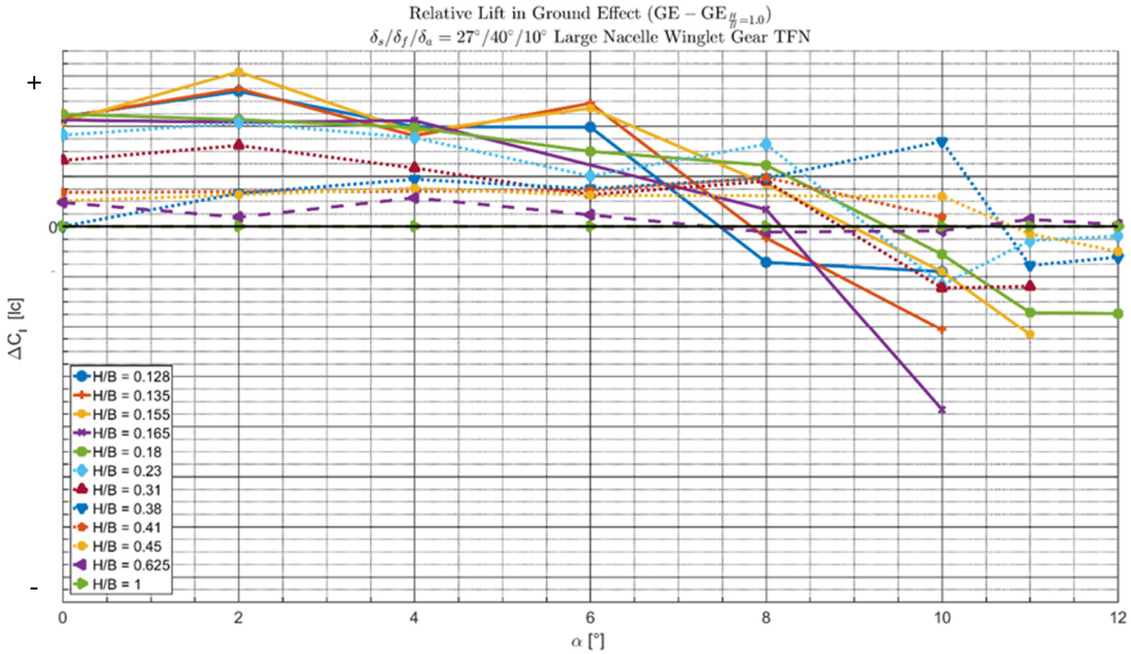

Figure 9.10 - Change in lift coefficient due to ground effect for a range of h/b for the large nacelle, winglet geometry with gear deployed in flightidle thrust conditions in landing configuration

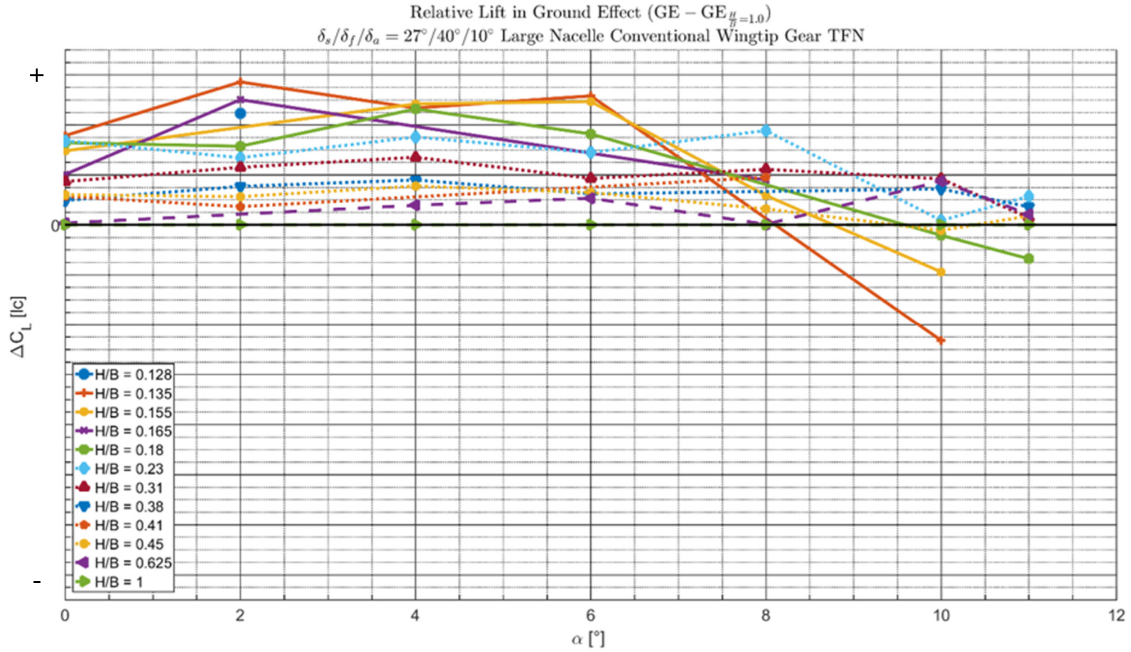

Figure 9.11 - Change in lift coefficient due to ground effect for a range of h/b for the large nacelle, conventional wingtip geometry with gear deployed in flightidle thrust conditions in landing configuration

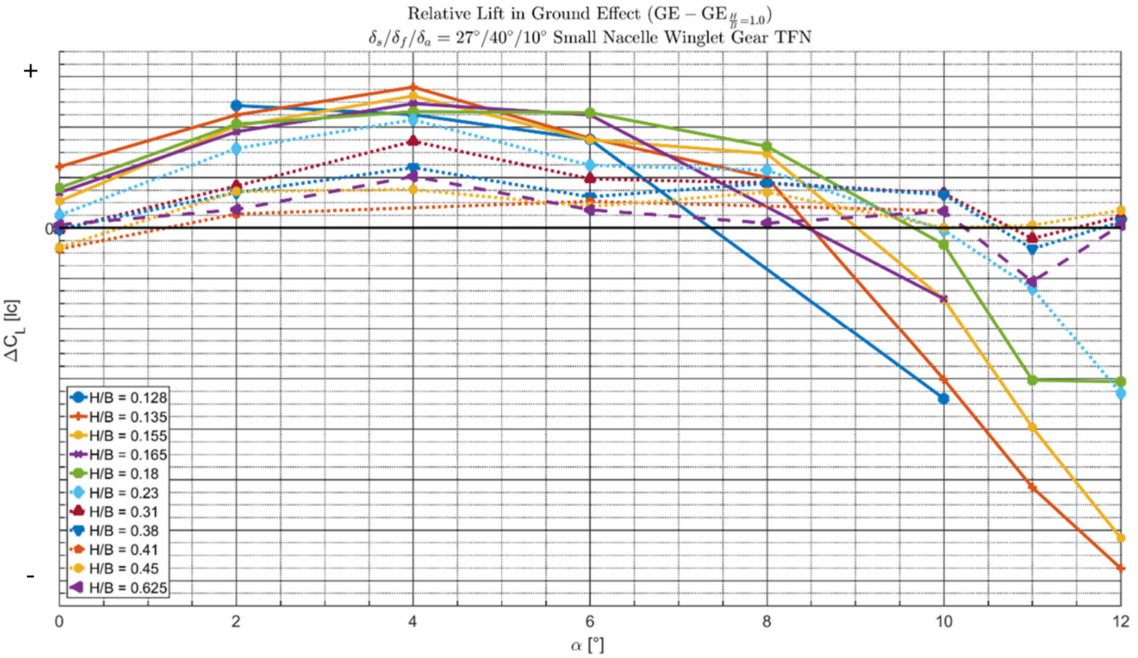

Figure 9.12 - Change in lift coefficient due to ground effect for a range of h/b for the small nacelle, winglet geometry with gear deployed in flightidle thrust conditions in landing configuration

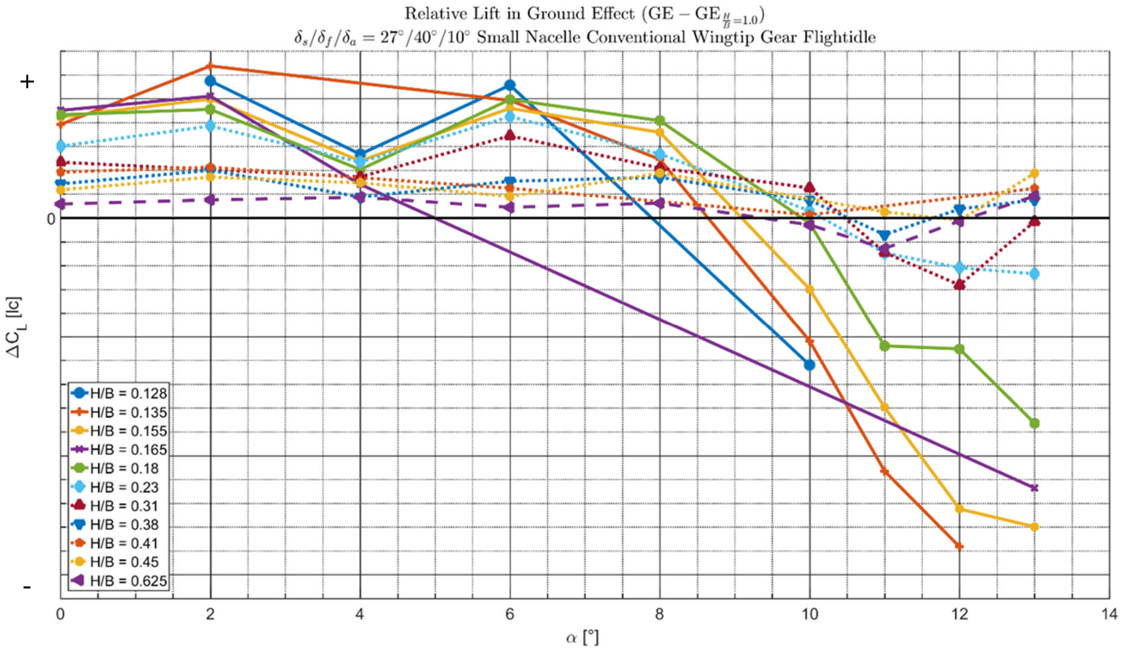

Figure 9.13 - Change in lift coefficient due to ground effect for a range of h/b for the small nacelle, conventional wingtip geometry with gear deployed in flightidle thrust conditions in landing configuration

9.3.3 Take-Off High-Lift configuration – MTO Thrust Conditions

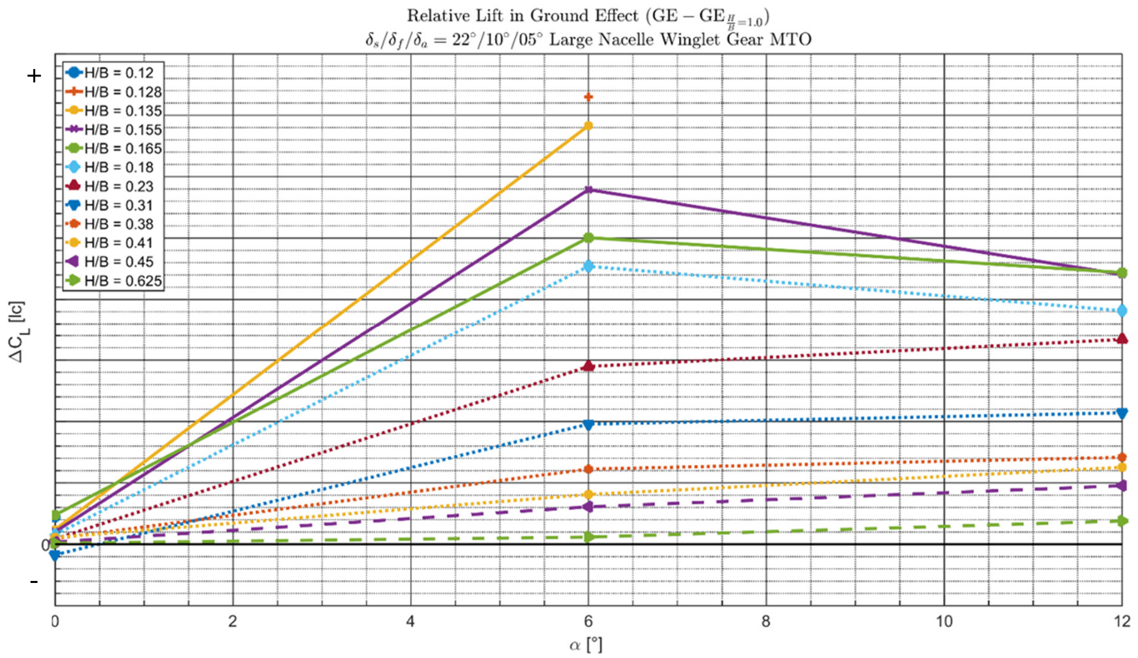

Figure 9.14 - Change in lift coefficient due to ground effect for a range of h/b for the large nacelle, winglet geometry with gear deployed in MTO thrust conditions in take-off configuration

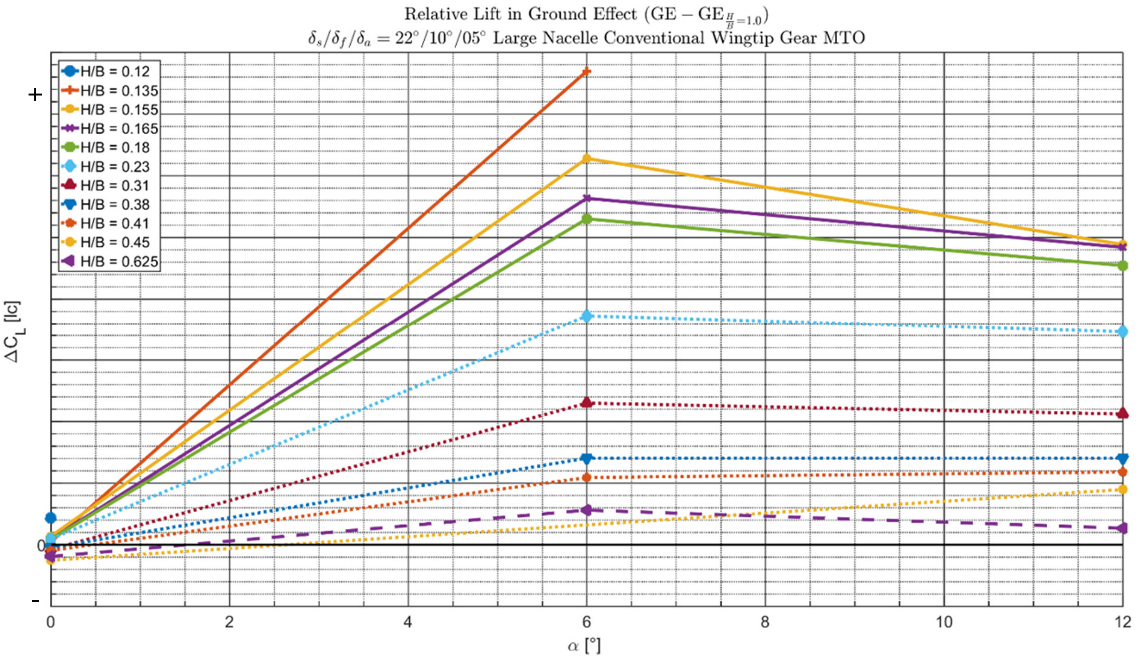

Figure 9.15 - Change in lift coefficient due to ground effect for a range of h/b for the large nacelle, conventional wingtip geometry with gear deployed in MTO thrust conditions in take-off configuration

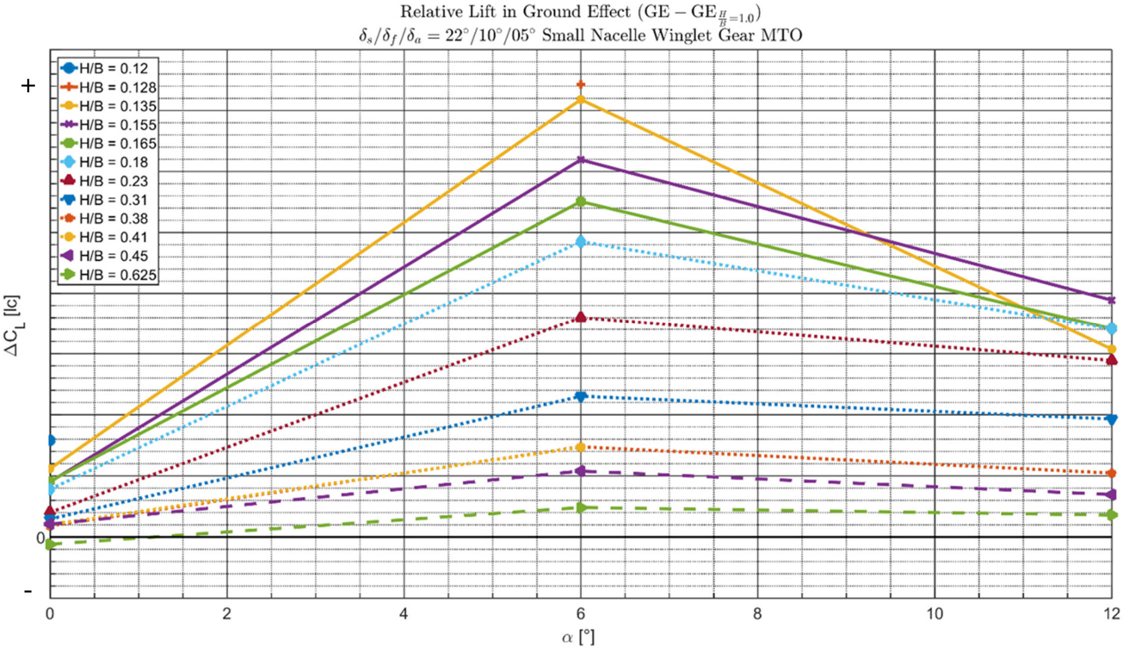

Figure 9.16 - Change in lift coefficient due to ground effect for a range of h/b for the small nacelle, winglet geometry with gear deployed in MTO thrust conditions in take-off configuration

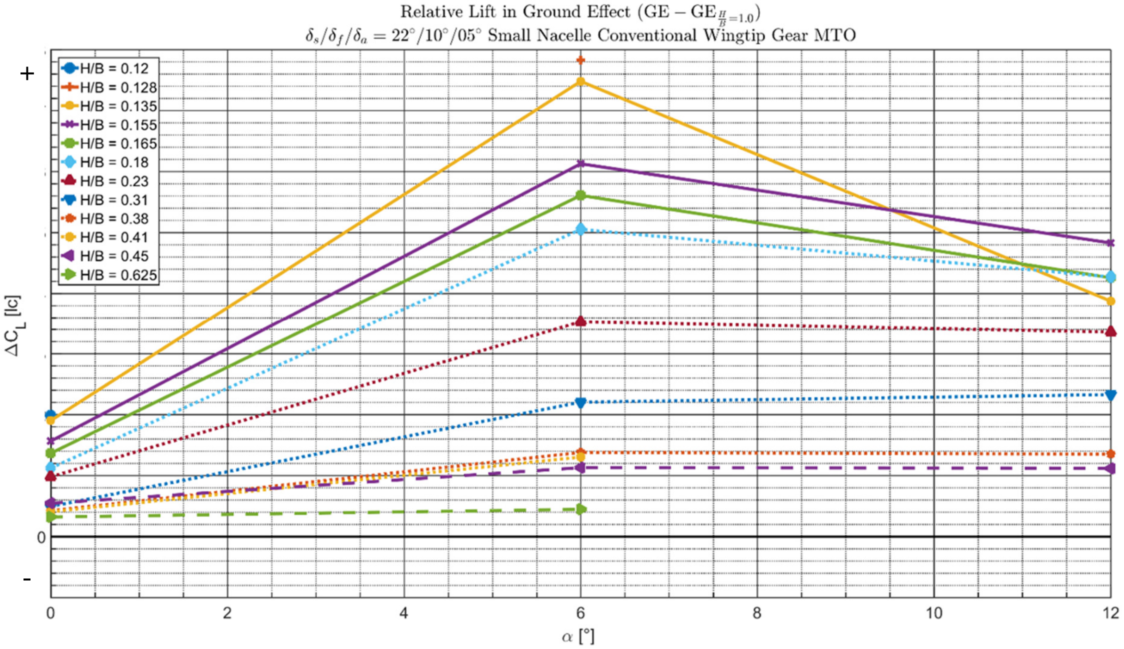

Figure 9.17 - Change in lift coefficient due to ground effect for a range of h/b for the small nacelle, conventional wingtip geometry with gear deployed in MTO thrust conditions in take-off configuration

9.4 Appendix D – Drag Increment Plots

In this appendix the drag increment data for the three high-lift configurations is presented, being the take-off configuration with MTO thrust settings, the landing configuration with MTO thrust settings and the landing configuration with flightidle thrust settings. For each configuration, the four data plots are provided, corresponding to the four geometry variants discussed in subsection 3.3.5.3. The scale of the Y-Axis is the same for all plots.

9.4.1 Landing High-lift configuration – MTO Thrust Conditions

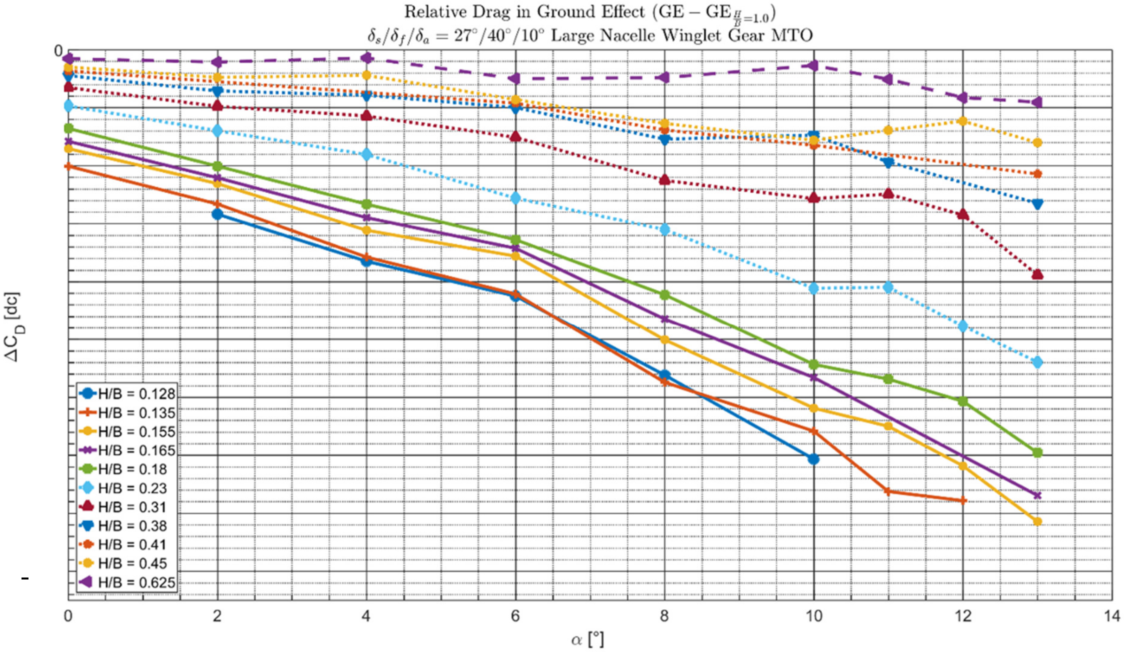

Figure 9.18 - Change in drag coefficient due to ground effect for a range of h/b for the large nacelle, winglet geometry with gear deployed in MTO thrust conditions in landing configuration

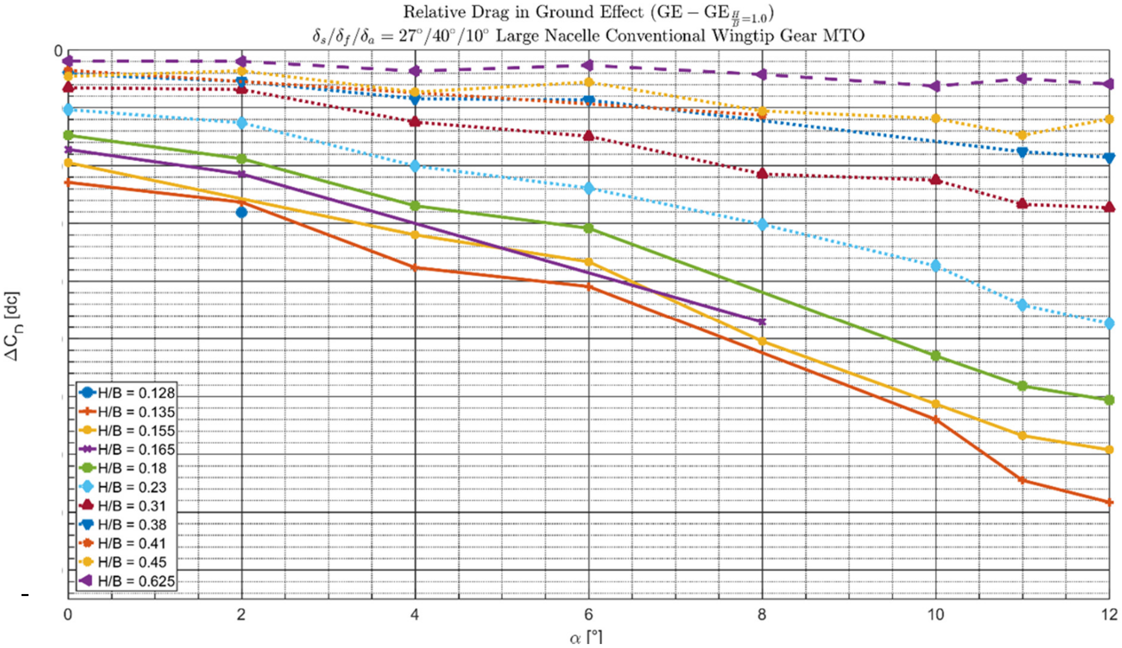

Figure 9.19 - Change in drag coefficient due to ground effect for a range of h/b for the large nacelle, conventional wingtip geometry with gear deployed in MTO thrust conditions in landing configuration

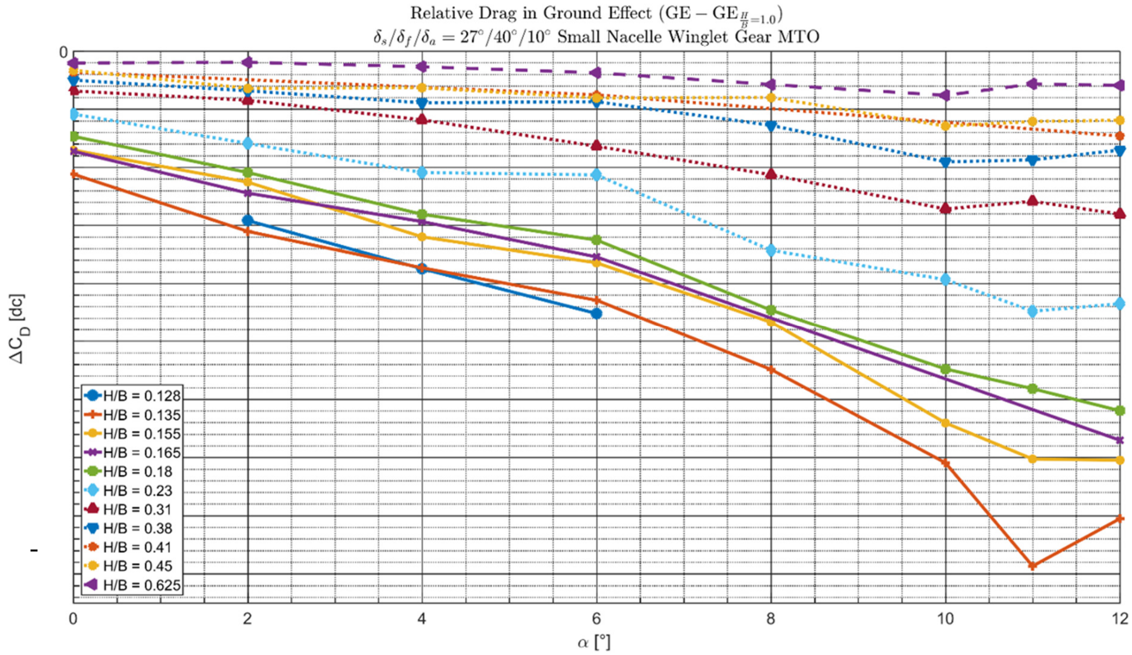

Figure 9.20 - Change in drag coefficient due to ground effect for a range of h/b for the small nacelle, winglet geometry with gear deployed in MTO thrust conditions in landing configuration

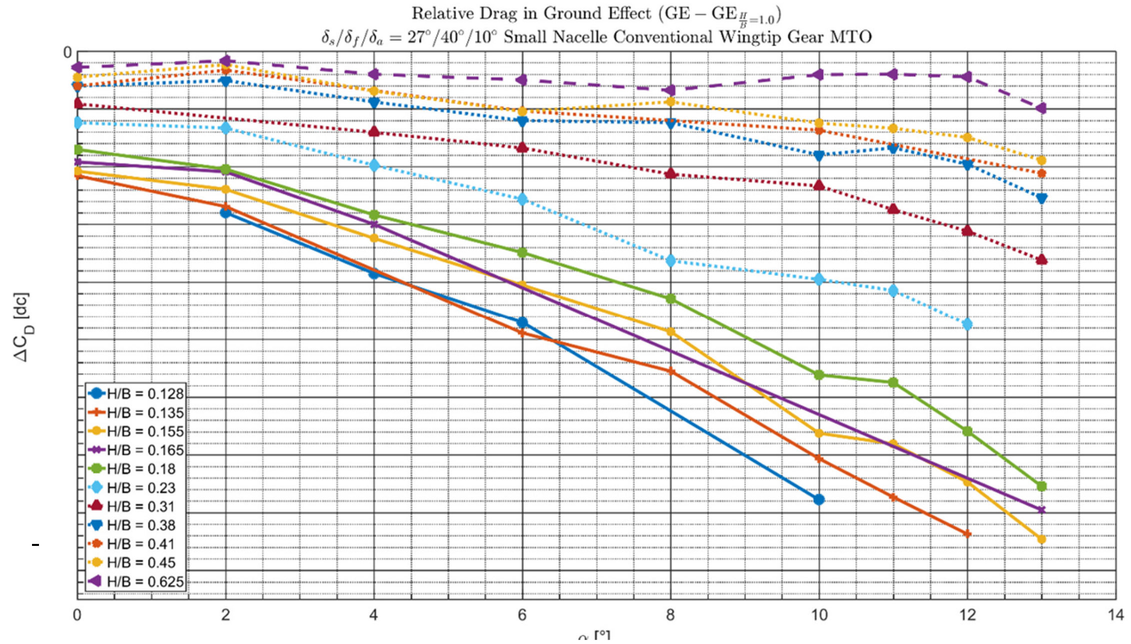

Figure 9.21 - Change in drag coefficient due to ground effect for a range of h/b for the small nacelle, conventional wingtip geometry with gear deployed in MTO thrust conditions in landing configuration

9.4.2 Landing High-lift configuration – Flightidle Thrust Conditions

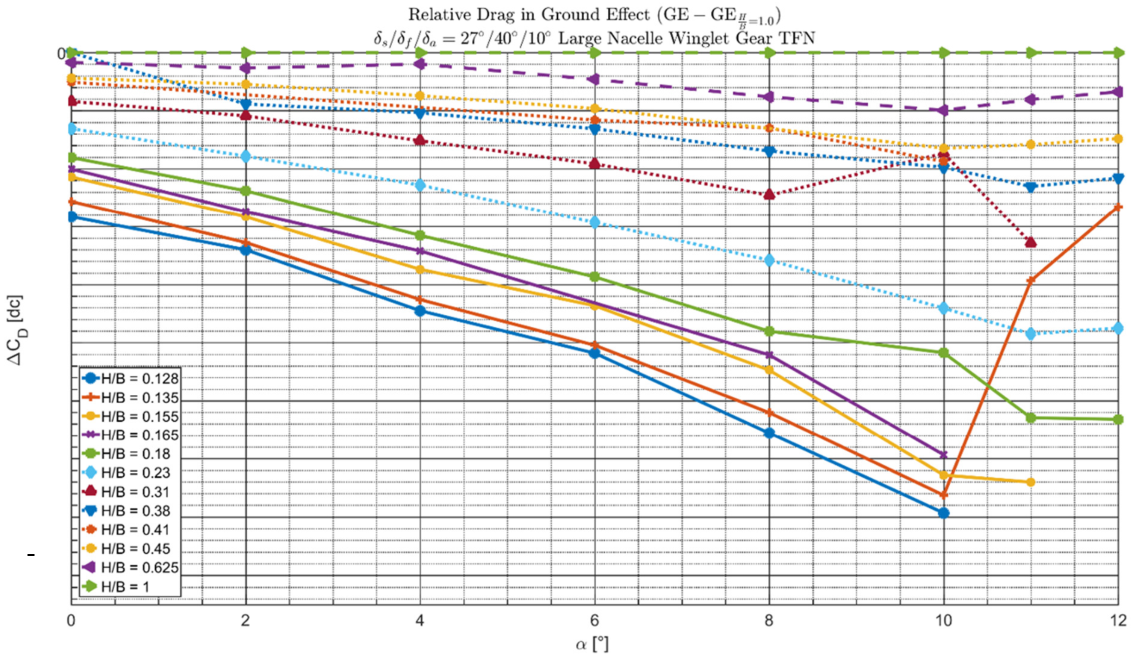

Figure 9.22 - Change in drag coefficient due to ground effect for a range of h/b for the large nacelle, winglet geometry with gear deployed in flightidle thrust conditions in landing configuration

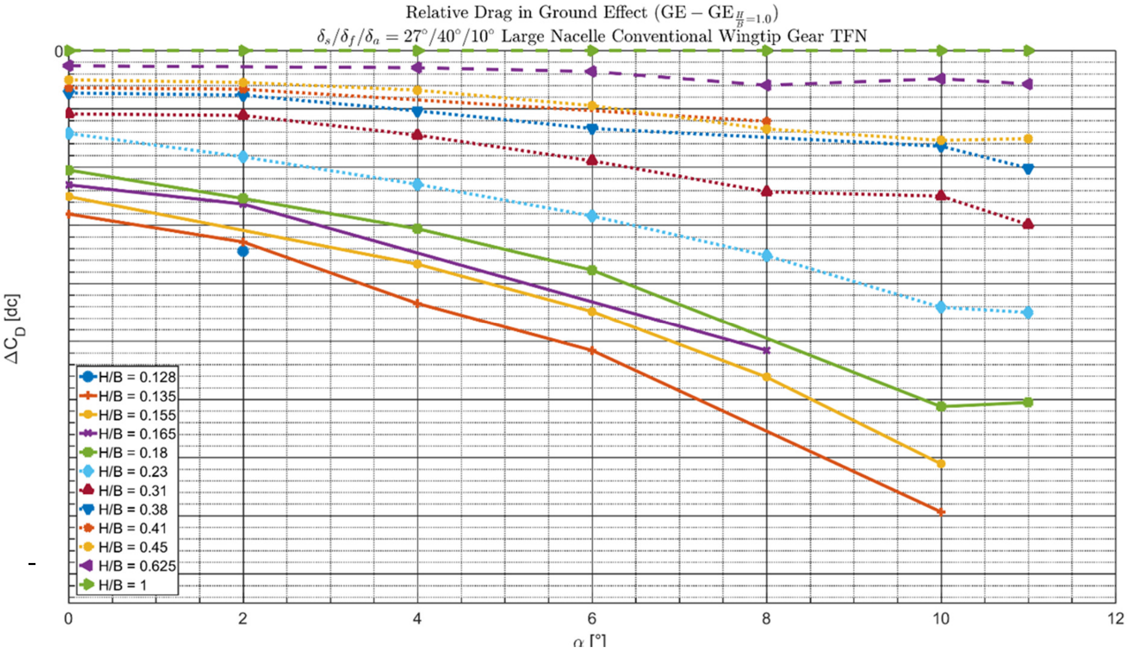

Figure 9.23 - Change in drag coefficient due to ground effect for a range of h/b for the large nacelle, conventional wingtip geometry with gear deployed in flightidle thrust conditions in landing configuration

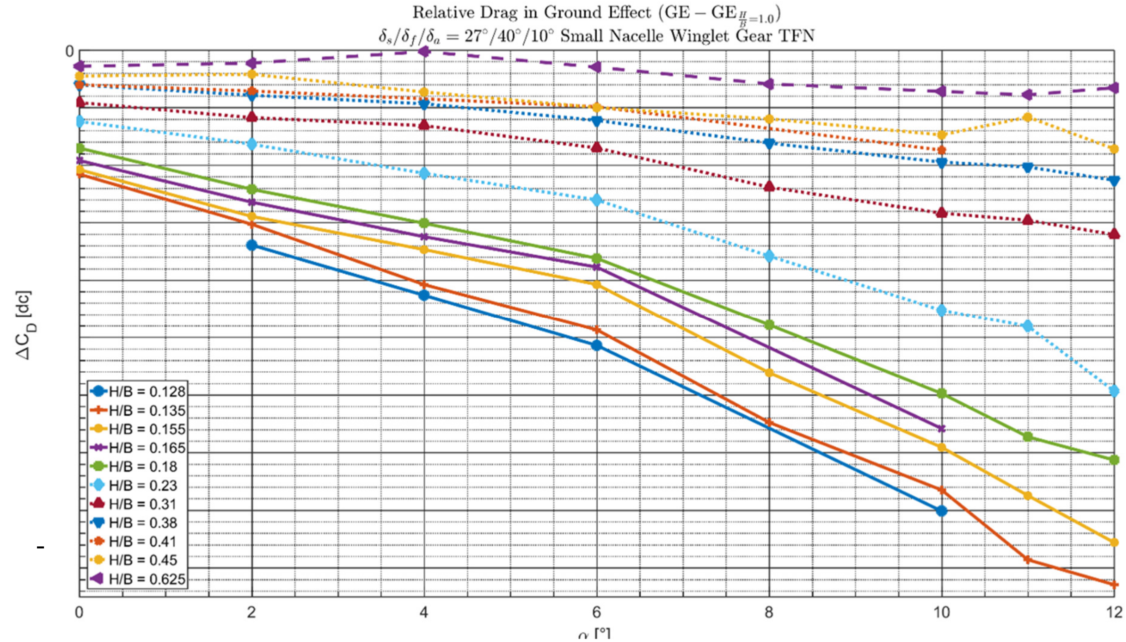

Figure 9.24 - Change in drag coefficient due to ground effect for a range of h/b for the small nacelle, winglet geometry with gear deployed in flightidle thrust conditions in landing configuration

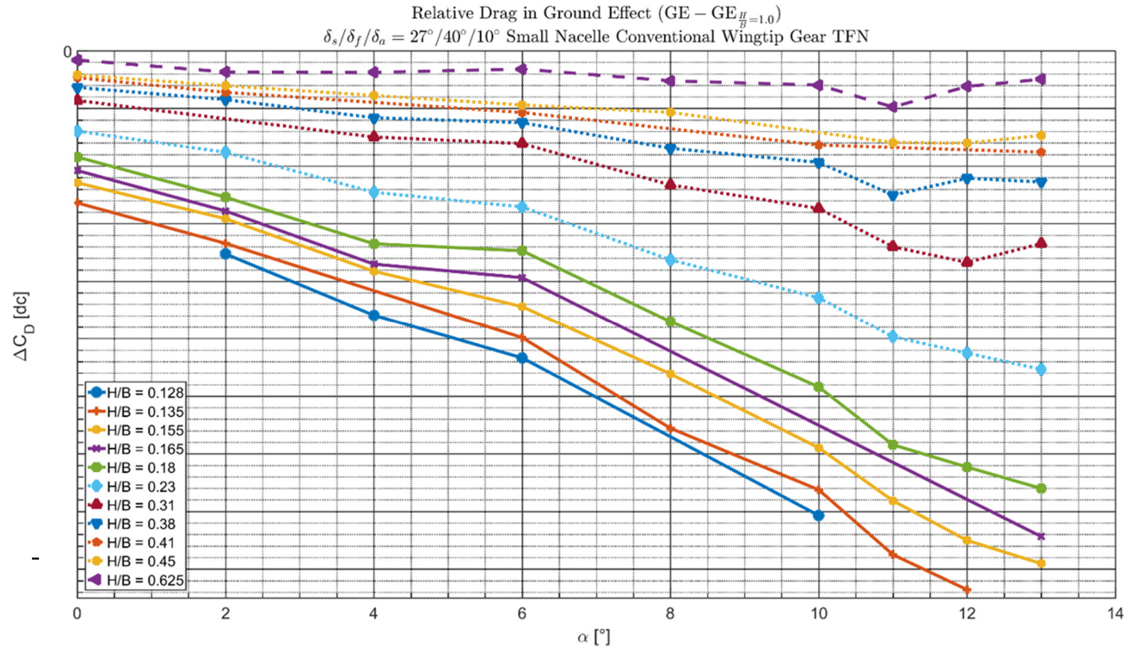

Figure 9.25 - Change in drag coefficient due to ground effect for a range of h/b for the small nacelle, conventional wingtip geometry with gear deployed in flightidle thrust conditions in landing configuration

9.4.3 Take-Off High-Lift configuration – MTO Thrust Conditions

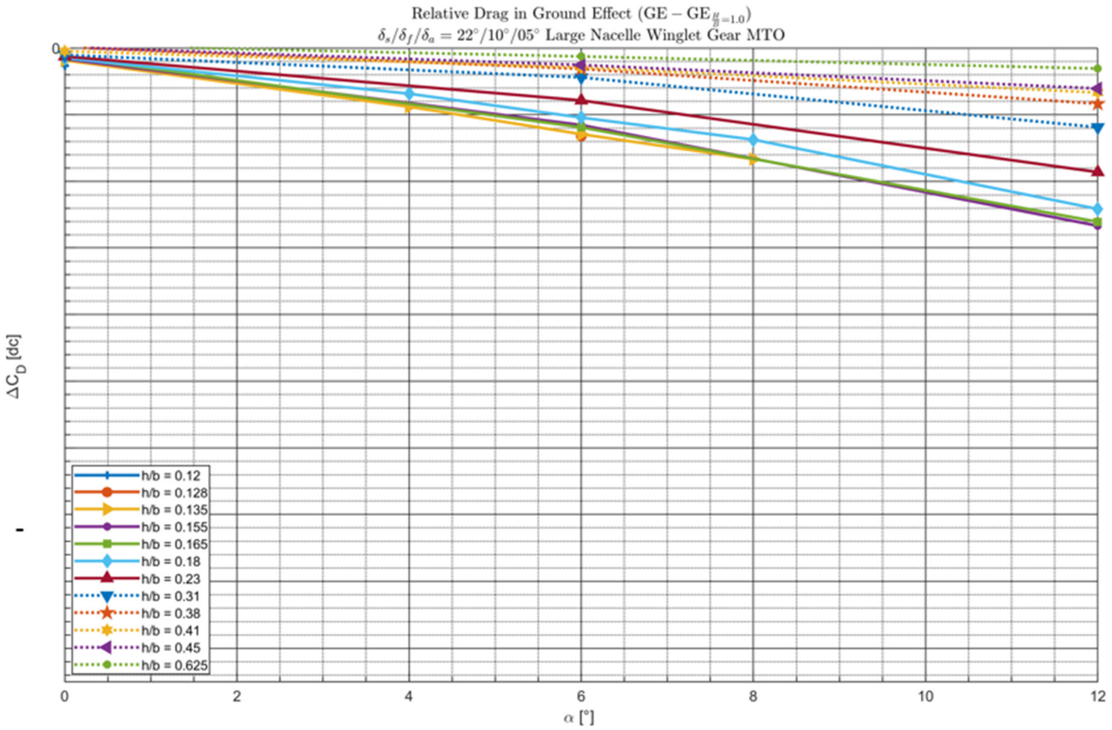

Figure 9.26 - Change in drag coefficient due to ground effect for a range of h/b for the large nacelle, winglet geometry with gear deployed in MTO thrust conditions in take-off configuration

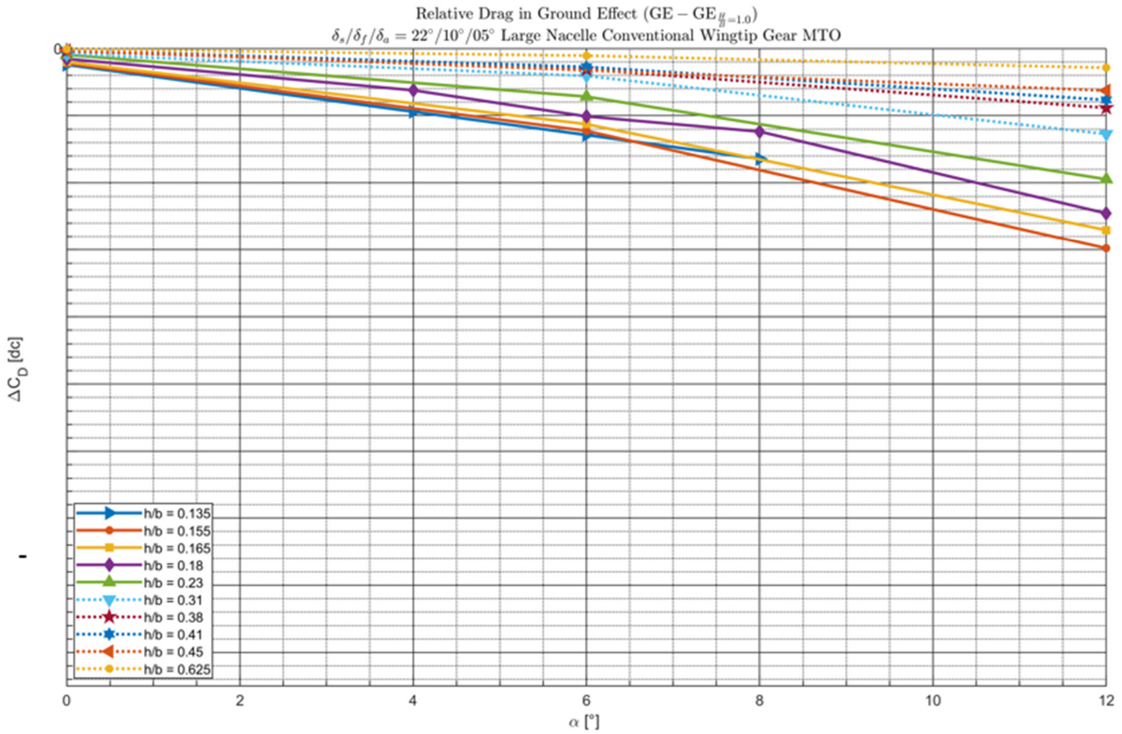

Figure 9.27 - Change in drag coefficient due to ground effect for a range of h/b for the large nacelle, conventional wingtip geometry with gear deployed in MTO thrust conditions in take-off configuration

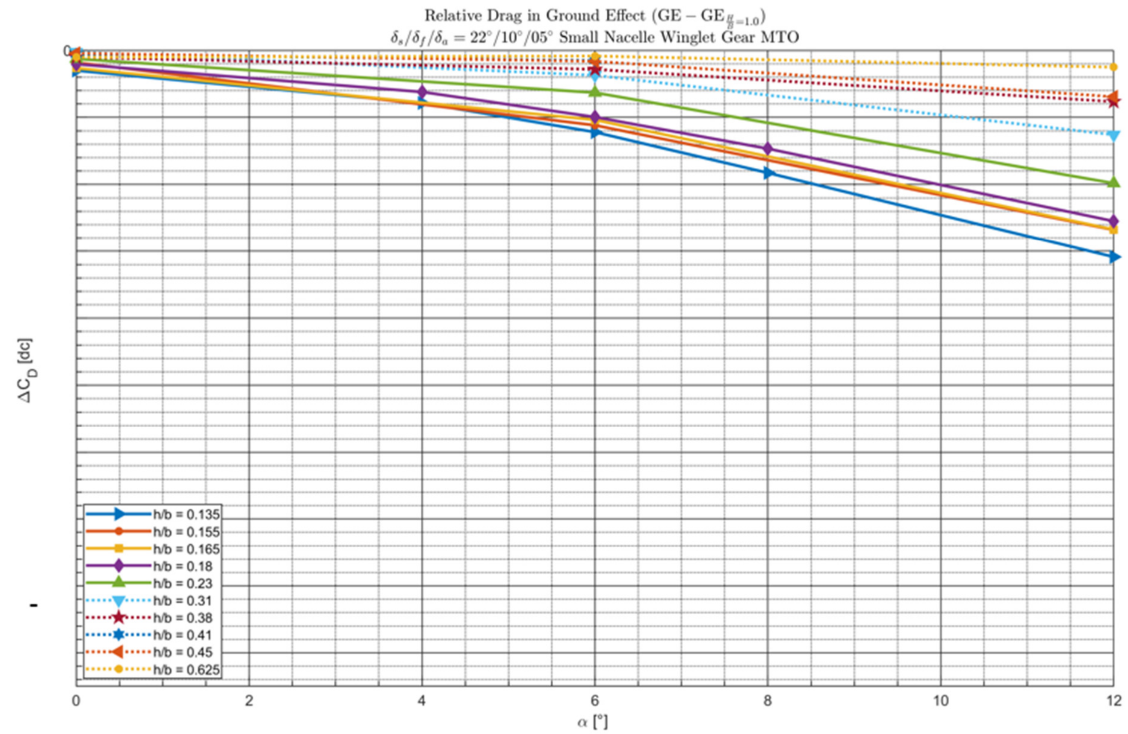

Figure 9.28 - Change in drag coefficient due to ground effect for a range of h/b for the small nacelle, winglet geometry with gear deployed in MTO thrust conditions in take-off configuration

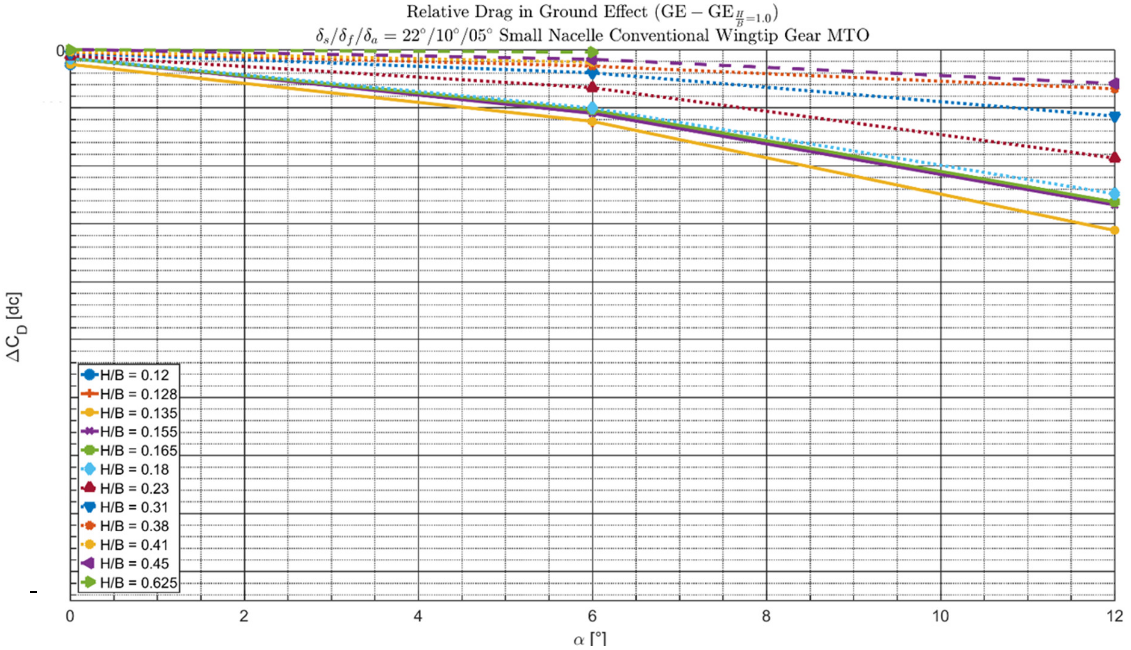

Figure 9.29 - Change in drag coefficient due to ground effect for a range of h/b for the small nacelle, conventional wingtip geometry with gear deployed in MTO thrust conditions in take-off configuration

9.5 Appendix E - Cut locations

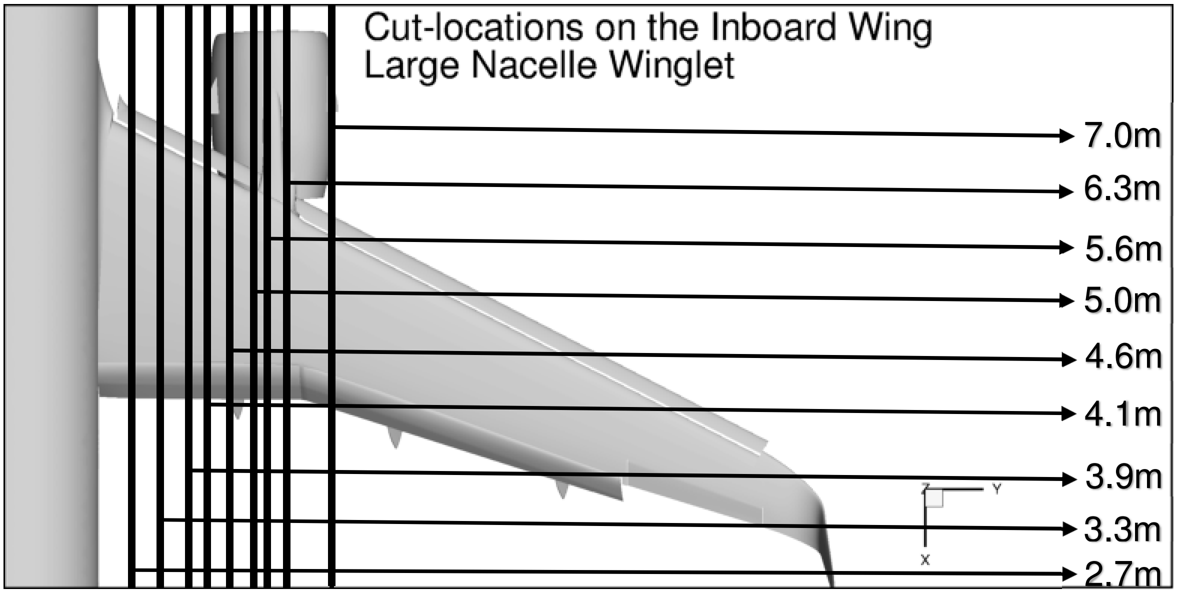

Figure 9.30 - Inboard Wing Cut Locations

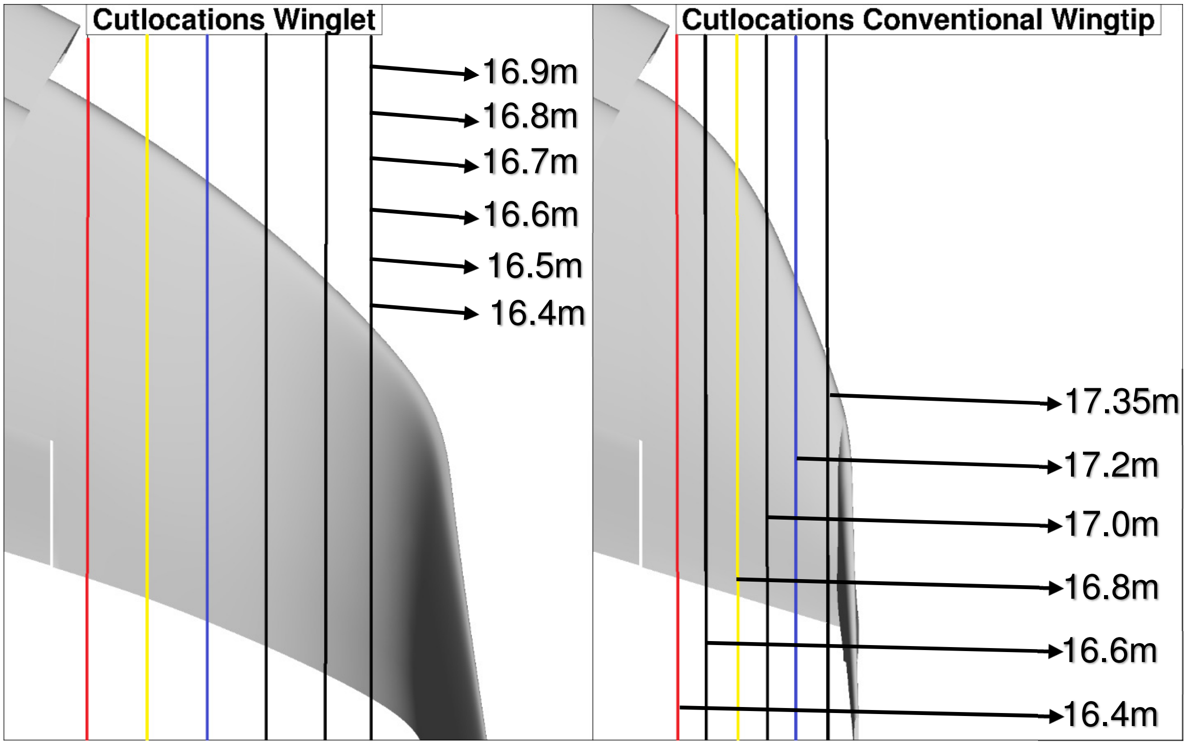

Figure 9.31 – Cut-locations on the wingtip area for the Winglet (left) and conventional Wingtip (right). Same colors correspond to same cut location. Scale is identical for both pictures.

9.6 Appendix F – Thrust Effect Pressure Plots

Slats

The locations of these cuts is visualized in Figure 9.30, located in Appendix E - Cut locations. Figure 9.32 and Figure 9.33, which show the C_p distribution around the inboard slat for $\alpha = 2.0$ and $\alpha = 12.0$, as well as the outboard slat in the region of the engine (6.3m and 7.0m respectively).

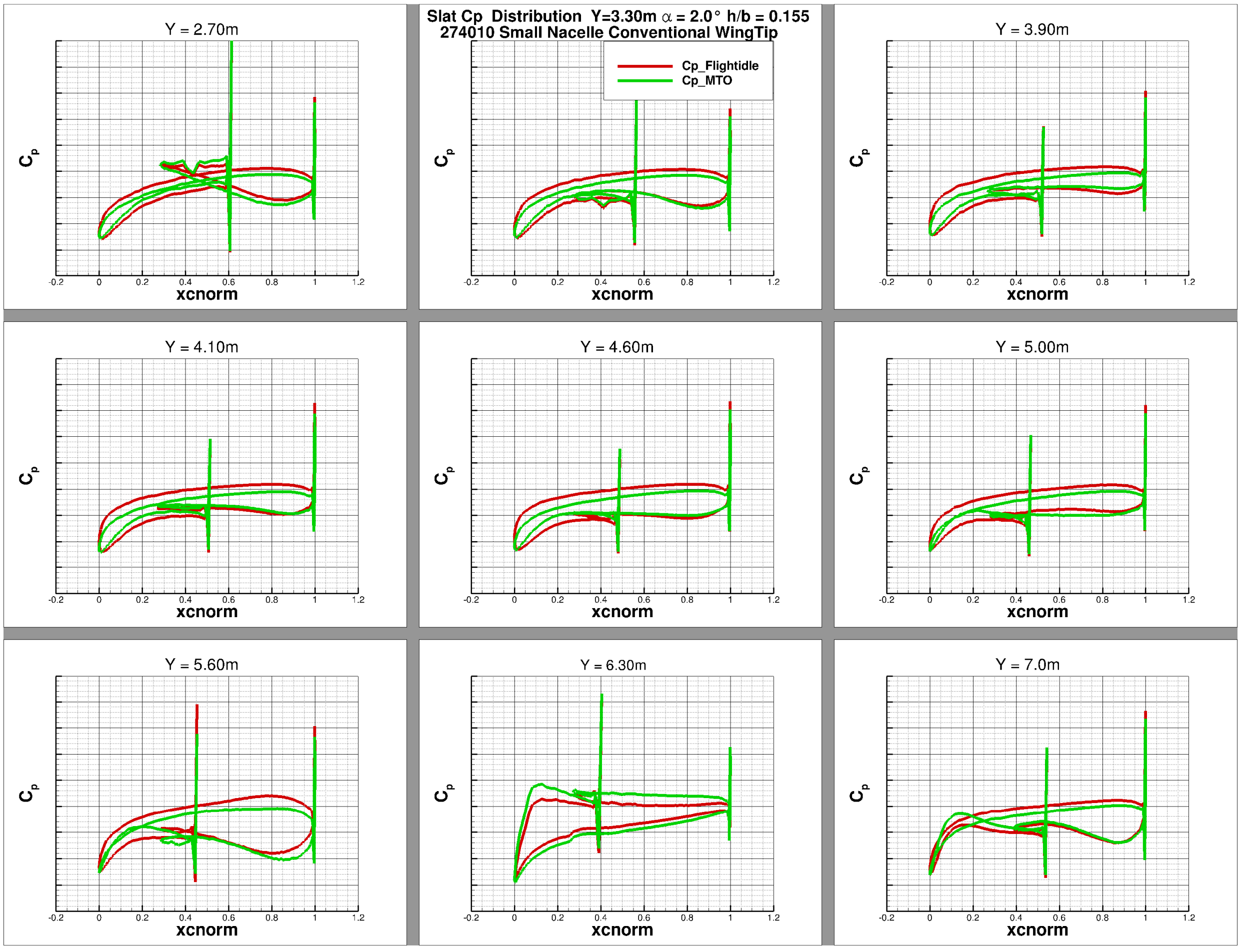

Figure 9.32 – Pressure Distribution on slats for MTO and Flightidle thrust settings $\alpha = 2.0° \; \frac{h}{b} = 0.155$

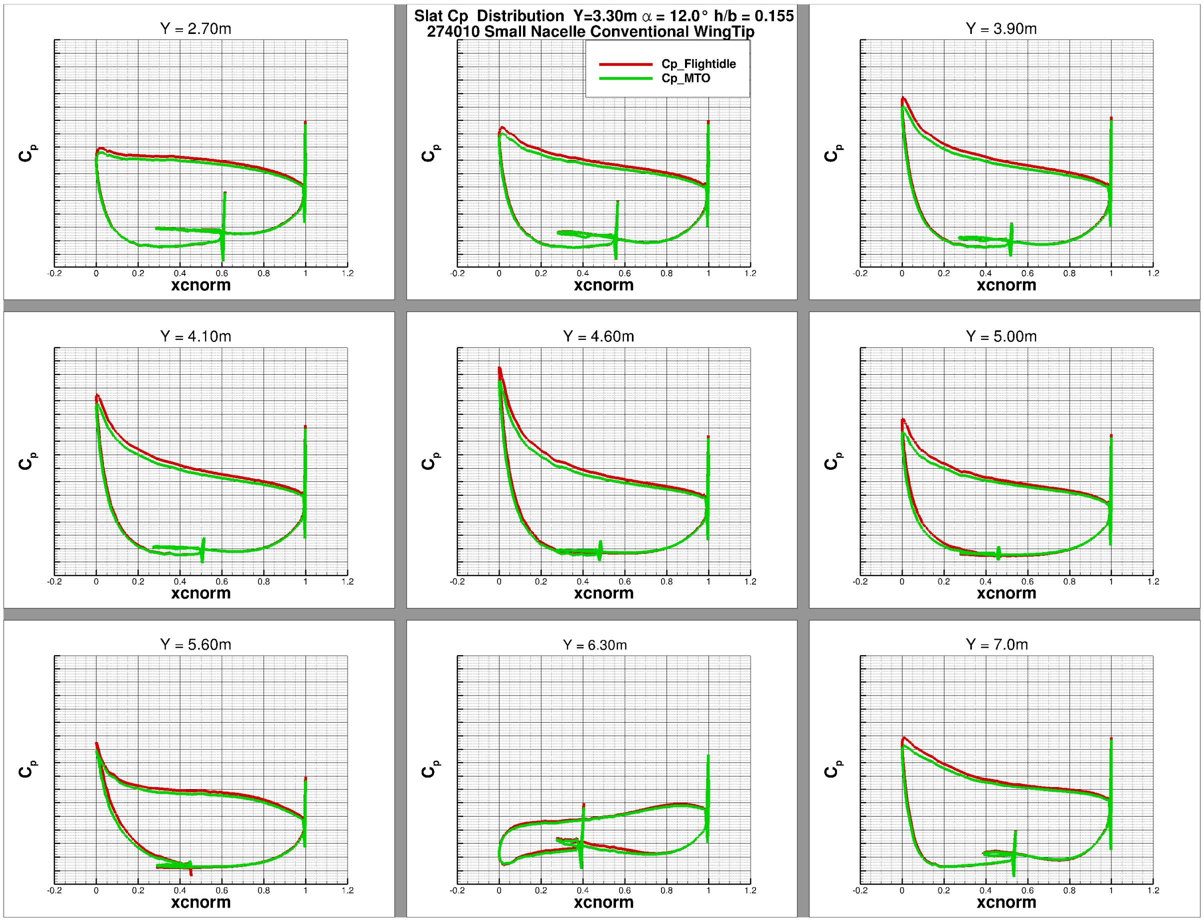

Figure 9.33 – Pressure Distribution on slats for MTO and flightidle thrust settings $\alpha = 12.0° \; \frac{h}{b} = 0.155$

Flaps

The flap gap effect can be observed in the flap C_p plots shown in Figure 9.34 and Figure 9.35 for respectively $\alpha = 2.0$ and $\alpha = 12.0$. At $Y = 2.7$, located very close to the fuselage and seen in the top left of, the influence of the engine on the flap is negligible. As the value of Y increases, the influence of the engine becomes visible and a higher suction peak on the flap leading edge is visible for the MTO engine settings case. This effect is also significantly increased with α.

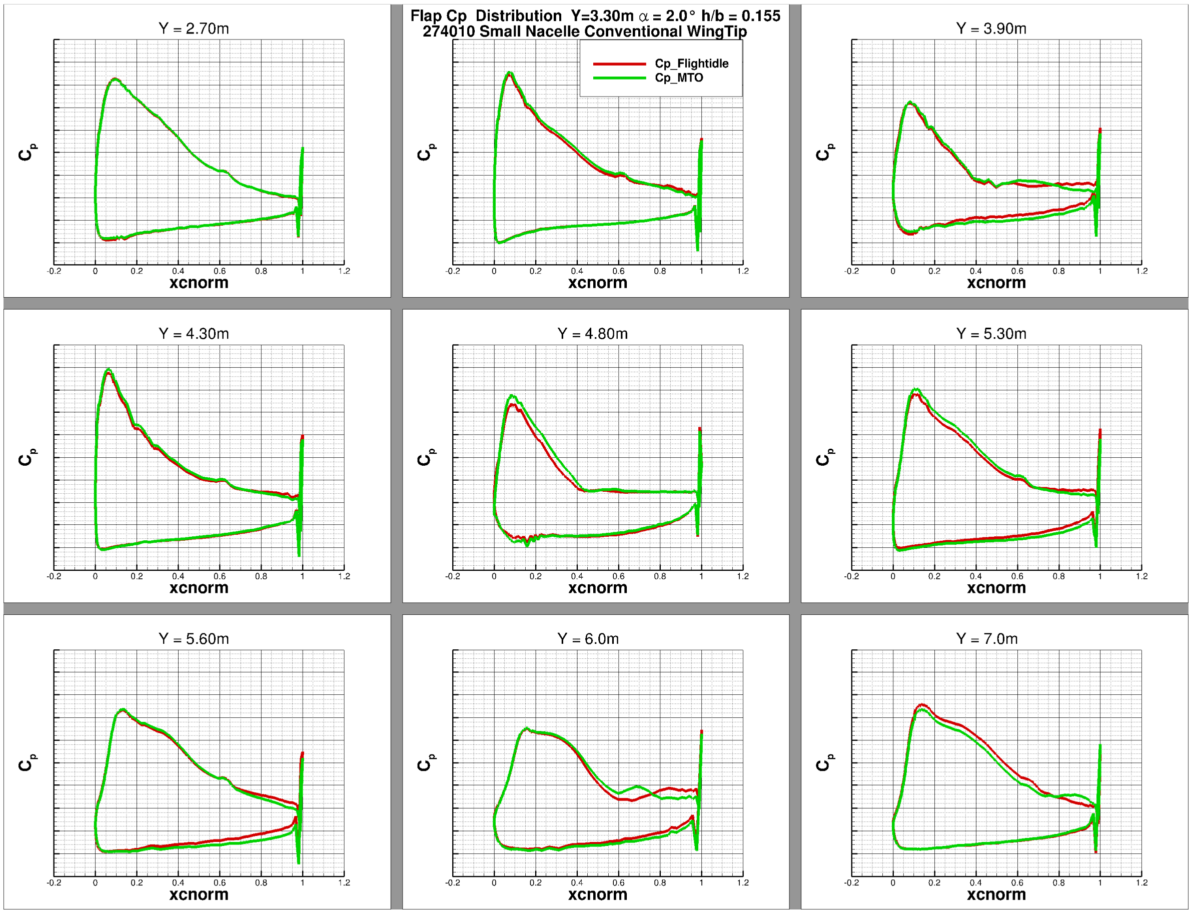

Figure 9.34 – Pressure Distribution on flaps for MTO and Flightidle thrust settings $\alpha = 2.0° \; \frac{h}{b} = 0.155$

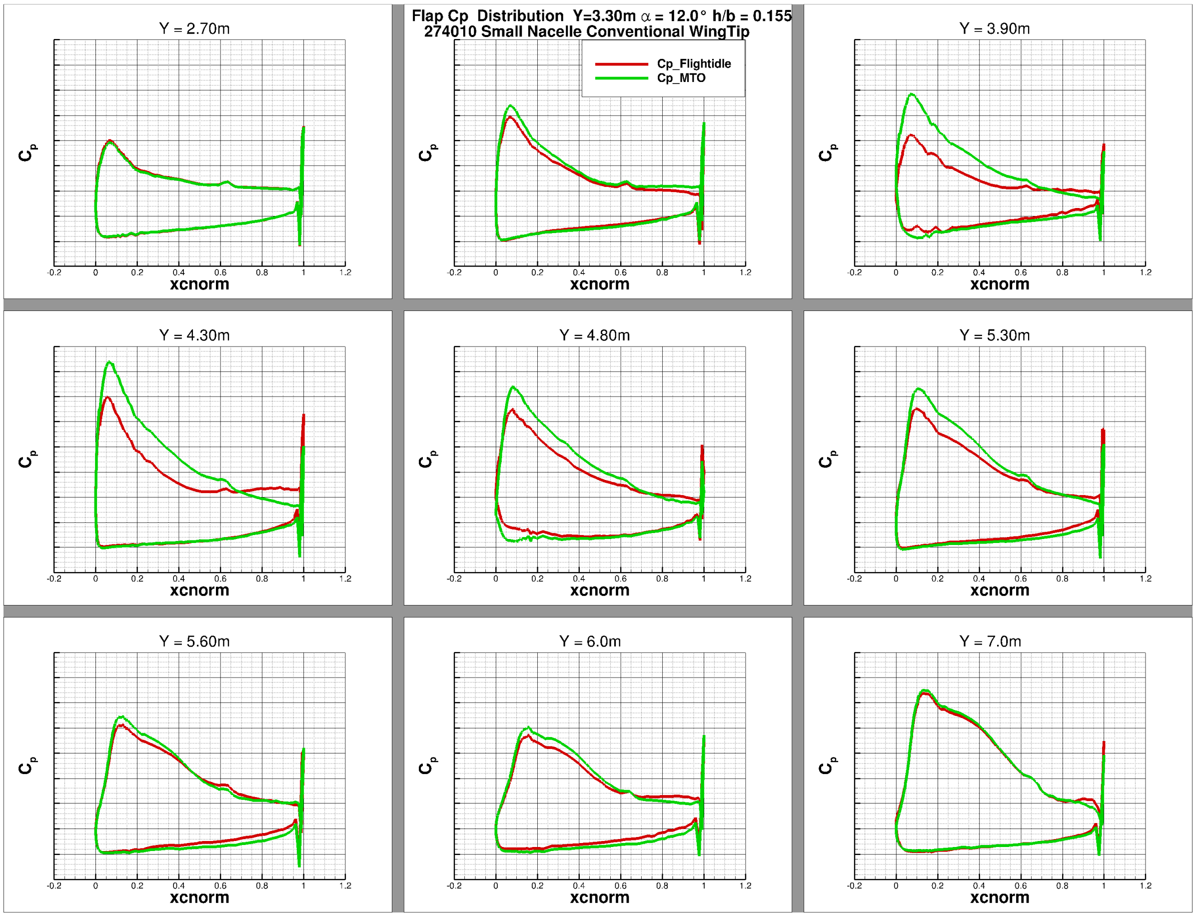

Figure 9.35 – Pressure Distribution on flaps for MTO and Flightidle thrust settings $\alpha = 12.0°$ $\frac{h}{b} = 0.155$

9.7 Appendix G – Wing Tip Pressure Coefficient Plots

9.7.1 Take-off High-Lift Configuration

9.7.1.1 Winglet

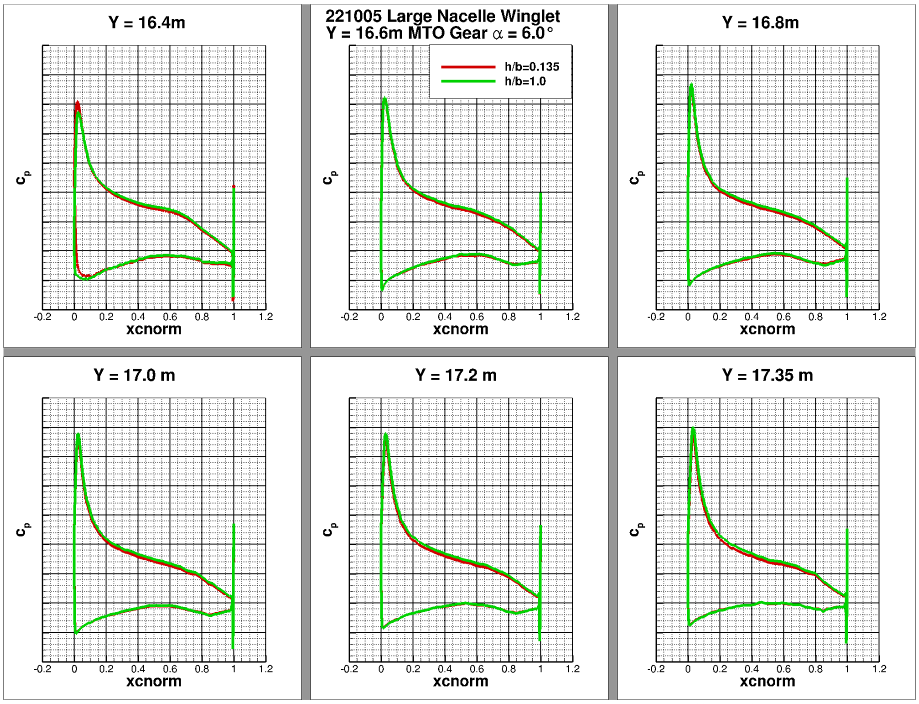

Figure 9.36 – C_P distribution at the wingtip at various cut locations for the take-off configuration, large nacelle and winglet geometry with gear deployed and maximum thrust setting applied at $\alpha = 6.0°$

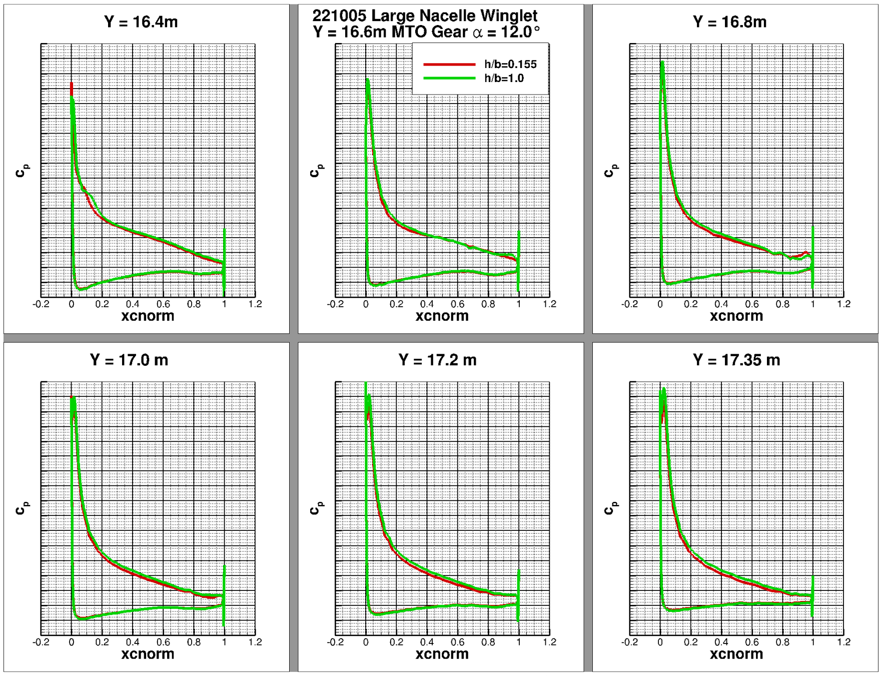

Figure 9.37 – C_P distribution at the wingtip at various cut locations for the take-off configuration, large nacelle and winglet geometry with gear deployed and maximum thrust setting applied at $\alpha = 12.0°$

9.7.1.2 Conventional Tip

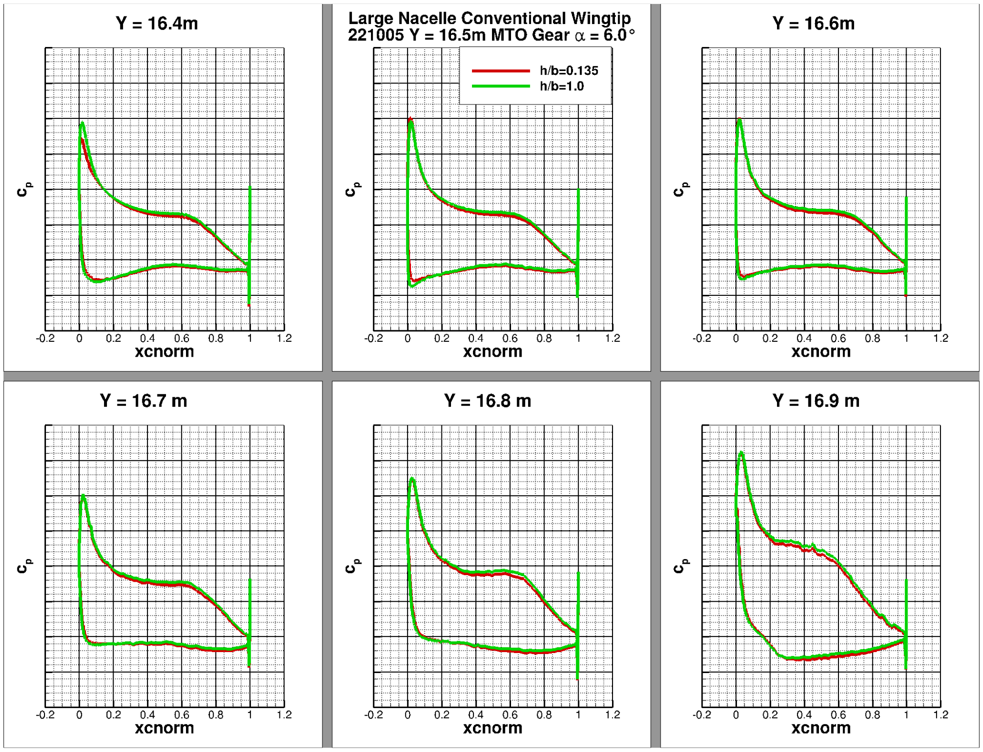

Figure 9.38 – C_P distribution at the wingtip at various cut locations for the take-off configuration, large nacelle and conventional wingtip geometry with gear deployed and maximum thrust setting applied at $\alpha = 6.0°$

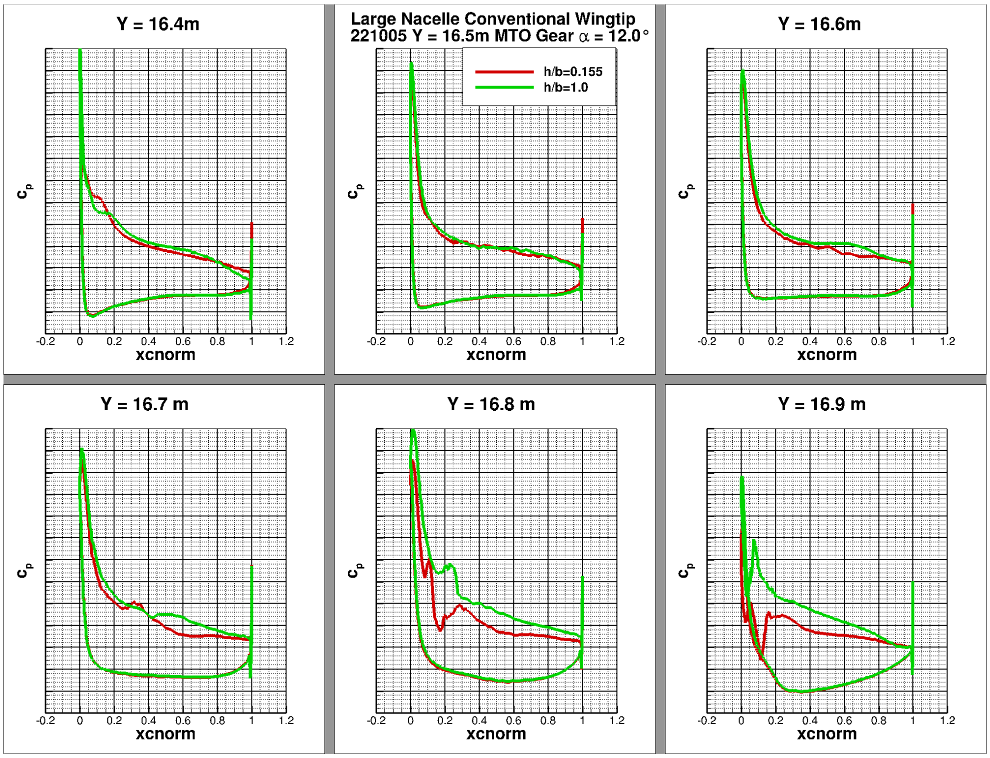

Figure 9.39 – C_P distribution at the wingtip at various cut locations for the take-off configuration, large nacelle and conventional wingtip geometry with gear deployed and maximum thrust setting applied at $\alpha = 12.0°$

9.7.2 Landing High-Lift Configuration

9.7.2.1 Large Nacelle Winglet Gear Geometry

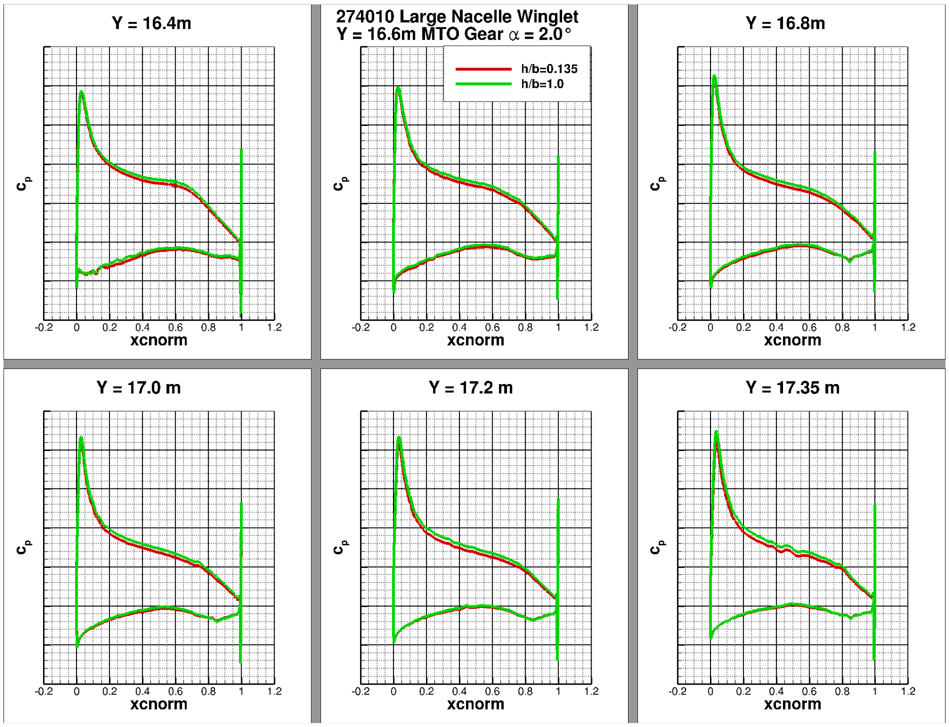

Figure 9.40 – C_P distribution at the wingtip at various cut locations for the landing configuration, large nacelle and winglet geometry with gear deployed and maximum thrust setting applied at $\alpha = 2.0°$

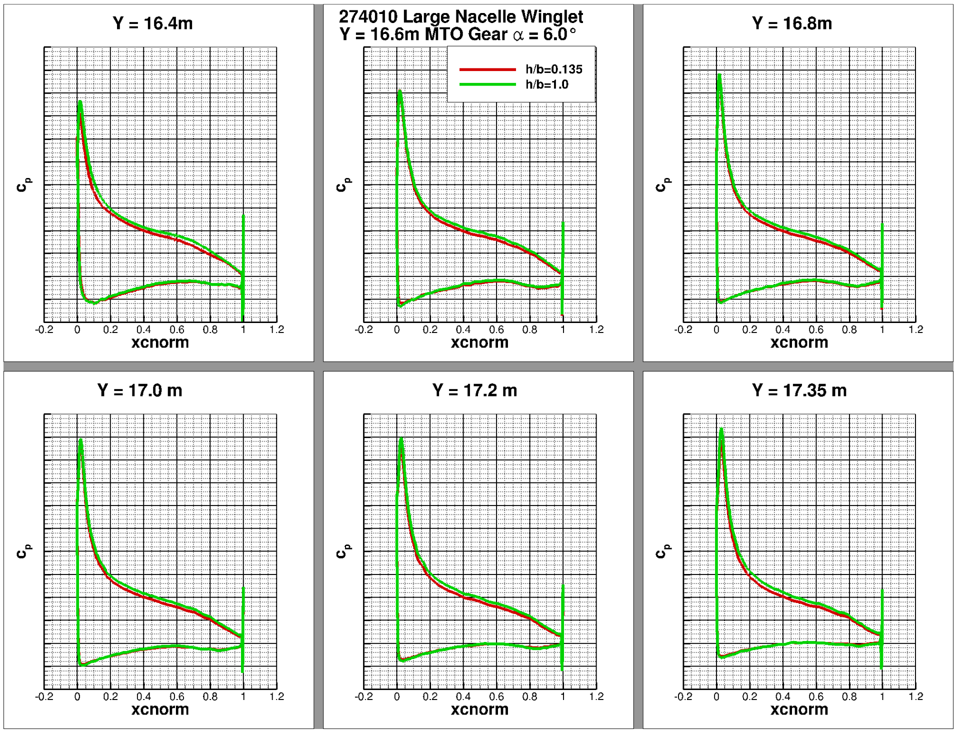

Figure 9.41 – C_P distribution at the wingtip at various cut locations for the landing configuration, large nacelle and winglet geometry with gear deployed and maximum thrust setting applied at $\alpha = 6.0°$

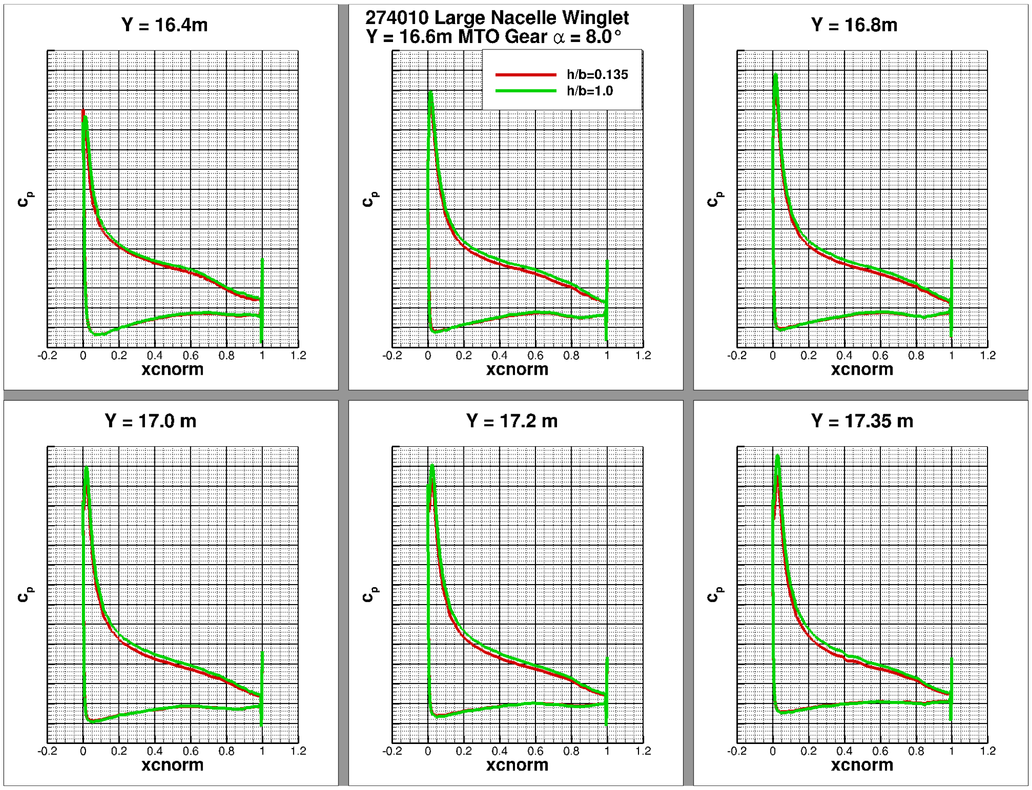

Figure 9.42 – C_P distribution at the wingtip at various cut locations for the landing configuration, large nacelle and winglet geometry with gear deployed and maximum thrust setting applied at $\alpha = 8.0°$

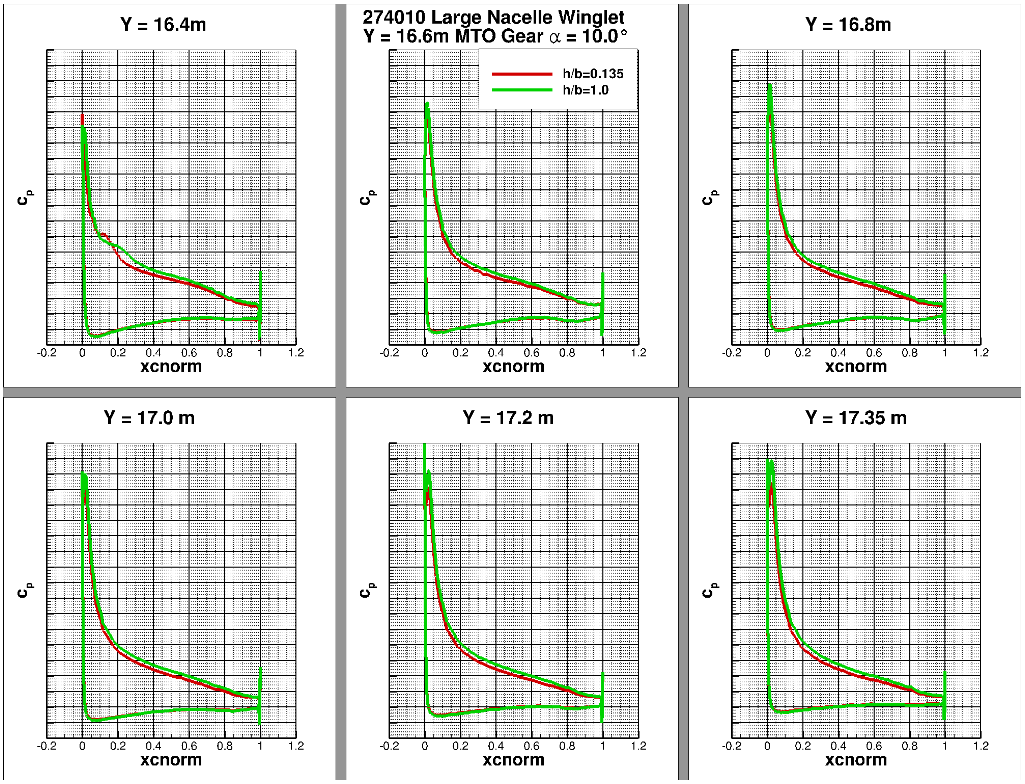

Figure 9.43 – C_P distribution at the wingtip at various cut locations for the landing configuration, large nacelle and winglet geometry with gear deployed and maximum thrust setting applied at $\alpha = 10.0°$

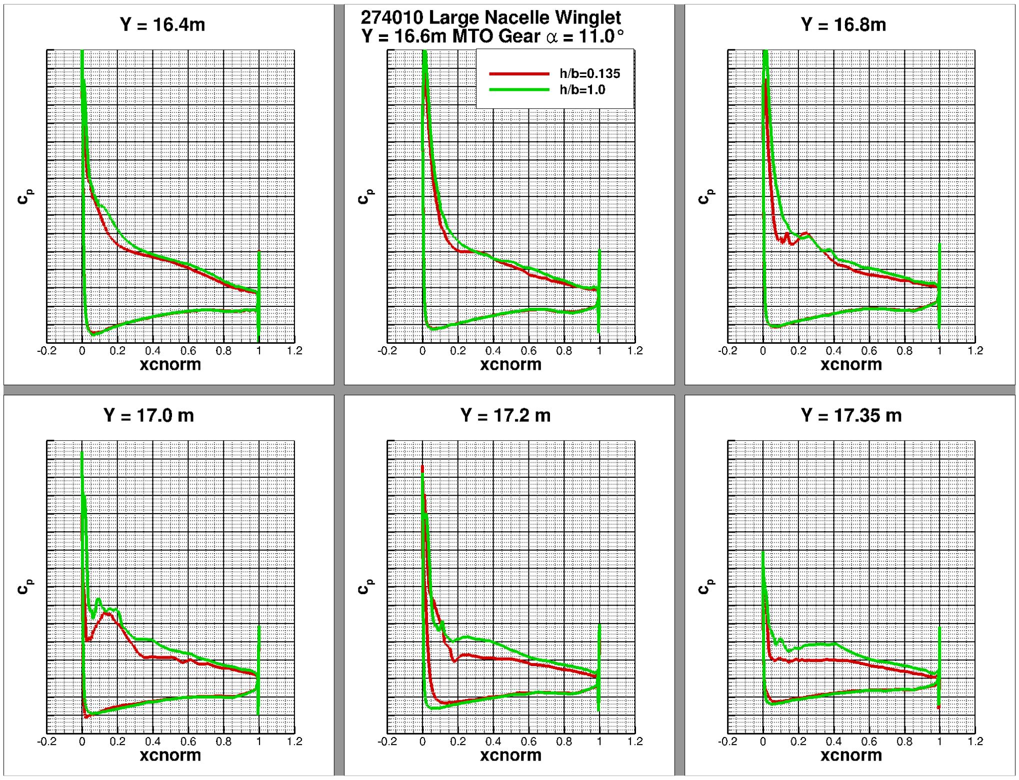

Figure 9.44 – C_P distribution at the wingtip at various cut locations for the landing configuration, large nacelle and winglet geometry with gear deployed and maximum thrust setting applied at $\alpha = 11.0°$

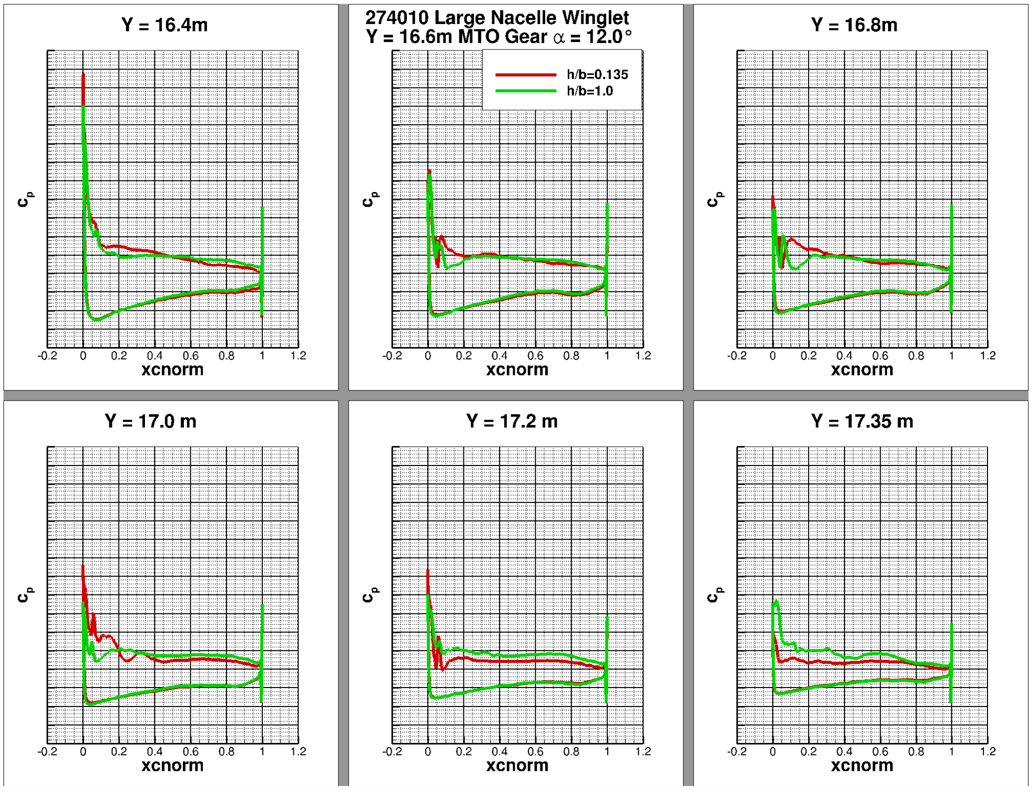

Figure 9.45 – C_P distribution at the wingtip at various cut locations for the landing configuration, large nacelle and winglet geometry with gear deployed and maximum thrust setting applied at $\alpha = 12.0°$

9.7.2.2 Large Nacelle Conventional Wingtip Gear Geometry

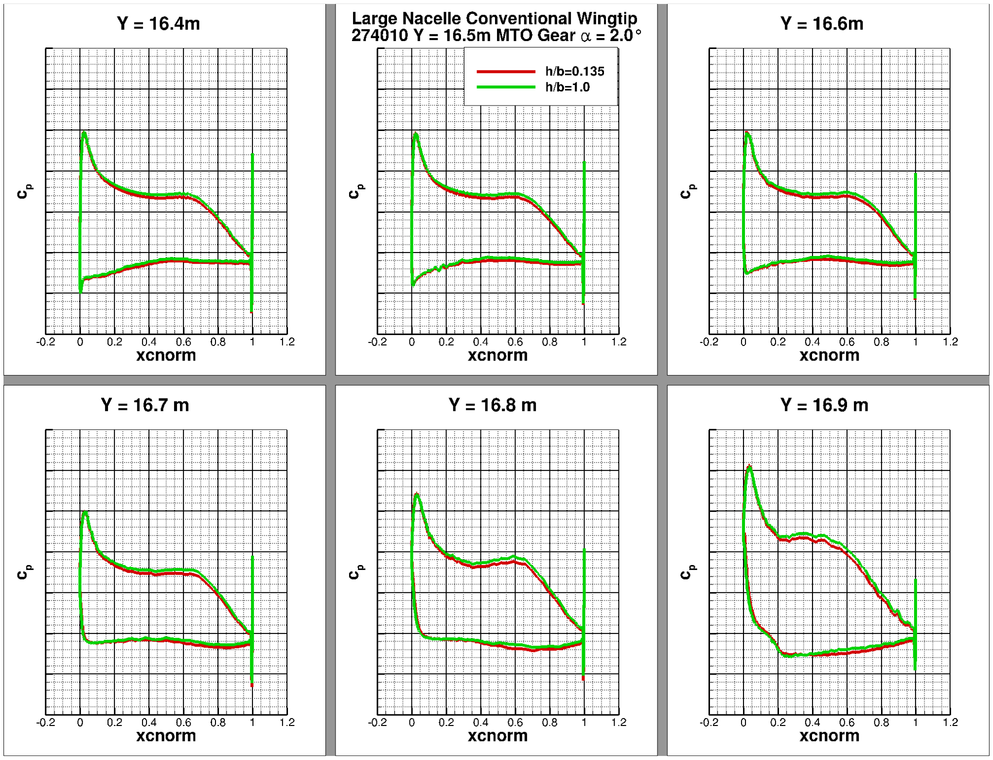

Figure 9.46 – C_P distribution at the wingtip at various cut locations for the landing configuration, large nacelle and conventional wingtip geometry with gear deployed and maximum thrust setting applied at $\alpha = 2.0°$

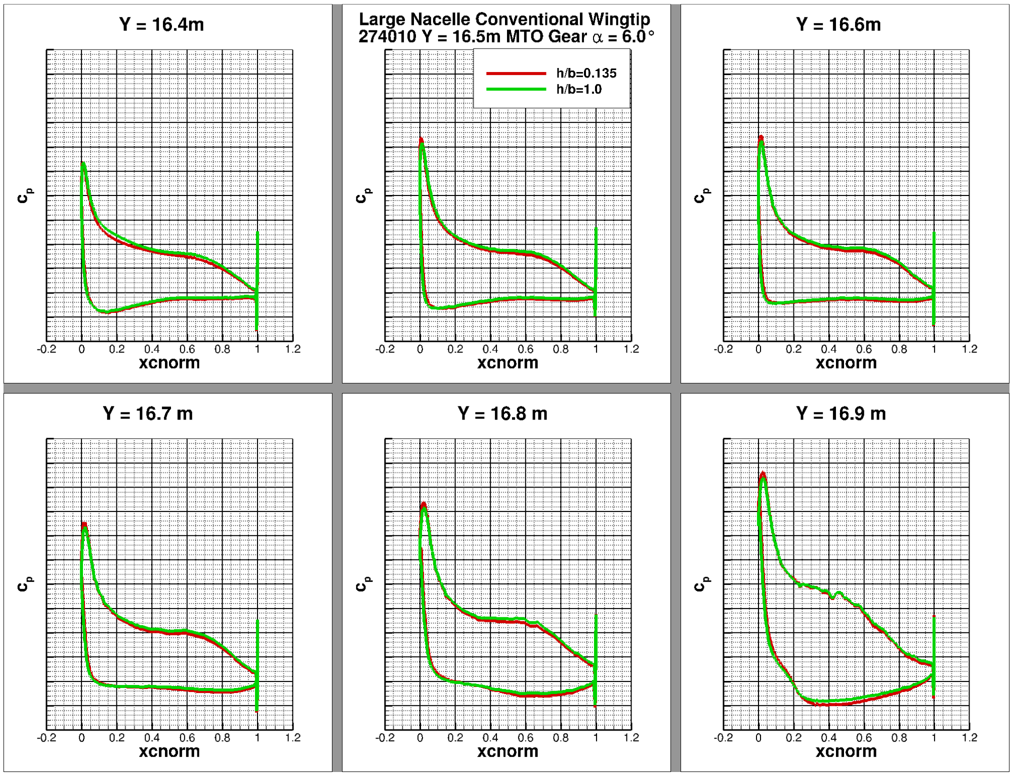

Figure 9.47 – C_P distribution at the wingtip at various cut locations for the landing configuration, large nacelle and conventional wingtip geometry with gear deployed and maximum thrust setting applied at $\alpha = 6.0°$

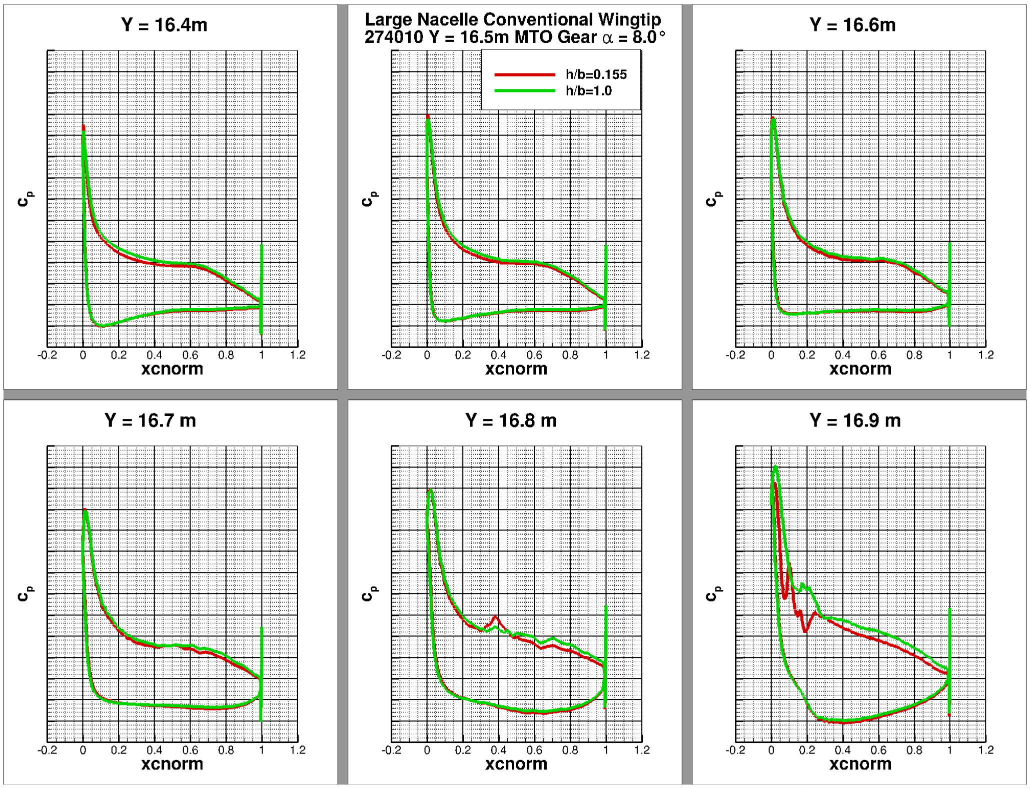
Y = 16.4m

Large Nacelle Conventional Wingtip 274010 Y = 16.5m MTO Gear α = 8.0°

Y = 16.6m

Y = 16.7 m

Y = 16.8 m

Y = 16.9 m

Figure 9.48 – C_P distribution at the wingtip at various cut locations for the landing configuration, large nacelle and conventional wingtip geometry with gear deployed and maximum thrust setting applied at $\alpha = 8.0°$

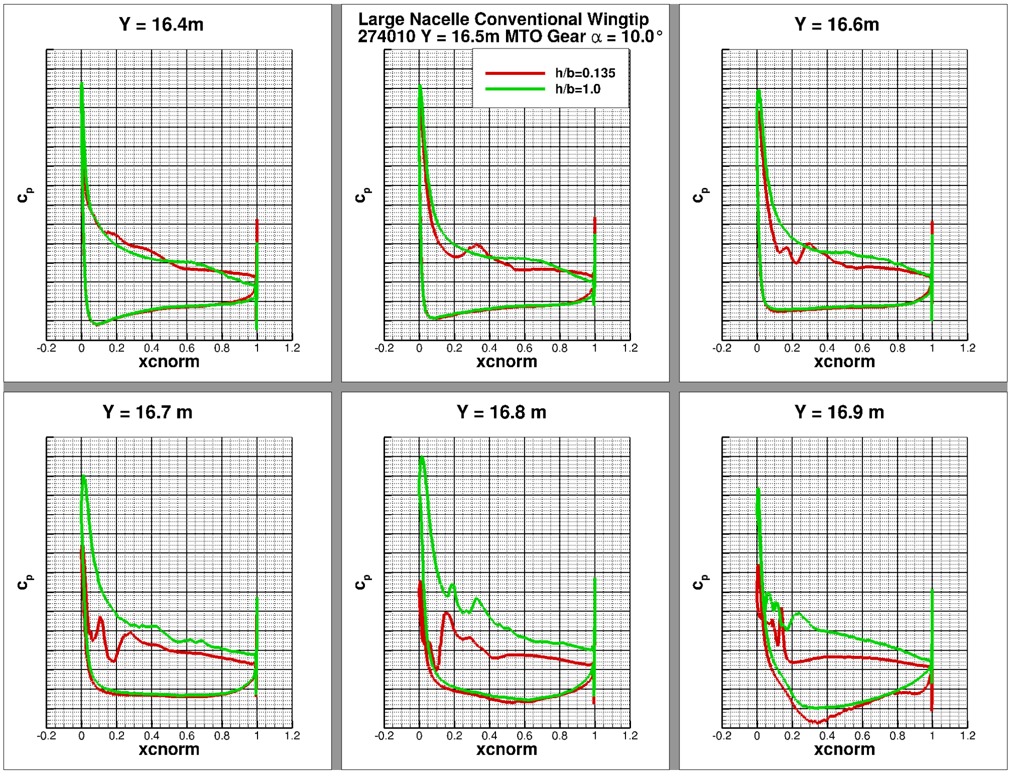
Y = 16.4m

Large Nacelle Conventional Wingtip 274010 Y = 16.5m MTO Gear α = 10.0°

Y = 16.6m

Y = 16.7 m

Y = 16.8 m

Y = 16.9 m

Figure 9.49 – C_P distribution at the wingtip at various cut locations for the landing configuration, large nacelle and conventional wingtip geometry with gear deployed and maximum thrust setting applied at $\alpha = 10.0°$

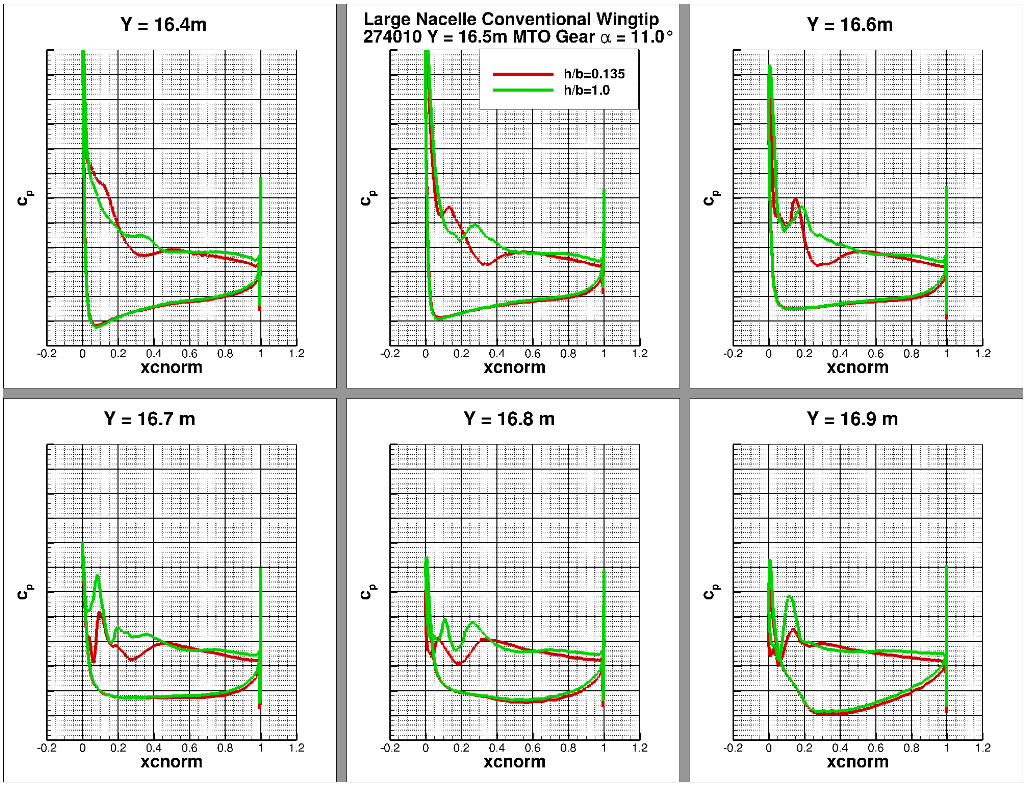

Figure 9.50 – C_P distribution at the wingtip at various cut locations for the landing configuration, large nacelle and conventional wingtip geometry with gear deployed and maximum thrust setting applied at $\alpha = 11.0°$

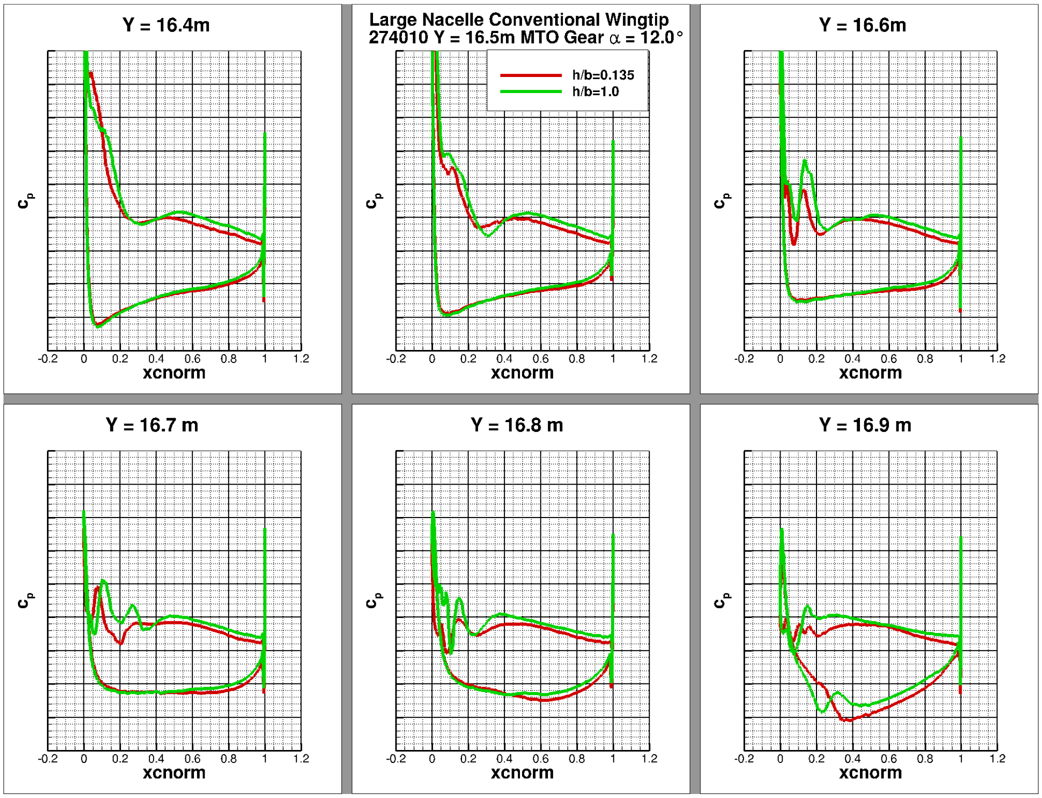

Figure 9.51 – C_P distribution at the wingtip at various cut locations for the landing configuration, large nacelle and conventional wingtip geometry with gear deployed and maximum thrust setting applied at $\alpha = 12.0°$

9.8 Appendix H –Total Pressure and Total Velocity change in ground effect

9.8.1 ΔP_{tot} Small Nacelle Conventional Wingtip flightidle thrust settings $\alpha = 6.0° \frac{h}{b} = 0.155$

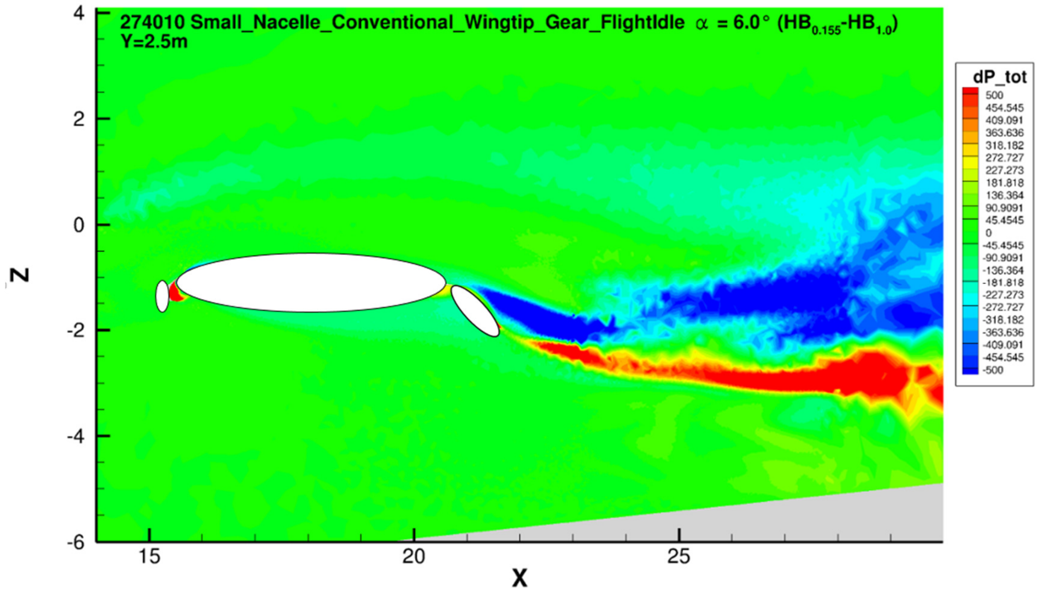

Figure 9.52 – Total pressure change (in Pa) due ground effect for the small nacelle, conventional winglet geometry in landing configuration with flightidle thrust settings $\alpha = 6.0°$

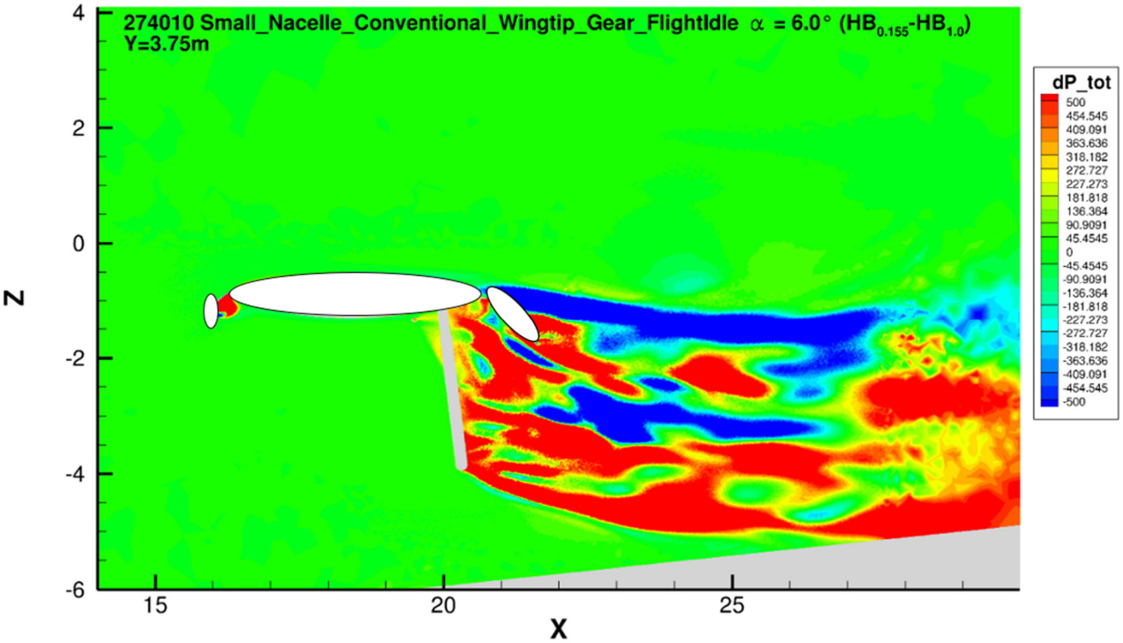

Figure 9.53 – Total pressure change (in Pa) due ground effect for the small nacelle, conventional winglet geometry in landing configuration with flightidle thrust settings $\alpha = 6.0°$

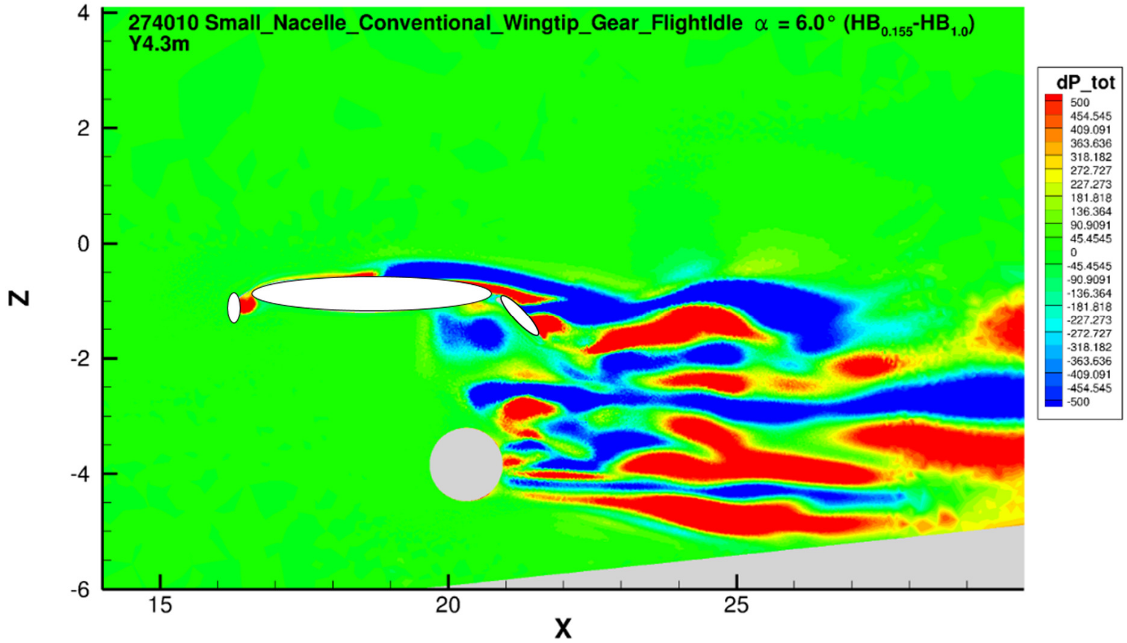

Figure 9.54 – Total pressure change (in Pa) due ground effect for the small nacelle, conventional winglet geometry in landing configuration with flightidle thrust settings $\alpha = 6.0°$

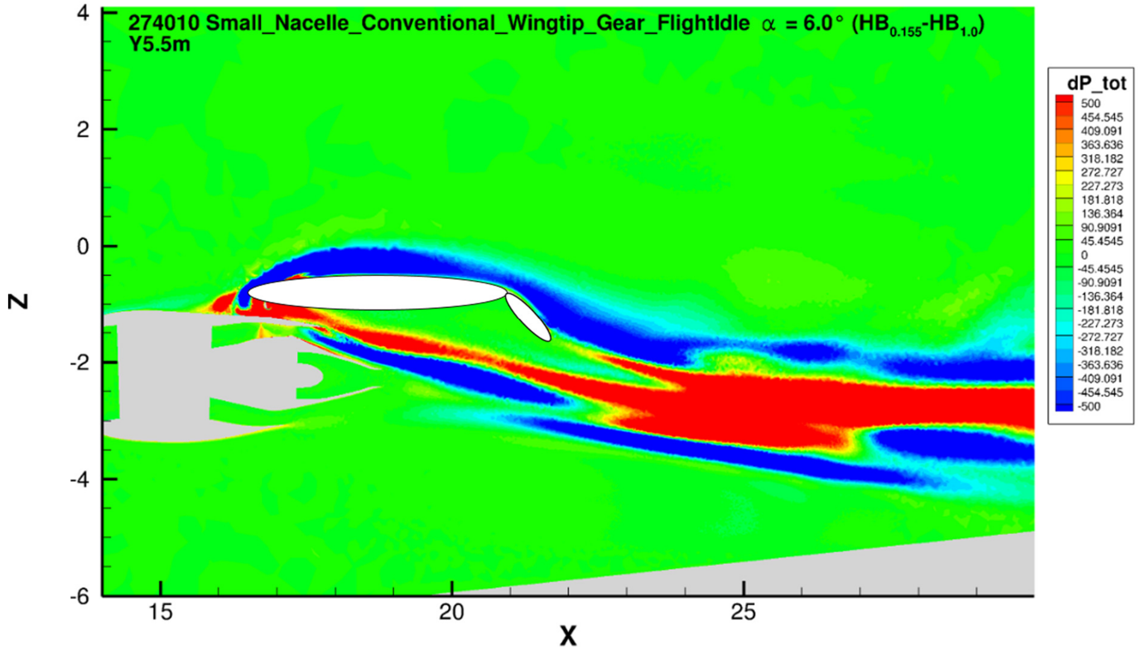

Figure 9.55 – Total pressure change (in Pa) due ground effect for the small nacelle, conventional winglet geometry in landing configuration with flightidle thrust settings $\alpha = 6.0°$

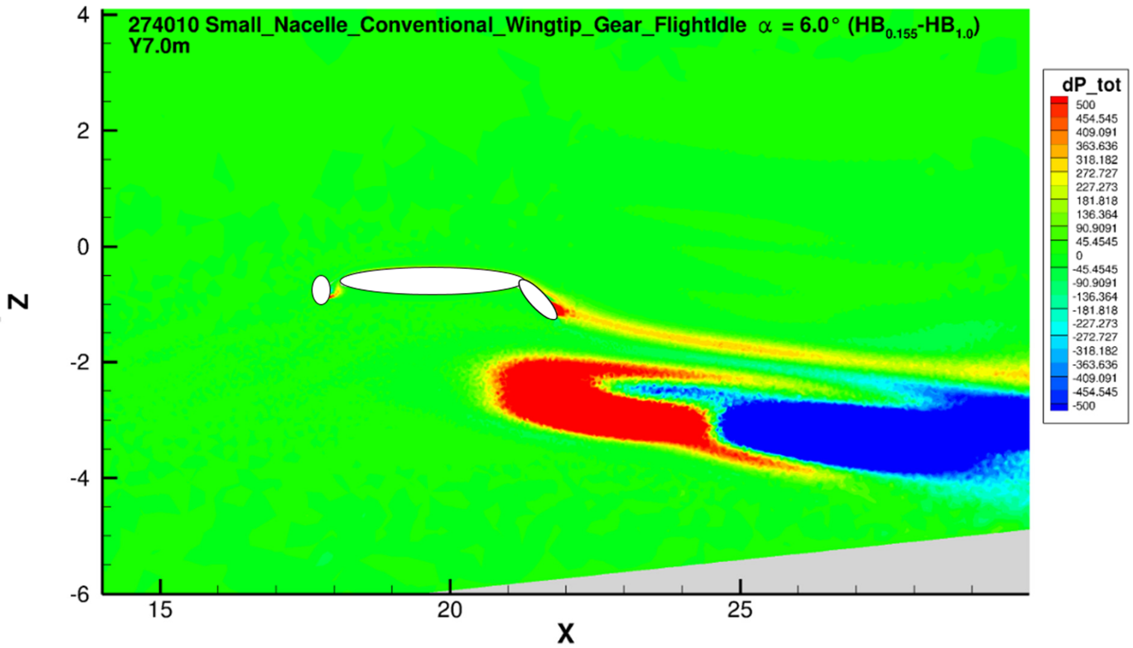

Figure 9.56 – Total pressure change (in Pa) due ground effect for the small nacelle, conventional winglet geometry in landing configuration with flightidle thrust settings $\alpha = 6.0°$

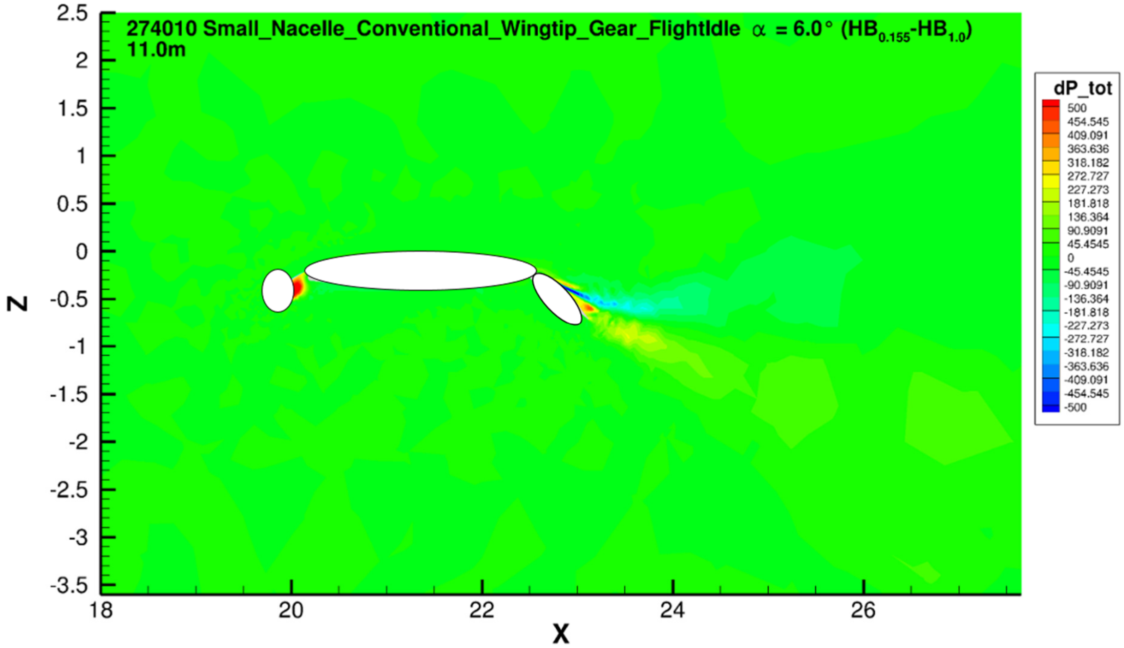

Figure 9.57 – Total pressure change (in Pa) due ground effect for the small nacelle, conventional winglet geometry in landing configuration with flightidle thrust settings $\alpha = 6.0°$

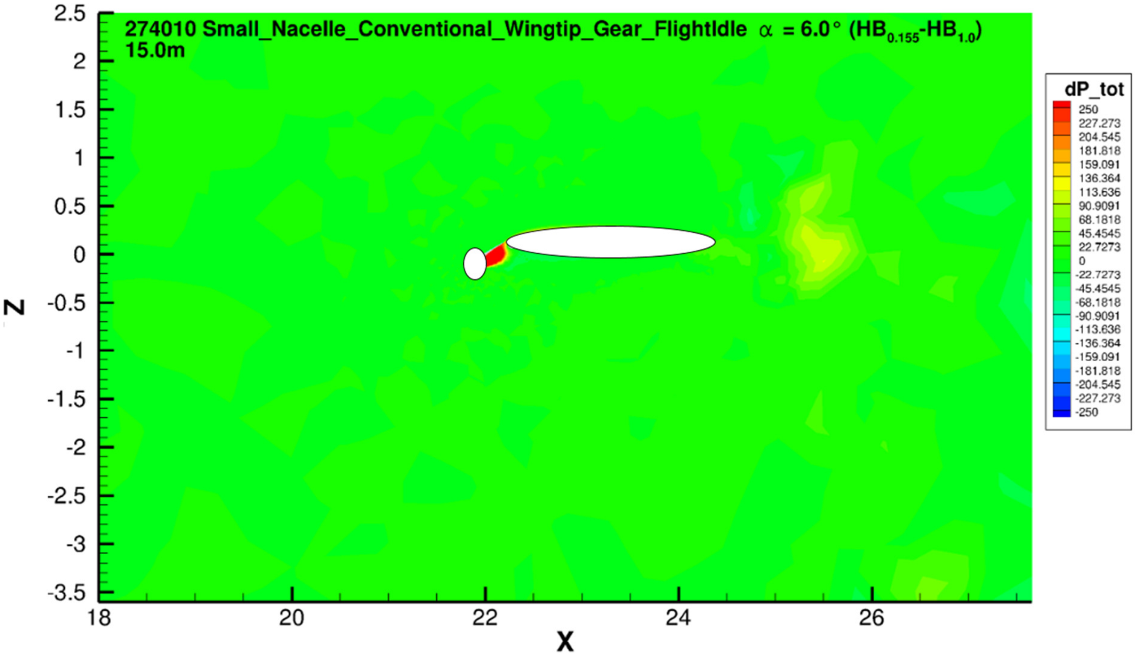

Figure 9.58 – Total pressure change (in Pa) due ground effect for the small nacelle, conventional winglet geometry in landing configuration with flightidle thrust settings $\alpha = 6.0°$

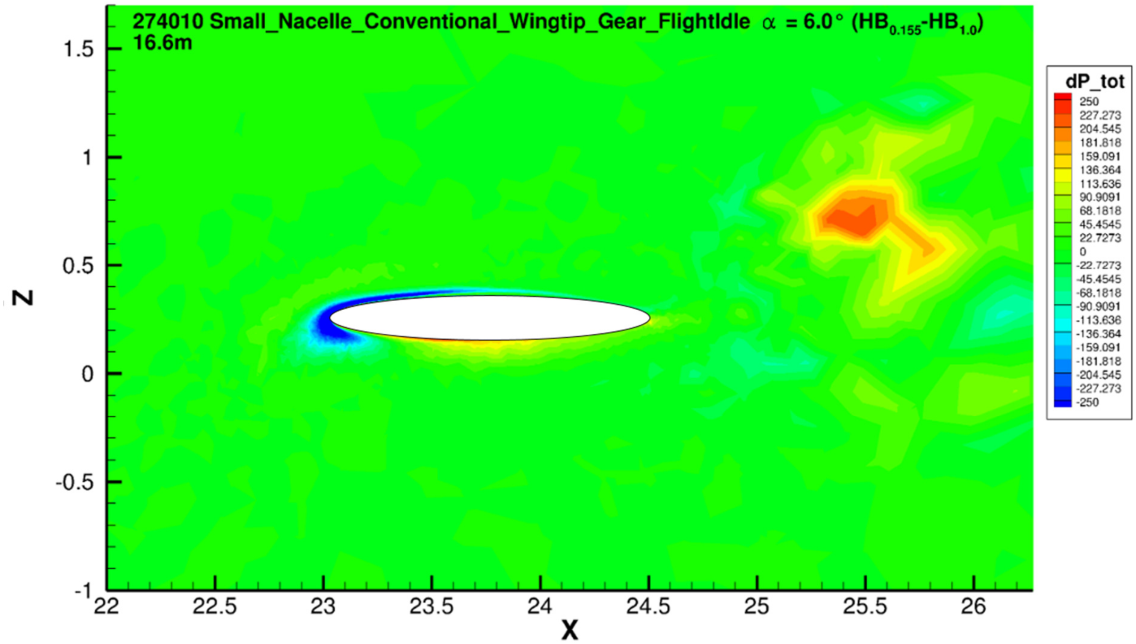

Figure 9.59 – Total pressure change (in Pa) due ground effect for the small nacelle, conventional winglet geometry in landing configuration with flightidle thrust settings $\alpha = 6.0°$

9.8.2 $\Delta \boldsymbol{P_{tot}}$ Small Nacelle Conventional Wingtip flightidle thrust settings $\boldsymbol{\alpha = 12.0° \ \frac{h}{b} = 0.155}$

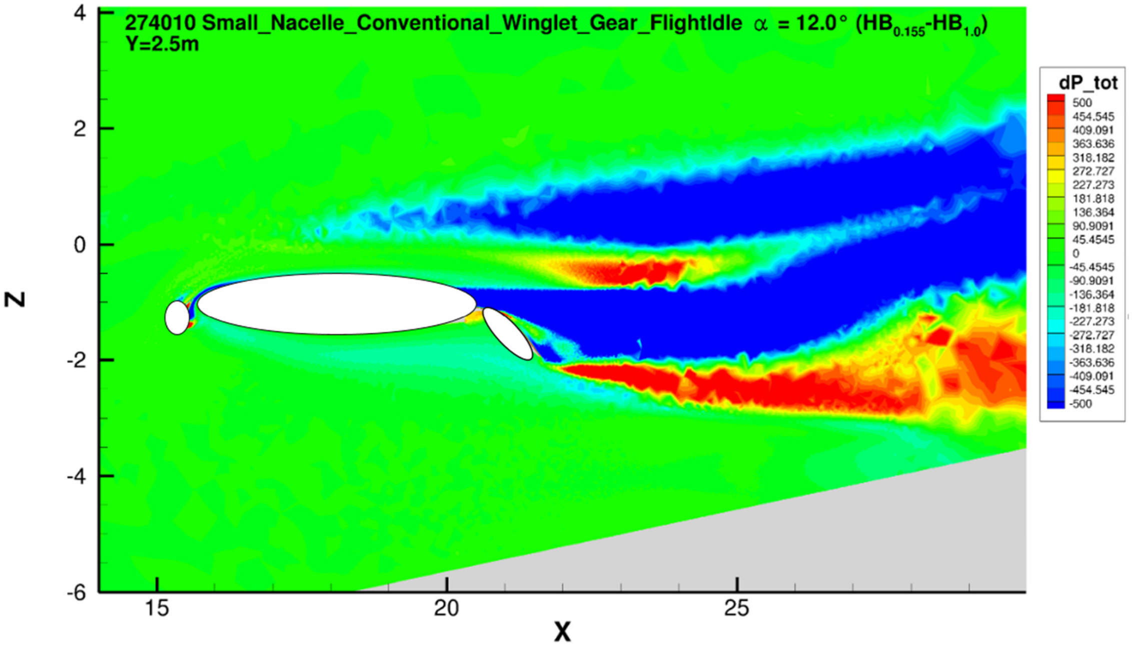

Figure 9.60 – Total pressure change (in Pa) due ground effect for the small nacelle, conventional winglet geometry in landing configuration with flightidle thrust settings $\alpha = 12.0°$

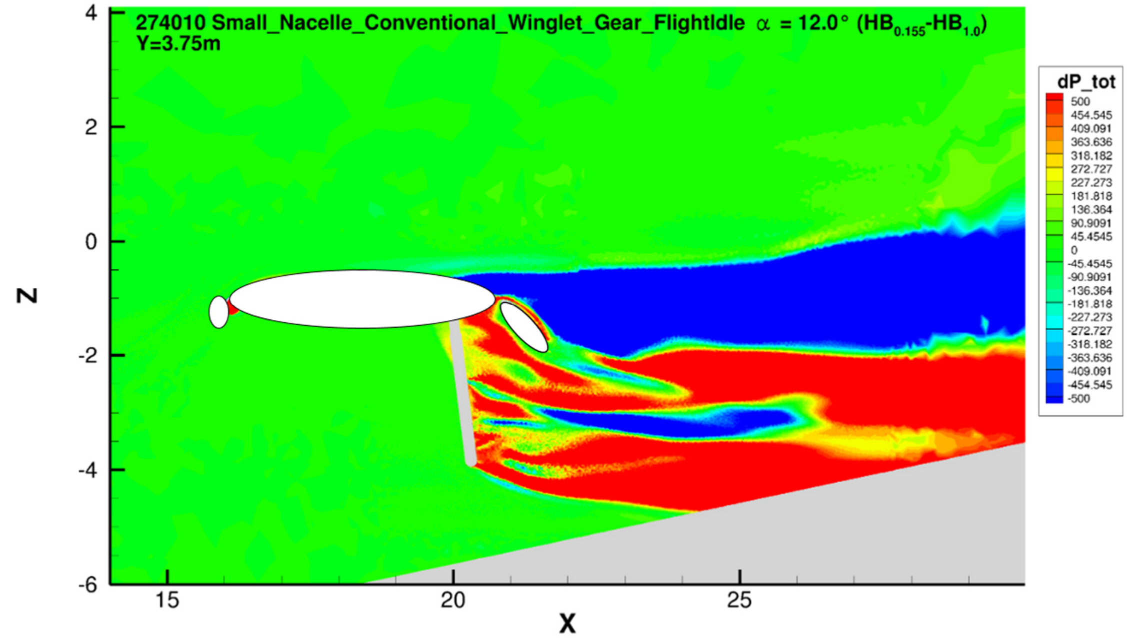

Figure 9.61 – Total pressure change (in Pa) due ground effect for the small nacelle, conventional winglet geometry in landing configuration with flightidle thrust settings $\alpha = 12.0°$

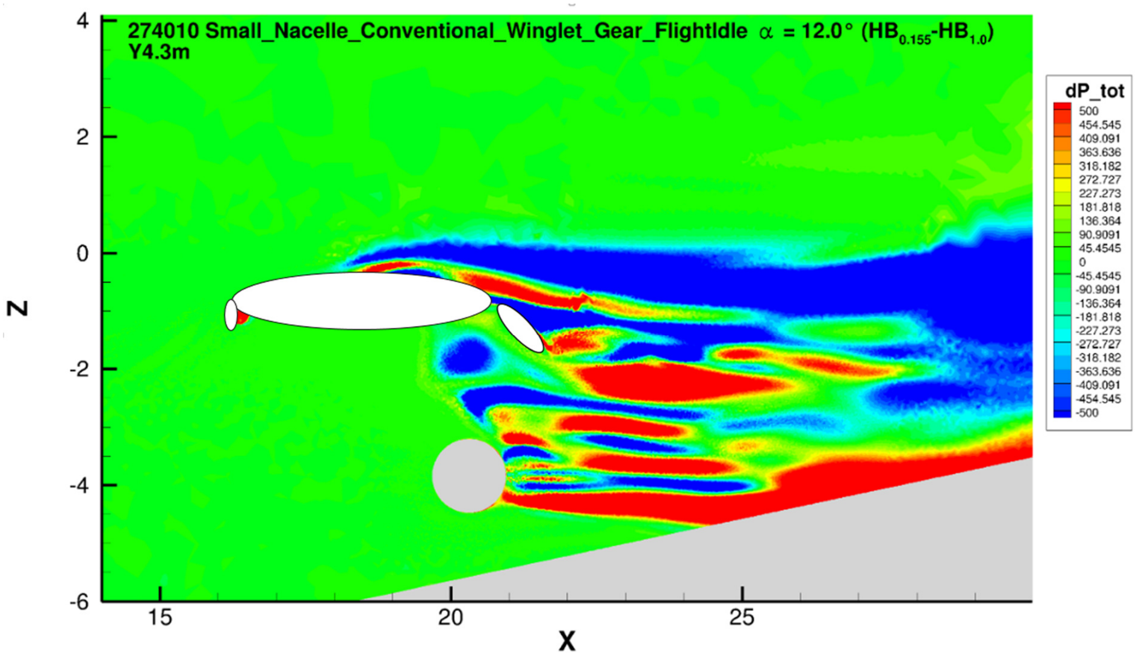

Figure 9.62 – Total pressure change (in Pa) due ground effect for the small nacelle, conventional winglet geometry in landing configuration with flightidle thrust settings $\alpha = 12.0°$

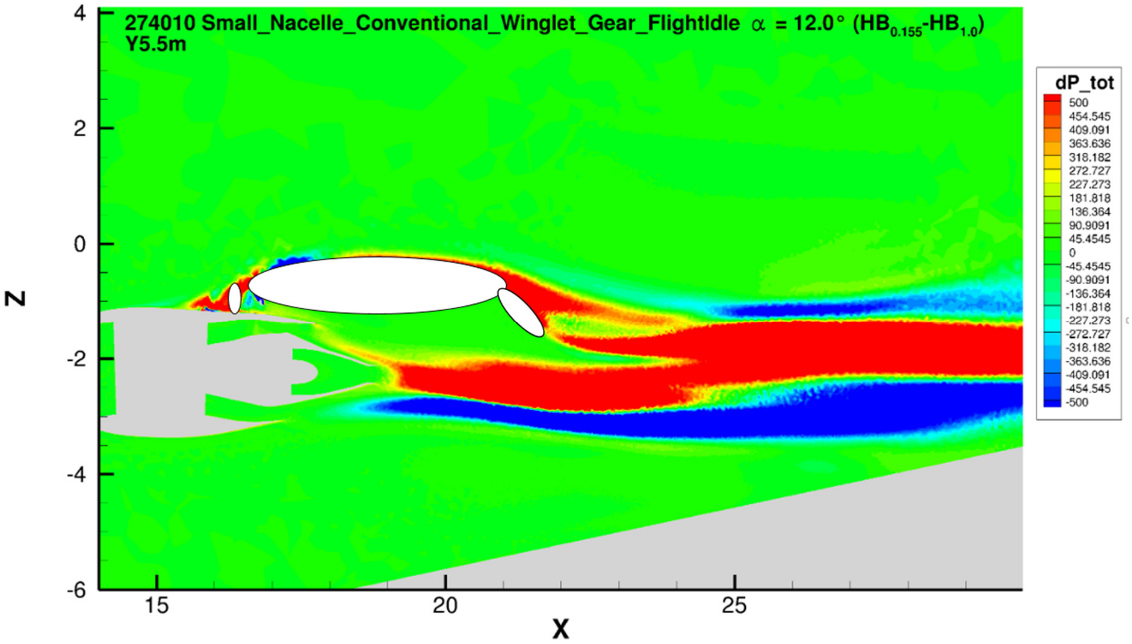

Figure 9.63 – Total pressure change (in Pa) due ground effect for the small nacelle, conventional winglet geometry in landing configuration with flightidle thrust settings $\alpha = 12.0°$

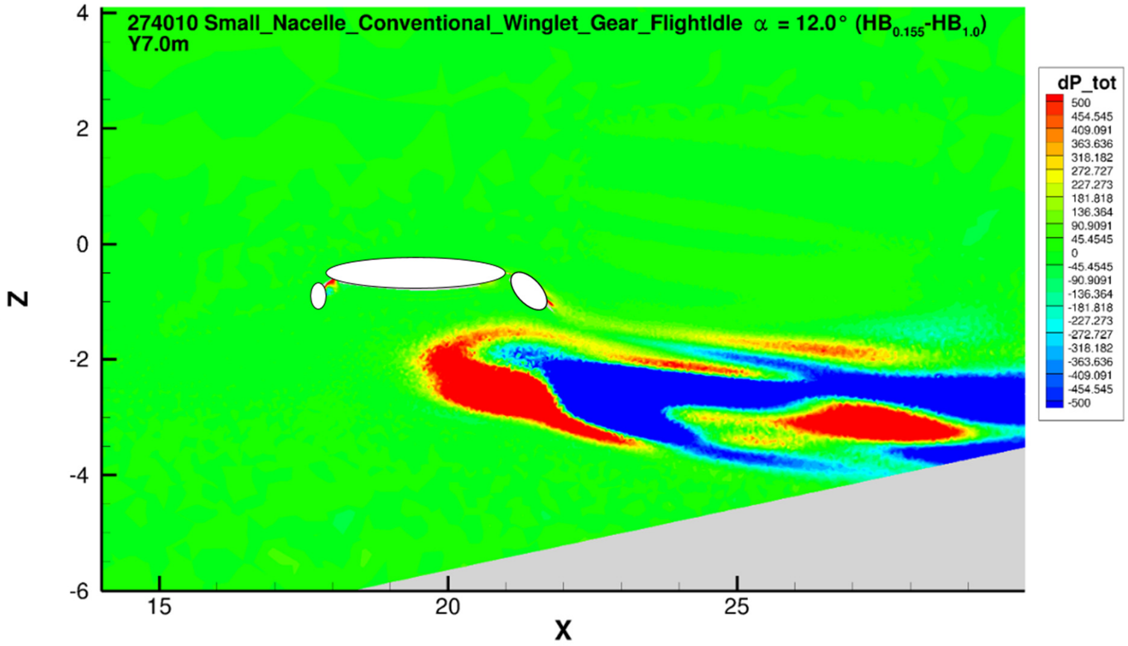

Figure 9.64 – Total pressure change (in Pa) due ground effect for the small nacelle, conventional winglet geometry in landing configuration with flightidle thrust settings $\alpha = 12.0°$

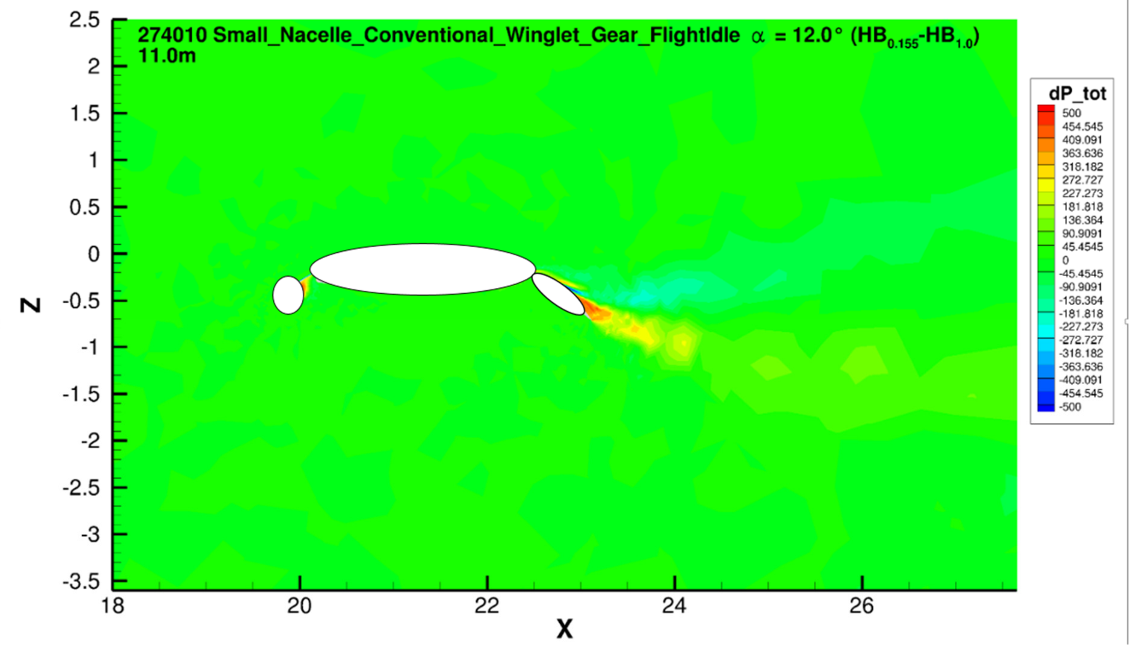

Figure 9.65 – Total pressure change (in Pa) due ground effect for the small nacelle, conventional winglet geometry in landing configuration with flightidle thrust settings $\alpha = 12.0°$

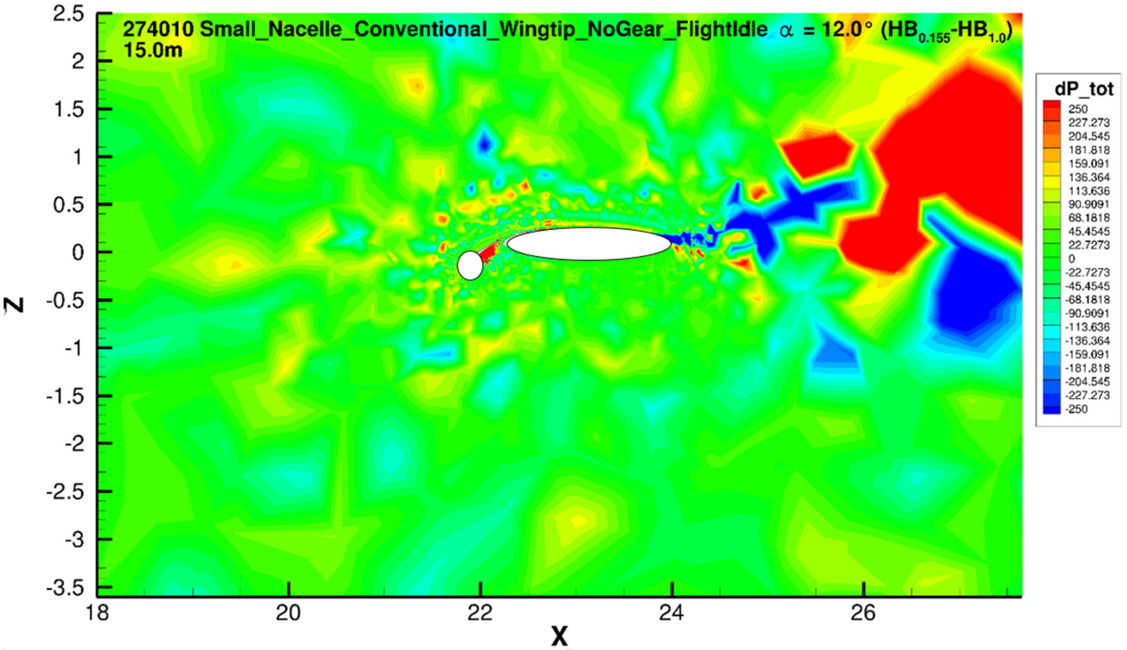

Figure 9.66 – Total pressure change (in Pa) due ground effect for the small nacelle, conventional winglet geometry in landing configuration with flightidle thrust settings $\alpha = 12.0°$

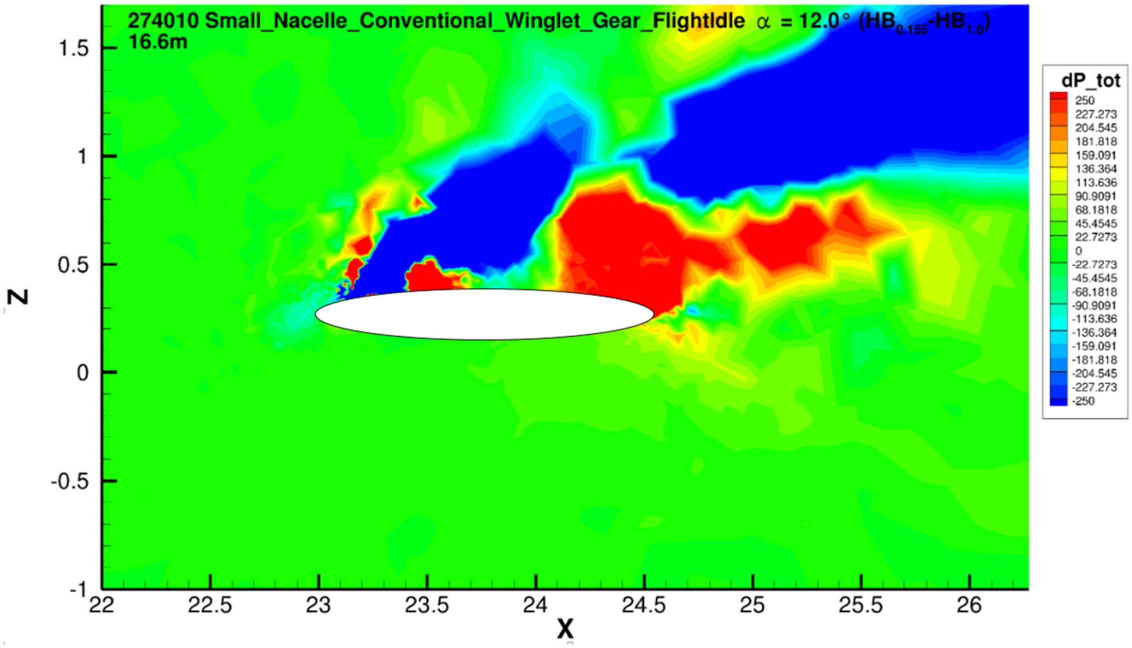

Figure 9.67 – Total pressure change (in Pa) due ground effect for the small nacelle, conventional winglet geometry in landing configuration with flightidle thrust settings $\alpha = 12.0°$

9.8.3 ΔV_{tot} Small Nacelle Conventional Wingtip flightidle thrust settings $\alpha = 6.0°\ \frac{h}{b} = 0.155$

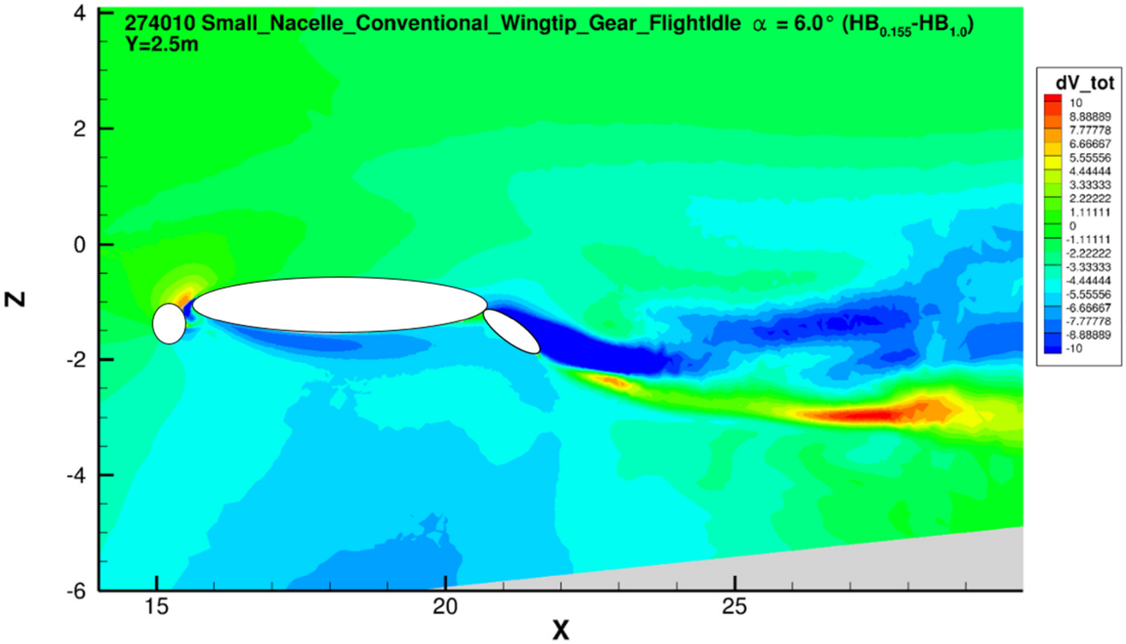

Figure 9.68 – Total velocity change (in m/s) due ground effect for the small nacelle, conventional winglet geometry in landing configuration with flightidle thrust settings $\alpha = 6.0°$

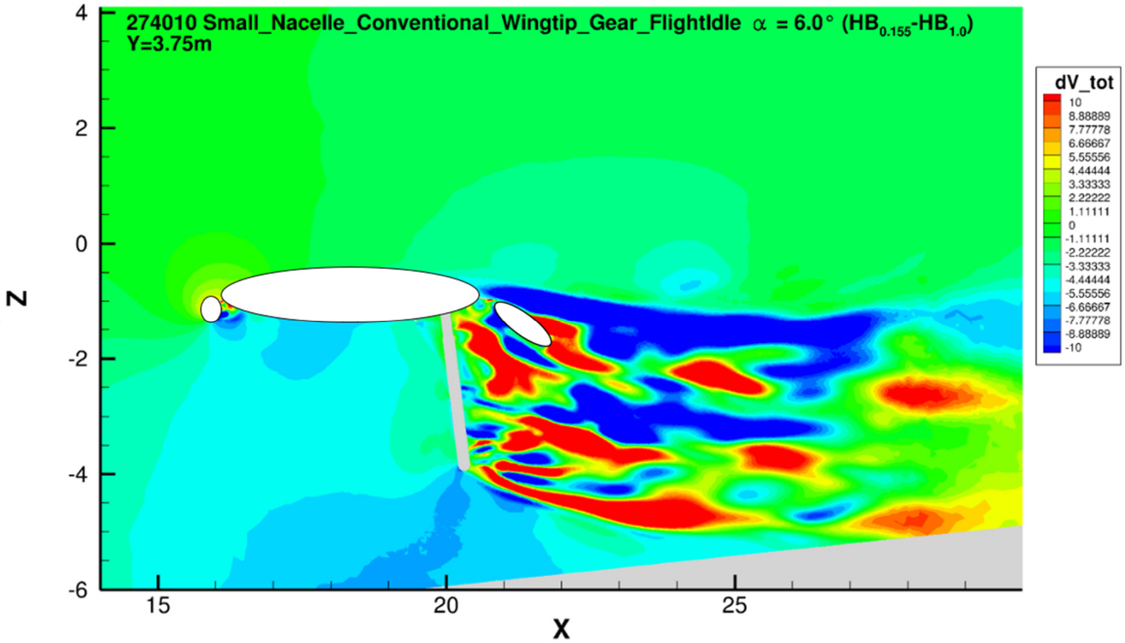

Figure 9.69 – Total velocity change (in m/s) due ground effect for the small nacelle, conventional winglet geometry in landing configuration with flightidle thrust settings $\alpha = 6.0°$

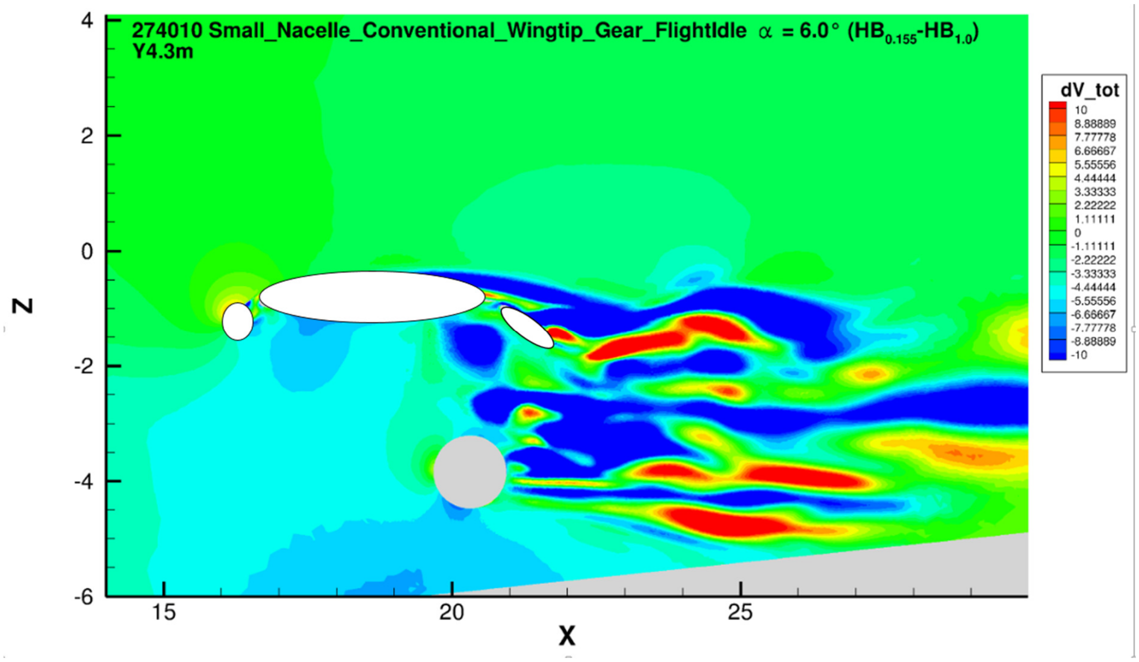

Figure 9.70 – Total velocity change (in m/s) due ground effect for the small nacelle, conventional winglet geometry in landing configuration with flightidle thrust settings $\alpha = 6.0°$

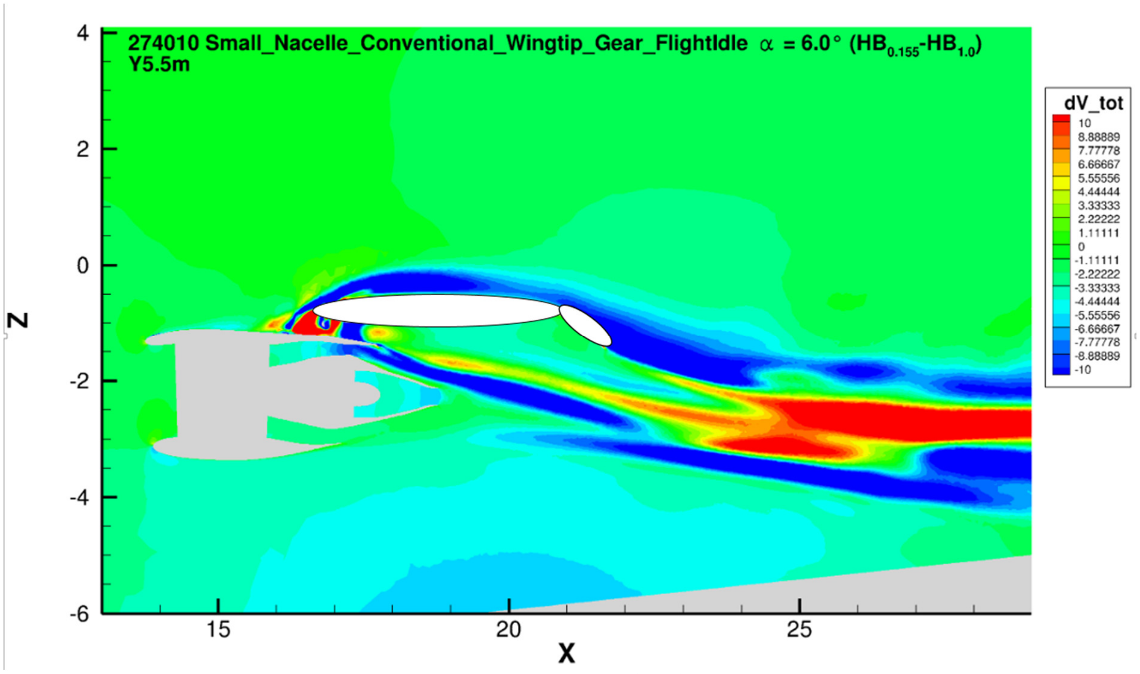

Figure 9.71 – Total velocity change (in m/s) due ground effect for the small nacelle, conventional winglet geometry in landing configuration with flightidle thrust settings $\alpha = 6.0°$

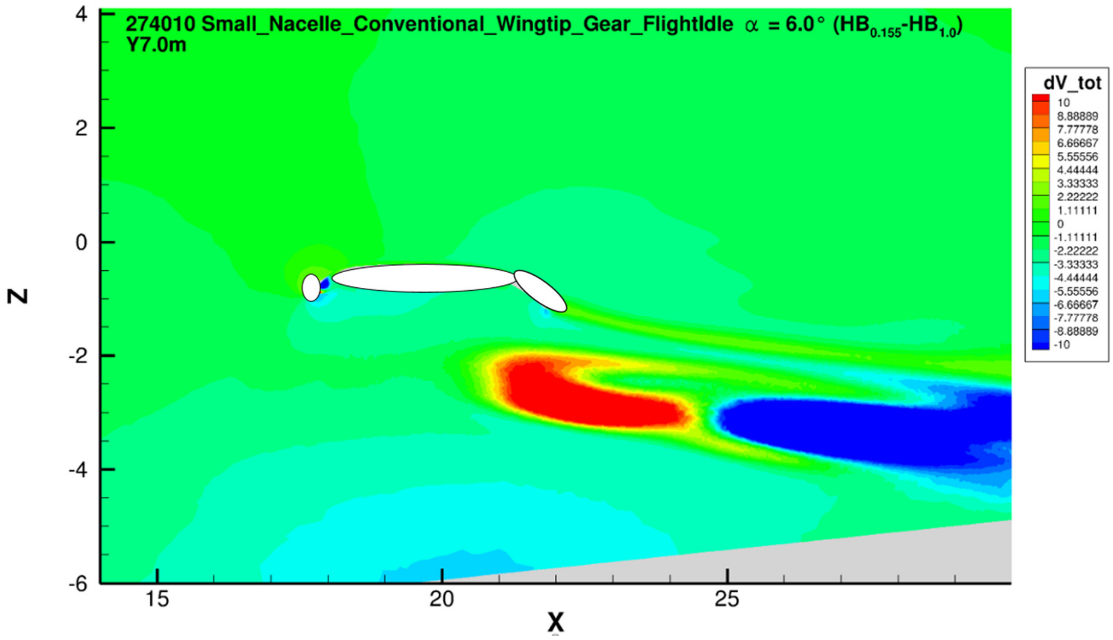

Figure 9.72 – Total velocity change (in m/s) due ground effect for the small nacelle, conventional winglet geometry in landing configuration with flightidle thrust settings $\alpha = 6.0°$

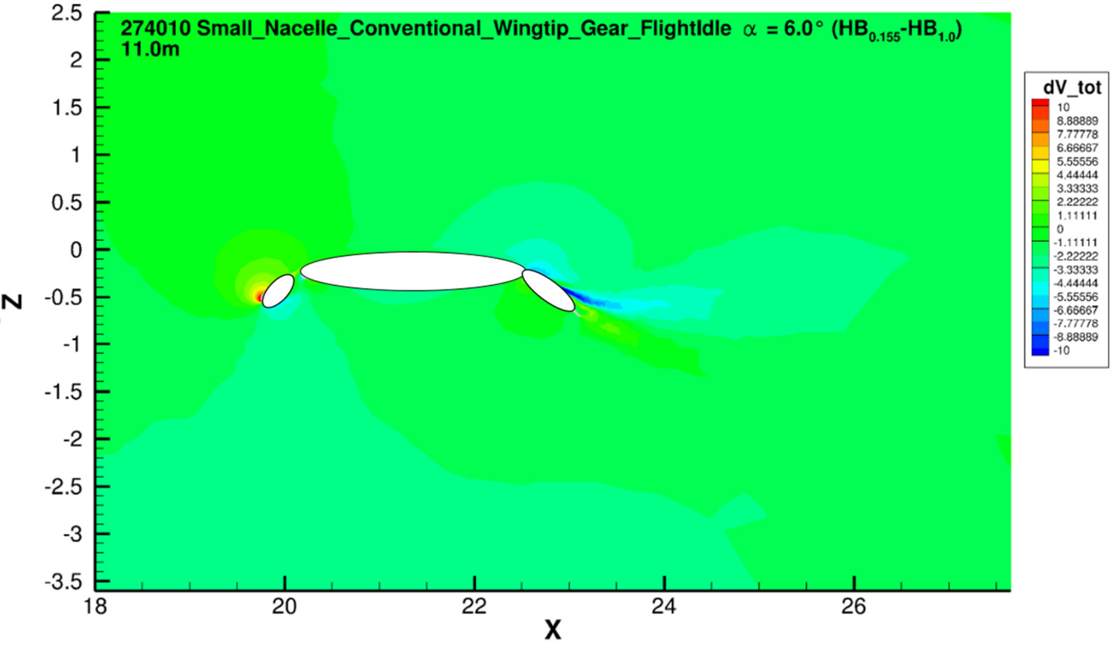

Figure 9.73 – Total velocity change (in m/s) due ground effect for the small nacelle, conventional winglet geometry in landing configuration with flightidle thrust settings $\alpha = 6.0°$

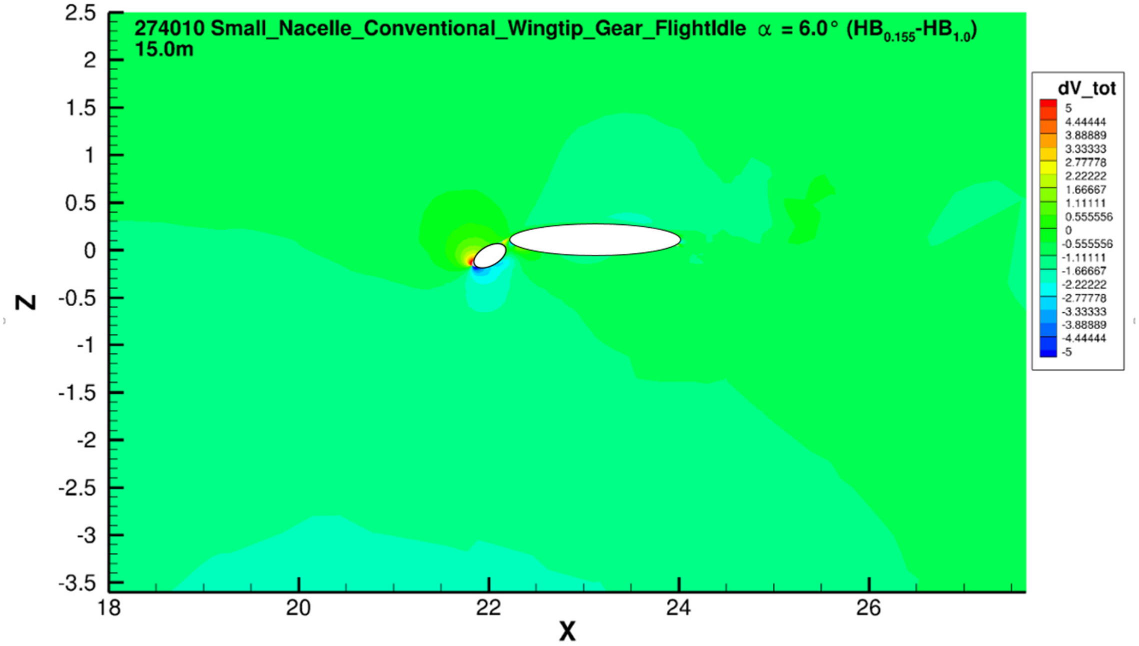

Figure 9.74 – Total velocity change (in m/s) due ground effect for the small nacelle, conventional winglet geometry in landing configuration with flightidle thrust settings $\alpha = 6.0°$

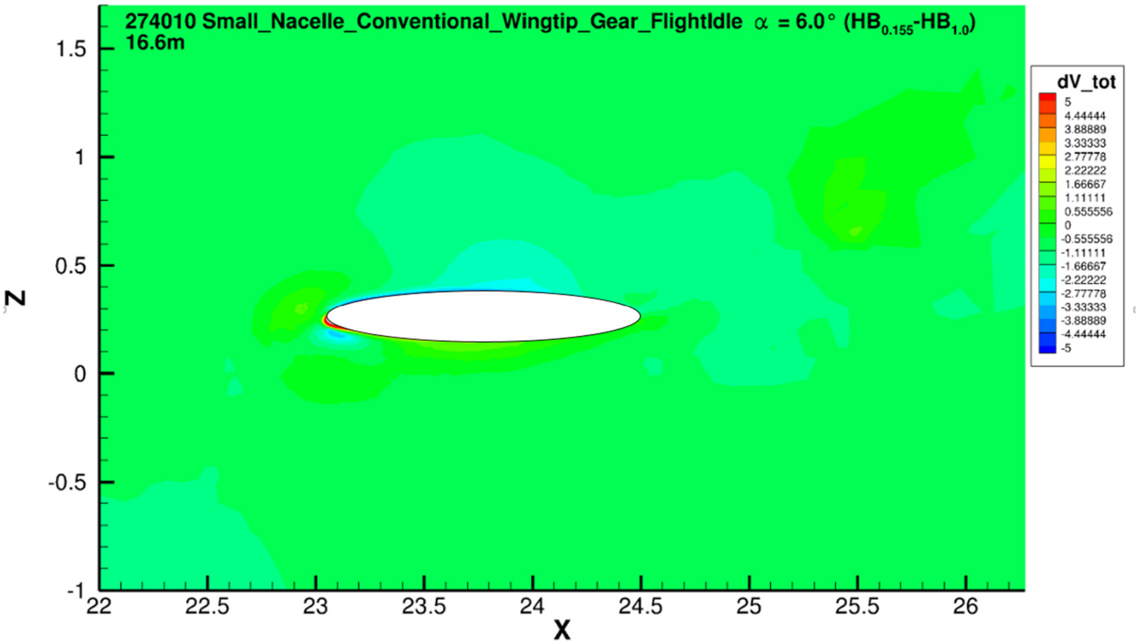

Figure 9.75 – Total velocity change (in m/s) due ground effect for the small nacelle, conventional winglet geometry in landing configuration with flightidle thrust settings $\alpha = 6.0°$

9.8.4 ΔV_{tot} Small Nacelle Conventional Wingtip flightidle thrust settings $\alpha = 12.0^\circ\ \frac{h}{b} = 0.155$

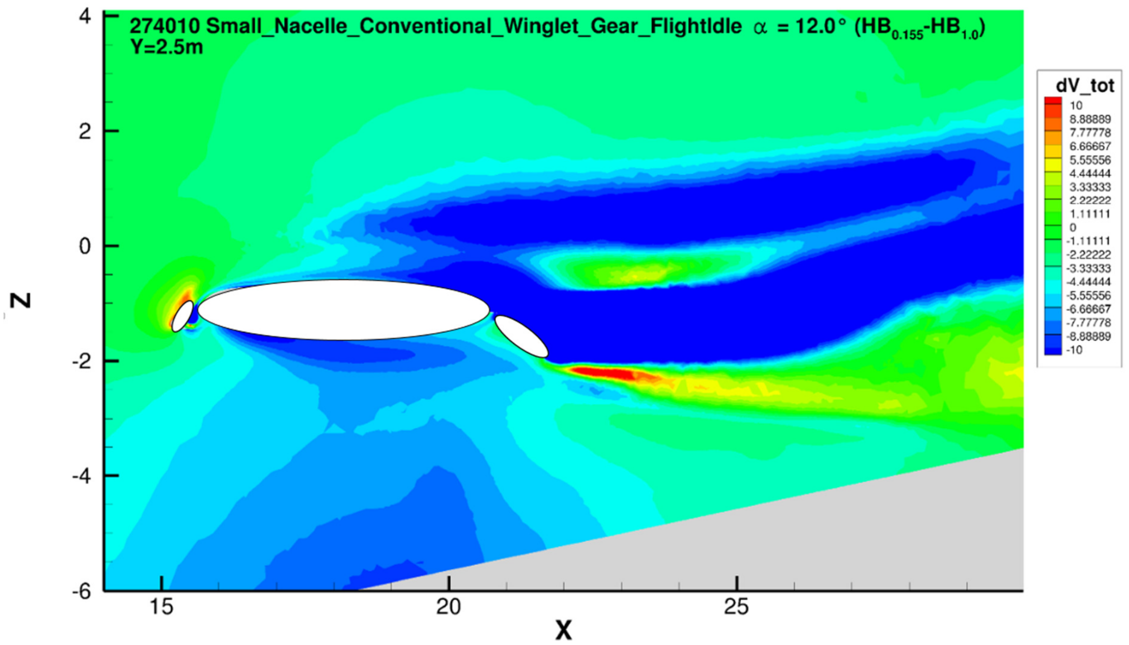

Figure 9.76 – Total velocity change (in m/s) due ground effect for the small nacelle, conventional winglet geometry in landing configuration with flightidle thrust settings $\alpha = 12.0°$

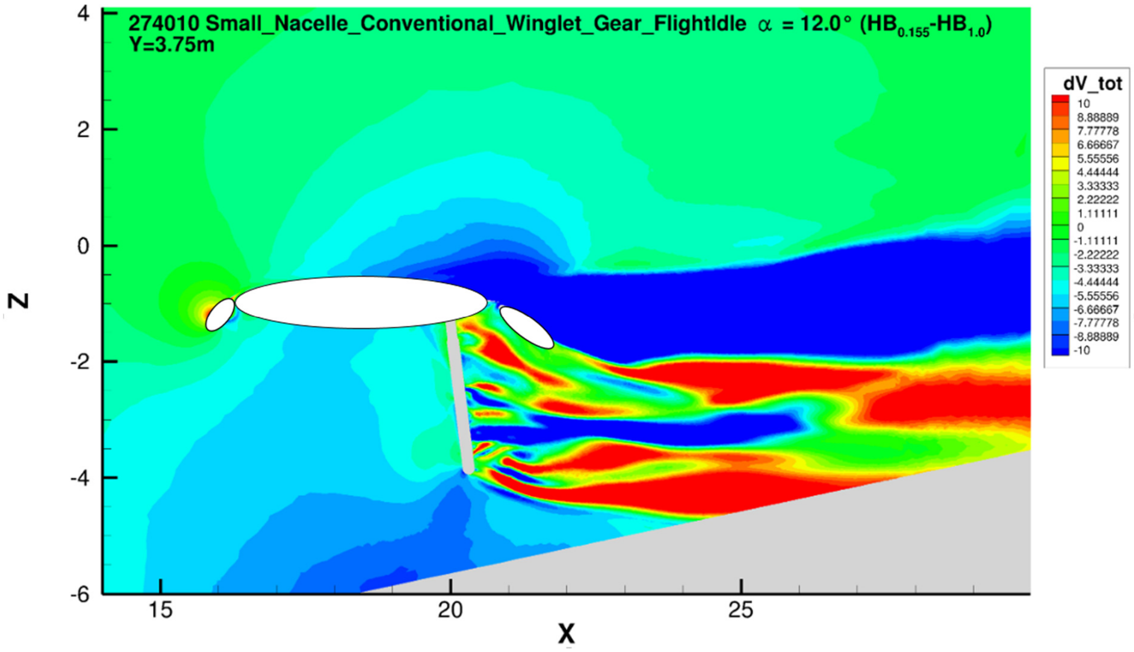

Figure 9.77 – Total velocity change (in m/s) due ground effect for the small nacelle, conventional winglet geometry in landing configuration with flightidle thrust settings $\alpha = 12.0°$

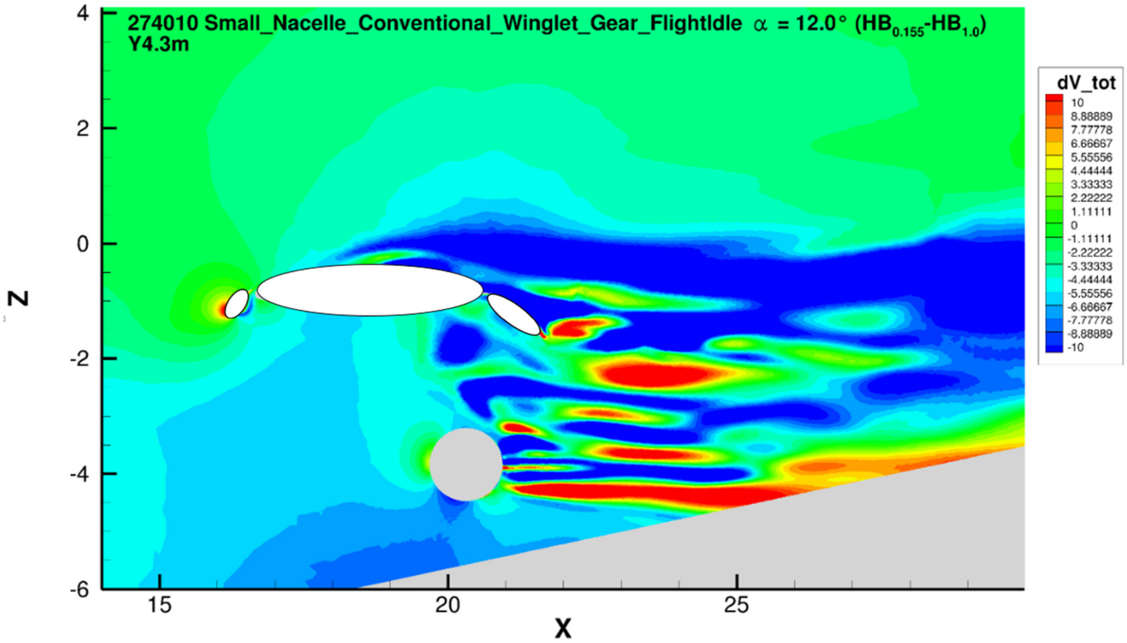

Figure 9.78 – Total velocity change (in m/s) due ground effect for the small nacelle, conventional winglet geometry in landing configuration with flightidle thrust settings $\alpha = 12.0°$

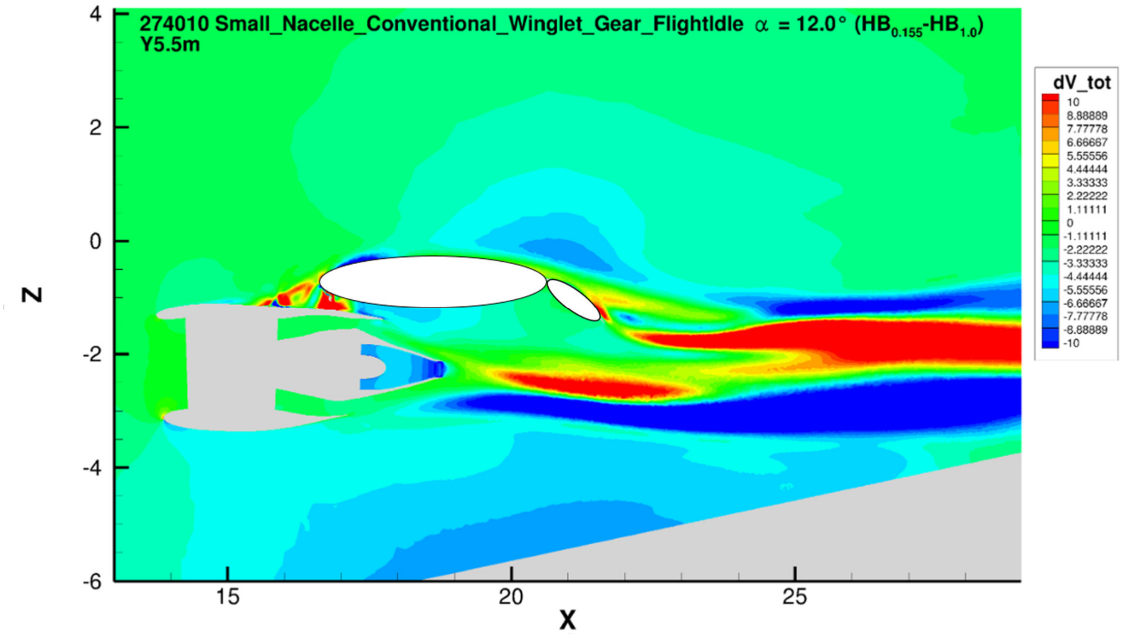

Figure 9.79 – Total velocity change (in m/s) due ground effect for the small nacelle, conventional winglet geometry in landing configuration with flightidle thrust settings $\alpha = 12.0°$

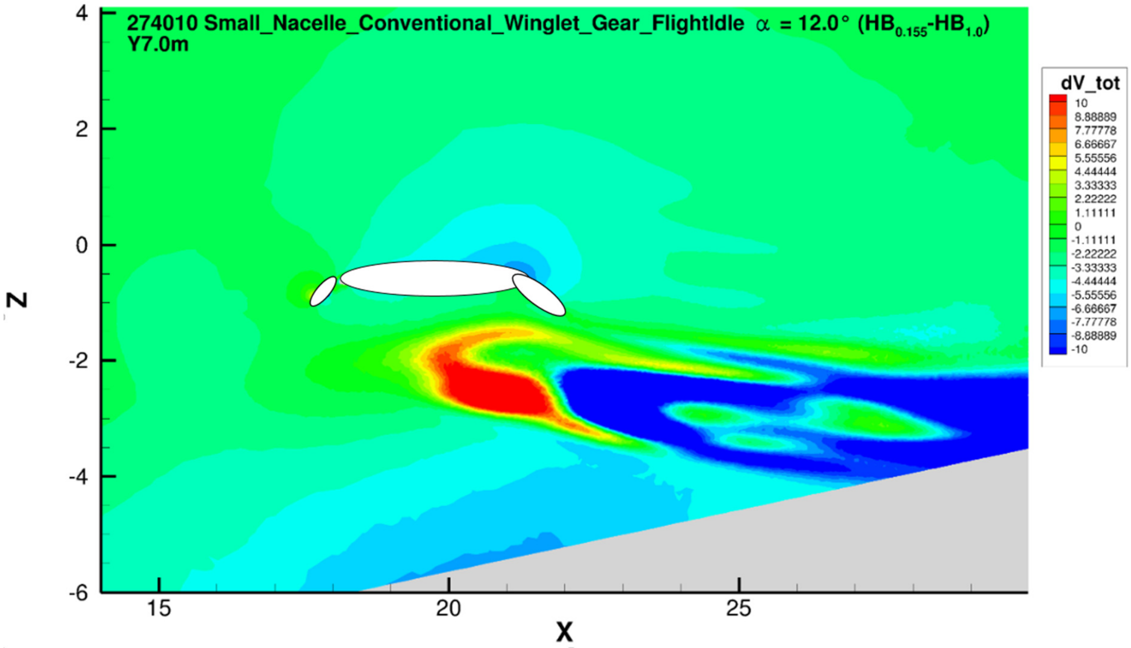

Figure 9.80 – Total velocity change (in m/s) due ground effect for the small nacelle, conventional winglet geometry in landing configuration with flightidle thrust settings $\alpha = 12.0°$

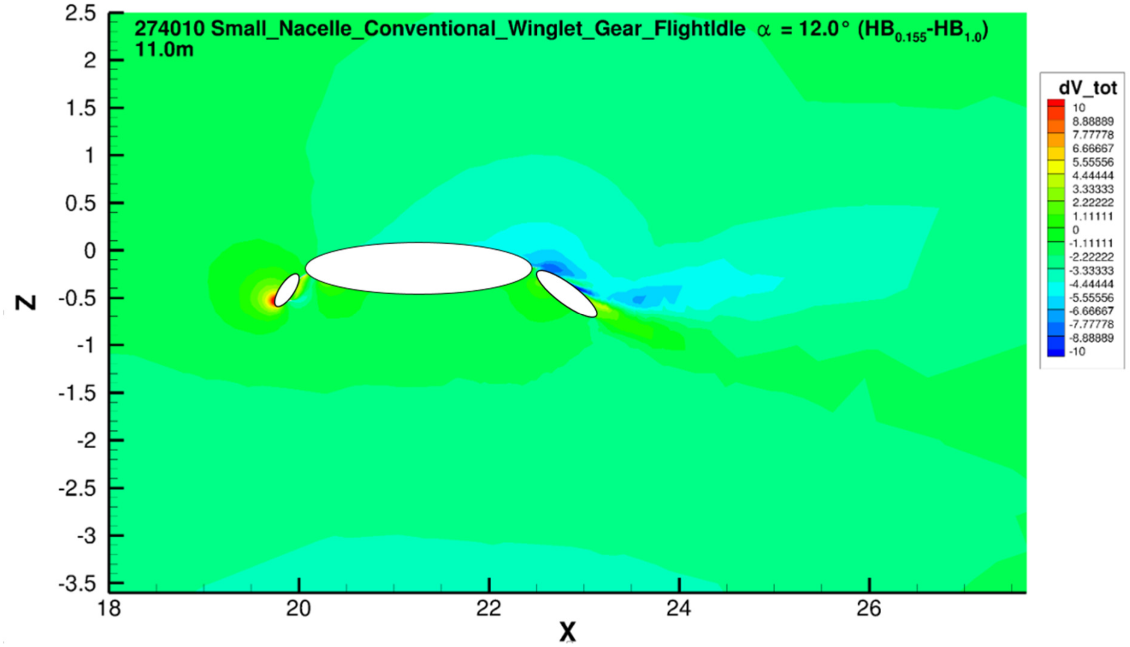

Figure 9.81 – Total velocity change (in m/s) due ground effect for the small nacelle, conventional winglet geometry in landing configuration with flightidle thrust settings $\alpha = 12.0°$

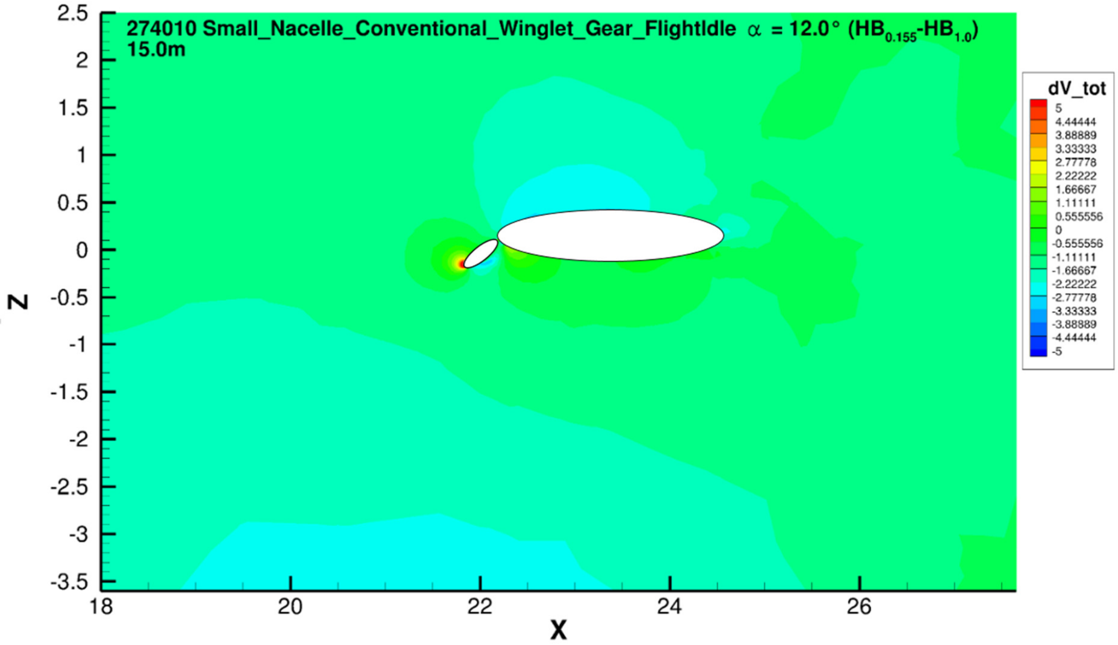

Figure 9.82 – Total velocity change (in m/s) due ground effect for the small nacelle, conventional winglet geometry in landing configuration with flightidle thrust settings $\alpha = 12.0°$

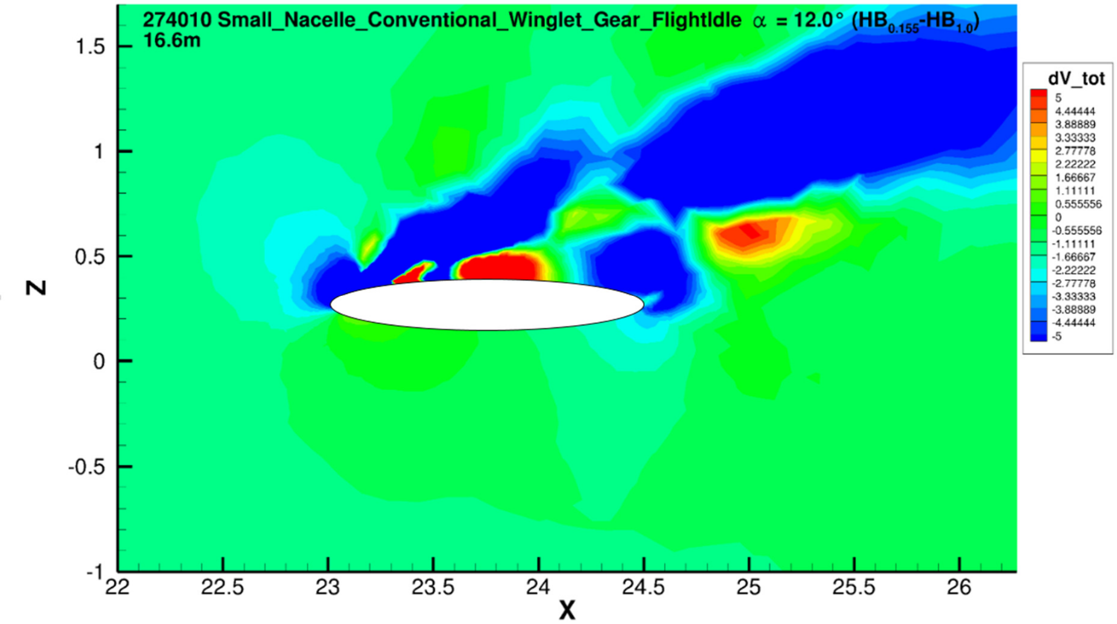

Figure 9.83 – Total velocity change (in m/s) due ground effect for the small nacelle, conventional winglet geometry in landing configuration with flightidle thrust settings $\alpha = 12.0°$

9.9 Appendix I – Spanwise Lift Distributions comparing different Geometries in the Landing High-Lift Configuration

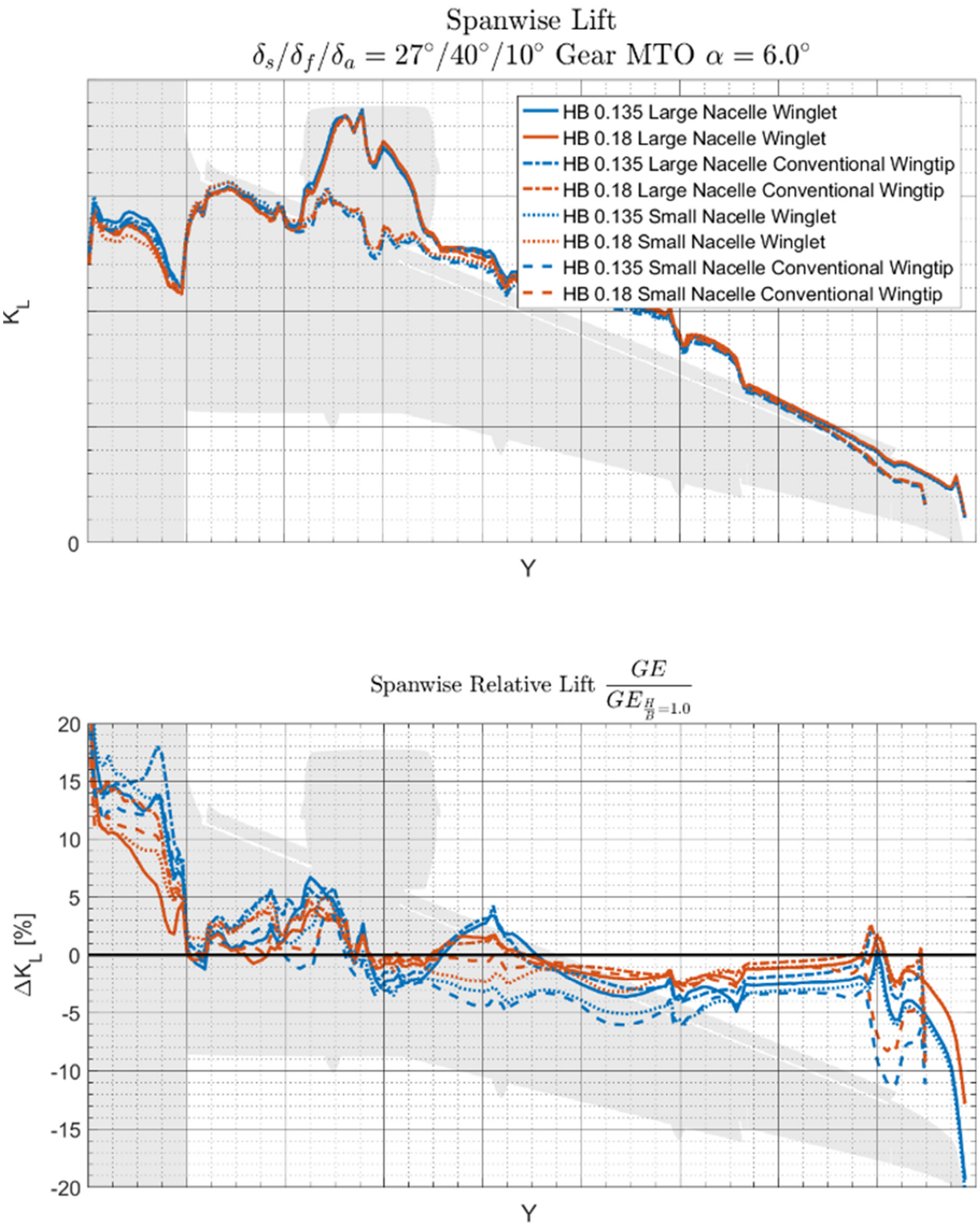

Figure 9.84 - Spanwise lift distribution for the large nacelle and small nacelle geometry with gear deployed and MTO thrust conditions at $\alpha = 6.0°$ $\frac{h}{b} = 0.135$ and $\frac{h}{b} = 0.18$ for the landing configuration

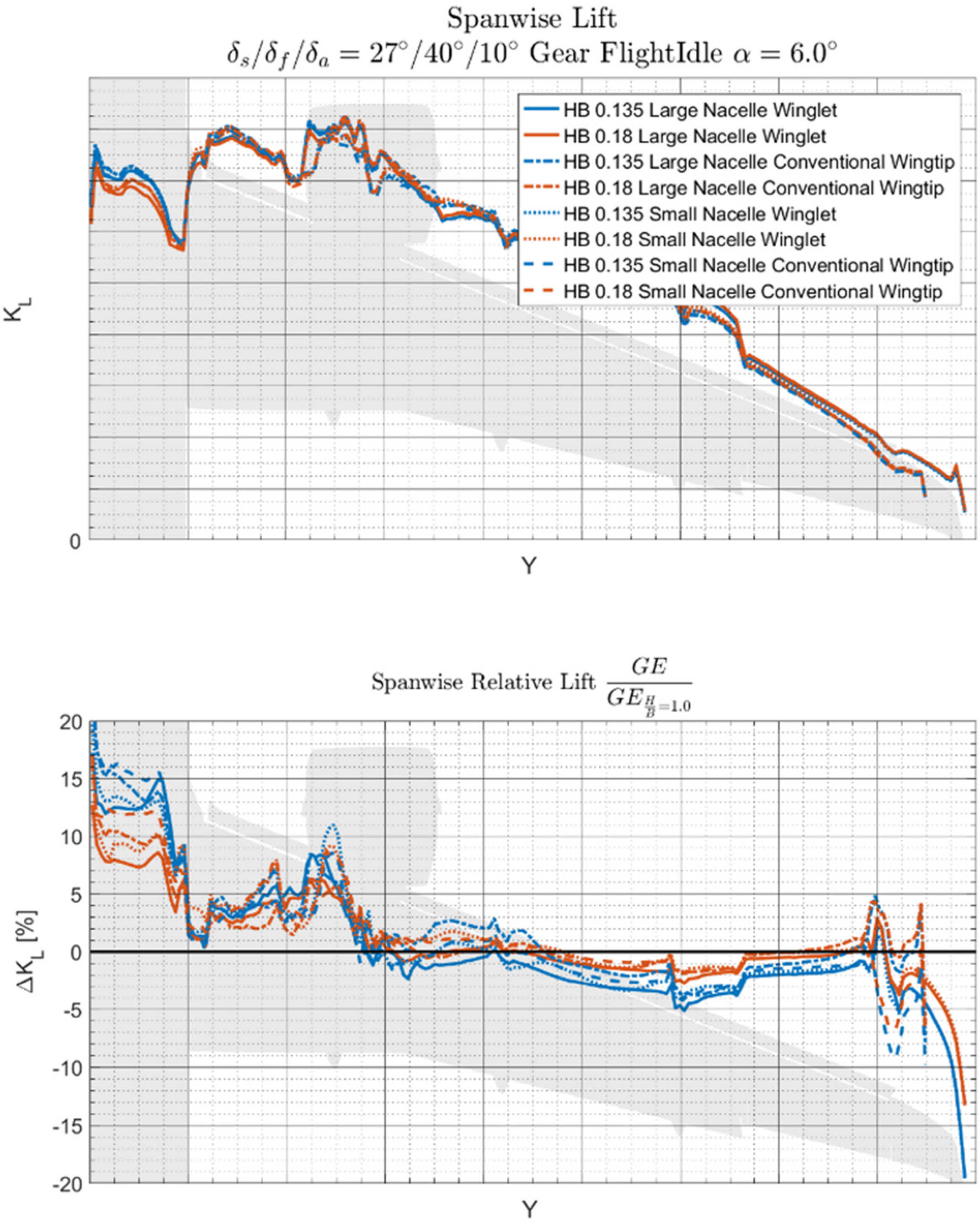

Figure 9.85 - Spanwise lift distribution for the large nacelle and small nacelle geometry with gear deployed and flightidle thrust conditions at $\alpha = 6.0°$ $\frac{h}{b} = 0.135$ and $\frac{h}{b} = 0.18$ for the landing configuration

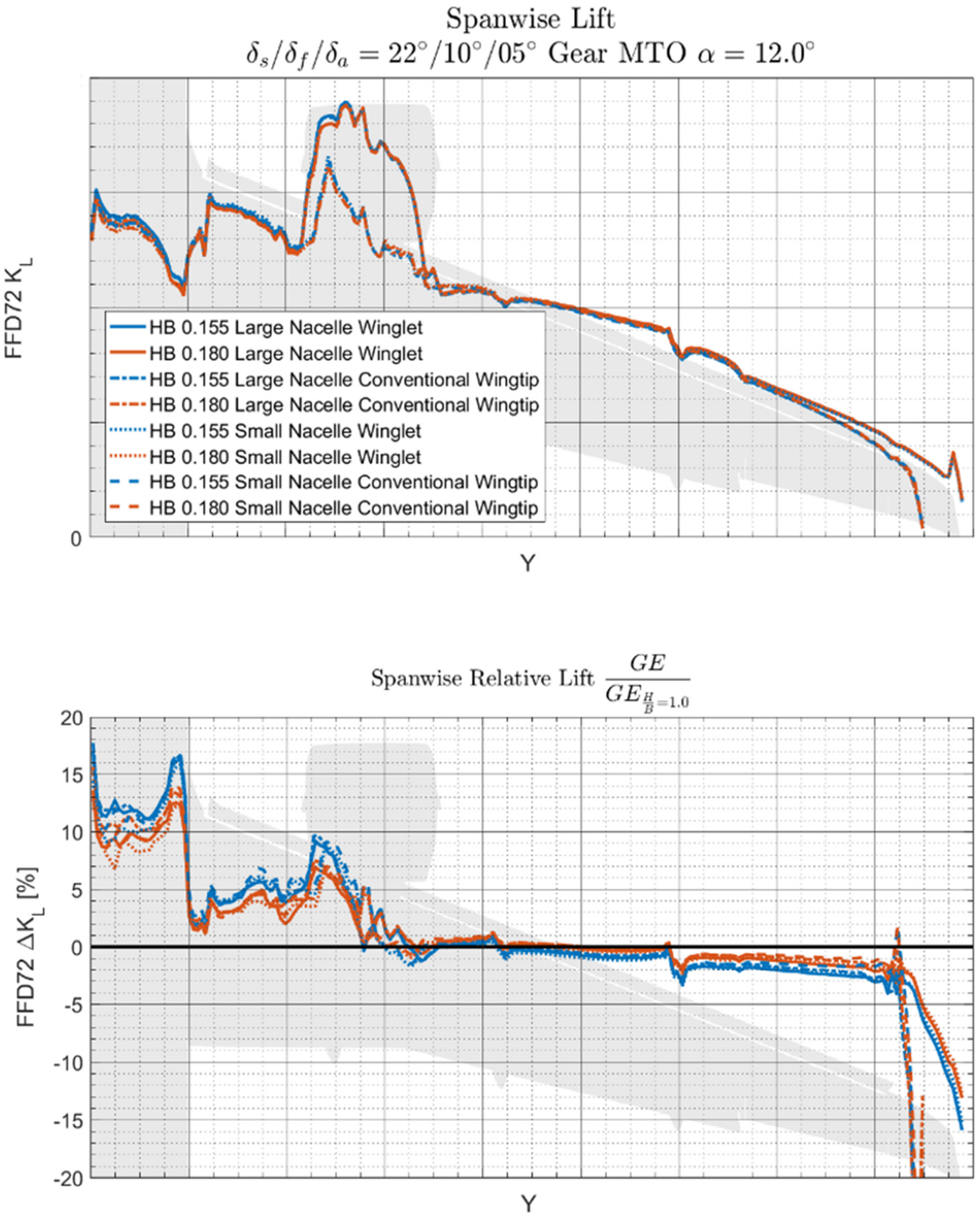

Figure 9.86 - Spanwise lift distribution for the large nacelle and small nacelle geometry with gear deployed and MTO thrust conditions at $\alpha = 12.0°$ $\frac{h}{b} = 0.155$ and $\frac{h}{b} = 0.18$ for the take-off configuration

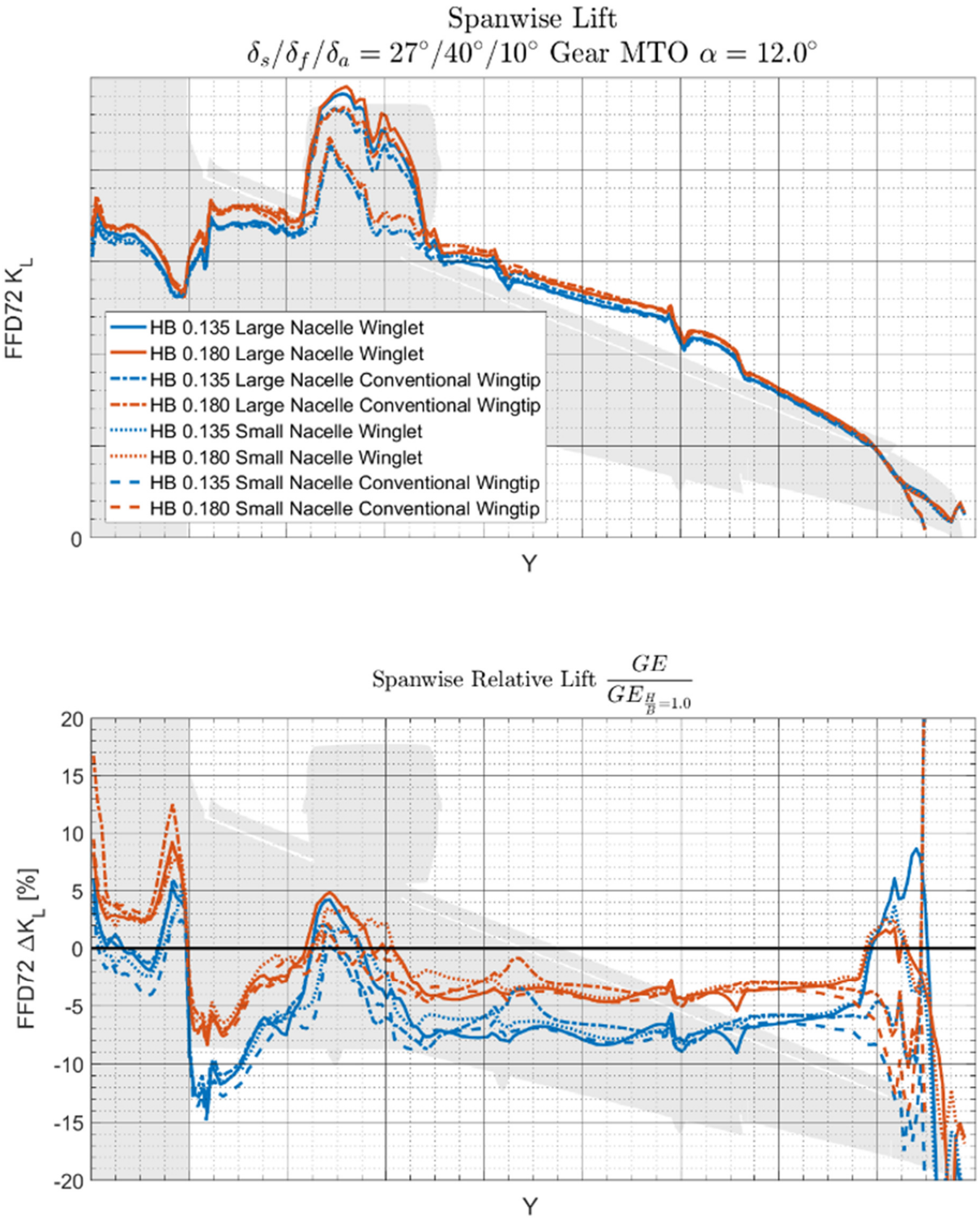

Spanwise Lift

$\delta_s/\delta_f/\delta_a = 27^\circ/40^\circ/10^\circ$ Gear MTO $\alpha = 12.0^\circ$

Spanwise Relative Lift $\frac{GE}{GE_{\frac{H}{B}=1.0}}$

Figure 9.87 - Spanwise lift distribution for the large nacelle and small nacelle geometry with gear deployed and MTO thrust conditions at $\alpha = 12.0°$ $\frac{h}{b} = 0.135$ and $\frac{h}{b} = 0.18$ for the landing configuration

9.10 Appendix J – Spanwise Drag Distributions comparing different Geometries

The total drag distribution at $\alpha = 6.0°$ and $\frac{h}{b} = 0.135$ for the take-off MTO, landing MTO and landing flightidle configurations are shown in Figure 9.88, Figure 9.89 and Figure 9.90 respectively. When comparing the two MTO thrust setting cases with the flightidle thrust setting, in the region of the engine small differences in relative drag reduction can be observed, which are encircled in Figure 9.88, Figure 9.89. For the flightidle case in Figure 9.90 these differences between the nacelle sizes are no longer present

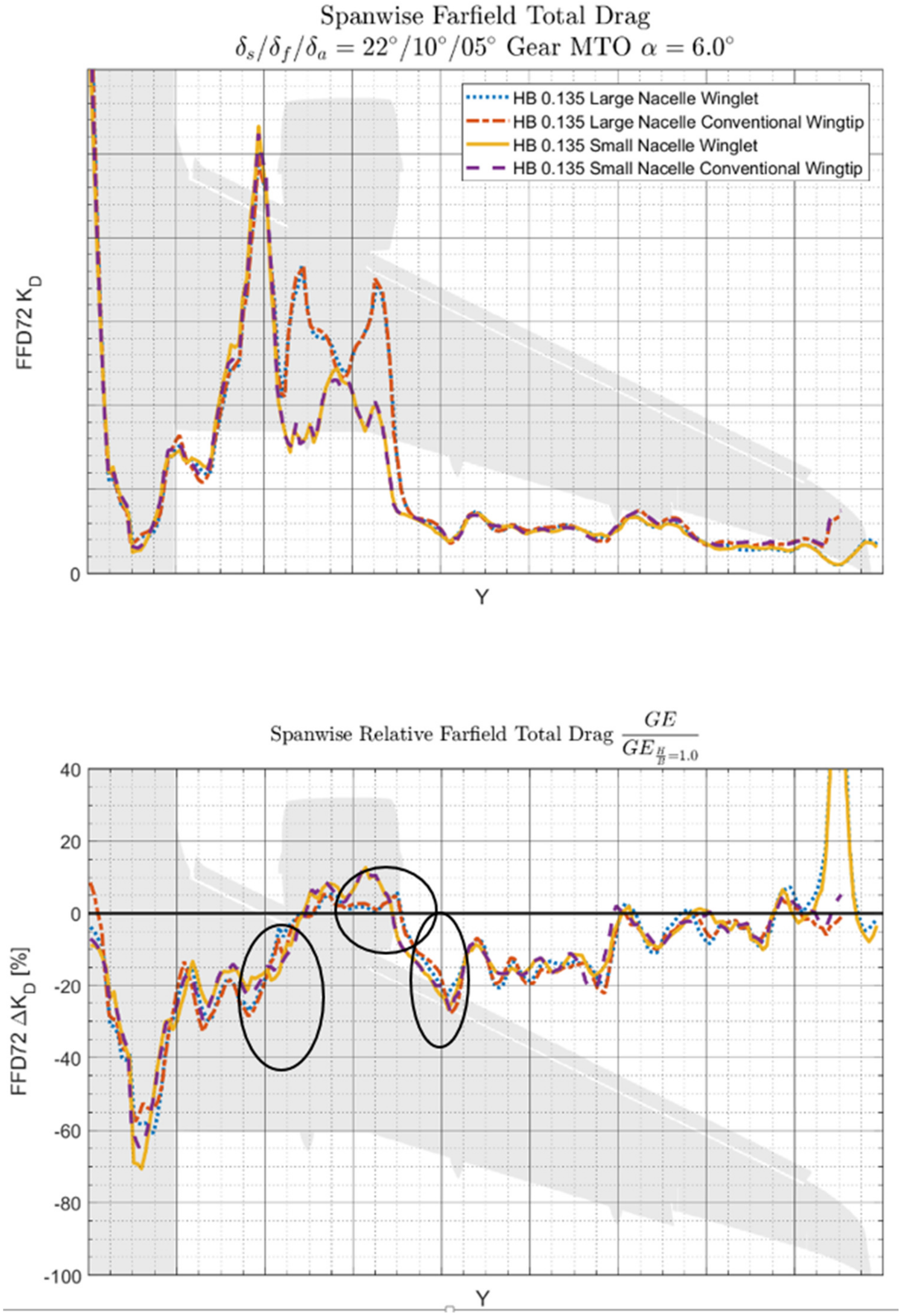

Figure 9.88 - Spanwise lift distribution for the large nacelle and small nacelle geometry with gear deployed and MTO thrust conditions at $\alpha = 6.0°$ $\frac{h}{b} = 0.135$ for the take-off configuration

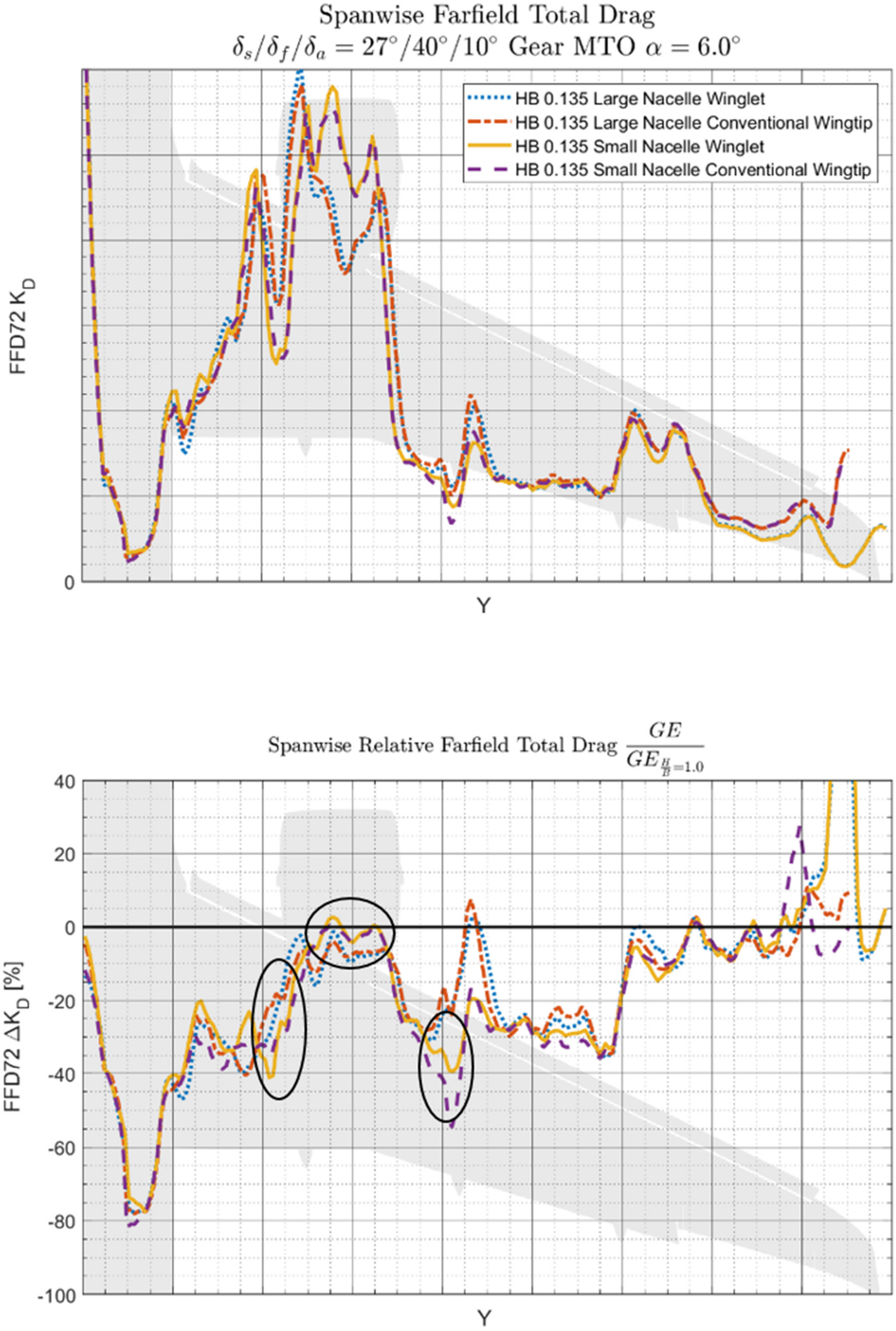

Figure 9.89 - Spanwise lift distribution for the large nacelle and small nacelle geometry with gear deployed and MTO thrust conditions at $\alpha = 6.0°$ $\frac{h}{b} = 0.135$ *for the landing configuration*

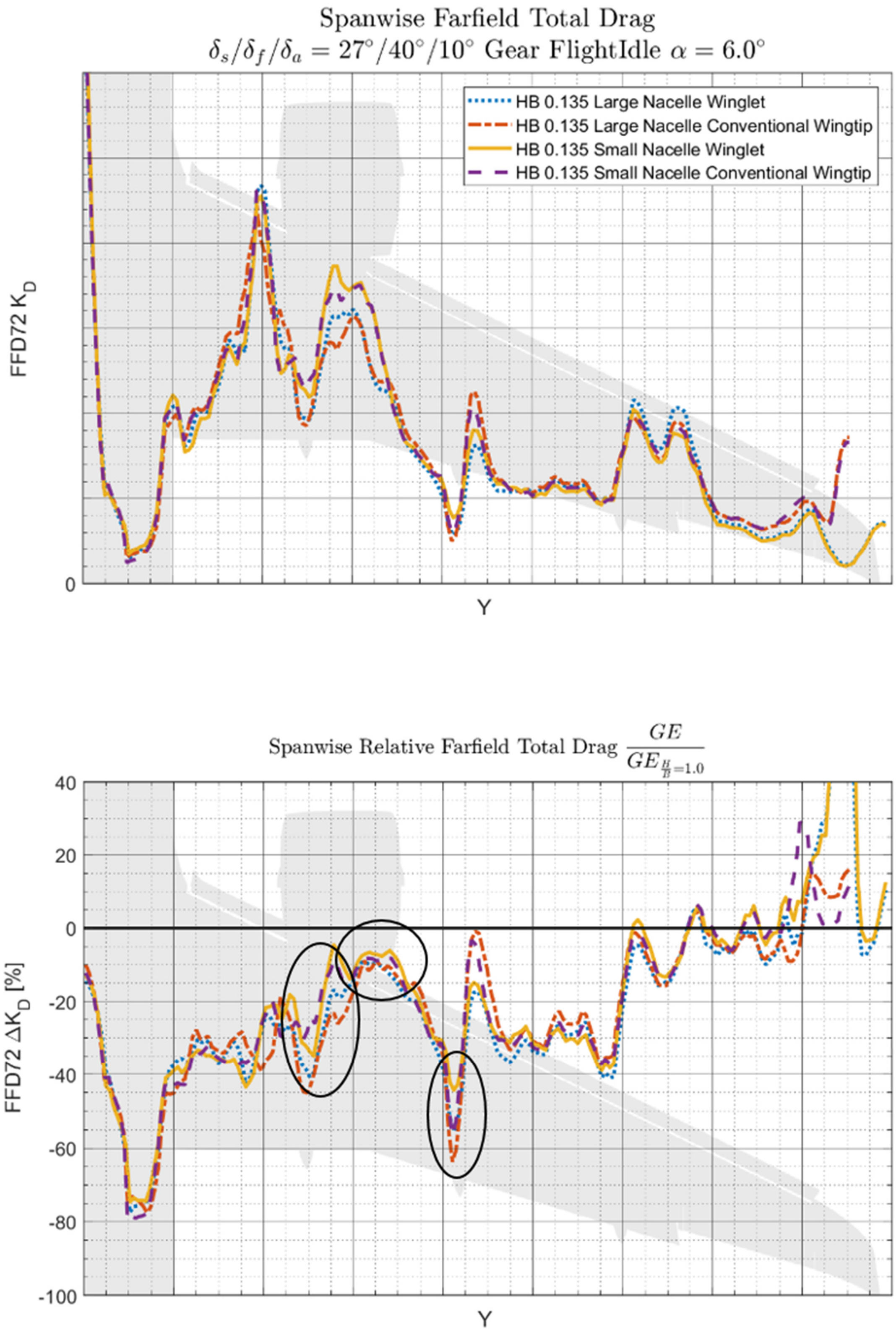

Figure 9.90 - Spanwise lift distribution for the large nacelle and small nacelle geometry with gear deployed and flightidle thrust conditions at $\alpha = 6.0°$ $\frac{h}{b} = 0.135$ *for the landing configuration*

9.11 Appendix K – Polynomial Surface Fit Plots

The Matlab 2017b function ‘fit’ is used to calculate the polynomial surface fit of a third degree as a function of α and $\frac{h}{b}$ using the default settings of this function. That results in the following polynomial equation:

$$\Delta\Delta C_L\left(\frac{h}{b},\alpha\right) = p_0 + p_{10}\alpha + p_{01}\frac{h}{b} + p_{20}\alpha^2 + p_{02}\left(\frac{h}{b}\right)^2 + p_{11}\alpha\frac{h}{b} + p_{30}\alpha^3 + p_{21}\alpha^2\frac{h}{b} + p_{12}\alpha\left(\frac{h}{b}\right)^2 + p_{03}\left(\frac{h}{b}\right)^3$$

$$\Delta\Delta C_D\left(\frac{h}{b},\alpha\right) = p_0 + p_{10}\alpha + p_{01}\frac{h}{b} + p_{20}\alpha^2 + p_{02}\left(\frac{h}{b}\right)^2 + p_{11}\alpha\frac{h}{b} + p_{30}\alpha^3 + p_{21}\alpha^2\frac{h}{b} + p_{12}\alpha\left(\frac{h}{b}\right)^2 + p_{03}\left(\frac{h}{b}\right)^3$$

An example of such a polynomial surface is provided in Figure 9.91, corresponding to the data from Figure 9.99 in **Fout! Verwijzingsbron niet gevonden.**.

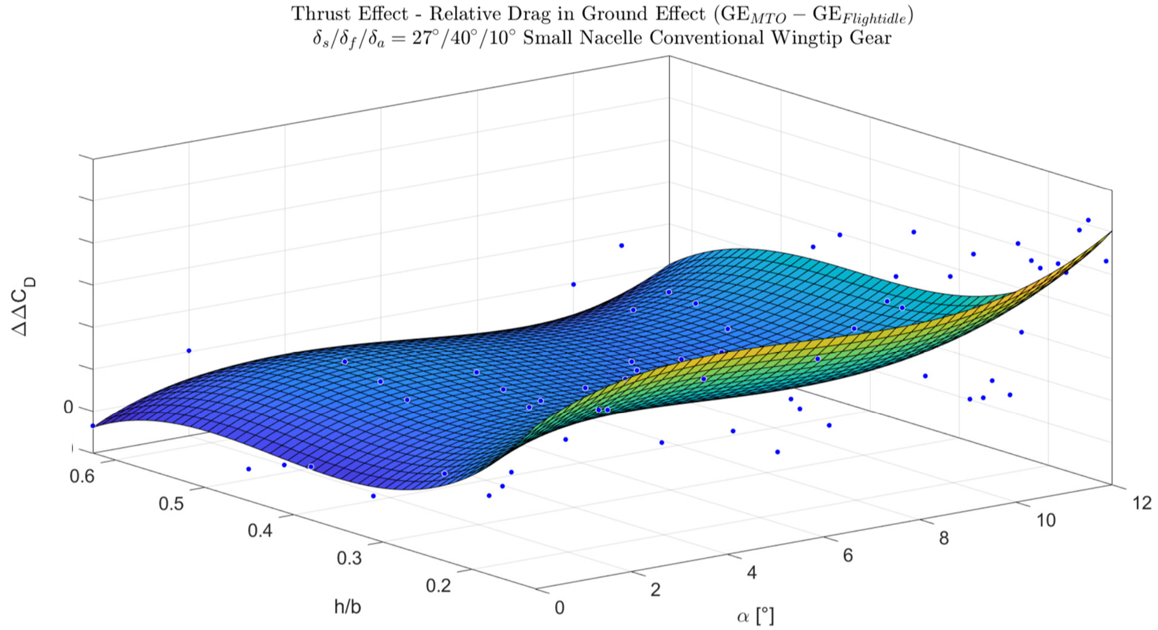

Figure 9.91 – Example polynomial surface fit of change to the incremental drag coefficient in ground effect due to engine thrust setting for a range of h/b for the small nacelle, conventional winglet geometry with gear deployed in landing configuration

9.11.1 Thrust Effect

9.11.1.1 Lift

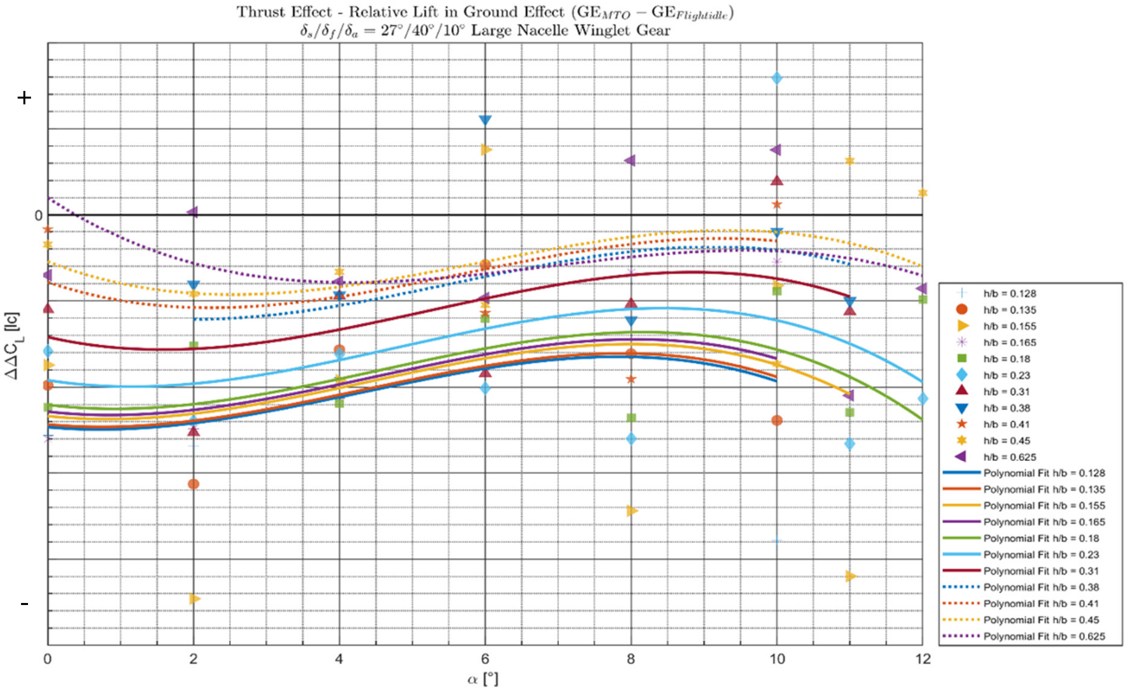

Figure 9.92 – Polynomial fit of change to the incremental lift coefficient in ground effect due to engine thrust setting for a range of h/b for the large nacelle, winglet geometry with gear deployed in landing configuration

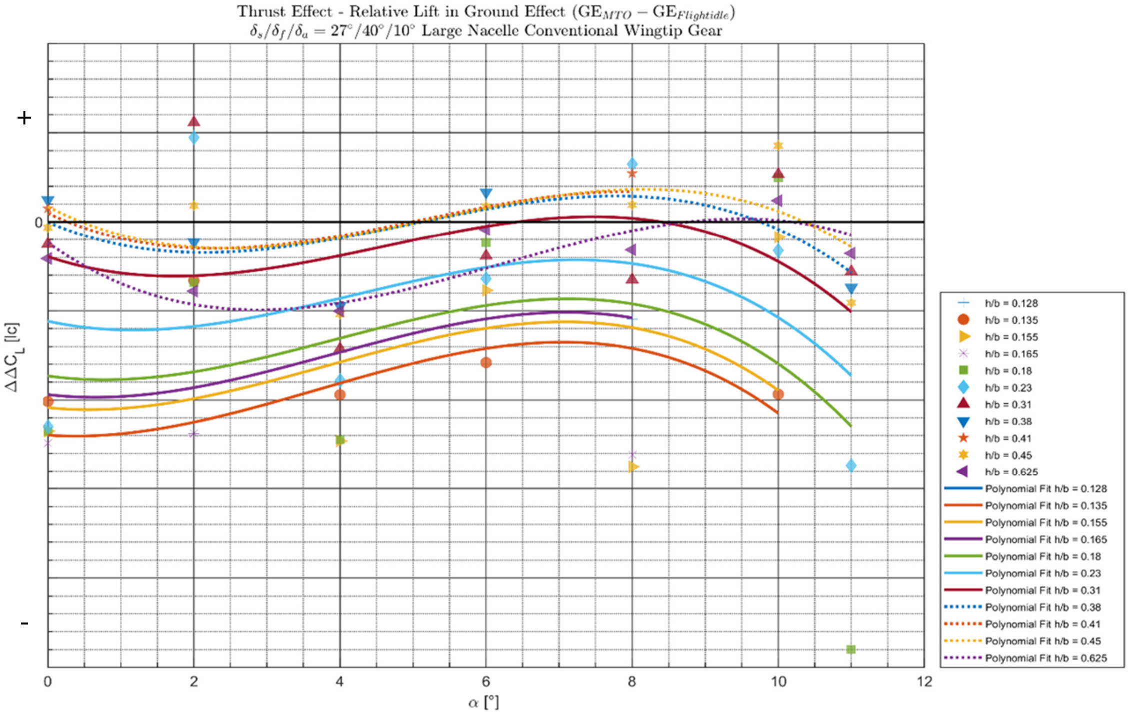

Figure 9.93 – Polynomial fit of change to the incremental lift coefficient in ground effect due to engine thrust setting for a range of h/b for the small nacelle, winglet geometry with gear deployed in landing configuration using a polynomial surface fit

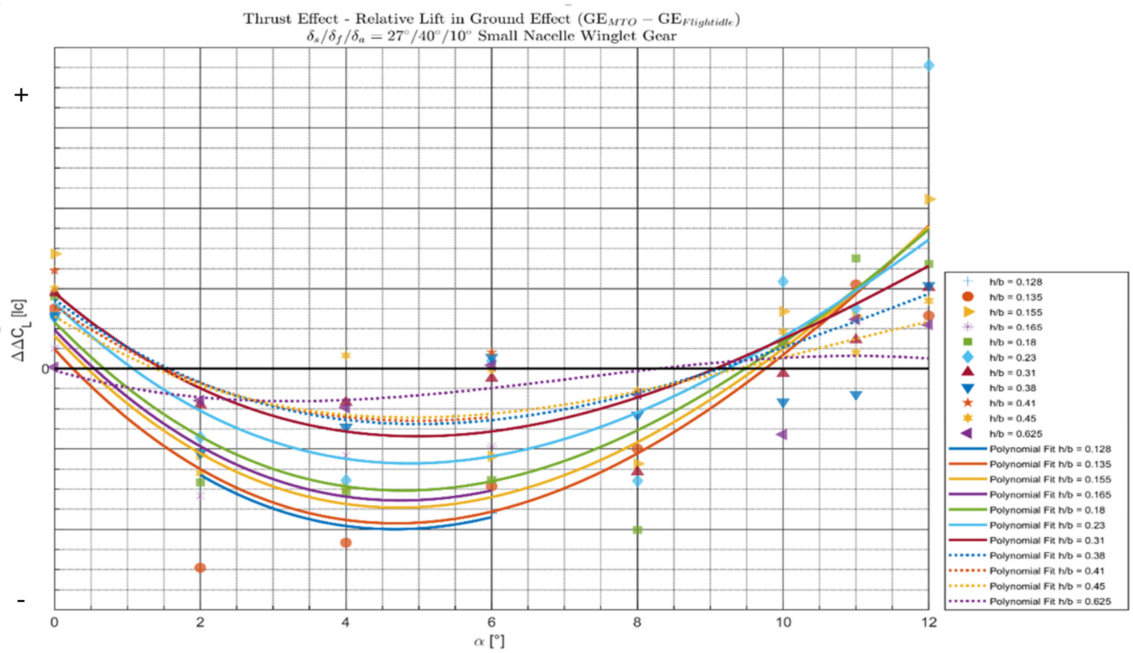

Figure 9.94 – Polynomial fit of change to the incremental lift coefficient in ground effect due to engine thrust setting for a range of h/b for the small nacelle, conventional wingtip geometry with gear deployed in landing configuration using a polynomial surface fit

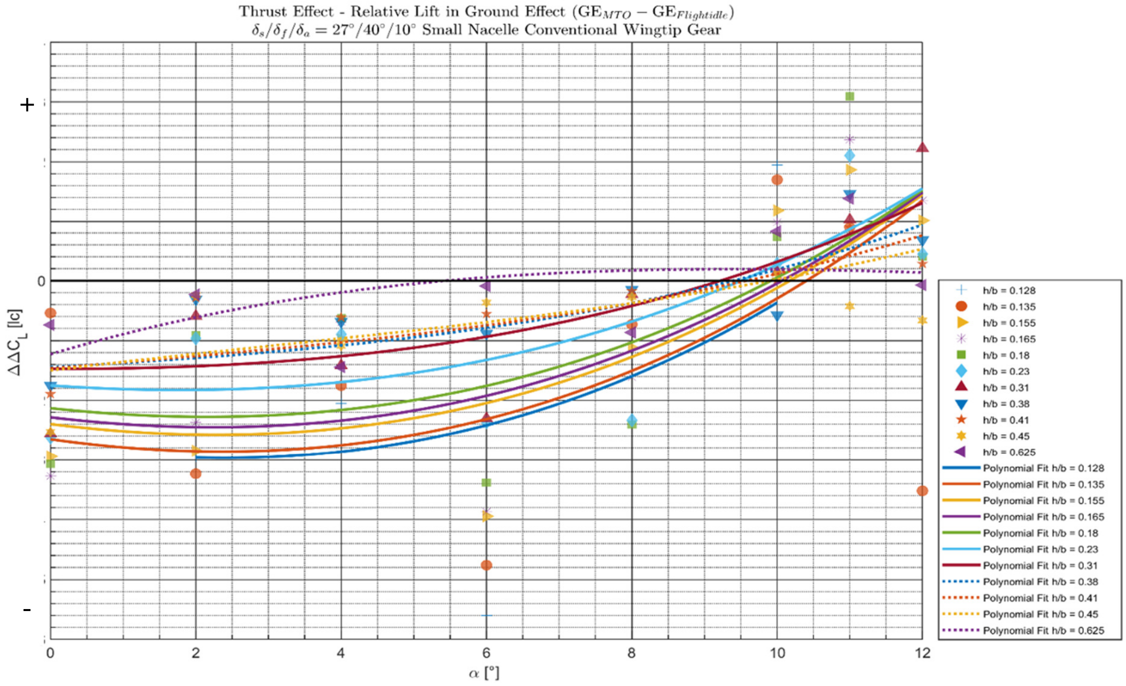

Figure 9.95 – Polynomial fit of change to the incremental lift coefficient in ground effect due to engine thrust setting for a range of h/b for the small nacelle, conventional wingtip geometry with gear deployed in landing configuration using a polynomial surface fit

9.11.1.2 Drag

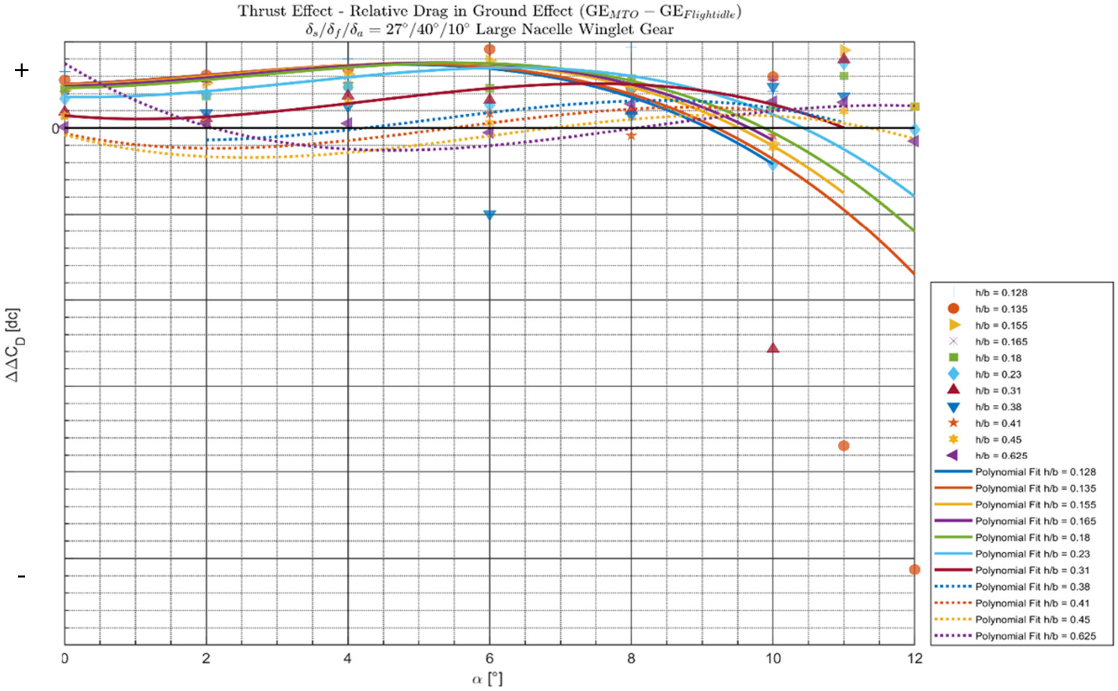

Figure 9.96 – Polynomial fit change to the incremental drag coefficient in ground effect due to engine thrust setting for a range of h/b for the large nacelle, winglet geometry with gear deployed in landing configuration using a polynomial surface fit

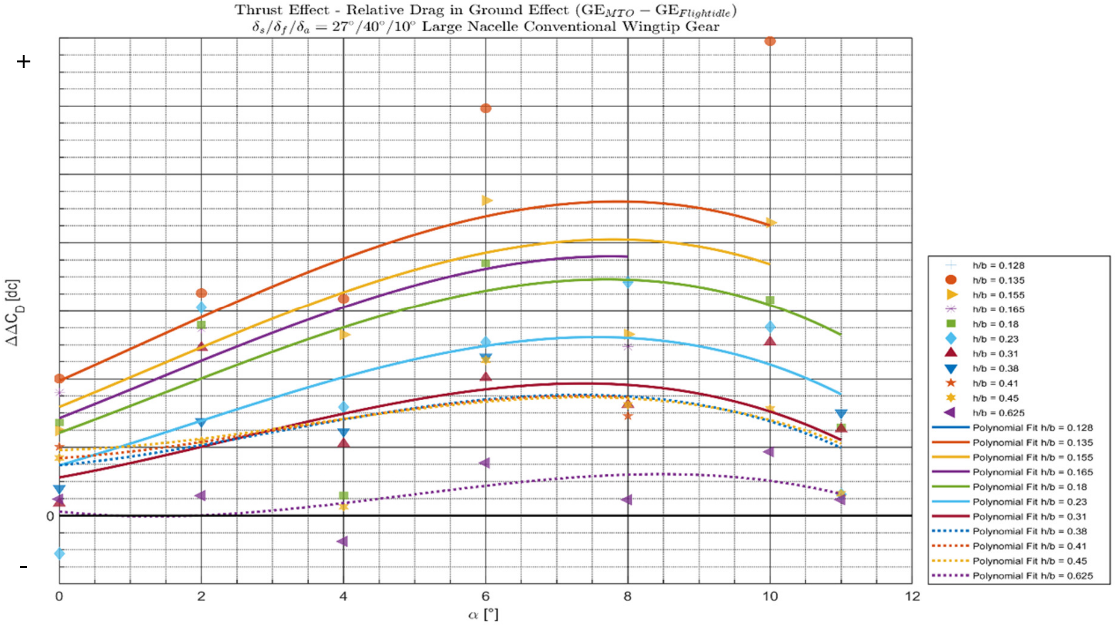

Figure 9.97 – Polynomial fit change to the incremental drag coefficient in ground effect due to engine thrust setting for a range of h/b for the large nacelle, conventional wingtip geometry with gear deployed in landing configuration using a polynomial surface fit

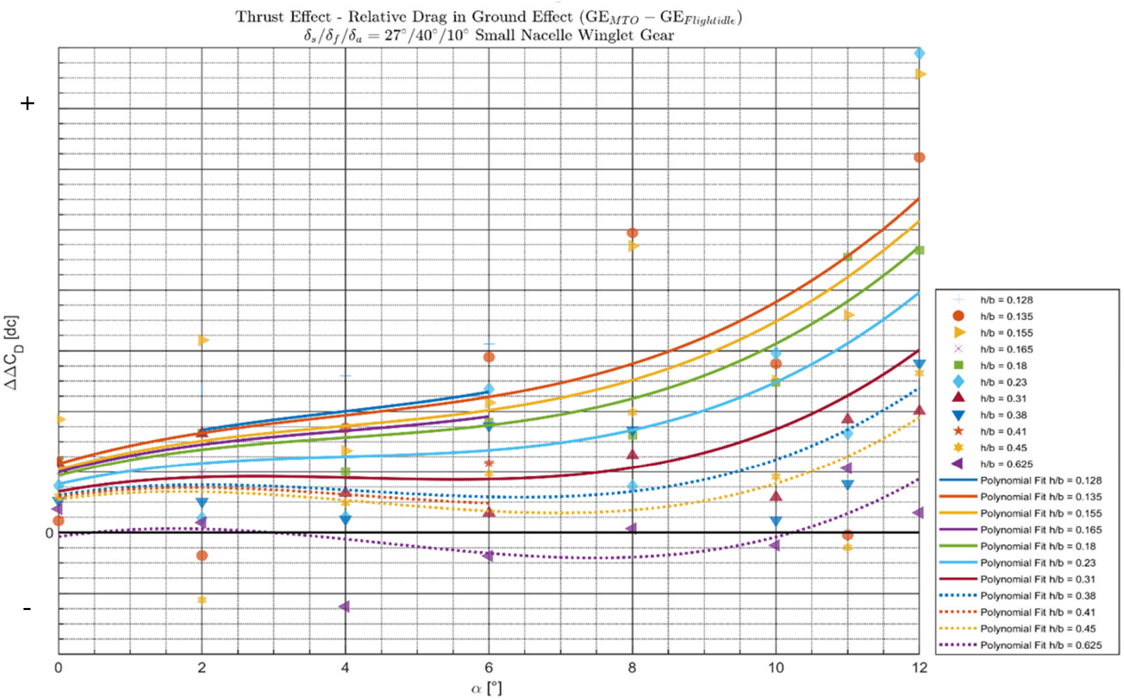

Figure 9.98 – Polynomial fit change to the incremental drag coefficient in ground effect due to engine thrust setting for a range of h/b for the small nacelle, winglet geometry with gear deployed in landing configuration using a polynomial surface fit

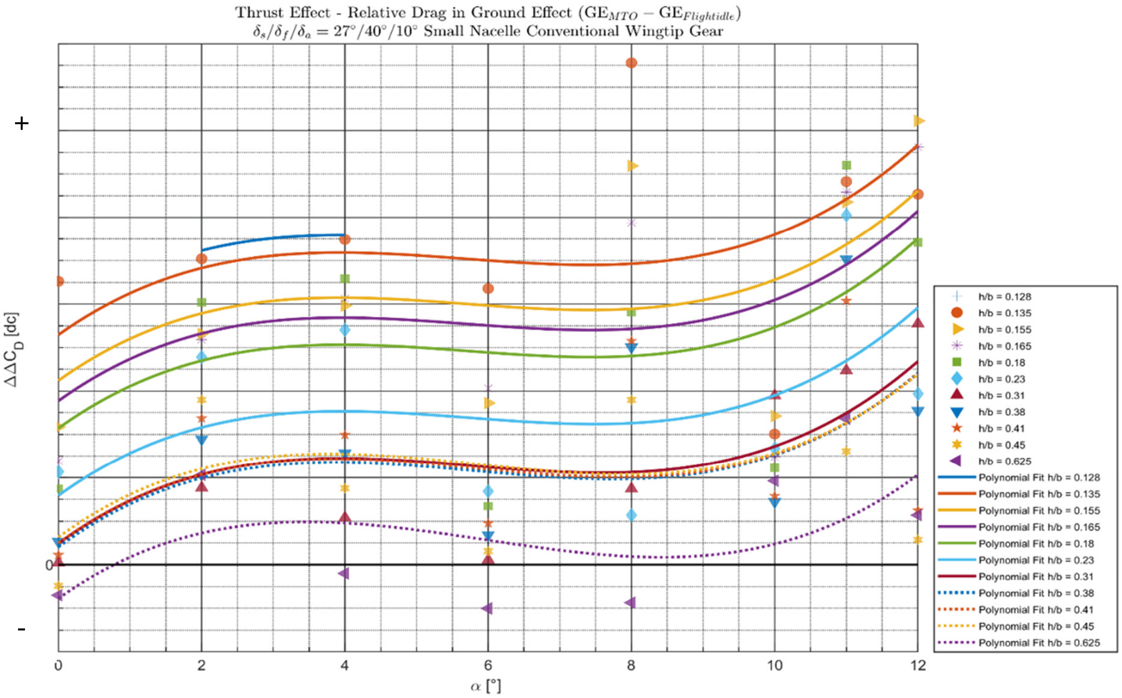

Figure 9.99 – Polynomial fit change to the incremental drag coefficient in ground effect due to engine thrust setting for a range of h/b for the small nacelle, conventional wingtip geometry with gear deployed in landing configuration using a polynomial surface fit

9.11.2 Gear Effect

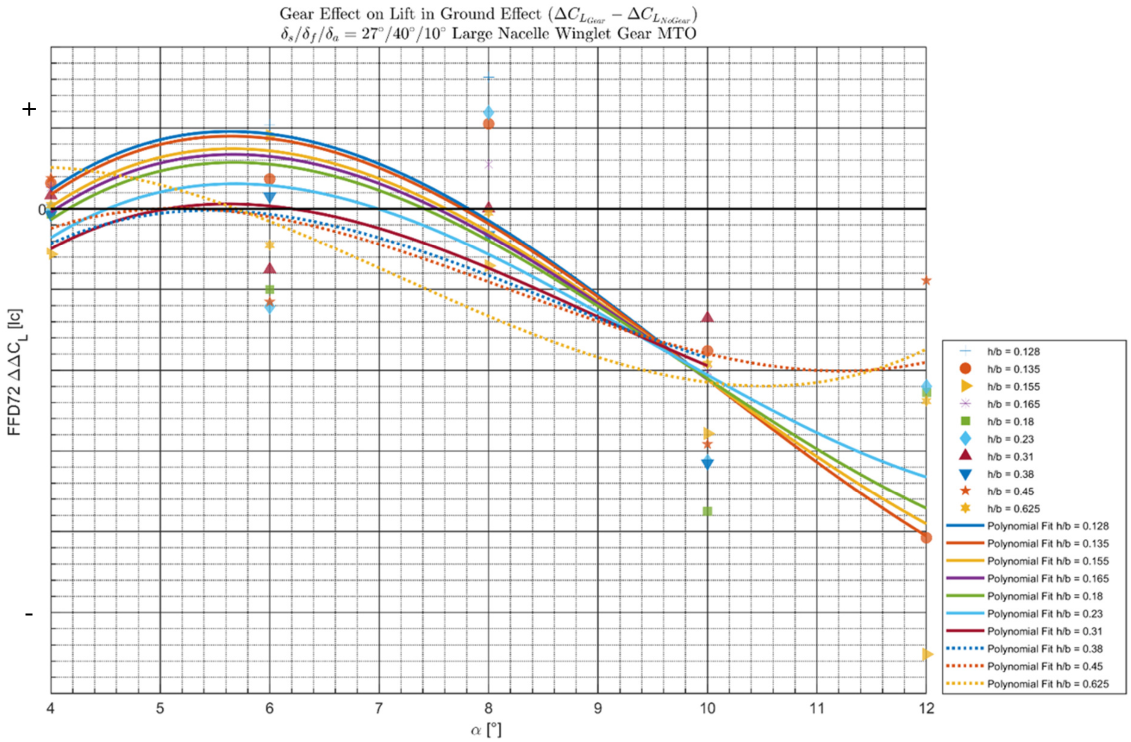

Figure 9.100 – Polynomial fit to the incremental lift coefficient change in ground effect due to gear effect for the large nacelle, winglet geometry with gear deployed in landing configuration with MTO thrust setting using a polynomial surface fit

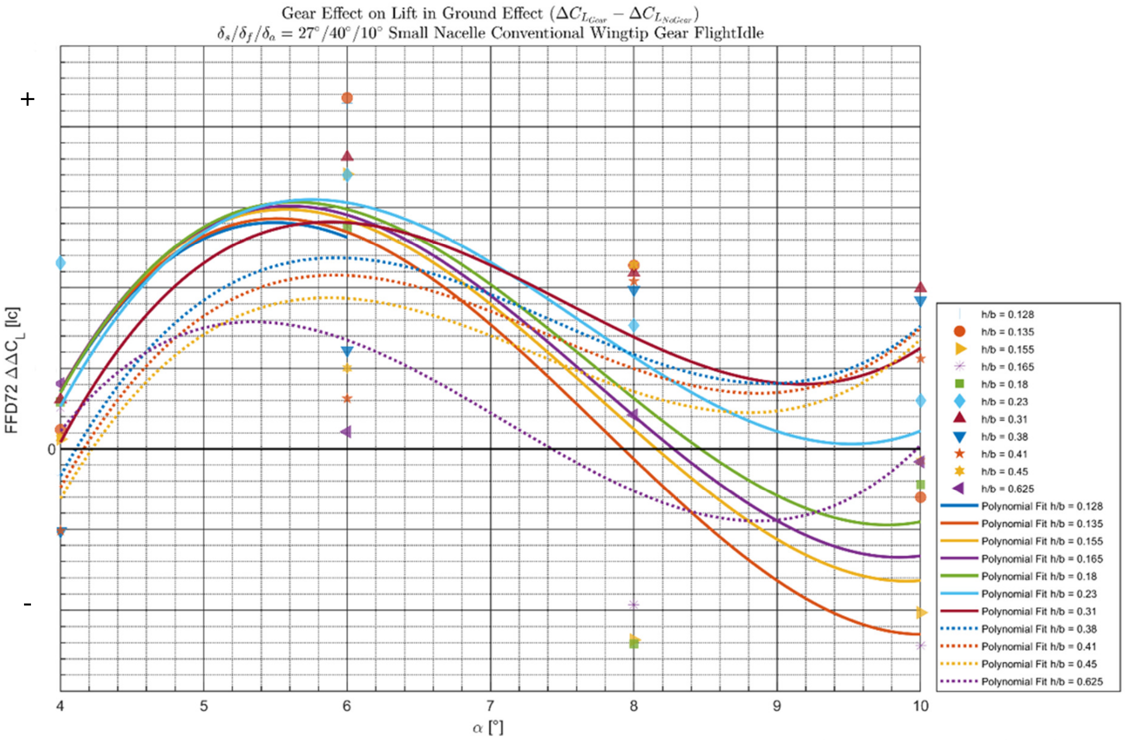

Figure 9.101 – Polynomial fit to the incremental lift coefficient change in ground effect due to gear effect for the small nacelle, conventional wingtip geometry with gear deployed in landing configuration with flightidle thrust setting using a polynomial surface fit

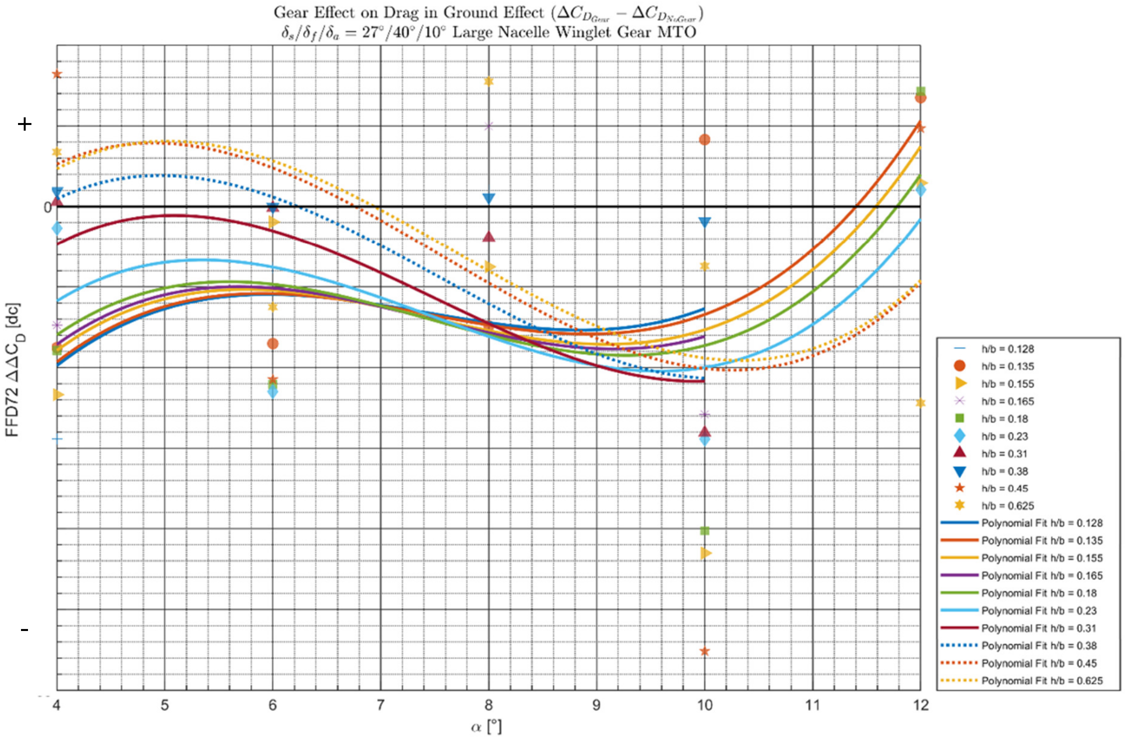

Figure 9.102 – Polynomial fit to the incremental drag coefficient change in ground effect due to gear effect for the large nacelle, winglet geometry with gear deployed in landing configuration with MTO thrust setting using a polynomial surface fit

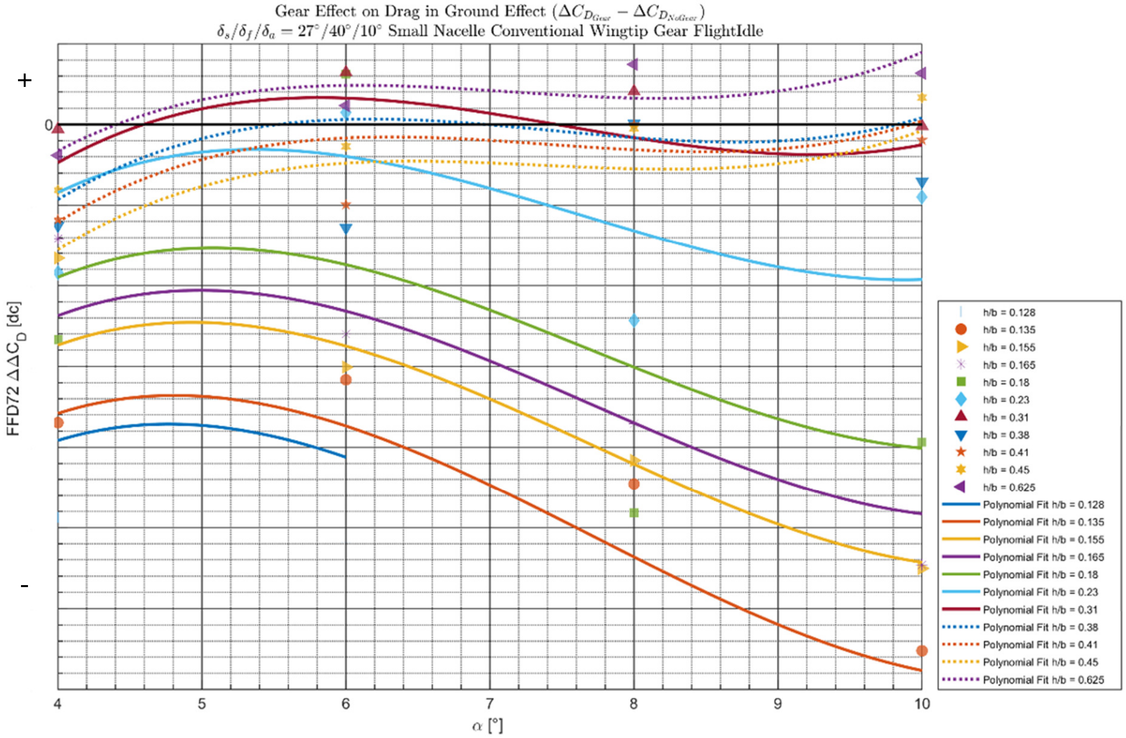

Figure 9.103 – Polynomial fit to the incremental drag coefficient change in ground effect due to gear effect for the small nacelle, conventional wingtip geometry with gear deployed in landing configuration with flightidle thrust setting using a polynomial surface fit

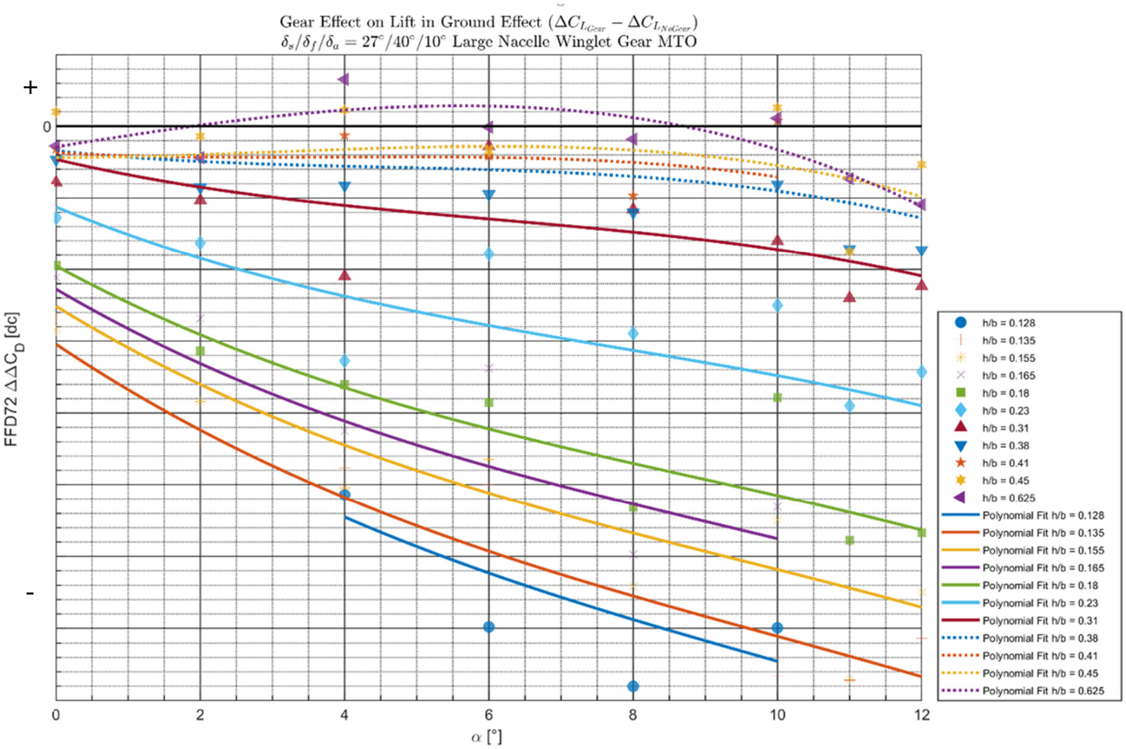

Figure 9.104 – Polynomial fit to the change to main landing gear drag in ground effect for the large nacelle, winglet geometry in landing configuration with MTO thrust setting using a polynomial surface fit

9.12 Appendix L – Interaction between Nose Landing Gear Wake and Inboard Leading-Edge

Figure 9.105 shows the zoomed out version of a number of streamlines which were placed close to the nose landing gear for the large nacelle, winglet geometry with MTO thrust setting at $\alpha = 12.0°$ and $h/b = 0.155$. The color on the streamlines indicate ratio of the total pressure, $\frac{P_{tot_{local}}}{P\_tot_{freestream}}$.

Therefore, it can be seen that the streamlines pass through the wake of the nose landing gear and the total pressure is reduced. These streamlines with reduced energy subsequently flow over the leading edge of the main wing, resulting in a loss of lift in this region. It is possible that this is one of the causes of the lift loss seen in this area on the spanwise absolute lift distribution shown in Figure 4.65 .

Figure 9.106 shows in closer detail how the streamlines pass the nose landing gear, while Figure 9.107 shows in detail how the same streamlines flow over the main wing. Finally Figure 9.108 shows streamlines placed at exactly the same location for the same flow solution but with the landing gear removed. It can be seen how there is now no reduction in total pressure before the flow reaches the mainwing.

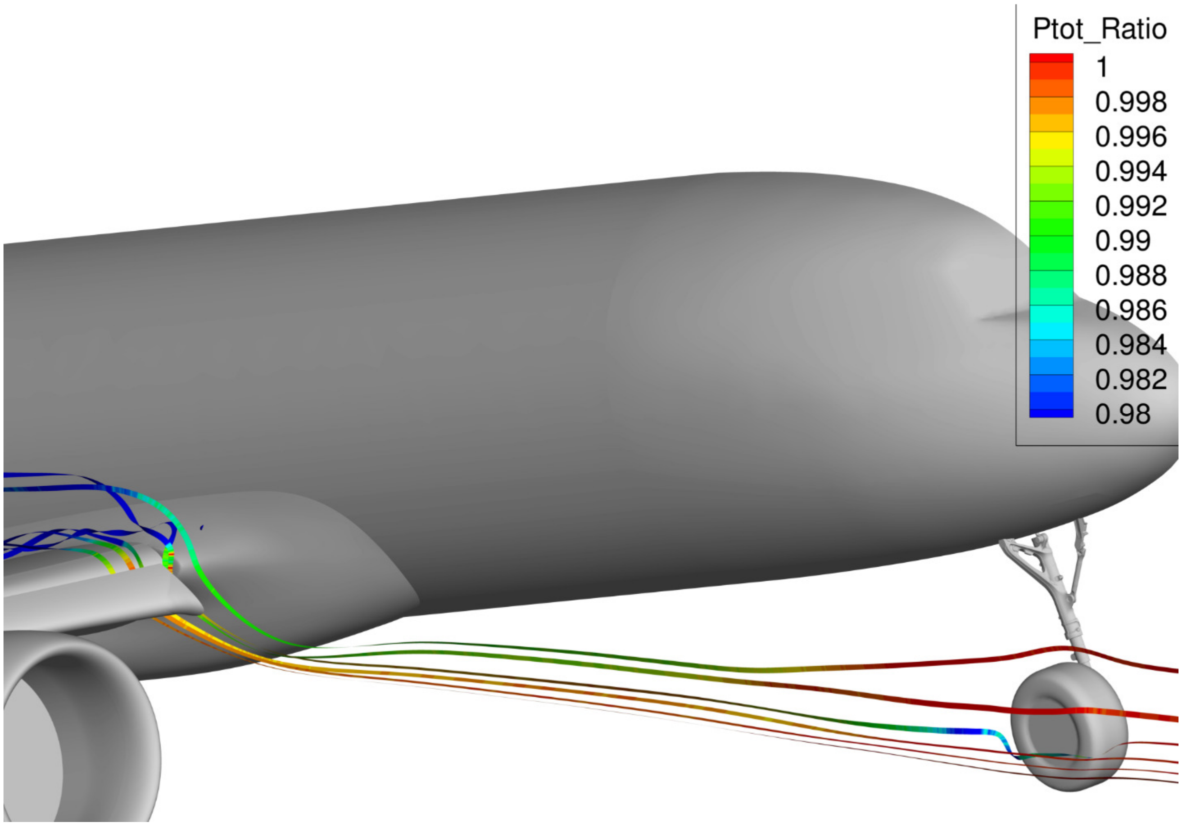

Figure 9.105 – Overview of streamlines passing through the wake of the nose landing gear after which they flow over the mainwing leading edge in ground effect for the large nacelle, winglet geometry with MTO thrust conditions $\alpha = 12.0°$ $\frac{h}{b} = 0.155$

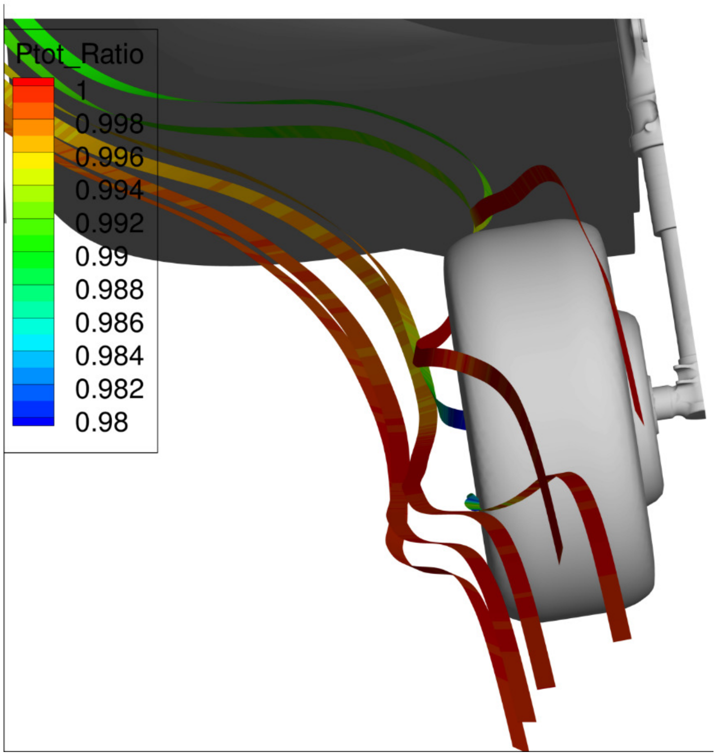

Figure 9.106 – Detail shot of the same streamlines flowing past the nose landing gear for the large nacelle, winglet geometry with MTO thrust conditions $\alpha = 12.0° \frac{h}{b} = 0.155$

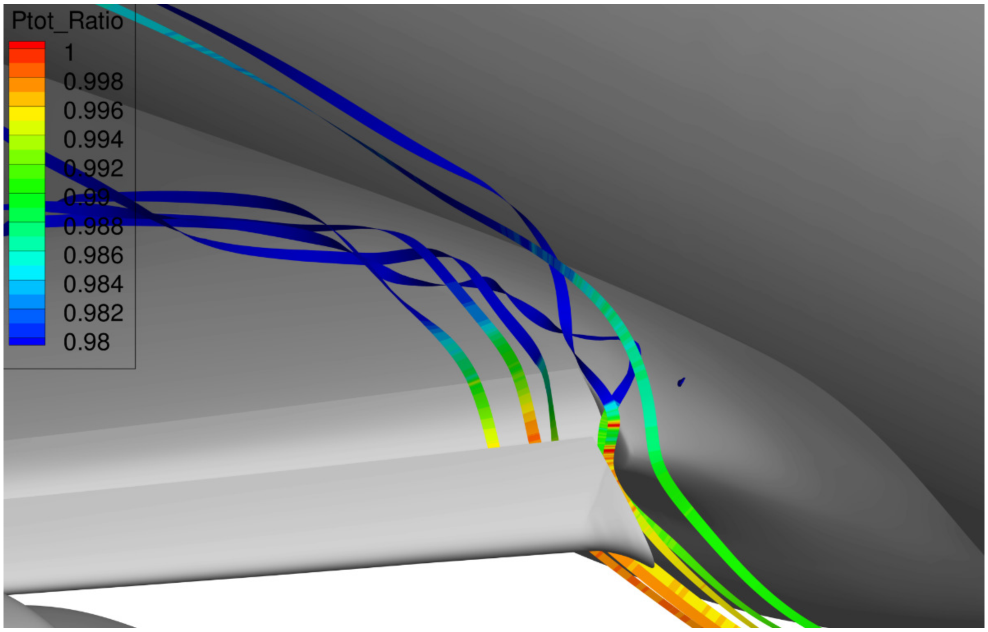

Figure 9.107 – Detail shot of the same streamlines flowing over the main wing leading edge and onglet for the large nacelle, winglet geometry with MTO thrust conditions $\alpha = 12.0° \frac{h}{b} = 0.155$

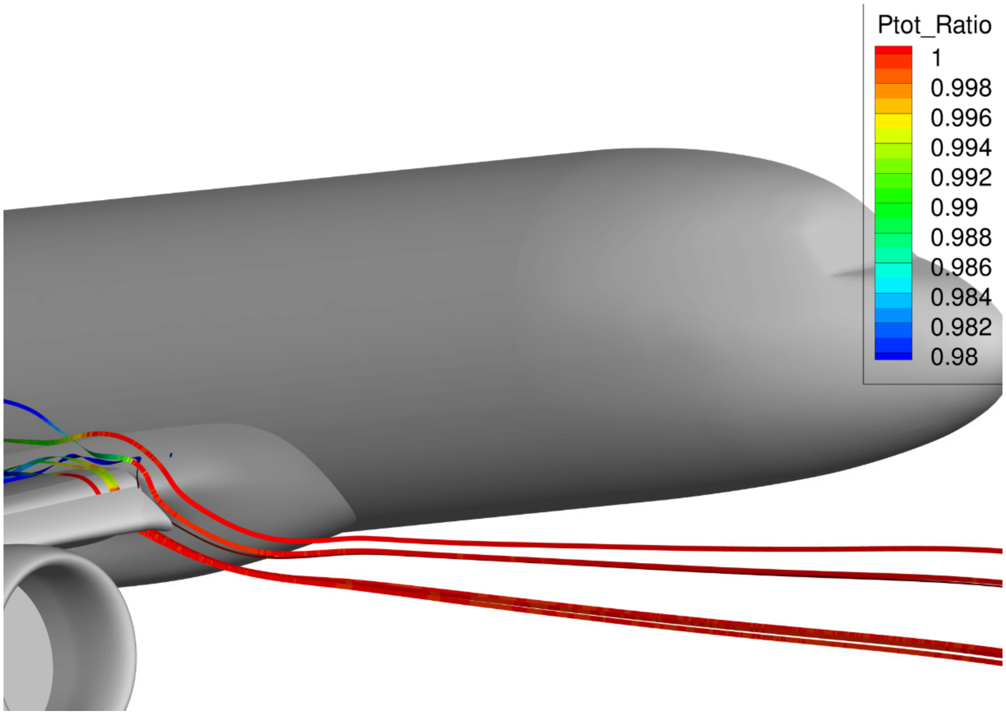

Figure 9.108 – Same streamlines as the previous three pictures with the landing gear now removed. No total pressure loss is now present until after the flow interacts with the wing leading edge. Large nacelle, winglet geometry with MTO thrust conditions $\alpha = 12.0° \frac{h}{b} = 0.155$

9.13 Appendix M – Total Pressure ISO-Surface Flow Visualization

During the thesis work an attempt was made to visualize the change in the three-dimensional flow due to ground effect. This was done by means of plotting the ISO-surface of the total pressure P_{tot}, at a value below the freestream total pressure P_{tot_∞}. The wake from the aircraft is visualized in this manner and the change in wake location and strength can be determined qualitatively.

Figure 9.109 and Figure 9.110 show the side view of the aircraft at $\frac{h}{b} = 0.128$ and $\frac{h}{b} = 1.0$ respectively. The wake of the main landing gear is deflected away from the ground due to the presence of the ground effect, shown in Figure 9.109, highlighted in region A. In Figure 9.110 the ground plane from Figure 9.109 is still present as a reference. In this case the wake is extends quite a bit below the reference ground plane.
In contrast the wake of the nose-landing gear, highlighted in region B for both figures, remains virtually unchanged due to ground effect. This can be understood by the fact that this is at $\alpha = 10.0°$, which means that the nose-landing gear is located significantly further away from the ground compared to the main landing gear. Thus the influence of the ground nose-landing gear is almost negligible in this case.

Figure 9.111 and Figure 9.112 shows the top down view of the same case. Of note is that the wake at the wing-fuselage junction is significantly thicker in the case of ground effect (region C). There is no clear change at the wingtip. Neither the wingtip wake nor the outboard slat vortex show a significant change in direction, which might be expected based on literature.

Figure 9.113 and Figure 9.114 show the final view of the same case. Of note is that the wake of the wing is angled upwards significantly due to ground effect and now envelops the VTP and rudder more significantly (region D). It can be expected that the rudder effectiveness will therefore decrease in ground effect, but this was not investigated since this is outside of the scope of the thesis.
The vortex from the onglet in region E is deflected upwards due to ground effect. The flap is hit by this vortex further backwards (in chordwise direction). This could be one of the reasons for earlier onset of stall in ground effect, which is discussed in subchapter 4.7.

It can be concluded from this section that the main influence of the ground effect on the wing wake is that it is deflected in upwards direction. The rudder becomes more immersed in the wake from the wing. There were no significant changes to nose-landing gear and wingtip wake observed.

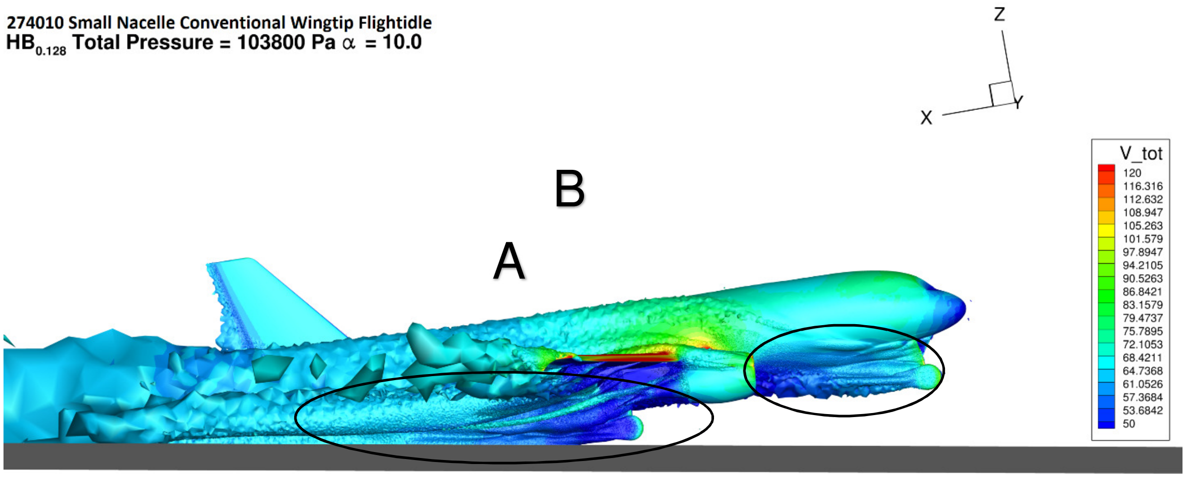

Figure 9.109 – Iso Surface of total pressure $\alpha = 10.0^{\circ} \frac{h}{b} = 0.128$

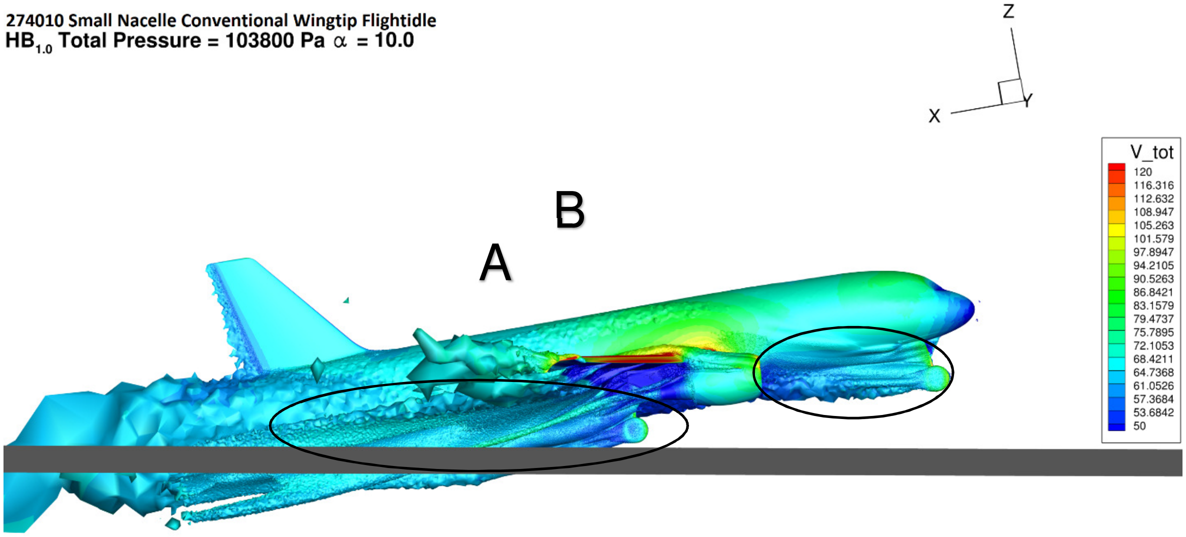

Figure 9.110 – Iso Surface of total pressure $\alpha = 10.0^{\circ} \frac{h}{b} = 1.0$

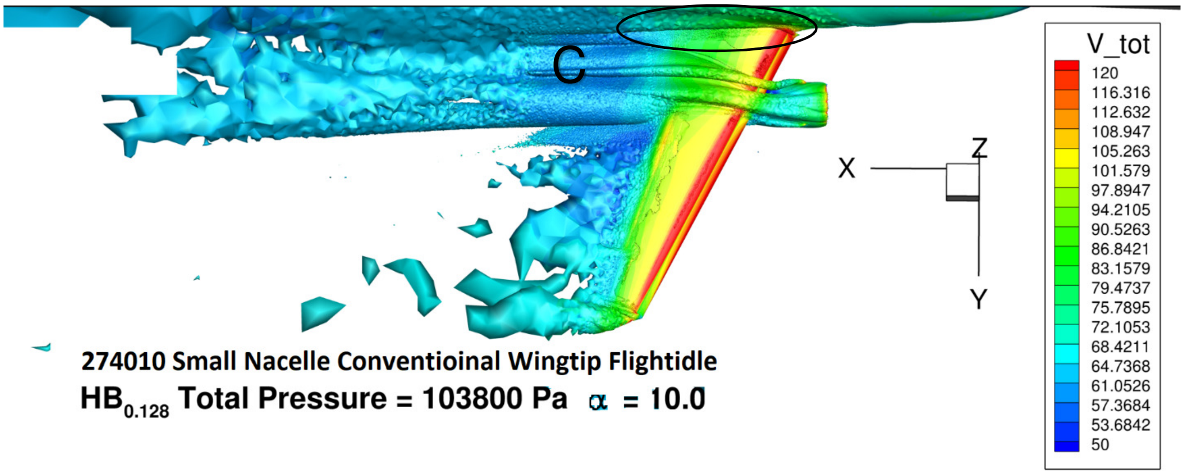

Figure 9.111– Iso Surface of total pressure $\alpha = 10.0° \, \frac{h}{b} = 0.128$

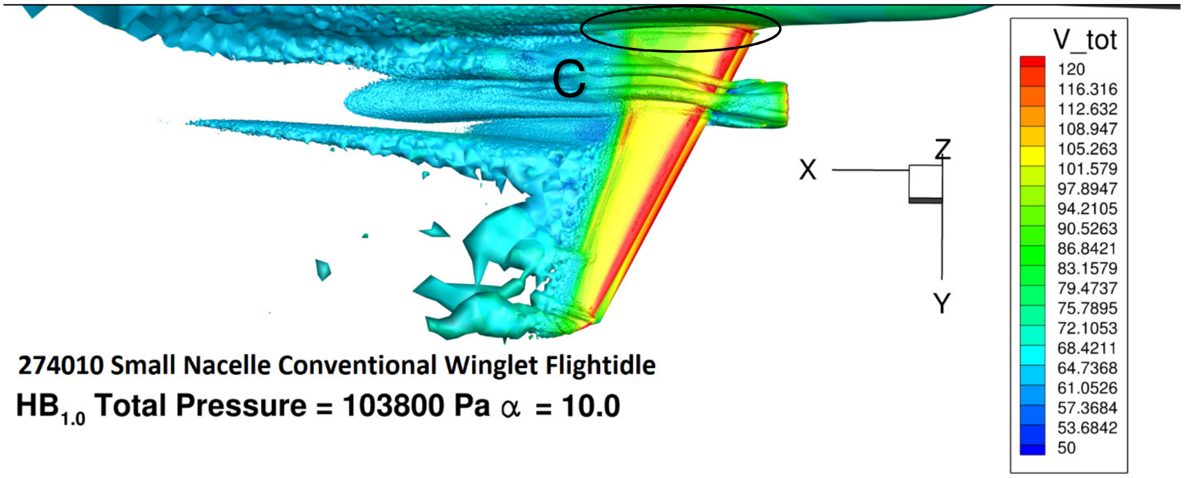

Figure 9.112 – Iso Surface of total pressure $\alpha = 10.0° \, \frac{h}{b} = 1.0$

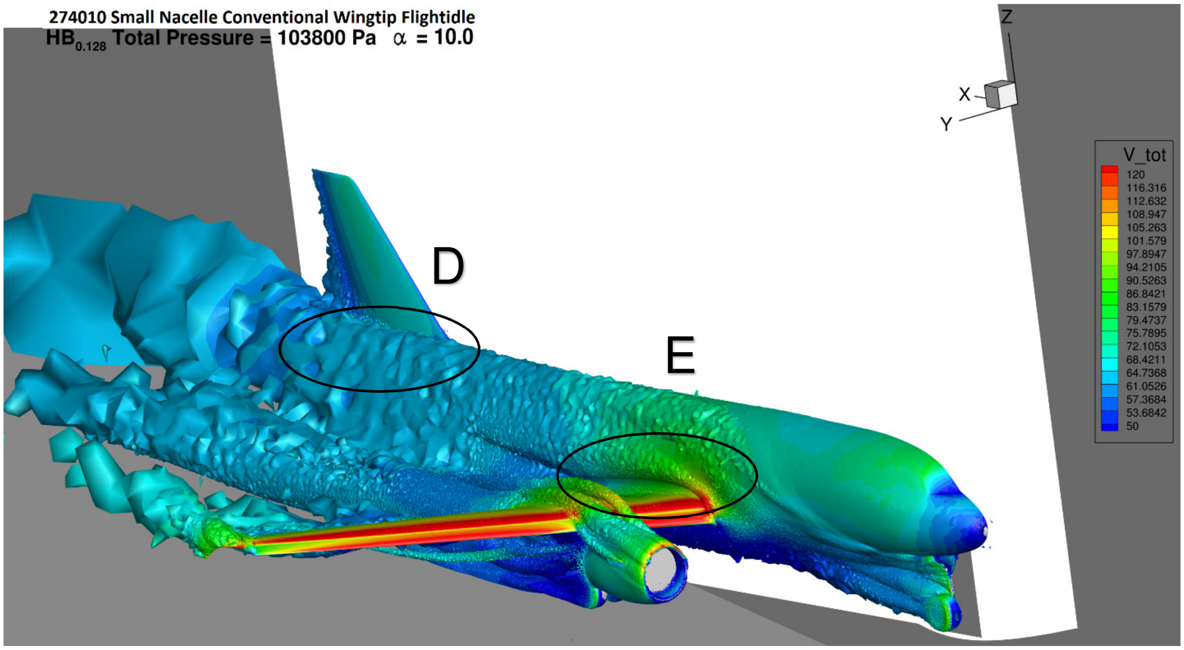

Figure 9.113– Iso Surface of total pressure $\alpha = 10.0° \frac{h}{b} = 0.128$

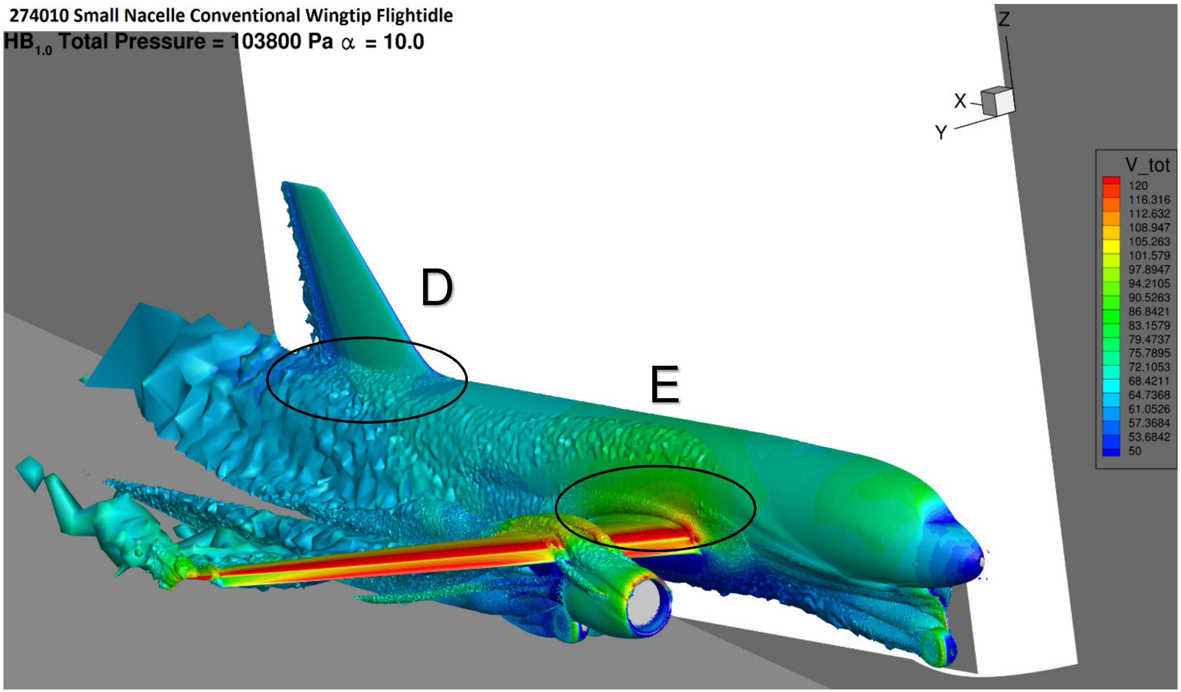

Figure 9.114 – Iso Surface of total pressure $\alpha = 10.0° \frac{h}{b} = 1.0$

9.14 Appendix N – Windtunnel and CFD Ground Effect Lift Increment Comparison for a Different Commercial Jet Aircraft

This data was obtained by the author during the internship at the same aerospace company.

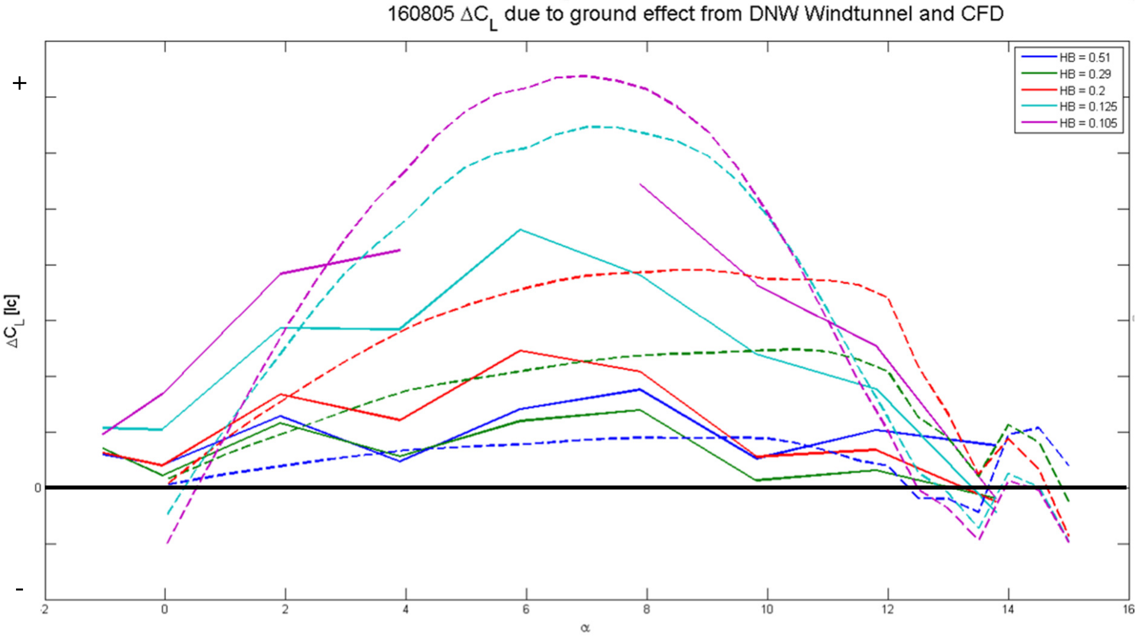

Figure 9.115 –Lift increment comparison between windtunnel (solid) and CFD (dashed) Conf 16/08/05 $(\delta_{slat}\ /\delta_{flap}/\delta_{ail})$

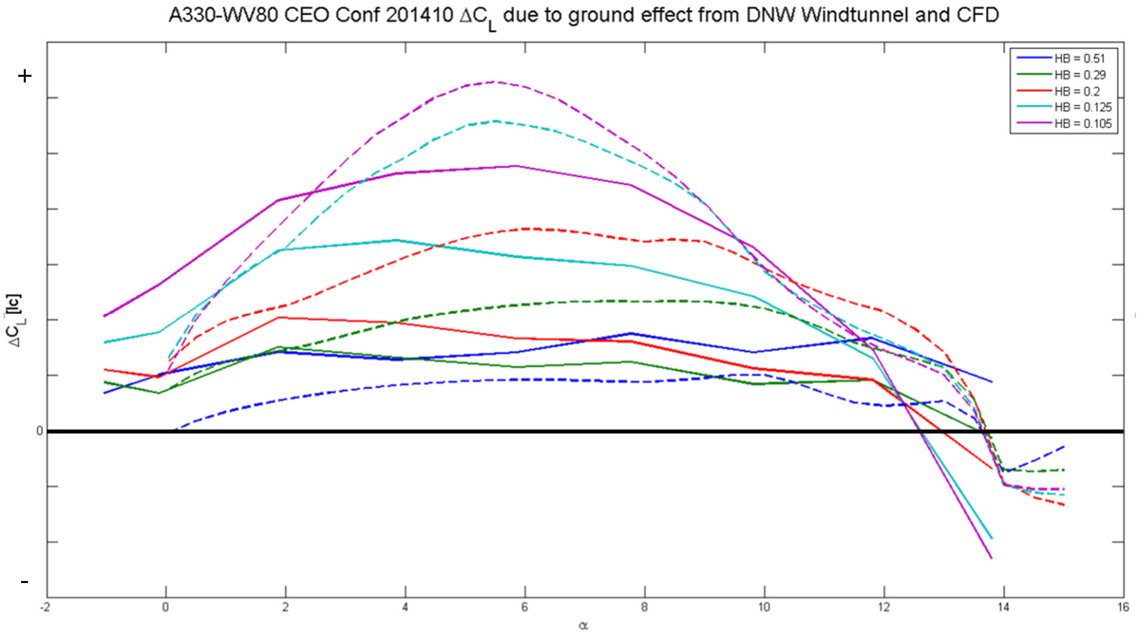

Figure 9.116 - Lift increment comparison between windtunnel (solid) and CFD (dashed) Conf 20/14/10 $(\delta_{slat}\ /\delta_{flap}/\delta_{ail})$

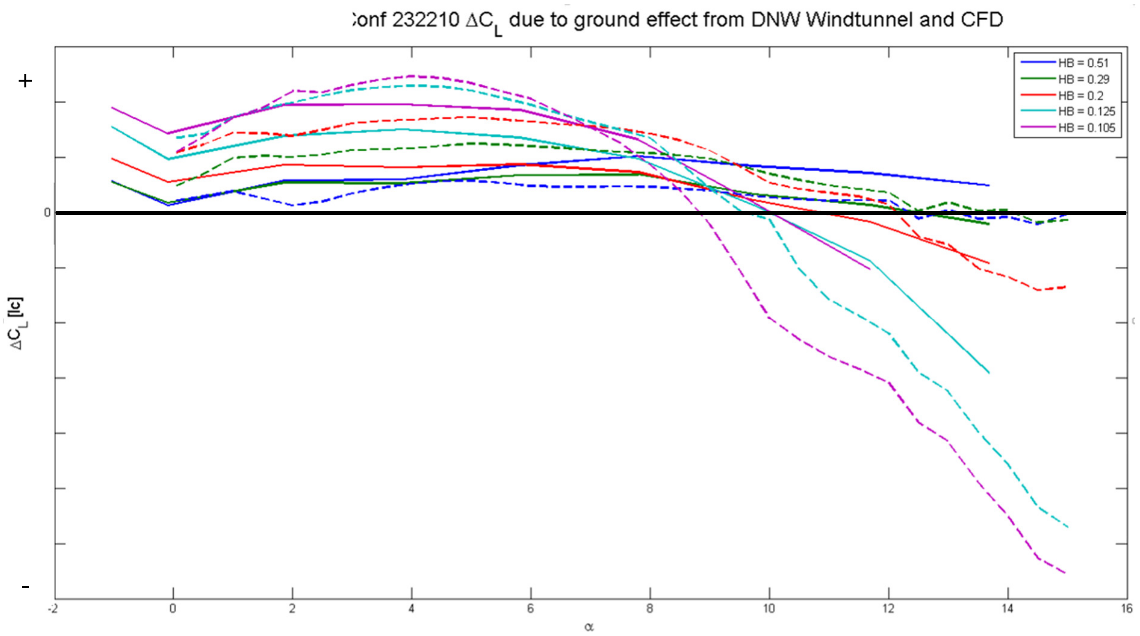

Figure 9.117 - Lift increment comparison between windtunnel (solid) and CFD (dashed) Conf 23/22/10 (δ_{slat} /δ_{flap}/δ_{ail})